

Search for heavy resonances decaying into the fully hadronic di-tau final state with the ATLAS detector

Dissertation

zur Erlangung des akademischen Grades

Doctor rerum naturalium

(Dr. rer. nat.)

vorgelegt der

**Fakultät Mathematik und Naturwissenschaften der
Technischen Universität Dresden**

von

Dipl.-Phys. Marcus Matthias Morgenstern

geboren am 21.04.1986 in Karl-Marx-Stadt (jetzt Chemnitz)

eingereicht am 23.01.2014



1. Gutachter: Jun.-Prof. Dr. Arno Straessner
2. Gutachter: Prof. Dr. Michael Kobel

Tag der Verteidigung: 21. März 2014

Kurzfassung

Die Entdeckung eines schweren neutralen Teilchens wäre ein direkter Hinweis auf neue Physik jenseits des Standardmodells der Teilchenphysik. In dieser Arbeit werden Suchen nach vorhergesagten neuen schweren neutralen Resonanzen, welche in zwei Tau-Leptonen zerfallen, vorgestellt. Die in der Analyse verwendeten Tau-Leptonen zerfallen dabei selbst in Hadronen, z.B. Pionen, und Neutrinos. Dabei werden sowohl neutrale Higgs-Bosonen im Rahmen des Minimalen Supersymmetrischen Standardmodells (MSSM), als auch Z' -Bosonen, welche von verschiedenen phänomenologischen Modellen mit erweiterten Eichgruppen vorhergesagt werden, betrachtet. Beide Analysen basieren auf dem vollständigen Datensatz von Proton-Proton-Kollisionen, aufgenommen vom ATLAS Detektor am "Large Hadron Collider" (LHC) im Jahr 2012. Der erweiterte Higgs-Sektor im MSSM weist auf zusätzliche schwere neutrale Higgs-Bosonen hin, welche in ungefähr 10% der Fälle in zwei Tau-Leptonen zerfallen. Da der dominierende Zerfall in zwei b -Quarks, $\phi \rightarrow b\bar{b}$, durch QCD-Multijet-Ereignisse überlagert wird, ist der Endzustand mit zwei Tau-Leptonen der sensitivste und damit der bevorzugte Kanal, um ein hypothetisches Signal zu entdecken. Der voll-hadronische Endzustand trägt mit 42% zu allen Zwei-Tau-Endzuständen bei und dominiert somit diesen Kanal. Insbesondere bei hohen transversalen Impulsen, bei denen der Hauptuntergrund durch QCD-Prozesse gering wird, ist die Sensitivität des voll-hadronischen Endzustandes vergleichbar mit, bzw. höher als in leptonischen Endzuständen.

Andere theoretische Erweiterungen des Standardmodells, welche hauptsächlich auf dem Konzept der "Großen Vereinheitlichung" (Grand Unified Theories - GUT) basieren, sagen ebenfalls neue schwere neutrale Teilchen voraus, welche an der TeV-Skala entdeckt werden können. Diese Resonanzen entspringen der erweiterten zugrundeliegenden Eichgruppe, wobei abhängig von der jeweiligen Struktur die Kopplung an Fermionen der dritten Generation bevorzugt ist. Dies motiviert die Suche nach Z' -Bosonen im voll-hadronischen Zwei-Tau-Endzustand, welche präsentiert wird.

Analysen, welche hadronisch zerfallende Tau-Leptonen involvieren, benötigen überdurchschnittlich performante Trigger- und Identifikationsalgorithmen, welche echte Tau-Leptonen mit einer hohen Akzeptanz selektieren und fehlrekonstruierte Tau-Kandidaten, welche durch Quark- oder Gluon-Jets initiiert werden, verwerfen. Im Rahmen dieser Arbeit wurde dazu ein neuer Algorithmus für den Tau-Trigger basierend auf multivariaten Klassifikatoren entwickelt, welcher als Standardalgorithmus im Trigger-Menü für die Datennahme im Jahr 2012 etabliert wurde. Weiterhin wurde der Identifikationsalgorithmus für die Tau-Identifikation basierend auf der log-likelihood-Methode für die Datennahme im Jahr 2011 optimiert, sowie das entsprechende Software-Framework für zukünftige Erweiterungen entwickelt.

Die Suche nach zusätzlichen neutralen Higgs-Bosonen im Rahmen des MSSM basiert auf den bei einer Schwerpunktsenergie von $\sqrt{s} = 8$ TeV aufgenommenen Proton-Proton-Kollisionsdaten des ATLAS-Detektors im Jahr 2012, welche einer integrierten Luminosität von 19.5 fb^{-1} entsprechen. Aktualisierte Selektionsschritte sowie neue Untergrundabschätzungsmethoden wurden im Rahmen dieser Arbeit entwickelt und führen zu signifikanten Verbesserungen der Sensitivität der Suchen. Keine Abweichungen von der Vorhersage des Standardmodells wurden beobachtet. Daher wurden Ausschlussgrenzen auf $\sigma(pp \rightarrow \phi) \times \text{BR}(\phi \rightarrow \tau\tau)$ bestimmt. Diese reichen von 13.0 pb bei 150 GeV zu 7.0 fb bei 1 TeV für Higgs-Bosonen welche in Assoziation mit b -Quarks produziert würden und von 23.6 pb bei 150 GeV bis zu 7.5 fb bei 1 TeV für den Produktionsmechanismus durch Gluon-Gluon-Fusion. Diese Ausschlussgrenzen können im Rahmen von verschiedenen Benchmark-Szenarien interpretiert werden. Dabei stellt das sogenannte m_h^{max} Szenario die "Standardkerze" dar und erlaubt den direkten Vergleich der erzielten Resultate zu früheren Analysen. Unter der Annahme dieses Benchmark-Szenarios können $\tan\beta$ -Werte zwischen 13.3 und 55 mit 95% Vertrauensniveau im betrachteten Massenbereich ausgeschlossen werden. Nach der Entdeckung eines SM-ähnlichen Higgs-Bosons durch die ATLAS und CMS Kollaborationen wurden neue Benchmark-Szenarien vorgeschlagen, welche die Eigenschaften des neu entdeckten Teilchens berücksichtigen. In dieser Arbeit wurden dazu die erzielten Resultate im Rahmen des $m_h^{\text{mod+}}$ ($m_h^{\text{mod-}}$) Szenarios interpretiert. Die erzielten Ausschlussgrenzen auf $\tan\beta$ reichen von 13.5 (13.3) bis 55 (52).

Abschließend wurde eine Suche nach schweren neutralen Resonanzen im Kontext von Z' -Bosonen durchgeführt. Da die zugrunde liegenden Selektionsschritte der Suche nach Higgs-Bosonen entsprechen,

wurde auch in dieser Analyse keine Abweichung von der Standardmodellvorhersage beobachtet. Entsprechend wurden Ausschlusslimits auf $\sigma(pp \rightarrow Z') \times \text{BR}(Z' \rightarrow \tau\tau)$ bestimmt. Dabei wurde der bayesianische Ansatz verfolgt. Aus den berechneten Ausschlussgrenzen auf $\sigma(pp \rightarrow Z') \times \text{BR}(Z' \rightarrow \tau\tau)$ lassen sich untere Grenzen auf die Masse des Z' -Bosons bestimmen. Im Rahmen des “Sequential Standard Model” konnten Z' -Bosonen mit $M_{Z'} < 1.9 \text{ TeV}$ mit 95% Glaubwürdigkeit ausgeschlossen werden. Dies stellt derzeit die weltbeste Ausschlussgrenze auf die Masse von Z' -Bosonen im Zwei-Tau-Endzustand durch ein Beschleunigerexperiment dar.

Abstract

The discovery of a heavy neutral particle would be a direct hint for new physics beyond the Standard Model. In this thesis searches for new heavy neutral particles decaying into two tau leptons, which further decay into hadrons, are presented. They cover neutral Higgs bosons in the context of the minimal supersymmetric extension of the Standard Model (MSSM) as well as Z' bosons, predicted by various theories with an extended gauge sector. Both analyses are based on the full 2012 proton-proton collision dataset taken by the ATLAS experiment at the Large Hadron Collider (LHC). The extended Higgs sector in the MSSM suggests additional heavy neutral Higgs bosons which decay into tau leptons in about 10% of the time. Given that the dominant final state, $\phi \rightarrow b\bar{b}$, suffers from tremendous QCD initiated backgrounds, the decay into two tau leptons is the most promising final state to discover such new resonances. The fully hadronic final state is the dominant one with a branching fraction of about 42%. It governs the sensitivity, in particular at high transverse momentum when the QCD multijet background becomes small.

Other theoretical extensions of the Standard Model, which are mainly driven by the concept of gauge unification, predict additional heavy particles arising from an extended underlying gauge group. Some of them further predict an enhanced coupling to fermions of the third generation. This motivates the search for Z' bosons in the fully hadronic di-tau final state.

One major challenge in physics analyses involving tau leptons is to have an outstanding performance of trigger and identification algorithms suitable to select real tau leptons with high efficiency, while rejecting fake taus originating from quark or gluon initiated jets. In this work a new tau trigger concept based on multivariate classifiers has been developed and became the default tau trigger algorithm in 2012 data-taking. An updated tau identification technique based on the log-likelihood approach has been provided for 2011 data-taking. Furthermore, a new framework has been developed to perform the tuning of the tau identification algorithm and exploited for the optimisation for 2012 data-taking, accordingly.

The search for new heavy neutral Higgs bosons in the context of the MSSM has been performed exploiting the full 2012 dataset corresponding to an integrated luminosity of 19.5 fb^{-1} taken at a centre-of-mass energy of $\sqrt{s} = 8 \text{ TeV}$. Updated event selection criteria and novel data-driven background estimation techniques have been developed and are suitable to increase the sensitivity of the analysis significantly. No deviations from the Standard Model prediction are observed, and thus 95% C.L. exclusion limits on the production cross section times branching ratio, $\sigma(pp \rightarrow \phi) \times \text{BR}(\phi \rightarrow \tau\tau)$, are derived exploiting the CL_s method. The exclusion ranges from 13.0 pb at 150 GeV to 7.0 fb at 1 TeV for Higgs boson production in association with b-quarks and from 23.6 pb at 150 GeV to 7.5 fb at 1 TeV for Higgs bosons produced via gluon-gluon fusion. The obtained exclusion limit on $\sigma(pp \rightarrow \phi) \times \text{BR}(\phi \rightarrow \tau\tau)$ can be related to an exclusion of the MSSM parameter space in the M_A - $\tan\beta$ -plane. Various benchmark scenario are considered. The "standard candle" is the m_h^{max} scenario, for which $\tan\beta$ values between 13.3 and 55 can be excluded at 95% C.L. in the considered mass range. Updated benchmark scenarios designed to incorporate the recently discovered SM-like Higgs boson were suggested and analysed as well. In the $m_h^{\text{mod+}}$ ($m_h^{\text{mod-}}$) scenario $\tan\beta$ values between 13.5 (13.3) and 55 (52) can be excluded.

Finally, a search for heavy neutral resonances in the context of Z' bosons was performed. As in the search for new Higgs bosons, no deviation from the Standard Model prediction is observed, and hence exclusion limits on the production cross section times branching ratio, $\sigma(pp \rightarrow Z') \times \text{BR}(Z' \rightarrow \tau\tau)$, and on the Z' boson mass are derived exploiting the Bayesian approach. Z' bosons with $M_{Z'} < 1.9 \text{ TeV}$ can be excluded at 95% credibility, and thus mark the strongest exclusion limit obtained in the di-tau final state by any collider experiment so far.

Contents

Kurzfassung	III
Abstract	V
1 Introduction	1
2 Theoretical Framework	3
2.1 Standard Model of Particle Physics	3
2.2 Electroweak Physics	4
2.3 Higgs Mechanism	6
2.3.1 Discovery of a Higgs particle	8
2.4 Supersymmetry	9
2.4.1 Motivation for Supersymmetry	10
2.4.2 SUSY breaking	12
2.5 Minimal Supersymmetric Extension of the Standard Model	12
2.5.1 Higgs Mechanism in the Context of the MSSM	13
2.5.2 Benchmark Scenarios and Radiative Corrections	15
2.6 Phenomenology of Heavy Z' bosons	18
2.6.1 Z - Z' -Mixing	18
2.6.2 Sequential Standard Model	19
2.6.3 E_6 Models	19
2.6.4 Left Right Symmetric Models	20
2.6.5 Technicolour Models	20
2.6.6 Topcolour Assisted Technicolour Models	20
2.6.7 Little Higgs Models	21
3 Experimental Status of Searches for Heavy Neutral Resonances	23
3.1 Indirect Constraints on Neutral MSSM Higgs Bosons	23
3.2 Direct Searches for Neutral MSSM Higgs Bosons	24
3.3 Indirect Constraints on Z' Bosons	29
3.4 Direct Searches for Z' Bosons	31
4 The ATLAS Experiment	37
4.1 The Large Hadron Collider	37
4.2 The ATLAS Detector	39
4.2.1 Coordinate System	40
4.2.2 Tracking System	40
4.2.3 Calorimeter System	42
4.2.4 Muon Spectrometer	45
4.2.5 Forward Detectors	47
4.2.6 Trigger System and Data Acquisition	47
4.3 Data-Taking in 2012	48
5 Monte Carlo Simulation	51
5.1 Hadron Hadron Interactions	51
5.2 Hadronic Jets	52
5.3 Monte Carlo Generators	52
5.3.1 Matrix Elements	52
5.3.2 Parton Shower	53
5.3.3 Merging of Matrix Elements and Parton Showers	54
5.3.4 Multiple Parton Interactions and Pile-up	54

5.3.5	Simulation of Tau Decays and QED Radiative Corrections	55
5.4	Detector Simulation	55
5.4.1	Full Simulation	56
5.4.2	Fast Simulation	56
6	Reconstruction of Physics Objects	57
6.1	Underlying Detector Objects	57
6.2	High-level Physics Objects	58
7	Tau Reconstruction and Identification	61
7.1	Tau Lepton Reconstruction	62
7.1.1	Building Tau Candidates	62
7.1.2	Track Association	62
7.1.3	Vertex Assignment	62
7.1.4	Neutral Pion Finder	63
7.1.5	Tau Energy Calibration	64
7.2	Tau Lepton Identification	66
7.2.1	Tau Identification Variables	66
7.2.2	Log-Likelihood Based Tau Identification	71
7.2.3	Boosted Decision Tree Based Tau Identification	75
7.2.4	Comparison of BDT and LLH Based Tau Identification	78
7.2.5	Measurement of the Performance of Tau Identification Algorithms	80
7.2.6	Electron Veto	82
7.2.7	Muon Veto	83
7.3	Triggering on Tau Leptons	84
7.3.1	Tau Trigger Menu in 2012	84
7.3.2	Development of a Multivariate Tau Trigger Menu	86
7.3.3	Performance Evaluation	88
7.3.4	Efficiency Measurement	89
8	Background Processes	93
8.1	Irreducible Backgrounds	93
8.1.1	$Z/\gamma^*(\rightarrow \tau\tau)+\text{jets}$	93
8.2	Reducible Backgrounds	94
8.2.1	QCD multijets	94
8.2.2	$W(\rightarrow \tau\nu)+\text{jets}$	95
8.2.3	Top Quark Pair and Single-Top Production	96
8.2.4	Electroweak Di-boson Production	97
8.2.5	Other Electroweak Backgrounds	98
9	Event Pre-selection	99
9.1	Event Cleaning	99
9.2	Light Lepton Vetoes	100
9.3	Trigger Requirements	101
9.4	Back-to-back Requirement	102
9.5	Opposite Sign Requirement	102
10	Background Estimation	105
10.1	Multijet Estimation	105
10.1.1	Multijet Estimation in the Single-Tau Triggered Category	105
10.1.2	Validation of QCD Multijet Estimation Using Fake-Factors	111
10.1.3	Multijet Estimation in the Di-Tau Triggered Category	116

10.1.4	Validation of QCD Multijet Estimation Using an ABCD Method	119
10.2	Fake Tau Estimation from MC	124
10.3	$Z/\gamma^* \rightarrow \tau\tau$ Control Region	129
11	Systematic Uncertainties	135
11.1	Experimental Systematic Uncertainties	135
11.1.1	Hadronic Tau Identification Efficiency	135
11.1.2	High- p_T Track Reconstruction Efficiency	137
11.1.3	Hadronic Tau Trigger Efficiency	138
11.1.4	Hadronic Tau Energy Scale	139
11.1.5	Charge Mis-Identification	139
11.1.6	Jet-to-Tau Fake-Rate	139
11.1.7	Jet Energy Scale	140
11.1.8	Missing Transverse Momentum Corrections	140
11.1.9	Luminosity	140
11.1.10	Multijet Estimation Using Fake-Factors	141
11.1.11	Multijet Estimation Using an ABCD Method	141
11.2	Theoretical Systematic Uncertainties on Simulated Background Cross Sections	143
11.2.1	Drell-Yan cross sections	143
11.2.2	W +jets cross sections	143
11.2.3	$t\bar{t}$ cross sections	144
11.2.4	Single-top cross sections	144
11.2.5	Electroweak Di-boson cross sections	144
12	Search for Neutral MSSM Higgs Bosons	145
12.1	Signal Simulation	145
12.1.1	MSSM Neutral Higgs Production in Association with b-Quarks	145
12.1.2	MSSM Neutral Higgs Production via Gluon-Gluon Fusion	147
12.2	Event Selection	149
12.2.1	Single-Tau Triggered Category	150
12.2.2	Di-Tau Triggered Category	152
12.3	Systematic Uncertainties	153
12.4	Results of the Combined Background Model	156
12.4.1	Single-Tau Triggered Category	157
12.4.2	Di-Tau Triggered Category	157
12.5	Results	163
12.6	Statistical Analysis of the Results	163
12.6.1	Hypothesis Testing	163
12.6.2	The CL_s Method	165
12.6.3	Construction of the Likelihood Function	165
12.6.4	Treatment of Systematic Uncertainties	167
12.6.5	Treatment of Statistical Uncertainties	168
12.6.6	Setting Upper Exclusion Limits	170
12.6.7	Calculation of Local Discovery Significance	171
12.6.8	Validation of the Minimisation Procedure	172
12.6.9	Validation using Pseudo Data	172
12.6.10	Exclusion Limit on MSSM Parameter Space	174
12.6.11	Upper Exclusion Limit on Generic 2HDM Models	176
12.6.12	Discovery Significance of the MSSM	178
12.7	Summary and Conclusion	180

13 Search for Heavy Z' Bosons	183
13.1 Signal Simulation	183
13.2 Event Selection	185
13.3 Results	187
13.4 Systematic Uncertainties	187
13.5 Statistical Interpretation	189
13.5.1 Bayesian Approach	189
13.5.2 Likelihood Model	190
13.5.3 Exclusion Limits	190
13.6 Summary and Conclusion	190
14 Summary and Outlook	193
A Auxiliary Information for the Theoretical Framework	197
A.1 Gamma Matrices	197
A.2 Quantum Electrodynamics	197
B Auxiliary Information for the Tau Trigger Optimisation	199
C Auxiliary Information for the Monte Carlo Simulation Samples	201
C.1 BSM Higgs MC Samples	201
C.2 Background MC Samples	201
D Auxiliary Information for the Search for Heavy Neutral Higgs Bosons	207
D.1 Higgs Production Cross Section	207
D.2 Pull Distributions of Nuisance Parameters Obtained from Pseudo Data	218
D.3 Scans of Negative Log-Likelihood	220
E Auxiliary Information for the Search for Z' Bosons	223
E.1 Full Simulation Signal Monte Carlo Samples	223
E.2 Systematics	223
Bibliography	231
List of Figures	247
List of Tables	253

1 Introduction

The underlying concept of particle physics, i.e. describing nature by a few fundamental building blocks, reaches back to the ancient Greeks, who already introduced the *atom*. In the past decade particle physics has accomplished outstanding progress and has been tested to an incredible precision by dozens of experiments. The concept of fundamental particles building stable matter is as simple as successful. In the early decades of the 20th century it has been found that stable matter, i.e. the atom, consists of protons, neutrons and electrons. As time passed further insight in the structure of these particles has been achieved, resulting in fundamental particles, the *quarks* which are the constituents of the proton and neutron, and the *leptons* with its most famous representative, the electron. Amazingly, stable matter surrounding us can be build out of three particles only, the electron and the up- and down-quark. The concept of the fundamental particles and their interactions are formulated in the *Standard Model* (SM) [1, 2, 3] developed in the 1960's, which is one of the most successful theories ever developed. It is a *quantum field theory* (QFT) describing the matter content and all known interactions, but gravity. Even though it has been tested by dozens of experiments since then, one open question remained until just recently: *How do particles acquire mass?* Already in 1964 Robert Brout, Francois Englert and Peter Higgs proposed a mechanism suitable to answer this question, the Higgs mechanism [4, 5, 6, 7, 8]. It took almost five decades to prove this mechanism experimentally. For this purpose huge collider experiments were build. The most powerful machine is the *Large Hadron Collider* (LHC) [9], located at the Franco-Swiss border at CERN. It is a proton-proton collider which started operation in 2008. Unfortunately, a magnetic connection failure occurred shortly after commissioning, and thus the collider had to be shut down for more than one year. After its restart in 2009 the LHC provided high energy proton beams colliding at centre-of-mass energies up to 7 – 8 TeV, which is the highest centre-of-mass energy ever reached in a collider experiment so far. After data-taking in 2012 had finished, the collider has been shut down for maintenance and is expected to ramp up in early 2015. During its first data-taking period both the collider and the experiments installed at the LHC exhibited an extraordinary performance. One of the experiments installed at the LHC is the ATLAS (*A Toroidal LHC ApparatuS*) detector [10] whose collected data is analysed in this thesis. The most outstanding day in the young history of the LHC was July, 4th, 2012 when the ATLAS and CMS (*Compact Muon Solenoid*) [11] collaborations announced the discovery of a new particle [12, 13]. Its properties are consistent with the predicted Higgs boson, and thus reveal the last remaining ingredient of the SM. Even though the SM provides a consistent picture of nature and is well proven, it is clear that it is only an effective theory embedded in an extended superior theory. These models are able to address various shortcomings of the SM such as providing a *dark matter* [14, 15, 16] candidate or solving the *fine-tuning problem* [17]. They are expected to emerge at the TeV scale, and thus are assumed to be detectable at the LHC. The most favoured extension of the SM is *supersymmetry* (SUSY) [18, 19]. It introduces a new symmetry concept between fermions and bosons, which leads to a duplication of the particle content. Further, it necessitates an extended Higgs sector. In its minimal version, the *Minimal Supersymmetric Standard Model* (MSSM) [20, 21, 22, 23], this results in five physically observable Higgs bosons. Three of them have neutral electric charge, while the remaining two are charged. The decay of the heavy neutral Higgs bosons into two tau leptons, τ , is favoured in a wide phase space region in many benchmark scenarios. Heavy in this context refers to masses between roughly $M \simeq 200 \text{ GeV}$ and $M \simeq 2 \text{ TeV}$. Thus the di-tau final state is an important probe of the Higgs sector in the MSSM. A search for heavy neutral Higgs bosons decaying into two tau leptons is documented in this thesis. In this analysis the fully hadronic final state, in which the two taus decay into hadrons, is considered. With a branching ratio of 42% it is the dominant final state. Since no hints for SUSY have been observed so far, other models extending the SM have been developed in order to describe nature up to very high energy scales. The *Planck scale*, at which gravity is supposed to become strong, such that its strength is in the order of the forces considered in the context of particle physics plays an important role. A very successful concept in particle physics during the last century is the unification of forces, as impressively shown by the *electroweak* unification of the weak and electromagnetic interaction. Hence theoretical models based on *Grand Unification* (GUT) have been developed. In these theories all forces unify at very high energy scales. One ingredient which enters in these models is an ex-

tended underlying gauge group. Additional gauge groups introduced in these theories predict new heavy gauge bosons, such as e.g. a heavy partner of the Z boson, the Z' boson. Depending on the underlying structure, the coupling to third generation fermions might be enhanced, which favours the di-tau final state as an essential probe for such a group of theories. A search for new heavy neutral resonances in the fully hadronic final state will be presented as well. The thesis is organised as follows:

Chapter 2 outlines the theoretical framework of particle physics beginning with an introduction of the SM and the Higgs sector. Problems which can not be addressed by the SM are discussed and possible solutions are provided in the discussion of various extended theories ranging from SUSY to GUT concepts.

Chapter 3 summarises the current experimental status of searches for new heavy neutral resonances considering both BSM Higgs bosons and Z' bosons. Beside direct searches also indirect constraints will be discussed.

Chapter 4 gives a brief overview of the LHC and the ATLAS detector.

Chapter 5 explains the key concepts of *Monte Carlo* (MC) simulation of proton-proton collisions.

Chapter 6 elaborates on the various background topologies arising from SM processes which enter in the search for new heavy neutral particles decaying into two tau leptons.

Chapter 7 briefly outlines the basic concepts of particle reconstruction used in the presented analyses.

Chapter 8 discusses the tau reconstruction and identification algorithms featured by the ATLAS experiment. Furthermore, advanced algorithms for triggering on hadronic tau decays are introduced.

Chapter 9 provides the applied event pre-selection on top of which the final event selection is performed.

Chapter 10 focuses on the data-driven and MC based background estimation techniques. Several improvements of the methodology w.r.t. previous analyses were developed in the process of this work and are discussed in detail here.

Chapter 11 introduces the experimental and theoretical systematic uncertainties which are common in the search for MSSM Higgs and Z' bosons.

Chapter 12 presents a search for heavy neutral Higgs bosons in the context of supersymmetric extensions of the SM.

Chapter 13 summarises the search for heavy neutral Z' bosons in the fully hadronic di-tau final state.

Chapter 14 closes with a summary of the presented analyses and puts the derived results in context of the current knowledge of these topics.

2 Theoretical Framework

This chapter will introduce the theoretical framework of modern particle physics. Sections 2.1 and 2.2 introduce the fundamental concepts of the *Standard Model* (SM), which provides a widely accepted and tested description of the nature of elementary particles and their interactions. Section 2.3 will introduce the Higgs mechanism followed by Sections 2.4 and 2.5 which cover extended theories approaching physics *beyond the Standard Model* (BSM). The focus is set to the Higgs sector in *supersymmetric* (SUSY) extensions of the SM, which builds the underlying theoretical framework for the presented search for new heavy neutral Higgs bosons. The chapter ends with a brief summary on various theoretical models predicting new heavy neutral gauge bosons. In the context of this thesis only a brief introduction on each topic can be given. The discussion is based on many excellent books and review articles [24, 25, 26, 17, 27, 28, 29], which the interested reader is referred to for further details.

2.1 Standard Model of Particle Physics

The Standard Model of particle physics is a relativistic *quantum field theory* (QFT) which describes the current knowledge of elementary particles and their interactions. It is based on a $SU(3)_C \times SU(2)_L \times U(1)_Y$ gauge group. The strong interaction is described by the $SU(3)_C$ part and the $SU(2)_L \times U(1)_Y$ group accounts for electroweak interactions, which are outlined in detail in Section 2.2. A central role in the formulation of field theories plays Noether's theorem [30, 31]. It states that a symmetry, i.e. an invariance of an action under a given symmetry transformation, leads to a conservation law. Gauge invariance of the Lagrangian together with the field strength tensor further implies dynamics. Thus, given the invariance of the Lagrangian under a local gauge transformation, the interactions between particles can be described, as impressively shown in the case of *Quantum Electrodynamics* (QED), which has been tested by dozens of experiments. The construction of a field theory based on the gauge principle is outlined in Appendix A.2 using the example of QED. Each gauge group is associated with a charge, which is the *colour charge*, C , in case of strong interactions, the *weak isospin*, \vec{I} , for weak interactions and the *electric charge*, Q , for QED. Particles carrying these charges can take part in the corresponding interaction. Elementary particles can be classified depending on their spin as matter particles and gauge bosons. The matter particles are fermions, i.e. they are spin- $\frac{1}{2}$ particles and are organised in three generations. They can be further categorised into quarks and leptons. The matter particle content of the SM and its associated charges are summarised in Table 2.1.

Interactions are mediated by gauge bosons, which are spin-1 particles. Electromagnetic interaction is transmitted by the photon, γ , which is massless and has no electric charge. Hence, it cannot interact with itself. The weak interaction, which describes e.g. the radioactive decay of nuclei, is mediated by the electrically charged W^\pm and the electrically neutral Z^0 bosons. They are both heavy compared to most of the particles described within the SM, with masses of $m_W = (80.385 \pm 0.015) \text{ GeV}$ and $m_Z = (91.1876 \pm 0.0021) \text{ GeV}$ [16], respectively. Given the Heisenberg uncertainty principle [32], which relates the uncertainty in simultaneous position and momentum measurements in quantum mechanics,

$$\Delta x \cdot \Delta p \geq \frac{\hbar}{2}, \quad (2.1)$$

or the energy-time relation:

$$\Delta E \cdot \Delta t \geq \frac{\hbar}{2}, \quad (2.2)$$

one can estimate the effective range, R_i^{eff} , of an interaction assuming the Yukawa hypothesis [33] by $R_i^{\text{eff}} = c \cdot \Delta t$. Hence, the effective range of the weak interaction is limited to distances of the order of 10^{-18} m . The charged W^\pm bosons have a weak isospin of $I_3 = \pm 1$, and hence can interact with each other, as well as with the Z boson. The strong interaction which describes e.g. the interactions within the proton, is mediated by gluons, which itself carry colour charge, and thus interact with each other. Even though the gluon is massless, the range of the interaction is restricted by the so-called *confinement*. Confinement states that quarks can not be observed as free particles, but occur only in colour neutral object, i.e.

Generation		Particle	Electric Charge, Q [e]	Weak Isospin, I_3	Mass, m [GeV]
I	e	electron	-1	$-\frac{1}{2}$	0.000511
	ν_e	electron neutrino	0	$+\frac{1}{2}$	—
	u	up quark	$+\frac{2}{3}$	$+\frac{1}{2}$	0.0023
	d	down quark	$-\frac{1}{3}$	$-\frac{1}{2}$	0.0048
II	μ	muon	-1	$-\frac{1}{2}$	0.105
	ν_μ	muon neutrino	0	$+\frac{1}{2}$	—
	c	charm quark	$+\frac{2}{3}$	$+\frac{1}{2}$	1.275
	s	strange quark	$-\frac{1}{3}$	$-\frac{1}{2}$	0.095
III	τ	tau lepton	-1	$-\frac{1}{2}$	1.777
	ν_τ	tau neutrino	0	$+\frac{1}{2}$	—
	t	top quark	$+\frac{2}{3}$	$+\frac{1}{2}$	173.5
	b	bottom quark	$-\frac{1}{3}$	$-\frac{1}{2}$	4.18

Table 2.1: Matter particle content of the Standard Model [16].

as hadrons. However, another feature of QCD is the so-called *asymptotic freedom*. This phenomenon describes the quarks and gluons as free particles at high energies, or equivalent at small distances, e.g. in high energy proton collisions. This is always a valid approach to consider for calculation in the high energy regime. Chapter 5 will elaborate in more detail how the two regimes enter in the phenomenology of hadron-hadron collisions. Table 2.2 provides a summary of interactions described by the SM and their associated gauge bosons.

Interaction	Gauge Boson	Mass [GeV]	Effective Range m
Electromagnetic	Photon (γ)	$< 1 \cdot 10^{-27}$	∞
Weak	W-boson (W^\pm)	80.385	$\sim 10^{-18}$
	Z-boson (Z^0)	91.188	
Strong	Gluon (g)	0	$< 10^{-15}$

Table 2.2: Fundamental interactions described by the Standard Model and mediating gauge bosons [16].

2.2 Electroweak Physics

Based on the gauge principle Glashow, Salam and Weinberg [1, 2, 3] developed a theoretical description of electroweak physics, which is known as the GSW model or Standard Model of electroweak physics. Low energy experiments implicate that the underlying theory has to be a chiral gauge theory. The chiral states of the fermion fields, ψ , are given as the left-handed, ψ_L , and right-handed, ψ_R , states by:

$$\psi_L = \frac{1}{2}(1 - \gamma_5)\psi \quad \psi_R = \frac{1}{2}(1 + \gamma_5)\psi, \quad (2.3)$$

in which $\gamma_5 = i\gamma_0\gamma_1\gamma_2\gamma_3$ is defined by the gamma matrices, γ_i (definition given in Appendix A.1). The Wu-experiment [34] has shown that parity conservation is violated in β -decays. It was observed that only

left-handed fermions take part in weak interactions. Furthermore, neutrinos are only observed in left-handed states while anti-neutrinos are only observed in right-handed states. This needs to be reflected by the underlying gauge group. The lowest group which leads to three gauge bosons is SU(2). To describe the unified electroweak interaction the direct product, $SU(2)_L \times U(1)_Y$, is chosen, with associated gauge fields, \vec{W}^μ , and B^μ , respectively. Thus the gauge part of the Lagrangian, \mathcal{L}_g , is given by¹:

$$\mathcal{L}_g = -\frac{1}{4}F_i^{\mu\nu}F_{\mu\nu}^i - \frac{1}{4}B^{\mu\nu}B_{\mu\nu}, \quad (2.4)$$

in which the field strengths for $SU(2)_L$, $F_i^{\mu\nu}$, are given by:

$$F_i^{\mu\nu} = \partial^\mu W_i^\nu - \partial^\nu W_i^\mu - g\epsilon^{ijk}W_j^\mu W_k^\nu, \quad (2.5)$$

and for $U(1)_Y$, $B^{\mu\nu}$,

$$B^{\mu\nu} = \partial^\mu B^\nu - \partial^\nu B^\mu, \quad (2.6)$$

respectively. The non-abelian structure due to SU(2) implies that the gauge fields do not evolve independently, but are coupled. The charge corresponding to $SU(2)_L$ is the weak isospin, T , while the hypercharge, Y , corresponds to $U(1)_Y$. They are related to the electric charge by the Gell-Mann-Nishijima relation [35, 36]:

$$Q = T_3 + Y. \quad (2.7)$$

Experimental observations demonstrate that left-handed fermions are arranged in a SU(2) doublet, while right-handed leptons are represented by a singlet. For down-type quarks the flavour eigenstates, (d', s', b') , are not equal to the mass eigenstates, (d, s, b) , but are related by the CKM² mixing matrix, V^{CKM} , [37, 16] according to $q'_i = \sum_j V_{ij}^{CKM} q_j$. The same holds for the neutrinos, for which the mass and flavour eigenstates are related by the PMNS³ matrix, $U_{\alpha,i}^{PMNS}$, [38] also called *neutrino mixing matrix*. The flavour eigenstates, $(\nu_e, \nu_\mu, \nu_\tau)$, are given by $\nu_f = \sum_i U_{\alpha,i}^{PMNS} \nu_i$. Interaction terms of fermions can be written in a convenient way by the covariant derivative, D^μ :

$$D^\mu = \partial^\mu + igT_a W^{a\mu} + ig'YB^\mu. \quad (2.8)$$

Thus the electroweak part of the Lagrangian of the Standard Model⁴ can be written as:

$$\mathcal{L} = \underbrace{-\frac{1}{4}F_i^{\mu\nu}F_{\mu\nu}^i - \frac{1}{4}B_{\mu\nu}B^{\mu\nu}}_{\text{kinetic energies and self-interactions of gauge bosons}} + \underbrace{\sum_f i\bar{\psi}_f D_\mu \gamma^\mu \psi_f}_{\text{kinetic energies and electroweak interactions of fermions}}. \quad (2.9)$$

The gauge fields in Eq. 2.9 are not the ones observed in nature, but they mix. The charged gauge bosons, W^\pm , observed in nature, are a mixture of the SU(2) states:

$$W_\mu^\pm = \frac{W_\mu^1 \mp iW_\mu^2}{\sqrt{2}}. \quad (2.10)$$

The neutral and electromagnetic currents are described by the W_μ^3 and B_μ fields. The photon cannot be assigned to the B_μ field, since this would imply a coupling of the photon to neutrinos. Hence, the physically observed gauge boson fields, Z_μ and A_μ , are given by the following mixture:

¹Here, the Einstein summation convention is used

²Cabibbo-Kobayashi-Maskawa

³Pontecorvo-Maki-Nakagawa-Sakata

⁴Note: in here no mass terms are considered, but can be introduced by the Higgs mechanism as discussed in Section 2.3.

$$\begin{pmatrix} Z_\mu \\ A_\mu \end{pmatrix} = \begin{pmatrix} \cos \theta_w & -\sin \theta_w \\ \sin \theta_w & \cos \theta_w \end{pmatrix} \begin{pmatrix} W_\mu^3 \\ B_\mu \end{pmatrix}, \quad (2.11)$$

in which θ_w denotes the Weinberg mixing angle. The latter can be related to the coupling constants by:

$$\tan \theta_w = \frac{g'}{g}. \quad (2.12)$$

So far the gauge bosons stay massless, which is in contrast to experimental data which has shown that only the photon is massless, while the W^\pm and Z^0 bosons are heavy. Explicit mass terms, however, would violate gauge invariance. Hence, a dedicated mechanism has to be introduced to yield mass terms for the gauge bosons. One possible way is given by the Higgs mechanism, which will be described in detail in the next section.

2.3 Higgs Mechanism

The Higgs (or Englert-Brout-Higgs) mechanism was introduced in the field of particle physics, by Peter Higgs et al in 1964 [4, 5, 6, 7, 8]. A new scalar field, the *Higgs field*, ϕ , is introduced to generate gauge invariant mass terms via *spontaneous symmetry breaking* (SSB). SSB means that the Lagrangian is invariant under a given symmetry, while the state with lowest energy (ground or vacuum state) is not. To share interaction with the gauge bosons the scalar field has to have non-vanishing weak isospin and hypercharge quantum numbers. Its simplest representation in the SM is given by a complex isospin doublet with hypercharge, $Y = \frac{1}{2}$:

$$\phi = \begin{pmatrix} \phi^+ \\ \phi^0 \end{pmatrix} = \begin{pmatrix} \phi_3 + i\phi_4 \\ \phi_1 + i\phi_2 \end{pmatrix}. \quad (2.13)$$

The four real scalar fields, ϕ_i , correspond to four *degrees of freedom* (d.o.f.). The Lagrangian of the Higgs mechanism consists of a dynamic term, \mathcal{L}^{kin} , the Higgs potential, $V(\phi)$, and a term generating masses of fermions, \mathcal{L}_{Yuk} :

$$\mathcal{L} = \underbrace{D_\mu \phi D^\mu \phi}_{\mathcal{L}^{kin}} - V(\phi) + \underbrace{\sum_f c_f (\bar{\psi}_f^L \phi^\dagger \psi_f^R + \bar{\psi}_f^R \phi \psi_f^L)}_{\mathcal{L}_{Yuk}}. \quad (2.14)$$

The most general, gauge invariant and renormalisable Higgs potential is given as:

$$V(\phi) = \mu^2 \phi^\dagger \phi + \lambda (\phi^\dagger \phi)^2, \quad (2.15)$$

with two free parameters, μ and λ . The parameter λ has to be positive, as otherwise the potential is unbounded from below. For $\mu^2 > 0$ only the trivial minimum, $\phi_i = 0$, exists. Thus μ^2 has to be negative to enable SSB. Figure 2.1 shows the Higgs potential for this configuration in the $\phi_1 - \phi_2$ -plane.

Calculating the minimum of the potential leads to the *vacuum expectation value* (vev), v :

$$v = \sqrt{\frac{-\mu^2}{\lambda}}. \quad (2.16)$$

There exists an infinite number of solutions for the minimum $\sum_i \phi_i^2 = v^2$. It can be shown that three degrees of freedom correspond to three massless bosons (see e.g. [39]), the *Goldstone bosons*, which are non-physical states. They can be absorbed by the gauge bosons using gauge transformation which leads to longitudinal polarisation components for the heavy gauge bosons, and thus mass terms. Using the *unitary gauge* it can be assumed without loss of generality that $\phi_1 = v^2$ and $\phi_i = 0$ ($i = 2, 3, 4$).

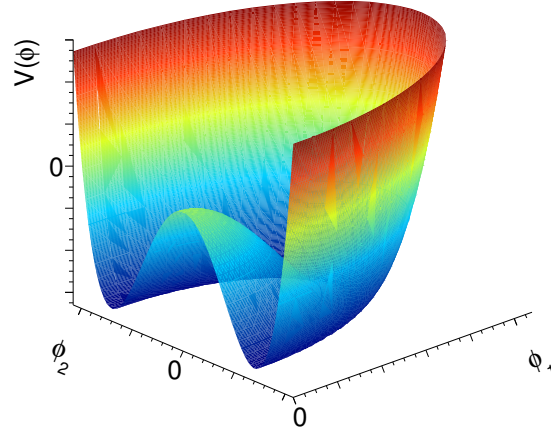


Figure 2.1: Higgs potential, $V(\phi)$, projected to $\phi_1 - \phi_2$ plane for negative μ^2 .

Excitations along the remaining d.o.f. around the vacuum state are considered as massive particles, i.e. the Higgs boson. Hence, the Higgs field can be written as:

$$\phi = \frac{1}{\sqrt{2}} \begin{pmatrix} 0 \\ v + H \end{pmatrix}, \quad (2.17)$$

with a scalar field H . The ground state is still invariant under $U(1)_{em}$, i.e. electric charge conservation is guaranteed, but not under $SU(2)_L \times U(1)_Y$, i.e.:

$$SU(2)_L \times U(1)_Y \rightarrow U(1)_{em}. \quad (2.18)$$

Taking the covariant derivative given in Eq. 2.8, the kinematic term yields (considering only terms proportional to v^2):

$$\mathcal{L}^{kin} = |D_\mu \phi|^2 = \left(\frac{gv}{2}\right)^2 W_\mu^+ W^{-\mu} + \frac{v^2}{8} \begin{pmatrix} W_\mu^3 & B_\mu \end{pmatrix} \begin{pmatrix} g^2 & -gg' \\ -gg' & g'^2 \end{pmatrix} \begin{pmatrix} W^{3,\mu} \\ B^\mu \end{pmatrix} + v^2 \lambda H^2 + O(H, H^2). \quad (2.19)$$

Using the mixing of W_μ^3 and B_μ defined in Eq. 2.11 the following mass terms for the gauge bosons, i.e. terms proportional to $V^\mu V_\mu$, arise:

$$\begin{aligned} M_Z &= \frac{v}{2} \sqrt{g^2 + g'^2}, \\ M_W &= \frac{gv}{2}, \\ M_\gamma &= 0. \end{aligned} \quad (2.20)$$

The mass term for the Higgs boson arises from the Higgs potential given in Eq. 2.15:

$$V(\phi) = \frac{\mu^2}{2} \begin{pmatrix} 0 & v + H \end{pmatrix} \begin{pmatrix} 0 \\ v + H \end{pmatrix} + \frac{\lambda}{4} \left| \begin{pmatrix} 0 & v + H \end{pmatrix} \begin{pmatrix} 0 \\ v + H \end{pmatrix} \right|^2 = \lambda v^2 H^2 + \dots, \quad (2.21)$$

which yields $m_H = \sqrt{2\lambda}v$. The masses of the fermions are generated by the Yukawa couplings, c_f , introduced "by hand". The Higgs mass formally depends on two parameters, λ and v , but the vev can be related to the Fermi constant, G_F :

$$v = \frac{1}{\sqrt{\sqrt{2}G_F}} \sim 246 \text{ GeV}. \quad (2.22)$$

Hence, the Higgs sector in the SM has only one free parameter chosen to be either λ or m_H . It cannot be constrained by theory, but has to be measured experimentally. The Higgs couplings to fermions and gauge bosons can be calculated in the same way as the mass terms, but considering only terms proportional to $\bar{\psi}_f \psi_f H$ and $V^\mu V_\mu H$, with V_μ being either Z_μ or W_μ^\pm . This leads to:

$$g_{Hff} = i \frac{m_f}{v} \quad g_{HVV} = -2i \frac{M_V^2}{v} \quad g_{HHVV} = -2i \frac{M_V^2}{v^2}. \quad (2.23)$$

Higgs self-couplings arise in the same way from terms proportional to H^3 (tri-linear coupling) and H^4 (quartic coupling):

$$g_{HHH} = -i \frac{M_H^2}{2v} \quad g_{HHHH} = -i \frac{M_H^2}{8v^2}. \quad (2.24)$$

2.3.1 Discovery of a Higgs particle

On July 4th, 2012 the ATLAS and CMS collaborations announced the discovery of a new boson [12, 13]. The observation of the ATLAS experiment was based on $4.6 - 4.8 \text{ fb}^{-1}$ of 2011 data taken at a centre-of-mass energy of $\sqrt{s} = 7 \text{ TeV}$ and $5.8 - 5.9 \text{ fb}^{-1}$ of 2012 data at $\sqrt{s} = 8 \text{ TeV}$. Since then the result has been updated to the full run-I dataset exploiting 20.7 fb^{-1} of 8 TeV data [40]. Searches for $H \rightarrow \gamma\gamma$, $H \rightarrow ZZ^{(*)} \rightarrow 4l$ and $H \rightarrow WW^{(*)} \rightarrow l\nu l\nu$ at $\sqrt{s} = 8 \text{ TeV}$ using the full dataset are combined with analyses of 2011 data of $H \rightarrow \gamma\gamma$, $H \rightarrow ZZ^{(*)}$, $H \rightarrow WW^{(*)}$, $H \rightarrow b\bar{b}$ and $H \rightarrow \tau\tau$. For the latter two an analysis of a subset of the full 8 TeV data corresponding to 13 fb^{-1} has been considered for the combination as well. The combination is performed using the CL_s approach using the *profile likelihood method* as test statistic (for details c.f. Section 12.6 or [41]). In the original publication of the observation a mass range between 111 GeV and 559 GeV could be excluded at 95% CL, except masses in range of 122 – 131 GeV in which an excess of events has been observed. The updated analysis including the extended dataset shows an excess of almost 10 standard deviations (σ) with an extracted mass of $125.2 \pm 0.2 \text{ (stat.)} \pm_{-0.6}^{+0.5} \text{ (syst.) GeV}$ in the $H \rightarrow \gamma\gamma$ and $H \rightarrow ZZ^* \rightarrow ll$ channels [40]. In the original publication a 5.9σ excess in the two channels combined with the analysis of $H \rightarrow WW^{(*)} \rightarrow l\nu l\nu$ has been observed, which exceeded the threshold of 5σ set to claim an observation. The observed local p_0 value as a function of the Higgs mass is shown in Figure 2.2 (left). Only the high mass resolution channels $H \rightarrow \gamma\gamma$ and $H \rightarrow ZZ^{(*)} \rightarrow 4l$ and $H \rightarrow WW^{(*)} \rightarrow l\nu l\nu$ are included (an updated version can be found in [40]). Both, $H \rightarrow \tau\tau$ and $H \rightarrow b\bar{b}$ do not show an excess at that time, because they had not enough sensitivity. A signal strength $\mu = 1.3 \pm 0.13 \text{ (stat.)} \pm 0.14 \text{ (syst.)}$ is obtained at $m_H = 125.5 \text{ GeV}$ considering all analysed channels. The obtained signal strength is in agreement with the SM hypothesis. The search in the di-tau final state has recently been updated [42] analysing the full $\sqrt{s} = 8 \text{ TeV}$ dataset. An excess at about 125 GeV of 4.1σ was observed. The signal strength is measured to $\mu = 1.4_{-0.4}^{+0.5}$, and will be considered for future combinations. The CMS experiment combined the same channels with slightly less data. An excess at $m_H = 125.3 \pm 0.4 \text{ (stat.)} \pm 0.5 \text{ (syst.) GeV}$ is observed in $H \rightarrow \gamma\gamma$ and $H \rightarrow ZZ^{(*)}$. The observed excess is compatible with the ATLAS observation. Figure 2.2 (right) presents the local p-value as a function of m_H for the individual channels and their combination (black line). A local significance of 5.0σ was achieved. It is lower than the ATLAS significance, because no excess was observed in $H \rightarrow WW^{(*)}$ and less data was analysed. Recently the measurement has been updated exploiting the full dataset which yields a best fit value of $m_H = 125.7 \pm 0.3 \text{ (stat.)} \pm 0.3 \text{ (syst.) GeV}$ [43]. The best fit value of the signal strength is evaluated to $\mu = 0.80 \pm 0.14$, which is compatible with the SM hypothesis as well as the ATLAS result. Figure 2.3 (right) demonstrates the best fit value of the signal strength in each channel entering the combination.

Since the decay into two photons is observed the new boson cannot be a spin one particle as stated by the *Landau-Yang-Theorem* [44, 45]. The decay into two W bosons indicates that it has neutral electric charge. However, to study whether the observed state is the SM Higgs boson or a state in the context of BSM theories with an extended Higgs sector, measurements of the properties have to be performed. For this purpose spin and parity have been measured in $H \rightarrow \gamma\gamma$ (not conclusive for CMS yet),

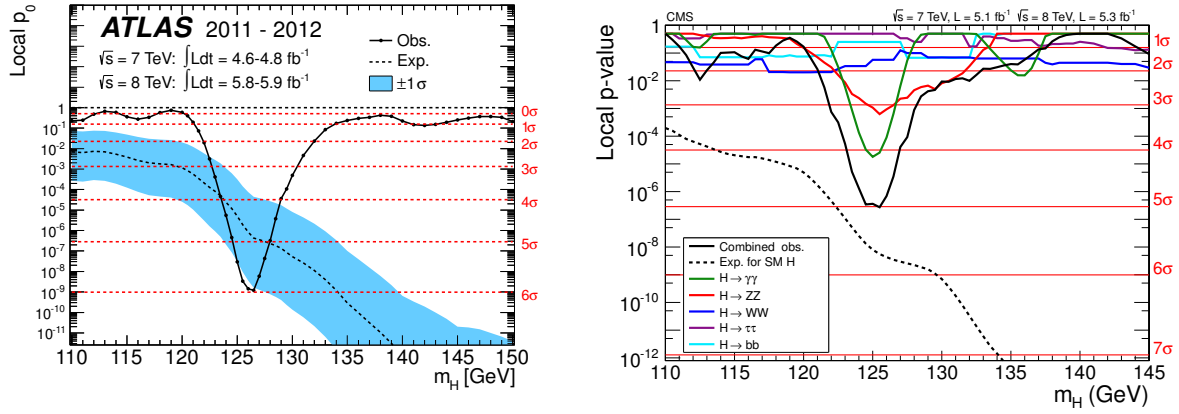


Figure 2.2: Observed local p_0 -value as a function of the Higgs mass, m_H . The left plot presents the combined results of the ATLAS collaboration, while the right plot shows the individual channels and combined results obtained by the CMS collaboration. The ATLAS collaboration presents a 5.9σ excess at 126 ± 0.4 (stat.) ± 0.4 (syst.) GeV [12], while CMS observes a 5.0σ excess at 125.3 ± 0.4 (stat.) ± 0.5 (syst.) GeV [13].

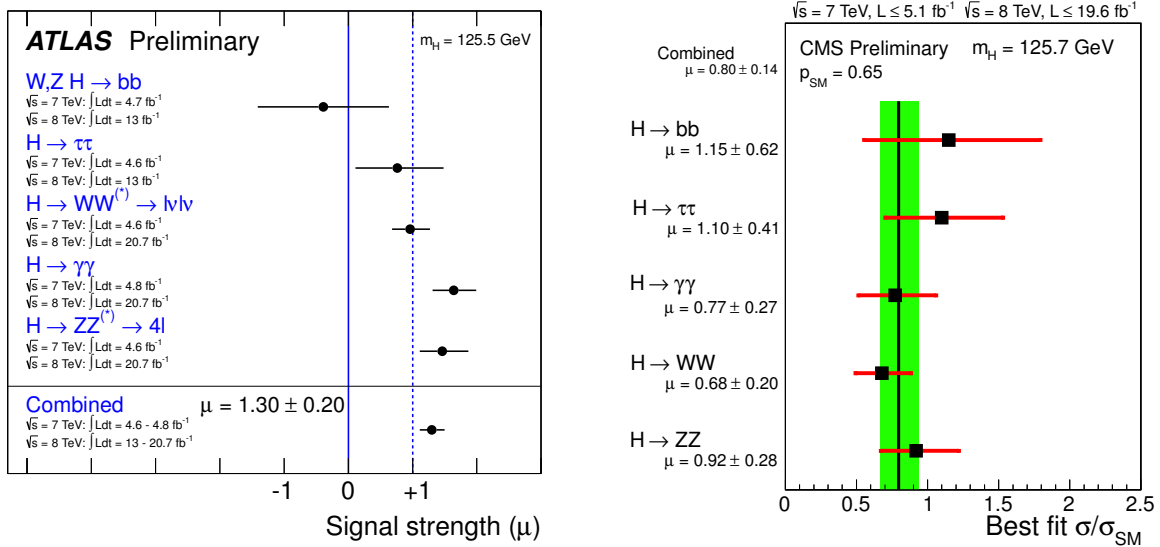


Figure 2.3: Observed best fit value of signal strength $\mu = \sigma/\sigma_{\text{SM}}$ for individual Higgs decay channels from ATLAS (left) [40] and CMS (right) [43].

$H \rightarrow ZZ^{(*)} \rightarrow 4l$ and $H \rightarrow WW^{(*)} \rightarrow l\nu l\nu$. The data taken by the ATLAS [46] and CMS [43] detector both favour $J^P = 0^+$ as predicted by the SM, while other models, like $J^P = 2^+$ are excluded at 95% C.L.

2.4 Supersymmetry

Supersymmetry is the most favoured extension of the Standard Model. Supersymmetry introduces a new symmetry between fermionic and bosonic degrees of freedom. The transformation is generated by the SUSY operator, Q , which is an anticommuting spinor, with:

$$Q|\text{fermion}\rangle = |\text{boson}\rangle \quad Q|\text{boson}\rangle = |\text{fermion}\rangle. \quad (2.25)$$

Since spinors are intrinsically complex objects, the hermitian conjugate, Q^\dagger , is a SUSY generator as well. The generators are fermionic operators, i.e. they carry spin angular momentum. Hence, supersymmetry is a space-time symmetry. The Coleman-Mandula theorem [47], which forbids the non-trivial combination

of internal and space-time symmetries, and its extension by Haag, Lopuszanski and Sohnius [48], highly restricts the form of such a symmetry. Indeed, it turned out that the supersymmetry algebra is the only possible extension of the Poincaré group. The algebra is defined by the following commutation relations:

$$\begin{aligned}\{Q, Q^\dagger \gamma_0\} &= 2\gamma^\mu P_\mu, \\ \{Q, Q\} &= \{Q^\dagger, Q^\dagger\} = 0, \\ [P^\mu, Q] &= [P^\mu, Q^\dagger] = 0,\end{aligned}\tag{2.26}$$

in which P^μ denotes the four-momentum generator of space-time translations. The particle spectrum of the Standard Model is extended by supersymmetric partners, which are arranged in supermultiplets. Fermionic and bosonic states in each supermultiplet are called superpartners. The SUSY generators commute with the SM group generators, hence the superpartners must have the same charges, e.g. electrical charge, as their corresponding SM partner. Furthermore, from the SUSY algebra it follows that the particles of each supermultiplet must have the same eigenvalues of $-P^2$, i.e. the same mass. However, none of them have been detected by experiments yet. Hence, supersymmetry cannot be an exact symmetry, but has to be broken. This will be addressed later.

2.4.1 Motivation for Supersymmetry

Although the SM describes nature well, it is clear that it is only an effective theory. There are many problems which can not be assessed by the SM. Some of these problems can be solved by SUSY and will be discussed in the following.

Grand Unification

One of the main goals in particle physics is the unification of all forces. *Grand Unified Theories* (GUTs) describe nature based on a unique interaction associated with a simple gauge group. The success of such theories has been shown in the formulation of the electroweak theory, for which the coupling constants of electromagnetic and weak interaction become identical at some energy scale. This is a generic feature of QFTs expressed by the *Renormalisation Group Equation* (RGE) [49] which defines the running of coupling constants. The coupling constants associated with the non-abelian gauge group, i.e. of weak and strong forces, decrease with increasing energy, while for the electromagnetic force it is vice versa. Thus a unification of the forces might be possible at high energies. The running of the coupling constants in the SM is demonstrated in Figure 2.4 (left). The coupling strengths differ by more than eight standard deviations [49], i.e. no unification can be achieved within the SM. New physics which enter between the electroweak and the Planck scale will change the slope of the running. If the mass of SUSY particles is of the order of 1 TeV, unification can be achieved as demonstrated in Figure 2.4 (right).

Dark Matter

The particle content of the SM excels in describing the nature of matter consisting of baryons (i.e. composite states of quarks, e.g. the proton and neutron) and electrons. However, global fits to the *cosmic microwave background* (CMB) data (e.g. from recent WMAP [14] and Planck [15] measurements) have shown that the baryonic contribution to the total mass of the Universe is just about 5% [14, 15, 16]. Other cosmological phenomena, like *rotation curves* or *gravitational lensing*, suggest the existence of *Dark Matter* (DM). Dark in this sense means that it does only interact weakly and is electric neutral. Supersymmetry provides a candidate for DM if *R-parity* defined as:

$$P_R = (-1)^{3(B-L)+2S},\tag{2.27}$$

in which $B(L)$ are the baryon (lepton) number and S the spin of the particle, is conserved. It was first introduced to avoid fast decay rates of the proton. *R-parity* assigns an additional quantum number to each

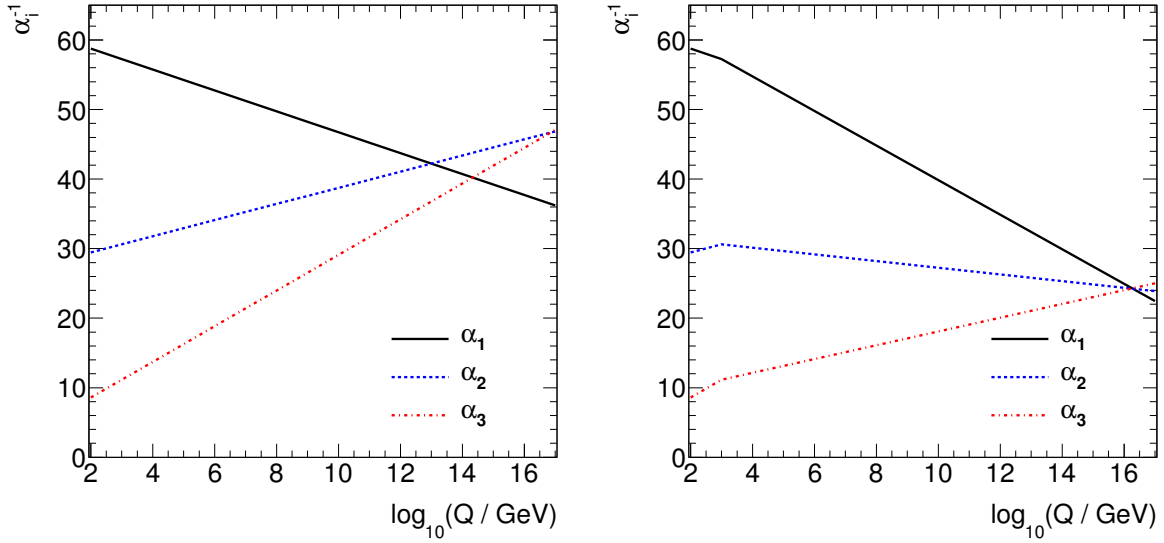


Figure 2.4: Evolution of the gauge coupling constants, $\alpha_i^{-1} = \frac{4\pi}{g_i^2}$, with $g_1 = \sqrt{\frac{5}{3}}g'$, $g_2 = g$ and $g_3 = g_s$ [16], from the GUT to the weak (M_Z) scale. In the SM (left) case no unification is observed, while in the MSSM (right) contributions from the superpartners lead to a unification at $Q \sim 2 \cdot 10^{16}$ GeV. The calculations are based on [50] (p. 199 ff.) taking $M_{\text{SUSY}} = 1$ TeV and $\alpha_i^{-1}(M_Z)$ from [49].

state in the theory, such that each SUSY particle has $P_R = -1$, while SM particles have $P_R = +1$. Decays of SUSY particles will always result in a final state with one remaining SUSY particle due to R -parity conservation. This *lightest supersymmetric particle* (LSP) is stable and has to be electrically neutral, and thus is a good candidate for DM.

Hierarchy Problem

Quantum loop corrections, Δm_H^2 , to the Higgs propagator relate the physical Higgs mass, m_H , to the *bare* mass, $m_{H,\text{bare}}$:

$$m_H = m_{H,\text{bare}} + \Delta m_H^2. \quad (2.28)$$

Figure 2.5 (left) shows an example for the fermion contributions to m_H^2 . Its contribution is given by [17]:

$$\Delta m_{H,f}^2 = -\frac{|\lambda_f|^2}{8\pi^2} \left[\Lambda_{\text{UV}}^2 - 3m_f \ln \frac{\Lambda_{\text{UV}}^2}{m_f} + \dots \right], \quad (2.29)$$

in which λ_f parametrises the coupling of the fermion to the Higgs, Λ_{UV}^2 is the cut-off scale to regulate the loop integral and m_f the fermion mass. The cut-off parameter defines the energy scale at which new physics would enter. Considering top-quark contributions for which $\lambda_f \sim 1$ and assuming the SM being valid up to the Planck scale, i.e. $\Lambda_{\text{UV}}^2 = m_{\text{P}}^2$, at which the gravitational force might become strong, Δm_H^2 becomes huge, $\Delta m_H^2 \sim \mathcal{O}(10^{30})$. To obtain an observable Higgs mass of 125 GeV the bare mass has to be fine-tuned to 34 digits. This is no problem, but seems unnatural. Boson contributions, shown exemplarily in Figure 2.5 (right), yield the same contribution in Λ_{UV}^2 to Δm_H^2 , but with a different sign. Thus, if SUSY would be exact, contributions from superpartners would cancel the divergent fermionic loop corrections. Although SUSY is not exact, the SUSY breaking scale defining Λ_{UV}^2 should be much smaller than m_{P}^2 , i.e. at the TeV scale, and thus a much smaller fine-tuning would be required.

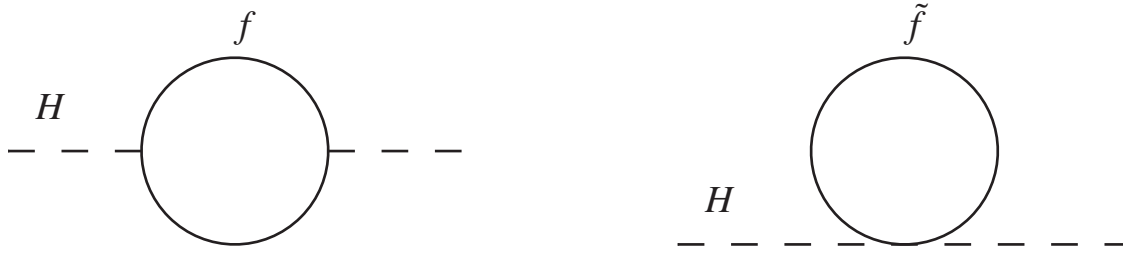


Figure 2.5: Examples for quantum loop corrections on the Higgs propagator entering the Higgs boson mass.

2.4.2 SUSY breaking

As mentioned in Section 2.4 SUSY cannot be exact, because otherwise the masses of the superpartners would be the same as their corresponding SM partner, and thus they would have been observed already. However, there are indications that constrain the SUSY breaking mechanism, e.g. if the energy scale at which the breaking takes place is above a few TeV, the hierarchy problem remains. From naturalness reasons *soft susy breaking* (SSB) scenarios are favoured, i.e. divergent SUSY breaking terms must not rise stronger than logarithmically. The SSB occurs by spontaneous symmetry breaking such that it is hidden at low energies. Many SUSY breaking mechanisms include a *hidden sector* which couples to the *visible sector* via renormalisable interactions. The breaking takes place in the hidden sector to which particles have no or only small couplings. Depending on the mediator of the breaking, soft SUSY breaking mechanisms can be classified into gravitation and gauge mediated scenarios. A detailed discussion on the breaking mechanism is beyond the scope of this thesis, but can be found e.g. in [17, 49].

2.5 Minimal Supersymmetric Extension of the Standard Model

The *Minimal Supersymmetric extension of the Standard Model* (MSSM) [20, 21, 22, 23] is the simplest supersymmetric extension of the SM. In this context "Minimal" refers to the fact that it introduces the smallest possible amount of new particles and interactions. As described in Section 2.4 each SM particle has a supersymmetric partner. For the fermions these are the *scalar partners of the fermions* (sfermions). The sleptons are the superpartners of the leptons and carry the same charges. They are labelled with a tilde ($\tilde{}$), i.e. the selectron is denoted as \tilde{e} . In the same way, the SUSY partners of the quarks are called squarks. Each of the sleptons and squarks is a spin-0 particle. Since fermions are chiral particles, each fermion is assigned to two sfermions. The coupling structure of the SM remains unchanged, for instance only the left-handed squarks, e.g. \tilde{u}_L and \tilde{d}_L , can couple to a W boson, but \tilde{u}_R and \tilde{d}_R do not. Sfermions and fermions are arranged in chiral supermultiplets. The gauge bosons get spin- $\frac{1}{2}$ superpartners, the gauginos. Each of the superpartner gets the SM name with a common suffix "-ino". They are the bino (\tilde{B}^0), winos ($\tilde{W}^+, \tilde{W}^0, \tilde{W}^-$) and gluino (\tilde{g}). The gauginos mix with the higgsinos, the fermionic partners of the scalar Higgs bosons, which results in four neutral mass eigenstates, the so-called neutralinos, and two charged mass eigenstates, the charginos. The sparticles are not sufficient to construct the MSSM, but two Higgs doublet fields enter in the Higgs sector. The additional Higgs doublet is necessary to avoid anomalies and to give mass to the up- and down-type fermions separately. Each of the doublets has four degrees of freedom, leading to 8 degrees of freedom for the Higgs sector in the MSSM. Hence, since three of them are absorbed by the gauge boson mass terms in an equivalent way as in the SM, five degrees of freedom remain. This leads to five physical Higgs bosons, three neutral ones, h^0, H^0, A^0 and two charged, H^\pm . The Higgs sector of the MSSM will be discussed in detail in Section 2.5.1. As outlined in Section 2.4.2 SUSY has to be broken. In the MSSM the soft SUSY breaking is introduced explicitly by adding corresponding terms, \mathcal{L}_{soft} , to the Lagrangian which parametrise the unknown breaking mechanism. A full review can be found in [17]. Qualitatively, the following terms are considered:

1. *Mass terms for the sfermions and Higgs bosons* represented by $m_{\phi_{ij}}^2 \phi_i^\dagger \phi_j$ with $\phi_{i,j}$ referring to the scalar partners of the SM fermions and to the scalar Higgses.

2. Mass terms for the gauginos, $M_i \tilde{V} \tilde{V}$, with $i = 1, 2, 3$ corresponding to the SM gauge groups and \tilde{V} referring to the gaugino superfields.
3. Trilinear couplings between scalar fields given as $A_{ijk} \phi_i \phi_j \phi_k$.
4. Bilinear scalar interaction term, $BH_u H_d$.

Soft SUSY breaking introduces 105 free parameters [51], which can be reduced within the *constrained* MSSM (cMSSM). This embraces the following assumptions [17]:

1. Gaugino masses are real and equal at the gauge unification scale, Λ_{UV}^2 , i.e. $M_1(\Lambda_{UV}^2) = M_2(\Lambda_{UV}^2) = M_3(\Lambda_{UV}^2) = m_{1/2}$. This presumes unification of gauge couplings at the GUT scale.
2. Universality of sfermion masses and trilinear couplings at the GUT scale, i.e. $m_{\tilde{Q}}^2 = m_{\tilde{u}}^2 = m_{\tilde{d}}^2 = m_{\tilde{L}}^2 = m_{\tilde{e}}^2 = m_0^2 \mathbb{1}$ in which $m_{i \neq 0}^2$ are diagonal mass matrices.
3. Universality of scalar Higgs mass terms at the GUT scale, i.e. $m_{H_u}^2 = m_{H_d}^2 = m_0^2$.

Taking these assumptions into account the number of free parameters is reduced to five, namely the universal sfermion and gaugino masses, $m_{1/2}$ and m_0 , respectively, the universal trilinear coupling, A_0 , the ratio of the vacuum expectation values of the two Higgs doublets, $\tan \beta$, and the sign of the higgsino mass terms, $\text{sign}(\mu)$.

2.5.1 Higgs Mechanism in the Context of the MSSM

In supersymmetric extensions of the Standard Model at least two Higgs doublet fields are required to give mass to up- and down-type fermions. Within the interpretation of the MSSM the Higgs sector is described by a two Higgs doublet model of type 2 (2HDM II) [27], a general model not restricted to supersymmetry. Two Higgs doublet fields are required since the second one cannot, unlike the SM case, be interpreted as the charge conjugate field of the other, as the superpotential prohibits terms of the form $(QH_d^\dagger)U$. Furthermore, the higgsinos, the superpartners of the Higgs field, would lead to gauge anomalies [26]. Thus the Higgs fields in the MSSM are given as:

$$H_u = \begin{pmatrix} H_u^+ \\ H_u^0 \end{pmatrix} \quad (Y = +\frac{1}{2}) \quad , \quad H_d = \begin{pmatrix} H_d^0 \\ H_d^- \end{pmatrix} \quad (Y = -\frac{1}{2}). \quad (2.30)$$

To break $SU(2)_L \times U(1)_Y$ gauge symmetry, SUSY breaking is required. This is called *radiative breaking*. The Higgs potential including the soft SUSY breaking parameters, $m_{H_u}^2$, $m_{H_d}^2$ and B_0 is then given by [52]:

$$V = \underbrace{(|\mu|^2 + m_{H_d}^2)}_{\tilde{m}_1^2} |H_d|^2 + \underbrace{(|\mu|^2 + m_{H_u}^2)}_{\tilde{m}_2^2} |H_u|^2 - \underbrace{\mu B_0}_{\tilde{m}_3^2} (H_u H_d + c.c.) + \frac{g^2 + g'^2}{8} (|H_d|^2 - |H_u|^2)^2 + \frac{1}{2} g^2 |H_d^\dagger H_u|^2. \quad (2.31)$$

Requiring that the potential is limited from below and that the gauge symmetry is broken to $U(1)_{em}$ leads to two conditions [17]:

$$\begin{aligned} 2\tilde{m}_3 &< 2|\mu|^2 + m_{H_u}^2 + m_{H_d}^2, \\ \tilde{m}_3^2 &> (|\mu|^2 + m_{H_u}^2)(|\mu|^2 + m_{H_d}^2). \end{aligned} \quad (2.32)$$

These conditions can only be fulfilled for $m_{H_u}^2 \neq m_{H_d}^2$. Some supersymmetry breaking mechanisms, like mSUGRA [53, 54, 55, 56, 57, 58, 59], require the masses to be equal at the GUT scale. In this case the

symmetry breaking occurs from different evolution of $m_{H_u}^2$ and $m_{H_d}^2$, described by the RGE. As in the SM, the Higgs fields acquire vev's:

$$H_u = \frac{1}{\sqrt{2}} \begin{pmatrix} 0 \\ v_u \end{pmatrix}, \quad H_d = \frac{1}{\sqrt{2}} \begin{pmatrix} v_d \\ 0 \end{pmatrix}. \quad (2.33)$$

The two vevs add up quadratically to the SM value, and the ratio becomes an important parameter as discussed later on:

$$\sqrt{v_d^2 + v_u^2} = v \sim 246 \text{ GeV}, \quad \tan \beta = \frac{v_u}{v_d}. \quad (2.34)$$

Minimising the potential leads to two relations:

$$\begin{aligned} \tilde{m}_1^2 &= \tilde{m}_3^2 \tan \beta + \frac{g^2 + g'^2}{8} (v_d^2 - v_u^2), \\ \tilde{m}_2^2 &= \tilde{m}_3^2 \cot \beta + \frac{g^2 + g'^2}{8} (v_d^2 - v_u^2). \end{aligned} \quad (2.35)$$

At tree level the phenomenology is thus described by two free parameter, $\tan \beta$ and one mass, e.g. \tilde{m}_3^2 . The two complex Higgs fields have eight degrees of freedom, three of them are absorbed by the gauge boson masses, while the remaining five yield five physical Higgs bosons, two neutral CP-even states h^0 , H^0 , one neutral CP-odd state, A^0 , and two charged Higgs bosons, H^\pm . Expansion of the Higgs fields around the vacuum state yield the physical states and the Goldstone bosons, G^0 , G^\pm as a mixture of the components of the Higgs fields:

$$\begin{aligned} \begin{pmatrix} G^0 \\ A^0 \end{pmatrix} &= \sqrt{2} \begin{pmatrix} \cos \beta & -\sin \beta \\ \sin \beta & \cos \beta \end{pmatrix} \begin{pmatrix} \text{Im}(H_d^0) \\ \text{Im}(H_u^0) \end{pmatrix}, \\ \begin{pmatrix} h^0 \\ H^0 \end{pmatrix} &= \sqrt{2} \begin{pmatrix} \cos \alpha & -\sin \alpha \\ \sin \alpha & \cos \alpha \end{pmatrix} \begin{pmatrix} \text{Re}(H_u^0) - v_u \\ \text{Re}(H_d^0) - v_d \end{pmatrix}, \\ \begin{pmatrix} G^- \\ H^- \end{pmatrix} &= \begin{pmatrix} \cos \beta & -\sin \beta \\ \sin \beta & \cos \beta \end{pmatrix} \begin{pmatrix} H_d^- \\ H_u^- \end{pmatrix}, \end{aligned} \quad (2.36)$$

with mixing angle α , $G^+ = (G^-)^\dagger$ and $H^+ = (H^-)^\dagger$. Diagonalising the mass matrices leads to masses for the Higgs bosons and the mixing angle which are given at tree level as [26]:

$$\begin{aligned} M_{H^\pm}^2 &= M_A^2 + M_W^2, \\ M_{h,H}^2 &= \frac{1}{2} \left[M_A^2 + M_Z^2 \mp \sqrt{(M_A^2 + M_Z^2)^2 - 4M_A^2 M_Z^2 \cos^2 2\beta} \right], \\ \tan 2\alpha &= \tan 2\beta \frac{M_A^2 + M_Z^2}{M_A^2 - M_Z^2} \quad \text{with} \quad -\frac{\pi}{2} < \alpha < 0. \end{aligned} \quad (2.37)$$

Two important relations can be derived from Equation 2.37:

$$\begin{aligned} M_h &< \min(M_Z, M_A) < M_H, \\ M_{H^\pm} &> M_W. \end{aligned} \quad (2.38)$$

The first relation directly implies that the mass of the lightest Higgs boson must be smaller than M_Z which has been ruled out by the LEP experiments [60]. However, this relation only holds at tree-level, but receives large radiative corrections, dominated by top and stop contributions, which push the upper bound to $M_h \lesssim 140 \text{ GeV}$ [27]. A detailed discussion on radiative corrections is given in Section 2.5.2. The masses of the gauge bosons and fermions are given by:

$$\begin{aligned} M_W &= \sqrt{\frac{g^2}{4} (v_d^2 + v_u^2)} & M_Z &= \sqrt{\frac{g^2 + g'^2}{4} (v_d^2 + v_u^2)}, \\ m_l &= \frac{\lambda_l}{\sqrt{2}} v_d & m_d &= \frac{\lambda_d}{\sqrt{2}} v_d & m_u &= \frac{\lambda_u}{\sqrt{2}} v_u, \end{aligned} \quad (2.39)$$

with the *Yukawa couplings* λ_l , λ_d , and λ_u . All neutral Higgs bosons couple to fermions, while, due to CP invariance, the A^0 boson does not couple to gauge bosons at tree level. The coupling strength can be related to the SM Higgs couplings. They are summarised in Table 2.3.

ϕ	$g_{\phi\bar{u}u}/g_{H^{SM}\bar{u}u}$	$g_{\phi\bar{d}d}/g_{H^{SM}\bar{d}d}$	$g_{\phi VV}/g_{H^{SM}VV}$
h^0	$\cos\alpha/\sin\beta$	$\sin\alpha/\cos\beta$	$\sin(\beta-\alpha)$
H^0	$\sin\alpha/\cos\beta$	$\cos\alpha/\cos\beta$	$\cos(\beta-\alpha)$
A^0	$\cot\beta$	$\tan\beta$	0

Table 2.3: MSSM Higgs boson couplings to gauge bosons and fermions with respect to SM Higgs couplings.

The μ -problem

There is still one puzzle remaining in the Higgs sector of the MSSM. The mass term μ in the Higgs potential (c.f. Eq. 2.31) can be arbitrarily large, e.g. in the order of the Planck mass. However, from phenomenology one expects μ to be in the order of the electroweak symmetry breaking scale, i.e. in the order of $10^2 - 10^3$ GeV. In principle this can be addressed by cancellations between μ and the soft SUSY mass breaking terms, which however seems unnatural. Thus, this problem is usually addressed by requiring the μ term to be absent at tree-level, but rather let it arise from vevs of some new fields entering in extended theories. This can be done by either extending the MSSM to the so-called *next-to-minimal supersymmetric standard model* (NMSSM)⁵ or by extending the underlying symmetry group, which will be discussed in detail in Section 2.6.

2.5.2 Benchmark Scenarios and Radiative Corrections

As mentioned above, radiative corrections have a significant impact on the Higgs sector in the MSSM. It affects both the Higgs masses as well as their couplings to fermions and gauge bosons. So far it has been shown that the Higgs sector at tree level can be described by two parameters, usually chosen to be $\tan\beta$ and M_A . Once radiative corrections are taken into account, the Higgs sector gets sensitive to the soft SUSY breaking parameters. From the experimental point of view it is not appropriate to use parametrisations with many degrees of freedom. Thus benchmark scenarios are developed to interpret the experimental results. There are benchmark scenarios for SUSY itself, e.g. the well known SPS points [61], but since this thesis will focus on the search for heavy Higgs bosons the discussion will concentrate on benchmark scenarios dedicated to the Higgs sector. In contrast to SUSY benchmarks which are defined by constraints at the GUT scale, the benchmarks considered here are defined by low energy parameters. They do not take into account experimental constraints from e.g. $B_s \rightarrow \mu^+\mu^-$, but rather define theoretically interesting or challenging scenarios. As mentioned above, at tree level the mass of the lightest Higgs has to be lower than M_Z , which has already been ruled out by the LEP experiments [60]. However, radiative corrections can push the mass above this threshold. They are dominated by contributions from top-stop and bottom-sbottom quarks. The corrections can be described within the renormalisation group approach which describes the running of parameters constrained at the GUT scale down to the electroweak scale. This is usually expressed in the $\overline{\text{DR}}$ scheme [62, 63]. For the lightest Higgs boson the one-loop correction is given as [27]:

$$\Delta M_h^2 \sim \frac{3\bar{m}_t^4}{2\pi^2 v^2 \sin^2\beta} \left[\log \frac{M_S^2}{\bar{m}_t^2} + 2 \frac{X_t^2}{2M_S^2} \left(1 - \frac{X_t^2}{6M_S^2} \right) \right], \quad (2.40)$$

⁵See e.g. [26] for a complete list of references.

with the averaged stop quark mass $M_S = \frac{1}{2}(m_{\tilde{t}_1} + m_{\tilde{t}_2})$, the stop mixing parameter, X_t , and the running $\overline{\text{MS}}$ top mass, \overline{m}_t . Depending on the choice of X_t one can distinguish the *no-mixing scenario* for which $X_t = 0$ and the *maximal mixing scenario* with $X_t = A_t - \mu \cot \beta \sim \sqrt{6}M_S$. In the maximal mixing scenario the lightest Higgs mass, M_h , gets maximised, and thus consistent with LEP data. However, the maximised lightest Higgs mass is not compatible with the recent measurements of the LHC experiments which favour a lighter h^0 boson. New benchmark scenarios based on the m_h^{max} scenario including the observation of the Higgs boson have been proposed, referred to as modified m_h^{max} scenarios, $m_h^{\text{mod+}}$ and $m_h^{\text{mod-}}$ [64]. They essentially differ in the stop mixing sector such that the observed state can be interpreted as h^0 . Furthermore, these scenario allow a wider accessible phase space in $M_A - \tan \beta$ which is strongly restricted in the m_h^{max} scenario (see [64] for a detailed discussion). However, the m_h^{max} scenario is still considered, as it allows an interpretation of the experimental results w.r.t. measurements by the LEP and Tevatron experiments. Table 2.4 summarises the parameter settings for the different scenarios considered in this thesis.

parameter	benchmark scenario		
	m_h^{max}	$m_h^{\text{mod+}}$	$m_h^{\text{mod-}}$
m_t [GeV]	173.2	173.2	173.2
M_{SUSY} [GeV]	1000	1000	1000
μ [GeV]	200	200	200
M_2 [GeV]	200	200	200
X_t^{OS}	$2M_{\text{SUSY}}$	$1.5M_{\text{SUSY}}$	$-1.9M_{\text{SUSY}}$
X_t^{MS}	$\sqrt{6}M_{\text{SUSY}}$	$1.6M_{\text{SUSY}}$	$-2.2M_{\text{SUSY}}$
	$A_b = A_\tau = A_t$	$A_b = A_\tau = A_t$	$A_b = A_\tau = A_t$
$m_{\tilde{g}}$ [GeV]	1500	1500	1500
$M_{\tilde{t}_3}$ [GeV]	1000	1000	1000

Table 2.4: Parameter setting of various MSSM Higgs benchmark scenarios considered in this thesis. Taken from [64].

For large $\tan \beta$ and M_A the masses of the H^0 and H^\pm bosons can be written in the ϵ -approximation [27]:

$$M_H \xrightarrow{M_A \gg M_Z} M_A \left[1 + \frac{M_Z^2 \sin^2 2\beta + \epsilon \cos^2 \beta}{2M_A^2} \right] \quad M_{H^\pm} \xrightarrow{M_A \gg M_Z} M_A \left[1 + \frac{M_W^2}{2M_A^2} \right]. \quad (2.41)$$

The masses of the heavier CP-even, the CP-odd and the charged Higgs bosons become degenerated. In the *decoupling regime* there is only one light Higgs boson, h^0 , and three heavy degenerated ones, $M_A \simeq M_H \simeq M_{H^\pm}$. The masses of the neutral MSSM Higgs bosons as a function of M_A are shown in Figure 2.6 for low and high $\tan \beta$ in the maximal-mixing scenario (left) and the modified maximal-mixing scenario (right).

Besides the masses, the couplings receive corrections due to higher order diagrams as well. This is approximated via one-loop calculations. The mixing angle, α , becomes an effective mixing angle, α_{eff} , given in the ϵ -approximation as [27]:

$$\tan 2\alpha_{\text{eff}} = \tan 2\beta \frac{M_A^2 + M_Z^2}{M_A^2 - M_Z^2 + \epsilon / \cos 2\beta}. \quad (2.42)$$

For large $\tan \beta$ the coupling of the lighter CP-even Higgs boson to fermions reaches the SM couplings, while for the heavier H^0 it goes to zero and vice versa for low $\tan \beta$. Thus the branching ratio for heavy Higgs bosons decaying into down-type fermions is enhanced. Higgs-fermion couplings are exposed

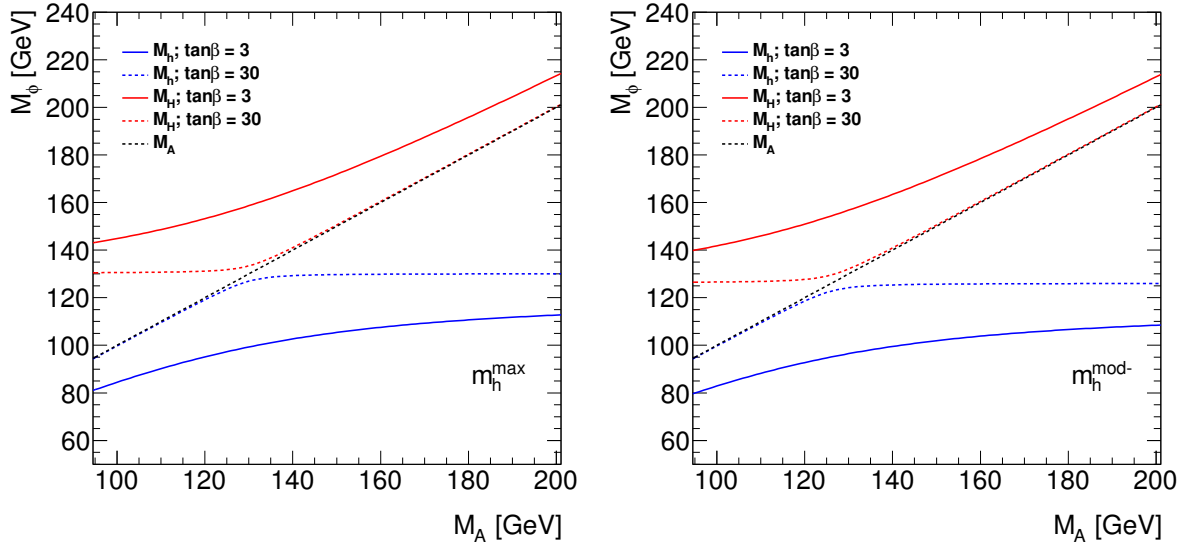


Figure 2.6: Masses of the neutral MSSM Higgs bosons as a function of M_A for $\tan\beta = 3$ (solid lines) and $\tan\beta = 30$ (dashed lines) in the m_h^{\max} (left) and $m_h^{\text{mod-}}$ (right) scenario. The calculation is done using FEYNHIGGS [65, 66, 67, 68]. The lightest Higgs boson in the m_h^{\max} scenario has a mass of $m_h \simeq 130$ GeV for high M_A and $\tan\beta$ which is inconsistent with experimental data. This is addressed in the $m_h^{\text{mod-}}$ scenario where $m_h \simeq 125$ GeV. For large $\tan\beta$ and high M_A the H^0 and A^0 bosons become degenerate in mass.

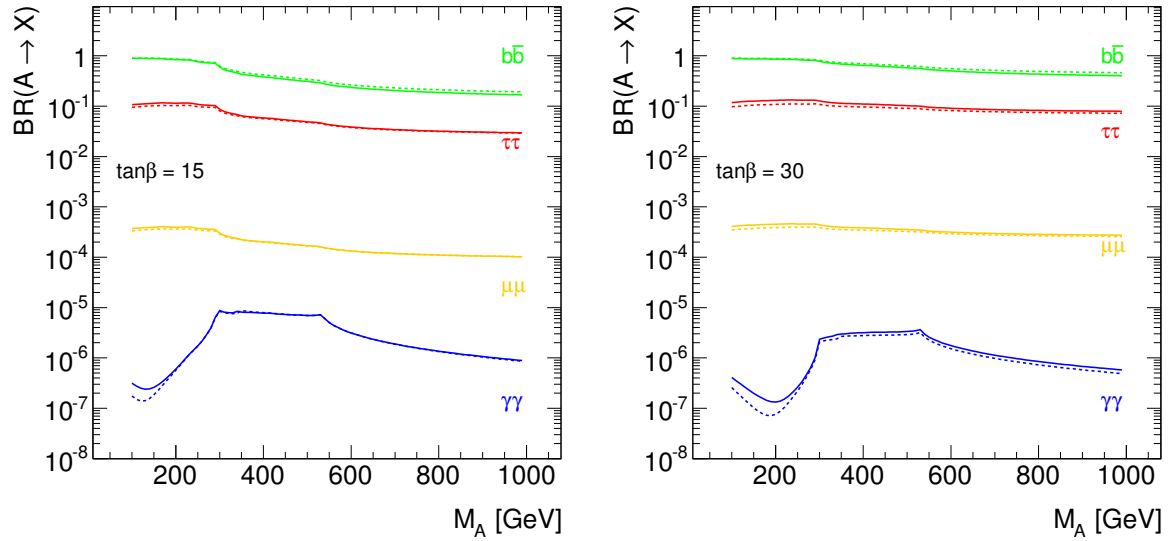


Figure 2.7: Branching ratios of the neutral CP-odd Higgs boson as a function of its mass for $\tan\beta = 15$ (left) and $\tan\beta = 30$ (right). The solid line mark the m_h^{\max} scenario, while dashed lines represent the $m_h^{\text{mod-}}$ scenario. As $\tan\beta$ becomes larger the branching ratio of the $\tau^+\tau^-$ final state becomes slightly smaller in the $m_h^{\text{mod-}}$ scenario, while the $b\bar{b}$ final state becomes slightly more dominant. The calculation was done using FEYNHIGGS [65, 66, 67, 68].

additional one-loop vertex corrections, Δ_f . The couplings of the heavy neutral Higgs bosons, A^0 and H^0 , to bottom quarks become modified [27]:

$$g_{Abb} \simeq \tan\beta \left[1 - \frac{\Delta_b}{1 + \Delta_b} \frac{1}{\sin^2\beta} \right] \quad g_{Hbb} \simeq \frac{\cos\alpha_{\text{eff}}}{\cos\beta} \left[1 - \frac{\Delta_b}{1 + \Delta_b} (1 - \tan\alpha_{\text{eff}} \cot\beta) \right]. \quad (2.43)$$

The same holds for the couplings to tau leptons. For large $\tan\beta$ the couplings to down-type fermions are enhanced, and thus a search in the $\tau^+\tau^-$ and $b\bar{b}$ final state are preferred. Figure 2.7 demonstrates the dependence of the coupling constants by showing the branching ratio of various decays of the A^0 boson, $BR(A \rightarrow X)$, for $\tan\beta = 15$ and $\tan\beta = 30$ as obtained in the m_h^{\max} and $m_h^{\text{mod-}}$ scenario.

2.6 Phenomenology of Heavy Z' bosons

New heavy gauge bosons are predicted by many extensions of the SM. The Z' boson enters the phenomenology of a variety of models which cannot be discussed in detail here, so the interested reader is pointed to a choice of review articles [28, 29, 69, 70]. Models containing Z' bosons can be categorised according to whether they arise from Grand Unification or not. Some representative examples will be discussed below. Generally speaking the Z' can be seen as a heavy version of the SM Z boson, although couplings, spin and other quantum numbers can be different. In *Kaluza-Klein* (KK) theories the Z' is interpreted as the KK excitation of the gravitino having spin two, while in R-parity violating SUSY models it can be associated to the sneutrino with spin zero. Other theories predict a spin one particle, e.g. in E_6 models (see below for details). A generic Z' does not necessarily have to have the same coupling structure as the SM Z , but it might be generation dependent. This makes the di-tau final state an important subject for searches in models which might not be accessible by the light lepton final states. However, family dependent couplings might lead to *Flavour Changing Neutral Currents* (FCNCs) which are strongly constrained by kaon and B hadron mixing ($K - \bar{K}$ and $B_{d,s} - \bar{B}_{d,s}$, respectively) [71, 72]. Generation dependent couplings can only occur if the generator, T' , of the additional $U(1)'$ gauge group does not commute with the $SU(2)_L$ generator.

2.6.1 Z - Z' -Mixing

In generic models including a new $U(1)$ gauge group, the Z and Z' bosons are not mass eigenstates, but mixing occurs. In general, there are two different scenarios how the mixing can occur, *kinematic mixing* or *mass mixing*. If the new gauge group is a simple $U(1)'$ the Lagrangian has to be invariant under $SU(2)_L \times U(1)_Y \times U(1)'$ transformations. The kinematic term of the Lagrangian can be written in the weak basis [29] as:

$$\mathcal{L}_{kin} = -\frac{1}{4}W_{\mu\nu}^a W_a^{\mu\nu} - \frac{1}{4}\tilde{B}_{\mu\nu}\tilde{B}^{\mu\nu} - \frac{1}{4}\tilde{Z}'_{\mu\nu}\tilde{Z}'^{\mu\nu} - \frac{\sin\chi}{2}\tilde{Z}'_{\mu\nu}\tilde{B}^{\mu\nu}, \quad (2.44)$$

with mixing parameter χ . As explained in Section 2.3 one can extract the fermion couplings which can be written in a simplified way as:

$$\bar{f}\left[gT_a W^a + g'Y\tilde{B} + \tilde{g}_{Z'}T'\tilde{Z}'\right]f, \quad (2.45)$$

with g and g' as defined in Section 2.2 and $\tilde{g}_{Z'}$ being the coupling constant corresponding to the new gauge group. The kinematic part of the Lagrangian can be diagonalised by transformation of the $U(1)$ fields, $\tilde{B} \rightarrow B - \tan\chi Z'$ and $\tilde{Z}' \rightarrow Z' / \cos\chi$, which leads to modified fermion couplings:

$$\bar{f}\left[gT_a W^a + g'YB + g_{Z'}(T' + \delta Y)Z'\right]f, \quad (2.46)$$

with $g_{Z'} = \frac{\tilde{g}_{Z'}}{\cos\chi}$ and $\delta = -g'\frac{\tan\chi}{g_{Z'}}$. If $\delta \neq 0$ mixing between Z and Z' occurs and the Z' coupling to fermions gets an additional component w.r.t. the SM hypercharge coupling g' . The mixing can also occur via SSB in the Higgs sector if the Higgs doublets do not transform as singlet under the new gauge group. Additional Higgs singlets, S_j , enter at the scale where the new gauge group is broken. Following the procedure outlined in Sections 2.3 and 2.5.1 the kinematic term of the Higgs Lagrangian can be written as:

$$\mathcal{L}_{H,kin} = \sum_{i=u,d} \left[\left(\frac{g}{\cos\theta_w} T_3 Z + g_{Z'} T' Z' \right) v_i \right]^2 + \sum_j \left[g_{Z'} T' v_{S_j} Z' \right]^2, \quad (2.47)$$

with the vevs $v_{u,d}$ (v_{S_j}) of the Higgs doublets (singlet). The quadratic terms in Equation 2.47 give rise to mass terms $M_Z Z^2$ and $M_{Z'} Z'^2$. If one of the Higgs doublets yield $T'H_i \neq 0$, mixing terms arise. The scale of the mixing will be set by the vev, and thus be in the order of M_Z^2 . The mass matrix is given as:

$$\mathcal{M} = \begin{pmatrix} M_Z^2 & \beta M_Z^2 \\ \beta M_Z^2 & M_{Z'}^2 \end{pmatrix}, \quad (2.48)$$

with

$$\beta = \frac{4 \cos \theta_w g_{Z'}}{g} \left[\sum_{i=u,d} T_3 T' v_i^2 \right] / \sum_{i=u,d} v_i^2. \quad (2.49)$$

Since \mathcal{M} is real it can be diagonalised by a simple rotation with angle ϕ . This yields the flavour eigenstates $Z = Z_1 \cos \phi - Z_2 \sin \phi$ and $Z' = Z_1 \sin \phi + Z_2 \cos \phi$, with $Z_{1,2}$ being the mass eigenstates with masses $M_{1,2}$. A non-zero mixing modifies the SM couplings of the Z to:

$$g_{Zff} = \frac{g}{\cos \theta_w} (T_3 - \sin^2 \theta_w Q) \cos \phi + g_{Z'} T' \sin \phi, \quad (2.50)$$

and thus implies modified partial widths of the Z decay into fermion pairs, $\Gamma(Z \rightarrow ff)$.

2.6.2 Sequential Standard Model

The *Sequential Standard Model* (SSM) introduces the Z' as a heavy partner of the SM Z boson with same couplings and quantum numbers, but higher mass. SSM models are not considered to be realistic, but serve as a *standard candle* in experimentell interpretations. Although it is not expected by gauge theories it might become realistic if couplings to exotics particles occur or the Z' is interpreted as an excited state in extra dimension models. Another realistic scenario might be to build a model with no couplings to SM fermions in the weak basis, but the couplings occur via Z – Z' –mixing (c.f. Section 2.6.1). Thus, the fermion couplings commensurate to the SM coupling reduced by $\sin \phi$.

2.6.3 E_6 Models

E_6 models are a famous ambassador of GUT theories with an extended gauge group leading to predictions of new heavy Z' bosons. One of these models is the *Exceptional Supersymmetric Standard Model* (ESSM) [73] which provides an alternative to the (N)MSSM. Originating from an E_6 gauge group, which gets broken at the GUT scale, it breaks down to the SM gauge group with an additional $U(1)_N$. The latter remains unbroken down to a scale near the EW scale. At this breaking scale the Z' enters the phenomenology of the ESSM. The matter content below the GUT scale can be described by three **27**-plets. It contains three Higgs doublet families, $H_{u,i}, H_{d,i}$, three additional quark $SU(2)$ -singlets, D_i, \bar{D}_i and three extra singlets under the SM gauge group, S_i . Only the third generation develops vevs where the Higgs doublets can be interpreted as outlined in Section 2.5.1. To provide gauge unification additional Higgs-like doublet supermultiplets have to be introduced, which however do not develop vevs. Exotic particles entering the matter content of the ESSM are expected to have masses in the order of 1 TeV. Gauge symmetry of $U(1)_N$ prevents a μ -term, and thus solves the μ -problem mentioned in Section 2.5.1. However, the E_6 gauge group cannot be broken in the conventional manner discussed previously, but by the so-called *Hosotani mechanism* [74]. The breakdown leads to either rank 5 or rank 6 gauge groups, but the rank 6 group can be reduced to an effective rank 5 gauge group if the vevs are sufficiently large [73]. The maximal subgroup E_6 can break down to, is $SO(10) \times U(1)_\psi$. Further breaking of $SO(10) \rightarrow SU(5) \times U(1)_\chi$ yields an extra $U(1)$ and the SM gauge sector included in $SU(5)$. The two $U(1)$ gauge groups can be expressed as a linear combination:

$$U(1)' = U(1)_\chi \cos \theta + U(1)_\psi \sin \theta, \quad (2.51)$$

which leads to specific models depending on the choice of χ, ψ and θ . If right handed neutrinos transform under $U(1)'$, stringent constraints on the Z' mass from cosmological and astrophysical data arise, leading

to $M_{Z'} > 4.3 \text{ TeV}$ [75]. Thus it is not of relevance for this analysis. If the right handed neutrinos do not carry the charge of $U(1)'$ the situation changes dramatically. They become very heavy and the SM neutrinos get their (low) masses via the *seesaw mechanism*. One advantage is that this provides an explanation for the baryon asymmetry in the universe.

2.6.4 Left Right Symmetric Models

Another popular class of GUT motivated theories involving Z' bosons are *Left Right Symmetric Models* (LRM). They are based on a $SU(2)_L \times SU(2)_R \times U(1)_{B-L}$ gauge group which may result from breaking of $SO(10)$ or E_6 . Since an additional $SU(2)$ group is involved in these theories they do not only predict a new heavy Z' boson, but also new heavy $W^{\pm'}$ bosons. The model is parametrised by $\kappa = \frac{g_R}{g_L}$ which in general is unequal to one. The mass ratio of the Z' and W' bosons is given as:

$$\frac{M_{Z'}^2}{M_{W'}^2} = \frac{\kappa^2(1 - x_w)\rho_R}{\kappa^2(1 - x_w) - x_w} > 1, \quad (2.52)$$

with $x_w = \sin^2 \theta_w$ and $\rho_R = 1$ or 2 depending on whether the $SU(2)_R$ symmetry is broken by a Higgs doublet or triplet. Thus the W' is always lighter than the Z' boson, which provides a good opportunity to test these models experimentally. The fermion couplings of the Z' are given as [76]:

$$g_{Z'ff} = g_Z \frac{1}{\sqrt{\kappa - (1 + \kappa)x_w}} [x_w T_{3,L} + \kappa(1 - x_w)T_{3,R} - x_w Q]. \quad (2.53)$$

2.6.5 Technicolour Models

The concept of *Technicolour* (TC) has been introduced in the late 1970's by Steven Weinberg [77] and Leonard Susskind [78]. It provides a new gauge force with properties similar to QCD, i.e. based on an extended gauge sector involving an additional non-abelian group $SU(N)$. This predicts new particles such as *technigluons* and *techniquarks*. In *Extended technicolour* (ETC) [79] models an extended gauge sector based on $SU(2)_h \times SU(2)_l$ is introduced in which new gauge bosons couple to both SM fermions and *technifermions*. EWSB is introduced by couplings of ordinary fermions to technifermion condensates. The gauge group structure introduces generation dependent transformations of fermions, in which leptons and quarks of the first and second family couple to $SU(2)_l$ (in which l refers to "light") and the third generation particles to the $SU(2)_h$ (h stands for "heavy"). The two $SU(2)$ gauge groups modify the charge operator to $Q = T_{3,l} + T_{3,h} + Y$. The Z' boson in these models couple only to left handed fermions with enhanced couplings to fermions of the third generation. Thus these models are of particular interest for this analysis, as the di-tau final state has a huge impact on the discovery or exclusion potential for these models.

2.6.6 Topcolour Assisted Technicolour Models

The large top mass suggests a dynamic electroweak symmetry breaking mechanism with a gauge structure depending on the fermion generation. *Topcolour Assisted Technicolour* (TC2) [80, 81] models address the dynamic electroweak symmetry breaking by assuming an extended gauge sector described by $G = SU(3)_1 \times SU(3)_2 \times U(1)_1 \times U(1)_2$ arising from a larger gauge group [69]. The large top mass is generated from two components, one fundamental component ϵm_t arising from e.g. ETC or the Higgs mechanism, and a dynamic term $(1 - \epsilon)m_t$ from topcolour dynamics occurring at the breaking scale, $\Lambda \sim 1 \text{ TeV}$. The scaling parameter ϵ is assumed to be small such that the fundamental component is of the order of the bottom mass. Fermions of the first and second generation will transform under $U(1)_1$ while the third generation fermions transform under $U(1)_2$. Thus, flavour changing neutral currents occur from mass mixing of the third generation fermions with the lighter fermions, but can be prevented by the choice of the fermion mixing angles [79]. The extended colour is broken to SM QCD ($SU(3)_c$) via a new scalar field, ϕ , which develops a vev. Thus three new *top-pions* enter the particle content of TC2 models

which have masses of the order of m_t . The Z' arises from the additional $U(1)_1$ gauge group. The mass term can be written as [79]:

$$M_{Z'} \simeq g_1 \frac{\Lambda}{\sin \theta' \cos \theta'}, \quad (2.54)$$

with g_1 being the coupling constant associated to $U(1)_1$, Λ the breaking scale and the mixing angle between B_μ and Z'_μ fields, θ' . From the perspective of these models the search in the di-tau channel is of great interest as the couplings are enhanced w.r.t. the di-electron and di-muon final states.

2.6.7 Little Higgs Models

Little Higgs models [82] are the most famous representative of non-GUT theories predicting new heavy gauge bosons. Quadratic divergencies occurring at one loop order, c.f. Section 2.4.1, are removed by new gauge bosons, fermions and Higgses. Partially broken global symmetries are present and address the divergencies. Contrary to SUSY the divergencies arising from contributions of gauge bosons and fermions are cancelled by the new gauge bosons and fermions. This yields stringent constraints on the couplings of the new particles. The extended underlying gauge group predicts new heavy Z' and W' bosons degenerated in mass, with the mass being of the order of 1 TeV. The *Littlest Higgs* model [83] shall serve as an example of Little Higgs extensions of the SM. The underlying field theory is based on a global $SU(5)$ gauge group, broken spontaneously to $SO(5)$ with vev, f , and a local $[SU(2) \times U(1)]^2$ gauge group. The local gauge group is broken to the SM gauge group, while the remaining group structure yields the heavy Z' and W' . The spontaneous symmetry breaking of the $SU(5)$ leads to 14 Goldstone bosons. Four of them give the longitudinal component of the new gauge bosons⁶, and thus give rise to their mass terms [82].

⁶Note: the breaking yields a heavy partner of the photon

3 Experimental Status of Searches for Heavy Neutral Resonances

In the last chapter the theoretical foundation and its constraints on searches for heavy neutral resonances are outlined. This chapter will summarise the current status of experimental data on this topic. Constraints can arise from both indirect and direct searches. New particles proposed by any theory can enter through radiative corrections to SM processes, and thus electroweak precision measurements can put limits on or give hints for new physics. Cosmological data, like searches for *cold dark matter* (CDM), puts also constraints on theories beyond the SM. These will be briefly introduced in Sections 3.1 and 3.3 for neutral BSM Higgs bosons and Z' bosons, respectively. Collider experiments allow for direct searches for these new particles. So far no new physics have been observed, and thus limits on the cross section of the production of these new particles are placed. These cross section limits can then be translated in the context of benchmark scenarios as discussed in Section 2.5.2. The current limits from the LEP, Tevatron and LHC experiments will be presented in Sections 3.2 and 3.4.

3.1 Indirect Constraints on Neutral MSSM Higgs Bosons

Beside direct searches (c.f. Section 3.2) high precision measurements of low energy observables yield constraints on the SUSY parameter space, and thus on the Higgs sector. Constraints on the parameter space describing the Higgs sector arise e.g. from measurements of $B \rightarrow X_s \gamma$, $B_s \rightarrow \mu\mu$, the anomalous magnetic moment of the muon, $(g-2)_\mu$, or the relic abundance of dark matter. A detailed review is given in e.g. [84, 85]. The recent discovery of a Higgs-boson outlined in Section 2.3.1 and its coupling measurements put further constraints on the MSSM Higgs sector. The inclusive radiative decay of $B \rightarrow X_s \gamma$ receives dominant loop contributions from SUSY particles, like stops and charginos, as well as from charged Higgs bosons. The recent result of the *Heavy Flavour Averaging Group* (HFAG) of the branching ratio of $b \rightarrow s \gamma$ of $(3.43 \pm 0.22) \cdot 10^{-4}$ [86] is close to the SM prediction. Thus, it puts severe constraints on the MSSM parameter space. Double neutral Higgs penguin diagrams⁷ enter the branching ratio calculation of the $B_s \rightarrow \mu\mu$ decay which can be interpreted as a two-sided bound on the product of the μ -parameter times the trilinear coupling, μA_t . The latest result on $\text{BR}(B_s \rightarrow \mu^+ \mu^-) = (2.9 \pm 0.7) \cdot 10^{-9}$ was published in 2013 by the CMS and LHCb collaborations [88]. Stau coannihilation with the lightest supersymmetric particle enters the DM relic density. The updated results of the *XENON-100* collaboration [89] are taken into account in the global fit of the MSSM parameter space. The calculation of the anomalous magnetic moment of the muon, $(g-2)_\mu$, receives dominant corrections from neutralinos, smuons, sneutrinos and charginos, and thus puts further constraints on the allowed parameter space, c.f. [84]. However, these are not included in the parameter scans mentioned below. As pointed out in Section 2.3.1 an enhanced coupling of the Higgs boson to photons is observed by the LHC experiments, but given the amount of data this is still compatible with both the SM and the MSSM assuming the decoupling limit. However, this could be a hint for SUSY corrections. As pointed out in Section 2.5.2 radiative corrections from sbottom squarks (Δ_b corrections) can change the effective couplings of $h^0 \rightarrow b\bar{b}$, and therefore affect the signal strength of $h^0 \rightarrow \gamma\gamma$. In the *vanishing coupling* regime, corrections to the effective mixing angle lead to a reduction of the b Yukawa coupling. This is not the case in the decoupling regime. A parameter scan in the *phenomenological MSSM* (pMSSM), which has 19 free parameters and the neutralino as LSP, has been performed based on a χ^2 probability test given the above mentioned measurements [85]. The scan in the M_A - $\tan\beta$ -plane for the pMSSM is shown in Figure 3.1 (left). The black points show the allowed parameter points fulfilling the LEP constraint of $M_h > 114 \text{ GeV}$ [60]. The dark and light green points represent allowed parameters at 90% and 68% C.L., respectively, including the mass and rate measurements of the LHC experiments. The direct $A^0/H^0 \rightarrow \tau\tau$ search limit is illustrated by the black line. For further details on the direct searches see Section 3.2. From Figure 3.1 it can be concluded that the data prefers large values of M_A and $\tan\beta$, i.e. the decoupling regime is preferred. However, the observed state can also be interpreted as the H^0 boson, which indicates a low M_A and moderate $\tan\beta$ (~ 10) and suppressed couplings of the h^0 boson to gauge bosons. This scenario can be

⁷Penguin diagrams mark a special class of higher order Feynman diagrams in particular important in B physics [87].

ruled out in the pMSSM as depicted in Figure 3.1 (right). The black dots mark the consistent parameter set including the flavour physics and dark matter results, while the red line presents the current CMS exclusion in $A^0/H^0 \rightarrow \tau\tau$. However, large Δ_b correction can lead to an enhanced $A^0/H^0 \rightarrow b\bar{b}$ decay width, and thus reduce the tau coupling strength. This makes the $A^0/H^0 \rightarrow \tau\tau$ limits less severe. In addition, decays into SUSY particles, in particular $H^0 \rightarrow \tilde{\tau}_1\tilde{\tau}_1$ and $A^0/H^0 \rightarrow \tilde{\tau}_1\tilde{\tau}_2$, can reduce the rate in the di-tau channel if the $\tilde{\tau}$ mass is low enough to be kinematically available. More scans can be found in [85]. It should be noted that the exclusion limits discussed here are only valid in the pMSSM. MSSM models constrained in other ways might yield different results.

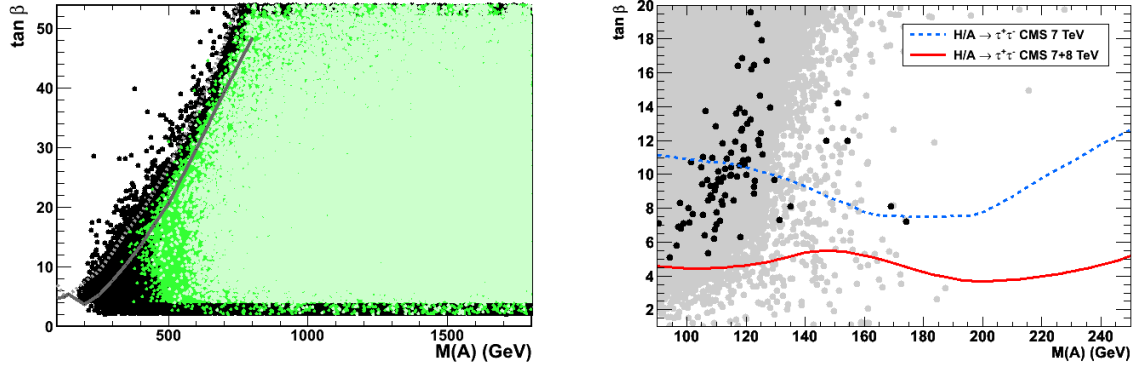


Figure 3.1: Allowed pMSSM parameter sets in the M_A - $\tan\beta$ -plane (left). The black dots represent accepted points consistent with the LEP exclusion of $M_h > 114$ GeV. Dark and light green points include the mass and decay rate measurements of the LHC experiments at 90% and 68% C.L., respectively. The exclusion limit from the direct search of $A^0/H^0 \rightarrow \tau\tau$ is demonstrated by the black line. In the right plot the allowed parameter space in the $\tan\beta$ - M_A -plane assuming the observed state to be the H^0 boson is represented by the grey dots. Including flavour physics and dark matter measurements put more stringent constraints as depicted by the black dots. In red the combined 7 TeV and 8 TeV CMS $A^0/H^0 \rightarrow \tau\tau$ exclusion limit is demonstrated. Taken from [85].

3.2 Direct Searches for Neutral MSSM Higgs Bosons

LEP Experiments

The four LEP experiments searched for MSSM Higgs bosons analysing e^+e^- collision data recorded at centre-of-mass energies between 91 GeV and 209 GeV. In Run1 ($\sqrt{s} = 91$ GeV) data corresponding to an integrated luminosity of 125 pb^{-1} was collected, while the Run2 ($\sqrt{s} = 133 \text{ GeV} - 209 \text{ GeV}$) data corresponds to 2.4 fb^{-1} . Higgs production via *Higgs-strahlung* and *pair production* are accessible. In *Higgs-strahlung* production processes the Higgs is accompanied by a Z boson. Depending on the decay modes of the Higgs and Z boson the collaborations searched for different event topologies, like $b\bar{b}$ final states or leptonic topologies. Higgs decays into quark and tau pairs are taken into account. All possible Z decays are considered, i.e. leptonic, hadronic and invisible ($Z \rightarrow \nu\bar{\nu}$). This leads to a variety of final states analysed. A summary is presented in [60]. Furthermore, Higgs cascade decays are considered in which a Higgs boson decays into two lighter Higgs bosons. Depending on the assumed benchmark scenario this can be either $A^0 \rightarrow h^0h^0$ (CP-conserving) or $h^0 \rightarrow A^0A^0$ (CP-violating). For Higgs pair production, i.e. $e^+e^- \rightarrow A^0h^0$, the di-tau and $b\bar{b}$ final states as well as cascade decays, e.g. $A^0h^0 \rightarrow h^0h^0h^0$ are investigated. No excess of data is observed w.r.t. the SM prediction. Thus exclusion limits exploiting the Frequentist approach, using the log-likelihood ratio as test statistic, are set. In Figure 3.2 model independent limits are presented. An upper bound is set on a scaling factor, S_{95} , defined as the ratio between the largest cross section consistent with data, σ_{max} , and a reference cross section, σ_{ref} . The latter depends on the production mechanism. For final states sensitive to *Higgs-strahlung* production the

reference cross section is taken as the SM prediction on Higgs production, while for pair production the MSSM Higgs production is considered. Details can be found in [60]. The left plot outlines the combined results and the di-tau final state results are presented in the right plot.

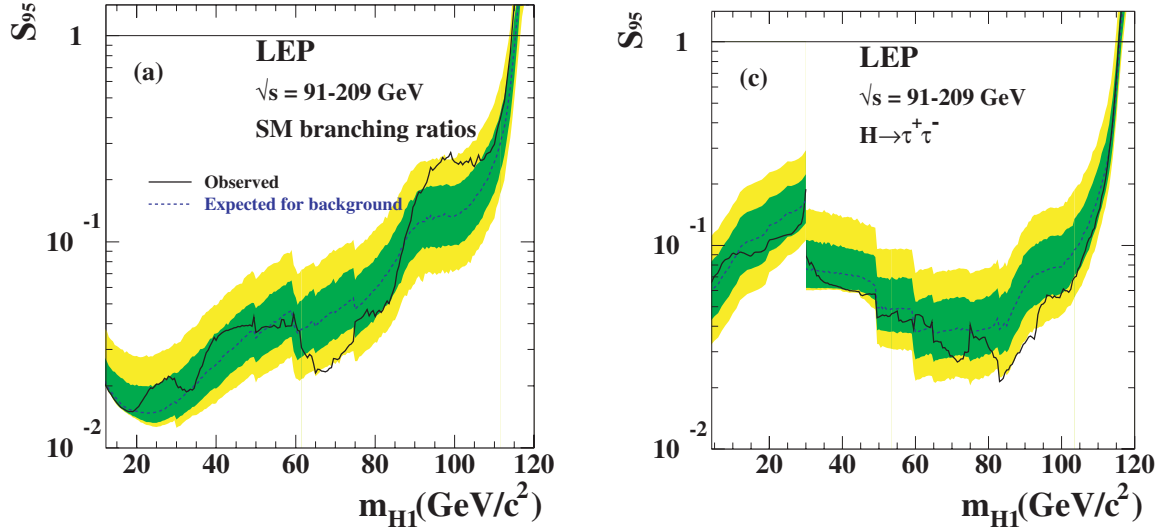


Figure 3.2: Upper bound on the scaling factor, S_{95} , as a function of the Higgs mass for the combined (left) and di-tau (right) LEP analyses [60]. The background only expectation, i.e. the SM, is represented by the blue dotted line with one and two sigma bands shown in green and yellow, respectively. The observed limit is shown by the black solid line.

From this, limits in different benchmark scenarios can be derived. Many different benchmarks were considered, like m_h^{\max} with no and maximal mixing, gluophobic or small- α_{eff} scenarios. In the context of this thesis the most relevant one is the interpretation within the CP-conserving m_h^{\max} scenario presented in Figure 3.3 in the M_A - $\tan\beta$ -plane.

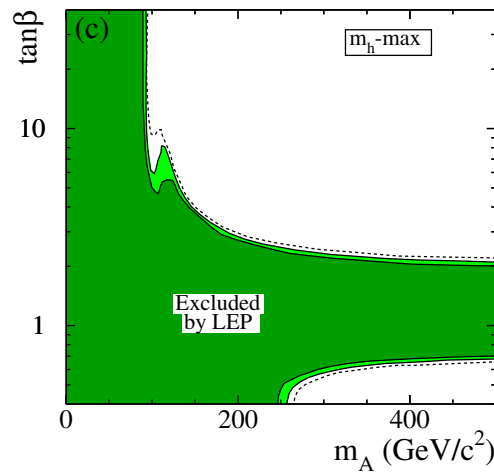


Figure 3.3: Observed exclusion limit at 95% C.L. (light-green) and 99.7% C.L. (dark-green) in the M_A - $\tan\beta$ -plane for the CP-conserving m_h^{\max} scenario. The expected exclusion limit is marked by the dashed lines [60].

Tevatron Experiments

The Tevatron experiments, CDF and DØ, performed searches for neutral MSSM Higgs bosons decaying into $b\bar{b}$ and $\tau^+\tau^-$ using data from $p\bar{p}$ -collisions at $\sqrt{s} = 1.96$ TeV. The most stringent limits are obtained from the di-tau analysis, which uses 1.8 fb^{-1} (CDF), and 2.2 fb^{-1} (DØ) [90] of data. Both semi-leptonic and fully-leptonic decays (only $e\mu$ channel) of the two tau leptons are investigated. CDF takes b-associated and gluon-fusion production mechanisms into account, while DØ only considers gluon-fusion. The exclusion limit is based on the invariant di-tau mass. The full shape is taken into account. Limits are set based on the modified Frequentist approach using the log-likelihood ratio as test statistic. In addition a *Bayesian approach* has been performed, but yields comparable results. Details on the latter can be found in [90]. The 95% C.L. exclusion limit on the cross section times branching ratio is shown in Figure 3.4 (left) as a function of M_A . This can be interpreted in the m_h^{max} scenario. Figure 3.4 (right) presents the limit in the M_A - $\tan\beta$ -plane assuming the m_h^{max} scenario.

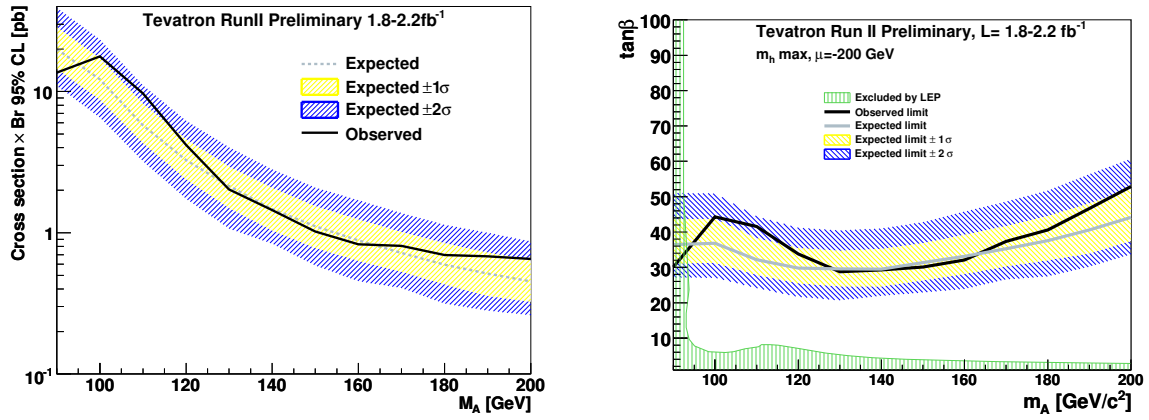


Figure 3.4: 95% C.L. exclusion limit on cross section times branching ratio for $\phi \rightarrow \tau\tau$ versus M_A (left). The solid line represents the observed limit, while the dashed line shows the expected sensitivity. The yellow and blue dashed areas mark the one and two sigma bands, respectively, of the expected limit. In the right plot the interpretation within the m_h^{max} scenario is presented as 95% C.L. exclusion limit in the M_A - $\tan\beta$ -plane. The region above the black solid line can be excluded at 95% C.L. The same colour scheme is applied. In addition the LEP exclusion is illustrated by the green solid line [90].

The search in the $b\bar{b}$ final state is based on 2.6 fb^{-1} (CDF) and 5.2 fb^{-1} (DØ) [91]. It is performed in the Higgs boson mass range between 90 GeV and 300 GeV. Final states with three or more b-tagged jets are taken into account. As in the di-tau analysis, the limit and combination is based on the modified Frequentist approach using the log-likelihood ratio as test statistic. Figure 3.5 shows the 95% C.L. exclusion limit on the cross section times branching ratio versus M_A (left) and the limit in the context of the m_h^{max} scenario in the M_A - $\tan\beta$ -plane (right). In the model independent limit excesses of 2.5σ at $M_\phi = 120$ GeV and 2.6σ at $M_\phi = 140$ GeV are observed. After taking into account the *look elsewhere effect* (for details see [92]) both excesses reduce to $\sim 2\sigma$, and thus no hint for new physics is obtained.

LHC Experiments

The multipurpose experiments, ATLAS and CMS, at the LHC have performed searches for neutral MSSM Higgs bosons as well. Both experiments investigated the di-tau final state. CMS also considered the $b\bar{b}$ final state, while ATLAS included the di-muon final state. The most sensitive search is the one in the di-tau channel [93, 94]. ATLAS uses 4.7 fb^{-1} of 2011 data taken at $\sqrt{s} = 7$ TeV. CMS exploits the 2011 dataset as well corresponding to 4.9 fb^{-1} . The ATLAS collaboration analysed the fully-leptonic ($\tau_e\tau_\mu$), the semi-leptonic ($\tau_{\text{lep}}\tau_{\text{had}}$) and the fully-hadronic ($\tau_{\text{had}}\tau_{\text{had}}$) final states. CMS only considers the

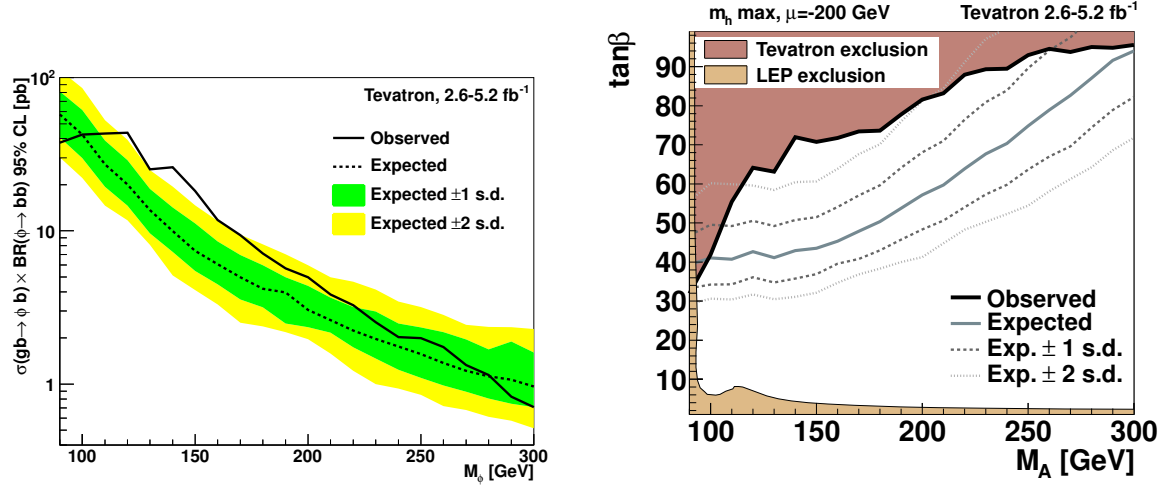


Figure 3.5: 95% C.L. exclusion limit on cross section times branching ratio for $\phi \rightarrow b\bar{b}$ versus M_A (left). The solid line represents the observed lower bound, while the dashed line shows the expected sensitivity. The green and yellow areas mark the one and two sigma bands, respectively, of the expected limit. In the right plot the interpretation within the m_h^{\max} scenario is presented as 95% C.L. exclusion limit in the M_A - $\tan\beta$ -plane. The black line shows the boundary of the observed exclusion limit, while the brownish area demonstrates the excluded area. The light dark line presents the expected sensitivity with the one and two sigma band represented by the dark and light dashed lines, respectively. In addition the LEP exclusion limits are demonstrated by light brown area [91].

first two. Both analyses are categorised into a b-vetoed, i.e. no selected b-tagged jet, and a b-tagged, i.e. at least one b-tagged jet, channel, which are combined in the limit. These two categories are sensitive to different production mechanisms, i.e. gluon-gluon fusion and b-associated production. Each analysis is based on a maximum likelihood fit of the invariant di-tau mass distribution. Both collaborations have developed advanced mass reconstruction algorithms to partially reconstruct the energy components of the neutrinos from the missing transverse energy. Details can be found in [95, 96]. Since no deviations from the background expectation is observed, exclusion limits based on the CL_s method are set. Figure 3.6 presents the 95% confidence level exclusion limit in the M_A - $\tan\beta$ -plane in the context of the m_h^{\max} scenario obtained by the ATLAS (left) and CMS (right) experiments. The LEP exclusion is shown as well by the dashed contour and the green area, respectively.

To allow an easy interpretation in different benchmark scenarios, the ATLAS collaboration also provides model independent limits set on the cross section times branching ratio. This is shown in Figure 3.7 for the gluon-gluon fusion and b-associated production, respectively. No deviation is observed either. For a given mass hypothesis all cross sections larger than the observed limit can be excluded. At high masses ($M_\phi \cong 400$ GeV) cross sections times branching ratios above $\sigma \sim 0.3$ pb can be excluded for both production mechanisms.

ATLAS has extended its range of searches by the di-muon final state. As pointed out in Figure 2.7 the branching ratio of $\phi \rightarrow \mu\mu$ is about two orders of magnitude lower than for the di-tau final state. However, the mass resolution is much better, and thus this search contributes to the low mass sensitivity. In Figure 3.7 the exclusion limit on the cross section times branching ratio obtained from the $\sqrt{s} = 7$ TeV data analysis is presented. Compared to the di-tau analysis a slightly higher integrated luminosity could be exploited. As predicted the excluded cross section is about two orders of magnitude lower than in the $\tau\tau$ final state.

CMS also investigated the $b\bar{b}$ final state using $2.7 - 4.8 \text{ fb}^{-1}$ of 2011 data [97]. The search was performed on 3 b-tagged jet final states, considering both the fully-hadronic and the semi-leptonic decays of the b-quarks. For the latter, only decays into muons are taken into account. In the fully-hadronic

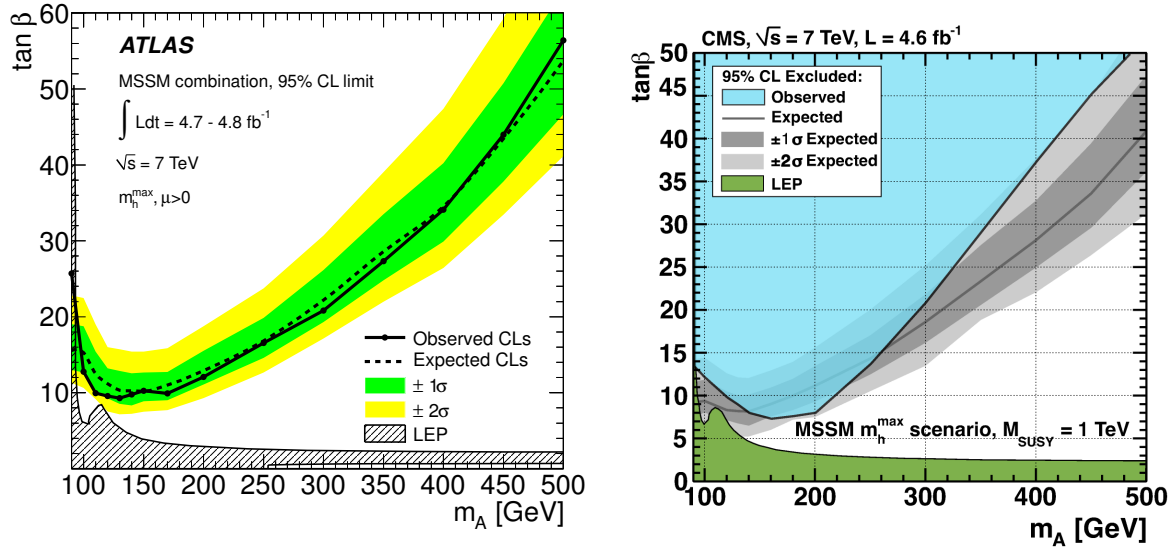


Figure 3.6: 95% C.L. exclusion limit of $\phi \rightarrow \tau\tau$ in the M_A - $\tan\beta$ -plane. The m_h^{\max} benchmark scenario is assumed. In the left figure the ATLAS result is presented, while the CMS exclusion is illustrated in the right figure. The solid black line represents the observed limit, while the dashed line shows the expected sensitivity. The green and yellow or light and dark grey areas mark the one and two sigma bands, respectively, of the expected limit. The blue area in the right plot flag the excluded parameter space at 95% C.L. In addition the LEP exclusion limits are demonstrated by the dashed and green area, respectively [93, 94].

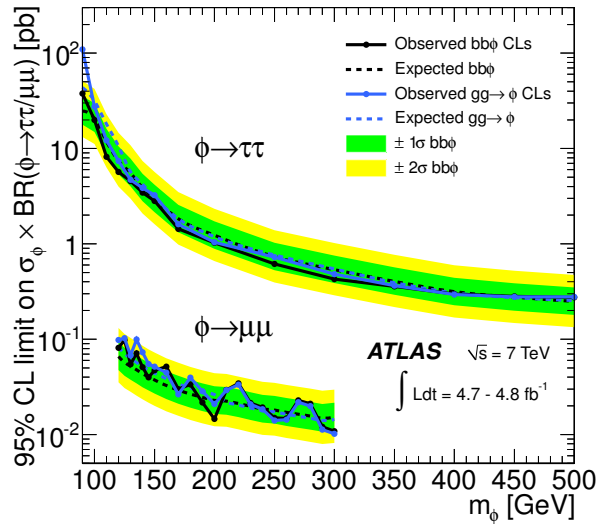


Figure 3.7: 95% C.L. exclusion limit on $\sigma_\phi \times \text{BR}(\phi \rightarrow \tau\tau/\mu\mu)$ as a function of the tested Higgs mass, m_ϕ . The black and blue dashed curves present the expected limit for b-associated and gluon-fusion production, respectively. The green and yellow bands represent the one and two sigma bands. The observed limits are marked by the solid lines. Limits for the di-tau channel are shown by the upper curves, while the lower ones summarise the di-muon final state [93].

analysis a χ^2 -fit of the invariant mass of the two highest- p_T b-jets is performed to obtain the limit. A binned likelihood fit is performed in the semi-leptonic analysis. No deviation from the background hypothesis assuming the SM prediction is observed and the exclusion limits are combined using the CL_s method. The model independent limit on the cross section times branching ratio is presented in

Figure 3.8 (left). Its interpretation in the m_h^{\max} scenario is shown in the right plot.

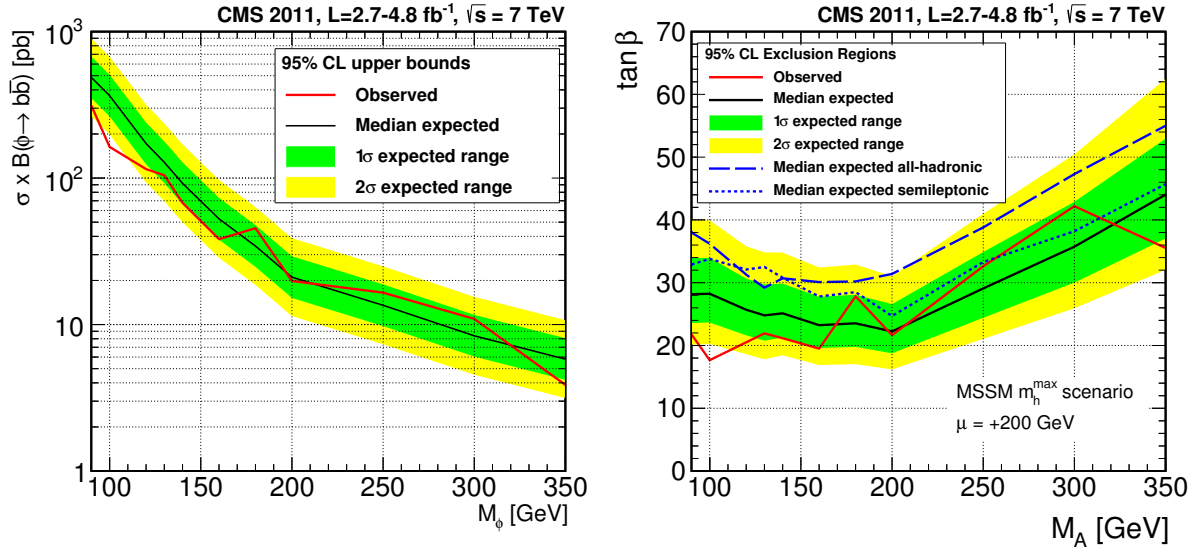


Figure 3.8: 95% C.L. exclusion limit on cross section times branching ratio for $\phi \rightarrow b\bar{b}$ versus M_ϕ (left). The red line represents the combined observed limit, while the black line shows the expected sensitivity. The green and yellow areas mark the one and two sigma uncertainty on the expected limit, respectively. In the right plot the interpretation within the m_h^{\max} scenario is presented as 95% C.L. exclusion limit in the M_A - $\tan\beta$ -plane. In blue the sensitivity of each sub-channel is demonstrated [97].

3.3 Indirect Constraints on Z' Bosons

Like for the MSSM Higgs sector, constraints from low energy experiments restrict the phase space of Z' bosons and put limits on either the mass or the mixing angle, accordingly. Severe constraints arise from Z measurements, both at and above the Z pole. High precision measurements at the Z pole put limits on the mixing angle, ϕ , while the mass remains unbound. If a Z' boson exists the mixing with the SM Z boson will change the couplings of the latter as pointed out in Section 2.6.1. A shift of the couplings would propagate to $\sin^2 \theta_W^{\text{eff}}$, and thus an upper bound on $|\phi|$ of a few 10^{-3} [29] can be derived from global fits of electroweak observables by LEP. The fit of the leptonic partial decay width, $\Gamma_{\ell\ell}$, and the leptonic mixing angle, $\sin^2 \theta_{\text{lepton}}^{\text{eff}}$, by LEP and SLD [98] is shown in Figure 3.9 (left). The prediction by the SM is indicated by the yellow band. In the right plot a comparison of measured values of SM observables w.r.t. their SM prediction is shown.

Measurements above the Z pole give rise to severe constraints on the couplings and the mass, while the limit on the mixing angle is rather low. The additional fermionic coupling term $\bar{f}\gamma_\mu(v_{f_{Z'}} - a_{f_{Z'}})fZ'^\mu$ affects the *forward-backward asymmetry*, A_{FB}^f , of fermionic scattering. Since no significant deviation from the SM is observed by the LEP experiments [98] 95% C.L. limits were put on $M_{Z'}$ in different models [98] which are summarised in Table 3.1. LRM and SSM models were investigated as well as specific E_6 models where the mixing angle ϕ is fixed (c.f. Section 2.6.3) and λ is assumed to be one. They correspond to $\phi = 0$ (χ); $\pi/2$ (ψ); $-\arctan \sqrt{5/3}$ (η).

In principle also the process $e^+e^- \rightarrow W^+W^-$ is sensitive to a potential Z' boson by gauge cancellations of the SM amplitudes which restore unitarity, but just at the scale where the new boson enters. The LEP experiments have not reached sufficient precision on the measurement, but LHC and a new linear e^+e^- collider like ILC can put limits from precision measurements of this process. Low energy experiments on the other hand can place constraints on the Z' mass. Left-right asymmetry, A_{LR} , measurements in polarised Møller scattering are sensitive to the effective mixing angle, x_{eff} , which can qualitatively be written as $x_{\text{eff}} = \sin^2 \theta_W^{\text{eff,SM}}(Q^2) + \text{new physics}$. A measurement of the weak mixing angle by the

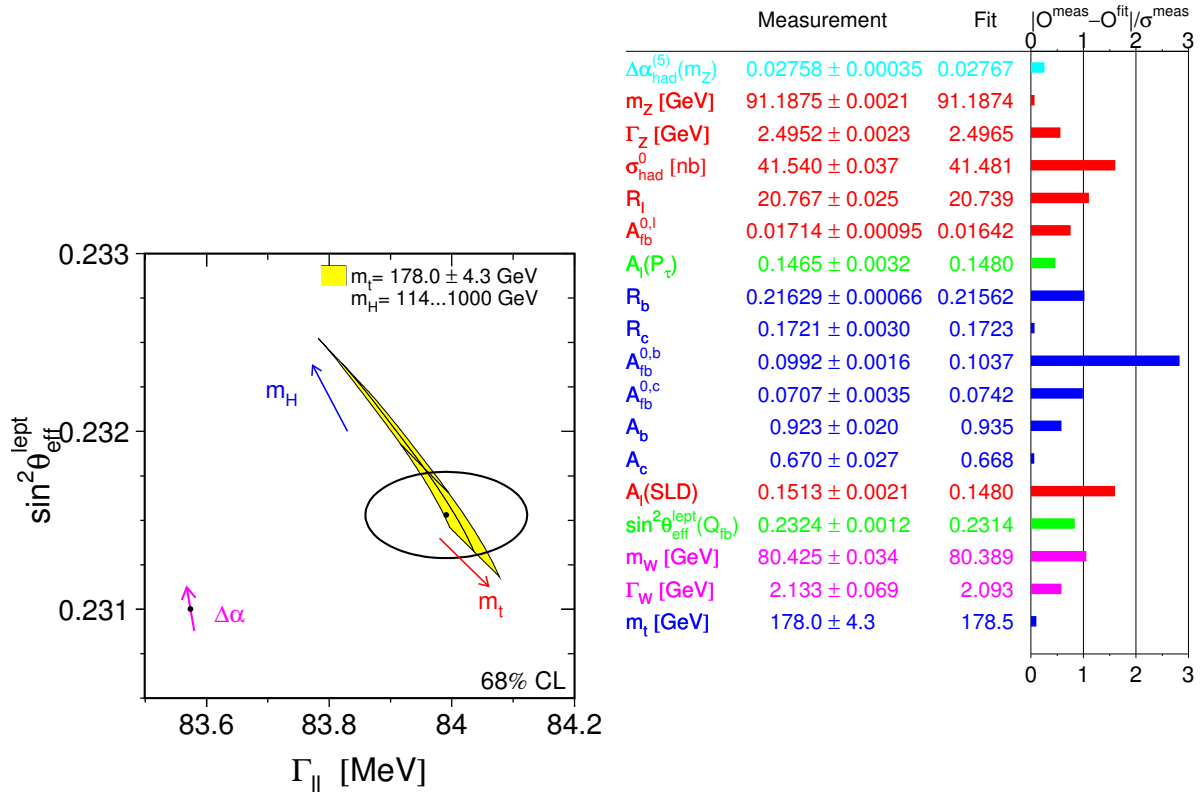


Figure 3.9: Left: Fit of the leptonic partial decay width of the Z boson and the leptonic mixing angle, $\sin^2 \theta_{\text{lepton}}^{\text{eff}}$, obtained from LEP and SLD data. The yellow band indicates the SM prediction. Right: Comparison of predicted and measured SM observables obtained from global fits of electroweak data. Both taken from [98].

	model	χ	ψ	η	LRM	SSM
95% C.L. limit on $M_{Z'}$ [GeV]		785	500	500	825	1760

Table 3.1: Lower limits on the Z' mass at 95% confidence level for E_6 (χ , ψ , η - see text for their corresponding choice of mixing parameters), LRM and SSM models derived from forward-backward asymmetry measurements at LEP and SLD [99]. For the constraints in the E_6 models, $\lambda = 1$ is assumed.

Z' model	SSM	ψ	χ	η
Observed limit [GeV] ($D\bar{O}$, $Z' \rightarrow ee$)	1023	891	903	923
Observed limit [GeV] (CDF, $Z' \rightarrow ee$)	963	851	862	877
Observed limit [GeV] (CDF, $Z' \rightarrow \mu\mu$)	1071	917	930	1071
Observed limit [GeV] (CDF, $Z' \rightarrow \tau\tau$)	399	—	—	—

Table 3.2: 95% C.L. observed limits on $M_{Z'}$ for various Z' models obtained by CDF [103, 105, 106] and $D\bar{O}$ [104] from searches in the di-lepton channels.

E-158 experiment at SLAC yield e.g. a constraint on $M_{Z'}$ in the $E_6 \chi$ model of $M_{Z'_\chi} \geq 1 \text{ TeV}$ [100] at 95% C.L. (assuming the coupling scale factor λ [29] to be one). Further limits arise from *atomic parity violation* (APV) measurements in heavy atoms. The parity violating interactions between the electrons and the nucleus can be parametrised by the weak charge, Q_W , which is model dependent. A hypothetical shift in Q_W thus would indicate an extension of the SM. The best limits are obtained from ^{133}Cs measurements [101] leading to $M_{Z'_\chi} \geq 750 \text{ GeV}$ [102].

3.4 Direct Searches for Z' Bosons

Tevatron Experiments

The Tevatron experiments have searched for new heavy resonances decaying into leptons. Both the CDF and $D\bar{O}$ collaborations investigated the di-electron final state. CDF analysed collision data corresponding to 2.5 fb^{-1} [103] while $D\bar{O}$ analysed 5.4 fb^{-1} [104]. The dominant background arise from Drell-Yan production, $Z/\gamma^* \rightarrow ee$, estimated from MC simulation. In addition electron fakes originating from jets in either QCD di-jet or $W(\rightarrow e\nu)$ +jets events yield a non negligible contribution. Since simulation of the fake-rate is not trivial, they are estimated from data control regions. None of the two experiments observe a significant deviation w.r.t. the SM prediction, and thus set exclusion limits on the cross section times branching ratio as well as on the Z' mass. The limits are derived from the invariant di-electron mass distribution. CDF uses an unbinned likelihood ratio test statistic, while $D\bar{O}$ exploits the log-likelihood ratio test statistic. Figure 3.10 shows the expected and observed 95% C.L. exclusion limits on $\sigma(p\bar{p} \rightarrow Z') \times \text{BR}(Z' \rightarrow ee)$ obtained by the CDF (left) and $D\bar{O}$ (right) collaborations. Predictions of the cross section times branching ratio from several models including E_6 and SSM are shown by the coloured lines. From this a limit on the Z' mass in each model can be derived. The observed 95% C.L. lower limit on the Z' mass for several models are summarised in Table 3.2. The larger dataset analysed by the $D\bar{O}$ collaboration allows to set slightly more stringent limits on both $\sigma(p\bar{p} \rightarrow Z') \times \text{BR}(Z' \rightarrow ee)$ and $M_{Z'}$.

The CDF collaboration extends its search for new heavy gauge bosons by the di-muon [105] and di-tau [106] channels. In the di-muon analysis 4.6 fb^{-1} of collision data were analysed, while the di-tau analysis is performed on 195 pb^{-1} , only. The latter only considers the hadronic final states, i.e. semi-leptonic and fully-hadronic decays of the di-tau system. The dominant backgrounds in both analyses arise from Drell-Yan production and are estimated by MC simulation. Both analyses do not observe a deviation from the SM prediction and set upper bounds on the Z' production cross section. In the di-muon

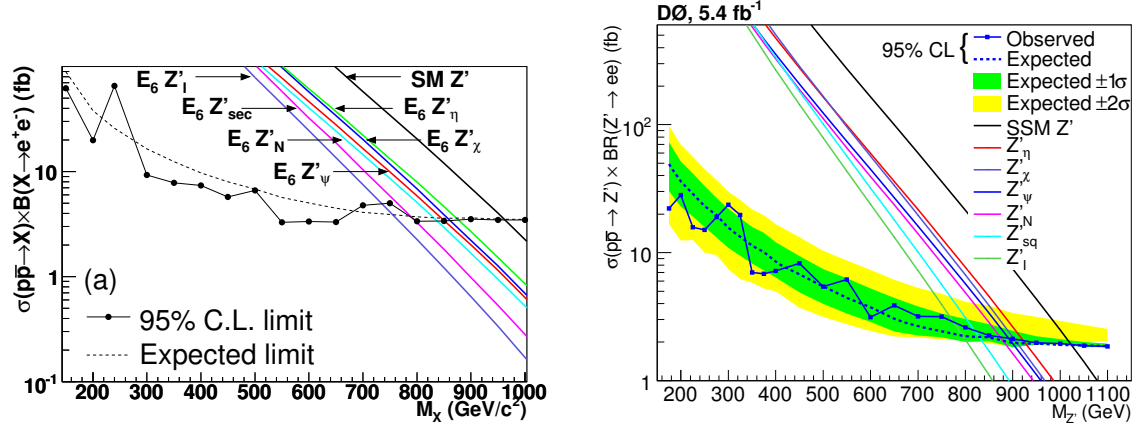


Figure 3.10: 95% C.L. upper bound on $\sigma(p\bar{p} \rightarrow Z') \times \text{BR}(Z' \rightarrow ee)$ depending on the Z' mass obtained by CDF [103] (left) and DØ [104] (right). The expected and observed limits on the cross section times branching ratio are marked by the dashed and solid black (left) and blue (right) lines. The coloured lines mark the theory predictions on $\sigma(p\bar{p} \rightarrow Z') \times \text{BR}(Z' \rightarrow ee)$ for the SSM and various E_6 models.

analysis an unbinned likelihood fit including the theory model of the full event kinematics as well as the muon p_T resolution of each event is used, while in the di-tau analysis a Bayesian approach is chosen (details on this method are given in Section 13.5). Rather than setting limits for specific Z' models a more generic approach was chosen by setting limits on $\sigma(p\bar{p} \rightarrow X) \times \text{BR}(X \rightarrow \tau\tau)$ for scalar and vector particles, which can be assigned to a SSM Z' boson (scalar) or a sneutrino (vector). Figure 3.11 (left) presents the observed and expected cross section limit obtained in the $Z' \rightarrow \mu\mu$ analysis as well as the SSM prediction represented by the blue line. The right plot shows the 95% C.L. upper bound on $\sigma(p\bar{p} \rightarrow X) \times \text{BR}(X \rightarrow \tau\tau)$ for a scalar (solid line) and vector (dotted line) particle hypothesis, as well as the SSM Z' and sneutrino theory prediction. The obtained lower limits on $M_{Z'}$ are summarised in Table 3.2.

LHC Experiments

The search for new heavy gauge bosons is continued at the LHC experiments, which, given the higher centre-of-mass energy and the higher luminosity, can extend the search towards much higher masses than the Tevatron experiments. Both ATLAS and CMS have started to search for deviations from the SM prediction in the light di-lepton channels [107, 108]. ATLAS analysed 5.9 fb⁻¹ of 8 TeV pp collision data in the e^+e^- final state and 6.1 fb⁻¹ in the di-muon channel. CMS combined the analysis of 5.3 fb⁻¹ of 7 TeV and 4.1 fb⁻¹ of 8 TeV data. As mentioned above the dominant background in both final states arise from Drell-Yan production whose shape is taken from MC simulation normalised in a data control region at the Z peak. The data driven approach significantly reduces the impact of systematic uncertainties. In the di-electron channel jet fakes from heavy flavour di-jet or γ +jet processes yield a non negligible background. Both experiments choose a data-driven approach to correct the jet-to-electron fake-rate. ATLAS exploits the *reversed electron identification technique* [109], while CMS measures the fake-rate in a jet enriched data sample and corrects its background simulation. No excess is observed in the invariant di-lepton mass distribution, and thus limits on the production cross section times branching ratio are set using the Bayesian approach [110, 111]. A flat uniform prior is assumed for the production cross section. CMS actually does not set a limit on $\sigma \times \text{BR}$, but rather on the ratio, $R_\sigma = \frac{\sigma_{Z'} \times \text{BR}(Z' \rightarrow \ell^+ \ell^-)}{\sigma_Z \times \text{BR}(Z \rightarrow \ell^+ \ell^-)}$, ($\ell = e, \mu$), of production cross section times branching ratio of a Z' boson to the SM Z boson. Figure 3.12 shows the expected and observed cross section limits obtained by ATLAS (left) and CMS (right). Using the theoretical prediction of the Z' production cross section and branching ratios these limits can be translated to model dependent limits on the Z' mass. Table 3.3 summarises the limits on $M_{Z'}$ in the SSM and various

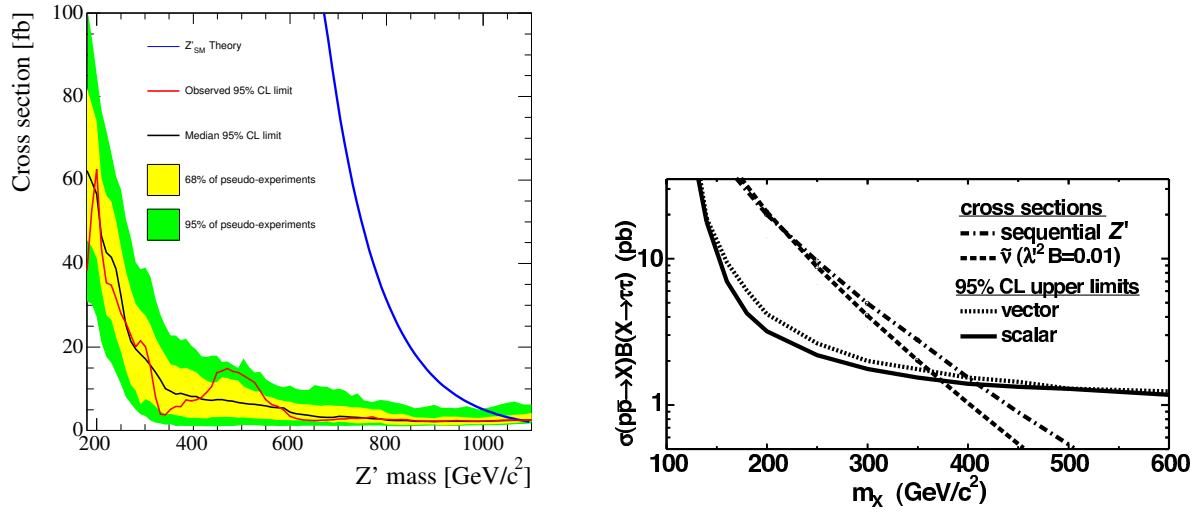


Figure 3.11: Left: Upper bound on the production cross section of Z' bosons as a function of the Z' mass obtained in the di-muon analysis [105] by the CDF collaboration. The expected and observed 95% C.L. exclusion limits are marked by the red and black line, respectively. The theory prediction assuming SM couplings are presented by the blue line. Right: Upper bound on production cross section times branching ratio for scalar and vector particle hypotheses in the di-tau channel [106] marked by the solid and dotted lines, respectively. Theory predictions assuming a Sequential Standard Model Z' and a sneutrino are shown by the dashed lines.

E_6 models.

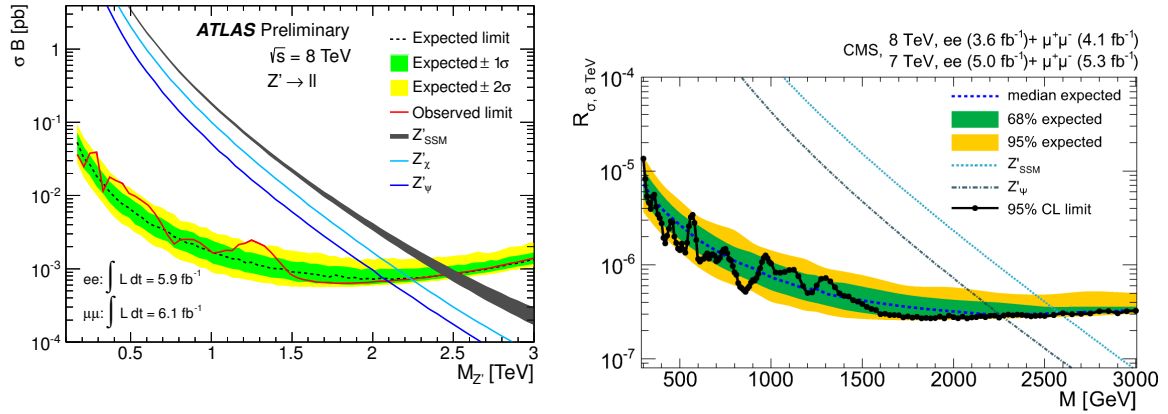


Figure 3.12: Left: 95% C.L. exclusion limit on $\sigma(pp \rightarrow Z') \times \text{BR}(Z' \rightarrow \ell\ell)$ obtained by the ATLAS experiment [107] as a function of $M_{Z'}$. The expected sensitivity is represented by the black dotted line with the one and two sigma bands shown in green and yellow, respectively. The red line shows the observed limit. Predictions by theory for the SSM (including theory uncertainties) and various E_6 models are shown in black and blue. Right: Exclusion limit on the production cross section times branching ratio of Z' bosons w.r.t. the SM Z boson, R_σ , as a function of the Z' mass obtained by the CMS collaboration [108] in the di-lepton channel. The dark blue dotted line shows the expected limit and the black solid line presents the observed limit at 95% C.L. One and two sigma bands are shown in green and yellow, respectively. Theory prediction in the SSM and $E_6 \psi$ model are marked by the black and light blue dotted lines.

Furthermore, both collaborations studied the di-tau final state using 4.6 fb^{-1} (ATLAS) [112] and 4.9 fb^{-1} (CMS) [113] of 7 TeV collision data. Both analyses cover the hadronic as well as the $\tau_e\tau_\mu$ -final states. As far as possible, backgrounds are estimated exploiting data-driven techniques. ATLAS estimates the QCD multijet background, dominant in the fully hadronic and semi-leptonic final states, using the fake-factor method ($\tau_{\text{lep}}\tau_{\text{had}}$) and an unbinned maximum likelihood fit in a data control region ($\tau_{\text{had}}\tau_{\text{had}}$), while CMS exploits the two-dimensional sideband extrapolation method (c.f. Section 10.1.3). Other backgrounds like $t\bar{t}$ or $Z/\gamma^* \rightarrow \ell\ell$ are estimated from data as well. Neither of the experiments observe a deviation from the SM, and thus set limits on $\sigma(pp \rightarrow Z') \times \text{BR}(Z' \rightarrow \tau\tau)$. ATLAS performs a cut-and-count analysis using the Bayesian approach (c.f. Section 13.5), while CMS uses the *effective visible mass* distribution (c.f. Eq. 1 in [113]) and sets the limit based on the modified Frequentist approach. Figure 3.13 shows the obtained 95% C.L. exclusion limits on the product of the production cross section and branching ratio. As explained above this can be translated into a limit on the Z' mass. ATLAS considers the interpretation within the SSM, only, while CMS considers the $E_6\psi$ model in addition. The obtained 95% C.L. lower bounds on $M_{Z'}$ are summarised in Table 3.3. As expected the exclusion limit in the SSM from the di-tau analysis is much lower than the one obtained in the light lepton analyses, but the cross section limits can still be used for interpretations in models predicting generation dependent couplings of the Z' boson.

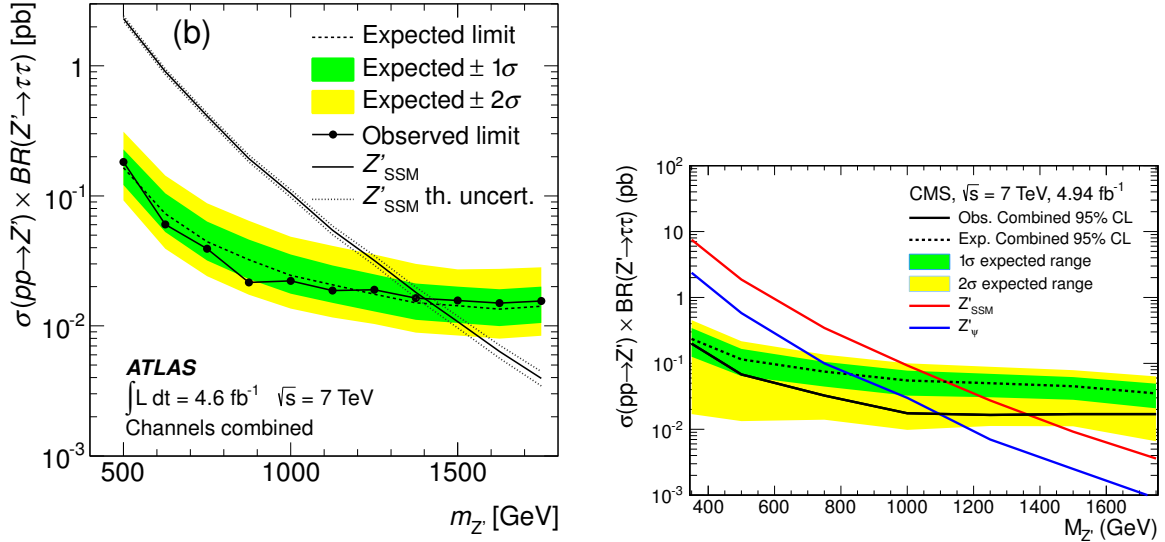


Figure 3.13: 95% C.L. exclusion limit on $\sigma(pp \rightarrow Z') \times \text{BR}(Z' \rightarrow \tau\tau)$ obtained by ATLAS [112] (left) and CMS [113] (right) as a function of Z' mass. The expected sensitivity is represented by the black dotted line with the one and two sigma bands shown in green and yellow, respectively. The black solid line shows the observed limit. Prediction by theoretical calculations for the SSM including theory uncertainties are shown in black (left) and red (right). CMS further present the cross section predictions in the $E_6\psi$ model which is represented by the blue solid line.

The constraints on the parameter space of extended phenomenological models presented in this chapter favour a heavy resonance occurring at the TeV scale, and thus motivate searches in the di-tau final state presented in this thesis. The analyses aim to either discovery new particles not yet excluded or to put more stringent constraints on the allowed parameter space.

Z' model	SSM	ψ	χ	η
Observed limit [GeV] (ATLAS, $Z' \rightarrow \ell\ell$)	2490	2090	2240	2150
Observed limit [GeV] (CMS, $Z' \rightarrow \ell\ell$)	2590	2270	—	—
Observed limit [GeV] (ATLAS, $Z' \rightarrow \tau\tau$)	1400	—	—	—
Observed limit [GeV] (CMS, $Z' \rightarrow \tau\tau$)	1400	1100	—	—

Table 3.3: 95% C.L. observed limits on $M_{Z'}$ for various Z' models obtained by ATLAS [107, 112] and CMS [108, 113] from searches in the di-lepton channels.

4 The ATLAS Experiment

The data analysed in this thesis was recorded by the ATLAS (*A Toroidal LHC ApparatuS*) [10] detector. The ATLAS experiment is installed at the *Large Hadron Collider* (LHC) at CERN⁸ located next to Geneva, Switzerland. It is a proton-proton collider and the largest particle physics experiment built so far. The designed centre-of-mass energy, \sqrt{s} , for proton-proton collisions is 7 TeV per beam, and thus it will provide the highest energies ever reached in a collider experiment. The LHC can also be filled with heavy ions preferably lead nuclei, to extend the physics program under investigation. Energies up to 5.5 TeV per nucleon can be achieved. After a magnetic connection failure in 2008, data-taking has started in 2009 and continued until the end of 2012. The data was taken at centre-of-mass energies of 900 GeV in 2009, up to 8 TeV in 2012. A technical stop in 2013/14 followed to reach the design parameters. However, it has been decided to increase the energy per beam only up to 6.5 TeV due to safety reasons.

A wide area of physics will be investigated by the different experiments installed at the LHC. The two high luminosity experiments, ATLAS and CMS (*Compact Muon Solenoid*) [11], investigate a variety of Standard Model and Beyond Standard Model physics. Both are multipurpose detectors to cope with the requirements of particle identification for searches of rare decays, such like excellent energy resolution for photon detection. The LHCb (*Large Hadron Collider beauty*) [114] experiment is designed to investigate b-quark physics and CP-violation. The ALICE (*A Large Ion Collider Experiment*) [115] experiment was build for studies related to heavy ion collisions, such as understanding the nature of the quark-gluon plasma.

The ATLAS and CMS experiments have been analysing the first data in 2010 mainly for the purpose of confirming the validity of the Standard Model at high energies. Several analyses have been performed for the understanding of the electroweak sector, e.g. W and Z cross section measurements [116]. Given the high energies, large production cross sections of rare processes can be achieved. Thus, for instance top quark processes, have been studied in detail [117]. Furthermore, a better understanding of soft QCD processes is of large interest, see e.g. [118]. This has a crucial impact on the *Monte Carlo* (MC) modelling of all physics processes. Beside the analysis of known processes the focus is on the observation of new physics processes. Originally, the main focus was on the search for the Higgs boson which has been achieved in 2012 as mentioned in Section 2.3.1. However, there are many more analyses searching for new particles in extended theories, in particular in the MSSM. Moreover, multiple analyses focusing on SUSY and other exotic processes are investigated and continuously optimised. An overview of the production cross sections of several physics processes is shown in Figure 4.1. The dominant processes are QCD events which have to be filtered in order to analyse low cross section processes such as Higgs production which have cross sections several orders of magnitude smaller than e.g. di-jet production.

4.1 The Large Hadron Collider

The Large Hadron Collider [9] is a particle collider installed at CERN. It can be operated with proton beams as well as with heavy ions, preferably lead nuclei. The LHC ring is installed in the tunnel of the former *Large Electron Positron* (LEP) collider and extends to 26.5 km in circumference. It consists of eight straight sections and eight arcs. In the arc sections large superconducting dipole magnets are needed to keep the beam on its nominal trajectory. The straight sections are used for acceleration and measurement of the quality of the beam profile and parameters. Starting from a hydrogen source, protons are first accelerated by the *Linac2* to 50 MeV. Next, the *Booster* (PSB) and *Proton Synchrotron* (PS) bring them to 1.4 GeV and 25 GeV, respectively. Furthermore, the structure of the bunch spacing is prepared. Before entering the LHC ring, the proton beams are ramped up to 450 GeV by the *Super Proton Synchrotron* (SPS). The entire accelerator complex installed at CERN is depicted in Figure 4.2.

The aim of the LHC and its experiments is to study particle physics at high energies, giving the design centre-of-mass energy of $\sqrt{s} = 14$ TeV for proton-proton collisions and an energy per beam of $E = 5.5$ TeV per nucleon for heavy ion collisions. Since this analysis deals with the discovery of new

⁸Conseil Européen pour la Recherche Nucléaire

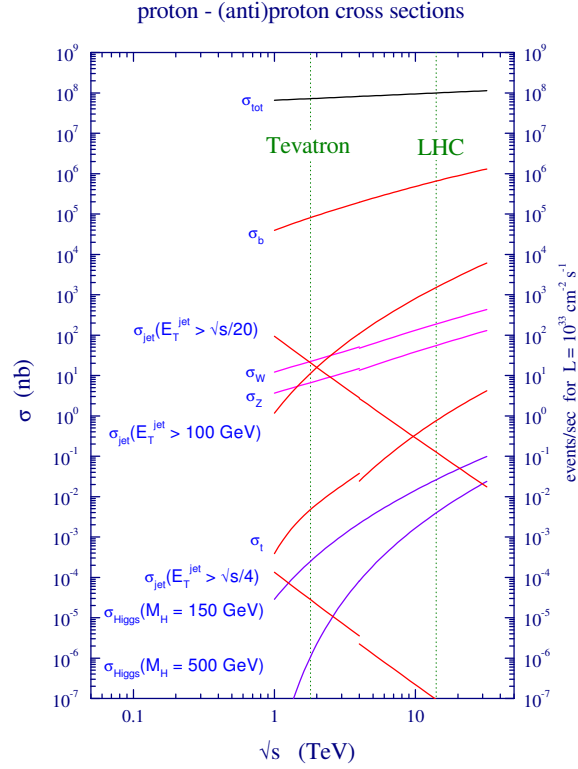


Figure 4.1: Cross sections of Standard Model processes at different centre-of-mass energy. The dashed lines indicate the design collision energy of the Tevatron and LHC colliders [119].

heavy resonances, the focus will be on proton-proton collision data. Running the LHC with protons and not with electrons (positrons) is necessary to reach high energies due to the energy loss, ΔE , by synchrotron radiation which is given for a proton per revolution by:

$$\Delta E = \frac{e^2 \beta^3 \gamma^4}{\epsilon_0 \beta^* 3R}, \quad (4.1)$$

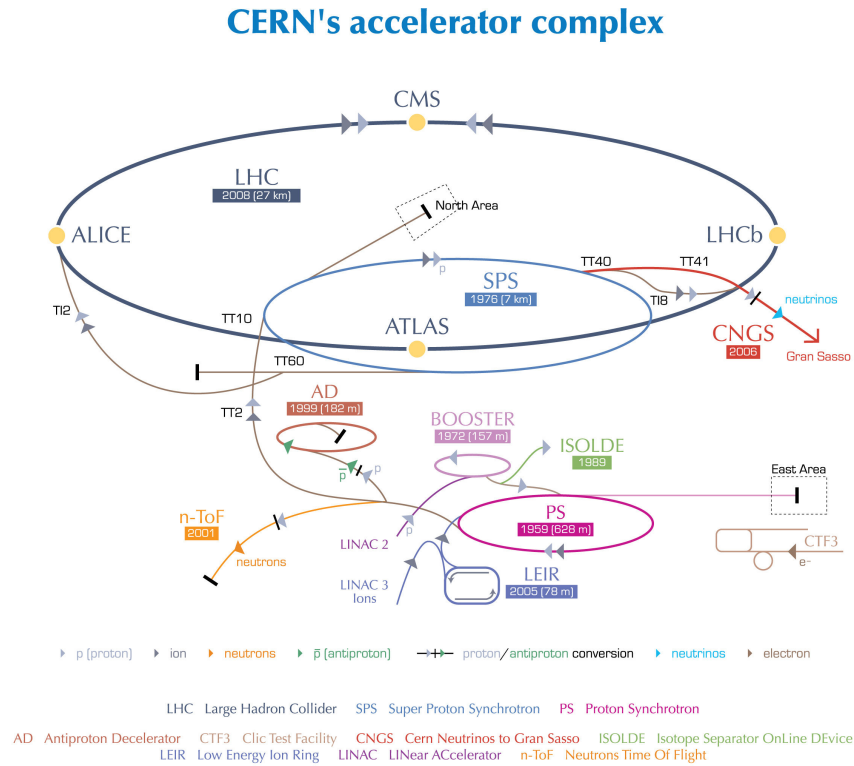
in which ϵ_0 denotes the dielectric constant, R the radius of the ring and $\beta = \frac{v}{c}$ the relativistic velocity. Since the relativistic factor, γ , is proportional to the inverse of the mass of the particle, the energy loss of an ultra-relativistic electron at the same energy is about $1.6 \cdot 10^{13}$ times larger than for a proton. Hence, it is energetically disfavoured to run a ring accelerator with electrons or positrons at the proposed centre-of-mass energy. Each proton beam consists of several proton bunches, each containing up to 1.6×10^{11} protons [121]. Running the LHC in 2012 configuration, each beam was composed of up to 1374 bunches [121]. The mean expected number of events, N_{event} , per second of a specific physics process with cross section, σ_{event} , is given by:

$$N_{event} = L \sigma_{event}, \quad (4.2)$$

with L being the luminosity. For a Gaussian beam profile it is defined as:

$$L = \frac{N_b^2 n_b f_{rev} \gamma}{4\pi \epsilon \beta^*} F. \quad (4.3)$$

In there, N_b and n_b denote the number of particles per bunch and the number of bunches per beam, respectively. Furthermore, it depends on the revolution frequency, f_{rev} , and the relativistic gamma factor, γ . Beam parameters, such as the normalised transverse beam emittance, ϵ , and the beta function at



European Organization for Nuclear Research | Organisation européenne pour la recherche nucléaire

© CERN 2008

Figure 4.2: Accelerator complex at CERN [120].

the collision point, β^* , enter the luminosity calculation as well. The geometrical luminosity reduction factor, F , depends on the crossing angle of the colliding beams at the interaction point. Both high luminosity experiments, ATLAS and CMS, aim for a design luminosity⁹ of $10^{34} \text{ cm}^{-2} \text{ s}^{-1}$. To control the proton beam on its nominal trajectory strong magnetic fields are required. These are provided by superconducting dipole magnets for the nearly circular trajectory, quadrupole magnets for focusing and higher multipole magnets for further optimisation of the beam profile and trajectory. For two proton beams two separate beam pipes are required, since they cannot share the same magnetic field. Since the LHC is installed in the former LEP tunnel, limited space rule out the usage of two distinct proton rings. Hence, a twin-bore magnet design was selected. For this the two beam pipes share the same cryostat and cold mass. The disadvantage of this design is the mechanic and magnetic coupling between the two rings. A magnetic field up to 8.33 T is provided by superconducting magnets. The LHC magnets are build by NbTi Rutherford cables cooled down to 1.7 K using superfluid helium. Given the low temperature of the LHC magnets the heat capacity of the cables is reduced significantly. Hence the energy deposition to cause a quench is reduced.

4.2 The ATLAS Detector

The ATLAS detector is one of the LHC experiments. It is a multipurpose detector designed to provide optimal performance for a variety of physics analyses. For instance for the discovery of the $H \rightarrow \gamma\gamma$ reaction, excellent energy resolution in the calorimeter has been crucial, while for top-quark measurements high secondary vertex reconstruction efficiencies and resolutions are important to properly identify b quark initiated jets. Furthermore, the detector has to sustain large radiation doses. In addition an efficient trigger system is required to deal with the high bunch crossing rate of 40 MHz. A schematic view

⁹Details on the conditions of 2012 data-taking are given below

of the entire detector is displayed in Figure 4.3. Each of the different subsystems providing the necessary information are addressed in the following sections.

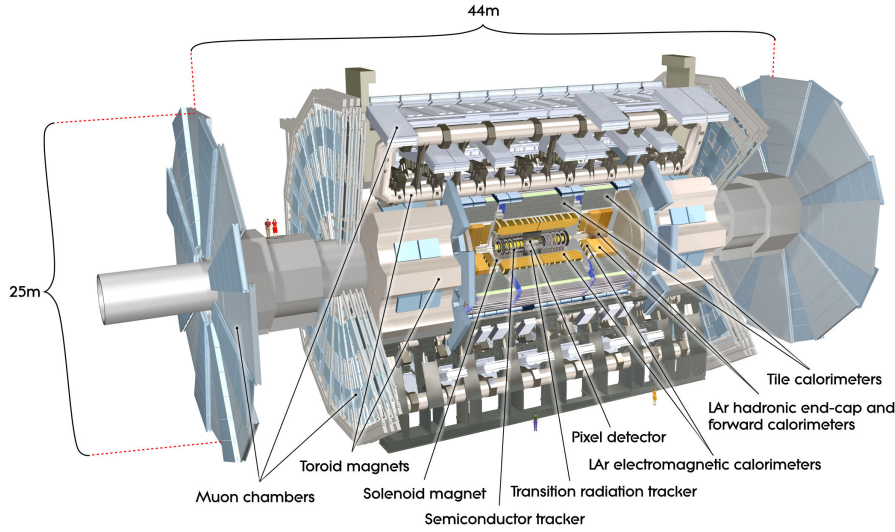


Figure 4.3: Cut-away view of the ATLAS detector [10].

4.2.1 Coordinate System

The origin of the ATLAS coordinate system is defined by the *interaction point* (IP). The z -axis is pointing along the beam pipe and the x - y -plane is transverse. The positive x -axis directs towards the centre of the LHC ring, while the positive y -axis points upwards. The ATLAS detector is split into an A-side (positive z -direction) and a C-side (negative z -direction) by the IP. Given the detector symmetry measured quantities are usually expressed in cylindrical coordinates in which the azimuthal angle, ϕ , is measured around the beam axis in the x - y plane w.r.t. the positive x -axis. The polar angle, θ , is defined with respect to the z -axis. An important quantity in hadron collider physics is the rapidity, y , defined as:

$$y = \frac{1}{2} \cdot \ln \frac{E + p_z}{E - p_z}. \quad (4.4)$$

Inclusive particle production as a function of y is invariant under longitudinal boosts. In the high energy limit, in which the particle mass is small compared to its energy, the rapidity can be approximated by the pseudo-rapidity, η , defined as:

$$\eta = -\ln \tan \frac{\theta}{2}, \quad (4.5)$$

which is used instead of the polar angle in hadron collider experiments. The spacial distance, ΔR , between two reconstructed objects is calculated as:

$$\Delta R = \sqrt{(\Delta\eta)^2 + (\Delta\phi)^2}. \quad (4.6)$$

Since the longitudinal momentum of the colliding partons is not known a priori in proton-proton collisions and the detector acceptance does not allow to reconstruct the momentum component along the beam pipe, transverse observables are defined in the x - y -plane, such as *transverse momentum*, p_T , *transverse energy*, E_T , and *missing transverse energy*, E_T^{miss} , which are frequently used in physics analyses.

4.2.2 Tracking System

Running the LHC in 2012 yields bunch-crossings each 50 ns resulting in about 1000 particles emerging from the interaction point and propagating through the ATLAS detector. Dealing with such high particle

densities while preserving the required momentum and vertex resolution is the aim of the tracking system, called *inner detector*. It is the system next to the beam pipe and consists of three sub-detectors, the pixel and silicon strip trackers and the *Transition Radiation Tracker* (TRT). The high resolution allows to precisely measure impact parameters and vertices. This information is important for tagging of heavy particles, such as τ leptons or B hadrons, which decay at a displaced vertex. This permits efficient identification algorithms for those particles. TRT measurements provide information to better distinct between electrons and charged pions. The layout of the inner detector is sketched in Figure 4.4. The

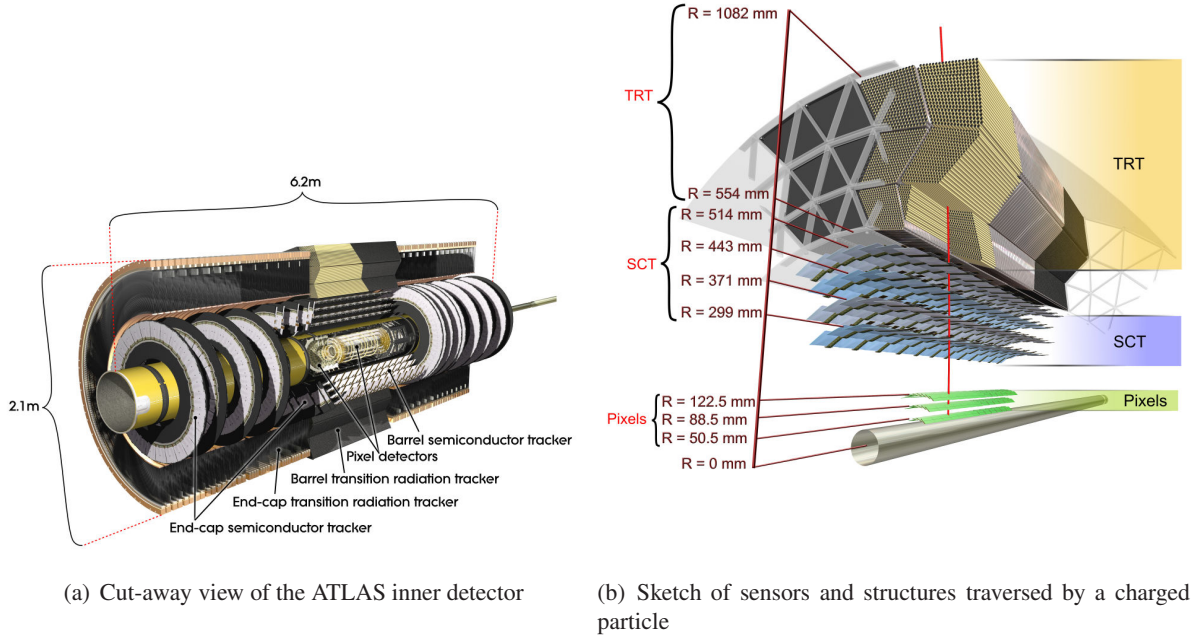


Figure 4.4: ATLAS inner detector [10].

pixel and silicon tracker systems cover an η range up to $|\eta| < 2.5$, while the TRT only covers $|\eta| < 2.0$. It is embedded in a 2 T magnetic field provided by the central solenoid and extends to 5.3 m in length and a diameter of 2.5 m. All sub-detectors are divided into a barrel part and an end-cap part. The resolution of track impact parameters has been measured using cosmic-ray data in 2008 [122]. For high- p_T tracks ($p_T > 30$ GeV) the longitudinal and transverse impact parameter resolutions have been determined to:

$$\begin{aligned}\sigma(d_0) &= (22.1 \pm 0.9) \mu\text{m} \\ \sigma(z_0) &= (112 \pm 4) \mu\text{m}.\end{aligned}\tag{4.7}$$

The transverse momentum resolution of single charged particles with $p_T > 30$ GeV has been evaluated to [122]:

$$\frac{\Delta p}{p} = (4.83 \pm 0.16) \cdot 10^{-4} \frac{p_T}{\text{GeV}}.\tag{4.8}$$

Since cosmic muons traverse the detector from top to bottom the quoted resolutions are only valid for the barrel region.

Pixel Detector

The innermost part of the inner detector is covered by the pixel detector which has to cope with very high radiation levels. The pixel detector provides precise space point measurements of charged particles. It is composed of three barrel layers and three end-cap disks covering the region of radii between 5.05 cm – 12.25 cm in the barrel and 49.5 cm – 65 cm in z -direction in the forward region around the IP. Hybrid silicon pixel sensors are employed. They consist of a silicon sensor and read-out chips. The

active sensor is a junction diode depleted by a bias voltage. A charged particle entering the sensitive depletion region creates electron-hole pairs by ionisation. The electrons drift to the cathode and are collected by tiny bump bonds. The pixel detector is designed to yield a spatial resolution of $10\text{ (10)}\mu\text{m}$ in $R-\phi$ and $115\text{ (105)}\mu\text{m}$ in z -direction in the barrel (forward) region.

Semi Conductor Tracker

The *Semi Conductor Tracker* (SCT) is the second high precision tracking device surrounding the pixel detector. It is based on silicon sensors as well, but segmented in strips. Semiconductors deployed in the SCT are produced with a pitch of $80\mu\text{m}$. Each module consists of four active sensors. Two detectors are wire-bound to achieve a two dimensional measurement of a track. The SCT consists of a barrel part with eight layers located at radii between $30\text{ cm} - 52\text{ cm}$ covering $|\eta| < 1.4$. To provide coverage over the full fiducial volume of the inner detector up to $|\eta| = 2.5$, the barrel part is supplemented by nine disks in the forward region on each side. It has an intrinsic resolution of $17\mu\text{m}$ in $R-\phi$ and $580\mu\text{m}$ in z -direction.

Transition Radiation Tracker

The inner detector is completed by the less precise Transition Radiation Tracker. It is based on straw tubes filled with a gas mixture of 70% Xenon, 27% carbon dioxide and 3% oxide. At the centre a gold-plated tungsten-rhenium wire with a diameter of $50\mu\text{m}$ is located. The wire is set to a high positive voltage. A charged particle traversing through a straw tube ionises the gas. The electrons drift with a constant velocity towards the cathode. Avalanching occurs near the wire due to the high electric field and leads to a measurable signal. Since the drift time is known, the location where the particle entered the straw tube can be calculated. Furthermore, the straw tubes are surrounded by polypropylene fibres/foils in the barrel/end-cap. This allows for an additional particle identification. Charged particles traversing the TRT cross many boundaries with different refraction indices. Ultra-relativistic particles ($\gamma \gtrsim 1000$) emit transition radiation photons at small angles in the direction of the incoming particle. These photons enter the active detector volume and are absorbed by the photoelectric effect due to the high Z of Xenon. Thus, they add an additional energy component to the measured current. The higher amplitude can be used to distinguish electrons and charged pions over a wide p_T range. This information is e.g. exploited by the tau identification, c.f. Section 7.2.6. The TRT provides on average 36 measured hits per track and has an intrinsic resolution of $130\mu\text{m}$ per straw tube. In contrast to the semiconducting tracking detectors the TRT only covers a fiducial volume up to $|\eta| < 2.0$.

Solenoid Magnet System

The inner detector is surrounded by a superconducting solenoid to bend charged particle trajectories. It is build of aluminium-copper-niobium-titanium wires operated at a current of 7.73 kA providing a 2 T magnetic field. The solenoid extends to 2.46 m in diameter and 5.3 m in length. To reduce the amount of material in front of the calorimeter, and thus reducing the deterioration of the energy measurement, the solenoid shares a common cryostat with the liquid argon calorimeter.

Figure 4.5 summarises the several sub-detectors in the inner detector and their coverage in pseudo-rapidity.

4.2.3 Calorimeter System

The calorimeter system is designed to absorb and measure the energy of all particles but muons and neutrinos, both interacting too weakly with matter. One important design goal is a high hermiticity in order to reconstruct missing transverse energy from the negative vectorial sum of energy deposits of all particles. Several components are used in the calorimeter. For high precision measurements of electrons and photons the *electromagnetic* (EM) calorimeter is equipped as first system covering a range of $|\eta| < 3.2$. Hadronically interacting particles are absorbed in the *hadronic* calorimeter. The calorimeter

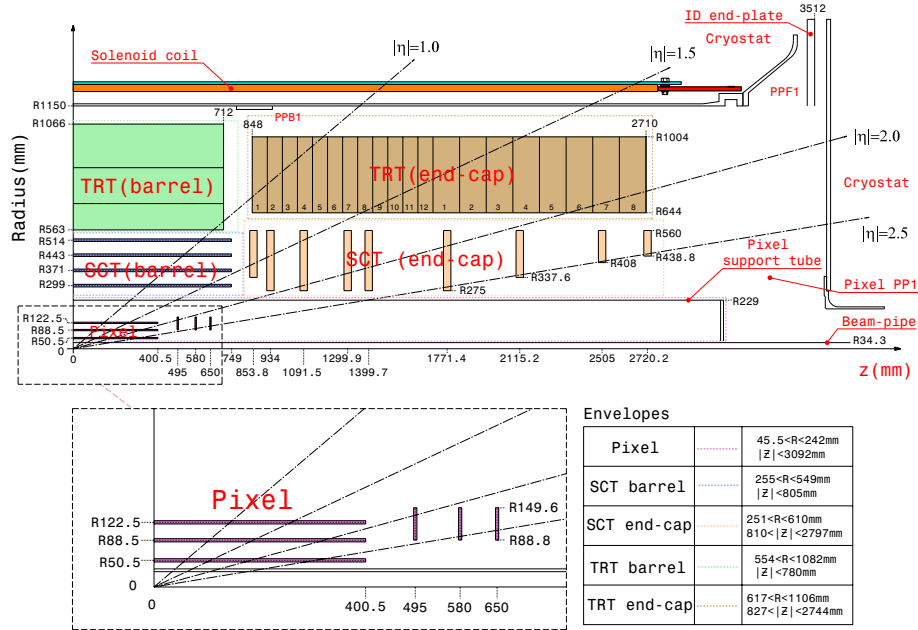


Figure 4.5: Part view of the ATLAS inner detector. Each sub-detector component and its coverage in pseudorapidity is shown [10].

system is completed by the forward calorimeters dedicated for energy measurements up to $|\eta| < 4.9$. Figure 4.6 shows the ATLAS calorimeter system.

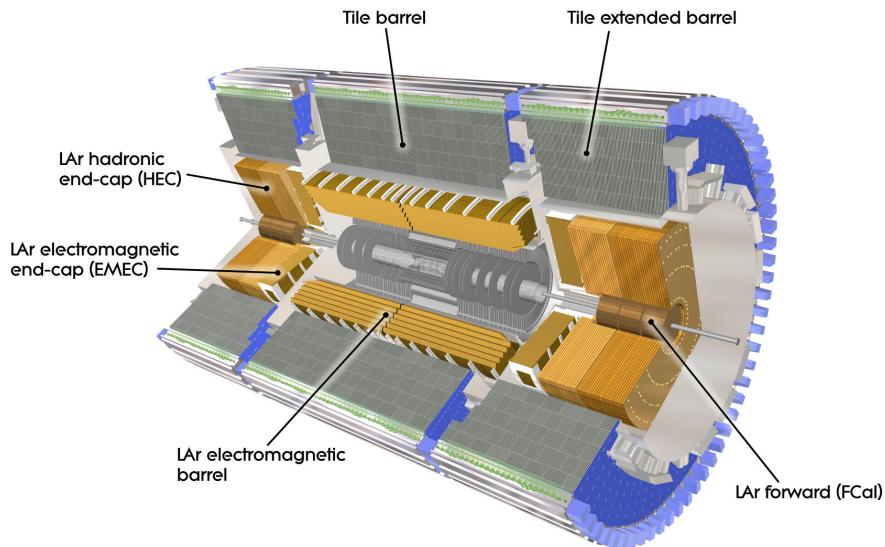


Figure 4.6: Sketch of the ATLAS calorimeter system [10].

Electromagnetic Calorimeter

The electromagnetic calorimeter (ECAL) exploits the *sampling* technology using *liquid argon* (LAr) as active material and lead as absorber. To provide a full coverage in ϕ , avoiding any cracks, an *accordion shape* absorber design as depicted in Figure 4.7 is used. In between copper electrodes on kapton are equipped to collect the signal from the active material. High energy electrons and positrons entering the electromagnetic calorimeter emit photons via bremsstrahlung, while prompt photons produce e^+e^- pairs

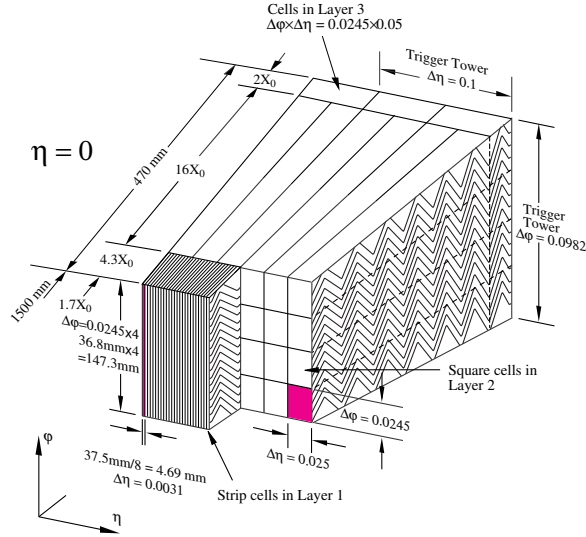


Figure 4.7: Schematic view of a barrel module of the electromagnetic calorimeter. Several layers with different granularity are shown [10].

which themselves emit photons. Thus, an electromagnetic particle shower is formed. Energy deposits by electrons and positrons ionise the argon in the gap. The ionisation electrons are collected in an electric field across the gap. The ECAL is split into a barrel and end-cap part with varying longitudinal sampling size and granularity in η . In the *high precision* region up to $|\eta| < 2.5$ three layers provide at least 24 radiation lengths (X_0), while at larger $|\eta|$ only two layers are installed. The barrel calorimeter is divided into two identical halves separated by a gap of 6 mm at $z = 0$. It provides coverage up to $|\eta| < 1.52$. Two wheels supplement the barrel on each side. Each wheel is subdivided into an inner and outer wheel covering $1.375 < \eta < 2.5$ and $2.5 < \eta < 3.2$, respectively. The overlap between barrel and end-cap calorimeters ensure a smooth transition. The end-cap calorimeters have a thickness of at least $26 X_0$. Material installed in front of the calorimeter, e.g. inner detector, read-out electronics etc., correspond to $2.3 X_0$ at $\eta = 0$. Thus, particle showers can start before the sensitive calorimeter system starts. To recover the missing shower energy a presampler is installed before the first layer of the ECAL. It consists of one active LAr layer extending to 1.1 (0.5) cm in thickness in the barrel (end-cap) region. Figure 4.8

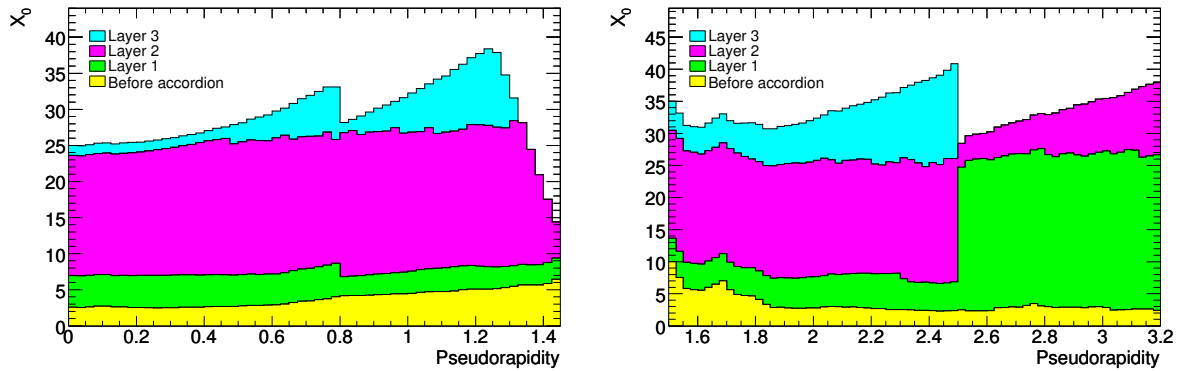


Figure 4.8: Cumulative amount of material in front of and in the ECAL in the barrel (left) and end-cap (right) region. Different layers are colour coded. The amount of material is expressed in terms of radiation lengths [10].

summarises the amount of material in terms of radiation lengths depending on the detector region. The first ECAL layer, referred to as η -layer, has the highest granularity of $\Delta\eta = 0.0031$ which allows to separate two photons, e.g. from neutral pion decays, $\pi^0 \rightarrow \gamma\gamma$. This information can be exploited by

the tau reconstruction in order to classify the tau decay mode (c.f. Chapter 7), but is also crucial for e.g. the $H \rightarrow \gamma\gamma$ analysis. As mentioned above the granularity is coarser at larger pseudorapidities but still sufficient for e.g. reconstruction of E_T^{miss} . The energy resolution of the ECAL is composed of a *noise* term a , a *sampling* term b and a *constant* term c :

$$\frac{\sigma_E}{E} = \frac{a}{E} \oplus \frac{b}{\sqrt{E}} \oplus c. \quad (4.9)$$

The noise term has been determined in an in-situ measurement using random triggers, cosmic and beam splash events as well as calibration data [123]. A good agreement with expected noise [124] is observed. Already in 2004 during test beam measurements [125] the sampling and constant term have been measured. Two different parametrisations of the calibration constants were used and show compatible results. The sampling and constant term have been derived to:

$$\begin{aligned} b &= (10.5 \pm 0.4)\% \cdot \sqrt{\text{GeV}} & \text{and} & & c &= (0.2 \pm 0.1)\% \\ b &= (10.2 \pm 0.4)\% \cdot \sqrt{\text{GeV}} & \text{and} & & c &= (0.2 \pm 0.2)\%. \end{aligned} \quad (4.10)$$

Using 2011 data the constant term was re-evaluated from a Z peak measurement in the di-electron channel [126].

Hadronic Calorimeter

The ECAL is enclosed by the *hadronic calorimeter* (HCAL) designed for energy measurement of jets and hadronically interacting particles, e.g. charged pions. It consists of three different types addressing specific needs. The barrel region is covered by the *Tile calorimeter* which extends to $|\eta| < 1.7$. It is a sampling calorimeter using iron as absorber and plastic scintillator tiles as active material. Hadrons entering the Tile calorimeter initiate showers by either electromagnetic or inelastic hadron interactions. Secondary particles produced excite the scintillator which emits light. The scintillator light is transported to *photo multipliers* (PMTs) via wavelength shifting fibres. The PMTs transform the incoming photons into an electric signal. In the centre, $\eta \simeq 0$, the Tile calorimeter has a thickness of 9.7 hadronic interaction length, sufficient to provide high energy resolution and avoid punch-through to the muon system. The higher radiation density in the forward region makes the Tile design unfeasible, but the intrinsic radiation hard LAr technology is used. The *Hadronic end-cap* (HEC) calorimeter, a copper LAr sampling calorimeter, overlaps with the Tile and covers $1.5 < |\eta| < 3.2$. In the very forward region, the *forward calorimeter* (FCAL) is installed. It consists of three layers, the first equipped with copper as absorber to measure electrons and photons and the remaining two made of tungsten. Each layer has longitudinal channels filled with rods and tubes. The rods are under high voltage while the tubes are grounded. The gaps in between are filled with liquid argon as active material. The overall amount of material in terms of interaction lengths in the HCAL is shown in Figure 4.9.

4.2.4 Muon Spectrometer

At LHC energies, muons are minimal ionising particles, and thus traverse the calorimeters without significant interaction. In order to provide a high precision measurement of muons the outermost part of the ATLAS detector is instrumented with the *muon spectrometer* (MS) shown schematically in Figure 4.10. Its purpose is two-fold: high precision measurement of muon momentum and fast detection for triggering. The momentum of the muon is measured by the bending of the trajectory. A high magnetic field is provided by huge toroid magnets installed radially and symmetrically around the beam pipe. The toroid magnet system consists of three air-toroids, each equipped with eight coils providing an almost circular magnetic field. In the central region up to $|\eta| < 1.4$ the barrel toroid provides a bending power - defined as the field integral $\int B_\perp dl$ along an infinite momentum muon trajectory in which B_\perp is the magnetic field component perpendicular to the muon direction - of $1.5 - 5.5 \text{ Tm}$. For $1.6 < |\eta| < 2.4$ the magnetic field is provided by the end-cap toroid device with a bending power of $1 - 7.5 \text{ Tm}$. In the

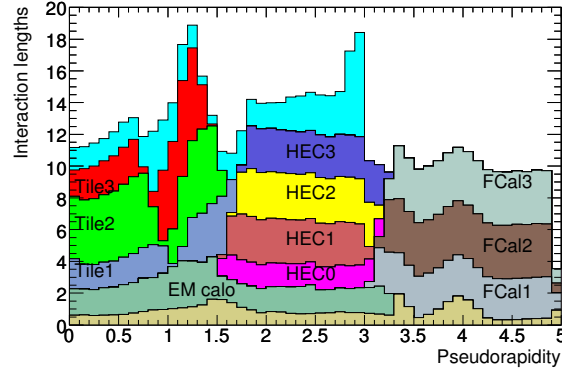


Figure 4.9: Cumulative amount of material in the HCAL. Different layers are colour coded. The amount of material is expressed in terms of hadronic interaction lengths [10].

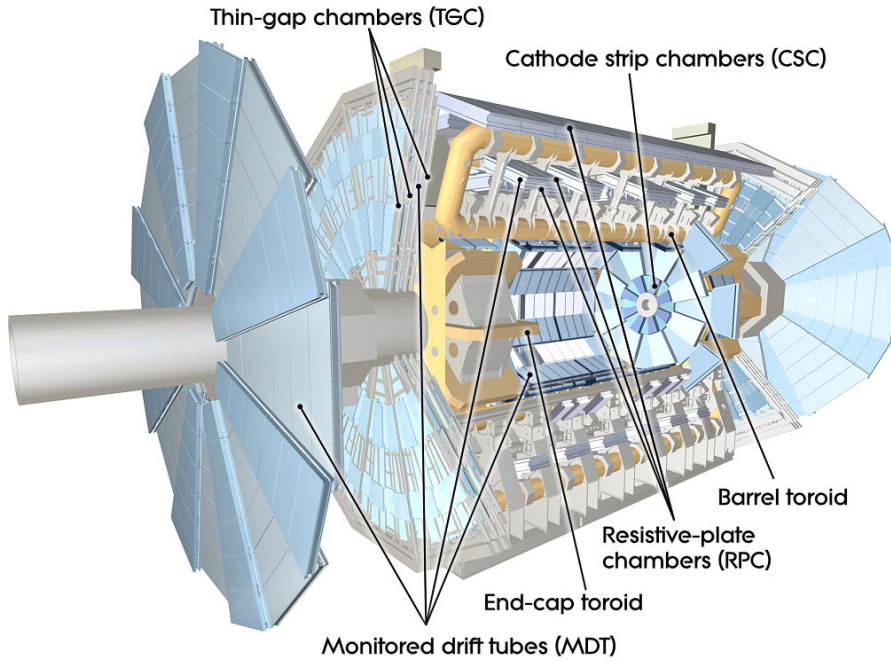


Figure 4.10: Sketch of the ATLAS muon system [10].

intermediate region, $1.4 < |\eta| < 1.6$, these two magnetic fields overlap providing lower bending power than the end-cap toroid coils. To achieve its design goals different detector types are installed which can be classified into high precision momentum and trigger devices. Over the full η range *Monitored Drift Tubes* (MDTs) are installed in the second and third layer while in the first layer they are only assembled up to $|\eta| < 2.0$. MDTs are cylindrical drift tubes made of aluminium and a tungsten-rhenium wire in the centre filled with a gas mixture of argon and carbon dioxide. The MDTs are supplemented by *Cathode Strip Chambers* (CSCs) which provide higher rate capacity and better time resolution. CSCs are multi-wire proportional chambers with tungsten-rhenium anode wires filled also with argon and carbon dioxide, but different mixing ratio. The cathode is segmented into strips. Both, MDTs and CSCs provide precise momentum information, but are too slow for trigger purpose. To cope with the stringent trigger requirements the muon system is equipped with dedicated detectors, *Resistive Plate Chambers* (RPCs) and *Thin Gap Chamber* (TGCs). RPCs are composed of two resistive plates arranged parallel. A high electric field between the two plates is applied causing an avalanche once a muon enters the sensitive volume. An intrinsic time resolution of 1.5 ns is achieved. TGCs are similar to multi-wire proportional

chambers with segments of radially and azimuthal wires. Operating the TGCs at saturation yields a high time resolution of 4 ns. Beside the fast response the TGCs complement the MDT measurement in the bending direction.

4.2.5 Forward Detectors

In addition to the "main" detector components, the ATLAS experiments involves a few forward devices dedicated to luminosity and beam condition measurements. Figure 4.11 outlines the forward detector alignment. The main luminosity detector of ATLAS is the *Cerenkov Integrating Detector* (LUCID)

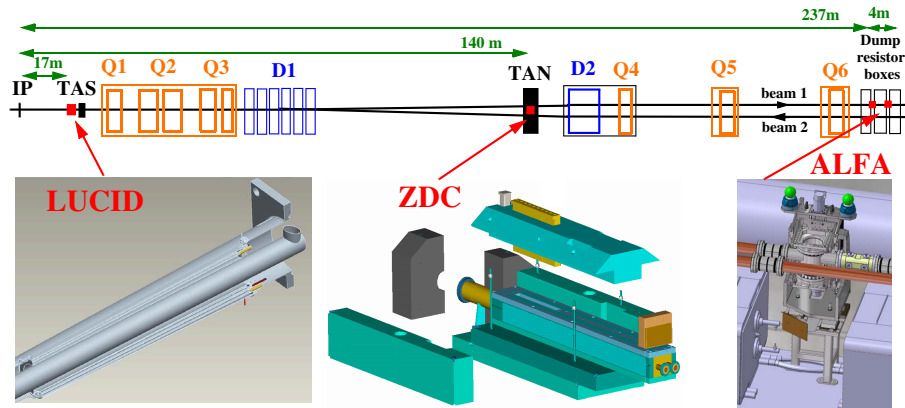


Figure 4.11: Location of the several forward detectors along the beam-line [10].

located at $z = \pm 17$ m and $|\eta| \sim 5.8$. A relative luminosity measurement is provided by measuring inelastic proton-proton scattering. The luminosity measurement is complemented by the *Zero Degree Calorimeter* (ZDC) located even further away at $z = \pm 140$ m, covering very small angles of $|\eta| > 8.3$, and the *Absolute Luminosity For ATLAS* (ALFA) detector. ALFA provides an absolute luminosity measurement used to calibrate LUCID. It is a scintillating fibre tracker inside roman pots located at $z = \pm 240$ m measuring elastic proton-proton scattering [127]. *Beam Condition Monitors* (BCMs) [128] supplement the forward detector collective.

4.2.6 Trigger System and Data Acquisition

The event rate of 40 MHz and a typical event size of a few MB makes it impossible to store all data. To cope with the high event rate a three level trigger system is installed to reduce the event rate to about 200 Hz. It aims to reject minimum bias events while preserving interesting events containing potentially new physics. The trigger system is based on both hardware and software systems. At *level-1* (L1) hardware based decisions are taken exploiting the information of the calorimeters and muon trigger chambers with reduced granularity. Single objects with large transverse momentum, like hadronically decaying taus, muons, jets, electrons, photons and the sum of the transverse energy (to trigger on missing transverse energy) are considered by the trigger algorithms. The L1 decision is based on several thresholds applied on these objects, e.g. on the energy sum in the calorimeters. Beside the pass/fail decision the L1 defines a *region-of-interest* (ROI) which contains information of the accepted objects, the passed threshold and the location in the detector, i.e. η and ϕ . Data accepted by the L1 is held by derandomising buffers, required to avoid any significant dead-time and then shipped to the *readout driver* (ROD). From the RODs the data is passed to the *high-level-trigger* (HLT). The L1 reduces the rate to about 75 kHz and has a latency of $2.5 \mu\text{s}$. The HLT is a software based system consisting of two stages, the *level-2* (L2) trigger and the *event filter* (EF). The L2 trigger exploits the full granularity in the RoIs and places further cuts to reduce the rate down to about 3.5 kHz with a latency of 40 ms. Events accepted by the L2 are handed over to the EF which runs a full event reconstruction executing algorithms close to offline reconstruction. On average this takes about 4 s per event and reduces the final rate to about 200 Hz which

is then written to tape and can be used for physics analysis. During this thesis a new *multivariate* (MV) EF algorithm to trigger on hadronically decaying tau leptons has been developed and used for 2012 data-taking. Therefore, the tau trigger chain is discussed in detail in Section 7.3. Figure 4.12 summarises the ATLAS trigger and data acquisition system.

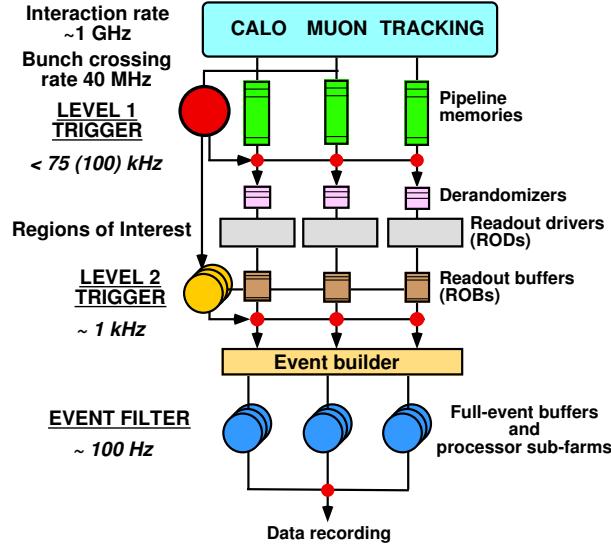


Figure 4.12: Block diagram of the ATLAS trigger and data acquisition system [124].

4.3 Data-Taking in 2012

The LHC was operated in 2012 at a centre-of-mass energy of $\sqrt{s} = 8 \text{ TeV}$ delivering an integrated luminosity of 22.8 fb^{-1} [129]. Most of the data-taking period was operated with 1374 proton bunches per beam and a bunch spacing of 50 ns [121]. The design value of 2808 bunches is planned to be achieved in run-II starting early 2015. ATLAS recorded 21.3 fb^{-1} of data corresponding to a data-taking efficiency of 93%. The integrated luminosity available for physics analyses corresponds to 20.3 fb^{-1} . The total integrated luminosity delivered by the LHC and recorded by ATLAS is shown in Figure 4.13. The peak instantaneous luminosity in 2012 was $7.73 \cdot 10^{33} \text{ cm}^{-2} \text{ s}^{-1}$, while the design luminosity of

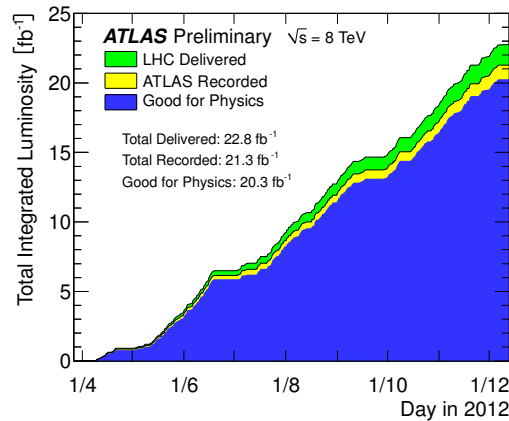


Figure 4.13: Total integrated luminosity delivered by LHC (green) and recorded by ATLAS (yellow) over the 2012 data-taking period [129]. The amount of data suitable for physics analyses is shown in blue.

$10^{34} \text{ cm}^{-2} \text{ s}^{-1}$ [10] is expected to be reached in run-II. However, the average number of interactions per bunch crossing already exceeds the expectation at the design luminosity because of the doubled bunch

spacing of 50 ns. In 2012 an average of almost 40 interactions per bunch crossing was accomplished. The instantaneous luminosity and the average number of interactions per bunch crossing over the data-taking period in 2012 are summarised in Figure 4.14. Table 4.1 summarises the data-taking periods and the

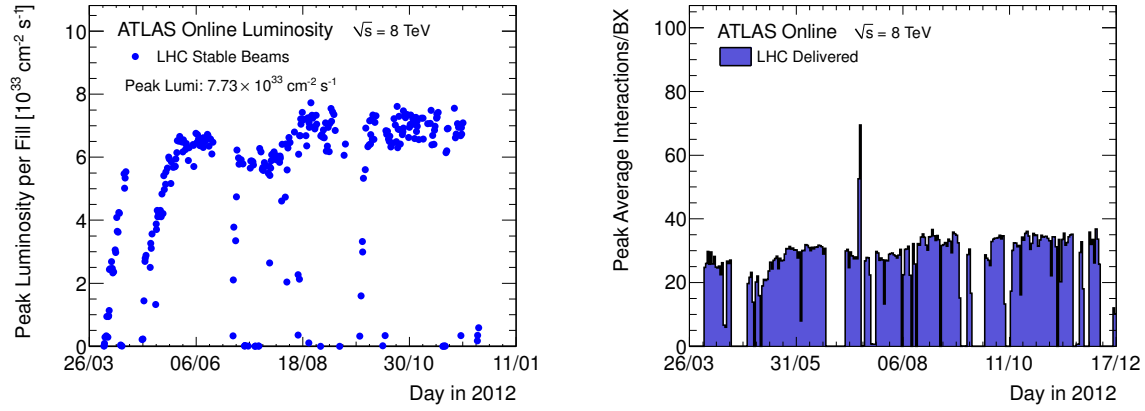


Figure 4.14: Evolution of peak luminosity per fill (left) and maximum number of interactions per bunch crossing (right) during 2012 data-taking [129].

run conditions in 2012. The recorded luminosity by ATLAS for each period including the data-taking efficiency are given as well.

Period	Start	End	Run-number range	Recorded Lumi [pb^{-1}]	Eff. [%]	μ_{max}
A	Apr-04	Apr-20	200804–201556	910	98	30
B	May-01	Jun-18	202660–205113	5594	98	31
C	Jul-01	Jul-24	206248–207397	1643	98	34
D	Jul-24	Aug-23	207447–209025	3598	98	34
E	Aug-23	Sep-17	209074–210308	2863	98	36
G	Sep-26	Oct-08	211522–212272	1404	98	34
H	Oct-13	Oct-26	212619–213359	1655	98	35
I	Oct-26	Nov-02	213431–213819	1149	98	34
J	Nov-02	Nov-26	213900–215091	2941	98	35
L	Nov-30	Dec-06	215414–215643	983	98	36
M	Dec-15	Dec-16	216399–216432	14	97	12

Table 4.1: Summary of pp collision data-taking periods in 2012 by the ATLAS detector. The average number of interactions per bunch crossing is denoted by μ_{max} [130].

5 Monte Carlo Simulation

Monte Carlo (MC) simulation is a key ingredient in particle physics analyses. It provides a crucial method to study and optimise the discovery potential for new physics as well as to study major and minor background processes. Detector simulation models the expected detector response providing output data in the same way as the real detector will do. To get a reliable estimate from the simulation it has to be tuned and compared to collision data. The following sections will first introduce the phenomenological concept behind the generation of physics processes and later discuss the various detector simulation models exploited in the presented analyses.

5.1 Hadron Hadron Interactions

Before entering the discussion on the actual MC simulation, the anatomy of hadron-hadron interactions is introduced. Dynamics of these interactions are described by the underlying SM Lagrangian. For high energy physics the *hard scattering* process is of interest. This involves processes at high energy scales, and thus short distances. Hence, *perturbative QCD* (pQCD) can be applied to calculate the cross sections of these processes. In pQCD the *partons*, i.e. the quarks and gluons, can be treated as free particles interacting with each other. On the other hand, not partons, but hadrons are actually measured by the detector. This is due to the *confinement* property of QCD, which states that at low energies colour charged particles do not exist as free particles, but only colourless particles exist (c.f. Section 2.1). This connects softer processes to the hard process which enter the calculation by gluon emissions in either the initial or final state. These emissions (including QED processes) will be referred to as *initial state radiation* (ISR) and *final state radiation* (FSR). Figure 5.1 displays the principle steps to be considered by calculations of proton-proton collisions.

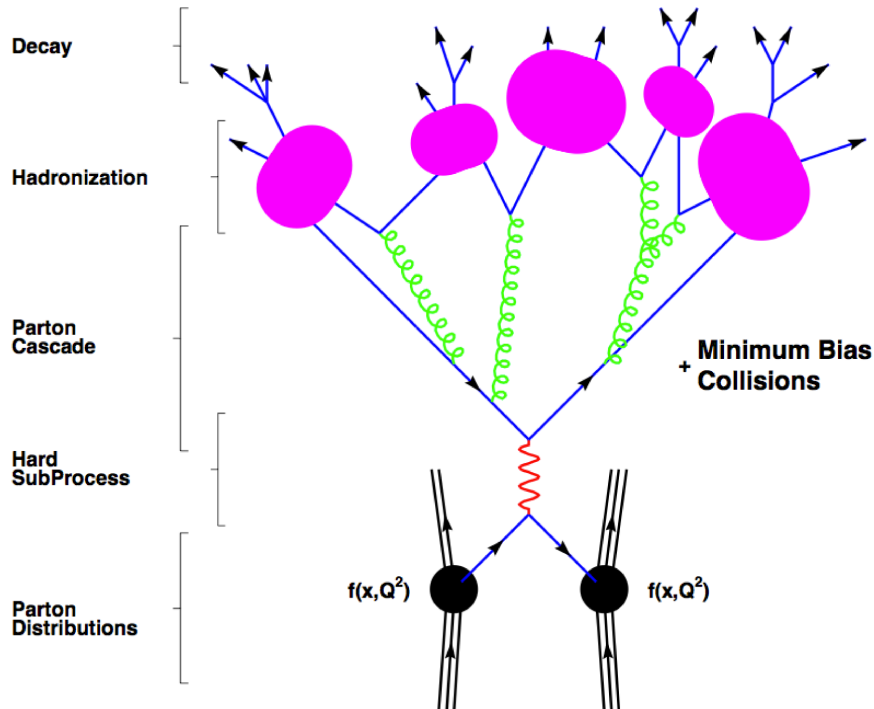


Figure 5.1: Illustration of a hard scattering event taking place at a hadron collider. For simplicity the initial state radiation as well as multiple interactions have been taken out. Taken from [131].

To simplify the discussion here it is assumed that only one parton out of each proton takes part in the hard scattering process. However, there can be multiple interactions per bunch crossing which will be discussed later. Calculations of hadron interactions start from the *differential cross section*, $\hat{\sigma}_{ij}$, for scattering processes of partons of species i and j . The differential cross section can be calculated from

the underlying theory, i.e. pQCD and electroweak theory. To predict the actual *hadronic cross section*, σ , of the scattering process, the differential cross section has to be convoluted with the probability of colliding partons i, j with their respective kinematics. The latter is described by *parton density functions* (PDFs), which can not be predicted by theory, but have to be measured experimentally. The hadronic cross section of the scattering of two partons i, j with momentum fractions x_1, x_2 is then given as:

$$\sigma = \sum_{i,j} \int \int dx_1 dx_2 (f_i(x_1, \mu_F^2) f_j(x_2, \mu_F^2)) \hat{\sigma}_{ij}. \quad (5.1)$$

In there it is assumed that the transverse component of the parton momentum can be neglected. The PDFs depend on the momentum fraction of the parton and the *factorisation scale*, μ_F . As mentioned above the PDFs have to be obtained by experiments, but the dependence on the factorisation scale can be calculated theoretically by the *DGLAP* equations [132, 133, 134] which evaluate the PDFs at a given μ_F . An additional scale enters once higher order QCD corrections are taken into account. Since they introduce large logarithms in the expansion they have to be resummed by *renormalisation*. Thus a dependence on the *renormalisation scale*, μ_R , enters the calculation from remaining finite correction terms. These are non universal and depend on μ_R at which α_S is evaluated. If one would perform the expansion to all orders of α_S the scale dependence would cancel exactly, although this is in practice not feasible. Thus the factorisation and renormalisation scale remain arbitrary, but typically they are chosen such that the remaining logarithms are small. The remaining scale dependence is then treated as systematic uncertainty of the theoretical prediction of the cross section. As shown later in Section 12.3 this will be taken into account in the analysis. Since the partons are colour charged particles they will emit *QCD bremsstrahlung* once they are accelerated, just like for charged particles in QED. These gluon radiations lead to ISR and FSR, and thus to a parton cascade, also called *parton shower*. The remnants of the protons will move on in the beam direction carrying a significant energy fraction of the initial beams. The partons evolving from the interaction will at some point reach an energy scale where they can not be treated by perturbative QCD anymore, but hadronise (c.f. confinement). This hadronisation can only be described by phenomenological models which is beyond the scope of this brief overview (c.f. [135, 136] for further details). Further, multiple interactions can take place at each bunch crossing leading to the so-called *pile-up* discussed below.

5.2 Hadronic Jets

A crucial concept at hadron colliders is the definition of a *jet*. As mentioned above a parton from the hard scattering process will radiate further partons, i.e. gluons and quarks, preferably in the same direction the initial parton moves. This results in a collection of hadrons observed as hadronic jet in the detector. The energy of the initial parton is thus carried by several constituents, such that the jet energy represents approximately the initial energy. To reconstruct jets the hadrons have to be clustered in order to assign them to a jet. Different algorithms differing in the definition of *narrowness* are available. There exist *cone* [137] and *sequential clustering* [138, 139, 140, 141] algorithms. The cone algorithms perform the hadron association by a geometrical matching depending on the η and ϕ of the constituents, while the sequential clustering algorithms are based on the relative difference in p_T .

5.3 Monte Carlo Generators

5.3.1 Matrix Elements

As aforementioned the hard process can be calculated from the underlying Lagrangian using the Feynman rules which lead to the *matrix element* (ME), \mathcal{M} , of the corresponding process. At tree level, i.e. loop contributions are not considered, this can be done in a generic way. However, configurations with soft or collinear partons lead to singularities in the ME. For soft emissions, the momentum of a gluon is much smaller than the momentum of the initial parton. Collinear singularities arise from partons radiated at very small angles. In the perturbative expansion these singularities cancel for inclusive observables

because the *real* emission divergencies are cancelled by their corresponding term in the *virtual* corrections.

5.3.2 Parton Shower

For fixed order matrix element calculations the ME provides only a proper description of the hard process for high energetic and well separated emissions. A common approach to calculate $2 \rightarrow n$ processes, with n final state partons, is to factorise the hard scattering process, e.g. the $2 \rightarrow 2$ process with highest momentum transfer, Q^2 , and emissions. The hard process will be calculated by the ME, while the emissions are handled by the so-called *parton shower* (PS), which models the evolution of partons from the scale associated to the hard process, where partons can be treated as free particles, down to the energy scale where the hadronisation starts and phenomenological models have to be adopted. The fundamental concept of the PS is the splitting probability measuring the likelihood of a parton a splitting into two partons b and c at a given energy scale Q^2 . This splitting probability is calculated exploiting the approximated ME in the soft and collinear limit. The probability is defined by a set of differential equations, the so-called DGLAP equations [132, 133, 134], and can be written as:

$$dP_{a \rightarrow bc} = \frac{\alpha_S}{2\pi} \frac{dQ^2}{Q^2} P_{a \rightarrow bc}(z) dz, \quad (5.2)$$

with z being the energy fraction of parton b w.r.t. the energy of the initial parton a and $P_{a \rightarrow bc}(z)$ the *splitting kernels*. The splitting kernels define the branching probability for a given process, like $g \rightarrow q\bar{q}$ or $q \rightarrow qg$ and are universal functions. Their actual definition can be found e.g. in [136]. The term $\frac{dQ^2}{Q^2}$ in Eq. 5.2 generates the collinear singularity. Soft divergencies arise for $z \rightarrow 1$ in the splitting kernels, except for $g \rightarrow q\bar{q}$. The splitting kernels are used to describe the PS as a series of branchings, which however, is divergent, resulting in total branching probabilities larger than one. This obviously does not provide a sufficient prescription, but rather so-called *Sudakov form factors* [142] are introduced to cover these inconsistencies and build the second component of the parton shower. The Sudakov form factor defines a no emission probability between two energy scales Q_1 and Q_2 . From the law of conservation of probabilities it follows that the probability that no branching occurs can be written as:

$$P_{\text{no branching}} = 1 - P_{\text{branching}}, \quad (5.3)$$

with the probability of a branching occurring in an infinitesimal time scale δQ (which is equivalent to a short scale due to the Heisenberg uncertainty principle) given as:

$$P_{\text{branching}} = \sum_{b,c} \int_z \frac{dP_{a \rightarrow bc}(x)}{dx} dx \delta Q^2. \quad (5.4)$$

Integrating over δQ yields the probability that no emission occurs at the scale Q starting at a high scale Q_{max} . The Sudakov form factor then becomes [136]:

$$F(Q^2, Q_{\text{max}}^2) = \exp \left(- \sum_{b,c} \int_{Q^2}^{Q_{\text{max}}^2} \frac{dQ'^2}{Q'^2} \int_z \frac{\alpha_S}{2\pi} P_{a \rightarrow bc}(x) dx \right). \quad (5.5)$$

The Sudakov form factor modifies the DGLAP equation in Eq. 5.2 which then reads as:

$$dP_{a \rightarrow bc} = \frac{\alpha_S}{2\pi} \frac{dQ^2}{Q^2} P_{a \rightarrow bc}(z) dz \cdot \exp \left(- \sum_{b,c} \int_{Q^2}^{Q_{\text{max}}^2} \frac{dQ'^2}{Q'^2} \int_z \frac{\alpha_S}{2\pi} P_{a \rightarrow bc}(x) dx \right). \quad (5.6)$$

Thus the Sudakov form factor ensures that the probability of a branching is always smaller or equal to one, because a branching of a parton can only occur if it has not occurred yet. The Sudakov form factor can also be seen as an approximation of the virtual corrections arising from loop diagrams. Still missing in this formulation are the non-universal finite terms of both the real and virtual MEs. However, the large

logarithmic terms from soft and collinear emission can be resummed by the Sudakov form factors, and thus they are suited for the simulation of the PS in the sense that it can randomly choose the point of emission. Furthermore, the formalism provides a link to the hadronisation process starting at low energy scales. Description of the parton shower for initial state radiation is more complicated, though, because the proton structure enters. This discussion is beyond the scope of this thesis, but a detailed description is given in e.g. [136].

5.3.3 Merging of Matrix Elements and Parton Showers

It has been shown above that the MEs allow a precise prescription of separated jets, while the PS can model the structure inside a jet. Both approaches provide a complementary concept to model the evolution of a jet. They both have advantages and disadvantages. The ME can give an exact prescription at a fixed order covering the entire phase space, but this comes at the cost of being computationally expensive and missing the logarithmic contributions. Parton showers on the other hand resum the dominant soft and collinear contributions at all orders, but are not able to provide a valid prescription of a hard emission at wide angles. Hence, to get a proper characterisation of the creation and evolution of jets one would like to merge both concepts. The merging is supposed to describe the hard emissions at leading order and leading log precision including soft emissions. However, a jet can be produced in the parton shower and the matrix element. This might lead to double counting, and thus a wrong description. One algorithm to perform the merging avoiding double counting is the CKKW (Catani, Krauss, Kuhn, Webber) matching algorithm [143, 144, 145] utilised in this analysis e.g. for the b-associated Higgs production generated by SHERPA [146]. It essentially splits the phase space at a *resolution scale*, μ , with one part described by the ME and the other by the PS which ensures the jet evolution down to the fragmentation scale where the hadronisation takes over. A reweighting procedure on the ME for all parton multiplicities is applied based on α_S at the branching scale including the appropriate Sudakov form factor to match the PS for the considered configuration. The concrete choice of the parameters specifying the CKKW algorithm, e.g. the matching scale, can have an impact on the generated event topology, and as unphysical parameter is subject to theoretical uncertainties which have to be taken into account. These will be included as systematic uncertainties in the search for neutral Higgs bosons. Details are given in Section 12.3.

5.3.4 Multiple Parton Interactions and Pile-up

Besides the hard process, soft processes, i.e. beam remnants and multiple interactions, need to be simulated. The remnants of the colliding protons, which do not take part in the hard scattering will continue moving in the direction of the beam, but are still connected to the hard collision via colour charge. This has to be taken into account by models designed for soft physics. Ref. [136] gives a detailed discussion of these models. In principle, they simulate multiple semi-hard $2 \rightarrow 2$ parton interactions. Using perturbative QCD calculations this results in singularities for vanishing transverse momentum of the outgoing partons. However, there is always a low transverse momentum scale where the non-perturbative regime takes over, and thus these singularities are not a problem here. To model the entire phase space of the multiple interactions, these $2 \rightarrow 2$ scatterings are simulated sequentially with decreasing transverse momentum of the outgoing partons until a cut-off scale is reached. The interaction between the proton remnants is called *multiple parton interaction* (MPI) and simulated by MC generators like PYTHIA [147] or JIMMY [148]. A second class of additional interactions which have to be simulated are pile-up collisions. Pile-up summarises the phenomenon of multiple proton-proton collisions which can be classified into *in-time pile-up* and *out-of-time pile-up*. The former one describes additional proton-proton collisions during a single bunch-crossing which lead to an overlay of the hard process with additional inelastic proton-proton collisions. At design luminosity collisions will take place each 25 ns. Thus the time between two bunch crossings is shorter than the detector signal (e.g. drift time in muon spectrometer tubes or LAr gaps), such that signals of previous bunch crossings overlay with the event of interest. This is called out-of-time pile-up. During the simulation the primary process is overlaid by a Poisson distributed number of *minimum bias events* which cover event and signal pile-up. In the data analysis further cor-

rections terms are applied on top of these simulations to match the actual data-taking conditions. Once a data-taking period is completed the entire simulation dataset can be reproduced, as for instance done after 2011 data-taking, accounting for the actual conditions in each run. However, this is not the case for the simulated samples utilised in this thesis, but rather a pile-up reweighting procedure is exploited. Details will be given in Section 9.1.

5.3.5 Simulation of Tau Decays and QED Radiative Corrections

On top of the multipurpose generators discussed above, two specialised generators are utilised in this thesis. For simulation of tau decays a dedicated tool called TAUOLA [149] is used for all generators, except SHERPA and PYTHIA8 which model the tau decay by themselves. TAUOLA is a FORTRAN library which is suitable to simulate both leptonic and hadronic tau decays including the entire decay topology, such as neutrinos, intermediate resonances in the decay of the tau lepton itself and spin correlations. To model QED radiative corrections, e.g. due to bremsstrahlung, another dedicated simulation library called PHOTOS [150] is utilised in this thesis, except for SHERPA, which has its own QED FSR modelling [151]. It is used to simulate corrections from photon radiation in the tau decays.

5.4 Detector Simulation

The Monte Carlo generators provide the four-vectors of each particle from the underlying physics process simulated using the above described methods. These four-vectors however, are not directly usable for physics analysis, but an additional step of the detector simulation is necessary. A framework called ATHENA [152] has been developed by the ATLAS collaboration which is suitable to perform the final step of simulating particle passage through the detector. Interactions of the final state particles with the detector material are simulated resulting in the final complete event description. This includes the shower evolution in the electromagnetic and hadronic calorimeters, displaced vertices of long lived particles as well as pile-up simulation. A huge amount of CPU hours is required to perform the entire detector simulation. To be able to simulate processes with large production cross sections it might not always be feasible to run the *full simulation* (FULLSIM), but rather rely on the so-called *fast simulation* (FASTSIM). Both FULLSIM and FASTSIM will be addressed below. Figure 5.2 illustrates the work flow of the ATLAS simulation and reconstruction chain.

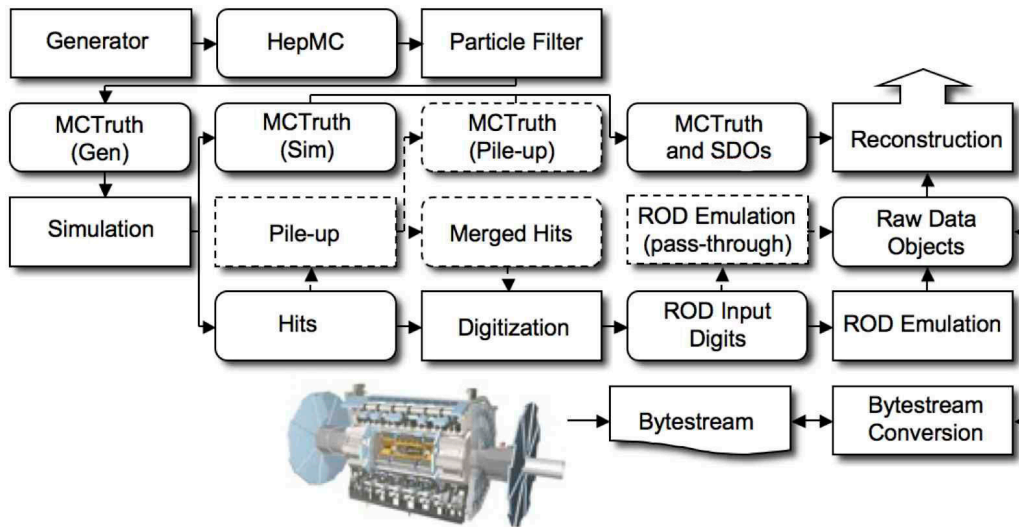


Figure 5.2: Work flow chart of the ATLAS reconstruction software chain [135] from event generation (top left) to reconstruction (top right). Squared-cornered and rounded boxes mark algorithms and persistent data objects, respectively. The dashed path represents additional calls if pile-up events are overlaid.

5.4.1 Full Simulation

The detector simulation is performed using GEANT 4 [153], a general purpose toolkit which can be used to simulate particle passage through matter. It gets a complete description of the detector and models the interactions of each particle traversing the detector. The detector model is stored in a dedicated database which holds all information for a single data-taking run, e.g. detector alignment. The full chain consists of three steps. First *hits* for each sub-detector are generated. They are the equivalent of energy deposits by a particle traversing a detector component. At this stage also the pile-up simulation is included via merging hits of the hard interaction and minimum-bias events simulated by e.g. PYTHIA. These hits are then digitised in the *digitisation* step. A digit is produced once the energy deposit exceeds a pre-defined voltage or current threshold in a given time window. The output is the *raw data object* (RDO) format which can be further reprocessed in later stages. The RDO contains the same information a data run includes, except it also comprises additional information provided by the generator, the so-called *truth record*, which can later be used for detailed studies. The final step is the *reconstruction* which transforms the digits back to particles using the same trigger and reconstruction algorithms as used for data reprocessing. Several data formats containing different levels of information can be produced starting with *event summary data* (ESD) including the full track and cell information, *analysis object data* (AOD) with a reduced amount of details and D3PD, the common analysis ntuple format utilised for physics analyses.

5.4.2 Fast Simulation

The full simulation chain takes up to 15 minutes per event on modern CPUs, and thus is not feasible for the simulation of physics processes with large production cross sections, like W +jets. Hence, dedicated fast simulation algorithms have been developed which are used within this thesis for the simulation of W +jets background samples. The common framework utilised is ATLFast-II [154] which exploits the *Fast Calorimeter Simulation* (FastCaloSim) [155] to simulate the calorimeter response. This results in a significant speedup, since simulation of the high granularity of the electromagnetic calorimeter is very time consuming. One advantage of ATLFast-II over the simpler version, ATLFast-I, is that it provides the full particle information, while ATLFast-I only provides the momenta of all particles. This allows to run the same reconstruction algorithms for data reprocessing and full simulation. The improvement in speedup arises from a simplified detector model. In the common setup both the inner detector and the muon system are modelled by full simulation, while the calorimeter system is described by FastCaloSim. The fast calorimeter simulation is based on parametrisations of the longitudinal and lateral energy profile, rather than simulating energy deposits of each particle. The input to calorimeter simulation are the generator information of each particle at the end of the inner detector. A detailed outline of the various fast simulation algorithms as well as their performance can be found in [135].

In this thesis the MSSM Higgs and the Z' production as well as several backgrounds are extracted from Monte Carlo simulation exploiting the techniques discussed above. Further details on the generators used and their setup are given in Sections 12.1 and 13.1 for the signal processes and Chapter 8 is dedicated to the modelling of electroweak backgrounds.

6 Reconstruction of Physics Objects

Elementary particles are not directly observed but have to be measured by means of their detector signature. This chapter outlines the reconstruction of physics objects such as electrons, muons, jets or missing transverse energy. First the underlying detector objects, i.e. *tracks* and *calorimeter clusters*, are introduced in Section 6.1. Based on these the higher level physics objects corresponding to elementary particles can be reconstructed and identified. Dedicated algorithms performing both steps will be discussed in Section 6.2. For hadronically decaying tau leptons this will be discussed extensively in Chapter 7 and will not be repeated here. However, the common pre-selection shared by both the Higgs as well as the Z' analysis will be addressed for all physics objects utilised in the analysis.

6.1 Underlying Detector Objects

Track Reconstruction

Track reconstruction is performed in three steps. In the *pre-processing* stage three dimensional space points are build from clusters formed by the signals in the pixel detector and the first layer of the SCT. TRT hits are combined to *calibrated drift circles* [156]. In the subsequent stage, the *track finding*, seeds for the track finding algorithms are formed out of the pixel and SCT space points. These seeds are extrapolated to the outer layers of the SCT to form *track candidates*. A track fit is performed on these track candidates, including outlier removal, ambiguity resolving and track-cluster association. Several algorithms for the track-fitting procedure are available, e.g. global- χ^2 , Kalman-filter [157] or Gaussian-sum filters (GSF) [158]. Next, fake tracks are removed by applying quality criteria, such as number of associated clusters or goodness of the track fit. The remaining selected tracks are then extrapolated to the TRT and refitted using all inner detector information. The quality of the refitted tracks is compared to the silicon-only fit in which, in case of bad fit results, outliers are labelled and removed from the track fit, but remain associated to the track. In addition, *backtracking* is performed which extends track segments in the TRT not matched to any silicon hit back into the silicon detectors. These extended tracks are combined with track segments in the pixel and SCT detector which are not selected as track seed. Such segments typically arise from particles decaying after the first layers. Thus, backtracking improves reconstruction of photon conversions and decays of long-lived particles. Finally, in the *post-processing* stage dedicated algorithms for vertex finding, secondary vertex fits and photon conversion finding are executed.

Calorimeter Cluster Reconstruction

Cluster reconstruction exploits the full three dimensional shower shape information in the calorimeters. Energy deposits are clustered by the *topological cluster* algorithm forming *topo-clusters* [159]. The clustering starts from a selection of cells whose signal exceeds a specific threshold chosen as four times the noise term, σ_{noise} , arising either from electronics or pile-up. Neighbouring cells around the seed cell are added if their measured energy exceeds two σ_{noise} . The cell association runs as long as no cell with $E > 2\sigma_{\text{noise}}$ remains. Next, all cells with positive energy are added to the cluster. Thus, the topo-cluster algorithm implicitly applies noise suppression. Finally, a search for local energy maxima is performed comparing cells within the cluster. If more than one maximum is found the cluster is split. This splitting is repeated until each cluster has exactly one local maximum. Since the calorimeters of the ATLAS experiment are non-compensating, i.e. electrons and hadrons of same energy yield different signals, cell energies are measured at an appropriate scale for electromagnetic showers, the so-called *EM-scale*. Hence, clusters have to be classified whether they are of electromagnetic or hadronic origin. The classification is based on shower shape variables. Finally, the clusters are calibrated accordingly by the *Local Hadron Calibration* (LC) [160].

6.2 High-level Physics Objects

Hadronic Taus

Hadronically decaying tau leptons are reconstructed and identified by the algorithms discussed in Chapter 7. For the presented studies they are required to have high transverse momentum, $p_T > 50 \text{ GeV}$, and be within the fiducial volume of the inner detector, $|\eta| < 2.47$, but not in the overlap region between barrel and end-cap (*crack region* of $1.37 < |\eta| < 1.52$). Furthermore, they have to have either exactly one or three associated tracks and an absolute charge of one. To reduce the amount of electron fakes, the loose BDT-based electron veto, referred to as eBDT, is applied. At this stage no jet discrimination based on the BDT identification criterion is requested to allow for data-driven background estimations. Section 10.2 will elaborate on this topic in detail.

Electrons

Electrons are reconstructed by matching tracks in the inner detector to clusters in the electromagnetic calorimeter [156]. The reconstruction has been significantly improved in 2012 using the GSF fitter. Electrons can loose a significant amount of energy in the inner detector due to bremsstrahlung. In the first years of data-taking until 2011 the track fitting was done assuming a pion hypothesis which could lead to track loss for later electron reconstruction. This has been improved by considering a dedicated electron hypothesis during the track fit [161]. In this thesis electrons are considered if $p_T > 15 \text{ GeV}$ and $|\eta| < 2.47$, excluding the crack region. The direction of the electron candidate is taken from the associated track if the sum of the number of hits in the SCT and the number of dead sensors is at least four. Otherwise, the direction is taken from the assigned ECAL cluster. Electron identification is applied on top of the reconstruction to ensure a good electron candidate. The electron identification is based on track quality requirements, electromagnetic shower shape information, track-to-cluster matching and number of TRT hits. Here, the *Loose++* working point is chosen corresponding to an efficiency of 95% [162, 163, 126].

Muons

Muons are reconstructed exploiting track measurement in the inner detector and the muon spectrometer (MS) [156]. MS tracks are extrapolated back to the ID and the quality is evaluated by a χ^2 -fit. In the fitting process corrections accounting for energy loss in the calorimeter system are taken into account. Depending on the p_T of the muon the momentum measurement is either taken from the MS for high- p_T muons ($p_T \gtrsim 30 \text{ GeV}$) or from the ID for low- p_T muons. Muons are selected if they exceed $p_T > 10 \text{ GeV}$ and are within the fiducial detector volume of $|\eta| < 2.5$. Track quality requirements corresponding to the recommendation by the *Combined Muon Performance Group* [164] are applied on top. If a b-layer hit is expected the corresponding cut is applied. Pixel and SCT hits including dead sensors have to be at least one or five, respectively. The sum of pixel and SCT holes must not exceed two. Depending on the location in the detector, different TRT quality criteria are placed. For tracks within $0.1 < |\eta| < 1.9$ at least six TRT hits are required and the number of outliers must not exceed 10%. The requirement on the outliers is dropped for tracks outside the η window and less than six TRT hits. On top the so-called *staco* identification algorithm [156] is applied, whereupon this analysis insists on the *loose* working point.

Jets

Several jet reconstruction algorithms are available [165, 166, 167] using either tracks, topo-clusters, cells or calo-towers as seeds. In the analyses presented in this thesis the anti- k_t algorithm [166] with a distance parameter $R = 0.4$ is used. The four-momenta of jets are calculated as the weighted sum of all associated clusters assuming zero mass for clusters. Cluster calibration is obtained from numerical inversion of the response in MC simulation [160] accounting for dead material and out-of-cluster energy loss in the tails

of the shower. The calibrated four-momentum is given as:

$$(E_{\text{jet}}, \vec{p}_{\text{jet}}) = \left(\sum_i^{\text{cells}} w(\rho_i, \vec{r}_i) \cdot E_i, \sum_i^{\text{cells}} w(\rho_i, \vec{r}_i) \cdot \vec{p}_i \right), \quad (6.1)$$

with weights, $w(\rho_i, \vec{r}_i)$, depending on the energy density, ρ_i , in the cell and its location, \vec{r}_i . Jets used in the presented analyses have to have $p_T > 30 \text{ GeV}$ and be within the fiducial volume of the calorimeter, $|\eta| < 4.5$. To ensure that the selected jets arise from the hard scattering rather than from a pile-up vertex an additional cut on the *jet vertex fraction* (JVF) [168, 169] of $|\text{JVF}| > 0.5$ is applied to all jets with $p_T < 50 \text{ GeV}$ and $|\eta| < 2.4$. The JVF is defined as the ratio of the scalar sum of transverse momenta of all tracks associated to the jet coming from the primary vertex to all associated tracks:

$$\text{JVF}(\text{jet}_i) = \frac{\sum_k^{\text{tracks}} p_T^k |vtx_{\text{primary}}|}{\sum_l^{\text{vertices}} \sum_m^{\text{tracks}} p_T^m |vtx_l|}. \quad (6.2)$$

If the jet is originating from the hard interaction vertex, i.e. the primary vertex, it will have a substantial fraction of tracks matching to the primary vertex leading to JVF values near one, while pile-up jets will tend to have very low values. By convention a value of -1 is assigned to all jets without any associated tracks.

Missing Transverse Energy

Neutrinos in the final state of the tau decay can not be reconstructed directly, but have to be considered via missing transverse energy. E_T^{miss} reconstruction is based on energy deposits in the calorimeter and momentum measurement in the muon spectrometer [170], with magnitude and direction given as:

$$E_T^{\text{miss}} = \sqrt{(E_x^{\text{miss}})^2 + (E_y^{\text{miss}})^2} \quad \phi^{\text{miss}} = \arctan \frac{E_y^{\text{miss}}}{E_x^{\text{miss}}}, \quad (6.3)$$

with

$$E_{x,y}^{\text{miss}} = E_{x,y}^{\text{miss,calo}} + E_{x,y}^{\text{miss},\mu}. \quad (6.4)$$

The calorimeter term is calculated from all cells calibrated accordingly to the reconstructed object they belong to. Non associated cells are taken into account via the *Cell-out* term. All physics objects are taken into account in the following order: electrons, photons, hadronic tau decays, jets and muons, such that:

$$E_{x,y}^{\text{miss,calo}} = E_{x,y}^{\text{miss,e}} + E_{x,y}^{\text{miss},\gamma} + E_{x,y}^{\text{miss},\tau} + E_{x,y}^{\text{miss,jets}} + E_{x,y}^{\text{miss,softjets}} + E_{x,y}^{\text{miss,calo}-\mu} + E_{x,y}^{\text{miss,Cell-out}}. \quad (6.5)$$

The jet contribution is split into a *soft jet* term for jets with $10 \text{ GeV} < p_T < 20 \text{ GeV}$ calibrated with the *local cell weights* (LCW) [160, 171] scheme and a jet term for jets with $p_T > 20 \text{ GeV}$ calibrated with the LCW+JES¹⁰. In order to reduce pile-up dependence, all contributions from jets with $p_T < 50 \text{ GeV}$ and $|\eta| < 2.4$ are weighted according to their JVF, calculated as defined in Equation 6.2. The *soft terms*, $E_T^{\text{miss,softjets}}$ and $E_T^{\text{miss,Cell-out}}$ are scaled by the so-called *soft-term vertex-fraction* (STVF) defined similar to JVF as the ratio of the sum of transverse momenta of all tracks not associated to any reconstructed object matched to the primary vertex to the sum of transverse momenta of all tracks not associated to any reconstructed object matched to any vertex [170]. The muon terms, $E_{x,y}^{\text{miss},\mu}$, are calculated from the sum of MS track momenta of all selected muons:

$$E_{x,y}^{\text{miss},\mu} = - \sum_{\text{selected } \mu} p_{x,y}^{\mu,\text{track}}. \quad (6.6)$$

In Monte Carlo simulation the calibration of physics objects are propagated through the E_T^{miss} calculation.

¹⁰jet energy scale [171]

7 Tau Reconstruction and Identification

Tau leptons, τ , play a crucial role in many physics analyses at the LHC. They are important in the analysis of Standard Model processes, e.g. the $Z \rightarrow \tau\tau$ cross section measurement [172], as well as in searches for new physics beyond the Standard Model, like in the search for neutral and charged MSSM Higgs bosons. Efficient reconstruction and identification (ID) algorithms of tau lepton decays are an essential ingredient for these analyses. With a mass of $m = 1.777 \text{ GeV}$ [16], the tau lepton is the heaviest lepton in the Standard Model. It can decay both leptonically and hadronically. It decays into light leptons, i.e. electrons and muons, with a probability of about 35 % and into charged and neutral hadrons in 65 % of all decays, respectively. All decay modes of tau leptons involve additional neutrinos in the final state. Leptonic decays of tau leptons are not distinguishable from primary electrons or muons. Hence, only hadronic tau decays, τ_{had} , are considered for reconstruction and identification. Tau leptons tend to decay into one or three charged hadrons (referred to as 1-/3-prong decays), mainly into pions, π^\pm , accompanied by additional neutral hadrons. Given the very low branching fraction ($\ll 1\%$) of taus decaying into more than three charged hadrons, they are not considered in physics analyses at ATLAS. The main decay modes of tau leptons and their branching fractions are summarised in Table 7.1.

Hadronic tau decays reveal low track multiplicities, i.e. one or three tracks, typical shower shapes and specific fractions of energy deposits in the electromagnetic and hadronic calorimeter. Other objects, like electrons or QCD jets, i.e. jets initiated by quarks and gluons, can mimic these detector signatures and hence fake tau candidates. The reconstruction and identification algorithms exploit this information. A three-fold approach is pursued to yield maximum performance in terms of tau acceptance and fake rejection. Discrimination against QCD jets is achieved by multivariate approaches exploiting *projective log-likelihood* (LLH) and *Boosted Decision Tree* (BDT) techniques [173]. They will be covered in Section 7.2 after the tau reconstruction has been introduced in Section 7.1. Discrimination against electrons is performed via a BDT which takes advantage of the narrower shower, the lower activity in the hadronic calorimeter and the higher transition radiation of electrons. Muons can fake tau decays as well, if they deposit energy in the calorimeter. A cut-based discrimination has been developed to minimise this effect. The light lepton vetos are outlined in Sections 7.2.6 and 7.2.7.

Furthermore, given the limited bandwidth of the ATLAS trigger system (c.f. Section 4.2.6), powerful algorithms are also required at the trigger level. In the context of this thesis a new tau identification at event filter stage exploiting multivariate techniques has been developed, which became the default algorithm in the EF tau trigger menu for 2012 data-taking. This will be discussed in detail in Section 7.3.

decay mode	branching fraction Γ_i/Γ
leptonic decays	
$\tau^\pm \rightarrow e^\pm + \nu_e + \nu_\tau$	17.83 %
$\tau^\pm \rightarrow \mu^\pm + \nu_\mu + \nu_\tau$	17.41 %
hadronic decays	
$\tau^\pm \rightarrow \pi^\pm + \nu_\tau$	10.83 %
$\tau^\pm \rightarrow \pi^\pm + \pi^0 + \nu_\tau$	25.52 %
$\tau^\pm \rightarrow \pi^\pm + 2\pi^0 + \nu_\tau$	9.30 %
$\tau^\pm \rightarrow \pi^\pm + \pi^\pm + \pi^\mp + \nu_\tau$	8.99 %
$\tau^\pm \rightarrow \pi^\pm + \pi^\pm + \pi^\mp + \pi^0 + \nu_\tau$	2.70 %

Table 7.1: Decay modes and branching fractions of hadronic tau decays [16].

7.1 Tau Lepton Reconstruction

The tau reconstruction aims to build tau candidates using tracking and calorimeter information [174]. It starts from building tau candidates out of reconstructed jets followed by track association. Details for each step will be outlined in Sections 7.1.1 - 7.1.5.

7.1.1 Building Tau Candidates

Candidates of hadronic tau decays reconstructed in the detector, τ_{had} , are seeded by jets reconstructed by the anti- k_t algorithm [166] with a distance parameter, $R = 0.4$. Calorimeter cells are clustered to topological clusters [159] calibrated by Local Hadron Calibration (LC) [160]. The LC applies weights depending on the reconstructed shower profile on topo clusters to account for non-compensation of the calorimeters, dead material and energy deposits outside the topo clusters. Only jets with $p_T > 10 \text{ GeV}$ and within the fiducial volume of the inner detector, $|\eta| < 2.5$, are considered. The direction of the tau candidate, i.e. η and ϕ , is calculated from the sum of the four-momenta of the jet constituents. The mass of each constituent is assigned to be zero [175]. Tau candidates have at this level by definition an assigned mass of zero, such that p_T equals $E_T = E \cdot \sin \theta$. Energy calibration applied to the seed jet is not appropriate for tau decays. Hence, a dedicated *tau energy scale* (TES) calibration is applied. Details are outlined in Section 7.1.5.

7.1.2 Track Association

Track assignment is a crucial ingredient to reconstruct n-prong tau decays properly. Tracks are counted in the *core region*, defined as a cone with opening angle $\Delta R < 0.2$ around the intermediate tau axis. To reduce fake assignment optimised selection requirements on reconstructed tracks are applied:

- transverse momentum, $p_T > 1 \text{ GeV}$
- number of pixel hits, $N_{\text{pixel}} \geq 2$
- number of pixel + SCT hits, $N_{\text{pixel+SCT}} \geq 7$
- distance of closest approach to primary vertex in transverse plane, $|d_o| < 1 \text{ mm}$
- distance of closest approach to primary vertex in longitudinal direction, $|z_o \cdot \sin \theta| < 1.5 \text{ mm}$.

The *primary vertex* (PV) is defined as the vertex with the maximum sum of transverse track momenta, $(\sum p_T^{\text{trk}})^2$ [176], of all associated tracks in the event. Track counting is extended to the *isolation annulus*, defined as a cone with $0.2 < \Delta R < 0.4$ around the intermediate tau axis. This information is used by the identification algorithms to suppress fake candidates.

7.1.3 Vertex Assignment

The primary vertex may be incorrectly assigned to a pile-up vertex. The probability for such mis-assignments increases with the number of pile-up collisions. Track assignment relies heavily on the assumption that the primary vertex corresponds to the hard interaction, because otherwise the tracks might fail the impact parameter criteria outlined above. To increase pile-up robustness, a vertex assignment algorithm called *Tau Jet Vertex Assignment* (TJVA) [174] has been developed. It is build on the *Jet Vertex Assignment* (JVA) [168] algorithm. For each jet it finds the vertex candidate with the highest Jet Vertex Fraction, JVF, defined as

$$\text{JVF} = \frac{\sum p_T^{\text{trk|vtx}}}{\sum p_T^{\text{trk}}}. \quad (7.1)$$

In the numerator the sum runs over all tracks assigned to a given vertex, while in the denominator the transverse momenta of all tracks within a jet are summed. Matching tracks to vertices follows the

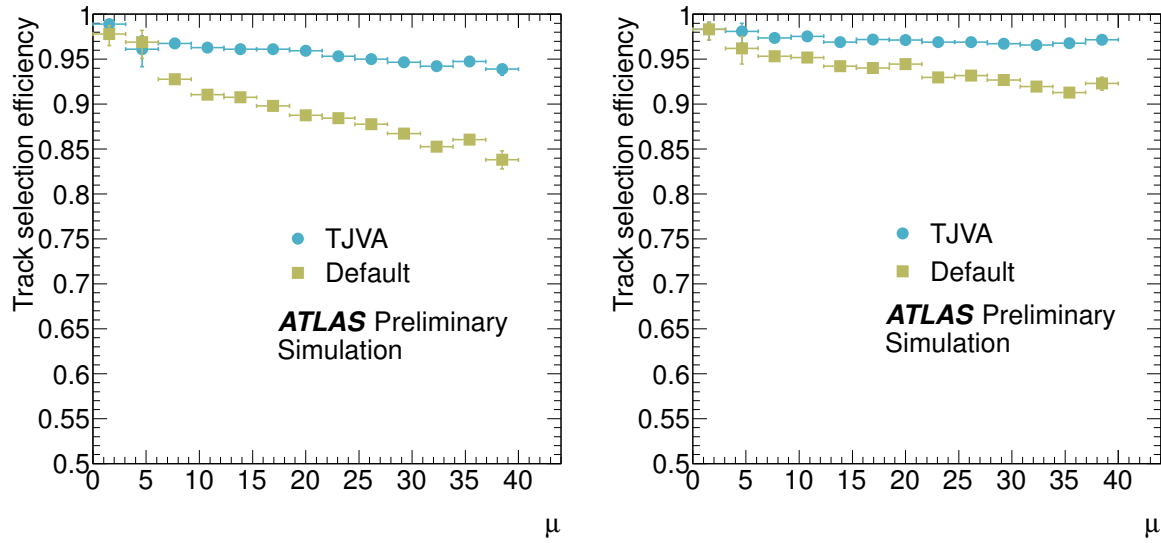


Figure 7.1: Track selection efficiency versus average interactions per bunch crossing, μ , of generated 1-prong (left) and 3-prong (right) τ_{had} candidates measured in Z/γ^* MC. Tau candidates are required to have $p_T > 15 \text{ GeV}$ and match to a generated tau within $\Delta R < 0.2$. Yellow boxes present the efficiency using default track assignment, while blue circles show the performance of the TJVA algorithm. The TJVA algorithm shows lower dependency on the number of pile-up interactions [174], thus providing stronger pile-up robustness.

procedure of JVF, but applies different track quality criteria optimised for tau decays. They are the same as given in Section 7.1.2, except for the impact parameter requirements which are dropped. Figure 7.1 presents the track selection efficiency versus the average number of interactions per bunch crossing for the default track selection algorithm and TJVA. Using TJVA yields much higher pile-up robustness.

7.1.4 Neutral Pion Finder

To obtain further information about the tau decay it is important to reconstruct its substructure, in particular to reconstruct the neutral pions. For this purpose a neutral pion finder algorithm based on calorimeter clusters has been developed [177]. It is designed to count the number of neutral pions utilising two distinct multivariate classifiers. This algorithm exploits Boosted Decision Trees, which will be explained in detail in Section 7.2.3. The first BDT is designed to decide whether there are any neutral pions accompanying the charged pions, while the second BDT is used to distinguish the tau decay in more detail, by classifying them into decay modes corresponding to $\tau^\pm \rightarrow \pi^\pm + \pi^0$, $\tau^\pm \rightarrow \pi^\pm + 2\pi^0$ and $\tau^\pm \rightarrow \pi^\pm + \pi^\pm + \pi^\mp + \pi^0$. Obviously this does not include all tau decay mode patterns, but covers the main decay channels, and thus provides further information which can be exploited later in e.g. the tau identification algorithms. Furthermore, this additional information will improve the energy resolution of the reconstructed tau lepton. The BDTs are trained using five variables which are sensitive to the neutral pion component in the calorimeter, such as the charged pion energy fraction in the electromagnetic calorimeter or the energy fraction in the presampler and strip layers w.r.t. the overall calorimeter energy. A complete list is given in [177]. If neutral pions are found by the BDT their four-vectors are calculated from calorimeter clusters after applying corrections for noise, underlying event and pile-up activity. An estimate of this is obtained in an isolation annulus around the track system, i.e. the charged pion direction, of size $0.2 < \Delta R < 0.4$. The estimated activity is then subtracted in the core region, i.e. $\Delta R < 0.2$, and only clusters surviving this subtraction are kept for later processing. Finally, a “ π^0 likeness score” is defined to select the cluster or pair of clusters with a high probability of being energy deposits of neutral pions. The likeness score is essentially the energy fraction in the presampler and strip layer w.r.t. the energy component of the charged pions. The exact definition is given in [177]. On top of

the pure π^0 finding an additional correction of hadronic energy contamination can be applied to reduce double counting of energy deposits which distorts the energy resolution of the neutral pions.

7.1.5 Tau Energy Calibration

Momentum Corrections

Even though the local hadron calibration improves the momentum resolution of hadronic tau decays w.r.t. EM scale calibration, it does not account for energy loss in front of the calorimeter, underlying event, pile-up and out-of-cone effects. These effects are accounted for in the tau energy calibration [178]. It is derived from Monte Carlo generated $W \rightarrow \tau\nu$, $Z/\gamma^* \rightarrow \tau\tau$ and $Z' \rightarrow \tau\tau$ events considering reconstructed τ_{had} candidates with $p_T > 15$ GeV which fulfil the medium BDT-based jet discrimination criteria (c.f. Section 7.2). Taking resolution effects into account, the TES can be applied on tau candidates with $p_T > 15$ GeV. The momentum is corrected by a calibration term, R , depending on the momentum at LC scale, p^{LC} , the reconstructed pseudorapidity, $|\eta_{\text{reco}}|$, and the number of associated tracks, n_p . Thus, the calibrated momentum of a τ_{had} candidate is given as:

$$p^{\text{cal}} = \frac{p^{\text{LC}}}{R(p^{\text{LC}}, |\eta_{\text{reco}}|, n_p)} . \quad (7.2)$$

To determine the calibration constants, the response, defined as the ratio between the LC scale momentum and the generated visible momentum, $p_{\text{vis}}^{\text{gen}}$, is fitted with a Gaussian function in bins of $p_{\text{vis}}^{\text{gen}}$ and $|\eta_{\text{reco}}|$ separately for generated 1-prong and 3-prong tau decays. The mean obtained from this fit is fitted by an empiric function to extract the momentum dependence of the calibration constants.

Pseudorapidity Corrections

The calibration corrects the tau momentum to about 1% - 2% of the final scale, but clusters reconstructed in poorly instrumented regions of the calorimeter yield a few percent deviation in some $|\eta|$ regions. The reconstructed energy of clusters in these regions is underestimated which results in a bias. A correction of $|\eta_{\text{reco}}|$ is derived from the average deviation of the reconstructed η w.r.t. the generated η_{gen} , $\eta_{\text{bias}} = < |\eta_{\text{reco}}| - |\eta_{\text{gen}}| >$, to account for the bias:

$$|\eta| = |\eta_{\text{reco}}| - \eta_{\text{bias}} . \quad (7.3)$$

Pile-up Corrections

The response is restored to unity by the momentum and pseudorapidity corrections, but deviations are observed as a function of pile-up events. The impact of pile-up collisions on the tau momentum is quantified as:

$$p_{\text{pile-up}} = A(|\eta_{\text{reco}}|, n_p)(N_{\text{PV}} - \langle N_{\text{PV}} \rangle) , \quad (7.4)$$

in which N_{PV} is the number of reconstructed primary vertices, $\langle N_{\text{PV}} \rangle$ the average number of PV and A a constant obtained from a linear fit in bins of $|\eta_{\text{reco}}|$ and n_p . The momentum contribution of pile-up collisions is used as an additional correction to the calibrated momentum, such that the final tau momentum is given as:

$$p^{\text{Final}} = \frac{p^{\text{LC}} - p_{\text{pile-up}}}{R(p^{\text{LC}}, |\eta_{\text{reco}}|, n_p)} . \quad (7.5)$$

Tau Energy Scale (TES) Uncertainty

Uncertainties on the TES arise from the calorimeter response, the choice of the MC event generator (including the choice of underlying event model and detector description) and non-closure of the calibration method. The calorimeter response can be estimated from single particle measurements, which

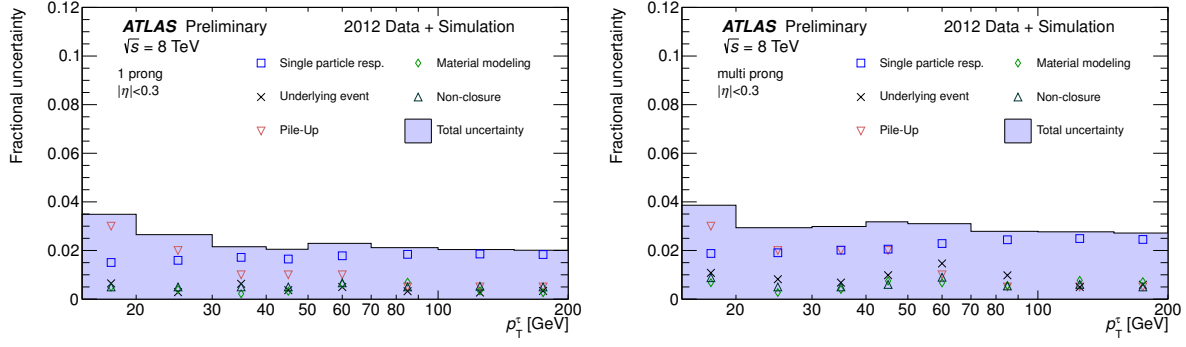


Figure 7.2: Total tau energy scale uncertainty for 1-prong (left) and multi-prong (right) tau decays as a function of p_T within $|\eta| < 0.3$. Individual components are depicted by different markers, while their combination is represented by the blue band [178].

decompose the hadronic tau decay into its decay products and convolve the constituents' response with the visible τ_{had} composition. This depends strongly on the kinematics of the tau decay, and hence three different measurements are exploited depending on the momentum and pseudorapidity of the tau. For low momentum ($p < 20 \text{ GeV}$) tau decays in the central region of the detector ($|\eta| < 1.7$) and higher momenta ($p < 60 \text{ GeV}$) in the end-cap ($1.7 < |\eta| < 2.5$), in-situ measurements are used. Combined test beam (CTB) data taken in 2004 [179] is used for high momentum tau decays in the barrel ($|\eta| < 0.8$), while for higher pseudorapidities MC simulation is taken. To estimate the uncertainty on the calorimeter response, MC simulation with no additional pile-up (in order to get a pure calorimeter response) is compared to data. For low momentum charged pions the energy of the assigned calorimeter clusters is compared to the momentum of the associated track in the inner detector (E/p -measurement). The high momentum π^\pm calorimeter response is constrained by CTB data and MC simulation produced using the test beam setup. A difference in the π^\pm response in the order of 0.5% is found [178]. Neutral pion response is taken from EM calorimeter response measured using $Z \rightarrow ee$ decays and minimum ionising muons in the Tile calorimeter. The EM scale uncertainty [126] measured from $Z \rightarrow ee$ decays is propagated to the TES uncertainty. Uncertainties on the cell energy measurement in the barrel region of the electromagnetic calorimeter are found to be 1.5%, while the scale uncertainty in the Tile calorimeter is found to be 3% [178]. Additional uncertainties arise from the shower shape modelling in MC simulation, which affects the shower energy density, leading to a different set of cells taken into account by the topo clustering algorithm. This also changes the LC weights assigned to the clusters. An uncertainty is extracted from a comparison of MC simulation data using two different hadronic shower models, *QGSP_BERT* [180, 181, 182] and *FTFP_BERT* [183], to CTB data. For 1-prong tau decays deviations of less than 0.5% are observed for the two shower models, while for multi-prong decays it is less than 1%. Dead material in front of the calorimeter, the underlying event model, non-closure of the calibration method and pile-up give additional uncertainties on the TES calibration. Monte Carlo simulation using a different detector model including extra material or using different MC tunes can be used to estimate the first two sources. Both yield an uncertainty of the order of 1%. Uncertainties related to pile-up are obtained from the p_T resolution in different bins of the number of reconstructed vertices. For both 1-prong and multi-prong tau decays the pile-up uncertainty is found to be between 3% at low- p_T and 0.5% at high- p_T . The non-closure contributes to about 1% to the final TES uncertainty. Details are outlined in [178]. The total tau energy scale uncertainty is depicted in Figure 7.2 for 1-prong (left) and multi-prong (right) tau decays for $|\eta| < 0.3$. Different markers show each component contributing to the final uncertainty, separately. In most of the phase space the global TES uncertainty is about 2% for 1-prong and 3% for multi-prong tau decays. A complete list can be found in [178].

7.2 Tau Lepton Identification

The large acceptance of quark and gluon initiated jets by the tau reconstruction algorithm necessitates high-performance identification algorithms. It exploits information of tau decay properties such as the narrow shower profile, to reject QCD jets while keeping real taus. For this purpose several algorithms based on different multivariate techniques have been developed and investigated w.r.t. their performance. The latter is quantified by the power of rejecting QCD jets at a given acceptance efficiency for real taus. To deal with evolving changes of the collision parameters such as different pile-up conditions, these algorithms are continuously optimised. During this thesis the *log-likelihood* (LLH) method has been tuned for 2011 data analysis [174]. An update was provided for 2012 data which will be summarised here. The procedure of tuning this algorithm remains the same.

7.2.1 Tau Identification Variables

The variables used for jet discrimination are outlined below. For real tau leptons MC simulated events of $Z/\gamma^* \rightarrow \tau\tau$, $W \rightarrow \tau\nu$ and $Z' \rightarrow \tau\tau$ processes have been used, while the background templates are extracted from data taken in 2012. Tau candidates used for signal templates are required to match a generated tau lepton decay. In data a di-jet selection has been applied to ensure a high purity of fake tau candidates. The data analysed corresponds to an integrated luminosity of $L = 20.3 \text{ fb}^{-1}$. Events are accepted if they pass the following selection criteria:

1. Good Runs List ¹¹ (data only):
data12_8TeV.periodAllYear_DetStatus-v61-pro14-02_DQDefects-00-01-00_PHYS_StandardGRL_All_Good.xml
2. at least one *primary vertex* (PV) reconstructed with at least four tracks
3. jet trigger
4. at least one reconstructed tau candidate with $p_T > 15 \text{ GeV}$ and $|\eta| < 2.3$

The following variables are considered by the identification algorithms:

Core energy fraction, f_{core} : Fraction of transverse energy in the core ($\Delta R < 0.1$) region of the tau candidate:

$$f_{\text{core}} = \frac{\sum_{i \in \{\text{all}\}}^{\Delta R_i < 0.1} E_{T,i}^{\text{EM}}}{\sum_{i \in \{\text{all}\}}^{\Delta R_i < 0.2} E_{T,i}^{\text{EM}}}, \quad (7.6)$$

where i runs over all cells associated to the tau candidate within $\Delta R < 0.1(0.2)$ of the intermediate tau axis, calibrated at the EM scale. This quantity measures the narrowness of the tau decay shower. Real tau decays are more collimated, and thus tend towards higher values, while QCD jets have a wider shower resulting in a smaller fraction. This quantity is sensitive to energy deposits originating from pile-up contribution. To increase the pile-up robustness a correction depending on the number of reconstructed vertices, N_{vtx} , is applied for tau candidates with $p_T < 80 \text{ GeV}$, i.e. $f_{\text{core}}^{\text{corr}} = f_{\text{core}} + 0.003 \cdot N_{\text{vtx}}$. The distributions for 1-prong and 3-prong tau candidates are shown in Figure 7.3.

Track radius, R_{track} : p_T weighted track width:

$$R_{\text{track}} = \frac{\sum_i^{\Delta R_i < 0.4} p_{T,i} \Delta R_i}{\sum_i^{\Delta R_i < 0.4} p_{T,i}}, \quad (7.7)$$

where i runs over all core and isolation tracks of the tau candidate, within $\Delta R_i < 0.4$. ΔR_i is defined relative to the intermediate tau axis and $p_{T,i}$ is the transverse momentum of the i -th track.

¹¹The Good Runs List applies quality criteria which ensure stable detector conditions and high quality of the selected proton-proton collision data. Further details are given in Section 9.1.

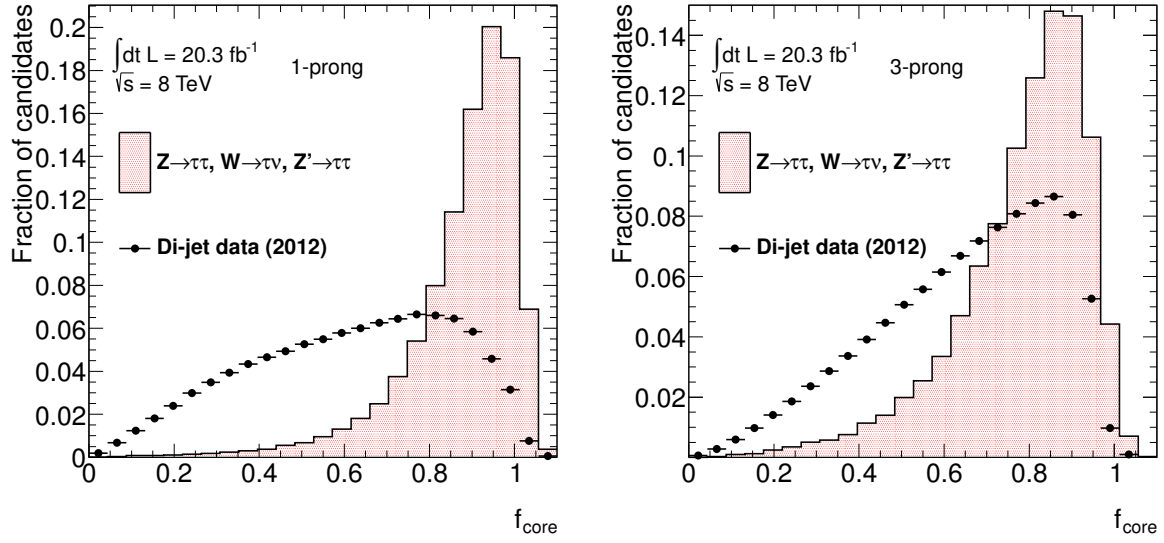


Figure 7.3: Core energy fraction, f_{core} , for reconstructed 1-prong (left) and 3-prong (right) tau candidates. The red dashed histogram shows the signal template obtained from MC simulation requiring a match to generated 1-/3-prong tau decays. In black the background template for QCD jets extracted from a di-jet selection in data is illustrated.

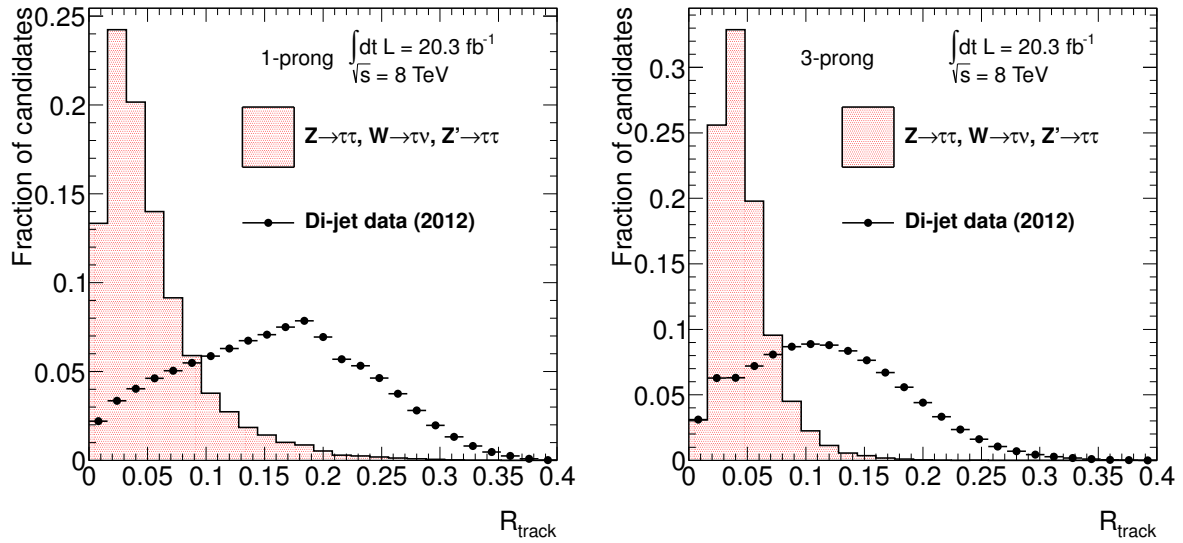


Figure 7.4: Average distance of tracks to intermediate tau axis, R_{track} , for reconstructed 1-prong (left) and 3-prong (right) tau candidates. The red dashed histogram shows the signal template obtained from MC simulation requiring a match to generated 1-/3-prong tau decays. In black the background template for QCD jets extracted from a di-jet selection in data is demonstrated.

Tau leptons have a lower track multiplicity, and thus tend to have smaller values of R_{track} , while QCD jets possess higher track multiplicities resulting in larger R_{track} . For 1-prong tau decays with no additional tracks in the isolation cone this quantity reduces to ΔR_{max} . The distributions for reconstructed 1-prong and 3-prong tau candidates are shown in Figure 7.4.

Leading track momentum fraction, f_{track} :

$$f_{\text{track}} = \frac{p_{T,1}^{\text{track}}}{E_T^\tau} + 0.003 \cdot N_{\text{vtx}}, \quad (7.8)$$

where $p_{T,1}^{\text{track}}$ is the transverse momentum of the highest- p_T track within $\Delta R < 0.2$ around the tau candidate axis and E_T^τ is the transverse energy of the tau candidate, calibrated at the EM energy scale. Since this variable is sensitive to energy contributions of pile-up events, a correction is applied. The low number of decay products of a tau decay results in a peak more close to one. For 1-prong tau candidates additional π^0 lead to f_{track} values different from one. The subtraction scheme applied in the cluster algorithm can yield values above one. In Figure 7.5 the distributions for 1-prong and 3-prong reconstructed tau candidates are presented.

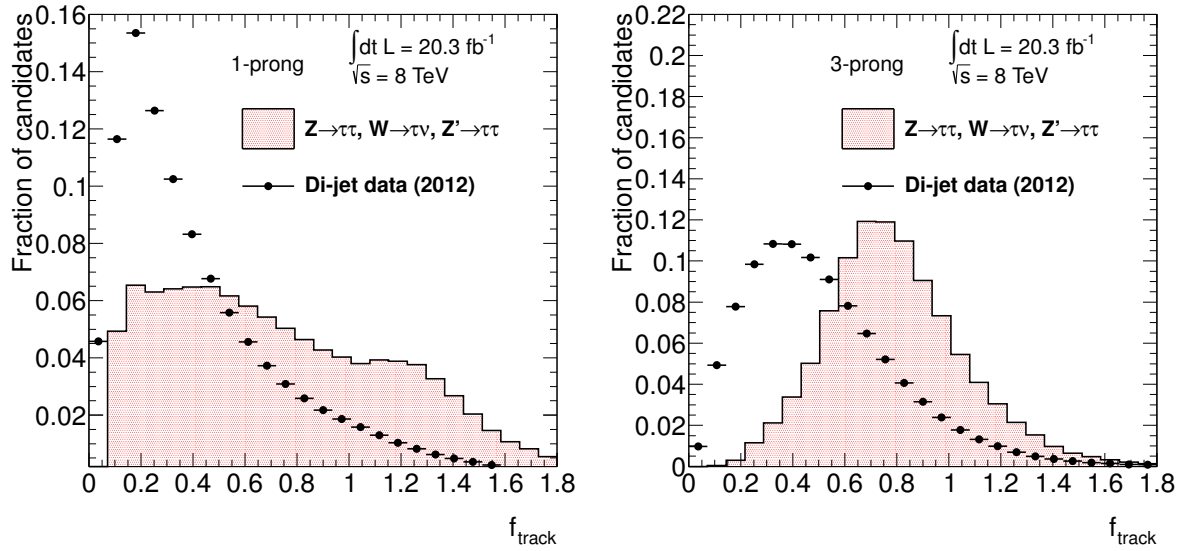


Figure 7.5: Momentum fraction of the highest- p_T track assigned to the tau candidate for 1-prong (left) and 3-prong (right) tau decays. The red dashed histogram shows the signal template obtained from MC simulation requiring a match to generated 1-/3-prong tau decays. In black the background template for QCD jets extracted from a di-jet selection in data is demonstrated.

Leading track IP significance, $S_{\text{lead track}}^{\text{IP}}$: impact parameter significance of the highest- p_T track of the tau candidate:

$$S_{\text{lead track}}^{\text{IP}} = \frac{d_0}{\delta d_0}, \quad (7.9)$$

with d_0 being the distance of closest approach of the leading track to the reconstructed PV in the transverse plane, and δd_0 its estimated uncertainty. This quantity is only considered for 1-prong tau decays. Its distribution is shown in Figure 7.6 (left).

Number of isolation tracks, $N_{\text{track}}^{\text{iso}}$: number of reconstructed tracks within the isolation annulus of $0.2 < \Delta R < 0.4$ around the tau candidate axis. QCD jets tend to larger number of tracks due to gluon splitting, while for real tau decays no additional tracks are expected. This quantity is only used for 1-prong tau candidates. Figure 7.6 (right) shows the distribution for real tau decays and QCD jets.

Track mass, m_{tracks} : invariant mass of the track system:

$$m_{\text{tracks}} = \sqrt{\left(\sum_{\text{tracks}} E\right)^2 - \left(\sum_{\text{tracks}} \vec{p}\right)^2}. \quad (7.10)$$

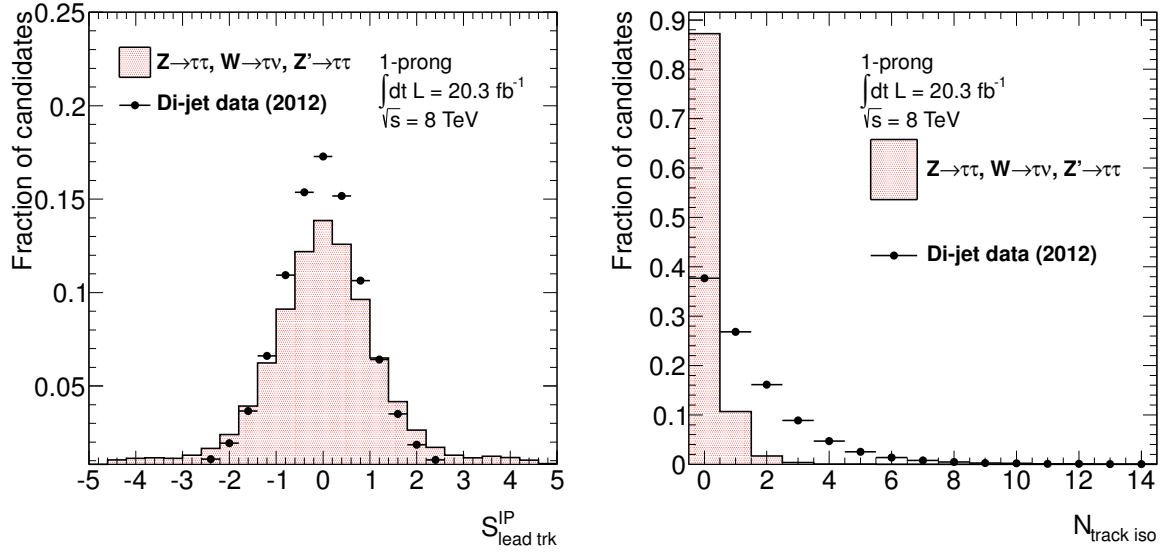


Figure 7.6: Impact parameter significance of the highest- p_T track for 1-prong tau candidates (left) and number of tracks within $0.2 < \Delta R < 0.4$ around the tau axis for reconstructed 1-prong tau candidates (right). The red dashed histogram shows the signal template obtained from MC simulation requiring a match to generated 1-prong tau decays. In black the background template for QCD jets extracted from a di-jet selection in data is demonstrated.

All tracks within $\Delta R < 0.4$ are considered. This quantity is only defined for multi-prong tau decays. For real tau decays it is expected to peak below the tau mass due to the neutrinos, whereas for QCD jets a broader distribution is observed. The distribution is shown in Figure 7.7 (left).

Maximum ΔR , ΔR_{max} : maximal ΔR between a track associated to the tau candidate and the tau axis. Only tracks within the core annulus are taken into account. The higher collimation of tau decays leads to smaller values of ΔR_{max} compared to QCD jets. Figure 7.7 (right) presents the corresponding signal and background templates. By construction this variable is only defined for multi-prong tau decays.

Transverse flight path significance, S_T^{flight} : decay length significance of the secondary vertex in the transverse plane:

$$S_T^{\text{flight}} = \frac{L_T^{\text{flight}}}{\delta L_T^{\text{flight}}}, \quad (7.11)$$

where L_T^{flight} is the reconstructed signed decay length, and $\delta L_T^{\text{flight}}$ is its estimated uncertainty. The vertex fit considers all tracks within the core region. It is only defined for multi-track tau candidates. The corresponding templates are depicted in Figure 7.8

Number of reconstructed neutral pions, N_{π^0} : number of reconstructed neutral pions exploiting the cluster based π^0 finder introduced above. Real tau leptons have a well defined spectrum of neutral pions in the hadronic final state, while QCD jets tend to have a larger amount of reconstructed neutral pions. The corresponding templates for real and fake taus is presented in Figure 7.9 for one- and three-prong tau decays. The cut-off at two π^0 is an artifact of the neutral pion finder algorithm.

Visible mass of the tau lepton, m_{τ}^{vis} : invariant mass of the track system and the neutral pions identified by the π^0 finder. Tau leptons have a well defined mass, while the invariant mass of quark and gluon jets is rather arbitrary. The visible mass does not include the energy component of the neutrinos. Figure 7.10 shows the visible invariant tau mass for one- and three-prong decays.

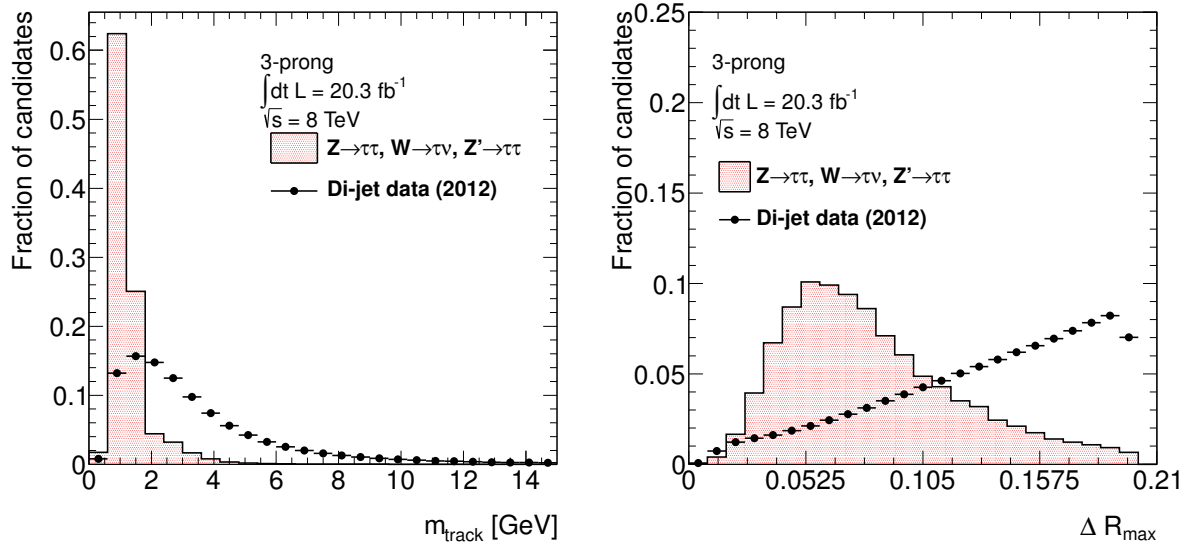


Figure 7.7: Invariant mass of the track system for 3-prong tau candidates (left) and maximum distance of tracks associated to the tau candidate within $\Delta R < 0.2$ w.r.t. tau axis for reconstructed 3-prong tau candidates (right). The red dashed histogram shows the signal template obtained from MC simulation requiring a match to generated 3-prong tau decays. In black the background template for QCD jets extracted from a di-jet selection in data is demonstrated.

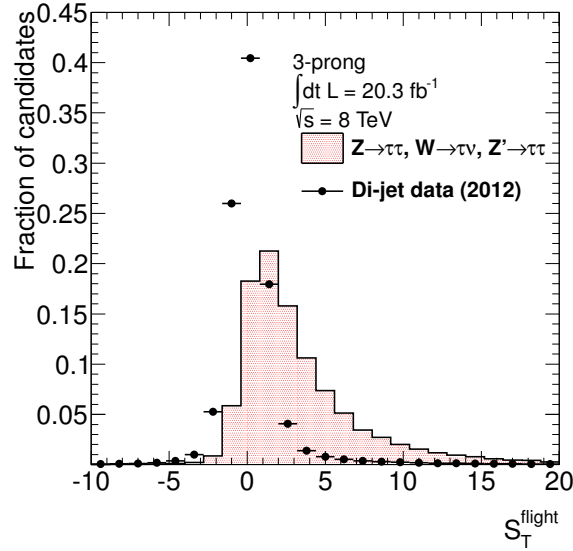


Figure 7.8: Transverse flight path significance for 3-prong tau candidates. The red dashed histogram shows the signal template obtained from MC simulation requiring a match to generated 3-prong tau decays. In black the background template for QCD jets extracted from a di-jet selection in data is demonstrated.

Transverse momentum ratio of track and neutral pion system w.r.t. the tau $p_T, p_T^{\tau, \pi^0} / p_T^\tau$: fraction of the summed charged and neutral pion transverse momentum w.r.t. the tau p_T . For tau leptons this ratio tends to be one, while for jets other neutral hadrons, like neutral kaons, lead to a significant shift towards smaller ratios. Figure 7.11 shows the p_T ratio for one- and three-prong decays.

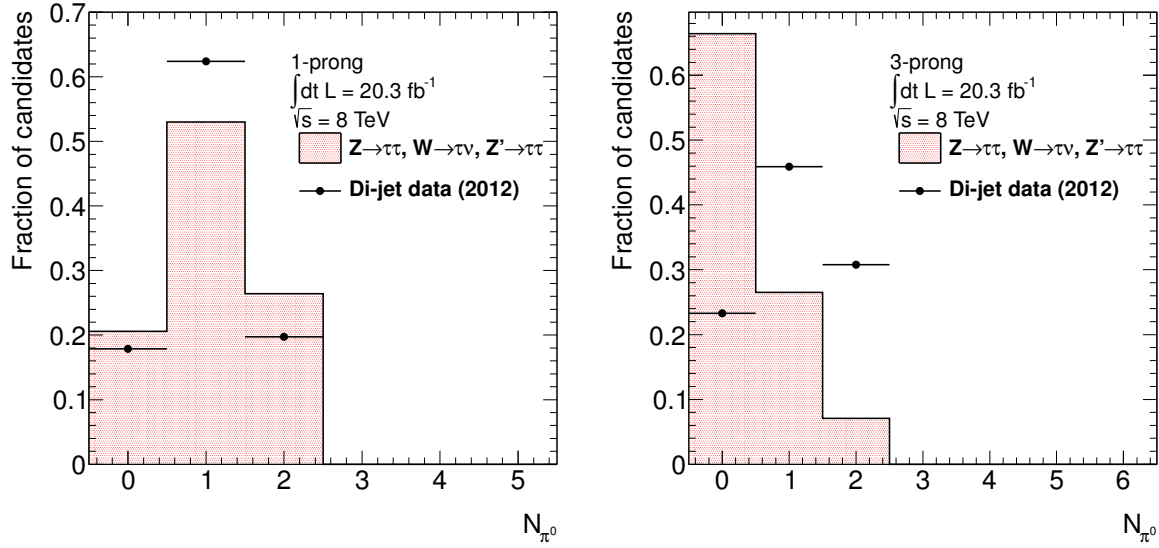


Figure 7.9: Number of reconstructed neutral pions using cluster based π^0 reconstruction for reconstructed 1-prong (left) and 3-prong (right) tau candidates. The red dashed histogram shows the signal template obtained from MC simulation requiring a match to generated 1-/3-prong tau decays. In black the background template for QCD jets extracted from a di-jet selection in data is demonstrated.

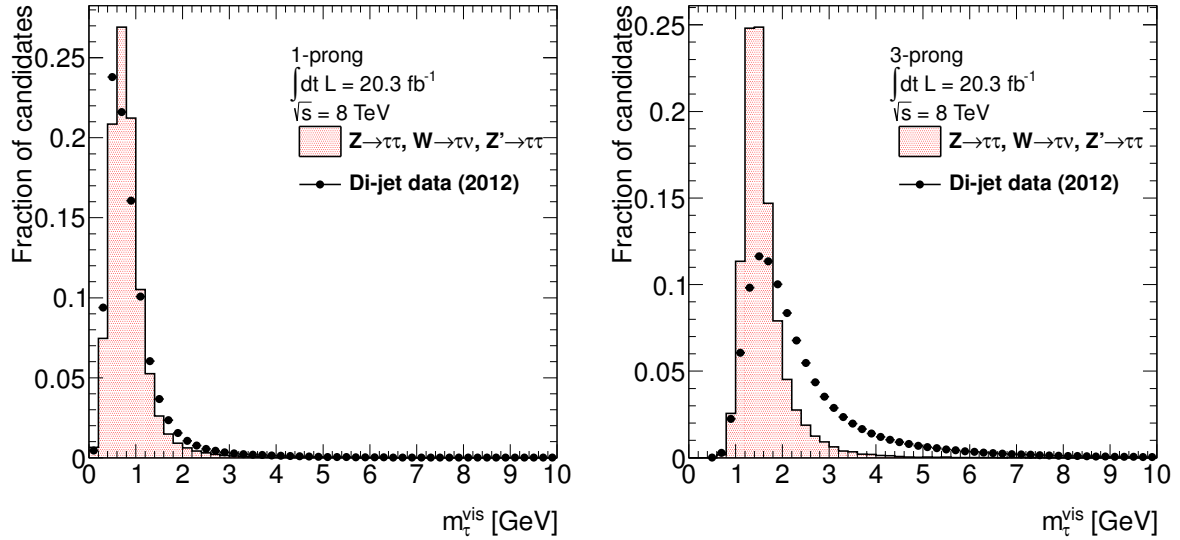


Figure 7.10: Visible invariant mass of the track and neutral pion system. The red dashed histogram shows the signal template obtained from MC simulation requiring a match to generated 1-/3-prong tau decays. In black the background template for QCD jets extracted from a di-jet selection in data is demonstrated.

7.2.2 Log-Likelihood Based Tau Identification

The likelihood-based tau identification is based on *probability density functions* (p.d.f.s) of several discriminating variables. For a given set of identification variables, x_i , the likelihood for being signal and background, $L_{S(B)}$, is defined as the product of p.d.f.s for signal and background events, $p_i^{S(B)}(x_i)$:

$$L_{S(B)} = \prod_{i=1}^N p_i^{S(B)}(x_i). \quad (7.12)$$

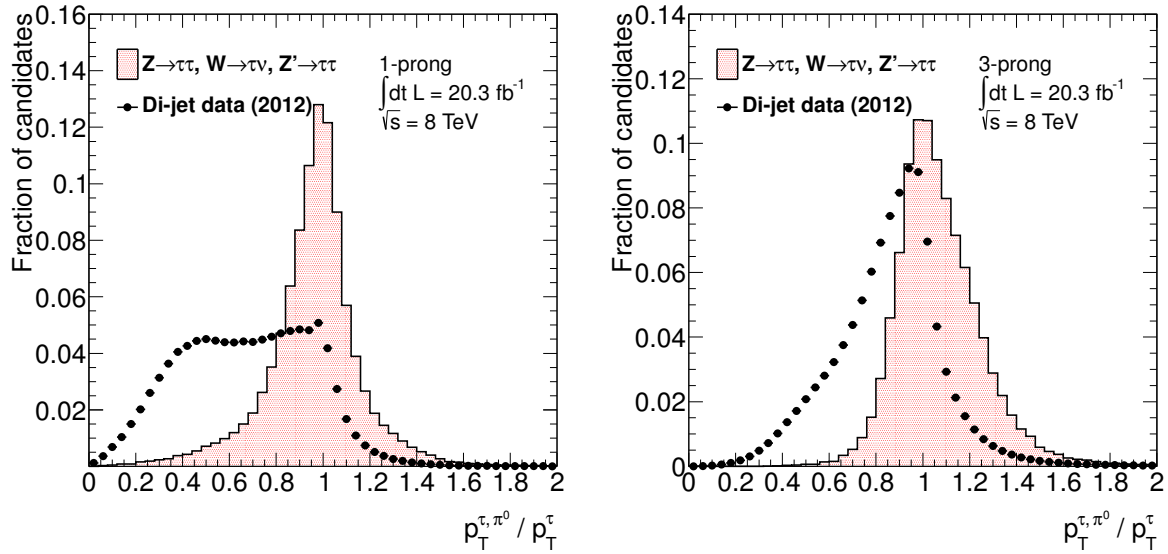


Figure 7.11: Ratio of the transverse momentum of the track and π^0 system w.r.t. the transverse momentum of the reconstructed tau candidate. The red dashed histogram shows the signal template obtained from MC simulation requiring a match to generated 1-/3-prong tau decays. In black the background template for QCD jets extracted from a di-jet selection in data is demonstrated.

Likelihood values are combined to the final discriminating log-likelihood score, S_{LLH} , by calculating a log-likelihood ratio of signal and background likelihoods:

$$S_{LLH} = \ln\left(\frac{L_S}{L_B}\right) = \sum_{i=1}^N \ln\left(\frac{p_i^S(x_i)}{p_i^B(x_i)}\right). \quad (7.13)$$

Cuts corresponding to predefined target signal efficiencies (working points) are applied on the score value. The optimisation is done in two steps. First the classifier is trained, followed by the evaluation of its performance in the testing (evaluation) step. The signal and background dataset are split into equal parts to perform each step on a statistically independent sample. The corresponding templates are extracted from the selected data outlined in Section 7.2.1.

Training

The training is used to obtain the p.d.f.s separately for 1-prong and 3-prong tau decays. To extract a clean signal template only tau candidates matching to a generated tau decay with the same number of charged hadrons are taken into account. Since the identification variables depend strongly on the tau decay kinematics they are binned in the transverse momentum, p_T , of the reconstructed tau candidate. Three different p_T bins are used: $p_T < 45$ GeV, $45 \text{ GeV} \leq p_T < 100$ GeV and $p_T \geq 100$ GeV. To avoid discontinuities at the bin borders an interpolation procedure is performed. It is applied if the tau p_T is within 10 GeV of a bin border, except for 1-prong tau decays where the interpolation is applied within a window of $[-30, +60]$ GeV for the last p_T bin. Let, L , be the likelihood value corresponding to the bin into which the tau falls, the likelihood value, L' , of the adjacent bin is calculated in addition. The following interpolation is applied to calculate the final likelihood value, L_{final} :

$$L_{final} = L \cdot \frac{10 + \delta}{20} + L' \cdot \frac{10 - \delta}{20}, \quad (7.14)$$

in which δ denotes the distance of the tau p_T , p_T^τ , to the bin border, $p_T^{bin-edge}$, i.e. $\delta = |p_T^\tau - p_T^{bin-edge}|$. The obtained LLH score distributions are shown in Figure 7.12 for 1-prong and 3-prong tau decays.

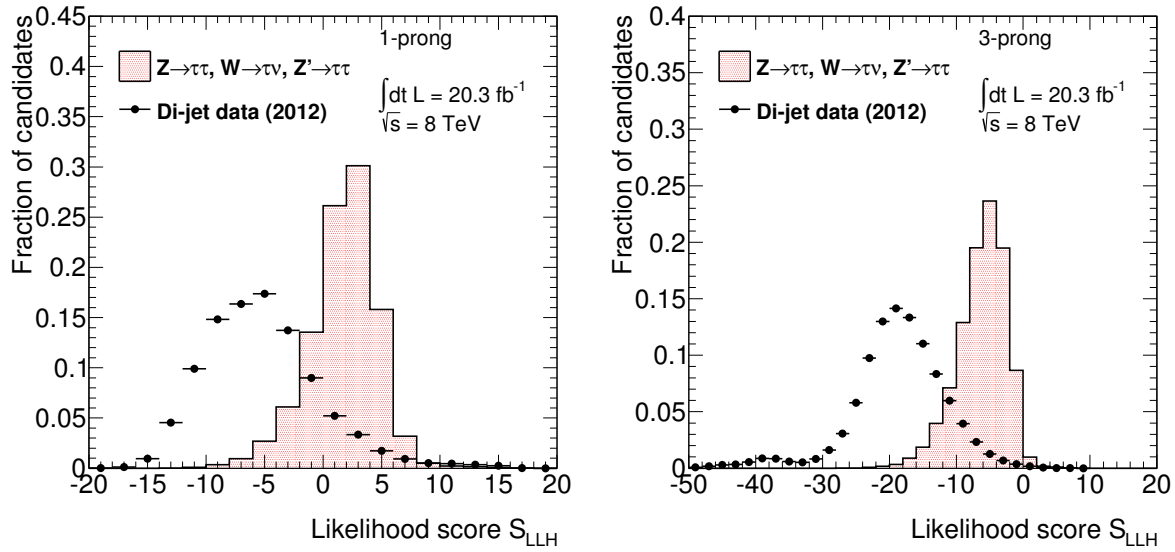


Figure 7.12: Distribution of the LLH discriminator for reconstructed 1- (left) and 3-prong (right) tau candidates. The red dashed histogram shows the signal template obtained from MC simulation requiring a match to generated 1-/3-prong tau decays. In black the background template for QCD jets extracted from a di-jet selection in data is demonstrated.

Performance Evaluation

The performance is evaluated on an statistically independent dataset. Looser requirements on the reconstructed tau candidates can be applied to match possible physics needs. The n-prong requirement for multi-prong taus is loosened including the two-track bin as well. The log-likelihood score is calculated based on the p.d.f.s defined in the training and cut values corresponding to pre-defined signal efficiencies are calculated. The signal efficiency is defined as the ratio of reconstructed 1-/3-prong tau candidates matched to a generated 1-/multi-prong tau decay within $\Delta R < 0.2$ passing a specific cut on the LLH score divided by the number of generated 1-/3-prong tau decays:

$$\epsilon_{1P/MP}^{\text{sig}} = \frac{N_{\text{passed}}^{1P/MP}}{N_{\text{generated}}^{1P/3P}}. \quad (7.15)$$

In there $N_{\text{passed}}^{1P/MP}$ is the number of reconstructed 1- or multi-prong tau candidates matched to a generated 1-/3-prong tau lepton passing the cut on the discriminator and $N_{\text{generated}}^{1P/3P}$ the number of generated 1-/3-prong taus. Thus it is not a pure identification efficiency, but rather a combined reconstruction and identification efficiency. The cut-values depend on p_T in order to provide flat signal efficiencies w.r.t. the generated visible transverse tau momentum. Working points corresponding to 70% (65%), 60% (55%) and 40% (35%) are provided for 1-(multi-)prong tau candidates. They are referred to as *loose*, *medium* and *tight*, respectively. The current LLH does not exploit the π^0 information, but rather a smaller set of variables summarised in Table 7.2. The obtained signal efficiency as a function of the transverse momentum of the tau candidate of the LLH algorithm is summarised in Figure 7.13.

Since the instantaneous luminosity increased in 2012, a larger number of pile-up events is expected. Furthermore, the collider parameters change during a data-taking period. To provide a constant performance of the tau identification the algorithms have to be robust against pile-up. Figure 7.14 shows the signal efficiencies for the pre-defined working points as a function of the average number of interactions per bunch crossing, μ , a measure for the pile-up activity. The efficiency stays flat up to $\mu \sim 40$ for multi-prong tau decays, which indicates the high robustness due to the dedicated corrections of pile-up sensitive input variables. Since 1-prong tau candidates are more prone to pile-up contamination a slight degradation with increasing μ is observed.

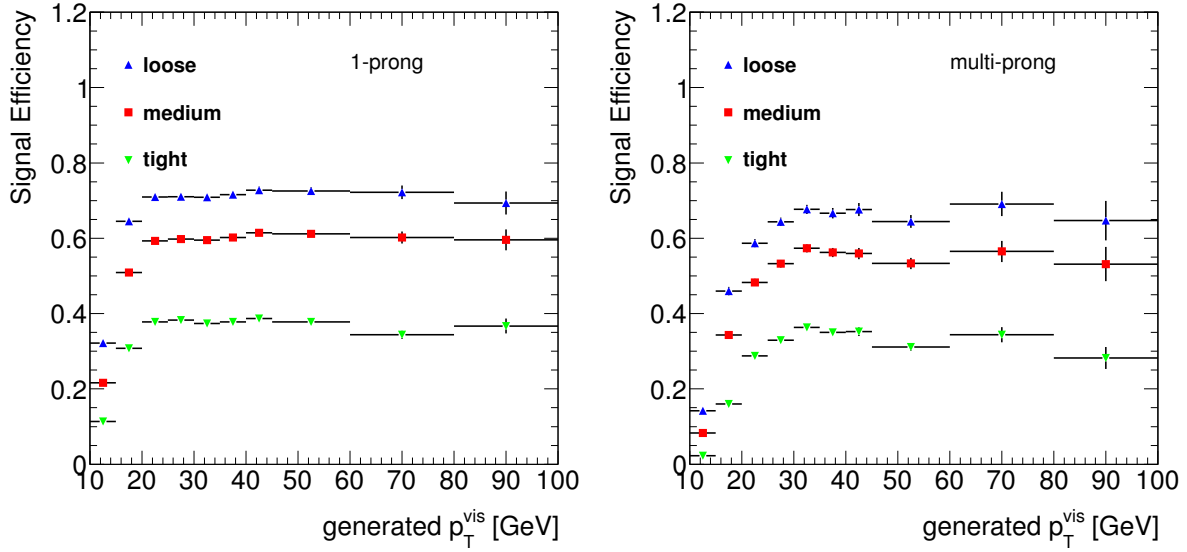


Figure 7.13: Tau identification efficiency for one- (left) and multi-prong (right) tau candidates versus the visible p_T of the generated tau lepton for the LLH algorithm. The loose, medium and tight working points are represented by the blue triangle, red squares and green triangles, respectively. The corresponding cuts on the LLH score are tuned such that the signal efficiency is flat w.r.t. the generated tau p_T .

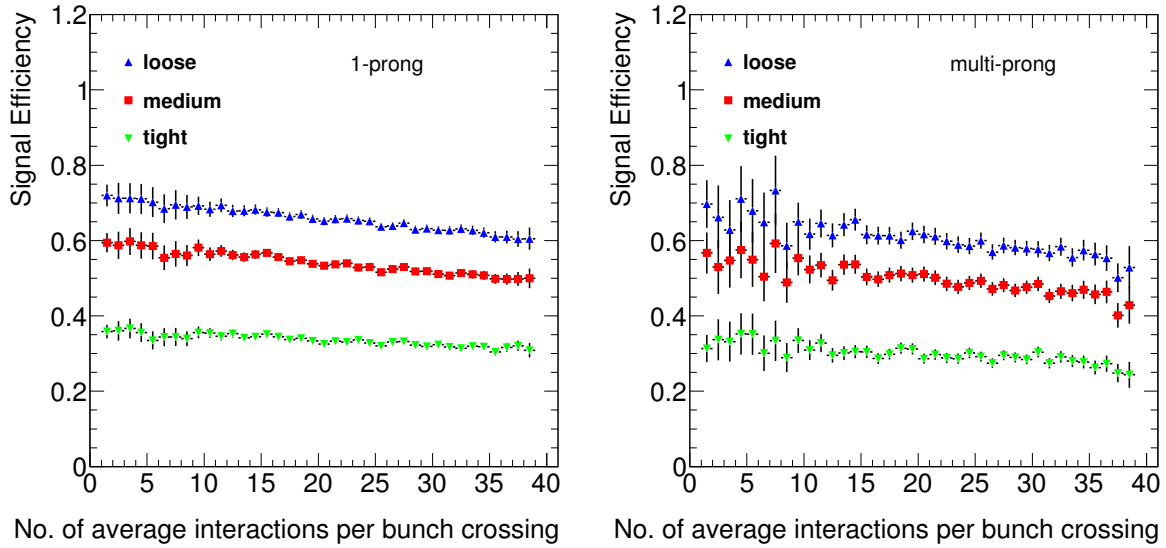


Figure 7.14: Tau identification efficiency for one- (left) and multi-prong (right) tau candidates versus the average number of interactions per bunch crossing for the LLH algorithm. The loose, medium and tight working points are represented by the blue triangle, red squares and green triangles, respectively.

Another figure of merit is the background efficiency, which gives a measure of the rate of rejecting fake tau candidates originating from quark or gluon initiated jets. It is defined analogous to the signal efficiency (c.f. Eq. 7.15), but obviously without the generator match requirement:

$$\epsilon_{1P/MP}^{\text{bkg}} = \frac{N_{\text{passed}}^{1P/MP}}{N_{\text{reco}}^{1P/MP}}, \quad (7.16)$$

with $N_{\text{passed}}^{1P/MP}$ being the number of reconstructed one- or multi-prong tau candidates passing the cut on

the discriminator and $N_{\text{reco}}^{\text{1P/MP}}$ the total number of reconstructed 1-/multi-prong tau candidates. The background efficiency has been measured on a statistically independent set of the di-jet data sample. Figure 7.15 presents the p_T dependence of the tau mis-identification efficiency for the LLH method. As the p_T dependence of the input variables to the multivariate classifiers is different between signal and background, the background efficiency is not flat in p_T . Furthermore, the actual background rejection rate reached in physics analyses strongly depends on the fake composition, i.e. the quark/gluon ratio, and thus on the applied selection criteria. The rejection rate can differ by more than a factor of two [184].

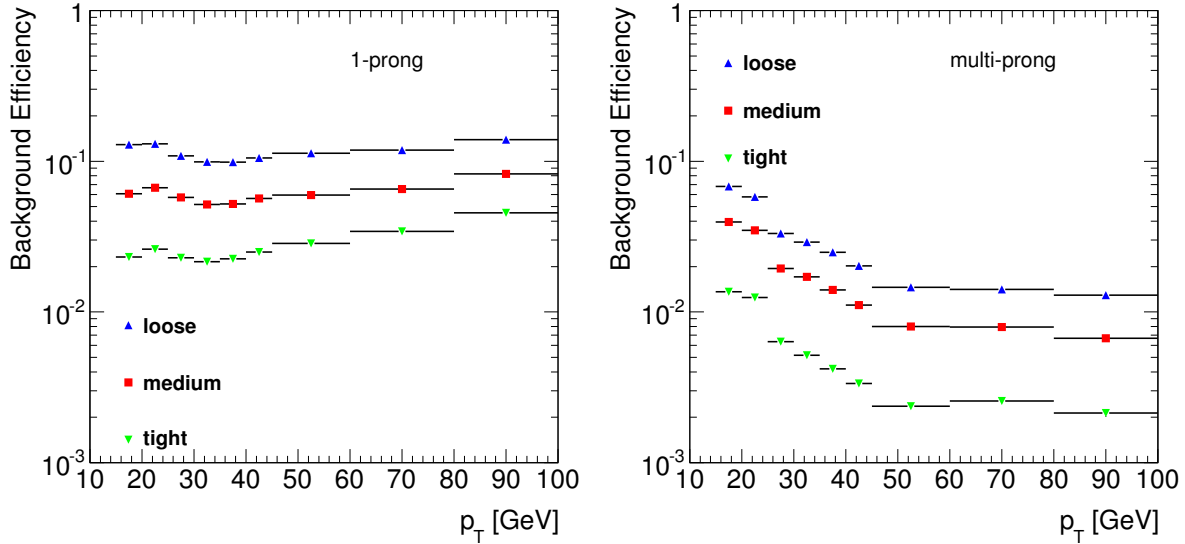


Figure 7.15: Tau mis-identification efficiency for one- (left) and multi-prong (right) tau candidates versus the p_T of the reconstructed tau candidate for the LLH algorithm. The loose, medium and tight working points are represented by the blue triangle, red squares and green triangles, respectively. The efficiency is measured in a di-jet enriched data sample.

Even though the mis-identification efficiency depends on the p_T of the tau candidate, it is supposed to be independent from the number of pile-up events. Figure 7.16 shows the mis-identification probability versus the number of average interactions per bunch crossing for the three predefined working points. A flat behaviour is observed which indicates the robustness against pile-up.

7.2.3 Boosted Decision Tree Based Tau Identification

A second multivariate algorithm based on boosted decision trees (BDTs) is trained for the tau identification. BDTs are based on simple *decision trees* (DTs), which build a binary tree structure by performing a series of *pass-fail-decisions* (cuts). The outline of a DT is depicted in Figure 7.17.

Starting from a *root node* objects are classified by a simple cut on one variable i . This leads to two *leaf nodes* which are subject to further cuts on a different training variable j . This has the advantage that in contrast to a simple cut-based approach, objects are not immediately discarded, but are kept until a *stopping criterion* is met. In case of tau identification the stopping criterion is defined by a requirement on the minimum number of objects in each leaf node at the current stage of the decision tree. Even though a DT possesses in general a better performance than a simple-cut-based approach, it still might be a *weak classifier*. Weak classifiers are just slightly better than random decision. For such classifiers a general technique called *boosting* has been developed. Boosting is not restricted to weak classifiers or decision trees, but can be applied to any classification method. Here, the *adaptive boosting* (AdaBoost) [186] algorithm is utilised. During the boosting process a combination of several classifiers is used to increase the performance. A weighted sum of these combinations builds the final discriminant. For BDTs each decision tree is trained on a weighted dataset, for which the weights depend on the performance of the previous DT. In particular, misclassified objects get a higher weight, and thus get highly profiled in

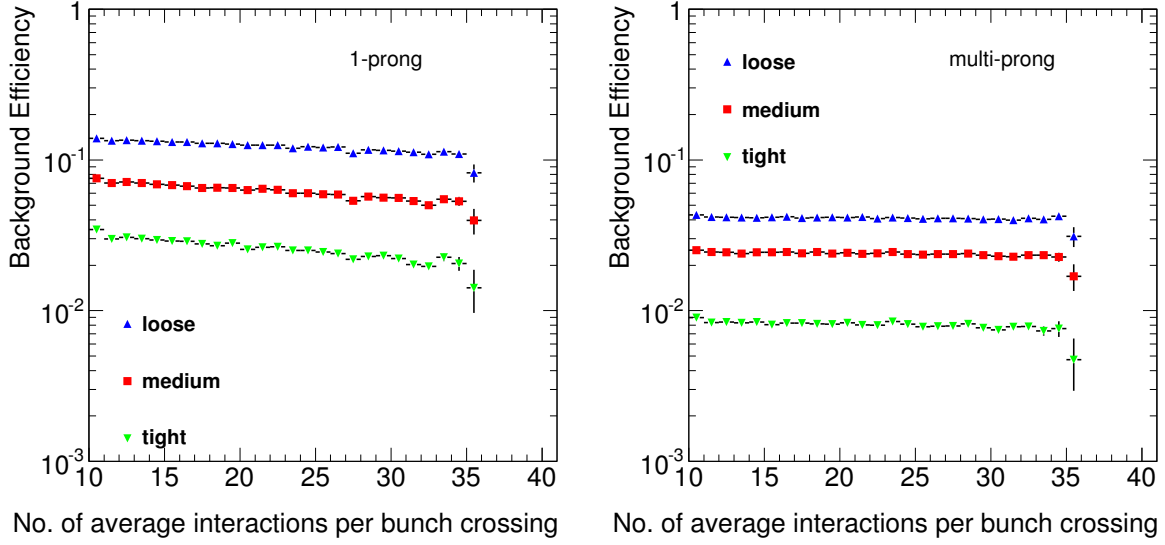


Figure 7.16: Tau mis-identification efficiency for one- (left) and multi-prong (right) tau candidates versus the average number of interactions per bunch crossing for the LLH algorithm. The loose, medium and tight working points are represented by the blue triangle, red squares and green triangles, respectively. The efficiency is measured in a di-jet enriched data sample.

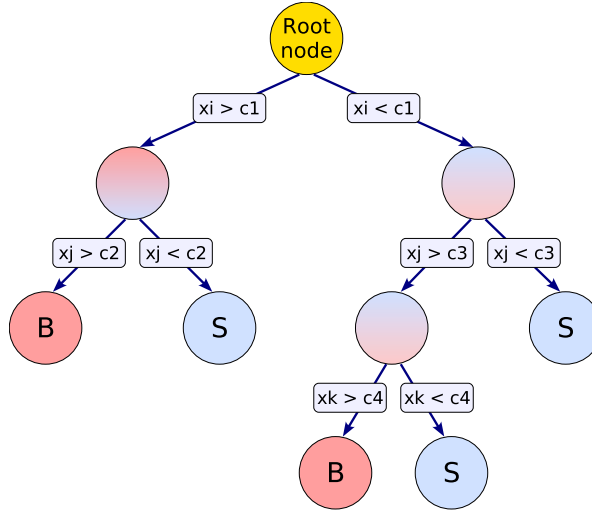


Figure 7.17: Schematic view of a decision tree. Starting from the root node the dataset is split into signal (blue) and background (red) leaves. Taken from [185].

the next training. Exploiting a *weighted majority voting scheme* yields the final continuous classifier, the BDT score. For further details on multivariate classification and boosting see e.g. [173]. In order to distinguish the BDT used for jet discrimination from other BDTs, it will be referred to as jBDT in the following. The input variables used by the jBDT are a subset of the above mentioned hadronic tau identification variables and are summarised in Table 7.2. The training and optimisation is performed using the *TMVA* toolkit [185]. In Figure 7.18 the distribution of the final discriminant, i.e. the BDT score, is displayed for one- and multi-prong hadronic tau candidates. Real tau candidates, represented by the red shaded area, tend to be classified with high BDT score values, while mis-identified jets tend to yield lower values. To obtain a flat signal efficiency the same procedure of flattening described above for the LLH method is applied.

As discussed above for the LLH-based tau identification, the signal efficiency is tuned to be flat w.r.t.

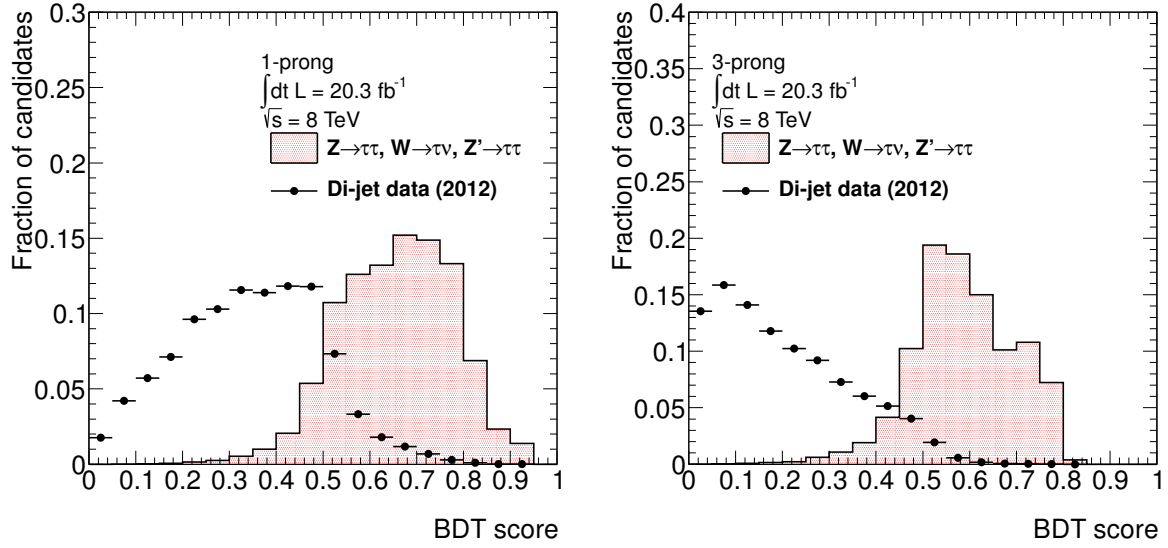


Figure 7.18: Distribution of the BDT discriminator for reconstructed 1- (left) and 3-prong (right) tau candidates. The red dashed histogram shows the signal template obtained from MC simulation requiring a match to generated 1-/3-prong tau decays. In black the background template for QCD jets extracted from a di-jet selection in data is demonstrated.

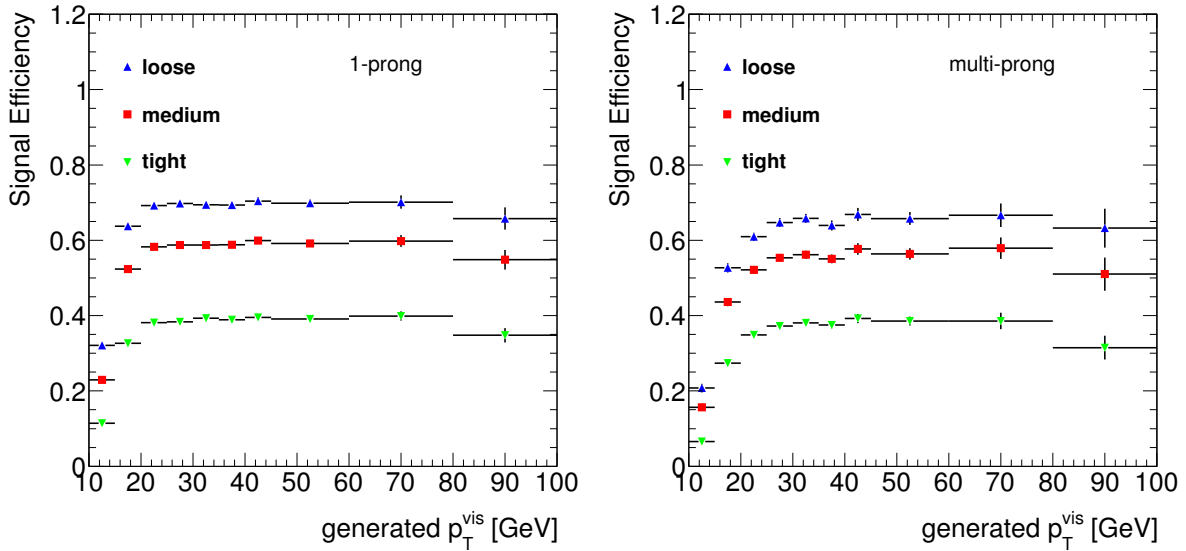


Figure 7.19: Tau identification efficiency for one- (left) and multi-prong (right) tau candidates versus the visible p_T of the generated tau lepton for the BDT algorithm. The loose, medium and tight working points are represented by the blue triangle, red squares and green triangles, respectively. The corresponding cuts on the BDT score are tuned such that the signal efficiency is flat w.r.t. the generated tau p_T .

the visible p_T of the matched generated tau lepton. Furthermore, since the same pile-up robust input variables are used in the training of the BDT classifier, a flat behaviour w.r.t. the average number of interactions per bunch crossing is expected. Figures 7.19 and 7.20 show the signal efficiency versus the visible p_T of the generated tau lepton and the number of interactions per bunch crossing, respectively, for the BDT algorithm. The expected behaviour is observed.

Since the BDT exploits an extended set of input variables a higher background suppression than provided by the LLH method is expected. Figures 7.21 and 7.22 present the p_T and pile-up dependence of

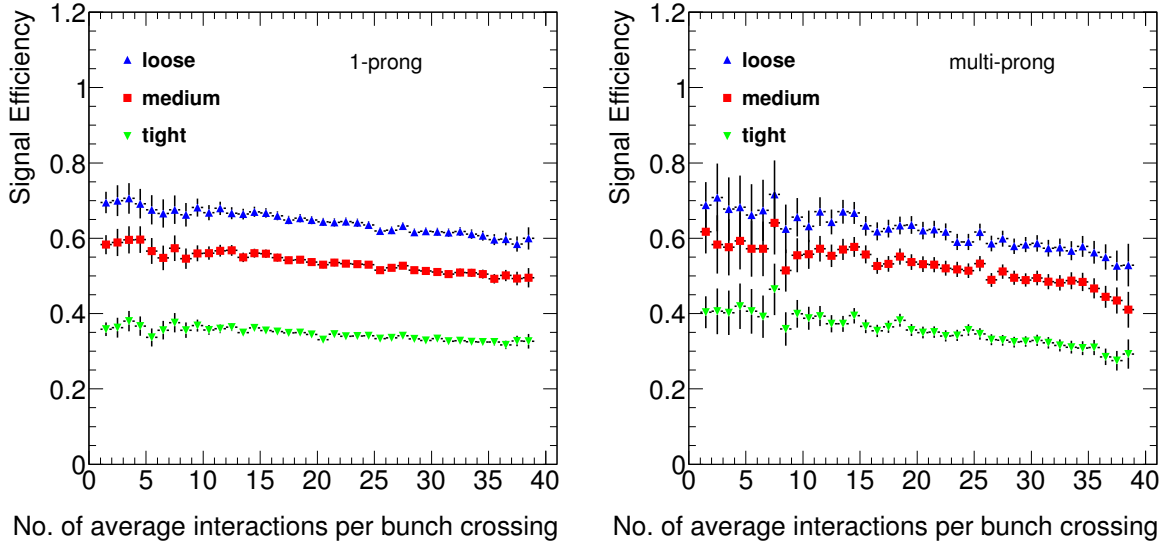


Figure 7.20: Tau identification efficiency for one- (left) and multi-prong (right) tau candidates versus the average number of interactions per bunch crossing for the BDT algorithm. The loose, medium and tight working points are represented by the blue triangle, red squares and green triangles, respectively.

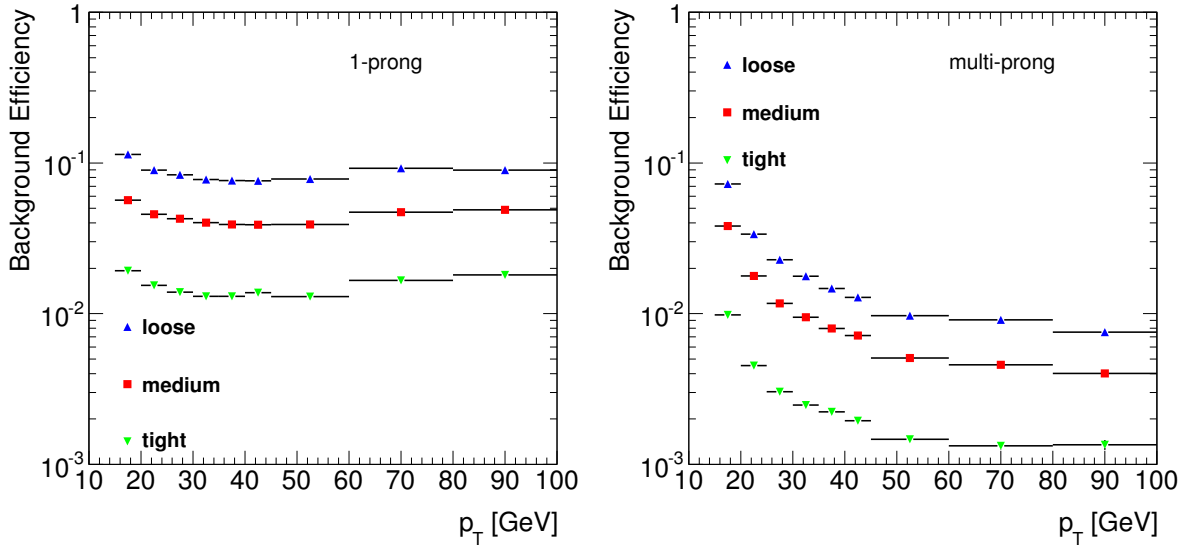


Figure 7.21: Tau mis-identification efficiency for one- (left) and multi-prong (right) tau candidates versus the p_T of the reconstructed tau candidate for the BDT algorithm. The loose, medium and tight working points are represented by the blue triangle, red squares and green triangles, respectively. The efficiency is measured in a di-jet enriched data sample.

the mis-identification efficiency for the BDT algorithm, respectively. As expected the mis-identification efficiency is up to a factor of two lower than obtained by the LLH technique. Again, a flat efficiency is observed as a function of the average number of interactions per bunch crossing.

7.2.4 Comparison of BDT and LLH Based Tau Identification

The final figure of merit to classify the performance of the tau identification algorithms is the background rejection rate at a given signal efficiency. Hence, the cuts on the discriminator scores are scanned through

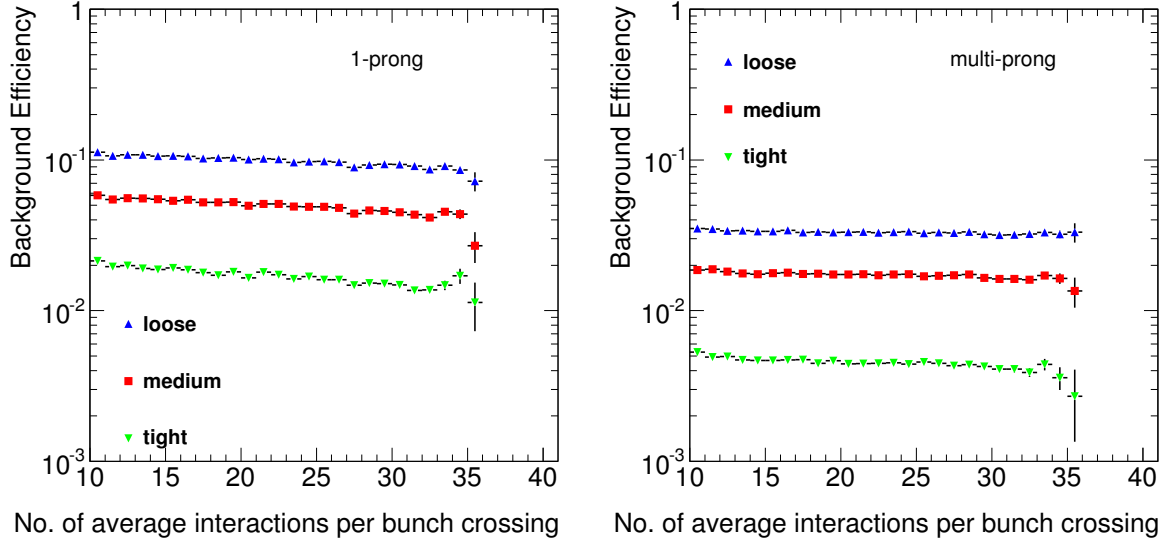


Figure 7.22: Tau mis-identification efficiency for one- (left) and multi-prong (right) tau candidates versus the average number of interactions per bunch crossing for the BDT algorithm. The loose, medium and tight working points are represented by the blue triangle, red squares and green triangles, respectively. The efficiency is measured in a di-jet enriched data sample.

variable	LLH		BDT	
	1-prong	3-prong	1-prong	3-prong
R_{track}	•	•	•	•
f_{core}	•	•	•	•
f_{track}	•	•	•	•
$S_{\text{lead track}}^{\text{IP}}$	•		•	
$N_{\text{track}}^{\text{iso}}$	•		•	
ΔR_{max}		•		•
m_{tracks}		•		•
$S_{\text{T}}^{\text{flight}}$		•		•
N_{π^0}			•	•
m_{τ}^{vis}			•	•
$p_{\text{T}}^{\tau, \pi^0} / p_{\text{T}}^{\tau}$			•	•

Table 7.2: Summary of identification variables used for LLH- and BDT-based jet discrimination. Different input variables (marked by the black bullets) are used for each classifier for 1-prong and 3-prong tau decays.

the entire interval of the discriminator calculating both signal and background efficiency. Figure 7.23 shows the background rejection versus the signal efficiency for one- and multi-prong tau candidates for the LLH and BDT technique. It can be seen that the BDT outperforms the LLH method as the background rejection is higher for all signal efficiencies. The reason is two-fold. First, the BDT training exploits an extended set of identification variables, in particular including π^0 information which leads to a gain in performance. Second, the BDT training takes advantage of the correlations of the identification variables, which are not considered by the LLH method. While the extension of the set of input variables

is trivial, the latter issue might be more complicated. However, for instance decorrelation algorithms exist and are implemented in tools designed for multivariate analyses, like TMVA, and thus might be applied in the future. Nevertheless, it is still important to provide both algorithms for the purpose of cross validation and to provide physics groups with alternatives, as the LLH method still might be more suitable in some phase space regions.

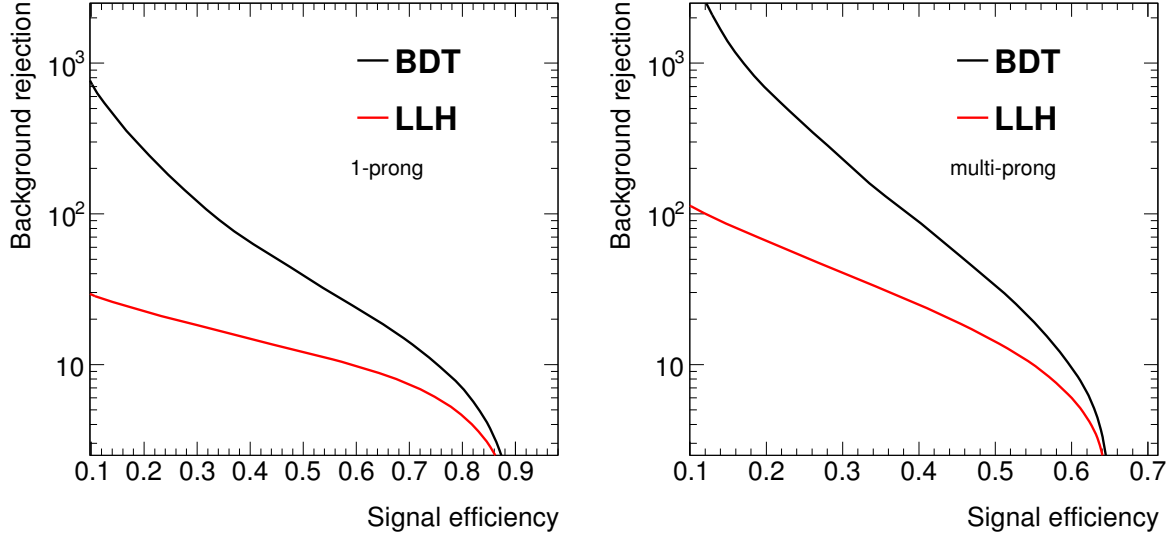


Figure 7.23: Background rejection versus signal efficiency for the LLH (red) and BDT (black) tau identification algorithms for 1- (left) and 3-prong (right) tau candidates. This represents the figure of merit during the optimisation. A clear performance overshoot of the BDT algorithm is observed, which arises from the extended set of training variables and the different underlying concept of the algorithms.

7.2.5 Measurement of the Performance of Tau Identification Algorithms

As outlined above the optimisation of the tau identification algorithms is based on MC simulation. Thus an evaluation of the performance with data is crucial to verify the quality of the modelling of the input variables and their correlations by simulation. This is the aim of the tau identification measurement, which derives *scale factors* for each working point. These scale factors cover potential mis-modelling effects and are applied as correction factors on the normalisation in the analysis. To measure the identification efficiency a pure tau sample has to be selected in data. The current measurement is based on a "tag-and-probe" style analysis [187] using $Z \rightarrow \tau_l \tau_h$ events, whereas the most recent measurement only considers the muon final state. The ID efficiency is then defined by the ratio of real taus after and before applying the identification requirement. However, in practice it is impossible to select a pure tau sample, but contamination from backgrounds have to be considered. A *template fit method* is performed to parametrise the yields before and after applying the identification criteria. These templates are based on the *extended track multiplicity* distribution, $N_{\text{track}}^{\text{ext}}$, defined in [174]. The dominant background arises from quark- and gluon-initiated jets occurring either in association with gauge bosons (electroweak component) or as multijet events (QCD component). Hadronic tau decays tend to be more collimated at a given transverse momentum than quark- or gluon-initiated jets which reflects in a shift in the N_{track} distribution. However, it is useful to include additional tracks in a wider cone to further improve the discrimination. For real tau decays no additional tracks are expected in an annulus of $0.2 < \Delta R < 0.6$ around the tau candidate axis, but might be distorted by pile-up tracks, whereas jets which mimic a tau decay tend to have a larger amount of associated tracks in this wider annulus. The association of tracks in the extended search region is based on its p_T and spatial distance. Details can be found in [174]. Figure 7.24 (left) shows the derived extended N_{track} distribution for the signal and several electroweak

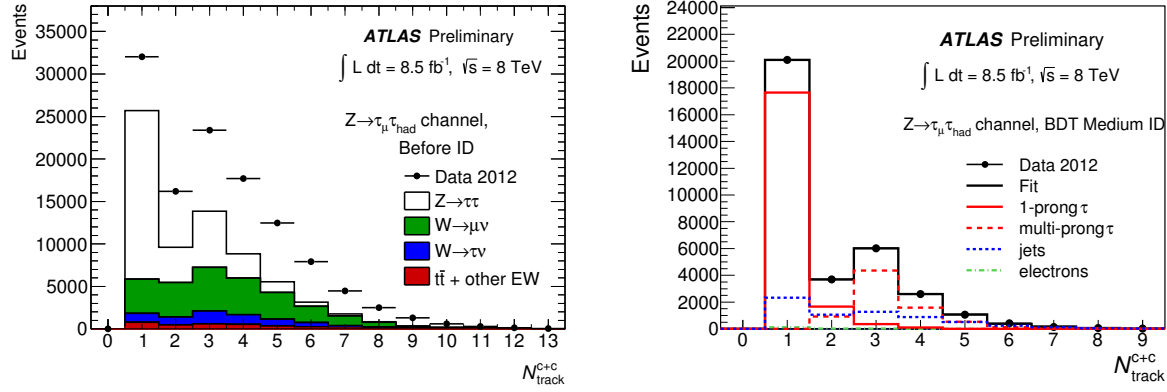


Figure 7.24: Left: Extended track distribution before applying the identification criterion. Signal and electroweak backgrounds are derived from MC simulated collision events and are represented by the coloured histograms. The data distribution is marked by the black dots. The missing multijet component is estimated from a data control region as discussed in the text. Right: Results of the template fit after applying jBDT medium identification for 1-prong probe tau candidates. Both taken from [174].

backgrounds and data after the $Z \rightarrow \tau_\mu \tau_{\text{had}}$ selection. As will be discussed below, the multijet component covering the discrepancy between the prediction by MC and data is derived from control regions in data, and thus is missing in the shown plot. The efficiency measured in data is defined by the number of taus passing a given threshold divided by the number of all taus. In MC simulation a matching to generated hadronic tau decays is performed. The ratio between the efficiency measured in MC simulation and data is defined as the scale factor

$$\text{SF} = \frac{\epsilon_{\text{data}}}{\epsilon_{\text{MC}}}. \quad (7.17)$$

Events considered for the analysis require an isolated trigger-matched muon serving as *tag* object and an additional hadronically decaying tau lepton as *probe* candidate. The full selection can be found in Table 1 in [174], but cuts have been tightened slightly in the updated version which will be published soon (c.f. [188]). A loose cut on the jBDT score is applied to the probe candidate which highly reduces the contamination from quark- and gluon-initiated jets, while the impact on the SF measurement is found to be negligible ($\sim 1\%$ [174]). Uncertainties are propagated through the SF calculation using the error propagation law. Different templates are then calculated using both MC simulation and collision data. Signal templates are derived separately for 1-prong and 3-prong probe tau candidates from PYTHIA $Z \rightarrow \tau\tau$ simulation events. Systematic uncertainties arise from the unknown quality of the tau decay modelling, which is estimated by performing the template fit with altered signal templates. These are derived from varied configurations of the simulation setup accounting for the choice of the generator and hadronic shower model, the detector geometry and the fragmentation model. Section 11.1.1 will elaborate in more detail on these samples. The systematic uncertainty is then taken as the difference between the nominal and the altered templates. To reduce the statistical component of the uncertainty the altered templates are obtained without applying the full tag-and-probe selection, which is a valid approach assuming the tag-and-probe selection and a potential mis-modelling effect are uncorrelated. The dominant background contribution for jets is estimated from same-sign data events, which serve as a signal free control region. This template will cover both the electroweak and strong interaction component of the jet backgrounds. Differences between the signal region, i.e. oppositely charged leptons, and the control region are taken as systematic uncertainty. This includes subtraction of same-sign electroweak and $t\bar{t}$ events estimated from MC simulation in the same-sign control region and correspondingly addition of their opposite-sign components in the signal region. Furthermore, uncertainties on the transfer ratio between OS and SS events, measured in an anti-isolated control region, i.e. where the isolation criterion on the muon is inverted, are propagated through the template. The control region with inverted isolation

criteria (anti-iso) is dominated by multijet events, and thus takes into account the charge distribution of multijet events. The background component arising from jet fakes can then be written as:

$$N_{\text{OS-SS}}(N_{\text{track}}^{\text{ext}}) = \left(N_{\text{SS}}^{\text{data}}(N_{\text{track}}^{\text{ext}}) - \sum_i^{\text{allMC}} N_{i,\text{SS}}^{\text{MC}}(N_{\text{track}}^{\text{ext}}) \right) \frac{N_{\text{OS}}^{\text{anti-iso}}(N_{\text{track}}^{\text{ext}})}{N_{\text{SS}}^{\text{anti-iso}}(N_{\text{track}}^{\text{ext}})} + \sum_i^{\text{allMC}} N_{i,\text{OS}}^{\text{MC}}(N_{\text{track}}^{\text{ext}}). \quad (7.18)$$

An additional template covering electron fakes is derived from $Z \rightarrow \tau\tau$ MC where the probe tau candidate is required not to match a generated hadronic tau decay. In Figure 7.24 (right) the templates and fit results [174] after application of the jBDT medium requirement are shown for 1-prong tau candidates.

The derived scale factors and their uncertainties are shown for the loose and medium jBDT working point in Figure 7.25 for 1- and 3-prong tau candidates. They are consistent with one and uncertainties are in the order of a few percent. The quoted uncertainties are the quadratic sum of statistical and systematic uncertainties. They will be used in the presented analyses to estimate the systematic uncertainty on the expected event yields for MC simulated events containing real taus. Details are given in Section 11.1.1.

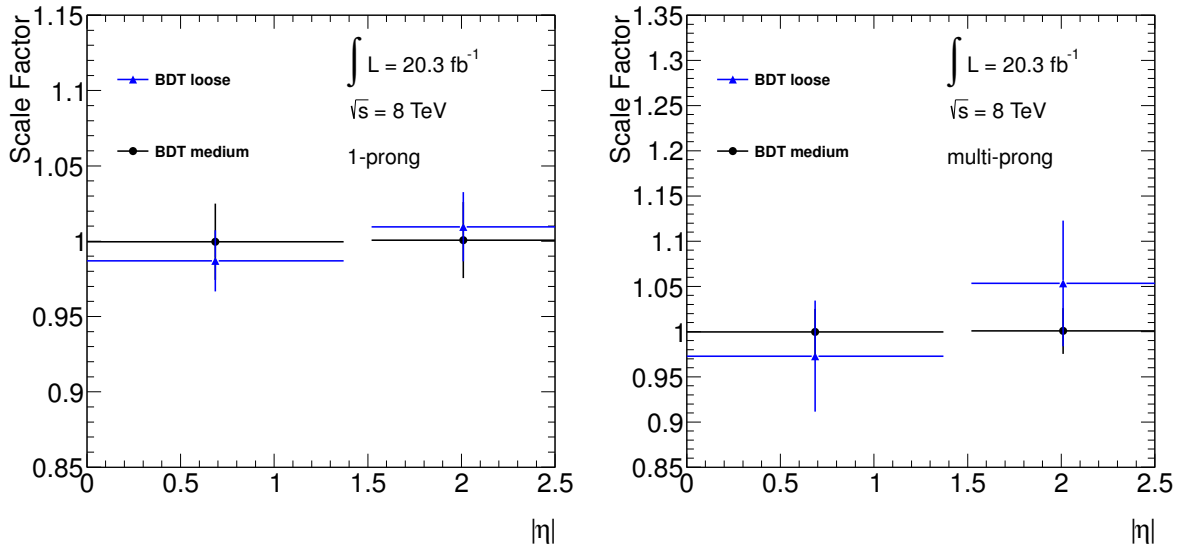


Figure 7.25: Tau identification scale factors for 1-prong (left) and 3-prong (right) tau candidates derived from a $Z \rightarrow \tau_\mu \tau_{\text{had}}$ analysis. Scale factors for the loose jBDT working point are marked by the blue triangles, while the black dots represent the jBDT medium working point. Error bars indicate the quadratic sum of statistical and systematic uncertainties.

7.2.6 Electron Veto

Optimisation

Electrons produce a track in the inner detector and an associated cluster in the electromagnetic calorimeter. This signature can mimic a hadronic 1-prong tau decay. To reduce the rate of electron fakes a BDT-based discrimination was developed. Tau decays tend to have wider and longer shower profiles than electrons which is exploited by the electron discrimination algorithm. Electrons also have a higher probability for transition radiation which is a powerful quantity entering the discriminant. The optimisation strategy follows the principles outlined in Section 7.2.3. Working points are provided for loose, medium and tight levels corresponding to signal efficiencies of 95%, 85% and 75%, respectively. The signal efficiency is defined as the fraction of reconstructed 1-prong tau decays passing the loose jBDT requirement matched to a generated τ_{had} within $\Delta R < 0.2$. The background rejection is defined w.r.t reconstructed electrons matched to generated electrons within $\Delta R < 0.2$. Both electron and tau candidates are required to have $p_T > 20 \text{ GeV}$. The optimisation is performed on simulated $Z \rightarrow \tau\tau$ (signal) and $Z \rightarrow ee$ (background) samples in four distinct $|\eta|$ regions; barrel ($|\eta| < 1.37$), crack region ($1.37 < |\eta| < 1.52$), end-cap

($1.52 < |\eta| < 2.0$) and forward end-cap $|\eta| > 2.0$. In each $|\eta|$ region the set of variables which yield the best performance in terms of background rejection is chosen. Figure 7.26 presents the background efficiency w.r.t. the signal efficiency obtained from simulated $Z \rightarrow \tau\tau$ and $Z \rightarrow ee$ events. The best performance is achieved in the barrel region, while in the forward region the performance degrades.

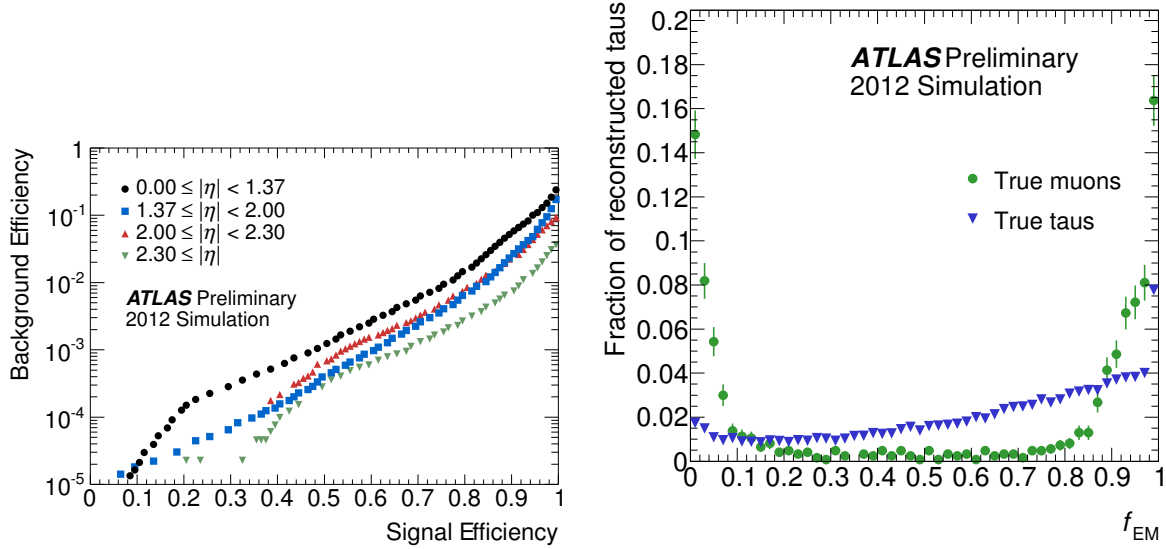


Figure 7.26: Background efficiency versus signal efficiency (left) of the electron discrimination algorithm measured in $Z \rightarrow \tau\tau$ and $Z \rightarrow ee$ MC simulation. Different colours/markers highlight different detector regions in which the electron veto algorithm has been optimised [187]. The right plot shows the electromagnetic energy fraction, f_{EM} , for tau candidates (blue triangles) and reconstructed muons (green circles) matched to generated objects. Distributions are obtained from $Z \rightarrow \tau\tau$ and $Z \rightarrow \mu\mu$ MC simulation [187].

Scale Factor Measurement

Like for the jet discrimination the electron veto performance is evaluated with data to derive scale factors which correct for any mis-modelling in the simulation. It is measured using 2012 data corresponding to 20.3 fb^{-1} . $Z \rightarrow ee$ events are selected by a tag-and-probe style analysis. Events are tagged if a reconstructed and identified electron (using the tight working point [189]) with $p_T > 35 \text{ GeV}$ and within the fiducial volume of the tracking system is found. As probe objects reconstructed τ_{had} candidates with $p_T > 20 \text{ GeV}$ and $|\eta| < 2.5$ are considered. The full event selection is outlined in [187]. Backgrounds remaining after this selection are QCD multijets, $W \rightarrow e\nu$, $Z \rightarrow \tau\tau$ and $t\bar{t}$. The multijet background is estimated from data, while others are estimated from simulation, but corrections factors derived from data versus MC comparisons in control regions are applied on top. Uncertainties on the correction factor of the electron discrimination efficiency are estimated by altering the event selection. Details can be found in [187]. Up to $|\eta| < 2.47$ uncertainties are about 20% except for the central ($|\eta| < 0.05$) and crack region ($1.37 < |\eta| < 1.52$) where they are significantly larger, extending up to 77%.

7.2.7 Muon Veto

At LHC energies muons are minimum ionising particles, and hence are unlikely to be reconstructed as a hadronic tau decay. However, if a cluster in the calorimeter is assigned to the muon track in the inner detector, it can mimic an 1-prong tau decay. The cluster can stem either from material ionisation by the muon with a large fraction of the energy deposited in the hadronic calorimeter, or it can come from an alternative source, such as collinear photon radiation off the muon or coincident overlap with a calorimeter cluster. In the latter case a large fraction of the energy will be deposited in the EM calorimeter, with

a small leak into the HCAL. These signatures can be expressed by the energy fraction in the electromagnetic calorimeter, f_{EM} . Low values of f_{EM} are expected for energy deposits by the muon itself, while high values of f_{EM} favour alternative sources of energy deposits building the cluster. A cut-based muon discrimination has been developed to reduce the amount of muon fakes. It is based on f_{EM} and f_{track} and optimised using simulated $Z \rightarrow \tau\tau$ (signal) and $Z \rightarrow \mu\mu$ (background) events. The electromagnetic energy fraction for tau candidates and muons, both matched to their corresponding generated object, is depicted in Figure 7.26 (right). Muon candidates are reduced by a factor of 2.5, while hadronic tau candidates are preserved by 96%.

7.3 Triggering on Tau Leptons

As pointed out in Section 4.2.6 a trigger system is crucial to cope with the high bunch crossing rate. Since tau leptons play an important role in many physics analyses, a dedicated tau trigger was designed to select hadronically decaying tau leptons. This is an extremely challenging task due to the high multijet production and its corresponding fake-rate. The trigger system is designed as a three step selection system as pointed out in Section 4.2.6. The following sections will first briefly introduce the outline of the L1 and L2 selection and menu used for 2012 data-taking. Next, an optimised EF trigger selection based on multivariate (MV) classification algorithms exploiting BDTs and LLHs will be discussed in detail. Section 7.3.4 closes with a brief discussion of the tau trigger efficiency measurement in data.

7.3.1 Tau Trigger Menu in 2012

L1 Tau Trigger

The L1 trigger is a hardware based system using information of the calorimeters and muon chambers with coarser granularity to retain a manageable rate. The L1 tau trigger uses both, electromagnetic and hadronic trigger towers of size $\Delta\eta \times \Delta\phi = 0.1 \times 0.1$. A core and an isolation region are defined. The core region is using a set of 2×2 trigger towers, i.e. $\Delta\eta \times \Delta\phi = 0.2 \times 0.2$, while the isolation region uses 4×4 trigger towers subtracting the core region. This is outlined in Figure 7.27. A cut on the transverse energy measured in the core region is applied by the L1 tau trigger. They are named like L1.TAUX, with X indicating the E_{T} threshold. The 2012 trigger menu supports thresholds of 8 GeV, 11 GeV, 15 GeV, 20 GeV and 40 GeV. These L1 trigger items can also be combined with other L1 triggers for e.g. electrons, muons or $E_{\text{T}}^{\text{miss}}$. To allow lower thresholds for combined triggers, e.g. lower cuts on $E_{\text{T}}^{\text{miss}}$ for combined tau+ $E_{\text{T}}^{\text{miss}}$ triggers, further items including isolation are supported. They are marked by an additional I in their name, e.g. L1.TAU8I. Isolation means that an additional energy cap of 4 GeV is applied on the sum of the transverse energy measured in the EM trigger towers in the isolation region.

L2 Tau Trigger

The L2 trigger is the first step in the HLT chain. It considers track and calorimeter information to select hadronic tau decays by considering the topology of a hadronic tau decay, i.e. the narrowness and low track multiplicity. The aim is to reject the overwhelming multijet background, while keeping as many real tau decays as possible. The L2 trigger algorithms are executed on the region-of-interest (RoI) defined by the L1 trigger. First, the position of the RoI gets refined by considering all calorimeter cells in $\Delta\eta \times \Delta\phi = 0.8 \times 0.8$. In the refined RoI the E_{T} is recalculated applying noise suppression thresholds on each cell. Furthermore, shower shape variables similar to the ones used by the offline algorithms are calculated. Finally tracking algorithms are executed and track-based variables are calculated. Several cuts are applied on a set of variables depending on the trigger item and whether it is an 1-prong or multi-prong tau candidate. The optimisation of the cuts are performed w.r.t. offline identification to yield optimal efficiencies for physics analyses. Variables considered are:

- the number of associated tracks, N_{track}

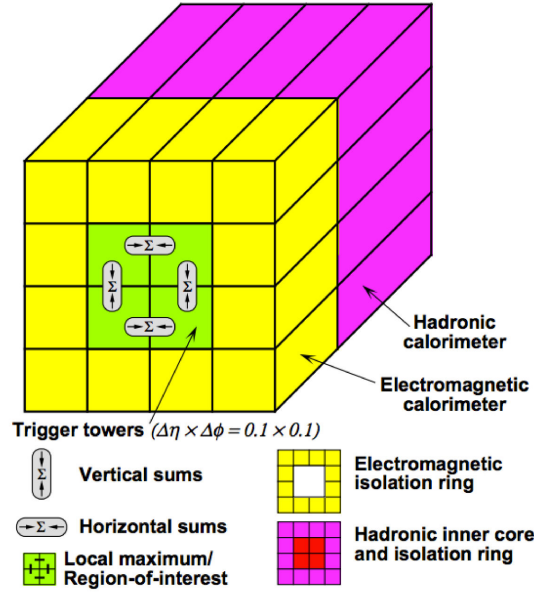


Figure 7.27: Schematic view of tau trigger towers [10].

- the transverse energy, E_T
- the leading track- p_T fraction w.r.t. the total E_T , f_{track}
- the average distance of tracks w.r.t. the RoI axis, R_{track}
- the energy fraction in the core region
- the scalar sum of track- p_T in the isolation annulus w.r.t. the core region.

The nomenclature of the L2 trigger items follows the one of the event filter items. They are named like `L2_tauXTi_medium1`, with X being the E_T threshold applied. By `medium` the identification level is defined, T refers to a tighter L1 threshold, i to the fact that isolation is applied at L1 and `medium1` (i.e. 1) to a tighter track selection than the "standard" medium working point. During 2012 data-taking a new collection of *topological tau triggers* has been added to the menu in order to increase the amount of low transverse momentum data, in particular relevant for the SM Higgs analyses in the di-tau final state. Since these are not subject to this thesis, those triggers will not be discussed.

EF Tau Trigger

In the last step of the trigger chain, the event filter applies algorithms very close to those used in the offline analysis for reconstruction and identification. Until end of 2011 a cut-based approach for identification was featured and tuned w.r.t. the corresponding cut-based offline ID. To further harmonise with the offline selection of hadronic tau decays used by the physics analyses and to improve the background rejection to cope with higher instantaneous luminosities in 2012 data-taking, a multivariate approach was implemented early 2012. Both algorithms used for the offline identification, i.e. Boosted Decision Trees and Log-Likelihoods, were investigated. The optimisation procedure follows very closely the one discussed for the offline ID above. There are important differences between trigger and offline identification, though. Given the limited amount of time available for each trigger algorithm, it is impossible to perform a complete vertex reconstruction. Thus the pile-up correction applied to the identification variables is not possible. To still ensure a reasonable robustness of the performance w.r.t. the number of pile-up events a cut on Δz_0 w.r.t. the leading track is applied. An upper threshold of 2 mm has been found to work well in keeping tracks associated to real taus while rejecting pile-up tracks efficiently, which tend to be more

displaced. To avoid a degradation already at L2, the Δz_0 cut has been added there as well. Figure 7.28 shows the trigger efficiency at each step in the trigger chain of the 20 GeV tau trigger item w.r.t. the number of reconstructed vertices for 2011 (left) [190] and 2012 (right) [191] data-taking. Comparing the inclusive L2 and EF efficiencies a significant improvement concerning the pile-up robustness is visible.

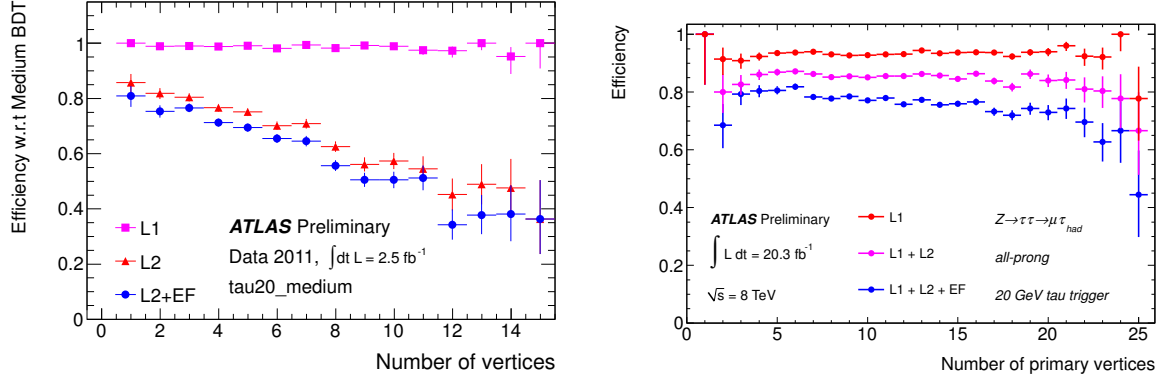


Figure 7.28: Tau trigger efficiency for the 20 GeV tau trigger item at all stages of the trigger chain versus the number of reconstructed vertices. The efficiency is calculated w.r.t. the jBDT medium offline identification efficiency. In (light) red the L1 efficiency is shown, while the (light) red and blue represent the inclusive L2 and EF efficiencies, respectively. The efficiency is measured in $Z \rightarrow \tau_\mu \tau_{\text{had}}$ data events selected by a tag-and-probe style analysis. The left plot [190] shows the measurement in 2011 data, while the right plot [191] shows the same for the complete 2012 dataset. A clear improvement of the pile-up robustness is visible at L2 and EF after implementation of the Δz_0 cut.

Another difference between online and offline selection is the tau energy calibration, which can cause shifts of calorimeter-based identification variables at trigger and offline level. However, this is accounted for during the training of the tau trigger ID. The problem is, though, that offline ID is subject to continuous optimisation, while the configuration at trigger level usually stays constant over the data-taking period and cannot be corrected later on, e.g. via reprocessing of data. Thus the BDT and LLH algorithms at trigger level have been optimised using an older version of the offline ID than mentioned above. Usually this is not a problem, though, because a retrained offline ID is supposed to give a higher performance, such that a degradation is unlikely, unless the selected phase space of real hadronic tau decays changes significantly, which would lead to a smaller overlap, and thus a lower combined trigger and offline ID efficiency. So far this has not been observed.

7.3.2 Development of a Multivariate Tau Trigger Menu

As mentioned before, a new tau trigger algorithm at EF stage has been developed featuring multivariate classifiers. The optimisation as well as the practical implementation follows closely the procedure of the offline identification tuning. Hence the details of each step will not be repeated here, but rather the discussion will focus on differences in the selection and the performance of the new algorithms.

Identification Variables

The MV-based EF trigger menu was developed in early 2012, and thus was tuned w.r.t. the offline ID at that time. Hence the set of identification variables is different to what is described above in Section 7.2, although the definition of the variables remain the same, except the pile-up correction, which is not applied at EF stage. Table 7.3 summarises the set of identification variables exploited by the LLH and BDT algorithms.

To extract the signal and background templates one needs to define an unbiased dataset, which requires that the trigger tau candidates match to the tau.NoCut chain, which does not apply identification

variable	Log-likelihood		Boosted-Decision-Tree	
	1-prong	multi-prong	1-prong	multi-prong
f_{core}	•	•	•	•
f_{trk}	•	•	•	•
R_{track}	•	•	•	•
$S_{leadtrack}$	•		•	
N_{trk}^{iso}	•		•	
S_T^{trk}		•		•
m_{trk}		•		•
ΔR_{max}		•		•

Table 7.3: Set of identification variables used by the LLH and BDT algorithms at event filter stage.

requirements. Since this results in an enormous rate due to jet fakes, one would need dedicated data-taking runs with an increased rate assigned to EF_tau_NoCut. This was done during the data-taking in 2011, but not in 2012. Hence the training relies on MC simulation for both the signal and the di-jet background. The same procedure was followed in the original training of the classifiers, as at that time no $\sqrt{s} = 8$ TeV data was available. Further information on the di-jet MC samples is given in Table 11.1. Figure 7.29 shows the core energy fraction for one- and three-prong tau candidates at EF level. For comparison the distributions obtained after offline reconstruction are overlaid. The observed difference in the templates at trigger and offline reconstruction stage arise from additional pile-up corrections applied for offline reconstructed tau candidates and different energy calibrations. Corresponding distributions of other identification variables can be found in Appendix B.

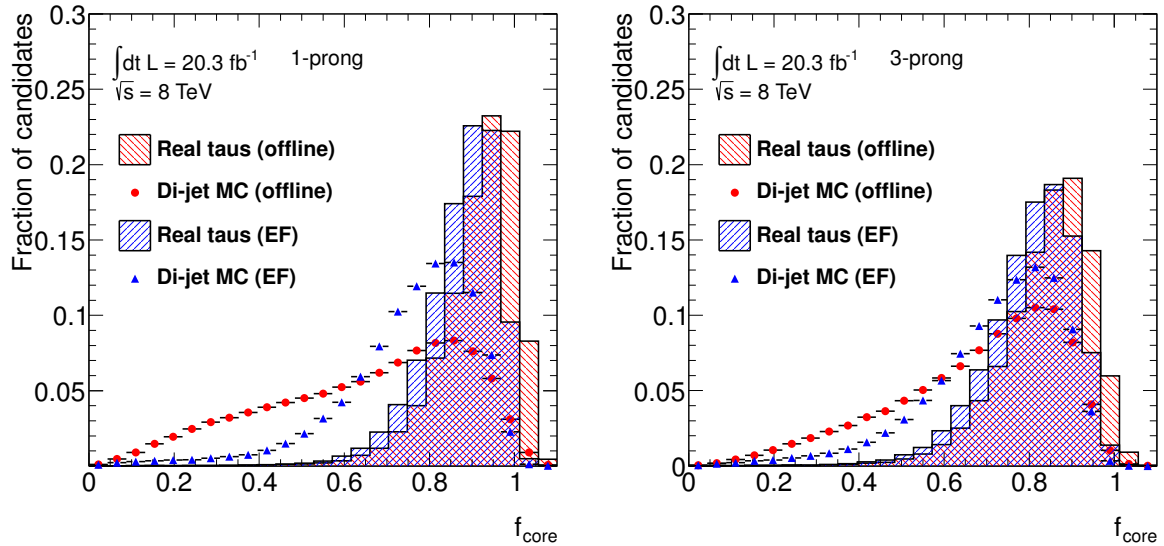


Figure 7.29: Core energy fraction for reconstructed 1-prong (left) and 3-prong (right) event filter tau candidates. The signal template is shown by the blue histogram, while the background template extracted from di-jet MC simulation is marked by the blue triangles. For comparison the corresponding distributions of the geometrically matched reconstructed tau candidate are overlaid in red. The difference in the trigger and offline templates arise from pile-up corrections applied only for offline reconstructed tau candidates and different energy calibrations.

Training of Multivariate Classifiers

The training and performance evaluation of the multivariate classifiers follows the procedure outlined in Section 7.2 for the offline identification algorithms. However, the matching conditions change slightly as they have to incorporate the additional EF stage. The signal efficiency is defined according to Eq. 7.15 as:

$$\epsilon_{1P/MP}^{\text{sig}} = \frac{N_{\text{passed}}^{1P/MP}}{N_{\text{total}}^{1P/MP}}, \quad (7.19)$$

with $N_{\text{passed}}^{1P/MP}$ being the number of 1- or multi-prong EF tau candidates passing the considered cut on the classifier score. They are further required to geometrically match a reconstructed tau candidate and a generated tau lepton. The matched reconstructed tau candidate is further required to pass the medium jBDT threshold. In the denominator $N_{\text{total}}^{1P/MP}$ accounts for the number of all one- or multi-prong EF tau candidates matched to a reconstructed one- or multi-prong tau candidate, which has to pass the medium jBDT criteria as well and further match to a generated tau lepton within $\Delta R < 0.2$. Additionally the

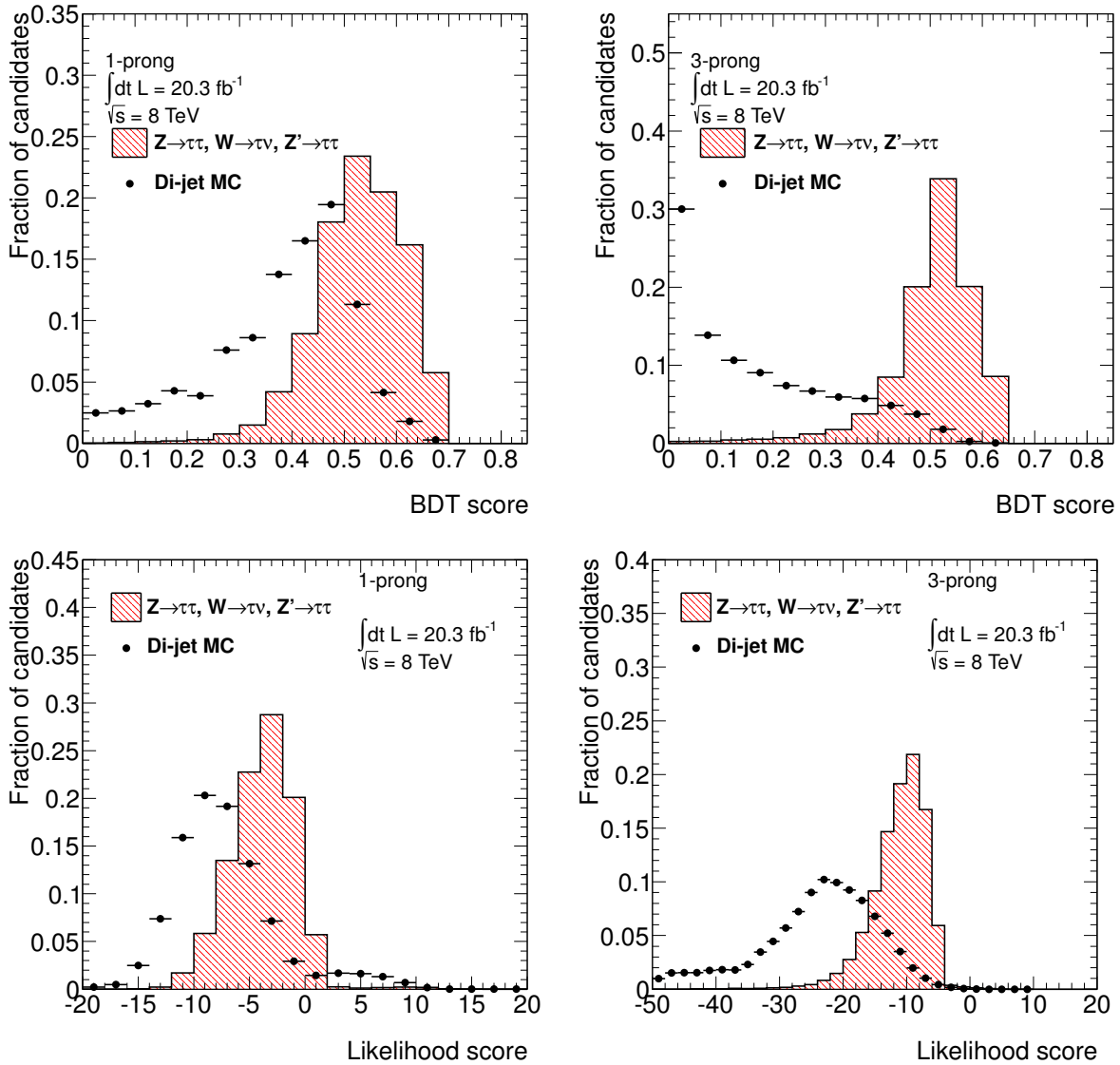


Figure 7.30: BDT (top row) and LLH (bottom row) scores for 1- and 3-prong EF tau candidates. The signal template is derived from MC simulated $Z/\gamma^* \rightarrow \tau\tau$, $W \rightarrow \tau\nu$ and $Z' \rightarrow \tau\tau$ events, while the background template is extracted from MC simulated di-jet events.

EF tau candidates are required to match in the number of tracks w.r.t. the offline tau candidate they are assigned to. The matching conditions depend on the prongness of the candidates and the considered trigger menu. For one-prong tau candidates, both the EF and the offline tau have to have one assigned track. In the case of multi-prong candidates the procedure is a bit more complicated. For the training of the classifiers only 3-prong tau candidates, both at EF and offline stage, are accepted, while for the evaluation of the performance the criteria is relaxed. Both 2- and 3-prong taus after offline reconstruction are allowed, while the selection of the EF taus depends on the considered menu. For the loose track selection items, i.e. `medium`, all candidates with less than seven assigned tracks, i.e. $N_{\text{track}} \in [2, 6]$, are considered, while for the tight track selection items, i.e. `medium1` and `tight1`, the track criteria is tightened to $N_{\text{track}} \in [2, 3]$. The background efficiency is defined accordingly by dropping the matching requirement to generated tau leptons and the offline track selection and identification criteria. The training is performed in the same way as discussed above, but for the LLH the interpolation next to the bin borders is always performed within 10 GeV. Figure 7.30 presents the derived LLH and BDT score distributions for one- and three-prong tau candidates.

7.3.3 Performance Evaluation

For the tau trigger the performance of the algorithms is crucial to meet the rate constraints of the read-out systems. The rate is driven by the background rejection of jet fakes. The figure of merit to decide which algorithm to run online is the background rejection versus the signal efficiency. Figure 7.31 presents the quantity for both algorithms for one- and multi-prong EF tau candidates. The BDT-based trigger algorithm outperforms the LLH method due to the reasons mentioned above. Given the rate constraints only one identification method can be applied online. This was chosen to be the BDT-based tau trigger ID.

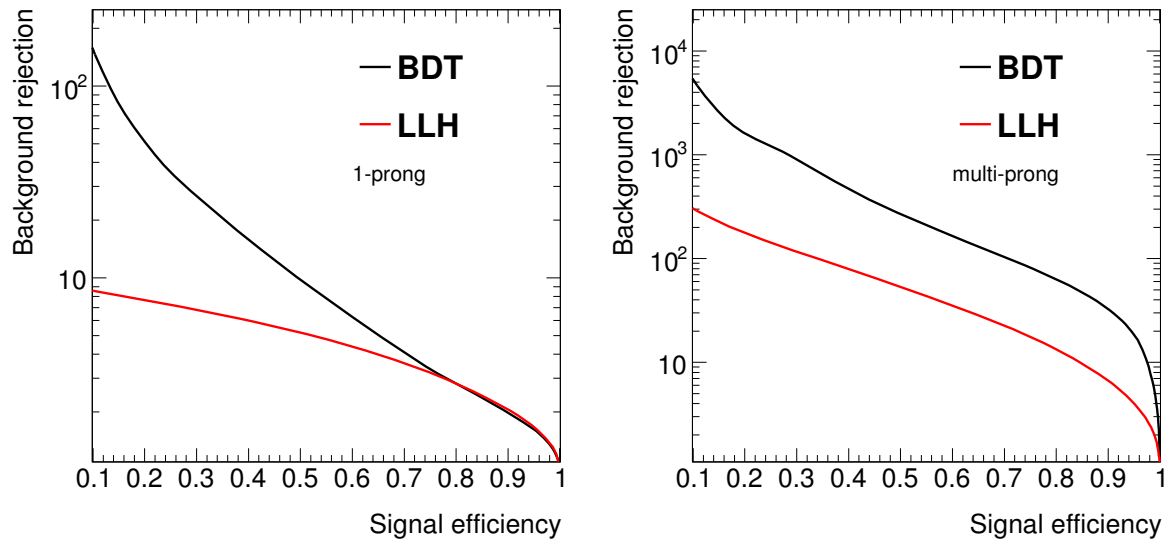


Figure 7.31: Fake rejection versus signal efficiency for one- (left) and multi-prong (right) EF tau candidates for the BDT- and LLH-based tau trigger identification algorithms.

As in the case of the offline tau identification the signal efficiency is tuned to be flat w.r.t. the transverse momentum of reconstructed tau candidate. The obtained signal efficiencies for the BDT algorithm is shown in Figure 7.32. The target efficiencies are tuned to maintain the rate constraints. Since the production cross section of jets faking an one-prong tau decay is much smaller than for multi-prong fakes due to the generally higher track multiplicity of quark and gluon initiated jets, the signal efficiency is higher. Obviously for real tau decays there is no difference between the `medium` and `medium1` configuration.

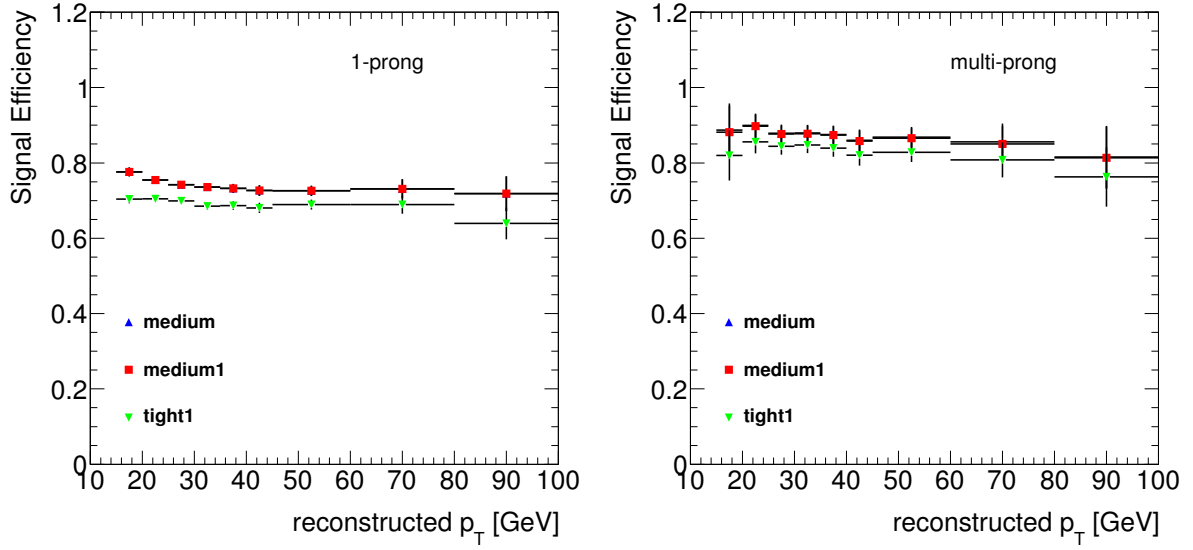


Figure 7.32: BDT-based tau trigger efficiency versus the reconstructed transverse momentum of the tau lepton for one- (left) and multi-prong (right) tau decays. The medium, medium1 and tight1 working points are represented by the blue triangles, red squares and green triangles, respectively.

As discussed before a flat signal efficiency leads to a p_T dependence of the mis-identification efficiency. This is shown in Figure 7.33. For jets faking an one-prong tau decay the medium and medium1 working points yield the same results, while for multi-prong fakes the mis-identification efficiency is smaller for the medium1 working point due to the tighter track requirement.

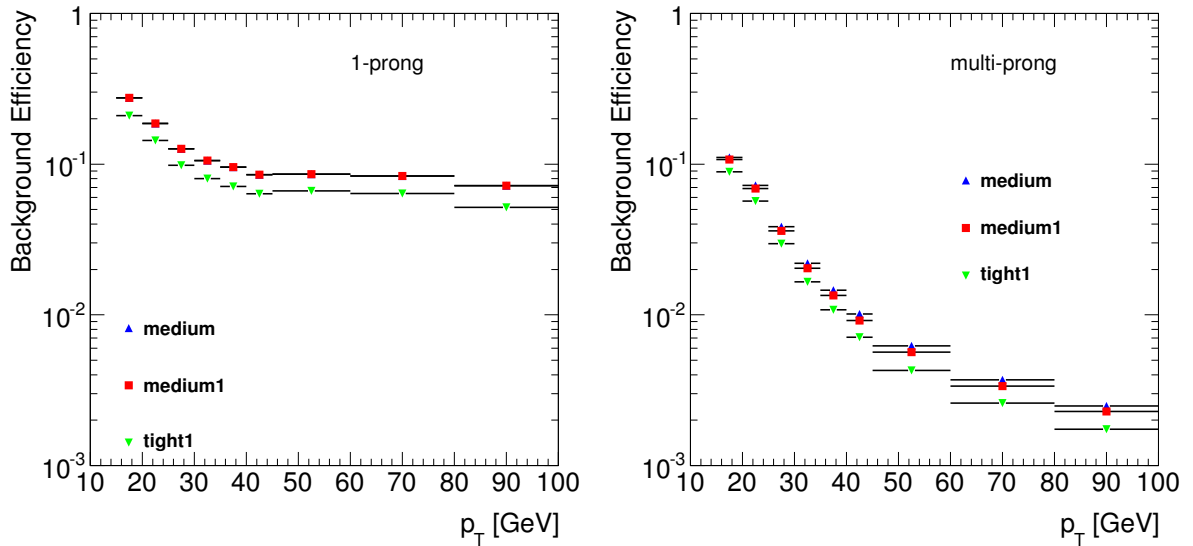


Figure 7.33: Mis-identification efficiency of the BDT-based tau trigger identification for one- (left) and multi-prong (right) tau decays obtained from MC simulated di-jet events. The medium, medium1 and tight1 working points are represented by the blue triangles, red squares and green triangles, respectively.

7.3.4 Efficiency Measurement

Since the optimisation of the tau trigger algorithms are performed exploiting MC simulated collision events, the performance obtained in the simulation has to be compared to proton-proton collision data. As for the offline identification, a tag-and-probe study is performed to measure the tau trigger efficiency. This tag-and-probe analysis is based on $Z/\gamma^* \rightarrow \tau_\mu \tau_{\text{had}}$ events, and is therefore only applicable for low- p_T tau leptons, i.e. $p_T \simeq 80$ GeV (c.f. Section 11 for a detailed discussion on the high- p_T treatment). The event selection follows the one explained in Section 7.2.5. Exactly one muon and one tau lepton with $22 \text{ GeV} < p_T^\mu < 40 \text{ GeV}$ and $p_T^\tau > 20 \text{ GeV}$ are required. To reduce contamination from W +jets and QCD multijet events the following criteria are applied in addition:

- E_T^{miss} alignment: $\sum_{\ell=\mu,\tau} \cos \Delta\phi(\ell, E_T^{\text{miss}}) > -0.15$
- transverse mass: $M_T = \sqrt{2p_T^\mu E_T^{\text{miss}} (1 - \cos \Delta\phi(\mu, E_T^{\text{miss}}))} < 50 \text{ GeV}$
- visible invariant mass: $M_{\text{vis}}(\mu, \tau) \in [40, 80] \text{ GeV}$.

This selection provides a high purity dataset enhanced in $Z/\gamma^* \rightarrow \tau_\mu \tau_{\text{had}}$ events. The estimation of the remaining backgrounds, mainly QCD multijet and W +jets events, follows the $H \rightarrow \tau_\mu \tau_{\text{had}}$ analysis [42, 192]. Further details on the selection and quality of the $Z/\gamma^* \rightarrow \tau_\mu \tau_{\text{had}}$ tag-and-probe analysis can be found in [193]. The configuration of the tau trigger menu was subject to several changes during 2012 data-taking as will be discussed in detail in Section 9.3. Hence the trigger efficiency is measured depending on the p_T , η and n-prong decay mode of the tau lepton and for three different ranges of data-taking periods according to specific trigger configurations. Furthermore, the tau trigger efficiency is measured for various thresholds of the offline tau identification. Similar to the efficiency measurement of the offline identification, scale factors are derived to quantify the discrepancy between data and MC simulation. Figure 7.34 presents the measured efficiencies as well as the scale factors for the EF_tau38T_medium1 trigger versus the p_T of the reconstructed tau candidate for one- and multi-prong tau decays in the barrel region ($|\eta| < 1.5$). The shown efficiencies are measured w.r.t. the loose jBDT criteria.

The derived scale factors are in agreement with one, except for the last bin, which suffers from low number of available events. The statistical precision in the turn-on region is rather low as well, but does not affect the presented analyses as the focus is on high- p_T tau leptons. The uncertainties on the scale factors are in the order of 1% to 10% depending on the track multiplicity, the η region (uncertainties tend to be larger in the end-cap region) and the required offline identification thresholds. The dominant source of the uncertainty is the low amount of available MC simulated collision events. An updated measurement is planned for early 2014, which will address this issue. For further details and additional working points consult [194].

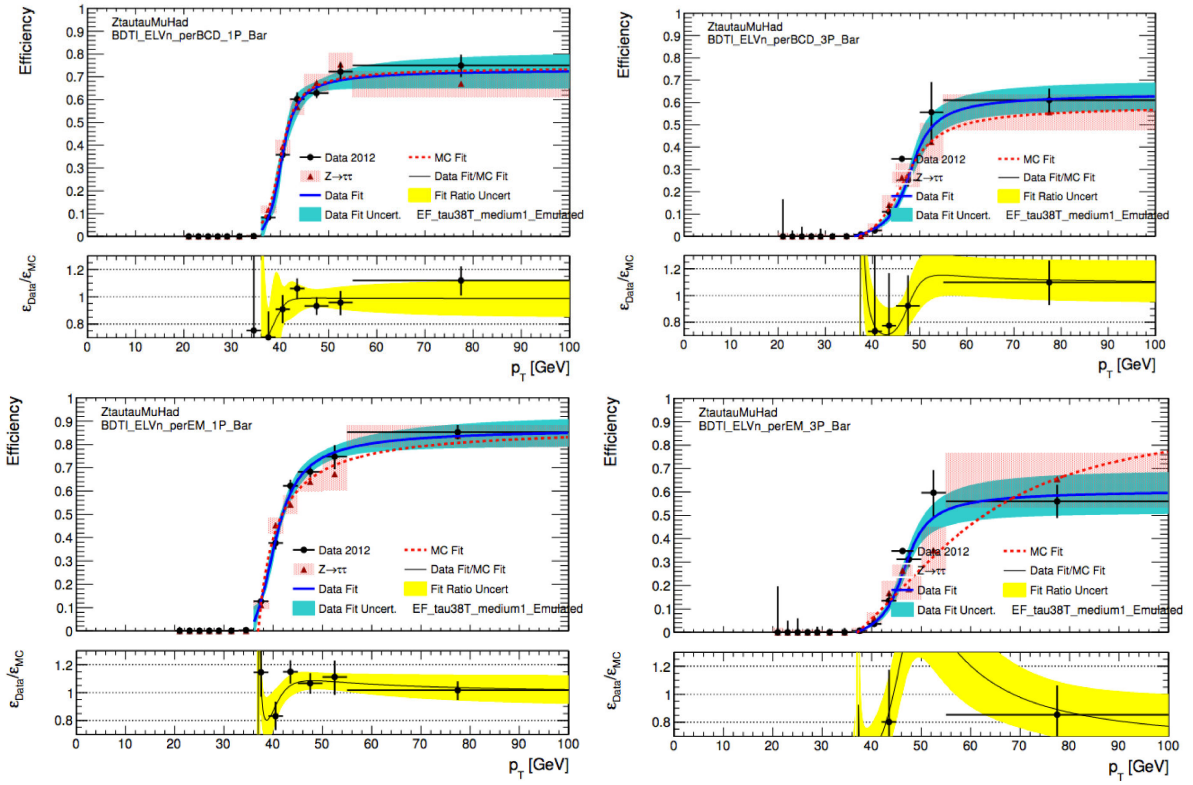


Figure 7.34: Tau trigger efficiency for EF_tau38T_medium1 derived from a $Z/\gamma^* \rightarrow \tau\tau$ tag-and-probe measurement for periods B-D (top) and periods E-L (bottom) data for 1-prong (left) and 3-prong (right) tau candidates. Taken from [194].

8 Background Processes

This chapter will discuss the background contributions from SM processes entering the analysis. Backgrounds can either be of irreducible or reducible nature. Reducible backgrounds arise from misinterpretation in the detector leading to fake candidates, e.g. electrons which mimic hadronic tau decays as discussed in Section 7.2.6. In principle they can be reduced completely, but in reality this will not be the case. On the other hand, irreducible background share the same final state and the same kinematics as the signal process, and thus one can not reduce them completely. However, they do not share the resonance topology at high invariant di-tau masses, but rather provide a steeply falling tail leading to a smooth background. For both types it is important to get a proper model of both their shapes and their normalisation. Some of them can be estimated from simulated collision events. For others, such as QCD multijet events, this will be not feasible, such that data-driven techniques have to be utilised. The latter ones will be discussed in detail in Chapter 10.

8.1 Irreducible Backgrounds

8.1.1 $Z/\gamma^*(\rightarrow \tau\tau)+\text{jets}$

The only irreducible background in this analysis arise from *Drell-Yan* production, $Z/\gamma^*(\rightarrow \tau\tau)+\text{jets}$. The decay into two tau leptons has a branching ratio of 3.37 % [16]. The Z is a narrow resonance with a width of $\Gamma(Z) = 2.49 \text{ GeV}$ [16]. Even though the spin is different from a Higgs boson or a Z' boson with spin zero, e.g. in R-parity violating SUSY models, the analysis of the final state involving two hadronically decaying tau leptons is not sensitive to the different spin. Thus $Z/\gamma^*(\rightarrow \tau\tau)+\text{jets}$ marks an irreducible background in the presented analyses. Some Feynman diagrams contributing to this process are shown in Figure 8.1. As can be seen the Z can be accompanied by additional jets which can be of heavy flavour origin, and therefore mimic the topology of b-associated Higgs production. Z and

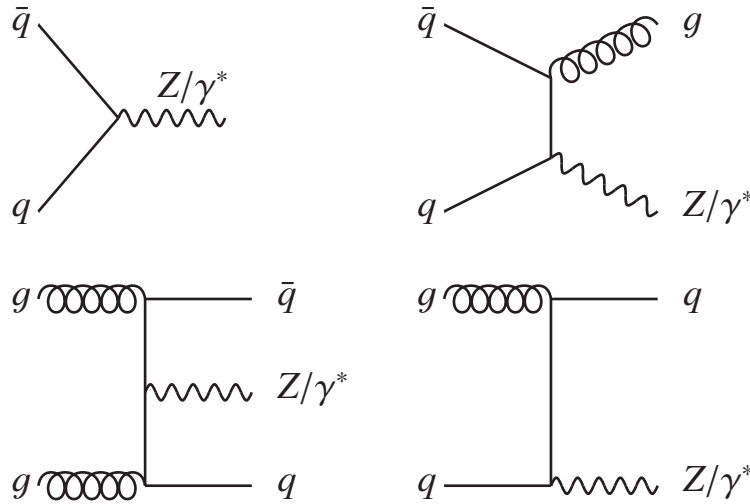


Figure 8.1: Examples of leading order Feynman diagrams of $Z/\gamma^*+\text{jets}$ production.

photon exchange, including interference, is taken into account, and thus the invariant di-tau mass is not restricted to the Z mass, but can be significantly higher. Since there is no signal-free data sample, this background is estimated from simulation using PYTHIA 8.165 [195]. For this background a *leading order* (LO) generator was chosen to allow for reweighting as Z' signal, which will be addressed in detail in Section 13.1. To get a proper modelling of this background the LO cross section has to be corrected using mass dependent k-factors. These k-factors are defined as the ratio of the *next-to-next-to-leading order* (NNLO) cross section derived using FEWZ 3.1.b2 [196] to the LO order prediction by PYTHIA. The NNLO cross sections are calculated using the *MSTW2008nnlo* [197, 198] PDF set. Electroweak corrections are taken into account at *next-to-leading order* (NLO). Finite width effects as well as spin correlations are taken into account by the FEWZ calculation. Figure 8.2 (left) shows the derived k-factors.

The mean value (red line) is used as an event weight applied according to the generated invariant di-tau mass. Uncertainties on the k-factors are derived from PDF and α_S variations at 90% C.L. using the MSTW error pdf set. The $\pm 1\sigma$ variations are presented by the blue and green line, respectively. They are used as a systematic uncertainty treated as a nuisance parameter in the limit calculation as pointed out in Section 11.2.1.

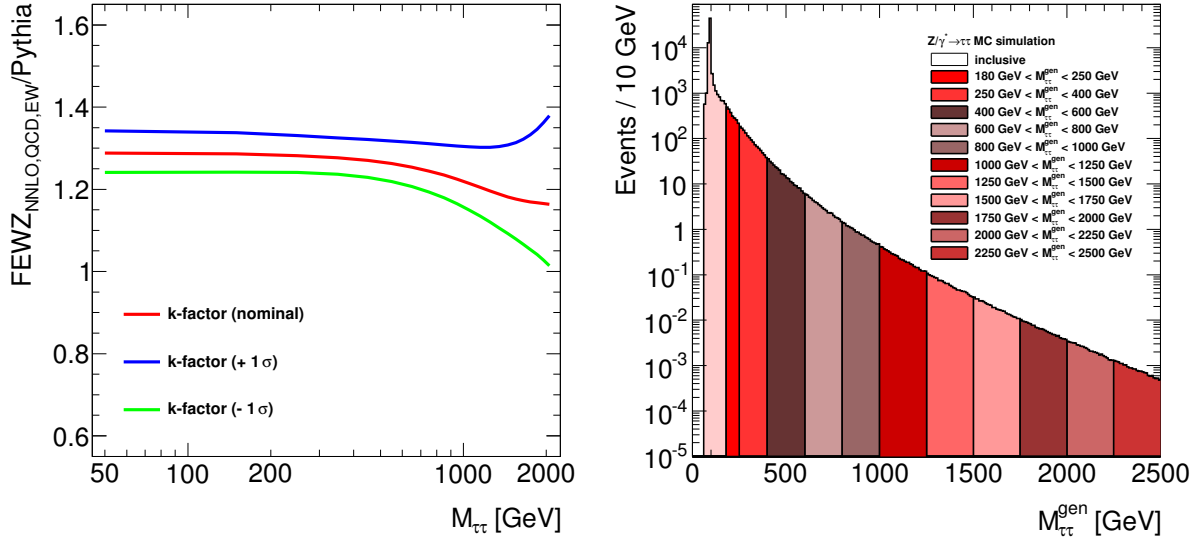


Figure 8.2: Left: NNLO correction factors (k-factors) for $Z/\gamma^* \rightarrow \tau\tau$ MC simulation samples as a function of the generated invariant di-tau mass calculated using FEWZ [196]. The mean correction factor is represented by the red line, while the blue and green line indicate the $\pm 1\sigma$ systematic uncertainties from PDF and α_S variation. Right: Generated invariant di-tau mass obtained from simulation data applying NNLO corrections via event weights.

To enhance the statistical precision at high invariant mass, the $Z/\gamma^*(\rightarrow \tau\tau)$ +jets MC production is performed in slices of the invariant di-tau mass. Eleven samples ranging from $M_{\tau\tau} = 180$ GeV to $M_{\tau\tau} = 2500$ GeV have been produced with equal statistics (c.f. Table C.3). To fill the low $M_{\tau\tau}$ phase space an inclusive sample has been added, but a cut on the generated invariant di-tau mass of $M_{\tau\tau} < 180$ GeV is applied to avoid an overlap with the dedicated sliced samples. The invariant mass distribution after applying the k-factors and corresponding luminosity weights is shown in Figure 8.2. The applied weights guarantee a smooth transition between each mass slice avoiding any discontinuities. Table C.3 in Appendix C.2 provides a summary of the samples used to model the $Z/\gamma^*(\rightarrow \tau\tau)$ +jets background component.

8.2 Reducible Backgrounds

8.2.1 QCD multijets

The dominant reducible background originates from QCD multijet events, which is the predominant process taking place at a hadron collider. Many different diagrams can contribute to final states involving quark and gluon initiated jets. Figure 8.3 summarises some of the LO contributions to di-jet production. Since the transverse momentum of the incoming protons, and thus the partons in the initial state, can be assumed to be zero for high energy protons, the two jets will likely traverse the detector in opposite directions leading to a back-to-back topology like the signal. Even though the rate of a jet faking a hadronic tau decay can be significantly suppressed by applying tau identification (c.f. Section 7.2.4), the huge production cross section (about six orders of magnitude larger than the signal production cross section, c.f. Figure 4.1) still leads to a dominant amount of selected background events. Furthermore, the large production cross section makes it practically impossible to generate a sufficient amount of MC

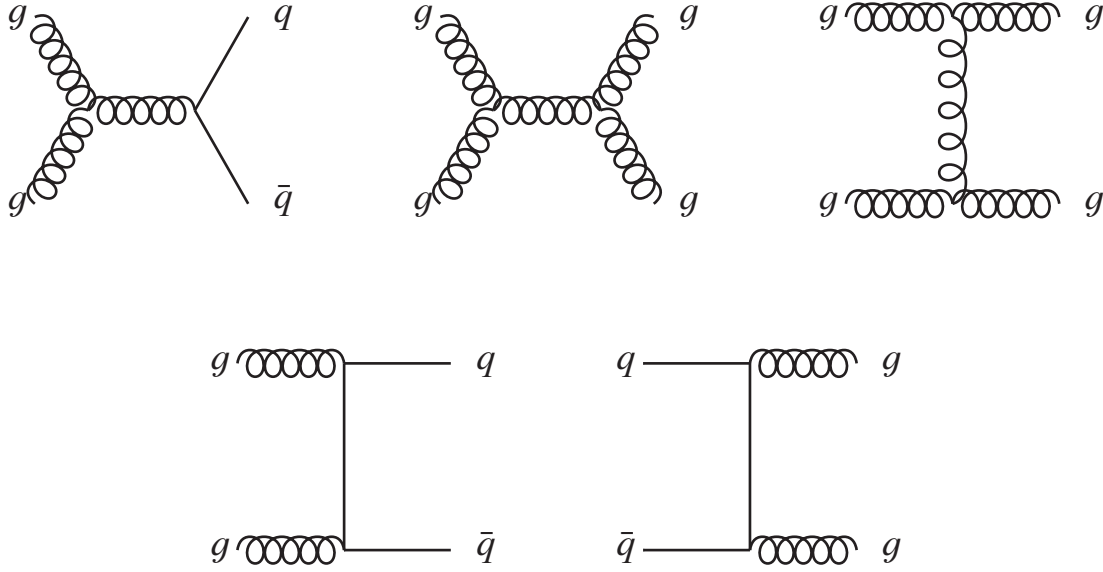


Figure 8.3: Leading order Feynman diagrams of QCD di-jet production.

statistics to estimate this background contribution from simulation. Beside this rather technical issue, the phenomenology of QCD processes is non trivial, and thus a proper modelling of the quark-gluon fractions is almost impossible. Therefore, it would lead to a badly modelled fake-rate prediction. Given these problems in the simulation, it is a standard procedure to estimate the QCD multijet contribution from data. Two different techniques are utilised in the presented search for new heavy resonances and will be discussed in detail in Section 10.1.

8.2.2 $W(\rightarrow \tau\nu)$ +jets

Another important background arises from W boson production accompanied by an additional jet. The W boson can decay into a tau lepton and a neutrino providing one real tau lepton in the final state. The branching ratio is $\text{BR}(W \rightarrow \tau\nu) = 11.25 \pm 0.20\%$ [16]. The second reconstructed tau candidate originates from the additional jet in the event which fakes the hadronic tau decay. The mass of the W boson is 80.38 GeV [16], and the inclusive production cross section is roughly ten times larger than Z boson production. Thus, even if the fake-rate is small, this background is not negligible. Figure 8.4 shows some Feynman diagrams contributing to $W(\rightarrow \tau\nu) + 1$ jet events. As can be seen from the left diagram there is a charge correlation between the lepton from the W decay and the accompanied quark-initiated jet. This will become important in the fake-rate measurement presented in Section 10.2. Events passing the event selection will most likely originate from $W(\rightarrow \tau\nu) + 1$ jet processes, where the recoiling jet has large transverse momentum to balance the boost of the W boson. Hence, the leading τ_{had} candidate will be a fake candidate from the recoil jet, while the sub-leading tau candidate will be the tau from the W decay. The real tau will have lower transverse momentum since a neutrino is involved in the W decay.

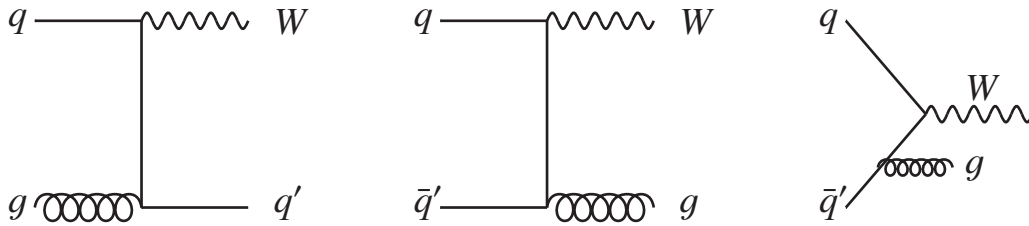


Figure 8.4: Examples of leading (left, middle) and next-to-leading (right) order Feynman diagrams of $W(\rightarrow \tau\nu)$ +jets production.

The $W(\rightarrow \tau\nu)$ +jets background is estimated from MC simulation using Sherpa 1.4.1 [146]. Dedi-

cated samples binned in the boost of the W boson, i.e. p_T^W , have been produced. In addition these samples are binned in the jet flavour of the accompanied jet. Filtered samples for light (u,d,s), c and b flavour have been produced. In particular b -jets tend to have a higher fake-rate than light flavour jets. Thus including the filter enhances the available statistics in the phase space of interest in this analysis. Four different bins of p_T^W have been simulated ranging from $p_T^W > 0$ GeV to $p_T^W > 500$ GeV. As for the simulation of the Z/γ^* background, the lowest p_T^W sample is inclusive, and thus a cut on $p_T^W < 70$ GeV has to be applied to avoid double counting due to the overlap. To permit a sufficiently high MC statistic in the inclusive samples they have been produced utilising ATLFast-II, rather than running the full simulation chain. This usually involves additional corrections to account for mis-modelling of the tau identification variables. However, given the low boost of the W boson in the inclusive sample, it does contribute only little, and thus no further corrections have been applied in this analysis. Details on the samples used to model the $W(\rightarrow \tau\nu)$ +jets background are given in Table C.4.

8.2.3 Top Quark Pair and Single-Top Production

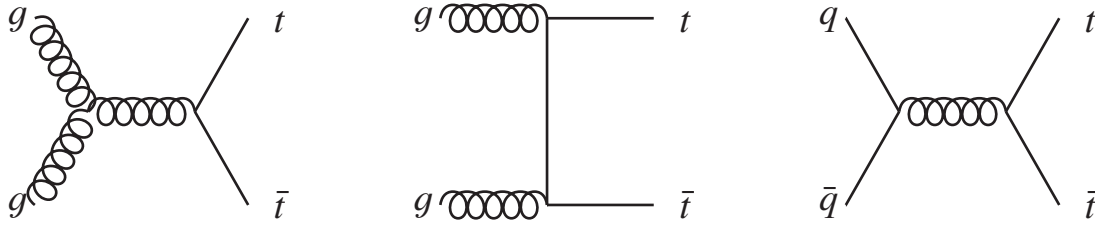


Figure 8.5: Leading order Feynman diagrams of $t\bar{t}$ production.

Another non-negligible background arises from top quark pair, $t\bar{t}$, production. Figure 8.5 shows the LO Feynman diagrams contributing to this process. The top quark decays almost to 100% into a W boson and a b -quark [16] forming a b -jet. Further decays of the W boson can involve real tau leptons in the final state. However, not only events with real tau leptons contribute to this process, but b -quark initiated jets can fake hadronic tau decays. Since the b -quark is rather heavy, the B hadrons formed by hadronisation decay at a displaced vertex, and thus can mimic a hadronic tau decay. Given the event selection this process can still be reduced significantly. Its shape and normalisation is extracted from MC simulation using MC@NLO 4.01 [199, 200, 201] for the matrix element and HERWIG 6.52 [202] for the parton shower. HERWIG is interfaced to Jimmy 4.31 [148] which takes care of the simulation of multiple interactions. Furthermore, CT10 [203, 204] is used as PDF set and the underlying event is simulated exploiting the AUET2 [205] tune. The $t\bar{t}$ cross section is calculated at NNLO in QCD including resummation of soft gluon terms at *next-to-next-to-leading logarithmic* (NNLL) order. The cross section calculation is performed using top++ 2.0 [206, 207, 208, 209, 210, 211]. Uncertainties on the production cross section from PDF and α_S uncertainties are evaluated following the PDF4LHC [212] prescription. PDF uncertainties are calculated using the MSTW2008 68% C.L. NNLO [197, 198], CT10 NNLO [203, 204] and NNPDF2.3 5f FFN [213] PDF sets. The obtained cross section is given as $\sigma(t\bar{t}) = 252.89^{+6.39}_{-8.64}$ (scale) $^{+11.67}_{-11.67}$ (PDF+ α_S) pb. Furthermore, an approximate calculation at NNLO+NNLL has been performed using Hathor 1.5 [214]. The obtained production cross section is about 3% larger. In Figure 8.6 the cross sections for various SM processes measured by the ATLAS experiment are shown and compared to the theoretical prediction. The measurement is based on the proton-proton collision dataset taken at centre-of-mass energies of 7 TeV and 8 TeV. A good agreement between the theoretical calculation and the measurement can be seen, and hence the assumed cross sections are reliable.

Two different samples have been produced with generator level filters applied to select fully hadronic decays of the two W bosons and the fully and semi-leptonic final states. The latter is referred to as no-fully hadronic sample.

An additional background component arise from single top-quark production, which involves Wt , s - and t -channel production. The corresponding Feynman diagrams are summarised in Figure 8.7. The Wt

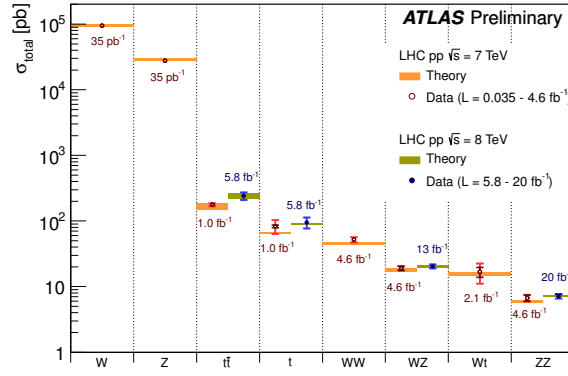


Figure 8.6: Summary of inclusive production cross section measurements for various SM processes, including $t\bar{t}$, single top-quark and electroweak di-boson processes, obtained by the ATLAS experiment. Theoretical predictions are marked by the orange and green bars for centre-of-mass energies of $\sqrt{s} = 7$ TeV and $\sqrt{s} = 8$ TeV, respectively. Taken from [215].

production has a similar final state as the $t\bar{t}$ process, involving two W bosons which can decay into two tau leptons. In the same way as discussed for the $t\bar{t}$ production, the b -quark in the final state can yield fake tau candidates. However, the production cross section is much smaller than for $t\bar{t}$, calculated at approximate NNLO+NNLL to be $\sigma(Wt) = 22.37 \pm 1.52$ pb [216]. In addition a top quark can be produced in an inelastic quark-quark scattering either in the s - or t -channel. The production cross section of the t -channel process is calculated at approximate NNLO+NNLL as well, $\sigma(t\text{-channel}) = 87.76^{+3.44}_{-1.91}$ pb [217], and thus has the largest contribution, while the s -channel production cross section is calculated at full NNLO, $\sigma(s\text{-channel}) = 5.61 \pm 0.22$ pb [218]. However, both processes only involve one W boson in the final state which could lead to a real hadronic tau decay. Thus, at least one fake tau has to be involved if such an event contributes to the background model. Hence, the contribution is rather small, and thus the $t\bar{t}$ and single top-quark background contributions are merged and are referred to as *Top* background in the following. The background model from single top-quark processes relies on MC simulation as well. For the Wt and s -channel production the same simulation chain as for the $t\bar{t}$ simulation is used, while the MC@NLO simulation of the t -channel production suffers from unphysical additional jets in the final state. Thus this contribution is modelled using AcerMC 3.8 [219] and PYTHIA 6.421 [147] for parton showering and hadronisation. As PDF set CTEQ6L1 [220] is used. The underlying event is simulated using the AUET2B [221] underlying event tune. A summary of the exploited samples is given in Table C.5.

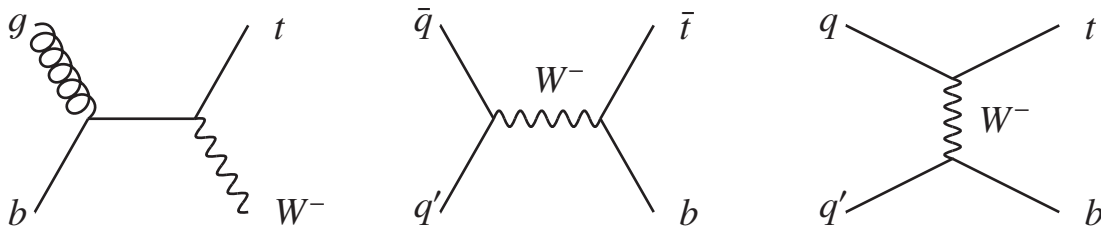


Figure 8.7: Leading order Feynman diagrams of single top-quark production in the Wt (left), s - (middle) and t -channel (right).

8.2.4 Electroweak Di-boson Production

A minor background arises from electroweak di-boson production. In WW production two real tau leptons accompanied by two neutrinos leading to sufficiently large missing transverse energy can occur in the final state, and thus mimic the signal process. Similar, ZZ final states with one Z boson decaying in the di-tau channel and the second Z decaying invisibly into neutrinos can lead to the same final state as

the signal process. However, given the boost of the Z boson the two tau leptons are unlikely to traverse in opposite direction, and therefore this background process can be suppressed rather well. Further, contributions from light leptons or hadronic final states can contribute. Missing decay particles of either of the two bosons, e.g. a light lepton in the WZ production, can yield further contributions. However, even given the wide variety of possible contribution, the production cross section of di-boson processes is small, and thus it marks only a minor background component. All these backgrounds are estimated from MC simulation using HERWIG 6.52 [202]. Samples are produced using the CTEQ6L1 PDF set and cross sections are calculated at NLO based on MCFM [222]. Table C.6 lists all samples.

8.2.5 Other Electroweak Backgrounds

Remaining backgrounds arise from light lepton decays in W and Z/γ^* production. The processes are the same as discussed above for the decay into tau leptons and their total number of expected events is the same given the lepton universality. However, since a dedicated light lepton veto is applied at the event selection stage these backgrounds can be reduced significantly, and thus mark a negligible background. Remaining events still have to be considered due to tau fakes from either the light leptons, in particular from electrons, or from accompanied jets produced at higher orders. For W production the same simulation chain as for $W(\rightarrow \tau\nu)+\text{jets}$ is used, while $Z/\gamma^*(\rightarrow \ell\ell)+\text{jets}$ processes are modelled using the Powheg [223, 224] generator interfaced to PYTHIA8 [195] for parton shower and hadronisation. Since Powheg provides a NLO prescription different k-factors to correct for two-loop contributions have to be applied. The NNLO cross sections are as well extracted from FEWZ and are applied as mass dependent k-factors as for $Z/\gamma^*(\rightarrow \tau\tau)+\text{jets}$. The k-factors and their systematic uncertainties derived from PDF and α_S variation are illustrated in Figure 8.8. Since the correction only includes two loop contributions they are smaller than the ones applied to $Z/\gamma^*(\rightarrow \tau\tau)+\text{jets}$ events. A summary of these samples is given in Tables C.3 and C.4 for $Z/\gamma^*(\rightarrow \ell\ell)+\text{jets}$ and $W(\rightarrow \ell\nu)+\text{jets}$, respectively.

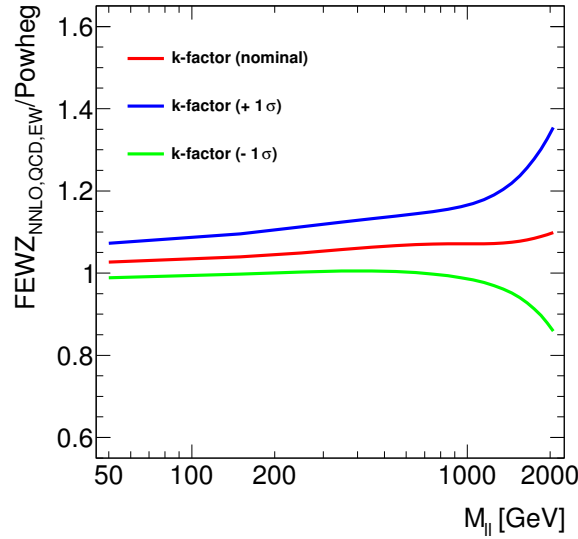


Figure 8.8: NNLO correction factors (k-factors) for $Z/\gamma^* \rightarrow \ell\ell$ MC simulation samples as a function of the generated invariant di-lepton mass calculated using FEWZ [196]. The mean correction factor is represented by the red line, while the blue and green line indicate the $\pm 1\sigma$ systematic uncertainties from PDF and α_S variation.

9 Event Pre-selection

A common pre-selection is applied to ensure high quality of selected data and reconstructed objects. Beside the event cleaning a pre-selection according to the event topology of a heavy resonance decaying into two tau leptons is applied. Each step of the selection will be addressed in the following.

9.1 Event Cleaning

Data Quality

Each *luminosity block* - a small period of data-taking of roughly two minutes - in each run gets a data quality flag assigned. This quality flag depends on the machine status, the conditions of each sub-detector and basic quality monitoring distributions of the data. A summary of these measurements are collected in so-called *Good Runs Lists* (GRLs). In this analysis the following GRL is used: `data12.8TeV.periodAllYear.DetStatus-v61-pro14-02.DQDefects-00-01-00_PHYS.StandardGRLAllGood.xml`. It requires all tracking and calorimeter detectors to be in good condition. Data events fulfilling these requirements corresponds to an integrated luminosity of 20.3 fb^{-1} . However, only data of period B onwards (c.f. Table 4.1) can be analysed here, as explained later. This leads to a total amount of analysed data corresponding to 19.5 fb^{-1} .

Removal of Incomplete Events

A new TTC¹² restart procedure was established in 2012 such that a run does not need to be restarted to recover certain sub-detectors flagged as being under "busy" conditions which blocks the readout [225]. This allows to recover certain detector systems in case of any occurring issue. However, this may lead to incomplete events in the following luminosity blocks. Each event gets a flag assigned which is asked for according to the recommendations of the *Data Preparation Group* [225].

Collision Cleaning

Collision cleaning is applied to ensure that there was at least one hard scattering. At least one reconstructed vertex with more than three associated tracks is required to remove bad collision events, e.g. beam-gas events.

Jet Cleaning

As pointed out earlier, tau leptons decaying hadronically are accompanied by neutrinos. Thus a good quality of the reconstructed missing transverse momentum is crucial. To ensure that no badly reconstructed jets are in the event, which distort the E_T^{miss} reconstruction, dedicated cleaning cuts are applied on data events. These cuts are designed to remove mis-reconstructed jets due to calorimeter noise or hardware problems. They are provided by the *JetEtMiss Working Group* [226]. The cleaning procedure as recommended for 2011 data analyses is still valid and applied in this analysis. These recommendations take several issues into account. Cuts on the energy fraction in the HEC and pulse shape comparisons discard events with HEC signal spikes. To remove events with noise in the EM calorimeter, selection criteria on the EM energy fraction and pulse shapes of the LAr calorimeter are placed. Finally, cuts on the charge fraction of jets, the EM energy fraction and the maximum energy fraction in the sampling layer reduce the non-collision background as well as contributions from cosmic events. Several thresholds are provided corresponding to different cut levels. In this thesis the *looser* working point is chosen. The jet cleaning is only applied to jets with $p_T > 20 \text{ GeV}$ and is used as an event-veto.

¹²Timing Trigger and Control System

Removal of Calorimeter Errors

Glitches in the calorimeter system lead to corrupted data events which have to be removed. All events suffering from noise bursts in the LAr calorimeter or which are affected by problems in the Tile calorimeter are removed. The Data Preparation Group provides bitsets which label the event as corrupt [225] or to be suffering from Tile calorimeter trips [227].

Pile-up Reweighting

Simulation of pile-up events is based on the expected conditions of 2012 data-taking. To account for changing data-taking conditions and discrepancies from the expectation, a reweighting procedure [228] is applied. Each MC simulated event gets a weight assigned corresponding to:

$$w(N_{int/xing}) = \frac{L_i}{N_i} \cdot \frac{N}{L}, \quad (9.1)$$

with L_i being the fraction of the luminosity corresponding to the generated average number of interactions per bunch crossing, $N_{int/xing}$, and L being the total luminosity of a given period. The number of MC events simulated with $N_{int/xing}$ is denoted by N_i , while N accounts for the total amount of simulated events. Figure 9.1 shows the number of average interactions per bunch crossing in simulated $Z/\gamma^* \rightarrow \tau\tau$ events before (red histogram) and after (blue histogram) the reweighting procedure is applied. Data events are marked by the black dots. Even after the reweighting a discrepancy between data and simulation is visible, which is expected since the longitudinal beam spot size simulated in MC is larger than in data.

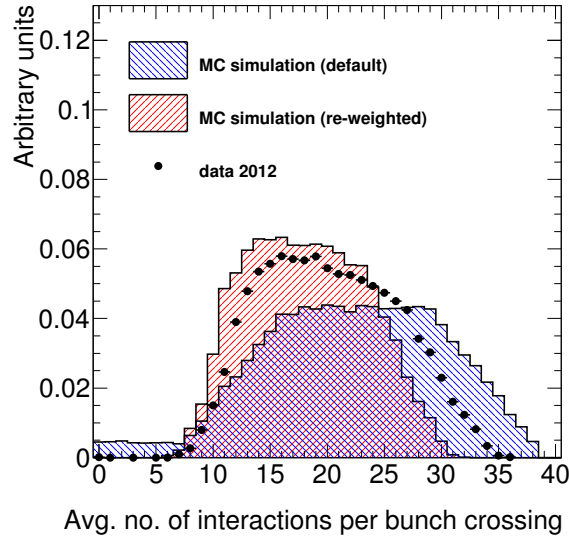


Figure 9.1: Average number of interactions per bunch crossing measured in $Z/\gamma^* \rightarrow \tau\tau$ MC simulated events and data. A reweighting procedure is applied to MC to correct for mis-modelling effects. The red and blue histograms show the distribution before and after reweighting. Data events are marked by the black dots. A clear improvement can be seen, but still a discrepancy remains due to different longitudinal beam spot size in MC simulated events compared to data.

9.2 Light Lepton Vetoes

The considered final state only consists of two hadronically decaying tau leptons and maybe additional jets, e.g. in b-associated Higgs production. However, electrons and muons can mimic tau decays and

additional jets may as well fake tau decays. To remove backgrounds from light lepton fakes, such as $Z/\gamma^*(\rightarrow ee)+\text{jets}$, $Z/\gamma^*(\rightarrow \mu\mu)+\text{jets}$, $W(\rightarrow e\nu)+\text{jets}$, $W(\rightarrow \mu\nu)+\text{jets}$ or di-boson production, each event containing at least on pre-selected electron or muon is discarded. This further ensures an orthogonal selection w.r.t. the fully and semi-leptonic final states such that no overlap between the channels in the combination of the results has to be considered.

9.3 Trigger Requirements

Events selected by a combination of a high- p_T single-tau (EF_tau125_medium1) and a relatively low- p_T di-tau (EF_2tau38T_medium1) trigger are accepted in this analysis. The combination was selected to allow for dedicated data-driven background estimation techniques for QCD multijet events as will be discussed in detail in Chapter 10. The single-tau trigger requires at least on reconstructed hadronically decaying tau lepton with $p_T > 125$ GeV. Identification requirements correspond to the *medium* working point as elaborated on in Section 7.3. It is seeded by L1_tau40 which requires a 40 GeV tau candidate at L1. At the second stage of the trigger chain a reconstructed tau lepton with at least one and not more than four associated tracks is required. A threshold on the reconstructed transverse momentum of 125 GeV is set. Furthermore, calorimeter isolation and tracking cuts according to the medium L2-ID level are applied. In the final EF processing the track requirement is tightened to be either 1, 2 or 3. The di-tau trigger requires the presence of at least two hadronic tau candidates with $p_T > 38$ GeV. The lowest unscaled trigger though is the asymmetric EF_tau29Ti_tau20Ti_medium1. However, it can not be exploited in this analysis due to the additional isolation criteria at L1, which would distort the QCD multijet estimation. The di-tau trigger is seeded by L1_2TAU20 placing a cut of $E_T > 20$ GeV on two reconstructed taus at L1. During the data-taking in 2012 several changes for purpose of bugfixes or performance improvements had to be implemented. However, the trigger simulation in MC was done before the data-taking started, and thus before the trigger menu was finalised. This leads to inconsistencies between simulation and data which have to be corrected. Figure 9.2 shows the jBDT score at Event Filter for the default configuration used for the MC simulation campaign and the recalculated scores using BDT configurations corresponding to data-taking conditions at period A and B, respectively. Unfortunately, not every change can be emulated. The impact parameter cut on Δz_0 at L2 and EF to reduce pile-up dependencies was only available from period B onwards (c.f. Table 4.1). The first implementation suffered from a bug for 1-prong tau candidates which was fixed in period C. Furthermore, period A misses the final BDT optimisation, but uses an older configuration. Since track-based variables are exploited by the EF jBDT, and tracks are removed in AODs, there is no way to emulate the trigger decision. Thus period A has to be discarded, which leads to the slightly lower integrated luminosity analysed in the fully hadronic di-tau searches. The missing track information in the AODs also affects the emulation of the Δz_0 cut, which however is small and covered by the systematic uncertainties. Table 9.1 summarises the trigger configuration in several data-taking periods in 2012 and in MC simulation.

Period	Run number range	Int. lumi. [pb^{-1}]	Details
A	200804-201556	794.02	No Δz_0 track selection Old BDT optimisation
B	202660-205113	5094.68	Imperfect Δz_0 track selection Reoptimised BDT
C-L	206248-215643	14392.8	Fixed Δz_0 track selection
MC simulation			Imperfect Δz_0 track selection Old BDT optimisation

Table 9.1: Summary of data periods, trigger configurations, and the integrated luminosity given in pb^{-1} used in the analyses.

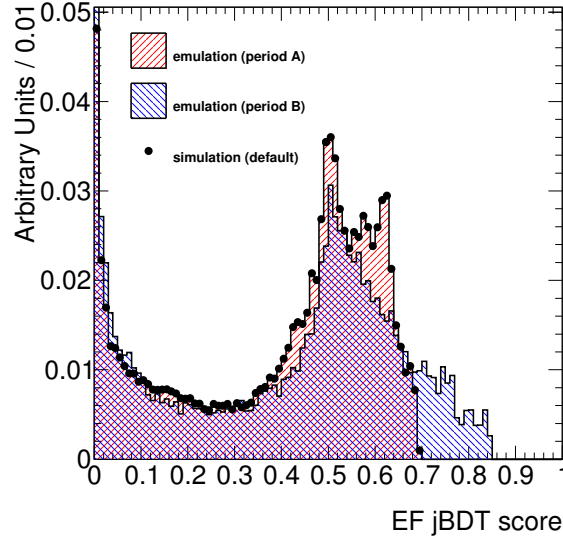


Figure 9.2: BDT discriminator at Event Filter measured in $Z/\gamma^* \rightarrow \tau\tau$ MC simulation. The default configuration used for simulation is depicted by the black dots. The red and blue histograms show the recalculated BDT score distribution using emulation based on the period A and B setup, respectively. The match of the black dots and red histogram indicates that period A configuration was used for the MC production campaign. All histograms are scaled to unit area using the same statistical dataset.

9.4 Back-to-back Requirement

A heavy resonance decaying into two leptons will lead to a back-to-back event topology in which the two taus propagate in opposite direction in the transverse plane. This is ensured by cutting on the difference of the polar angle, $\Delta\phi(\tau_1, \tau_2) > 2.7$, between the two highest- p_T taus, $\tau_{1,2}$. Figure 9.3 shows the angular distance in the transverse plan, $\Delta\phi$, between the two selected tau candidates after applying the event cleaning and light lepton vetoes. For illustration the signal expectations for $M_A = 200$ GeV and $\tan\beta = 15$ assuming the m_h^{\max} scenario are presented by the red and blue lines for b-associated and gluon fusion production mechanism, respectively. Since no data-driven QCD multijet estimation is applicable at this stage, it is taken as the difference between data and prediction of all other backgrounds estimated from MC simulation. The black vertical line indicates the cut value.

9.5 Opposite Sign Requirement

Charge conservation leads to two oppositely charged leptons in the decay of a neutral particle. Thus, the two highest- p_T tau candidates are required to have opposite charge, i.e. $Q_{\tau_1} \cdot Q_{\tau_2} = -1$.

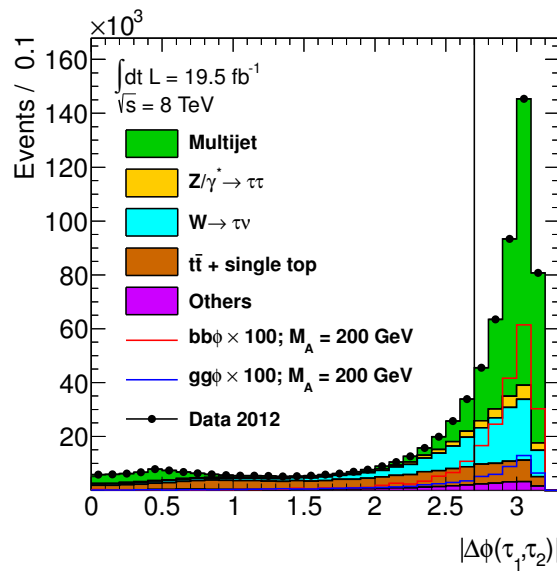


Figure 9.3: Angular distance between the two selected tau candidates after event cleaning and light lepton veto cuts are applied. The multijet contribution is taken as the difference between data and predictions of other processes estimated from MC simulation. All other contributions are estimated from MC simulation. The signal is illustrated by the red and blue lines indicating the b-associated and gluon fusion production, respectively. It is shown for $M_A = 200$ GeV and $\tan\beta = 15$ assuming the m_h^{\max} scenario. The signal strength is scaled by a factor of 100. The cut value is indicated by the black vertical line.

10 Background Estimation

In this chapter the background estimation techniques will be presented. QCD multijet background events are estimated exploiting data-driven approaches, while other dominating components like $Z/\gamma^* \rightarrow \tau\tau$ events and backgrounds arising from jet-to-tau fakes are taken from Monte Carlo simulation. Section 10.1 will elaborate on the various QCD multijet estimation techniques. In Section 10.2 the modelling of the jet-to-tau fake-rate will be discussed. The Chapter closes with a discussion on the control region designed to test the model of $Z/\gamma^*(\rightarrow \tau\tau)+\text{jets}$ events in Section 10.3.

10.1 Multijet Estimation

The dominant background up to moderate masses ($M_X \simeq 350 \text{ GeV}$) originates from QCD multijet events. Even though the fake-rate is small, the huge production cross section of di-jet events makes this background the most significant component. The estimation of this background cannot rely on MC simulation, as it is impossible to generate sufficient statistics. Furthermore, the modelling of quark-gluon fractions, and thus the prediction of the fake-rate is complicated and might lead to a wrong estimate. Hence, data-driven methods have been developed to estimate the QCD multijet contribution. The methods differ in the single-tau triggered (STT) and di-tau triggered (DTT) categories, as will be outlined below. In Sections 10.1.1 and 10.1.3 the concepts of the data-driven estimation in the STT and DTT categories, respectively, are outlined. Before unblinding the data in the signal regions it has to be ensured that the predicted background models provide an adequate prescription. For this purpose additional control regions are defined, which can be used to test the model of the background. This will be summarised in Sections 10.1.2 and 10.1.4, respectively.

10.1.1 Multijet Estimation in the Single-Tau Triggered Category

The two-dimensional sideband extrapolation method (*ABCD method*) exploited in the 2011 analysis to estimate the multijet background works well for low mass di-tau triggered events, but suffers from low available statistics at high mass. Thus a new technique based on *fake-factors* was developed and applied in the presented analyses. The concept is based on the fact that the leading τ_{had} has to match to the trigger, but the sub-leading tau candidate does not. The trigger match leads to a bias of the jBDT score distribution, because a lower level of identification criteria is already applied by the trigger. However, the sub-leading tau candidate remains unbiased and its jBDT score distribution can be used to define control regions from which the contribution of QCD multijet events can be extracted. In Figure 10.1 the jBDT score distributions for the pre-selected tau candidates for 1-prong (left) and 3-prong (right) decays are summarised. The above mentioned bias towards higher jBDT values of the leading tau candidate is clearly visible in the top row plots. By inverting the identification requirement on the sub-leading τ_{had} a control region is defined. Given the loose working point this corresponds roughly to a cut of 0.6 on the jBDT score. This yields a multijet enriched control region with almost no contamination by signal or other backgrounds. Table 10.1 summarises the event yields in the control region.

To estimate the QCD multijet contribution in the signal region, the data in the control region is weighted by an event-by-event weight derived in a dedicated data control region. These weights are referred to as tau-ID fake-factors, $f_{\tau\text{-ID}}$, which are calculated in a tag-and-probe measurement of di-jet data. They are defined as the ratio of the number of probe jets passing the identification criterion selected in the di-jet tag-and-probe measurement, $N^{\text{pass } \tau\text{-ID}}$, and the number of the selected probe jets failing the identification criterion, $N^{\text{fail } \tau\text{-ID}}$:

$$f_{\tau\text{-ID}}(p_T, N_{\text{tracks}}) = \frac{N^{\text{pass } \tau\text{-ID}}(p_T, N_{\text{tracks}})}{N^{\text{fail } \tau\text{-ID}}(p_T, N_{\text{tracks}})} \bigg|_{\text{di-jet}}. \quad (10.1)$$

The normalisation and shape of the QCD multijet background, N_{multijet} , of any variable x in the signal region, i.e. where the sub-leading tau passes ID, is predicted by weighting each event where the sub-

cut	$gg \rightarrow A \rightarrow \tau_{\text{had}} \tau_{\text{had}}$	$b\bar{b}A \rightarrow \tau_{\text{had}} \tau_{\text{had}}$	$Z/\gamma^* \rightarrow \tau\tau + \text{jets}$	$W \rightarrow \tau\nu + \text{jets}$	Top	Others	SM Total	Data
Loose BDT τ_1	43.8 ± 0.8	420.2 ± 8.0	465.0 ± 25.5	774.7 ± 12.9	241.7 ± 9.2	25.3 ± 1.6	$(15.1 \pm 0.3) \times 10^2$	43.16×10^3
Fail Loose BDT τ_2	7.2 ± 0.3	68.5 ± 3.2	59.0 ± 8.2	14.9 ± 0.7	6.7 ± 1.3	0.3 ± 0.1	80.9 ± 8.3	42.15×10^3
Opposite signs	6.4 ± 0.3	60.4 ± 3.0	55.0 ± 8.2	11.4 ± 0.6	5.3 ± 0.9	0.2 ± 0.1	71.9 ± 8.3	21.89×10^3
$\Delta\phi(\tau_1, \tau_2) > 2.7$	5.1 ± 0.3	53.6 ± 2.9	20.0 ± 1.1	7.3 ± 0.4	3.1 ± 0.7	0.2 ± 0.1	30.6 ± 1.3	14.83×10^3

Table 10.1: Event yields in the multijet enriched control region, constructed by inverting the tau identification requirement, in the single-tau triggered category used to estimate the multijet background contribution in the signal region. For illustration signal expectations corresponding to $M_A = 400$ GeV and $\tan\beta = 40$ assuming the m_h^{max} benchmark scenario are summarised in the first two columns. Uncertainties quoted are of statistical origin.

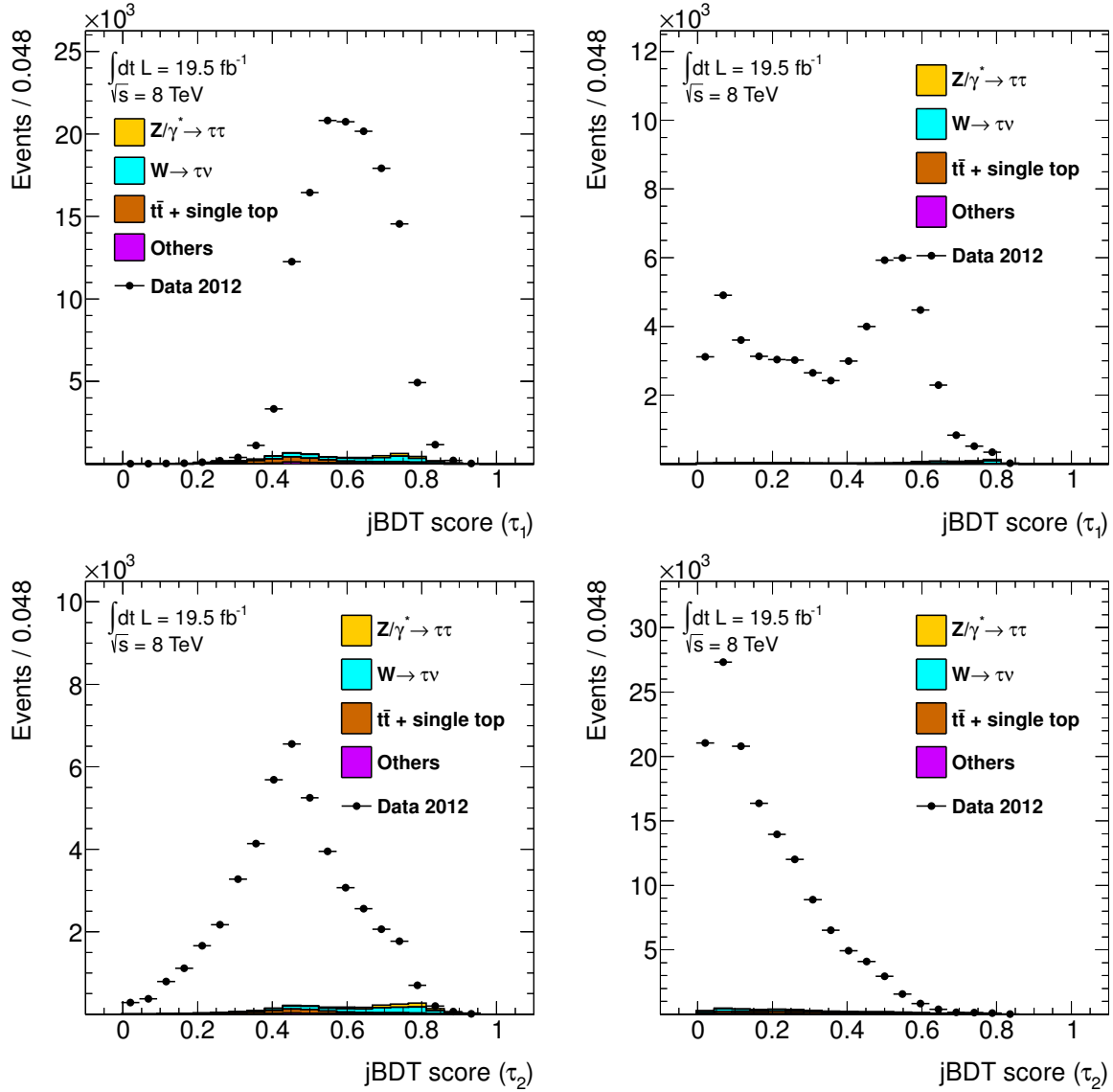


Figure 10.1: Tau identification jBDT scores of the leading (top) and sub-leading (bottom) tau candidate reconstructed as 1-prong (left) and 3-prong (right) decay after the trigger match is applied. Non-multijet contributions are estimated from MC simulation. A clear bias of the leading τ_{had} jBDT score distribution is seen due to the trigger matching criterion.

leading τ_{had} fails the ID requirement by its fake-factor:

$$N_{\text{multijet}}(p_T, N_{\text{tracks}}, x) = f_{\tau\text{-ID}}(p_T, N_{\text{tracks}}) \times N_{\text{data}}^{\text{fail } \tau\text{-ID}}(p_T, N_{\text{tracks}}, x). \quad (10.2)$$

Di-jet Control Region

As mentioned above the fake-factors are derived in a data control region optimised for a high purity selection of di-jet events. Events triggered by any single-jet trigger are excepted. Given the high rate of jet production at the LHC, the low- p_T jet triggers are pre-scaled. The lowest unpre-scaled jet trigger is EF_j360_a4tchad, which selects anti- k_t ($R = 0.4$) jets on EF level with an E_T threshold of 360 GeV. Table 10.2 summarises the trigger selection and the corresponding pre-scales.

Furthermore, at least two reconstructed tau candidates are required, each fulfilling $p_T > 50$ GeV. As *tag* jet the highest- p_T tau candidate is considered, while the sub-leading tau candidate serves as the *probe* object. As in the selection of the signal region, the p_T threshold on the tag side is raised to 150 GeV (c.f.

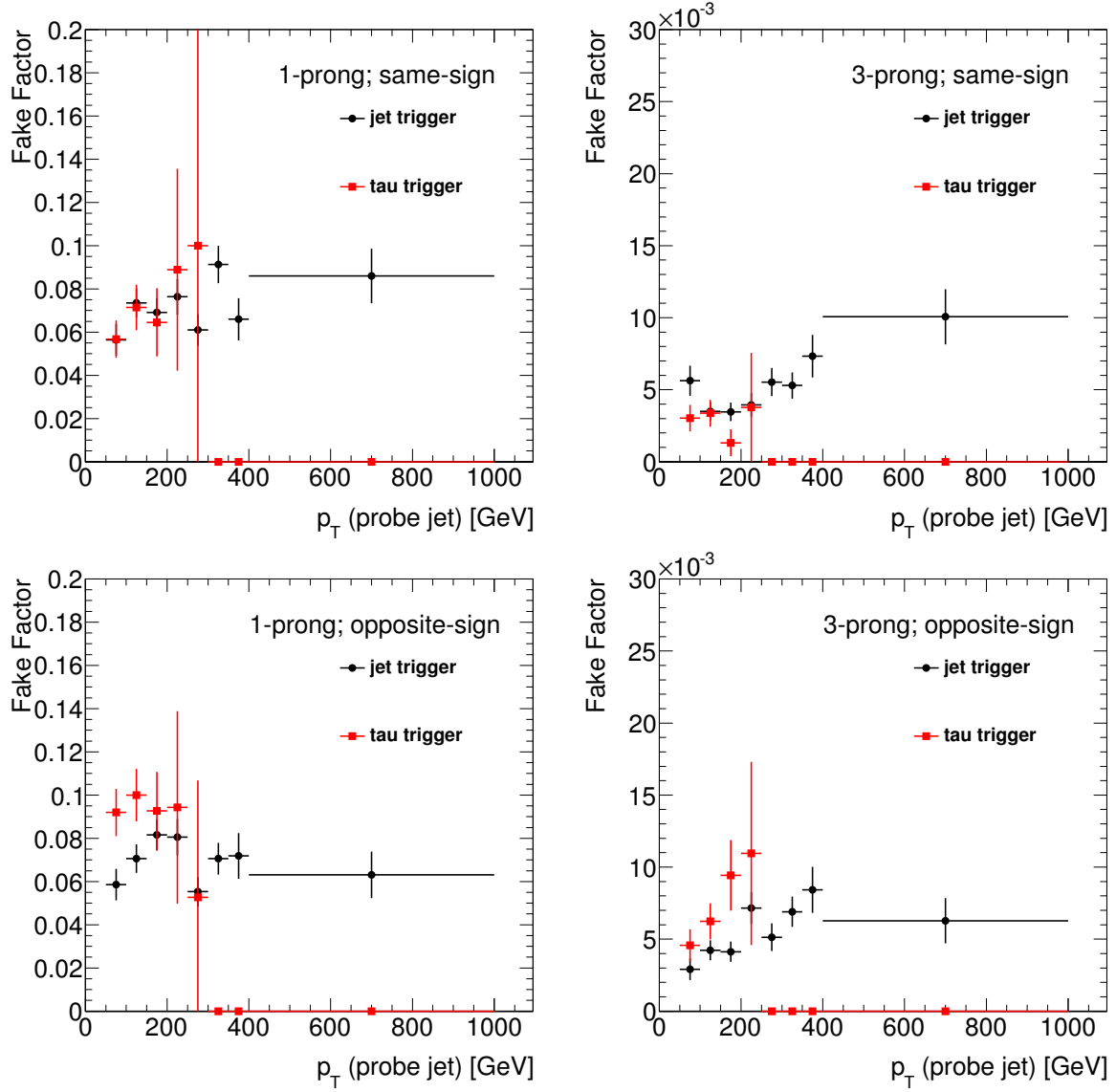


Figure 10.2: Fake-factors measured in a di-jet tag-and-probe style analysis for 1-prong (left) and 3-prong probe jets (right) as a function of the probe jet transverse momentum for jet and tau-triggered events marked by the black dots and red boxes, respectively. Fake-factors measured in same-sign events are shown in the top row, while in the bottom row they are calculated for oppositely charged tag and probe jets.

Trigger	pre-scale
EF_j110_a4tchad	2066
EF_j145_a4tchad	559
EF_j180_a4tchad	257
EF_j220_a4tchad	77.6
EF_j360_a4tchad	1
EF_tau125_medium1	1

Table 10.2: Summary of triggers used for the di-jet tag-and-probe fake-factor measurement with pre-scale factors for low- p_T jet triggers are given. They are used to calculate the correct normalisation. The single-jet triggers select anti- k_t ($R = 0.4$) jets on EF level with E_T thresholds between 110 GeV and 360 GeV.

Section 12.2.1). On top a tight eBDT requirement is asked for to reduce contamination by electrons originating from e.g. $Z/\gamma^*(\rightarrow ee)+\text{jets}$ events. Furthermore, a large imbalance in p_T between the two jets can lead to a very poor modelling of the fake-rate due to mispredictions of the quark-gluon ratio, because not typical di-jet events, but rather multijet events are selected. Thus a lower threshold on the p_T balance of the two selected jets of 30% is placed, i.e. $p_T^{\text{probe}}/p_T^{\text{tag}} \geq 0.3$. In the signal region a single-tau trigger requirement is applied in the selection instead of jet triggers. Hence, the dependence of the fake-factors on the trigger has been investigated. Figure 10.2 shows the obtained fake-factors for tau and jet triggered events for one- and three-prong tau decays. The top row presents the measurement in same-sign events, while in the bottom row the fake-factors obtained in opposite-sign events are shown. For same-sign events the obtained fake-factors do not show any significant dependence on the trigger. For high- p_T di-jet events the amount of events selected by the single-tau trigger becomes very small due to isolation requirements, which are not applied by the jet-triggers. For events with oppositely charged jets a significant deviation is observed at rather low- p_T . This is expected as the tau trigger will likely select $Z/\gamma^*(\rightarrow \tau\tau)+\text{jets}$ events, which distort the measurement. However, assuming that the composition of multijet events in same- and opposite-sign events is the same, the fake-factors obtained by the measurement of jet-triggered events is reliable. A bias on the estimate of the multijet background may also arise from the selected event topology. In particular events with a high jet multiplicity may yield a bias due to a difference in the selected quark-gluon fraction. For this purpose the fake-factors have been measured for events with various jet multiplicities. Figure 10.3 summarises the measured fake-factors for events with zero to four additional jets in the events. Apparently, the available amount of data significantly decreases with increased jet multiplicity, which results in large statistical uncertainties on the measured fake-factors. However, no systematic deviation is observed. The large statistical uncertainty for di-jet events in the lowest p_T bin arises from the p_T balance of the two jets.

A further cross check has been performed to ensure that the impact of the identification requirement in the signal region has no impact on the fake-factors. For this purpose the fake-factors have been measured applying various thresholds on the jBDT score of the tag jet. This emulates the tau trigger selection to some extent, which might bias the quark-gluon fraction. The obtained fake-factors are shown in Figure 10.4. For the tightest cut of jBDT > 0.3 the available amount of events drops significantly resulting in huge statistical uncertainties. However, no significant discrepancy of the measured fake-factors is observed.

The aforementioned measurements justify the calculation of the fake-factors considering both opposite- and same-sign events without any additional jBDT requirement on the tag jet. The final fake-factors used to estimate the QCD multijet background contribution are summarised in Figure 10.5. The evaluation of the systematic uncertainties will be outlined in Section 11.1.10.

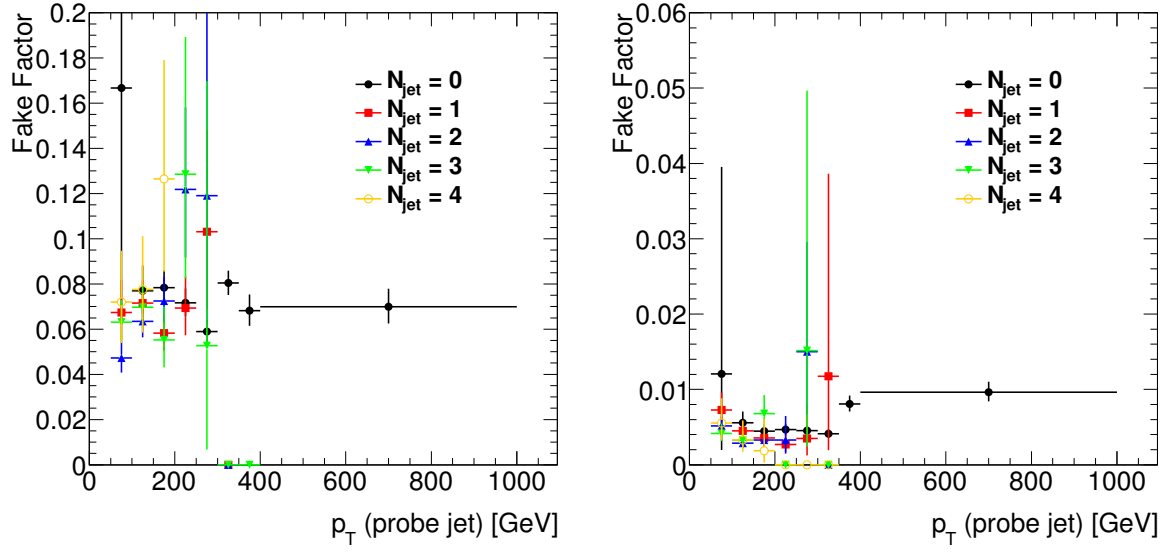


Figure 10.3: Fake-factors measured in a di-jet tag-and-probe style analysis for 1-prong (left) and 3-prong probe jets (right) as a function of the probe jet transverse momentum for various numbers of additional jets in the events. Fake-factors have been derived from same-sign di-jet events to reduce the amount of real tau contamination.

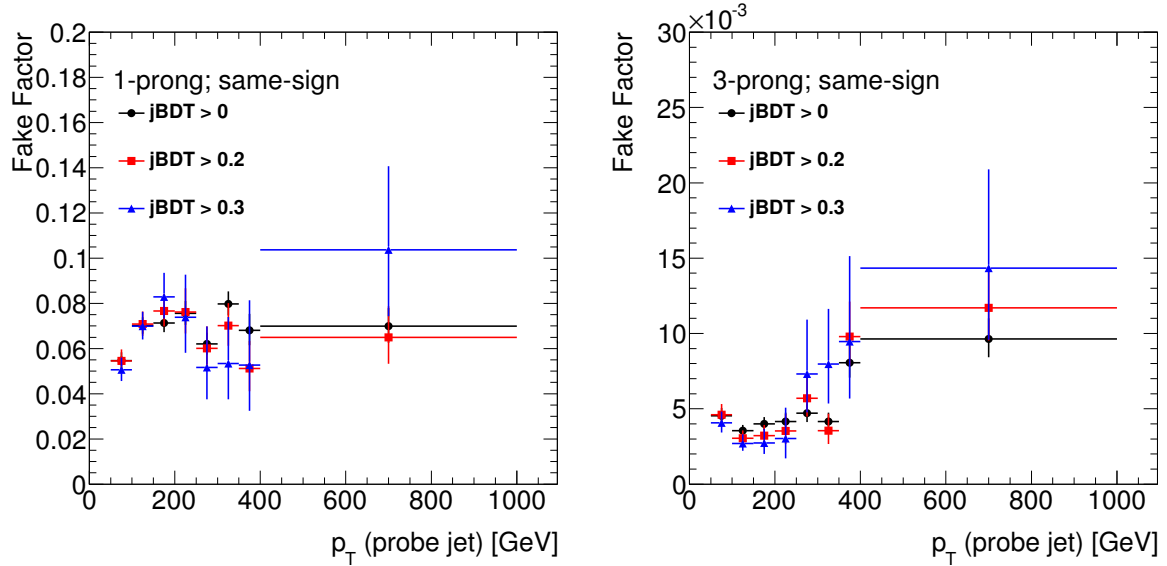


Figure 10.4: Fake-factors measured in a di-jet tag-and-probe style analysis for 1-prong (left) and 3-prong probe jets (right) as a function of the probe jet transverse momentum for various thresholds applied on the jBDT score of the tag jet. Fake-factors have been derived from same-sign di-jet events to reduce the amount of real tau contamination.

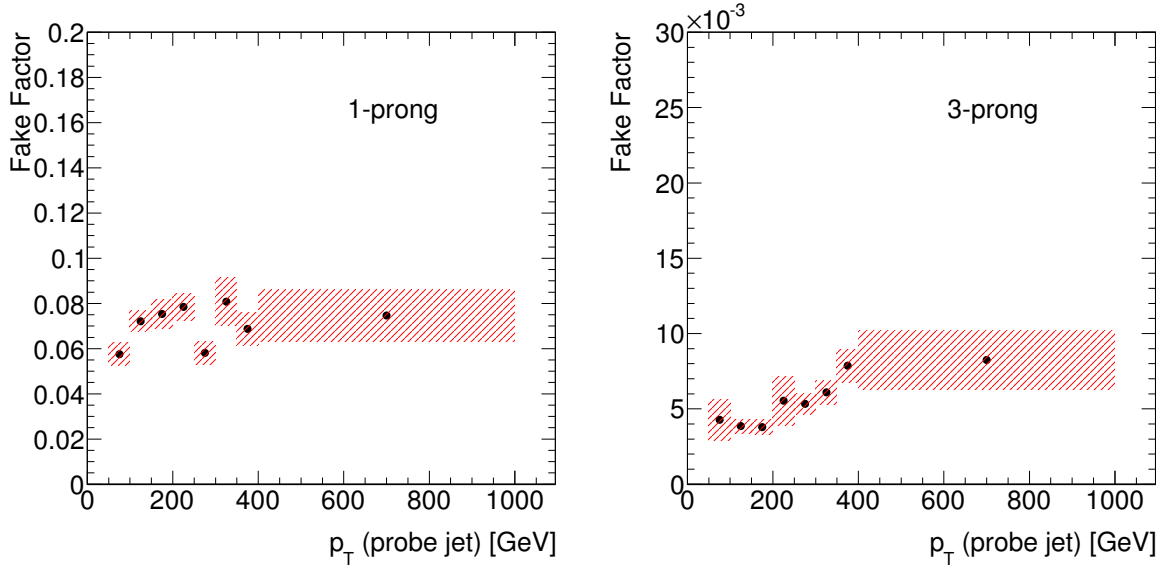


Figure 10.5: Fake-factors measured in a di-jet tag-and-probe analysis for 1-prong (left) and 3-prong probe jets (right) as a function of the probe jet transverse momentum. The central value is marked by the black dots, while the red dashed areas indicate the systematic uncertainties.

10.1.2 Validation of QCD Multijet Estimation Using Fake-Factors

Before analysing the data in the signal region it has to be validated that the background model provides an adequate prescription. This is in particular crucial for backgrounds estimated from data. To validate the QCD multijet model obtained by the tau-ID fake-factor method a control region has been designed to compare the estimated backgrounds from SM processes with data. It has to be guaranteed that no signal, or at least only a negligible amount, enters in this control region. Furthermore, to be meaningful, the control region has to be as close as possible to the signal region. The same selection criteria as in the signal region are applied to define the control region, but the charge requirement is inverted, such that the two selected tau candidates are required to have same electric charge. The fake-factor method is then applied in the same way as in the signal region by defining a further control region of inverted tau-ID requirement on the sub-leading tau candidate. All other backgrounds are estimated from simulation, applying the same corrections, like fake-weights (see below), as in the signal region. The expected and observed event yields are summarised in Table 10.3.

Figure 10.6 shows some kinematic key distributions of the two selected tau candidates in the same-sign control region. In the top row the p_T distributions of the leading and sub-leading τ_{had} candidates are depicted. The bottom row present the angular distributions. A good agreement within the statistical and systematic uncertainties is observed. Figure 10.7 illustrates the track multiplicity distributions of the two selected tau candidates. As for the kinematic distributions a good agreement between data and the background model is observed. Event based observables are shown in Figure 10.8. The left hand plot shows the E_T^{miss} distribution, while the right hand plot shows the scalar sum of the transverse energy of all reconstructed objects. Neither of them is directly used in the single-tau triggered selection, but the E_T^{miss} enters the m_T^{tot} calculation (c.f. Eq. 10.3), and thus a proper modelling is crucial. Again a reasonable agreement between the background model and the data is observed. Finally, the visible and total transverse mass distributions are presented in Figure 10.9. The *total transverse mass*, m_T^{tot} , is defined as:

$$m_T^{\text{tot}} = \sqrt{2p_{T1}p_{T2}C + 2|E_T^{\text{miss}}|p_{T1}C_1 + 2|E_T^{\text{miss}}|p_{T2}C_2}, \quad (10.3)$$

with p_{T1} and p_{T2} being the transverse momentum of the two selected tau leptons and C defined as $C = 1 - \cos \Delta\phi$ with $\Delta\phi$ being the angle between the two tau leptons in the transverse plane. C_1 and C_2 are defined analogously with $\Delta\phi$ measuring the angle between the missing transverse energy and the leading

cut	$gg \rightarrow A \rightarrow \tau_{\text{had}} \tau_{\text{had}}$	$b\bar{b}A \rightarrow \tau_{\text{had}} \tau_{\text{had}}$	multijet	$Z/\gamma^* \rightarrow \tau\tau + \text{jets}$	$W \rightarrow \tau\nu + \text{jets}$	Top	Others	SM Total	Data
Preselection	34.6 ± 0.7	338.3 ± 7.2	621.5 ± 5.6	266.6 ± 17.1	62.6 ± 1.4	22.1 ± 1.9	1.7 ± 0.4	974.6 ± 18.2	1017
Same signs	0.5 ± 0.1	4.0 ± 0.7	299.5 ± 3.9	5.6 ± 0.7	10.7 ± 0.4	2.9 ± 0.2	0.2 ± 0.0	318.9 ± 4.0	327
$\Delta\phi(\tau_1, \tau_2) > 2.7$	0.4 ± 0.1	3.6 ± 0.7	206.5 ± 3.3	4.2 ± 0.5	6.1 ± 0.3	1.2 ± 0.1	0.1 ± 0.0	218.1 ± 3.3	205

Table 10.3: Event yields in the same-sign multijet enriched control region in the single-tau triggered category used to validate the multijet background model based on tau-ID fake-factors. For illustration signal expectations corresponding to $M_A = 400$ GeV and $\tan\beta = 40$ assuming the m_h^{max} benchmark scenario are summarised in the first two columns. Uncertainties quoted are of statistical origin.

and sub-leading tau lepton, respectively. Since the m_T^{tot} distribution is used as the final discriminating variable in the statistical interpretation of the presented searches for new particles, their modelling is crucial. A very good agreement can be seen, except for the first bin, which suffers from low statistics. This, however, is non-significant, since the large statistical uncertainty prevents a clear conclusion, and furthermore a heavy resonance would appear at higher values of m_T^{tot} . Also the visible mass is predicted reasonably well and agrees within the statistical and systematic uncertainties.

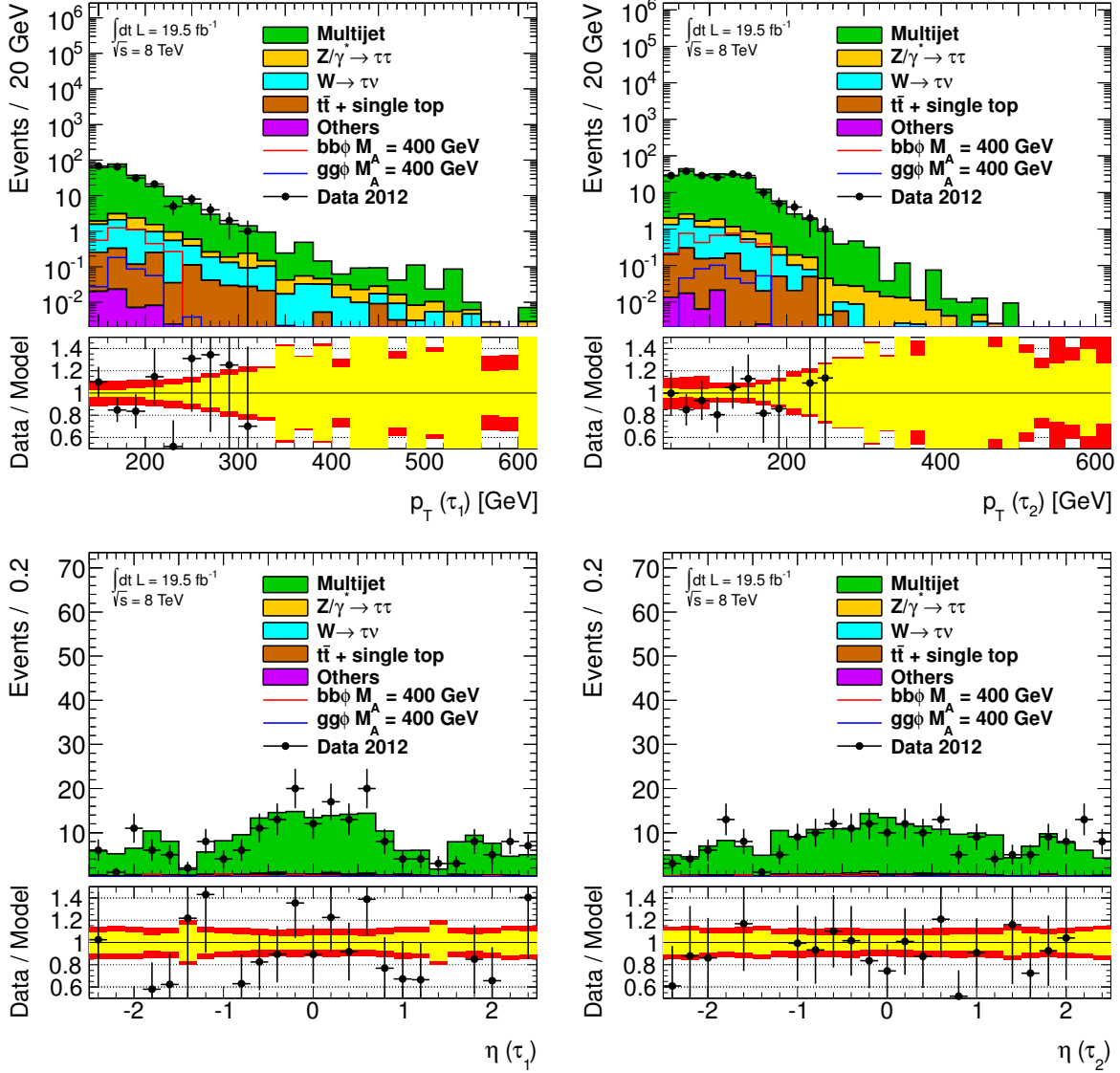


Figure 10.6: Kinematic distributions of the leading (left) and sub-leading (right) tau candidates in the same-sign control region. The multijet contribution is estimated using tau-ID fake-factors. All other contributions are estimated from MC simulation. Others include di-boson production and W/Z light lepton, i.e. e, μ , decays. The signal shown for illustration corresponds to $M_A = 400$ GeV and $\tan\beta = 40$ assuming the m_h^{max} benchmark scenario. The statistical and systematic uncertainties on the model are indicated by the yellow and red bands in the ratio, respectively.

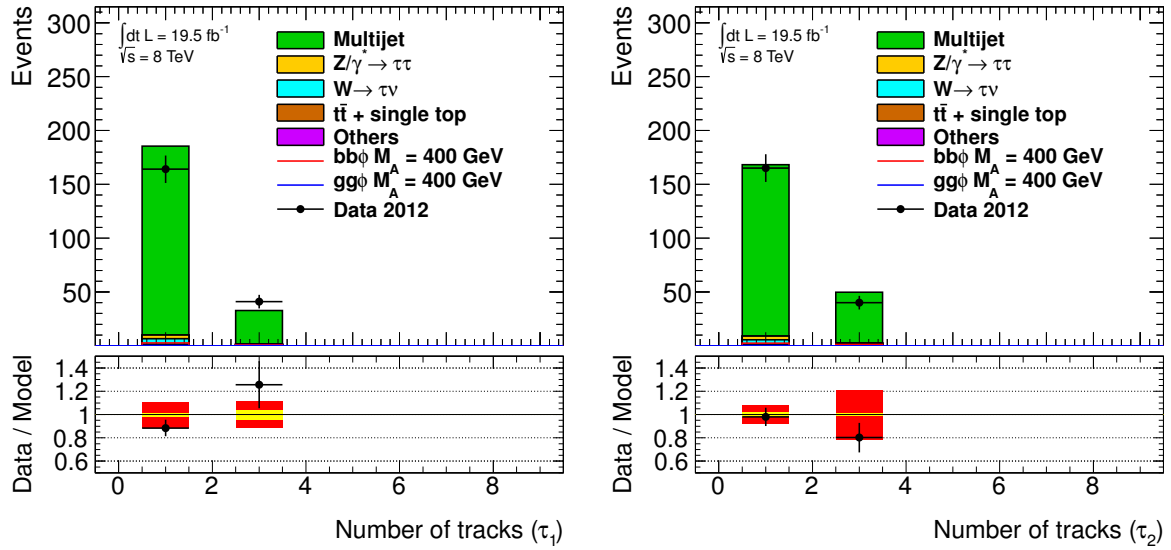


Figure 10.7: Track multiplicity distributions for the leading and sub-leading tau candidates in the same-sign control region. The multijet contribution is estimated using tau-ID fake-factors. All other contributions are estimated from MC simulation. Others include di-boson production and W/Z light lepton, i.e. e, μ , decays. The signal shown for illustration corresponds to $M_A = 400$ GeV and $\tan\beta = 40$ assuming the m_h^{\max} benchmark scenario. The statistical and systematic uncertainties on the model are indicated by the yellow and red bands in the ratio, respectively.

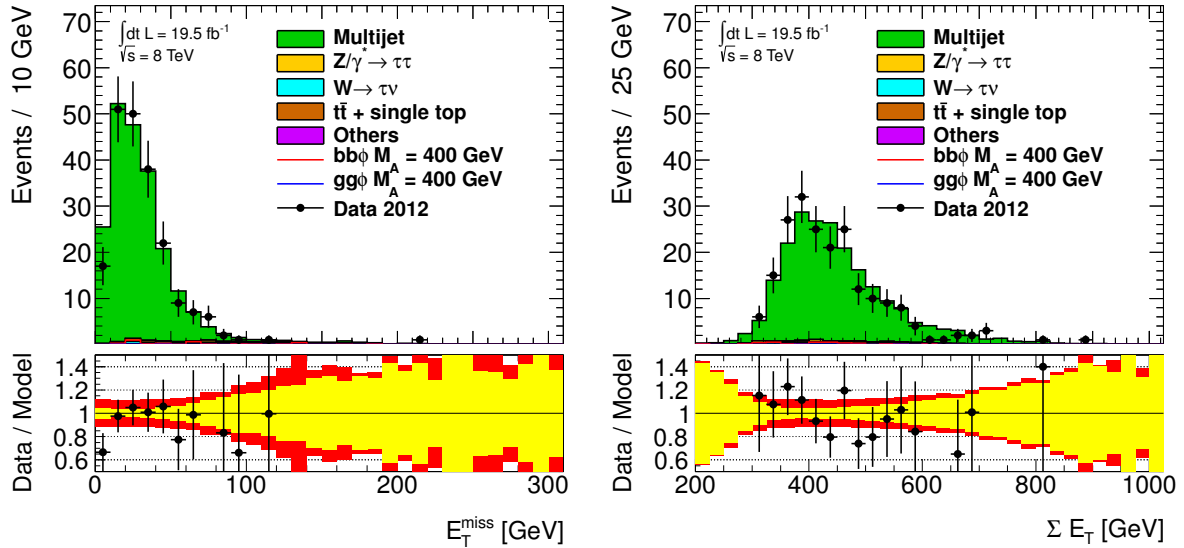


Figure 10.8: Key event distributions in the same-sign control region. The multijet contribution is estimated using tau-ID fake-factors. All other contributions are estimated from MC simulation. Others include di-boson production and W/Z light lepton, i.e. e, μ , decays. The signal shown for illustration corresponds to $M_A = 400$ GeV and $\tan\beta = 40$ assuming the m_h^{\max} benchmark scenario. The statistical and systematic uncertainties on the model are indicated by the yellow and red bands in the ratio, respectively.

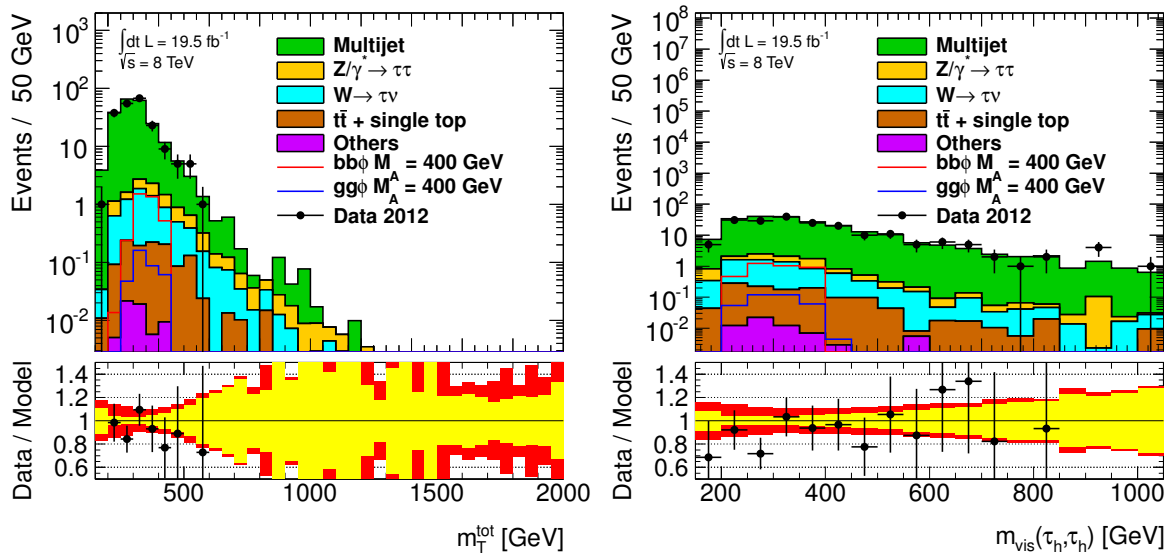


Figure 10.9: Total transverse mass and visible mass distributions in the same-sign control region. The multijet contribution is estimated using tau-ID fake-factors. All other contributions are estimated from MC simulation. Others include di-boson production and W/Z light lepton, i.e. e, μ , decays. The signal shown for illustration corresponds to $M_A = 400$ GeV and $\tan\beta = 40$ assuming the m_h^{\max} benchmark scenario. The statistical and systematic uncertainties on the model are indicated by the yellow and red bands in the ratio, respectively.

10.1.3 Multijet Estimation in the Di-Tau Triggered Category

In the di-tau triggered category the aforementioned fake-factor method is not applicable, because a trigger match to both selected tau candidates is required. Given the identification requirement applied at EF stage, this leads to a bias of the jBDT score distribution of the sub-leading tau candidate. This is shown in Figure 10.10 which presents the jBDT score distributions of the sub-leading tau candidate after the match to the trigger chain is applied.

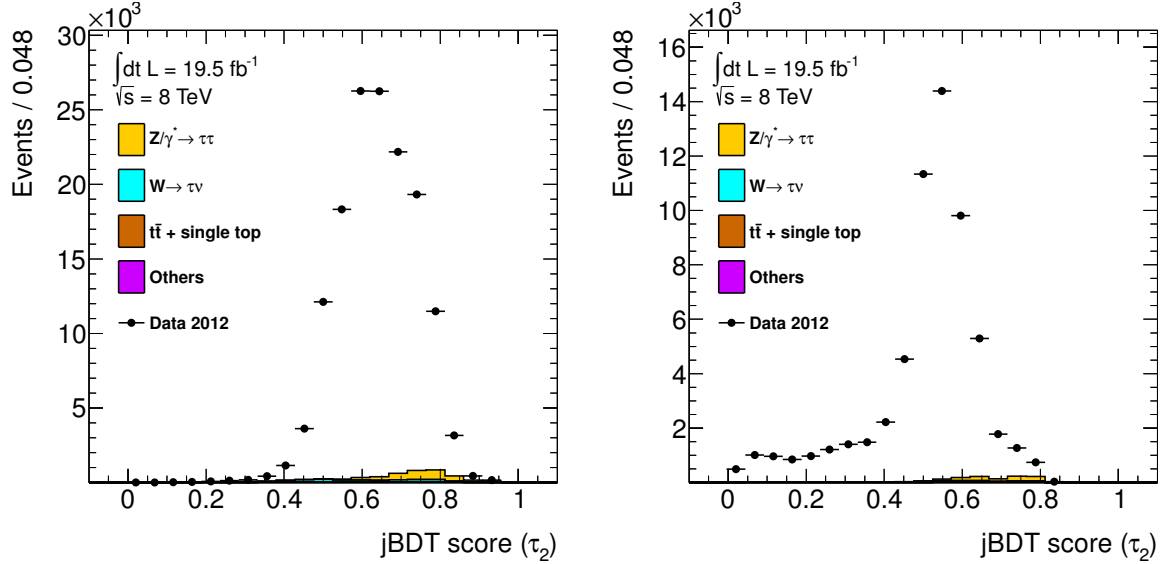


Figure 10.10: Tau identification jBDT scores of the sub-leading tau candidate reconstructed as 1-prong (left) and 3-prong (right) decay after the trigger match is applied. Non-multijet contributions are estimated from MC simulation. Others include di-boson production and W/Z light lepton, i.e. e, μ , decays. Contrary to the STT selection, a clear bias of the jBDT score distribution is seen due to the trigger matching criterion.

A clear shift towards higher jBDT score values is visible, and thus prevents the application of the fake-factor method. Hence, a two-dimensional sideband extrapolation (ABCD) method is deployed. It is based on four mutually exclusive data samples. Three of them serve as control regions enhanced with QCD multijet events, while the remaining sample corresponds to the signal region in which the multijet contributions has to be estimated. The entire phase space is split into these four regions by classifying events depending on the charge product of the two selected tau candidates and the measured missing transverse energy. The control regions are then defined by inverting one or both of either the requirement on the charge product, the so-called same-sign (SS) control regions, or the E_T^{miss} requirement, which leads to the low- E_T^{miss} ($E_T^{\text{miss}} < 10 \text{ GeV}$) or high- E_T^{miss} ($E_T^{\text{miss}} > 10 \text{ GeV}$) control regions. This leads to the following four data samples:

- **Region A:** events where the two tau candidates have opposite charge and $E_T^{\text{miss}} > 10 \text{ GeV}$
- **Region B:** events where the two tau candidates have same charge and $E_T^{\text{miss}} > 10 \text{ GeV}$
- **Region C:** events where the two tau candidates have opposite charge and $E_T^{\text{miss}} < 10 \text{ GeV}$
- **Region D:** events where the two tau candidates have same charge and $E_T^{\text{miss}} < 10 \text{ GeV}$

To get a proper estimate of the QCD multijet background in the signal region, both the shape and the normalisation have to be determined. The shape can be extracted from region B, while the normalisation can be calculated from the event yields in regions C and D. This assumes that the shapes of the final discriminating variable, as well as of other important kinematic and event variables, are the same in opposite-sign and same-sign events. These assumptions have been validated by comparing these shapes.

Figure 10.11 shows the distributions of key kinematic variables for each of the selected τ_{had} candidates in opposite- and same-sign data samples. Contributions from electroweak processes, like $Z/\gamma^* \rightarrow \tau\tau$, are subtracted using the prediction by MC simulation. In addition a *Kolmogorov-Smirnov* (KS) [229, 230] test has been performed to verify that the shapes arise from the same underlying distribution. A KS value of one indicates that the shapes are the same, while a low KS value indicates a disagreement between the underlying distributions. The tau kinematic variables show a reasonable agreement, except the η distribution which shows some disagreements. However, since η is not sensitive to the signal it does not degrade the analysis.

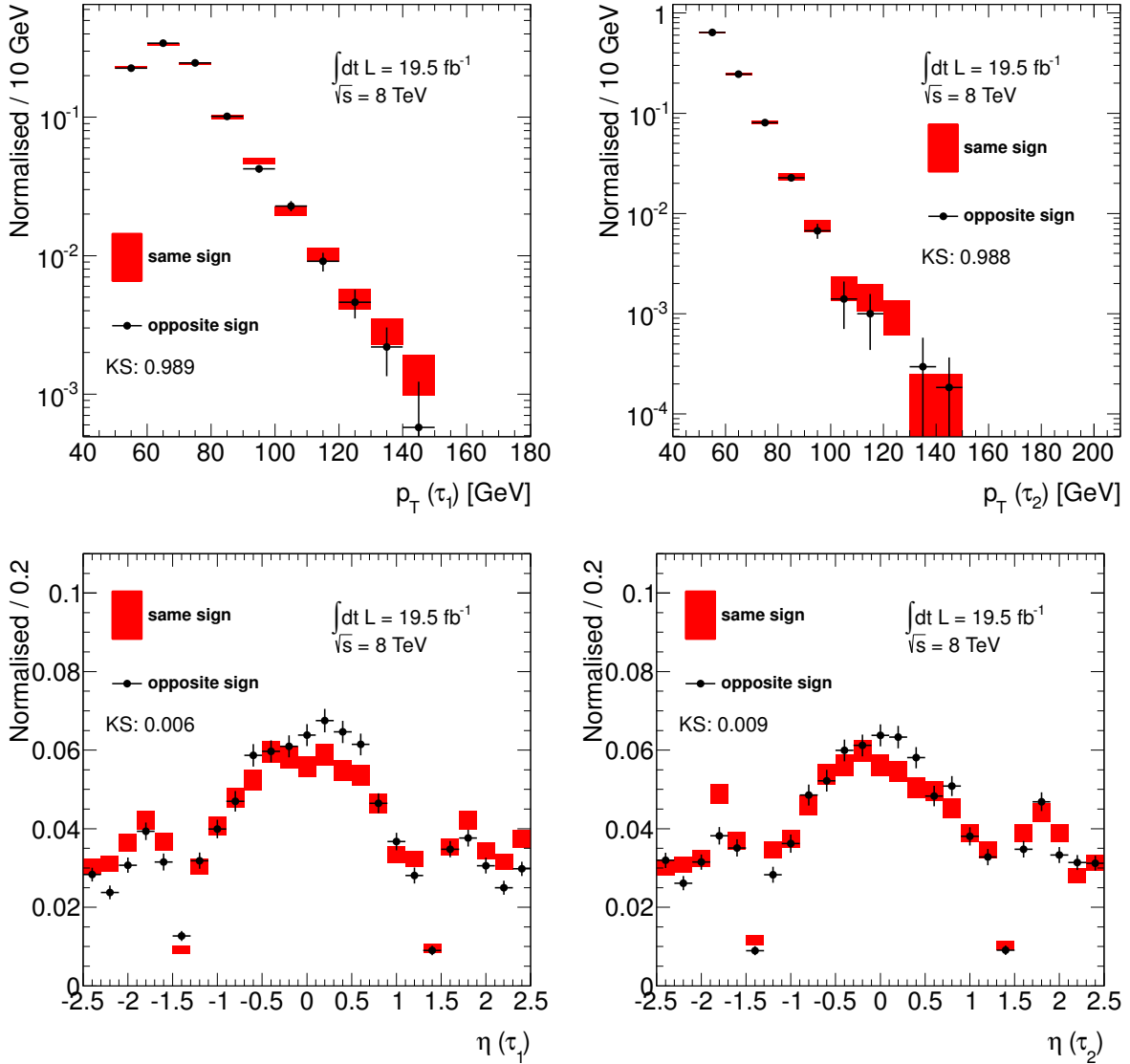


Figure 10.11: Shape comparison of key kinematic variables of the two selected τ_{had} candidates measured in opposite- and same-sign data samples. In red the distributions of same-sign events is presented, while the black dots indicate events with oppositely charged τ_{had} candidates. The quoted uncertainties are of statistical nature. All distributions are normalised to unit area. The distributions of the leading and sub-leading τ_{had} candidate are displayed in the left and right column, respectively. KS values quoted in the plots are an indicator of the agreement between the shapes.

Besides the agreement of kinematic variables of the selected τ_{had} candidates, key event variables, like $E_{\text{T}}^{\text{miss}}$ or $m_{\text{T}}^{\text{tot}}$, are crucial. Figure 10.12 presents the missing transverse energy, the scalar sum of

the transverse energy, $\sum E_T$, the visible mass, m_{vis} , and the total transverse mass, m_T^{tot} . A reasonable agreement is observed, although the visible mass distribution exhibits some disagreement. This issue has been observed in previous analyses as well, but so far no conclusion on the cause was reached. A likely explanation is that the p_z component is different in opposite- and same-sign events, but there is no way to measure the momentum component along the beam pipe. However, this might explain why the transverse projection, which is not sensitive to the p_z component, is described very well. Furthermore, the shift in the visible mass distribution occurs at higher mass where the DTT category is insensitive and replaced by the STT category. The latter exploits a different approach of multijet background estimation, which is insensitive to the same-sign shapes

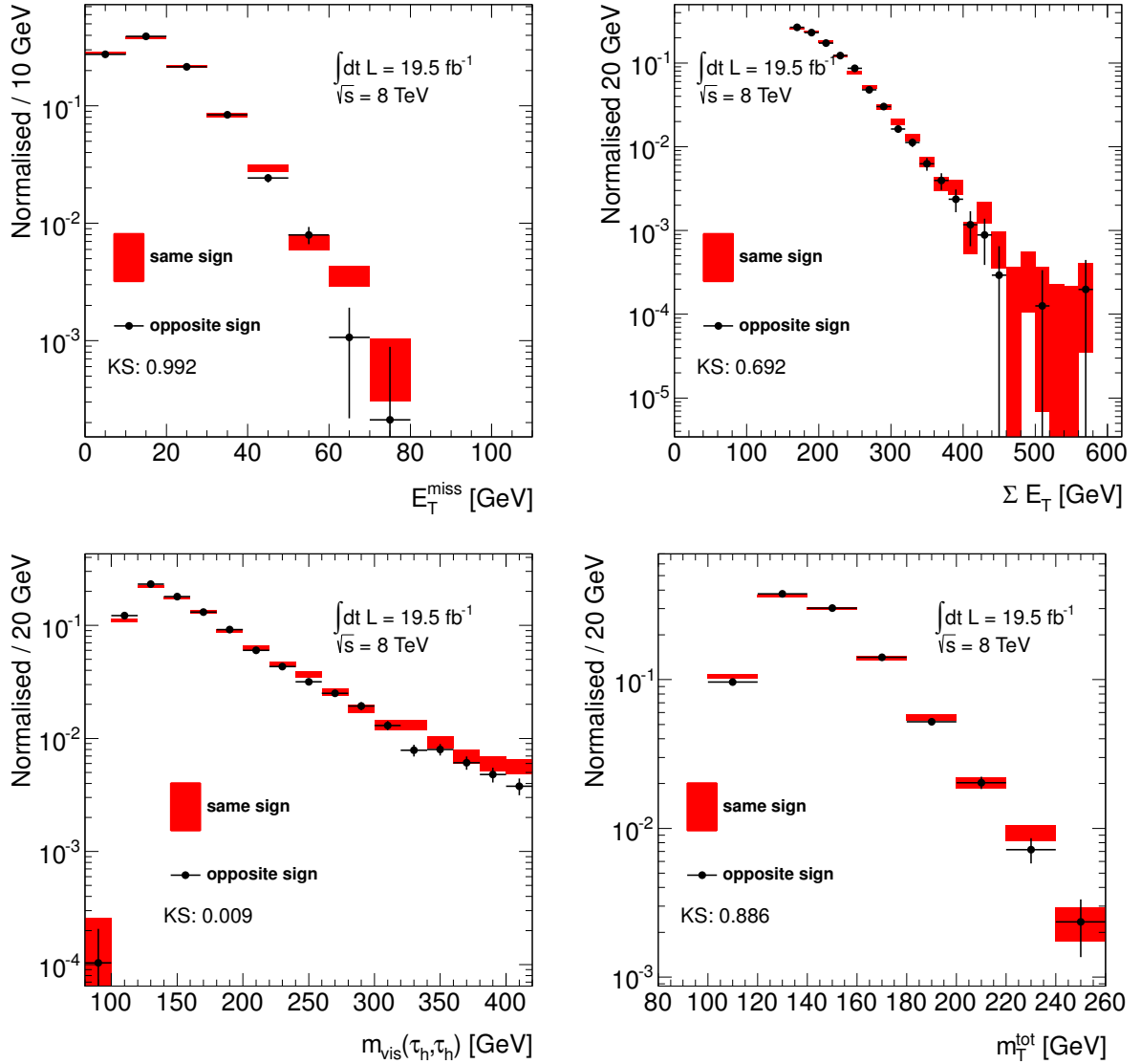


Figure 10.12: Shape comparison of key event variables in opposite- and same-sign data samples. In red the distributions of same-sign events is presented, while the black dots indicate events with oppositely charged τ_{had} candidates. The quoted uncertainties are of statistical nature. All distributions are normalised to unit area. The E_T^{miss} and $\sum E_T$ distributions are shown in the top row, while in the bottom row the visible and total transverse mass are presented. KS values quoted in the plots are an indicator of the agreement between the shapes.

The QCD multijet contribution in the signal region is then estimated as the shape obtained in region B multiplied by a transfer factor, R_{qcd} , which is obtained as the ratio of the event yields in region C and

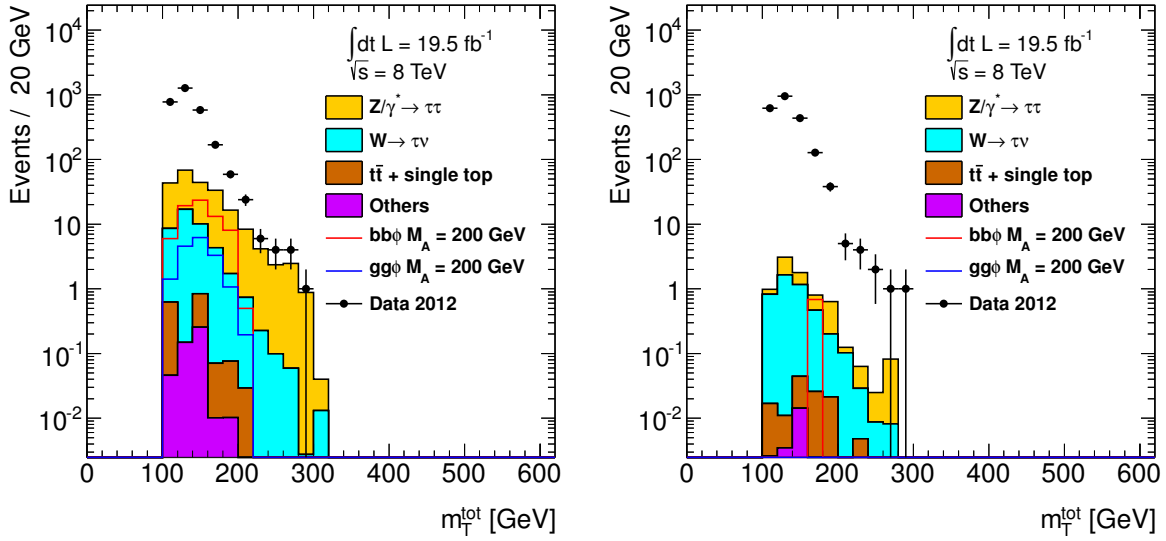


Figure 10.13: Total transverse mass, m_T^{tot} , distribution in the low- E_T^{miss} control region for opposite-sign (left) and same-sign (right) events. All non-multijet backgrounds are estimated from MC simulation. Others include di-boson production and W/Z light lepton, i.e. e, μ , decays. The signal shown for illustration corresponds to $M_A = 200$ GeV and $\tan\beta = 15$ assuming the m_h^{max} benchmark scenario.

D, i.e.:

$$N_{\text{multijet}}(x)|_{\text{signal-region}} = R_{\text{qcd}}(N_{\text{data}}(x)|_{\text{region B}} - N_{\text{MC}}(x)|_{\text{region B}}), \quad (10.4)$$

with

$$R_{\text{qcd}} = \frac{N_{\text{data}}|_{\text{region C}} - N_{\text{MC}}|_{\text{region C}}}{N_{\text{data}}|_{\text{region D}} - N_{\text{MC}}|_{\text{region D}}}. \quad (10.5)$$

A proper estimate is only obtained if the purity of multijet events is sufficiently high, i.e. there is no (or negligible) signal contamination, as well as only small contributions from other SM processes. Figure 10.13 shows the m_T^{tot} distributions in the low- E_T^{miss} opposite-sign (left) and same-sign (right) control region. As can be seen there is only little contribution from non-multijet events, and thus a high purity of multijet events in data is guaranteed.

The observed and expected event yields in each of the control regions and the signal region is further summarised in Table 10.4. As expected, the largest signal contamination appears in the opposite-sign low- E_T^{miss} sample, while for same-sign events the signal contribution can be neglected. In addition the non-multijet backgrounds account for less than 1% in the same-sign control regions, but roughly 7% in region C. As pointed out above, the MC prediction is subtracted from data events in each control region. Thus all systematic uncertainties on the MC estimate have to be taken into account. This will be addressed in detail in Chapter 11.

10.1.4 Validation of QCD Multijet Estimation Using an ABCD Method

As pointed out in Section 10.1.2 it is crucial to validate the performance of the considered technique deployed for the estimation of a background component. To test the ABCD method, additional orthogonal QCD multijet enriched control regions have been designed, which are again as similar to the nominal configuration as possible. These are based on inverted tau-ID criteria. The same selections of the regions A-D, as discussed above, are applied, but the two selected τ_{had} candidates are required to fail the tau identification requirement. To reduce the amount of QCD multijet events in the final signal region, the tau identification requirement is tightened to the medium working point (c.f. Section 12.2.2). But, simply inverting the medium requirement would yield a significant contamination of signal events, and

	A	B	C	D
$b\bar{b}A \rightarrow \tau_{\text{had}}\tau_{\text{had}}$	411.83 ± 13.30	0.59 ± 0.46	70.59 ± 5.55	0.69 ± 0.68
$gg \rightarrow A \rightarrow \tau_{\text{had}}\tau_{\text{had}}$	93.89 ± 3.47	0.62 ± 0.24	16.76 ± 1.45	0.00 ± 0.00
$Z/\gamma^* \rightarrow \tau\tau + \text{jets}$	763.24 ± 26.07	30.17 ± 3.24	180.95 ± 14.58	3.16 ± 0.50
$W \rightarrow \tau\nu + \text{jets}$	409.29 ± 7.11	48.29 ± 1.27	41.16 ± 2.68	4.31 ± 0.46
Top	77.17 ± 4.82	4.43 ± 0.20	1.19 ± 0.67	0.10 ± 0.03
Others	3.31 ± 0.19	0.40 ± 0.19	0.47 ± 0.19	0.02 ± 0.01
Data	8229	5634	2892	2194
signal cont. [%]	—	0.02	3.02	0.03

Table 10.4: Expected event yields together with statistical uncertainties in the signal and control regions used to estimate the multijet background exploiting an two-dimensional sideband extrapolation method. For comparison the expected signal yields for $M_A = 200$ GeV and $\tan\beta = 15$ assuming the m_h^{max} benchmark scenario are shown. The contamination in the control regions is much smaller than 1%, except in the opposite-sign low E_T^{miss} control region.

	A	B	C	D
$b\bar{b}A \rightarrow \tau_{\text{had}}\tau_{\text{had}}$	1.35 ± 0.73	0.02 ± 0.01	< 0.01	< 0.01
$gg \rightarrow A \rightarrow \tau_{\text{had}}\tau_{\text{had}}$	0.61 ± 0.26	< 0.01	0.12 ± 0.12	< 0.01
$Z/\gamma^* \rightarrow \tau\tau + \text{jets}$	11.40 ± 1.89	6.09 ± 0.62	1.03 ± 0.22	0.61 ± 0.15
$W \rightarrow \tau\nu + \text{jets}$	59.93 ± 1.58	16.95 ± 0.64	6.08 ± 0.61	1.26 ± 0.15
Top	6.78 ± 0.44	2.55 ± 0.20	0.23 ± 0.03	0.10 ± 0.02
Others	0.83 ± 0.05	0.20 ± 0.02	0.06 ± 0.01	0.02 ± 0.00
Data	7616	6559	2915	2468
signal cont. [%]	0.03	< 0.01	< 0.01	< 0.01

Table 10.5: Expected event yields together with statistical uncertainties in the fail tau identification control regions used to validate the multijet background estimation based on the two-dimensional sideband extrapolation method. For comparison the expected signal yields for $M_A = 200$ GeV and $\tan\beta = 15$ assuming the m_h^{max} benchmark scenario are shown. The signal contamination in the control regions is much smaller than 1%.

thus both tau candidates have to fail the loose threshold. This leaves a gap in the selected phase space and reduces the available statistics slightly, but provides a high purity multijet enriched control region. Table 10.5 summarises the expected and observed event yields.

Key kinematic distributions of the two selected τ_{had} candidates are presented in Figure 10.14. A good agreement between the predicted background model and the data is observed. Figure 10.15 shows the track multiplicity distributions of the two tau candidates. Event based observables are depicted in Figure 10.16. Both the E_T^{miss} and the $\sum E_T$ variables are well modelled. Finally, Figure 10.17 presents the total transverse and visible mass distributions. In particular for the m_T^{tot} distribution a proper modelling is crucial as it is used as the final discriminating variable. It can be seen that the background prediction agrees very well with the data within statistical and systematic uncertainties.

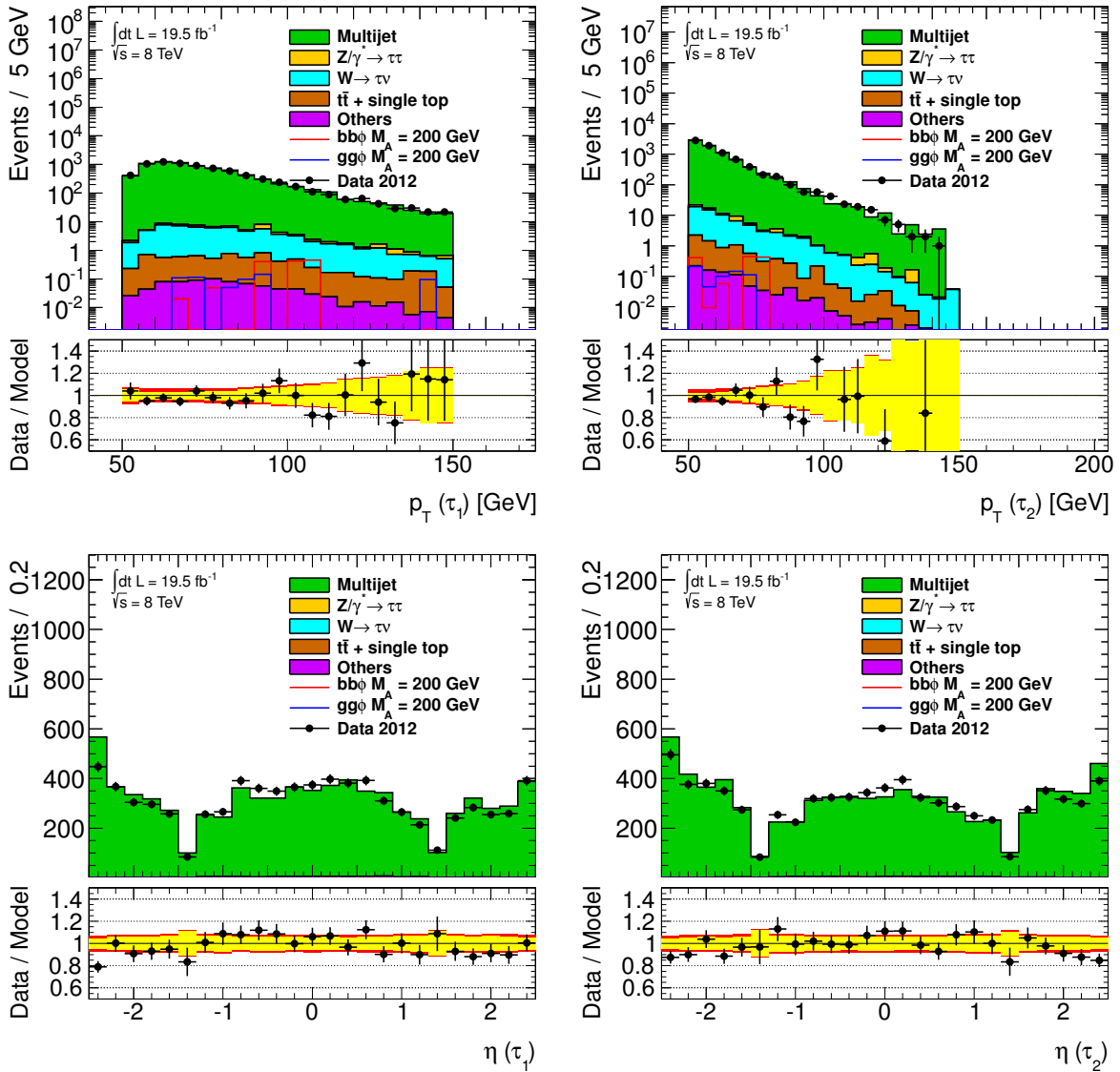


Figure 10.14: Kinematic distributions of the leading (left) and sub-leading (right) tau candidates in the fail-ID control region. The multijet contribution is estimated using a two-dimensional sideband extrapolation method. All other contributions are estimated from MC simulation. Others include di-boson production and W/Z light lepton, i.e. e, μ , decays. The signal shown for illustration corresponds to $M_A = 200$ GeV and $\tan\beta = 15$ assuming the m_h^{max} benchmark scenario. The statistical and systematic uncertainties on the model are indicated by the yellow and red bands in the ratio, respectively.

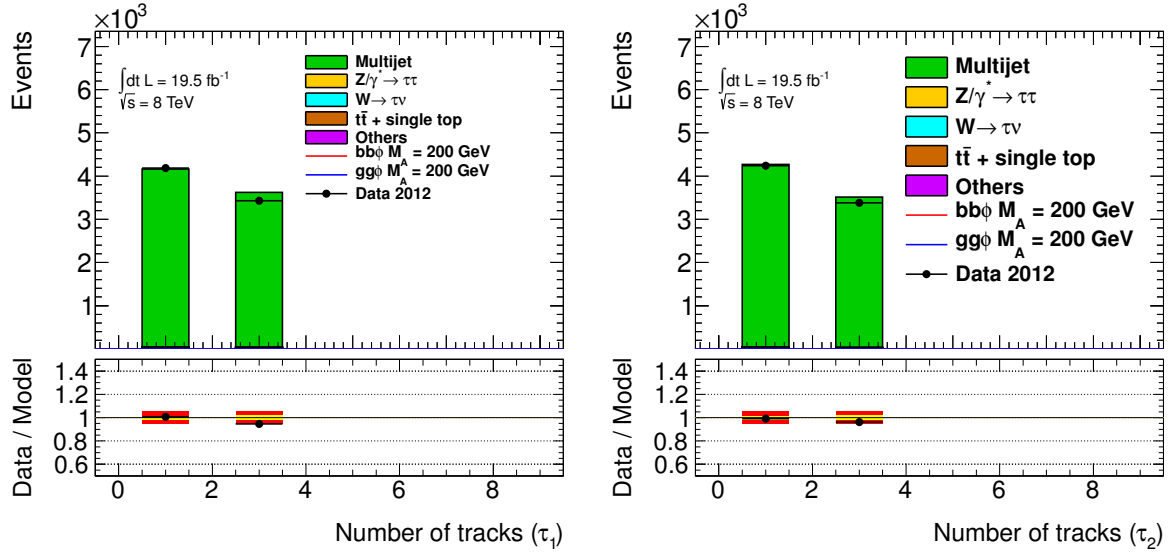


Figure 10.15: Track multiplicity distributions for the leading and sub-leading tau candidates in the fail-ID control region. The multijet contribution is estimated using a two-dimensional sideband extrapolation method. All other contributions are estimated from MC simulation. Others include di-boson production and W/Z light lepton, i.e. e, μ , decays. The signal shown for illustration corresponds to $M_A = 200$ GeV and $\tan\beta = 15$ assuming the m_h^{\max} benchmark scenario. The statistical and systematic uncertainties on the model are indicated by the yellow and red bands in the ratio, respectively.

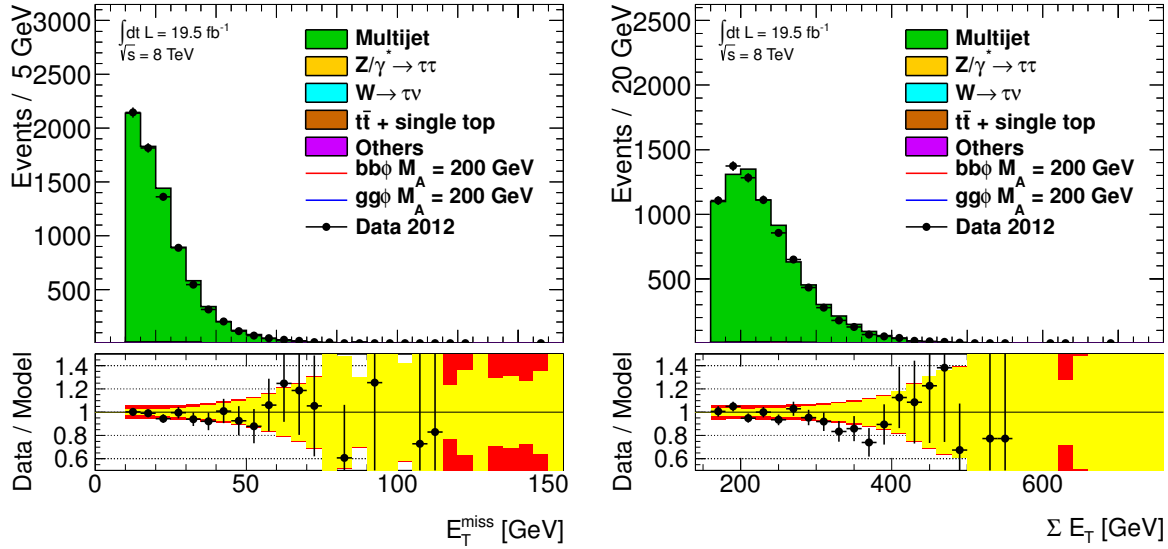


Figure 10.16: Key event distributions in the fail-ID control region. The multijet contribution is estimated using a two-dimensional sideband extrapolation method. All other contributions are estimated from MC simulation. Others include di-boson production and W/Z light lepton, i.e. e, μ , decays. The signal shown for illustration corresponds to $M_A = 200$ GeV and $\tan\beta = 15$ assuming the m_h^{\max} benchmark scenario. The statistical and systematic uncertainties on the model are indicated by the yellow and red bands in the ratio, respectively.

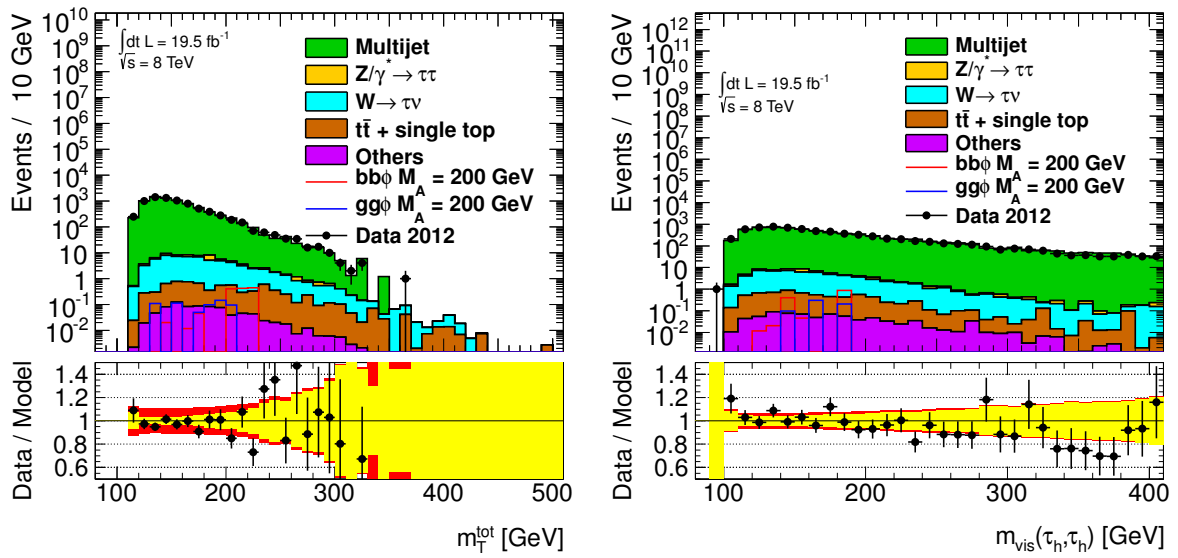


Figure 10.17: Total transverse mass and visible mass distributions in the fail-ID control region. The multijet contribution is estimated using a two-dimensional sideband extrapolation method. All other contributions are estimated from MC simulation. Others include di-boson production and W/Z light lepton, i.e. e, μ , decays. The signal shown for illustration corresponds to $M_A = 200$ GeV and $\tan\beta = 15$ assuming the m_h^{\max} benchmark scenario. The statistical and systematic uncertainties on the model are indicated by the yellow and red bands in the ratio, respectively.

10.2 Fake Tau Estimation from MC

Background contributions arising from jets which are not of QCD multijet origin are estimated from MC simulation. In particular this regards $W(\rightarrow \tau\nu)$ +jets events, in which the sub-leading tau presumably originates from the decay of the W boson and the leading tau is faked by an additional jet. It is known that the prediction of the jet-to-tau fake-rate is badly modelled by the MC simulation. Figure 10.18 shows the fake-rate obtained for one- and three-prong tau candidates in MC simulation and in data. Here the loose jBDT tau identification working point is chosen. The MC simulation overestimates the fake-rate, and thus would overestimate the total event yield of such processes, which would lead to a degradation in the sensitivity of the analysis.

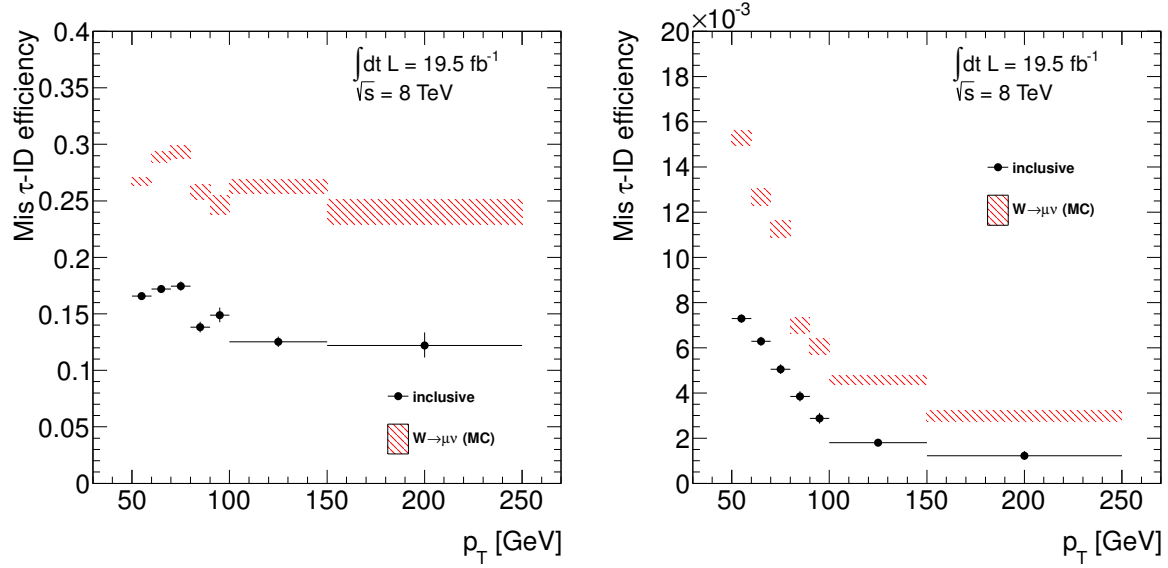


Figure 10.18: Tau identification fake-rate for the loose jBDT tau identification working point measured in $W(\rightarrow \tau\nu)$ +jets MC and data events for 1- (left) and 3-prong (right) tau decays. The fake-rate predicted by MC is depicted by the red dashed histogram, while the data measurement is represented by the black dots. Quoted uncertainties are of statistical origin.

Furthermore, backgrounds arising from jet-to-tau fakes estimated from MC simulation usually suffer from low statistics, in particular in the tails of the distribution, i.e. at high mass. Both issues can be addressed by a weighting procedure based on a data-driven estimation of the jet-to-tau fake-rate. This requires that the jet discrimination is not applied in the pre-selection, because otherwise a bias would yield an incorrect estimation of these backgrounds. The fake-rate is measured in a $W(\rightarrow \mu\nu)$ +jets control region. Rather than applying the jBDT requirement, each event with fake taus is weighted according to the fake-rate. This corrects the predicted event yield, and furthermore artificially enhances the available statistics, since no tau candidate is discarded by the jBDT requirement. As pointed out in Section 7.3 the EF applies a selection similar to the offline jBDT algorithm. Hence, the additional trigger bias has to be taken into account by measuring combined trigger+offline identification fake-rates.

Selection of Control Region

To select a clean sample of $W(\rightarrow \mu\nu)$ +jets events in data a series of cuts is applied. Good quality data is ensured by the application of a Good Runs List and event cleaning cuts as discussed in Section 9.1. Events are triggered by a combination of single-muon triggers, `EF_mu24i_tight` or `EF_mu36_tight`, which select muons on EF level with p_T thresholds of 24 GeV and 36 GeV, respectively, and apply the tight EF muon identification. Furthermore, `EF_mu24i_tight` requires isolation on EF level. The isolation criterion is defined by a threshold of 12% on the ratio of the sum of the transverse momentum of all inner detector tracks within a cone of $\Delta R < 0.2$ (excluding the muon track) and the p_T of the muon.

Further, an isolated high- p_T ($p_T > 26$ GeV) muon passing medium identification is required. Isolation of muons is ensured by requiring the energy deposits around the muon candidate within a cone of size $\Delta R < 0.2$ to be less than 6% of the muon p_T , i.e. $E_T^{\text{cone} < 0.2}/p_T < 6\%$. This reduces the amount of events where the muon is produced inside a jet, e.g. from B hadron decays. $W(\rightarrow e\nu)$ +jets and $Z(\rightarrow ee)$ +jets events are reduced by applying an electron veto, i.e. events with at least one pre-selected electron (c.f. Section 6.2) are discarded. A di-muon veto, i.e. a veto on events with an additional pre-selected muon, reduces the contamination of $Z(\rightarrow \mu\mu)$ +jets. QCD multijet events are reduced by raising the muon p_T requirement to 40 GeV. One reconstructed tau candidate is required used as probe candidate for the jet-to-tau fake-rate measurement. Since a hard neutrino is involved in the decay of the W boson, the event topology suggests that the E_T^{miss} points in the plane between the selected muon and tau candidate. A cut on $\sum_{\ell=\mu,\tau} \cos \Delta\phi(\ell, E_T^{\text{miss}}) < -0.15$ GeV is applied accordingly. This strongly reduces background contributions from the semi-leptonic decay of $Z/\gamma^*(\rightarrow \tau\tau)$ +jets. To summarise, the following selection criteria are applied to construct the $W(\rightarrow \mu\nu)$ +jets control region:

Pre-selection

- Good Runs List:
data12.8TeV.periodAllYear.DetStatus-v61-pro14-02.DQDefects-00-01-00_PHYS.StandardGRL.All.Good.xml
- Trigger: single-muon trigger with p_T thresholds on EF level of 24 GeV and 36 GeV and tight identification: EF_mu24i_tight or EF_mu36_tight
- Event cleaning: as defined in Section 9.1
- Electron veto: no pre-selected electrons (c.f. Section 6.2)
- Muon selection: at least one pre-selected muon with $p_T > 26$ GeV passing medium identification
- Di-muon veto: no further pre-selected muon
- Trigger match: the selected muon is required to have fired the trigger
- Muon isolation: the selected muon is required to be isolated ensured by $E_T^{\text{cone} < 0.2}/p_T < 6\%$

Event-selection

- Tau selection: one reconstructed tau candidate with $p_T > 50$ GeV
- Muon- p_T : increased cut on muon p_T of 40 GeV
- E_T^{miss} direction: E_T^{miss} has to point between the selected muon and the tau lepton, i.e. $\sum_{\ell=\mu,\tau} \cos \Delta\phi(\ell, E_T^{\text{miss}}) < -0.15$.

cut	$W \rightarrow \mu\nu + \text{jets}$	$Z/\gamma^* \rightarrow \mu\mu + \text{jets}$	$W \rightarrow \tau\nu + \text{jets}$	Top	Others	Data
Pre-selection	87.8×10^6	12.1×10^6	30.8×10^5	73.4×10^4	62.9×10^4	18.4×10^7
electron veto	87.7×10^6	12.0×10^6	30.7×10^5	64.3×10^4	58.2×10^4	18.3×10^7
One preselected muon with $p_T > 26$ GeV	80.2×10^6	11.4×10^6	22.5×10^5	60.8×10^4	46.4×10^4	15.3×10^7
Di-muon veto	80.1×10^6	38.9×10^5	22.4×10^5	49.3×10^4	42.1×10^4	14.2×10^7
Muon isolation	76.8×10^6	37.4×10^5	21.4×10^5	41.0×10^4	39.8×10^4	93.3×10^6
One preselected τ	18.2×10^5	63.1×10^3	98.9×10^3	21.1×10^4	33.6×10^3	27.3×10^5
Muon $p_T > 40$ GeV	13.5×10^5	49.3×10^3	48.4×10^3	15.2×10^4	19.4×10^3	16.8×10^5
$\Sigma \cos \Delta\phi < 0.15$	78.5×10^4	21.5×10^3	19.0×10^3	74.6×10^3	76.7×10^2	89.9×10^4

Table 10.6: Number of events passing the $W(\rightarrow \mu\nu)$ +jets selection criteria. Background contributions from $Z/\gamma^*(\rightarrow \tau\tau)$ +jets, $Z/\gamma^*(\rightarrow ee)$ +jets, $W(\rightarrow e\nu)$ +jets and di-boson production are summarised as *Others*.

The obtained event yields are summarised in Table 10.6. The purity is about 87%. The dominant background contribution originates from $t\bar{t}$ and single top-quark events, which is in the order of 8.2%. Furthermore, $Z/\gamma^*(\rightarrow \mu\mu)+\text{jets}$ contributions amount to 2.4%. The impact of these backgrounds on the measured fake-rate is found to be small and expected to be covered by the systematic uncertainties.

Figure 10.19 shows the $\sum_{\ell=\mu,\tau} \cos \Delta\phi(\ell, E_T^{\text{miss}})$ distribution after the pre- and full event-selection. It can be seen that the background arising from QCD multijet events (assumed as the difference between data and MC) tend to be centred around zero and can be significantly reduced by the cut on $\sum_{\ell=\mu,\tau} \cos \Delta\phi(\ell, E_T^{\text{miss}}) < -0.15$.

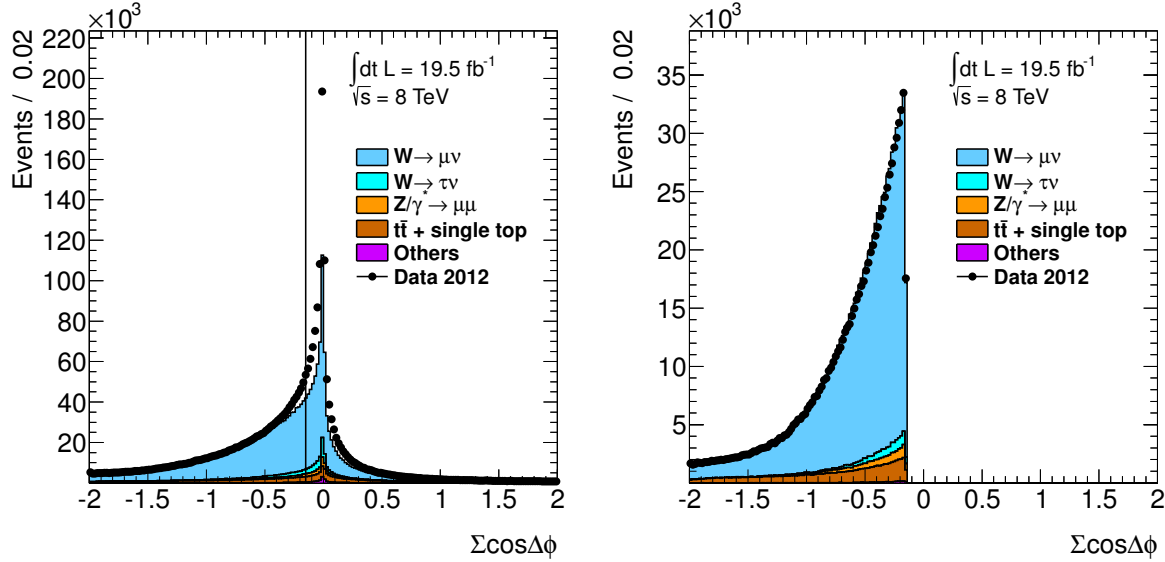


Figure 10.19: $\sum_{\ell=\mu,\tau} \cos \Delta\phi(\ell, E_T^{\text{miss}})$ distribution after the pre-selection (left) and after the full event selection (right). The excess in data around $\sum_{\ell=\mu,\tau} \cos \Delta\phi(\ell, E_T^{\text{miss}}) \simeq 0$ is due to QCD multijet events not modelled in this control region.

Measurement of the Jet-to-Tau Fake-Rate

The jet-to-tau fake-rate is measured from events selected by the aforementioned criteria applying a tag-and-probe style analysis. Only the highest- p_T tau candidate is considered as probe object. The mis-identification efficiency is then defined as the ratio of probe candidates passing a certain level of identification w.r.t. to the entire set of probe candidates, i.e. it has the same definition as the tau identification efficiency defined in Eq. 7.16, but only considers tau fakes originating from jets. Further, the fake-rate is parametrised by the charge product of the selected tag muon and the probe tau candidate. The obtained tau mis-identification efficiency for the loose and medium jBDT working points are shown in Figure 10.20 for one- and three-prong fake candidates, separately. A clear difference between same and opposite charge of the tag-and-probe object is observed and has to be taken into account accordingly in the final application of the fake-rate as event weight. Part of the discrepancy arise from different quark-gluon ratios in the two phase space regions (c.f. Section 8.2.2). However, this does not cover the full range observed in the measurement. There is some missing component, which can not be addressed at the moment, but advanced techniques have to be developed in the future, which might be able to get a deeper understanding of this issue. One idea would be a tagging algorithm, which precisely tags a jet as being of quark or gluon origin. This would then allow for a fake-rate measurement parametrised by the quark-gluon fraction, providing a more precise model of the jet-to-tau fake-rates. However, this is still under development and will not be available before run-II data-taking will start.

As pointed out above a combined tau trigger and identification fake-rate has to be measured in addition, in order to provide proper weights for events where the fake tau candidate has fired the corresponding trigger. Since the identification configuration applied at the trigger level is common for all

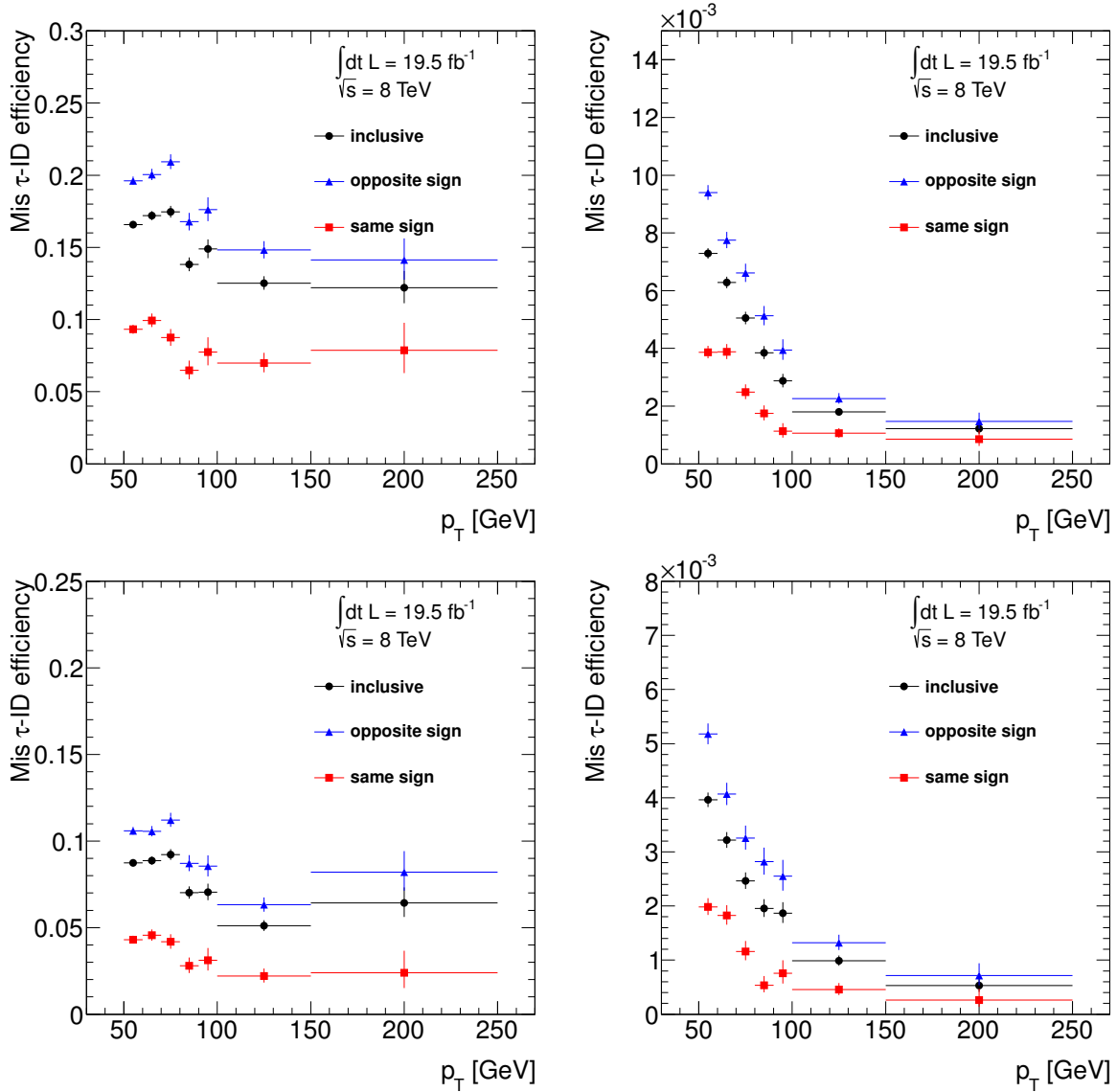


Figure 10.20: Tau mis-identification efficiency measured in $W(\rightarrow \mu\nu)+\text{jets}$ data events for the jBDT loose (top) and medium (bottom) identification working point for 1-prong (left) and 3-prong (right) tau candidates. The mis-identification efficiency is parametrised by the charge product of the selected muon and the probe fake tau candidate. The blue triangles mark opposite-sign events, while the red squares show the fake efficiency for same-sign events. For illustration the mis-identification efficiency for the inclusive selection is represented by the black circles. The fake-rate in opposite-sign events is about a factor of two larger than measured in same-sign events, which is treated in the analysis accordingly.

items (c.f. Section 7.3) any trigger item applying the medium identification criterion is suitable for this measurement. Hence, the `EF_tau38T_medium1` is chosen. Since the single-tau trigger is not running in the main menu, due to too high rates, the *resurrected* decision is taken in data. This re-runs the trigger decision for each RoI if the event is selected by one of the main triggers. The derived jet-to-tau fake-rates are depicted in Figure 10.21 for 1- and 3-prong tau candidates for the loose and medium offline tau identification working points.

The measured jet-to-tau fake-rates are applicable for one of the dominant backgrounds arising from $W(\rightarrow \tau\nu)+\text{jets}$ events. To apply them to other background components, like $t\bar{t}$ events, it has to be validated, that they have a similar quark-gluon fraction, as the fake-rate will depend strongly on the jet

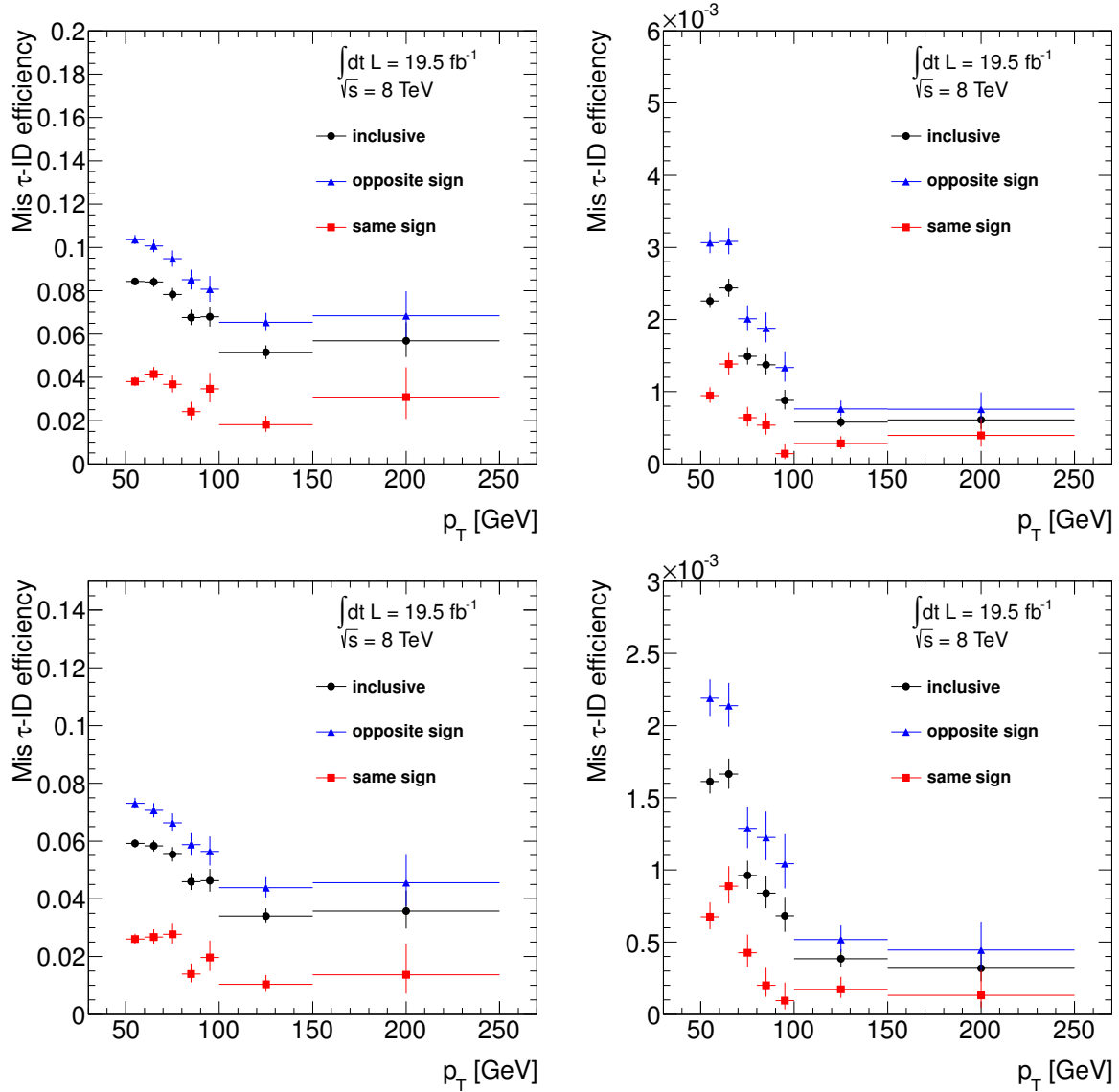


Figure 10.21: Combined tau trigger and identification fake-rate measured in $W(\rightarrow \mu\nu)$ +jets data events for the jBDT loose (top) and medium (bottom) identification working point for 1-prong (left) and 3-prong (right) tau candidates. The trigger identification is obtained from the EF_tau38T_medium1 tau trigger. The mis-identification efficiency is parametrised by the charge product of the selected muon and the probe fake tau candidate. The blue triangles mark opposite-sign events, while the red squares show the fake efficiency for same-sign events. For illustration the mis-identification efficiency for the inclusive selection is represented by the black circles. The fake-rate in opposite-sign events is about a factor of two larger than measured in same-sign events, which is treated in the analysis accordingly.

composition. Figure 10.22 shows the quark fraction of the fake tau candidates as a function of their p_T for various background components involving fake taus. As expected the quark fraction in $t\bar{t}$ events is larger than in the $W(\rightarrow \mu\nu)$ +jets control region. However, given that the fake tau candidates arise dominantly from quark initiated jets in all backgrounds, the application of the fake-weights seems reasonable. A potential bias arising from the different fake composition will be addressed by the assigned systematic uncertainty discussed in Section 11.1.6.

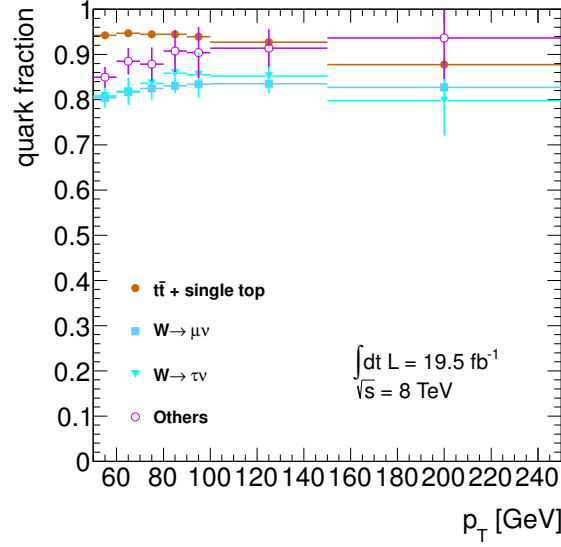


Figure 10.22: Quark fraction of fake tau candidates obtained from MC simulation for various background processes versus the transverse momentum.

10.3 $Z/\gamma^* \rightarrow \tau\tau$ Control Region

The remaining dominant background not addressed so far, is $Z/\gamma^* \rightarrow \tau\tau$. As pointed out in Section 8.1, both the shape and the normalisation are estimated from MC simulation. Hence, a $Z/\gamma^* \rightarrow \tau\tau$ enriched data sample would be desirable to gain confidence in the model. However, as also discussed in Section 8.1 it is an irreducible background, which shares the same final state as the signal. Furthermore, only the di-tau triggered category provides sufficient statistics for this purpose, which on the other hand is dominated by QCD multijet events. Thus, the only possible data sample enriched in $Z/\gamma^* \rightarrow \tau\tau$, which does not suffer from large signal or multijet contamination, consists of boosted Z/γ^* events. This control region can be constructed by applying the di-tau triggered selection except the back-to-back requirement. To ensure a large boost of the intermediate resonance, the back-to-back requirement is replaced by requiring the two taus propagating in the same direction, i.e. $\cos \Delta\phi(\tau_1, \tau_2) > 0.2$. Furthermore, the E_T^{miss} should point in the same direction due to the neutrinos moving in the same direction. This is guaranteed by cutting on $\cos \Delta\phi(\tau_2, E_T^{\text{miss}}) > 0$. Another cut of $\Delta R(\tau_1, \tau_2) < 1.5$ is applied to select the boosted event topology. Finally, to reduce the contamination by QCD multijet events, a lower cut on the magnitude of the missing transverse energy of 10 GeV is applied. To preserve statistics, the $\sum E_T$ cut applied in the DTT selection is dropped. The selection of the $Z/\gamma^* \rightarrow \tau\tau$ control data sample can be summarised as:

- baseline di-tau triggered selection without the back-to-back requirement,
- inverted back-to-back requirement: $\cos \Delta\phi(\tau_1, \tau_2) > 0.2$,
- neutrino propagation in direction of the boosted Z boson: $\cos \Delta\phi(\tau_2, E_T^{\text{miss}}) > 0$,
- two preselected taus propagating in same direction: $\Delta R(\tau_1, \tau_2) < 1.5$,
- large missing transverse energy: $E_T^{\text{miss}} > 10 \text{ GeV}$.

The QCD multijet contamination is estimated exploiting the ABCD method as used in the nominal di-tau triggered selection, but adapting the control samples. Table 10.7 summarises the expected and observed event yields in the $Z/\gamma^* \rightarrow \tau\tau$ control region. Contributions from SM Higgs decays can be neglected. The total SM prediction agrees with the observed number of data events within statistical uncertainties. The purity is 95%, while the signal contamination is less than 1%, and thus can be considered as signal

free. Kinematic distributions of the leading and sub-leading tau candidates are presented in Figure 10.23. The track multiplicity distributions of the two tau candidates are shown in Figure 10.24. Figure 10.25 and 10.26 summarise the modelling of the E_T^{miss} and $\sum E_T$ distributions as well as the mass distributions. An adequate agreement within statistical and systematic uncertainties is observed for all distributions.

cut	$gg \rightarrow A \rightarrow \tau_{\text{had}}\tau_{\text{had}}$	$b\bar{b}A \rightarrow \tau_{\text{had}}\tau_{\text{had}}$	multijet	$Z/\gamma^* \rightarrow \tau\tau + \text{jets}$	$W \rightarrow \tau\nu + \text{jets}$	Top	Others	SM Total	Data
$\cos\Delta\phi(\tau_1, \tau_2) > 0.2$	7.2 ± 1.0	5.2 ± 1.6	117.4 ± 7.3	901.6 ± 44.3	41.5 ± 1.7	26.9 ± 2.2	1.3 ± 0.4	$(10.9 \pm 0.4) \times 10^2$	1427
$\cos\Delta\phi(\tau_2, E_{\text{T}}^{\text{miss}}) > 0$	6.8 ± 1.0	3.7 ± 1.3	50.5 ± 4.9	746.1 ± 40.4	22.0 ± 1.0	14.5 ± 1.9	0.5 ± 0.3	833.7 ± 40.8	920
$\Delta R(\tau_1, \tau_2) < 1.5$	4.8 ± 0.8	2.3 ± 1.1	23.9 ± 3.7	732.3 ± 40.1	13.7 ± 0.8	9.7 ± 1.4	0.5 ± 0.3	780.1 ± 40.3	802
$E_{\text{T}}^{\text{miss}} > 10 \text{ GeV}$	4.8 ± 0.8	2.3 ± 1.1	20.4 ± 3.5	708.6 ± 39.4	13.5 ± 0.8	9.3 ± 1.4	0.5 ± 0.3	752.2 ± 39.6	760

Table 10.7: Expected and observed event yields in the $Z/\gamma^* \rightarrow \tau\tau$ control sample. Others include di-boson production and W/Z light lepton, i.e. e, μ , decays. The total SM prediction is the sum of all non signal contributions. For illustration the expected signal event yields for $M_A = 200 \text{ GeV}$ and $\tan\beta = 15$ are shown assuming the $m_{\text{h}}^{\text{max}}$ benchmark scenario. The QCD multijet background is estimated from data control regions exploiting the ABCD method.

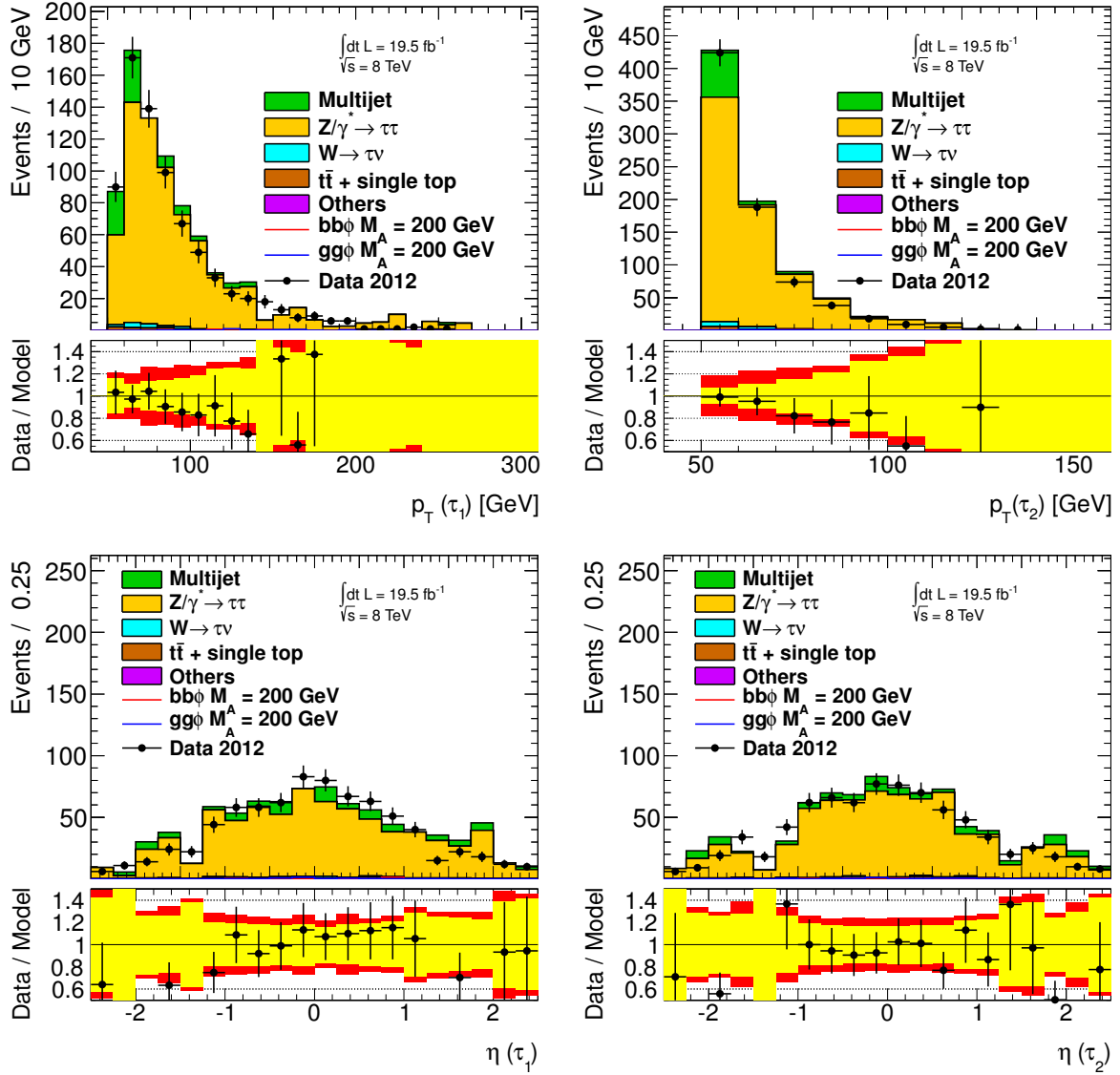


Figure 10.23: Kinematic distributions of the leading (left) and sub-leading (right) tau candidates in the $Z/\gamma^* \rightarrow \tau\tau$ control region. The multijet contribution is estimated using the ABCD method. All other contributions are estimated from MC simulation. Others include di-boson production and W/Z light lepton, i.e. e, μ , decays. The statistical and systematic uncertainties on the model are indicated by the yellow and red bands in the ratio, respectively. For illustration the MSSM Higgs signal expectation for $M_A = 200$ GeV and $\tan\beta = 15$ assuming the m_h^{\max} benchmark scenario is shown in red for b-associated production and in blue for gluon fusion.

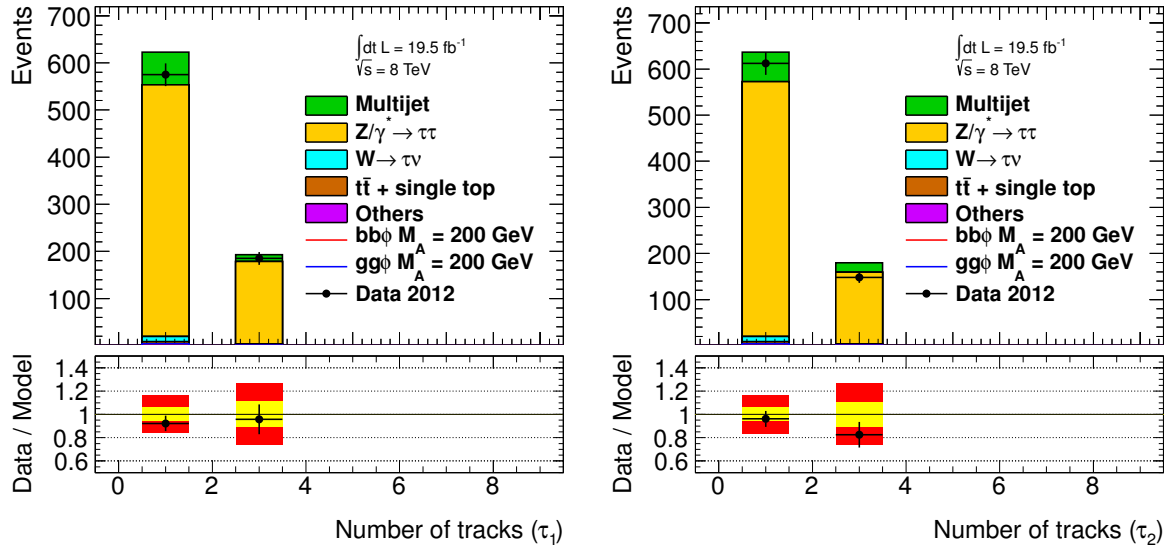


Figure 10.24: Track multiplicity distributions for the leading and sub-leading tau candidates in the $Z/\gamma^* \rightarrow \tau\tau$ control region. The multijet contribution is estimated using the ABCD method. All other contributions are estimated from MC simulation. Others include di-boson production and W/Z light lepton, i.e. e, μ , decays. The statistical and systematic uncertainties on the model are indicated by the yellow and red bands in the ratio, respectively. For illustration the MSSM Higgs signal expectation for $M_A = 200$ GeV and $\tan\beta = 15$ assuming the m_h^{\max} benchmark scenario is shown in red for b-associated production and in blue for gluon fusion.

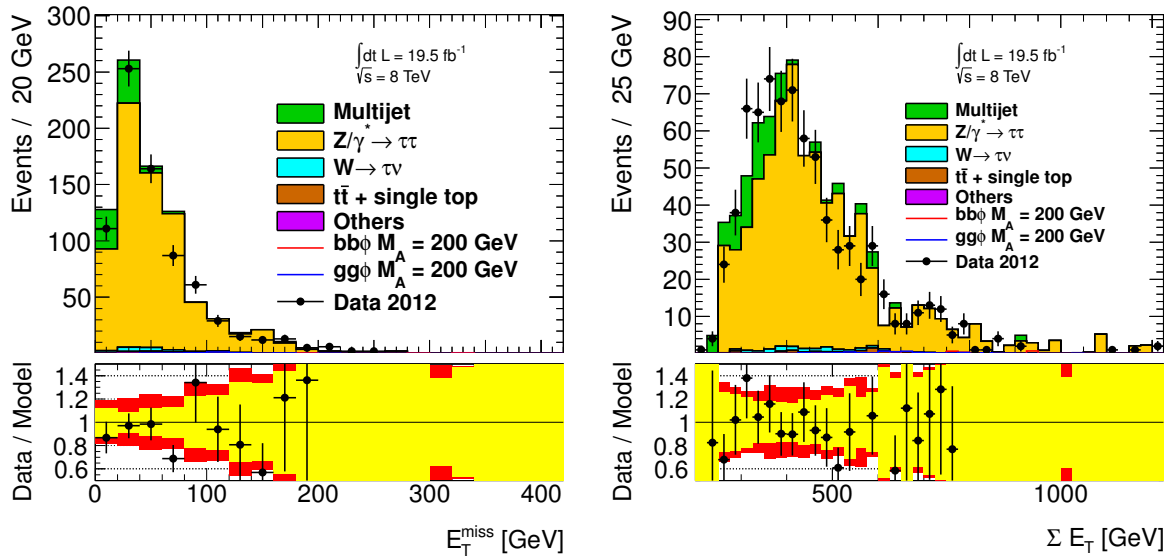


Figure 10.25: Key event distributions in the $Z/\gamma^* \rightarrow \tau\tau$ control region. The multijet contribution is estimated using the ABCD method. All other contributions are estimated from MC simulation. Others include di-boson production and W/Z light lepton, i.e. e, μ , decays. The statistical and systematic uncertainties on the model are indicated by the yellow and red bands in the ratio, respectively. For illustration the MSSM Higgs signal expectation for $M_A = 200$ GeV and $\tan\beta = 15$ assuming the m_h^{\max} benchmark scenario is shown in red for b-associated production and in blue for gluon fusion.

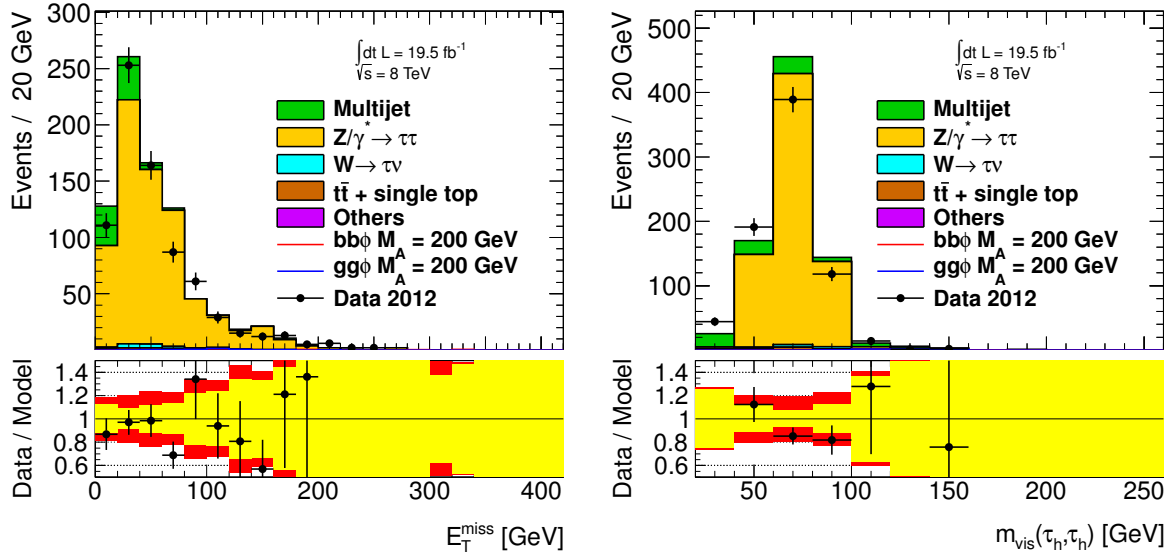


Figure 10.26: Total transverse mass and visible mass distributions in the $Z/\gamma^* \rightarrow \tau\tau$ control region. The multijet contribution is estimated using the ABCD method. All other contributions are estimated from MC simulation. Others include di-boson production and W/Z light lepton, i.e. e, μ , decays. The statistical and systematic uncertainties on the model are indicated by the yellow and red bands in the ratio, respectively. For illustration the MSSM Higgs signal expectation for $M_A = 200$ GeV and $\tan\beta = 15$ assuming the m_h^{\max} benchmark scenario is shown in red for b-associated production and in blue for gluon fusion.

In this chapter several background estimation techniques for the dominant background components in searches for heavy neutral resonances decaying into two hadronically decaying tau leptons have been introduced and validated in various control regions. The validation shows that they provide a proper model of these background components, and hence they are applied in both the MSSM Higgs and the Z' analysis discussed later.

11 Systematic Uncertainties

The normalisation and shapes of the signal and background distributions are subject to statistical and systematic uncertainties. The latter will be elaborated on in the following sections. They arise from experimental and theoretical sources. Experimental systematics originate either from imprecise simulation or from the method used to obtain the background model. Simulation of pile-up conditions and object reconstruction are the main sources. They are evaluated by variation of the median value by its uncertainty, taking the difference in the expected event yield as final uncertainty. These uncertainties can affect both the shape of a distribution, like TES, and/or the normalisation of the background prediction, e.g. the $\text{jet} \rightarrow \tau$ fake-rate. Uncertainties on the modelling of the detector response from electrons and muons are not considered as they are found to be negligible, c.f. [231]. Systematic uncertainties on the signal and background cross sections arise from the use of fixed order loop calculations.

11.1 Experimental Systematic Uncertainties

11.1.1 Hadronic Tau Identification Efficiency

The uncertainty on the tau identification efficiency is one of the dominant uncertainties on real tau decays, and thus has a large impact on both the signal as well as on dominant backgrounds like $Z/\gamma^* \rightarrow \tau\tau$. As pointed out in Section 7.2.5 the tau identification efficiency is measured in a $Z/\gamma^* \rightarrow \tau\tau$ tag-and-probe analysis. From this measurement an uncertainty of 2–7 % is assigned depending on the track multiplicity and η of the tau candidate. Obviously, also the choice of the working point has an impact on the concrete uncertainty. However, this measurement is restricted to low- p_T taus of $p_T \lesssim 100 \text{ GeV}$. This raises the question whether this is applicable for high- p_T taus as well. Hence, the fidelity of the simulation of hadronic tau decays has to be quantified which brings up the problem that there is no abundant source of real tau leptons up to $p_T \sim 800 \text{ GeV}$. The question can however be rephrased, as the actual matter to address is if the modelling of tau decays is any worse at high- p_T or not. Any degradation has to be addressed by inflating the uncertainty measured by the tag-and-probe analysis. A potential mis-modelling can arise either from issues in the modelling of

1. the τ decay, or
2. the detector response.

Since at low- p_T the simulation of tau decays works very well it is unlikely that this will get worse at high- p_T . To get a handle on this the tau identification efficiency has been determined at high- p_T using different setups of the MC simulations. For this purpose a variety of $Z' \rightarrow \tau\tau$ MC samples for $M_{Z'} = 1000 \text{ GeV}$ have been produced with:

1. the nominal configuration of PYTHIA using the *QGSP_BERT* [180, 182, 181] shower model
2. an altered shower model - *QGSP* [180] and *FTFP_BERT* [183, 181]
3. a varied detector model including extra material
4. a different ATLAS underlying event tune - *A2* [221].

Figure 11.1 shows the tau identification efficiency for the loose jBDT working point as a function of the reconstructed tau- p_T obtained in various MC simulation samples for 1- and 3-prong tau candidates matched to a generated hadronic tau decay within a spatial distance of $\Delta R < 0.2$. A good agreement is observed up to $p_T \sim 400 \text{ GeV}$, while for higher transverse momenta the statistical uncertainty is rather large, but the ratio of the various simulation configurations compared to the nominal setup is still in agreement with being one. This supports the assumption that tau decays are well modelled at high- p_T and no degradation has to be considered.

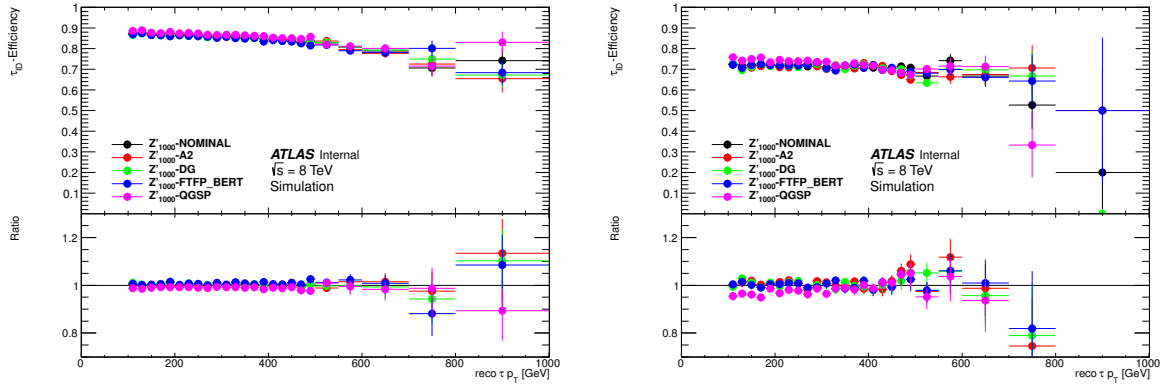


Figure 11.1: Tau identification efficiency for the loose jBDT working point for 1- (left) and 3-prong (right) tau candidates as a function of the reconstructed tau transverse momentum [232]. The efficiency has been measured in various MC samples of $Z' \rightarrow \tau\tau$ ($M_{Z'} = 1000$ GeV) produced using different configurations (see text for details). Considered tau candidates have to match to a generated hadronic tau decay within $\Delta R < 0.2$. In the ratio the relative difference w.r.t. the nominal MC setup is shown. The colour code corresponds to the legend shown in the upper plot.

Since the modelling of hadronic tau decays is described well by simulation the remaining issue to address is the detector response at high- p_T . This is investigated measuring the mis-identification probability in di-jet events comparing predictions by MC simulation to data. For this purpose, a di-jet sample has been selected in data. The selection cuts are similar to the di-jet tag-and-probe analysis utilised in the fake-factor measurement, c.f. Section 10.1.1. Events are accepted if they are triggered by a single-jet trigger (see Table 10.2). Since no tau triggers enter this selection the full 2012 dataset corresponding to 20.3 fb^{-1} can be analysed. The selection follows the tag-and-probe style approach requiring the two jets to be back-to-back which is guaranteed by cutting on $\cos \Delta\phi(\text{jet}_{\text{tag}}, \text{jet}_{\text{probe}}) < -0.95$. Furthermore, the two jets have to be well balanced in p_T , $\left| \frac{p_{T,\text{tag}} - p_{T,\text{probe}}}{p_{T,\text{tag}}} \right| < 0.05$. This selection ensures a high purity di-jet sample with both jets originating from the hard scattering, and thus avoiding selection of jets originating from gluon emission which might be poorly modelled. To further reduce contamination by photons and electrons the probe candidate is required to pass the loose eBDT veto. Furthermore, both jets are required not to be in the crack region ($1.37 < |\eta| < 1.52$). The effect on the hadronisation model is further minimised by considering only probe jets with one or three assigned tracks. The same selection is applied in MC. For this purpose, samples generated utilising PYTHIA are used. Table 11.1 summarises the set of samples. Events are generated in several bins of the jet- p_T with a flat distribution in p_T . To get a smooth p_T spectrum of the jets, event weights are applied accordingly.

Sample	generator	p_T range [GeV]	cross section [pb]	filter efficiency	Exp. Events (20.3 fb^{-1})	Simulated Events
J2W		80–200	2.6×10^7	4.0×10^{-3}	2.1×10^9	6.0×10^6
J3W		200–500	5.4×10^5	1.2×10^{-3}	1.3×10^7	6.0×10^6
J4W		500–1000	6.4×10^3	7.1×10^{-4}	9.3×10^4	6.0×10^6
J5W		1000–1500	4.0×10^1	2.2×10^{-3}	1.7×10^3	3.0×10^6
J6W		1500–2000	4.2×10^{-1}	4.7×10^{-3}	4.0×10^1	2.5×10^6
J7W		2000– ∞	4.1×10^{-2}	1.5×10^{-2}	1.2×10^1	3.0×10^6

Table 11.1: Summary of simulated MC di-jet events used to estimate the tau mis-identification probability.

A comparison of the prediction by MC simulation to data shows an overall adequate agreement (see [232, 233]), except the ϕ distribution. The latter is shown in Figure 11.2 for one and three track

jets. A clear excess in data around $\phi \simeq -2$ is visible. This has already been observed in 2011 data (c.f. [234, 112]). The reason could be tracked down to be dead pixel sensors in the inner detector which lead to track loss, and thus migration effects of high track multiplicity jets towards 1- or 3-track jets [233]. These dead modules are not simulated in the detector simulation, and therefore are not predicted by MC. However, since the tau identification is expected to be symmetric in ϕ this will not lead to a bias in the mis-identification efficiency. Therefore, the ϕ region in question is cut out by requiring the probe jet not to be within $\phi \in [-2.5, -2.0]$.

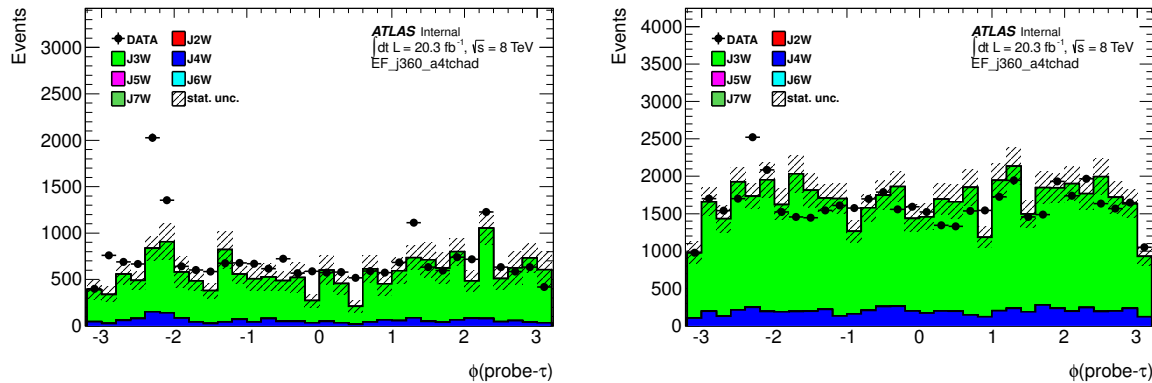


Figure 11.2: Distribution of the polar angle of the probe jet for 1- (left) and 3-prong (right) jets in the di-jet sample [232]. Estimates from MC simulation are stacked, while data is represented by the black points. A clear excess in data around $\phi \simeq -2$ is visible.

Figure 11.3 shows the mis-identification probability for 1- and 3-prong probe jets as a function of the jet- p_T . Cuts on the jBDT score are placed such that the mis-identification probability corresponds roughly to the efficiency of the loose jBDT working point. An overall mis-modelling is observed, but expected (c.f. Section 10.2). However, no significant p_T dependence is measured, so it can be assumed that there is no deterioration of the modelling of the detector response at high- p_T . To quantify any possible dependence a first order polynomial fit on the data over MC ratio is performed. The uncertainty on the slope of the fit is taken to inflate the tau identification efficiency from the $Z/\gamma^* \rightarrow \tau\tau$ tag-and-probe measurement at high- p_T . To avoid an extreme inflation at very high- p_T a cut-off is defined which is taken from the uncertainty of a constant fit assuming that there is no p_T dependence. Taken the results from both fits the following prescription for the systematic uncertainty of the tau identification is derived for 1- and 3-prong tau candidates:

$$\begin{aligned}\Delta\epsilon^{1\text{-prong}} &= \Delta\epsilon_{\text{low-}p_T}^{1\text{-prong}} + 0.011\% / \text{GeV} \cdot (p_T - 100 \text{ GeV}) \\ \Delta\epsilon^{3\text{-prong}} &= \Delta\epsilon_{\text{low-}p_T}^{3\text{-prong}} + 0.0076\% / \text{GeV} \cdot (p_T - 100 \text{ GeV})\end{aligned}\quad (11.1)$$

11.1.2 High- p_T Track Reconstruction Efficiency

For high- p_T tau candidates the track reconstruction efficiency decreases due to track merging effects. The probability of overlapping tracks which cannot be distinguished as single tracks by the track reconstruction algorithms increases with increasing p_T due to higher collimation of the tau decay products. Thus, high- p_T 3-prong tau candidates are likely to be reconstructed as 2-prong candidates. This is illustrated in Figure 11.4, which shows the fraction of generated three-prong tau decays reconstructed as 2-, 3- or 4-prong tau candidate. It shows that for taus with $p_T > 150 \text{ GeV}$ the fraction of correctly reconstructed taus decreases, while the fraction of 2-prong reconstructed tau candidates increases due to merging of tracks. Track reconstruction has been studied in detail in [235, 236] which showed that the modelling of merged and shared hits in the inner detector by MC simulation is in good agreement with data. However, it is not possible to directly measure the track efficiency loss in data and MC and in doing so provide

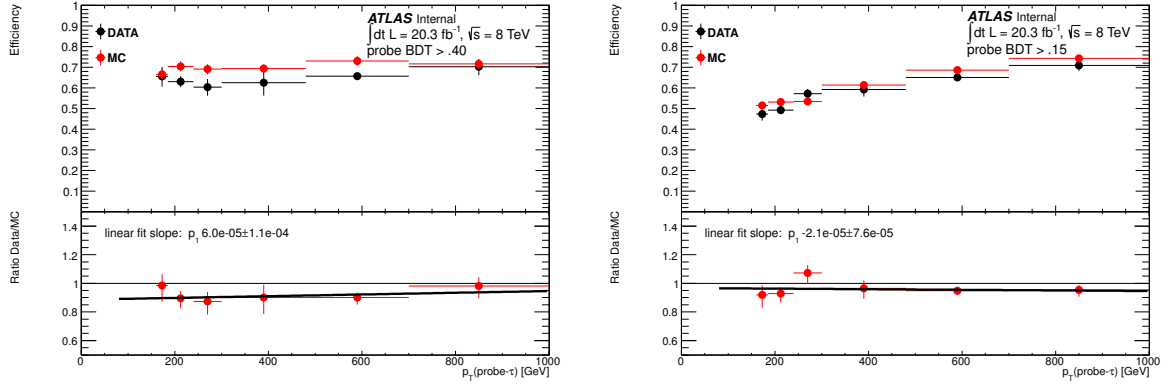


Figure 11.3: Tau mis-identification efficiency for 1- (left) and 3-prong (right) tau candidates as a function of the probe jet- p_T in data (black) and simulation (red) [232]. The cuts on the jBDT score are chosen such that the mis-identification efficiency corresponds to roughly the same efficiency as for the loose jBDT working point.

a systematic uncertainty. Thus, a conservative estimate of the track efficiency loss of 50% is assumed. As shown in Figure 11.4 the degradation becomes significant for tau candidates with $p_T > 150$ GeV and increases by roughly 10% per 100 GeV. From this the following prescription is derived:

$$\begin{aligned}
 p_T \leq 150 \text{ GeV} &: \text{no additional uncertainty} \\
 p_T > 150 \text{ GeV} &: \Delta\epsilon_{3\text{-prong}} = 0.05 \cdot (p_T / \text{GeV} - 150)\%
 \end{aligned}
 \tag{11.2}$$

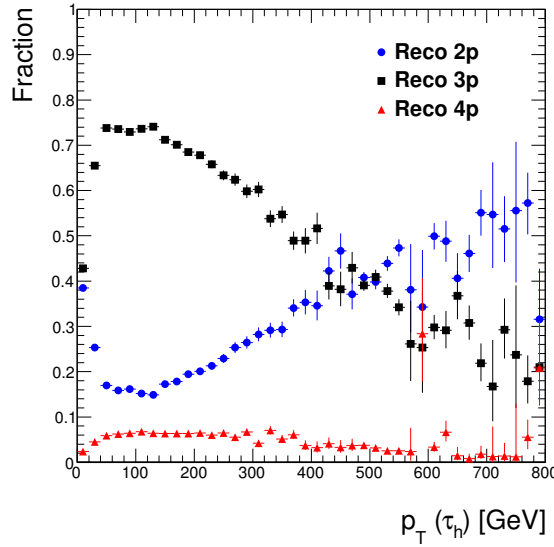


Figure 11.4: Fraction of generated 3-prong tau decays reconstructed as 2- (blue), 3- (black) or 4- (red) prong tau candidate as a function of the reconstructed transverse momentum of the tau. A strong degradation of correctly reconstructed tau candidates is observed for taus with $p_T > 150$ GeV, while the fraction of tau candidates with two assigned tracks increases due to track merging [232].

11.1.3 Hadronic Tau Trigger Efficiency

The uncertainty on the hadronic tau trigger efficiency is evaluated by a tag-and-probe measurement using $Z \rightarrow \tau_l \tau_h$ events. Details are outlined in Section 7.3.4. However, like the evaluation of the hadronic

tau identification efficiency this measurement is limited to low- p_T tau decays. Scale factors obtained by the tag-and-probe measurement are applicable in the di-tau triggered category for reconstructed tau candidates with $p_T < 100$ GeV. Above this threshold they are no longer applicable, but rather an envelope around the discrepancies of the low- p_T uncertainties (c.f. Figure 7.34) is constructed. This accounts for mis-modelling effects in the simulation. An uncertainty of 10% covers the spread and is assigned for all taus with $p_T > 100$ GeV. Additional high- p_T effects from the detector response are covered by the inflation of the hadronic tau identification efficiency uncertainty.

11.1.4 Hadronic Tau Energy Scale

The calibration of the tau energy scale and the determination of its uncertainty has been discussed in detail in Section 7.1.5. It is a major uncertainty in the presented analyses, since shifting the tau energy up or down influences the event yields as taus after applying the corrections might pass or fail the p_T cuts. Furthermore, it effects the shape of the mass distribution which has to be taken into account during the statistical analysis of the data. The concrete method will be addressed in Section 12.6.4. The uncertainty on the TES is binned in p_T and η and separately derived for one- and three-prong decays. It amounts to approximately 2 – 3 % and is applied as a shift of the transverse momentum for each tau.

11.1.5 Charge Mis-Identification

The two selected tau candidates entering the final statistical analysis are required to have opposite electric charge. Thus, a mis-identification of the charge can effect the analysis and has to be taken into account as a potential source of systematic uncertainty. The charge flip probability has been determined for electrons, muons and taus in the $Z' \rightarrow \tau\tau$ search using 2011 data [234] (Appendix E). While for high- p_T electrons there is a non negligible probability of charge mis-identification due to bremsstrahlung, and thus wrong track assignment, this is found to be negligible for hadronic tau decays, i.e. for charged pions. This has been re-evaluated in the 2012 analysis. Since muons and charged pions have comparable mass, the charge flip probability can be estimated from the p_T resolution of muons in the inner detector. The resolution of the muon p_T , σ_μ , has been evaluated to be 0.36 TeV^{-1} in the central region of the detector ($|\eta| < 1.05$) and 0.66 TeV^{-1} in the forward region ($1.7 < |\eta| < 2.0$) [237]. Even though the majority of tau candidates in the presented analyses are found to be in the central region (see e.g. Figure 12.10) the systematic uncertainty is estimated in a conservative manner assuming $\sigma_\mu = 0.66 \text{ TeV}^{-1}$. From the p_T resolution the charge flip probability can be calculated by the negative-momentum probability which has been measured in $Z/\gamma^*(\rightarrow \tau\tau)$ +jets MC, taking the sample corresponding to an invariant di-tau mass of $2250 \text{ GeV} < M_{\tau\tau} < 2500 \text{ GeV}$. Figure 11.5 shows the estimated fraction of charge flipped tau candidates versus the p_T of the leading track as obtained in MC requiring $m_T^{\text{tot}} > 850 \text{ GeV}$ to match the expected tau spectrum for very heavy resonances. Indeed, the charge flip probability increases at high- p_T , but since several decay products occur in the hadronic decay of a tau lepton the mean leading track- p_T for a decay of a 2 TeV resonance is about 400 GeV. This results in a charge mis-identification probability of much less than 1%, and thus can be neglected here.

11.1.6 Jet-to-Tau Fake-Rate

The uncertainty on the jet-to-tau fake-rate arises from the statistical precision of the fake-rate measurement. Hence, the statistical uncertainty of the measured fake-rate is taken as systematic uncertainty. However, it can only be guaranteed that the measured fake-rate can be applied to W +jets events, as the quark-gluon fraction is expected to be the same in the $W(\rightarrow \mu\nu)$ +jets control region utilised to measure the fake-rate and the dominating $W(\rightarrow \tau\nu)$ +jets background. For other background components the quark-gluon ratio might be different, in particular for components involving top-quarks, which tend to have a larger quark fraction (c.f. Figure 10.22). Since these background components are small compared to the dominating $Z/\gamma^*(\rightarrow \tau\tau)$ +jets, QCD multijet and $W(\rightarrow \tau\nu)$ +jets backgrounds, a conservative 60%

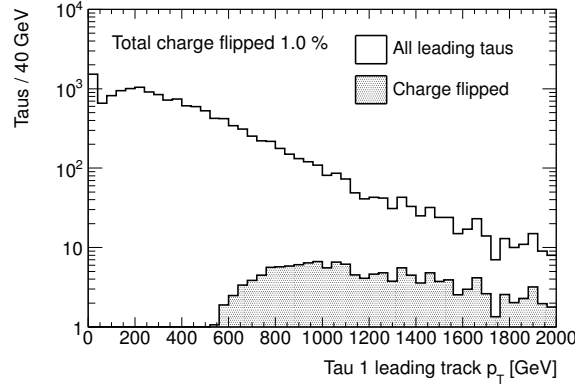


Figure 11.5: Fraction of charge flipped tau candidates as a function of the leading track transverse momentum estimated in $Z/\gamma^*(\rightarrow \tau\tau)$ +jets MC simulation with $2250 \text{ GeV} < M_{\tau\tau} < 2500 \text{ GeV}$. To match the spectrum of tau candidates entering the analysis a cut of $m_T^{\text{tot}} > 850 \text{ GeV}$ is applied [232].

systematic uncertainty is assigned. This is motivated by the difference of the jet-to-tau fake-rate measured in opposite- and same-sign events, which cover the largest possible deviation one can expect (see Figure 10.20).

11.1.7 Jet Energy Scale

The *jet energy scale* (JES) is calibrated using MC simulation. Like the TES this is subject to further corrections and uncertainties. First, a correction obtained by a data-to-MC comparison is derived and applied to each jet in MC. A tool has been designed by the JetEtMiss working group which applies the calibration [238]. Uncertainties on the final calibration arise from pile-up, close-by jets and the flavour composition. Exploiting several in-situ measurements the uncertainty for various components are derived and provided by another tool utilised in the presented analyses [238]. Details on the JES uncertainty measurement can be found in [239]. The correction is applied such that the energy of each jet is shifted up and down by the corresponding uncertainty. These correction terms are binned in jet- p_T and η . Since jets only enter the analysis via the E_T^{miss} calculation this uncertainty is a minor component, while for other channels like in the semi-leptonic MSSM Higgs analysis it is an important source due to the event categorisation based on the number of selected b-jets. The inclusive JES uncertainty is of the order of up to 5% depending on the p_T and η of the jet.

11.1.8 Missing Transverse Momentum Corrections

The E_T^{miss} is calculated as the imbalance of the sum of the transverse moment of all particles in the event (c.f. Eq. 6.5). Thus, the uncertainty on the E_T^{miss} calculation arises from two sources. First, the momentum resolution and scale of all particles, like taus or jets, have to be propagated to the E_T^{miss} calculation. This is done by recalculating E_T^{miss} after shifting the particle momenta within their uncertainty, e.g. TES or JES. Secondly, the soft term contribution (c.f. Section 6.2) which is evaluated by $Z \rightarrow \ell\ell$ in-situ measurements [170] needs to be taken into account. The soft term corrections as well as the recalculation of the E_T^{miss} are provided by a dedicated tool developed by the JetEtMiss working group [240] and applied in the analyses accordingly. Further details can be found in [238, 170].

11.1.9 Luminosity

The delivered luminosity is measured by several dedicated detectors, c.f. Section 4.2.5, using *van der Meer* scans. Uncertainties on this measurement arise from emittance growth, the fit model or the pile-up correction. The method of the luminosity measurement and the evaluation of its uncertainty is described

in [241]. For 2012 data an uncertainty of 2.8% is quoted. This affects the normalisation of the signal and backgrounds estimated from MC simulation and is propagated through the multijet estimation using the two-dimensional sideband extrapolation method.

11.1.10 Multijet Estimation Using Fake-Factors

In Section 10.1.1 the QCD multijet estimation based on fake-factors has been introduced. To estimate the expected background yields arising for QCD multijet events, the fake-factors derived inclusively in the charge product of the two probe jets are used. This might be subject to systematic uncertainties as the fake-rate can differ in opposite- and same-sign events due to different quark/gluon compositions. Hence the fake-factors have been derived in events with oppositely and equally charged jets. Figure 11.6 shows the obtained fake-factors for one- and three-prong probe jets. Within statistical uncertainties they agree, although there might be a trend towards slightly higher values for opposite-sign events and slightly lower fake-rates in same-sign events. This could either be due to contamination by real tau leptons in opposite-sign events arising from $Z/\gamma^* \rightarrow \tau\tau$ production or from a higher quark fraction, which both lead to a higher fake-rate. Hence this is subject to a systematic uncertainty, which is derived from the maximum deviation between fake-factors obtained inclusively and the ones measured in opposite- and same-sign events. In case the statistical uncertainty is larger than the deviation between the fake-factors, it is taken instead. The derived systematic uncertainties range between 6% and 30% depending on the p_T of the probe jet and its track multiplicity. The QCD multijet contribution is estimated with the nominal fake-factors scaled up and down by one sigma. The difference in the event yield, and, in case of the MSSM Higgs analysis, on the shape of the final discriminating variable, is accounted for in the limit setting as nuisance parameters.

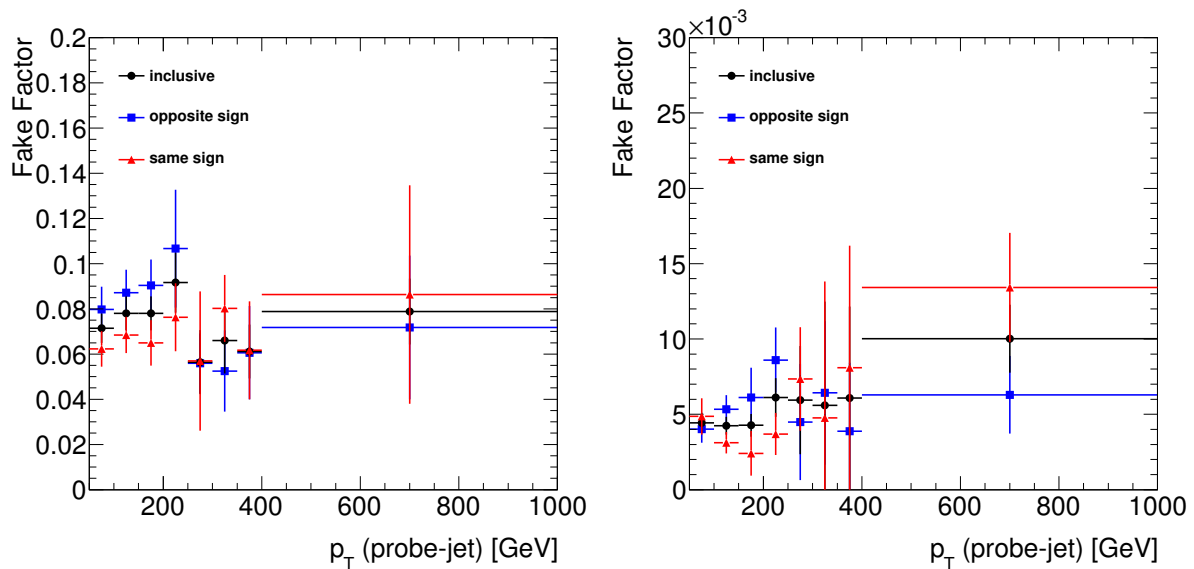


Figure 11.6: Tau-ID fake-factors derived in opposite- (blue squares) and same-sign (red triangles) events for one- (left) and three- (right) prong probe candidates compared to the inclusive (black dots) measurement.

11.1.11 Multijet Estimation Using an ABCD Method

The QCD multijet contribution in events triggered by the di-tau trigger is estimated exploiting the ABCD method (c.f. Section 10.1.3). This technique is based on two assumptions. First it assumes that the transfer factor, R_{qcd} , which is used to scale the shape in the same-sign data sample, is uncorrelated to E_T^{miss} . This assumption is tested by altering the definition of the control sample. Rather than calculating R_{qcd} in the low- E_T^{miss} control region it is calculated in a fail-ID control sample, which is defined in the

same way as the low- E_T^{miss} control sample, but rather than requiring $E_T^{\text{miss}} < 10 \text{ GeV}$ the two selected tau candidates are required to fail the loose jBDT criterion. This results also in a QCD multijet enriched control sample. Table 11.2 summarises the expected and observed event yields in the low- E_T^{miss} and fail-ID opposite- and same-sign control regions.

process	low- E_T^{miss} OS	low- E_T^{miss} SS	fail-ID OS	fail-ID SS
$Z/\gamma^* \rightarrow \tau\tau + \text{jets}$	180.95	3.16	12.43	6.70
$W \rightarrow \tau\nu + \text{jets}$	41.16	4.31	66.01	18.21
Top	1.19	0.10	7.01	2.65
Others	0.47	0.02	0.89	0.22
Data	2892	2194	10531	9027
Data - MC	2668.23	2186.40	10444.66	8999.23
R_{qcd}	1.22		1.16	

Table 11.2: Expected and observed event yields in the opposite- and same-sign control samples used to derive the R_{qcd} transfer factor from events either failing the E_T^{miss} requirement or the tau identification criteria on the two selected tau candidates. The calculated R_{qcd} values are shown in the last row. From the difference a systematic uncertainty of 4.9 % is deduced on the normalisation of the QCD multijet background.

The difference of the obtained transfer factor between the two control samples is taken as a systematic uncertainty on the normalisation of the QCD multijet background which evaluates to 4.9 %. The second assumption of the ABCD method is that $R_{\text{qcd}}(m_T^{\text{tot}})$ is constant. Figure 11.7 shows $R_{\text{qcd}}(m_T^{\text{tot}})$ measured in the low- E_T^{miss} and fail-ID control sample.

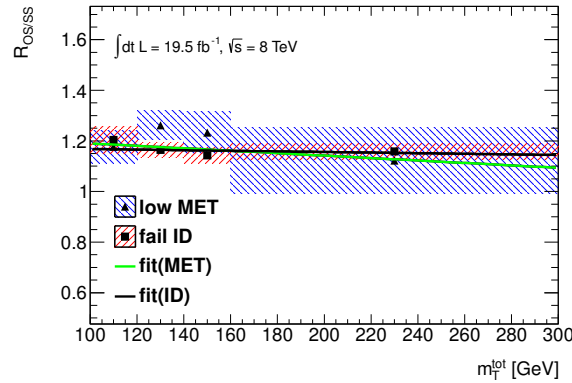


Figure 11.7: QCD transfer factor, R_{qcd} , as a function of the total transverse mass, m_T^{tot} , determined in the low- E_T^{miss} (blue) and fail-ID (red) control sample. A linear fit as defined in Eq. 11.3 is applied to quantify the dependence. The maximum difference of either of the fit in the control regions is taken as systematic uncertainty on the shape of the QCD multijet estimation.

A slight dependence is observed which might lead to a shift of the m_T^{tot} template assigned to the QCD multijet background. To take this dependence into account a linear fit of R_{qcd} is performed in both control samples. The fit function is defined as:

$$R_{\text{qcd}}(m_T^{\text{tot}}) = a \cdot (m_T^{\text{tot}} - \langle m_T^{\text{tot}} \rangle) + \langle R_{\text{qcd}} \rangle, \quad (11.3)$$

with $\langle m_T^{\text{tot}} \rangle$ being the mean value of the m_T^{tot} distribution and $\langle R_{\text{qcd}} \rangle$ the central value of R_{qcd} obtained from the integral in each control region (c.f. Table 11.2). To avoid any bias it has been validated that the

mean value of m_T^{tot} is in agreement in the opposite-sign and same-sign control region, but obviously it is different in the low- E_T^{miss} and fail-ID control samples. These constraints ensure that the uncertainty is not overestimated. The fit parameters are evaluated to:

$$\begin{aligned} \text{low } E_T^{\text{miss}}: \quad R_{\text{qcd}}(m_T^{\text{tot}})|_{\text{low } E_T^{\text{miss}}} &= -0.00047 \cdot (m_T^{\text{tot}} / \text{GeV} - 136.02 \text{ GeV}) + 1.22 \\ \text{fail ID:} \quad R_{\text{qcd}}(m_T^{\text{tot}})|_{\text{fail-ID}} &= -0.00012 \cdot (m_T^{\text{tot}} / \text{GeV} - 160.60 \text{ GeV}) + 1.16. \end{aligned} \quad (11.4)$$

As final systematic uncertainty on this assumption the maximum difference between the nominal R_{qcd} value and either of the two fits is taken as a shape uncertainty. Since the fit is performed in both control samples, i.e. low- E_T^{miss} and fail-ID, with $\langle R_{\text{qcd}} \rangle$ being fixed, the nuisance parameters assigned to the two components will be strongly correlated.

11.2 Theoretical Systematic Uncertainties on Simulated Background Cross Sections

The cross sections used to scale the MC driven backgrounds are subject to systematic uncertainties which arise from their fixed order loop calculation. Table 11.3 summarises the assigned cross section uncertainties for all MC based background processes. Details on their evaluation are given below.

Process	Uncertainty on σ_{prod} (%)
$W+\text{jets}$	27.5
$Z/\gamma^*+\text{jets}$	< 10 (mass-dependent)
$WW/WZ/ZZ$	5
$t\bar{t}$	10
single-top	13

Table 11.3: Uncertainties on the cross section for all background processes estimated from MC simulation [242]. The mass-dependent uncertainties on the simulated $Z/\gamma^*+\text{jets}$ background are described in the text and amount to less than $\sim 10\%$ in the relevant mass range.

11.2.1 Drell-Yan cross sections

The $Z/\gamma^* \rightarrow \tau\tau$ background is estimated from simulation using the leading order generator PYTHIA. The cross section is calculated at NNLO in QCD including electroweak corrections at NLO using FEWZ 3.1.b2 [196]. A correction factor (*k-factor*) is determined from the ratio of the NNLO cross section w.r.t. the LO cross section from PYTHIA, c.f. Section 8.1. The derivation of the k-factors follows the procedure defined in [243]. Uncertainties on these k-factors arise from PDF and α_S variations at 90% C.L. evaluated exploiting the MSTW PDF error sets and uncertainties on higher order electroweak corrections. This does not include photon-induced di-tau production and W/Z final state radiation, but these are expected to be small and have no impact on the sensitivity. The one sigma variations are shown in Figure 8.2 and Figure 8.8 for $Z/\gamma^* \rightarrow \tau\tau$ and $Z/\gamma^* \rightarrow \ell\ell$, respectively.

11.2.2 $W+\text{jets}$ cross sections

The uncertainty on the inclusive cross section of single vector boson production has been evaluated to be 4%-5% [244]. The cross section calculation up to NNLO in QCD has been implemented in several tools, e.g. FEWZ [196] or ZWPRODMS [245]. A comparison of the different programs shows a good agreement between the calculated cross section which agrees within 0.5%. Furthermore, uncertainties from scale (μ_F, μ_R) as well as from PDF and α_S variation are taken into account [242]. An additional uncertainty of 24% for each additional jet [244] is assumed. Since only processes with at least one additional jet enter the analysis the overall systematic uncertainty assigned to the $W+\text{jets}$ cross section is evaluated to be 27.5%.

11.2.3 $t\bar{t}$ cross sections

The $t\bar{t}$ cross section has been calculated at approximate NNLO+NNLL in QCD utilising Hathor. PDF and α_S uncertainties have been evaluated using the MSTW2008 PDF set at 90% C.L. (c.f. Section 8.2). All uncertainties are added in quadrature and evaluate to 10% [244, 246].

11.2.4 Single-top cross sections

The single-top cross section uncertainties have been evaluated in a similar way as for $t\bar{t}$ processes, c.f. Section 8.2 for details. An overall uncertainty of 13% [244, 246] is assigned to the cross section of each component of the single-top production, i.e. s -/ t -channel and Wt production.

11.2.5 Electroweak Di-boson cross sections

As mentioned above the uncertainty on vector boson production has been found to be in the order of 5%. Following the arguments in [244, 246] an uncertainty of 5% is assigned to the WW , WZ and ZZ production cross section.

12 Search for Neutral MSSM Higgs Bosons

This chapter presents a search for heavy neutral Higgs bosons decaying into two tau leptons. Only the fully hadronic final state is considered. Results are interpreted in the context of the MSSM. As discussed above the di-tau final state is the most promising one to observe a potential signal. Given the branching ratios of tau lepton decays, the fully hadronic final state provides the largest contribution ($\text{BR}(\phi \rightarrow \tau_{\text{had}}\tau_{\text{had}}) \simeq 4\%$). In particular for heavy Higgs bosons ($M_A \gtrsim 350 \text{ GeV}$) the sensitivity of the combined search is dominated by the $\tau_{\text{had}}\tau_{\text{had}}$ channel. In the low masses region the fully and semi-leptonic decay provide better sensitivity due to larger QCD multijet background suppression. In Section 12.1 the simulation of the signal processes is discussed. The event selection applied on top of the pre-selection addressed in Chapter 9 is outlined in Section 12.2. Additional systematic uncertainties which have to be taken into account on top of the experimental and theoretical uncertainties outlined in Chapter 11 are introduced in Section 12.3. The validation of the background model is presented in Section 12.4. In Section 12.5 the obtained results are summarised. The concepts used to perform the statistical interpretation of the results are introduced in Section 12.6. The observed data is interpreted as exclusion limit in the M_A - $\tan\beta$ -plane in the context of the MSSM assuming various benchmark scenarios, and in a generic interpretation by setting upper limits on the production cross section times branching ratio. The results are discussed in Sections 12.6.10 and 12.6.11, respectively. Finally, in Section 12.7 the search for heavy neutral Higgs bosons will be summarised and classified in the context of the current experimental status of these searches.

12.1 Signal Simulation

This section will elaborate on the MC simulation of the MSSM Higgs production in the fully hadronic di-tau final state. Two distinct generation processes have been considered. The Higgs boson can be produced either in association with b-quarks or via gluon-gluon fusion. Each of them will be discussed in detail below. Besides the MC simulation, cross section calculations have been performed in order to obtain results in specific benchmark scenarios (c.f. Section 2.5.2). For this thesis the m_h^{max} scenario has been chosen as baseline benchmark. Even though it is theoretically strongly disfavoured in the light of the observed Higgs boson at $M_\phi \simeq 125 \text{ GeV}$, it practically is still a favoured benchmark scenario to allow comparisons to previous search results by LEP, Tevatron and the LHC. In addition, modified benchmark scenarios have been proposed and are examined.

12.1.1 MSSM Neutral Higgs Production in Association with b-Quarks

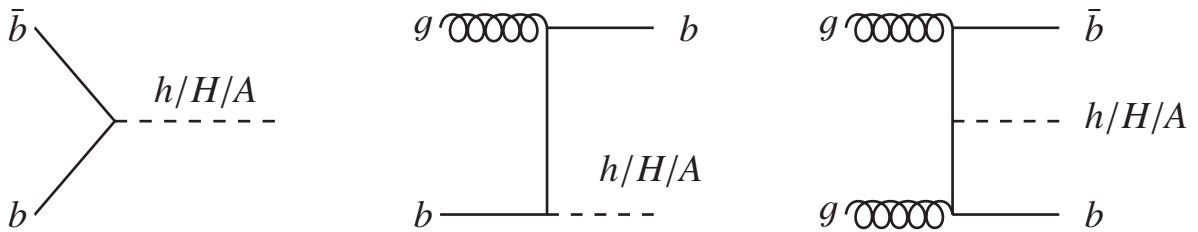


Figure 12.1: Examples of tree-level Feynman diagrams for neutral Higgs boson production in association with b-quarks.

Contrary to the SM, the b Yukawa coupling is enhanced in the MSSM in particular for large $\tan\beta$ (c.f. Section 2.5.2). Thus for the considered search for heavy neutral Higgs bosons the Higgs production in association with b-quarks is the dominant process. Figure 12.1 presents some leading order Feynman diagrams of contributing processes. They can be classified depending whether a b-quark occurs in the final state or not. However, the presented search is performed inclusive in the number of jets, i.e. all final states are considered, whereas other analyses, like the search in the semi-leptonic di-tau final state, exploit dedicated b-tagged and b-vetoed selections. The total production cross section can be calculated exploiting

perturbative expansion as the b-quark mass is large compared to the QCD scale, i.e. $m_b \gg \Lambda_{\text{QCD}}$. Since b-quarks are not directly considered as partons of the proton, the incoming b-quarks have to be produced via gluon splitting. This can be taken into account in the calculation of the total cross section in two different ways. In the so-called *four flavour scheme* (4FS) [247, 248] the b-quarks are not considered being partons of the protons. Hence the dominating LO processes contributing to the total cross section are gluon-gluon or quark-anti-quark annihilation, i.e. $gg \rightarrow b\bar{b}\phi$ and $q\bar{q} \rightarrow b\bar{b}\phi$, respectively. However, the gluon-gluon annihilation process yields large logarithms of $\ln\left(\frac{\mu_F}{m_\phi}\right)$ from collinear $b\bar{b}$ pairs evolving from gluon splitting. The factorisation scale in the collinear region is valid up to $\mu_F \sim \frac{m_\phi}{4m_b}$ [249, 250, 251]. Thus, for $m_\phi \gg 4m_b$ the logarithms become divergent, which is the case in the considered search. These logarithmic terms can however be resummed once one introduces the b-quark PDF as done in the *five flavour scheme* (5FS) [252]. In doing so, the dominant LO process becomes b-quark pair annihilation, $b\bar{b} \rightarrow \phi$. Performing the perturbative expansion to all orders, both the 4FS and 5FS will yield the same results. In practice the calculation is restricted to fixed order, though. Hence both schemes take different contributions into account, and thus lead to different numerical results. To combine the two schemes a matching procedure has been developed, called *Santander matching* [253]. This matching scheme provides a prescription to interpolate between the asymptotic limits of either very light or very heavy Higgs bosons by introducing weights depending on the Higgs mass. In the limit of very heavy Higgs bosons, i.e. $\frac{m_\phi}{m_b} \rightarrow \infty$, the cross section is taken from the 5FS calculation. On the other hand for very light masses, and thus small logarithms, i.e. $\ln \frac{m_\phi}{m_b} = 2$ [253], the cross section is taken from the 4FS calculation. In the intermediate region both are combined by a weighting procedure according to [254]:

$$\sigma_{\text{tot}} = \frac{\sigma^{\text{4FS}} + w(m_\phi) \cdot \sigma^{\text{5FS}}}{1 + w(m_\phi)}, \quad (12.1)$$

with weights:

$$w(m_\phi) = \ln \frac{m_\phi}{m_b}. \quad (12.2)$$

The 4FS cross sections have been calculated at NLO QCD precision [247, 248], while the 5FS calculation is performed up to NNLO [252]. Figure 12.2 shows the production cross section of all three neutral

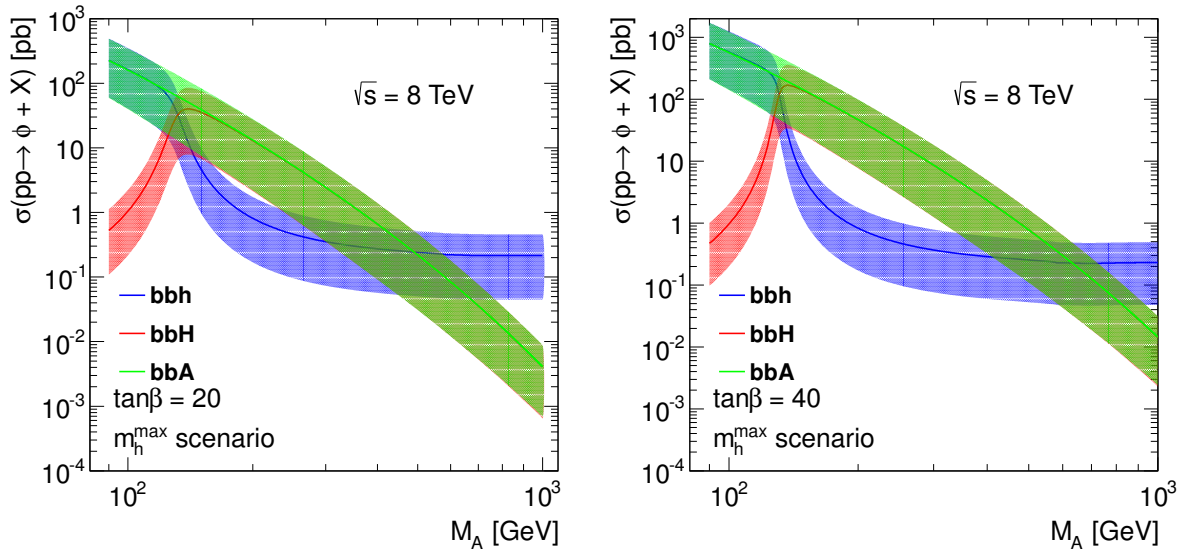


Figure 12.2: Total cross section of Higgs production in association with b-quarks versus M_A in the m_h^{max} scenario for $\tan\beta = 20$ (left) and $\tan\beta = 40$ (right). Different colours indicate the three neutral Higgs bosons. The dashed areas mark the uncertainty on the cross section from μ_F , μ_R , α_S and PDF variation [255]. The Santander matching has been applied to merge 4FS and 5FS calculations.

Higgs bosons as a function of M_A for moderate and high $\tan\beta$. The cross section is derived in the context of the m_h^{\max} scenario applying the Santander matching. For the $b\bar{b} \rightarrow \phi$ cross section calculation BBH@NNLO [252] has been featured using FEYNHIGGS [65, 66, 67, 68] to rescale the Yukawa couplings according to the MSSM prediction. Uncertainties on the predicted production cross section arise from variations of the renormalisation and factorisation scale, α_s and PDF set. The corresponding evaluation is presented in [255] and marked by the dashed areas in Figure 12.2.

The cross sections for the A^0 and H^0 bosons in the m_A - $\tan\beta$ -plane are shown in Figure 12.3 for the m_h^{\max} scenario. Numerical values for selected $\tan\beta$ values are summarised in Appendix D.1. Corresponding values for the $m_h^{\text{mod}+}$ and $m_h^{\text{mod}-}$ scenarios are given in Appendix D.1 as well.

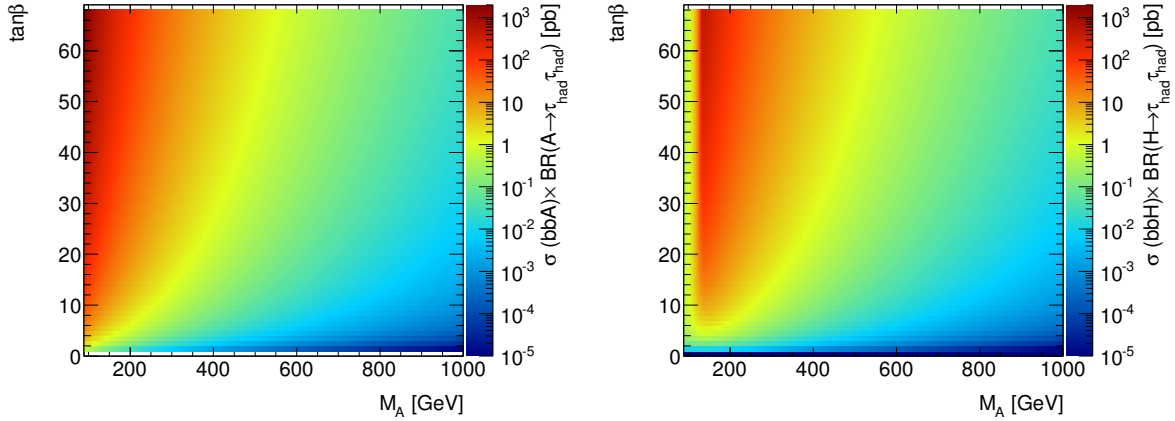


Figure 12.3: Production cross section times branching ratio for Higgs production in association with b-quarks versus M_A in the m_h^{\max} scenario for the A^0 (left) and H^0 (right) boson.

MC simulated collision events used to extract the signal template in this analysis have been produced using the SHERPA generator [146]. It generates generic two parton processes at leading order according to $2 \text{ partons} \rightarrow \tau\tau + n \text{ partons}$ with $n \leq 3$. A collection of 23 samples between $m_\phi = 100 \text{ GeV}$ and $m_\phi = 1 \text{ TeV}$ has been produced assuming $\tan\beta = 20$. Even though the Higgs decay width is restricted to the generated $\tan\beta$ value, no bias for larger $\tan\beta$, as used in the statistical analysis of the m_h^{\max} scenario (c.f. Section 12.6.10), is expected, as the resolution of the reconstructed invariant di-tau mass is much coarser than the $\tan\beta$ dependence of the Higgs width. Figure 12.4 shows the generated invariant di-tau mass for several mass hypotheses. The right plot presents the total decay width of the heavy neutral Higgs bosons assuming the m_h^{\max} benchmark scenario calculated with FEYNHIGGS for moderate and high values of $\tan\beta$. The decay width is of the order of a few GeV, and thus much smaller than the mass resolution in the di-tau final state.

12.1.2 MSSM Neutral Higgs Production via Gluon-Gluon Fusion

In the SM, the Higgs production via gluon-gluon fusion is the dominant production process. Since the Higgs boson can not couple directly to gluons, these processes always involve a quark loop to connect the gluons and the Higgs boson. Figure 12.5 shows Feynman diagrams as examples of processes contributing to the gluon-gluon fusion production.

In the SM, these quark loops are dominated by top quark contributions due to the large Yukawa coupling. In the MSSM the situation changes significantly, in particular for heavy Higgs bosons and large $\tan\beta$ as it is the case in the presented analysis. As pointed out in Section 2.5.2, higher order corrections involving b-quarks can be large. Hence they have to be considered in the calculation of MSSM production cross sections. For the m_h^{\max} scenario the cross sections have been calculated using ggh@nnlo [256] at NNLO in QCD for diagrams involving only top quarks, while other diagrams including b-quarks and top-bottom interference have been calculated at NLO precision using HIGLU [257]. For the considered scenarios this is sufficient as squark contributions to the loop are suppressed by $M_Z^2/M_{\tilde{q}}^2$ [258]. However,

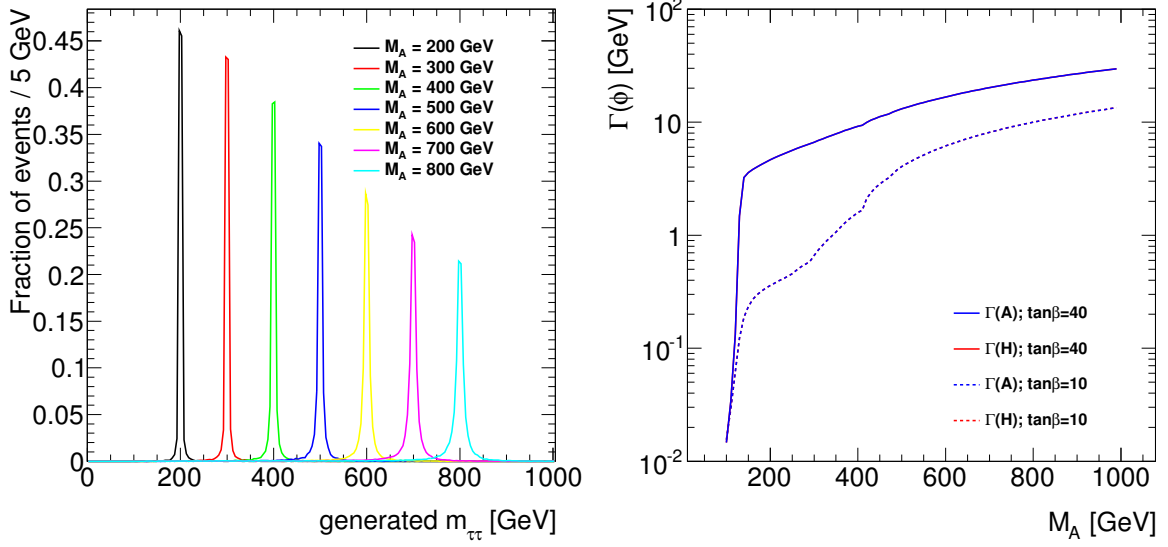


Figure 12.4: Left: Generated invariant di-tau mass, $M_{\tau\tau}$, for various mass points. Right: Total decay width, $\Gamma(\phi)$, as a function of M_A for heavy neutral Higgs bosons for $\tan\beta = 10$ (dashed lines) and $\tan\beta = 40$ (solid lines).

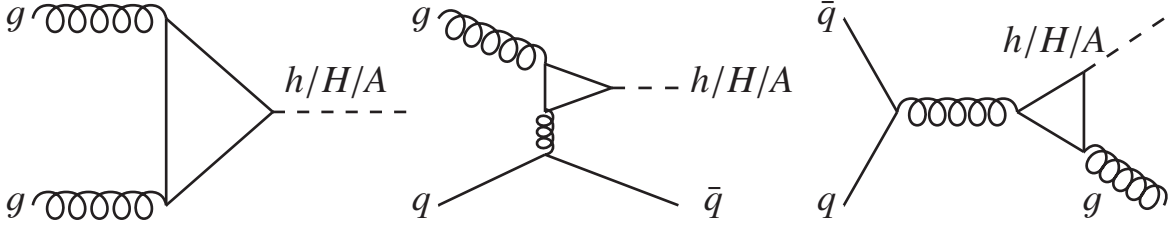


Figure 12.5: Examples of Feynman diagrams of MSSM Higgs production via gluon-gluon fusion.

a new tool SUSHI [259] has been developed which is capable of performing NNLO calculations including dominant squark contributions. These become relevant in benchmark scenarios involving light squark masses [258]. However, these models are not considered in this thesis. The uncertainties on the production cross section arise again from PDF, α_s and scale uncertainties. The PDF+ α_s uncertainties have been evaluated using the MSTW2008 PDF prescription. However, in contrast to e.g. the calculation of the top cross section, a conservative approach is pursued by considering only the NLO set. Further details are given in [258]. Figure 12.6 shows the obtained cross sections including their respective uncertainties for the neutral Higgs bosons in the m_h^{\max} scenario as a function of M_A for $\tan\beta = 20$ and $\tan\beta = 40$, respectively. Compared to the Higgs production in association with b-quarks the cross section is about a factor of ten smaller in the M_A - $\tan\beta$ space relevant for this analysis. Since the event selection will be inclusive, i.e. without designed selection criteria sensitive to a single production mechanism, the reduced cross section will directly translate to a strongly reduced amount of selected events in the gluon-gluon production process.

The production cross section times branching ratio, $\sigma(gg \rightarrow \phi) \times BR(\phi \rightarrow \tau_{\text{had}}\tau_{\text{had}})$, of the A^0 and H^0 boson in the entire phase space considering the m_h^{\max} scenario is presented in Figure 12.7. The given values are used to scale the signal in the statistical analysis in the m_h^{\max} scenario. Numerical values are given for completeness in Appendix D.1 for the considered benchmark scenarios.

The POWHEG MC generator was employed to produce the MC simulation samples used in this analysis for gluon-gluon fusion production. The same set of mass points as for the b-associated production have been generated. A complete list of the samples used in this analysis including some relevant details are given in Table C.2 in Appendix C.1.

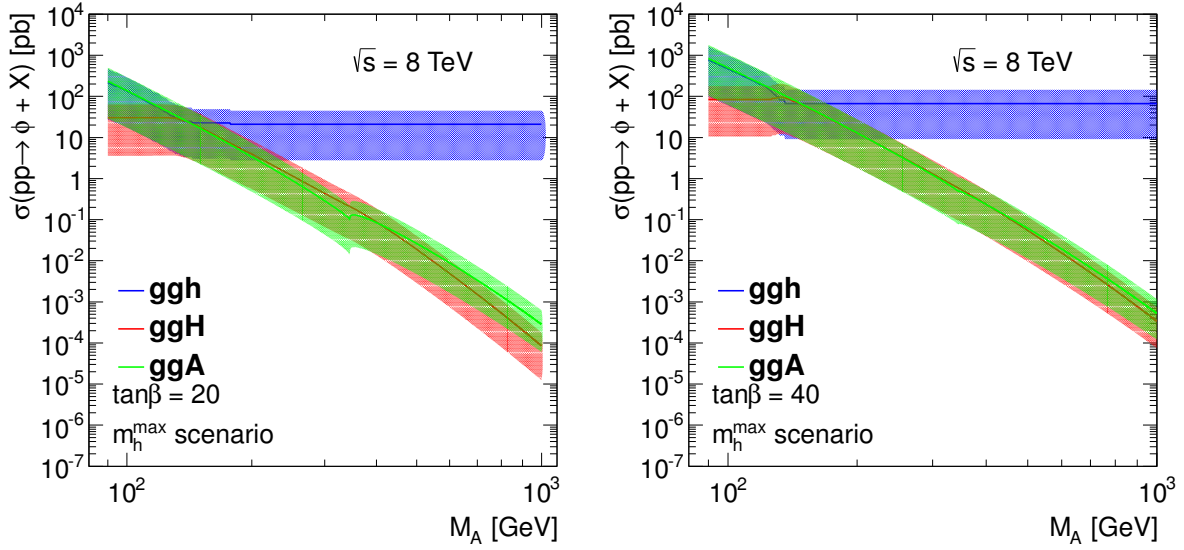


Figure 12.6: Total cross section of Higgs production via gluon-gluon fusion versus M_A in the m_h^{\max} scenario for $\tan\beta = 20$ (left) and $\tan\beta = 40$ (right). Different colours indicate the three neutral Higgs bosons. The dashed areas mark the uncertainty on the cross section from μ_F , μ_R , α_S and PDF variation [258].

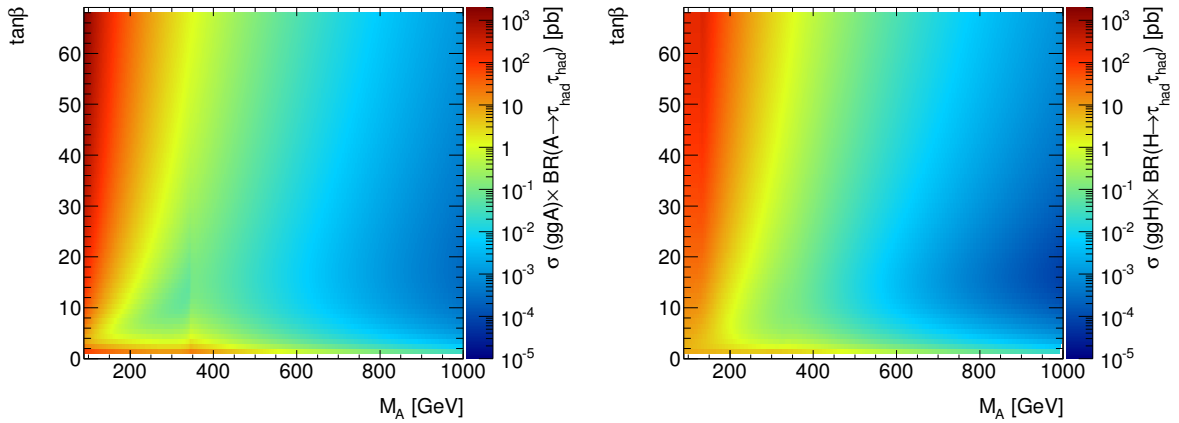


Figure 12.7: Production cross section times branching ratio for Higgs production via gluon-gluon fusion versus M_A in the m_h^{\max} scenario for the A^0 (left) and H^0 (right) boson.

12.2 Event Selection

This section will summarise the event categorisation applied on top of the loose pre-selection discussed in Chapter 9. The analysis is split into two mutually exclusive phase space regions depending on the trigger by which the events were accepted. Light Higgs bosons are dominantly selected by the di-tau triggered (DTT) category, while heavy Higgs bosons are more likely to pass the single-tau triggered (STT) selection. However, the event selection is not optimised for specific mass hypotheses. The main advantage of the categorisation is the ability to feature dedicated techniques to estimate the QCD multijet background as outlined in Section 10.1. The following sections will elaborate on the concrete selection cuts applied in each category.

12.2.1 Single-Tau Triggered Category

The single-tau triggered category requires the event to be accepted by the lowest unprescaled single-tau trigger, EF_tau125_medium1. As discussed in Section 11.1.3 there is no abundant source of high- p_T taus to measure the trigger efficiency for the single-tau trigger. Hence, relying on the modelling of the turn-on region by MC simulation is delicate. However, since the trigger identification algorithms are trained such that they provide a flat efficiency versus the transverse momentum of the tau candidate firing the trigger, it is suitable to consider events in this region. Figure 12.8 shows the trigger efficiency for the EF_tau125_medium1 trigger as a function of the p_T of the reconstructed tau candidate which fired the trigger, measured in $Z/\gamma^* \rightarrow \tau\tau$ MC simulated collision events. A cut of $p_T > 150$ GeV is applied to avoid the turn-on region.

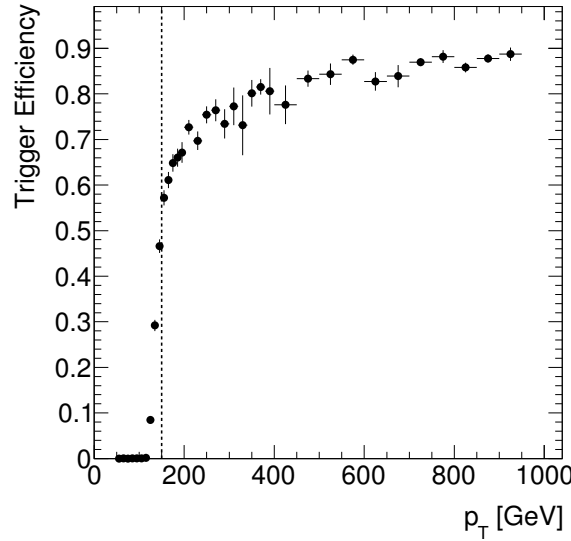


Figure 12.8: Trigger efficiency for EF_tau125_medium1 versus the transverse momentum of the matched reconstructed tau candidate measured in MC simulated $Z/\gamma^* \rightarrow \tau\tau$ events. A steep turn-on region can be observed above 125 GeV. The cut-value on the p_T of the highest- p_T tau candidate of 150 GeV is indicated by the black dotted line.

Hence, the leading tau candidate is required to geometrically match to the EF RoI corresponding to the EF_tau125_medium1 chain within $\Delta R < 0.2$ and to fulfil $p_T > 150$ GeV. Furthermore, both pre-selected tau candidates are required to pass the loose jBDT criterion. Table 12.1 summarises the expected and observed event yields after applying the selection criteria according to the STT category. For illustration the expected signal yields corresponding to $M_A = 400$ GeV and $\tan\beta = 40$ are shown separately for production in association with b-quarks and via gluon-gluon fusion. The sum of all electroweak and QCD backgrounds is given as SM Total. Quoted uncertainties are of statistical origin only. In addition the expected signal yields for b-associated and gluon-gluon fusion Higgs production for all mass points are shown in Tables 12.2 and 12.3, respectively. The low mass points have been dropped as their contribution is negligible. It can be seen that the expected signal yield increases with increasing mass of the hypothetical Higgs boson, which is expected due to the tight kinematic cuts. For very heavy Higgs bosons this trend reverses as the cross section decreases stronger than the acceptance efficiency increases. This is also reflected in Figure 12.9 (left) which shows the cut acceptance efficiency of the full STT selection as a function of M_A for both production processes. As expected it continuously increases as the p_T of the tau candidates become harder with increasing mass.

cut	$gg \rightarrow A \rightarrow \tau_{\text{had}}\tau_{\text{had}}$	$b\bar{b}A \rightarrow \tau_{\text{had}}\tau_{\text{had}}$	multijet	$Z/\gamma^* \rightarrow \tau\tau + \text{jets}$	$W \rightarrow \tau\nu + \text{jets}$	Top	Others	SM Total	Data
Preselection	34.6 ± 0.7	338.3 ± 7.2	621.5 ± 5.6	266.6 ± 17.1	62.6 ± 1.4	22.1 ± 1.9	1.7 ± 0.4	974.6 ± 18.2	1017
Opposite signs	34.1 ± 0.7	334.3 ± 7.1	322.0 ± 4.0	261.0 ± 17.1	51.9 ± 1.3	19.2 ± 1.9	1.5 ± 0.4	655.7 ± 17.7	690
$\Delta\phi(\tau_1, \tau_2) > 2.7$	27.6 ± 0.6	302.7 ± 6.8	216.3 ± 3.3	113.7 ± 2.4	33.5 ± 1.0	10.2 ± 1.4	0.7 ± 0.2	374.4 ± 4.5	373

Table 12.1: Expected event yields for SM backgrounds and Higgs signal for $m_A = 400$ GeV and $\tan\beta = 40$ assuming the m_h^{max} benchmark scenario for the STT selection. The statistical uncertainty is shown. Others include di-boson production and W/Z light lepton, i.e. e, μ , decays.

	Preselection	Opposite signs	$\Delta\phi(\tau_1, \tau_2) > 2.7$
$M_A = 200 \text{ GeV}$	26.0 ± 9.5	25.7 ± 9.5	5.3 ± 4.8
$M_A = 250 \text{ GeV}$	91.1 ± 12.2	90.9 ± 12.2	39.1 ± 7.9
$M_A = 300 \text{ GeV}$	201.1 ± 10.9	199.7 ± 10.9	147.5 ± 9.4
$M_A = 350 \text{ GeV}$	358.8 ± 10.1	351.6 ± 10.0	304.4 ± 9.4
$M_A = 400 \text{ GeV}$	338.3 ± 7.2	334.3 ± 7.1	302.7 ± 6.8
$M_A = 450 \text{ GeV}$	251.3 ± 4.5	247.4 ± 4.5	228.2 ± 4.3
$M_A = 500 \text{ GeV}$	180.6 ± 2.9	177.5 ± 2.9	162.8 ± 2.7
$M_A = 600 \text{ GeV}$	81.5 ± 1.2	79.8 ± 1.2	74.9 ± 1.1
$M_A = 700 \text{ GeV}$	38.2 ± 0.5	37.4 ± 0.5	35.3 ± 0.5
$M_A = 800 \text{ GeV}$	17.3 ± 0.2	16.9 ± 0.2	16.0 ± 0.2
$M_A = 900 \text{ GeV}$	8.8 ± 0.1	8.5 ± 0.1	8.1 ± 0.1
$M_A = 1000 \text{ GeV}$	4.1 ± 0.1	4.0 ± 0.1	3.8 ± 0.0

Table 12.2: Expected signal event yields together with the statistical uncertainty in the STT category for Higgs bosons produced in association with b-quarks. Signal expectations corresponding to Higgs boson masses between $M_A = 200 \text{ GeV}$ and $M_A = 1000 \text{ GeV}$ and $\tan\beta = 40$ assuming the m_h^{\max} benchmark scenario are shown.

	Preselection	Opposite signs	$\Delta\phi(\tau_1, \tau_2) > 2.7$
$M_A = 200 \text{ GeV}$	42.4 ± 5.8	42.0 ± 5.8	2.5 ± 1.4
$M_A = 250 \text{ GeV}$	41.5 ± 3.2	40.7 ± 3.2	12.3 ± 1.7
$M_A = 300 \text{ GeV}$	42.8 ± 1.9	42.1 ± 1.9	25.5 ± 1.5
$M_A = 350 \text{ GeV}$	44.7 ± 1.2	43.6 ± 1.2	32.5 ± 1.0
$M_A = 400 \text{ GeV}$	34.6 ± 0.7	34.1 ± 0.7	27.6 ± 0.6
$M_A = 450 \text{ GeV}$	22.0 ± 0.4	21.7 ± 0.4	18.6 ± 0.4
$M_A = 500 \text{ GeV}$	13.1 ± 0.2	12.8 ± 0.2	11.0 ± 0.2
$M_A = 550 \text{ GeV}$	6.7 ± 0.1	6.6 ± 0.1	5.6 ± 0.1
$M_A = 600 \text{ GeV}$	4.6 ± 0.1	4.5 ± 0.1	4.0 ± 0.1
$M_A = 700 \text{ GeV}$	1.7 ± 0.0	1.6 ± 0.0	1.4 ± 0.0
$M_A = 800 \text{ GeV}$	0.7 ± 0.0	0.7 ± 0.0	0.6 ± 0.0
$M_A = 900 \text{ GeV}$	0.3 ± 0.0	0.3 ± 0.0	0.2 ± 0.0
$M_A = 1000 \text{ GeV}$	0.1 ± 0.0	0.1 ± 0.0	0.1 ± 0.0

Table 12.3: Expected signal event yields together with the statistical uncertainty in the STT category for Higgs bosons produced via gluon-gluon fusion. Signal expectations corresponding to Higgs boson masses between $M_A = 200 \text{ GeV}$ and $M_A = 1000 \text{ GeV}$ and $\tan\beta = 40$ assuming the m_h^{\max} benchmark scenario are shown.

12.2.2 Di-Tau Triggered Category

In order to recover the sensitivity in the light Higgs mass regime, a second category is considered in this analysis. To avoid any overlap with the STT selection the DTT category is designed to be mutually exclusive. It only considers events failing the single-tau trigger requirement, and requires the event to be accepted by the di-tau trigger, EF_2tau38T_medium1. Furthermore, the p_T of the leading tau candidate has to be less than 150 GeV . These two cuts ensure orthogonality between the two categories which

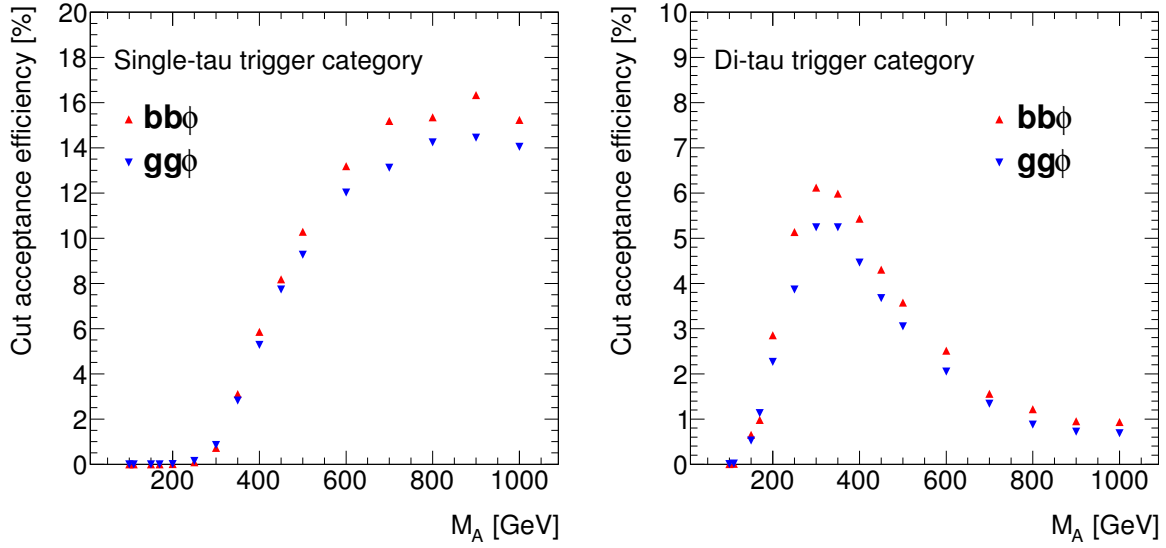


Figure 12.9: Cut acceptance efficiency versus the tested Higgs mass hypothesis for the STT (left) and DTT (right) selection. Higgs production in association with b-quarks is marked by the red triangles, while the blue triangles mark the gluon-gluon fusion process.

simplifies the statistical combination of them later in the limit setting. Since these events are triggered by a di-tau trigger, the trigger match criterion is extended to be fulfilled by both pre-selected tau candidates. By this selection the multijet background becomes very large. To reduce the backgrounds from tau fakes the identification requirement is tightened such that both tau candidates have to pass the medium jBDT threshold. To further reduce the contribution from QCD multijet events and in order to span the required grid for the two-dimensional sideband extrapolation method a cut on the missing transverse energy of $E_T^{\text{miss}} > 10 \text{ GeV}$ is introduced. Finally, it has been found that a cut on the scalar sum of the transverse energy of all reconstructed objects, $\sum E_T$, further improves the background rejection. A cut of $\sum E_T > 160 \text{ GeV}$ is applied. Table 12.4 summarises the expected and observed event yields for signal and background processes. For illustration the $M_A = 200 \text{ GeV}$ and $\tan\beta = 15$ signal hypothesis assuming the m_h^{max} scenario is shown, which reflects the sensitivity of this selection. It can be seen that the QCD multijet background is by far the dominant contribution to the total background, followed by the $Z/\gamma^* \rightarrow \tau\tau$ production, in good agreement with the expectation.

Tables 12.5 and 12.6 summarise the expected signal yields for all relevant mass hypotheses for $\tan\beta = 15$ for the Higgs production mechanism in association with b-quarks and in gluon-gluon fusion, respectively. In Figure 12.9 (right) the cut acceptance is shown for the DTT selection for both production mechanisms. It can be seen that the acceptance increases with increasing mass up to $M_A \sim 300 \text{ GeV}$, which is due to the still fairly tight kinematic cuts and decrease for very heavy Higgs bosons. The latter is expected as the STT category takes over in this regime. Furthermore, the overall acceptance efficiency is about a factor of two to three lower than in the STT category, which is again expected due to the tighter selection. In particular the tighter identification criteria at both the EF and the offline level lead to a degradation of the acceptance. Still the DTT category is suitable to extend the search range to lighter Higgs bosons.

12.3 Systematic Uncertainties

The experimental and theoretical systematic uncertainties have been discussed in detail in Chapter 11. However, in Chapter 5 it has been discussed that the MC simulation of collision events depends on configuration parameters, which can not be determined from first principle, e.g. the factorisation scale. The choice of these unphysical parameters introduce further systematic uncertainties which will be covered by the acceptance uncertainty. To get an estimate of this component, MC simulated samples have been

cut	$gg \rightarrow A \rightarrow \tau_{\text{had}} \tau_{\text{had}}$	$b\bar{b}A \rightarrow \tau_{\text{had}} \tau_{\text{had}}$	multijet	$Z/\gamma^* \rightarrow \tau\tau + \text{jets}$	$W \rightarrow \tau\nu + \text{jets}$	Top	Others	SM Total	Data
Preselection	173.8 ± 4.7	642.5 ± 16.7	$(29.9 \pm 0.2) \times 10^3$	$(26.9 \pm 0.7) \times 10^2$	952.6 ± 10.5	222.1 ± 7.1	9.4 ± 0.5	$(33.8 \pm 0.2) \times 10^3$	33.78×10^3
$p_T < 150 \text{ GeV}$	169.9 ± 4.7	639.0 ± 16.6	$(29.8 \pm 0.2) \times 10^3$	$(25.2 \pm 0.6) \times 10^2$	920.2 ± 10.5	209.2 ± 7.0	8.7 ± 0.5	$(33.5 \pm 0.2) \times 10^3$	33.49×10^3
Opposite signs	168.7 ± 4.6	637.3 ± 16.6	$(16.6 \pm 0.1) \times 10^3$	$(24.6 \pm 0.6) \times 10^2$	817.5 ± 10.3	193.4 ± 6.9	7.9 ± 0.4	$(20.1 \pm 0.1) \times 10^3$	20.06×10^3
$\Delta\phi(\tau_1, \tau_2) > 2.7$	118.0 ± 3.9	534.6 ± 15.2	$(13.5 \pm 0.1) \times 10^3$	$(12.1 \pm 0.4) \times 10^2$	513.5 ± 8.6	78.4 ± 4.9	4.1 ± 0.3	$(15.3 \pm 0.1) \times 10^3$	15.30×10^3
$E_T^{\text{miss}} > 10 \text{ GeV}$	99.6 ± 3.6	450.8 ± 14.0	$(86.1 \pm 0.8) \times 10^2$	924.3 ± 32.3	461.7 ± 8.0	77.2 ± 4.8	3.6 ± 0.2	$(10.1 \pm 0.1) \times 10^3$	10.29×10^3
$\Sigma E_T > 160 \text{ GeV}$	93.9 ± 3.5	411.8 ± 13.3	$(67.7 \pm 0.8) \times 10^2$	763.2 ± 26.1	409.3 ± 7.1	77.2 ± 4.8	3.3 ± 0.2	$(80.3 \pm 0.8) \times 10^2$	8229

Table 12.4: Expected event yields for SM backgrounds and Higgs signal for $m_A = 200 \text{ GeV}$ and $\tan\beta = 15$ assuming the m_h^{max} scenario for the DTT selection. The statistical uncertainty is shown. Others include di-boson production and W/Z light lepton, i.e. e, μ , decays.

	Preselection	$p_T < 150 \text{ GeV}$	Opposite signs	$\Delta\phi(\tau_1, \tau_2) > 2.7$	$E_T^{\text{miss}} > 10 \text{ GeV}$	$\sum E_T > 160 \text{ GeV}$
$M_A = 150 \text{ GeV}$	596.8 ± 19.9	594.5 ± 19.9	589.6 ± 19.8	440.9 ± 17.1	343.0 ± 15.1	259.4 ± 13.1
$M_A = 170 \text{ GeV}$	467.3 ± 25.1	467.2 ± 25.1	462.1 ± 25.0	377.8 ± 22.7	303.6 ± 20.3	261.2 ± 18.8
$M_A = 200 \text{ GeV}$	642.5 ± 16.7	639.0 ± 16.6	637.3 ± 16.6	534.6 ± 15.2	450.8 ± 14.0	411.8 ± 13.3
$M_A = 250 \text{ GeV}$	411.6 ± 9.5	404.0 ± 9.4	400.1 ± 9.4	347.1 ± 8.7	307.0 ± 8.2	294.6 ± 8.0
$M_A = 300 \text{ GeV}$	199.1 ± 3.7	183.9 ± 3.6	181.4 ± 3.6	161.1 ± 3.3	144.6 ± 3.2	140.6 ± 3.1
$M_A = 350 \text{ GeV}$	92.4 ± 1.6	69.3 ± 1.4	68.6 ± 1.4	61.6 ± 1.3	55.4 ± 1.2	54.5 ± 1.2
$M_A = 400 \text{ GeV}$	48.7 ± 0.8	28.7 ± 0.6	28.4 ± 0.6	25.6 ± 0.6	23.5 ± 0.6	23.2 ± 0.5
$M_A = 450 \text{ GeV}$	23.0 ± 0.4	10.6 ± 0.2	10.5 ± 0.2	9.3 ± 0.2	8.5 ± 0.2	8.4 ± 0.2

Table 12.5: Expected signal event yields together with the statistical uncertainty in the DTT category for Higgs bosons produced in association with b-quarks. Signal expectations corresponding to Higgs boson masses between $M_A = 150 \text{ GeV}$ and $M_A = 450 \text{ GeV}$ and $\tan\beta = 15$ assuming the m_h^{max} benchmark scenario are shown. The statistical uncertainty is shown.

	Preselection	$p_T < 150 \text{ GeV}$	Opposite signs	$\Delta\phi(\tau_1, \tau_2) > 2.7$	$E_T^{\text{miss}} > 10 \text{ GeV}$	$\sum E_T > 160 \text{ GeV}$
$M_A = 150 \text{ GeV}$	285.4 ± 9.2	276.3 ± 9.1	273.4 ± 9.0	153.7 ± 6.8	119.3 ± 5.9	101.1 ± 5.5
$M_A = 170 \text{ GeV}$	255.7 ± 8.9	250.6 ± 8.8	248.3 ± 8.7	156.9 ± 6.9	126.9 ± 6.2	114.2 ± 5.9
$M_A = 200 \text{ GeV}$	173.8 ± 4.7	169.9 ± 4.7	168.7 ± 4.6	118.0 ± 3.9	99.6 ± 3.6	93.9 ± 3.5
$M_A = 250 \text{ GeV}$	74.8 ± 1.6	70.9 ± 1.6	70.3 ± 1.6	51.9 ± 1.4	46.3 ± 1.3	45.3 ± 1.3
$M_A = 300 \text{ GeV}$	31.4 ± 0.6	27.7 ± 0.6	27.5 ± 0.6	21.9 ± 0.5	20.0 ± 0.5	19.7 ± 0.5
$M_A = 350 \text{ GeV}$	15.7 ± 0.3	11.4 ± 0.2	11.3 ± 0.2	9.4 ± 0.2	8.6 ± 0.2	8.6 ± 0.2
$M_A = 400 \text{ GeV}$	8.3 ± 0.1	4.6 ± 0.1	4.5 ± 0.1	3.8 ± 0.1	3.5 ± 0.1	3.5 ± 0.1
$M_A = 450 \text{ GeV}$	3.7 ± 0.1	1.6 ± 0.0	1.6 ± 0.0	1.3 ± 0.0	1.2 ± 0.0	1.2 ± 0.0

Table 12.6: Expected signal event yields together with the statistical uncertainty in the DTT category for Higgs bosons produced via gluon-gluon fusion. Signal expectations corresponding to Higgs boson masses between $M_A = 150 \text{ GeV}$ and $M_A = 450 \text{ GeV}$ and $\tan\beta = 15$ assuming the m_h^{max} benchmark scenario are shown.

produced with altered configurations. Since this is computationally very expensive, it has only been done for the signal processes choosing four different mass points, which to some extent can cover the entire mass range under investigation, and the dominant backgrounds, i.e. $Z/\gamma^*(\rightarrow \tau\tau)+\text{jets}$ and $W(\rightarrow \tau\nu)+\text{jets}$ events. The acceptance uncertainty is evaluated from the difference in the event yields between the nominal and altered configurations. Effects from PDF uncertainties which affect the initial state partonic cross section (c.f. Eq. 5.1) are estimated by replacing the nominal PDF set with another one depending on the generator featured for the production. This is not the most reliable strategy to estimate the uncertainty, which would be considering the error PDF set. However, the number of components of these error sets can exceed 50, which is impractical to evaluate. Hence, the PDF set is replaced by another one which is supposed to provide the largest reasonable difference compared to the nominal one, and thus will yield a conservative estimate. Table 12.7 summarises the choice of the nominal and altered PDF sets exploited for the various processes under investigation.

Process	Generator	Nominal PDF set	Altered PDF set
$bb\phi$	SHERPA	CT10	CTEQ6L1
$gg\phi$	POWHEG	CT10	CTEQ6L1
$Z/\gamma^*(\rightarrow \tau\tau)+\text{jets}$	PYTHIA	CTEQ6L1	NNPDF21NLO [260]
$W(\rightarrow \tau\nu)+\text{jets}$	SHERPA	CT10	CTEQ6L1

Table 12.7: Summary of PDF sets used to estimate the acceptance uncertainty for Higgs production in association with b-quarks and gluon-gluon fusion as well as for the dominant backgrounds.

Furthermore, the amount of initial and final state radiation may vary by altering the matching scale in the ME-PS matching (c.f. Section 5.3.3). Hence, the matching scale has been varied accordingly. In SHERPA the CKKW algorithm is featured to perform the matching. The nominal scale is set to $\sqrt{20 \text{ GeV} / \sqrt{s}}$. The up- and downward fluctuations are derived by setting the scale to $\sqrt{30 \text{ GeV} / \sqrt{s}}$ and $\sqrt{15 \text{ GeV} / \sqrt{s}}$, respectively. For the POWHEG generator the amount of ISR and FSR radiation can be tuned by dedicated parameters. Following the recommendations by the ATLAS collaboration these parameters have been varied. The nominal renormalisation and factorisation scales are chosen to be $\mu_F = \mu_R = M_\phi$. An uncertainty is derived by scaling μ_F by a factor of two, while μ_R is scaled by 10%. In POWHEG they are both treated fully correlated, i.e. both are simultaneously scaled up or down, while in SHERPA they are treated uncorrelated following the recommendations by the authors of the generators [261]. For each variation new MC simulated collision events are produced. The event selection is applied at generator level using the RIVET [262] framework. The difference in the observed event yields is taken as systematic uncertainty. Each component is summed in quadrature, which yields the total uncertainty. Table 12.8 summarises the total acceptance uncertainty for each process and considered mass point.

The experimental systematics on the expected signal and background yields are summarised in Table 12.9 and Table 12.10 for the STT and DTT channels after the full event selection is applied. The dominant uncertainties on the signal arise from the modelling of hadronic tau decays, i.e. hadronic tau trigger and identification efficiencies and TES. Expected background yields are effected by two different sources. In phase space regions where the multijet background dominates, the main systematic uncertainty arises from the multijet estimation technique, while for very high masses where the Z/γ^* background becomes dominant, the uncertainties related to the modelling of hadronic tau decays plays the major role.

12.4 Results of the Combined Background Model

After performing the above presented selection, key kinematic and event distributions have been analysed. Backgrounds are estimated exploiting the techniques discussed in Chapter 8. The following sec-

tions will summarise the quality of the background model in the STT and DTT signal regions.

12.4.1 Single-Tau Triggered Category

In the STT category the dominant background arising from QCD multijet events is estimated using the fake-factor technique, which in contrast to the ABCD method is suitable to provide a good model up to very high- p_T , i.e. for very heavy resonances. This significantly improves the quality of the background model. Given the large available statistics in the control region, the uncertainty on the QCD multijet background is dominated by the systematic uncertainties. The next dominant background contribution originates from $Z/\gamma^*(\rightarrow \tau\tau)$ +jets events. This is expected, as these events contain two real tau leptons in the final state as well. Furthermore, once the Z/γ^* is produced off-shell, the same final state topology will be seen by the detector. The assigned model is improved w.r.t. previous analyses by the dedicated high invariant di-tau mass samples utilised here. Both backgrounds contribute 88.1% to the overall background from SM processes. The remaining 11.9% are dominated by $W(\rightarrow \tau\nu)$ +jets events with small contributions from $t\bar{t}$ and single-top and a negligible amount of light lepton fakes. Figure 12.10 presents some key kinematic distributions of the two selected tau candidates, with the p_T given in the top row η in the bottom row, respectively. For illustration the expected signal distribution is shown for $M_A = 400$ GeV and $\tan\beta = 40$ assuming the m_h^{\max} scenario. The lower plots show the ratio between data and expected background event yields including the statistical and systematic uncertainties on the full background template shown in yellow and red, respectively. Figure 12.11 shows the track multiplicity distribution of the two selected tau leptons. The reconstructed missing transverse energy, entering the calculation of m_T^{tot} , and the scalar sum of E_T is presented in Figure 12.12.

12.4.2 Di-Tau Triggered Category

The background model in the DTT category is validated in the same way as presented above for the STT channel. The performance is presented in Figures 12.13 - 12.15. As discussed previously, the most important background is again arising from QCD multijet events, which is by far the dominant contribution to the overall background model. This component is extracted from a two dimensional

Process	Acceptance Unc. [%] - STT	Acceptance Unc. [%] - DTT
$bb\phi$ ($M_\phi = 250$ GeV)	± 28.2	± 6.4
$bb\phi$ ($M_\phi = 300$ GeV)	± 13.2	± 4.7
$bb\phi$ ($M_\phi = 500$ GeV)	± 3.0	± 5.2
$bb\phi$ ($M_\phi = 700$ GeV)	± 2.8	± 4.6
$gg\phi$ ($M_\phi = 250$ GeV)	± 8.3	± 1.3
$gg\phi$ ($M_\phi = 400$ GeV)	± 1.5	± 1.8
$gg\phi$ ($M_\phi = 500$ GeV)	± 1.2	± 1.7
$gg\phi$ ($M_\phi = 700$ GeV)	± 2.7	± 1.2
$Z/\gamma^*(\rightarrow \tau\tau)$ +jets (incl.)	—	± 15.0
$Z/\gamma^*(\rightarrow \tau\tau)$ +jets ($250 \text{ GeV} < M_{\tau\tau} < 400 \text{ GeV}$)	± 6.3	—
$Z/\gamma^*(\rightarrow \tau\tau)$ +jets ($250 \text{ GeV} < M_{\tau\tau} < 400 \text{ GeV}$)	± 2.3	—
$W(\rightarrow \tau\nu)$ +jets ($70 \text{ GeV} < p_T^W < 140 \text{ GeV}$)	± 74.1	± 22.1
$W(\rightarrow \tau\nu)$ +jets ($140 \text{ GeV} < p_T^W < 280 \text{ GeV}$)	± 14.7	± 19.4
$W(\rightarrow \tau\nu)$ +jets ($280 \text{ GeV} < p_T^W < 500 \text{ GeV}$)	± 13.8	± 16.9
$W(\rightarrow \tau\nu)$ +jets ($p_T^W > 500 \text{ GeV}$)	± 12.5	± 46.0

Table 12.8: Systematic uncertainties arising from acceptance uncertainties estimated from altered generator configuration for various processes. Entries marked by — can not be evaluated due to too low selection efficiency.

	$Z/\gamma^* \rightarrow \tau\tau + \text{jets}$	multijet	$W \rightarrow \tau\nu + \text{jets}$	Top	Others	SM Total	bbA ($M_A = 400 \text{ GeV}$)	ggH ($M_A = 400 \text{ GeV}$)
Expected Events	113.67 \pm 2.42	216.29 \pm 3.34	33.52 \pm 1.02	10.22 \pm 1.42	0.66 \pm 0.17	374.36 \pm 4.54	302.7 \pm 6.8	27.6 \pm 0.6
Multijet fake-factor	—	± 11.3	—	—	—	± 6.6	—	—
MC fake-weight	± 1.7	—	14.7 -12.8	33.1 -28.1	33.2 -25.6	2.8 -2.5	< 0.1	< 0.1
JES	—	—	—	—	—	—	—	—
MET (res.)	—	—	—	—	—	—	—	—
MET(scale)	—	—	—	—	—	—	—	—
τ -3p	± 0.7	—	± 0.3	± 0.4	< 0.1	± 0.3	± 0.4	± 0.4
τ -ID	± 6.5	—	± 3.4	± 5.2	± 0.1	± 2.4	± 6.5	± 6.5
τ -trigger low- p_T	—	—	—	—	—	—	—	—
τ -trigger high- p_T	± 9.8	—	± 2.4	± 7.5	—	± 3.4	± 10.0	± 10.0
TES real	6.5 -5.6	—	4.1 -8.0	18.0 -10.8	<0.1 -7.5	± 2.8	± 6.4	± 6.1
TES fake	0.6 -0.1	—	6.3 -5.4	3.0 -2.4	± 6.9	0.8 -0.6	—	—
k-factor $Z/\gamma^* \rightarrow \ell\ell$	—	—	—	—	<0.1 -1.0	—	—	—
k-factor $Z/\gamma^* \rightarrow \tau\tau$	4.3 -3.4	—	—	—	—	1.3 -1.0	—	—

Table 12.9: Summary of detector and theory related systematic uncertainties in the STT category. Quoted numbers are relative uncertainties given in %. Entries marked by — are either not applicable or evaluated to zero. For illustration the effects on the gluon-gluon fusion and b-associated Higgs production for $M_A = 400 \text{ GeV}$ and $\tan\beta = 40$ assuming the m_h^{max} benchmark scenario are summarised in the last two columns.

	$Z/\gamma^* \rightarrow \tau\tau + \text{jets}$	multijet	$W \rightarrow \tau\nu + \text{jets}$	Top	Others	SM Total	bbA ($M_A = 200 \text{ GeV}$)	ggH ($M_A = 200 \text{ GeV}$)
Expected Events	763.24 \pm 26.07	6773.94 \pm 75.14	409.29 \pm 7.11	77.17 \pm 4.82	3.31 \pm 0.19	8026.95 \pm 80.00	411.8 \pm 13.3	93.9 \pm 3.5
$R_{OS/SS}$	—	± 4.9	—	—	—	—	—	—
MC fake-weight	± 4.7	± 0.6	± 5.2	29.4 -26.0	21.2 -16.4	± 0.5	< 0.1	< 0.1
JES	—	—	—	—	—	—	—	—
MET (res.)	-0.1 0.1	< 0.1	-0.1 <0.1	< 0.1	< 0.1	< 0.1	-0.4 <0.1	-0.2 -0.3
MET(scale)	± 0.2	< 0.1	-0.2 <0.1	< 0.1	< 0.1	< 0.1	<0.1 -0.1	-0.2 <0.1
τ -3p	—	—	—	—	—	—	—	—
τ -ID	± 6.6	± 0.5	± 3.6	± 5.0	± 0.2	± 0.4	± 6.5	± 6.5
τ -trigger low- p_T	± 18.0	± 1.6	± 10.6	± 12.7	0.6 -0.6	± 1.0	± 9.4	± 9.6
τ -trigger high- p_T	± 3.1	± 0.1	± 0.7	± 3.0	< 0.1	± 0.2	± 10.2	± 9.8
TES real	± 8.0	-0.6 0.8	3.7 -5.9	2.7 -4.0	0.4 -5.5	± 0.4	4.1 3.6	-2.8 3.2
TES fake	0.2 -0.2	<0.1 0.1	2.6 -2.3	1.1 -1.3	4.5 -5.5	< 0.1	—	—
k-factor $Z/\gamma^* \rightarrow \ell\ell$	—	—	—	—	<0.1 -0.2	< 0.1	—	—
k-factor $Z/\gamma^* \rightarrow \tau\tau$	3.9 -3.3	-0.3 0.2	—	—	—	0.1 -0.1	—	—

Table 12.10: Summary of detector and theory related systematic uncertainties in the DTT category. Quoted numbers are relative uncertainties given in %. Entries marked by — are either not applicable or evaluated to zero. For illustration the effects on the gluon-gluon fusion and b-associated Higgs production for $M_A = 200 \text{ GeV}$ and $\tan\beta = 15$ assuming the m_h^{max} benchmark scenario are summarised in the last two columns.

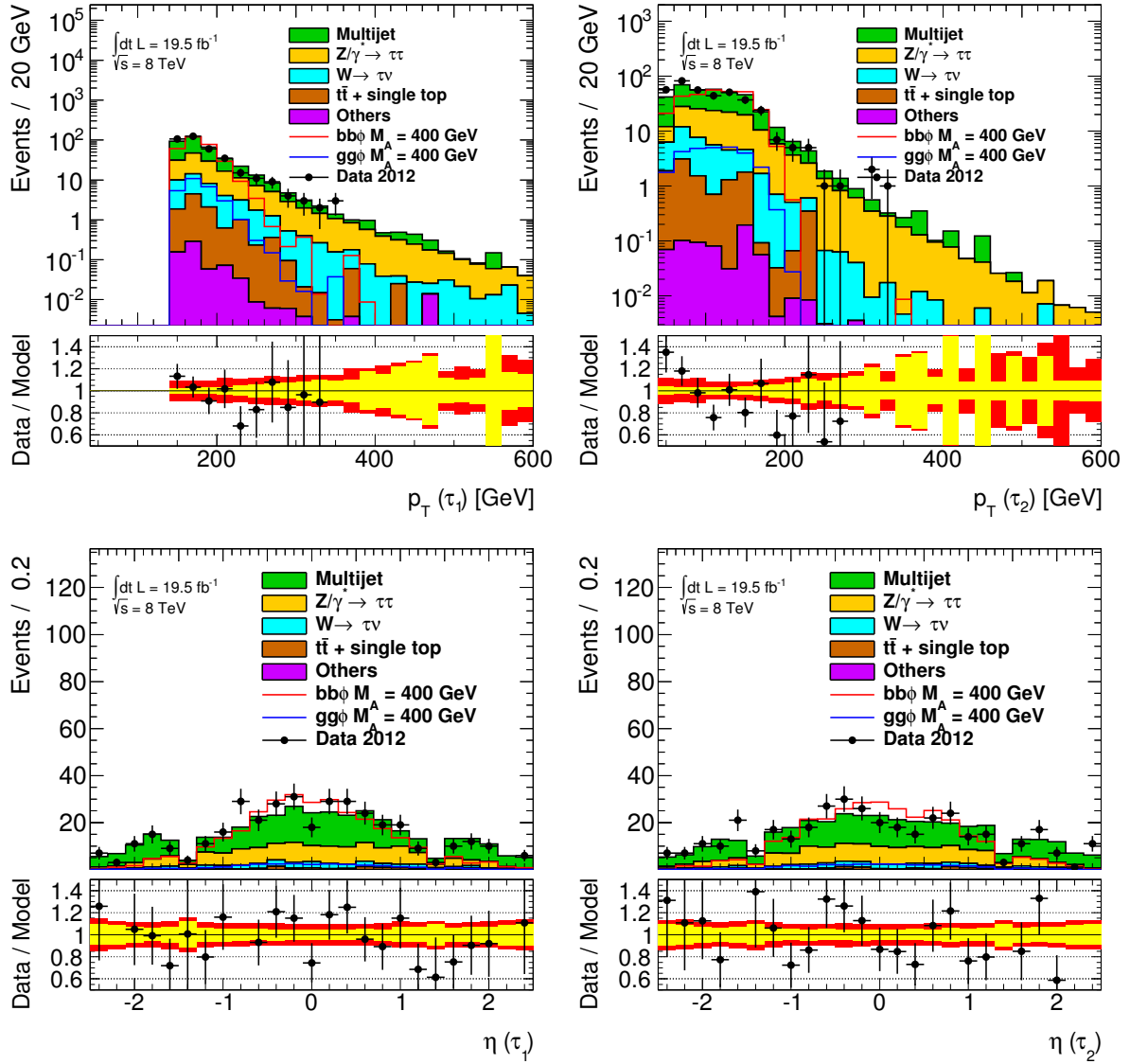


Figure 12.10: Kinematic distributions of the leading (left) and sub-leading (right) tau candidates in the STT signal region. The multijet contribution is estimated using tau-ID fake-factors. All other contributions are estimated from MC simulation. Others include di-boson production and W/Z light lepton, i.e. e, μ , decays. The signal shown for illustration corresponds to $M_A = 400$ GeV and $\tan\beta = 40$ assuming the m_h^{\max} scenario. The statistical and systematic uncertainties on the model are indicated by the yellow and red bands in the ratio, respectively.

side band method as outlined in Section 10.1.3. It sums up to about 85% of the total SM background. $Z/\gamma^*(\rightarrow \tau\tau)+\text{jets}$ is the second most important component which is about a factor of ten smaller than the QCD multijet background. Another 5% consists of $W(\rightarrow \tau\nu)+\text{jets}$ events estimated from MC simulation, with correction factors for the jet-to-tau fake-rate from a data control sample applied on top. Further backgrounds from $t\bar{t}$, single-top and lepton fake events provide only a minor component.

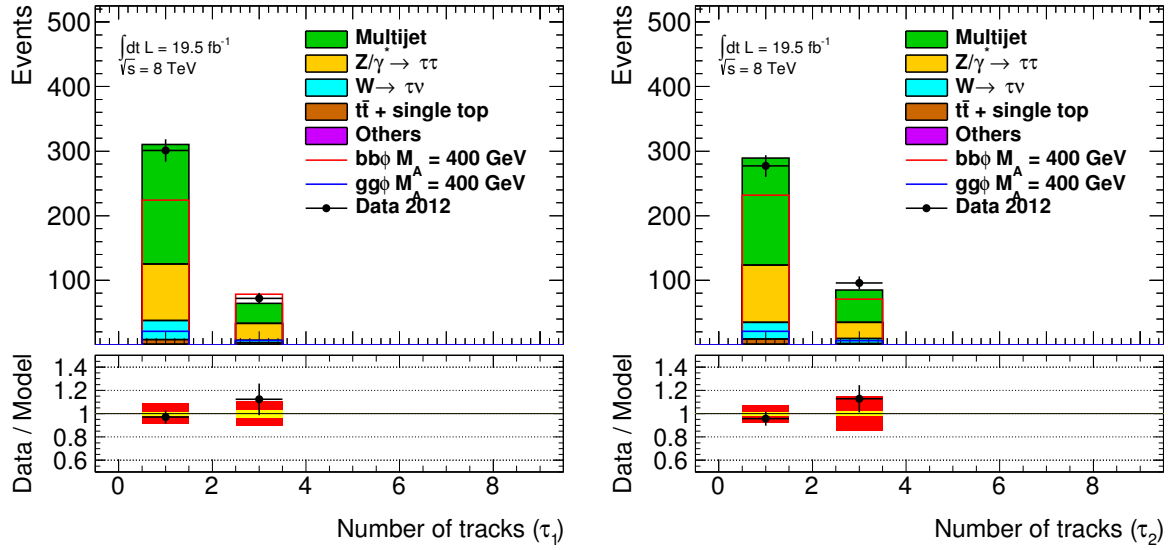


Figure 12.11: Track multiplicity distributions for the leading and sub-leading tau candidates in the STT signal region. The multijet contribution is estimated using tau-ID fake-factors. All other contributions are estimated from MC simulation. Others include di-boson production and W/Z light lepton, i.e. e, μ , decays. The signal shown for illustration corresponds to $M_A = 400$ GeV and $\tan\beta = 40$ assuming the m_h^{\max} scenario. The statistical and systematic uncertainties on the model are indicated by the yellow and red bands in the ratio, respectively.

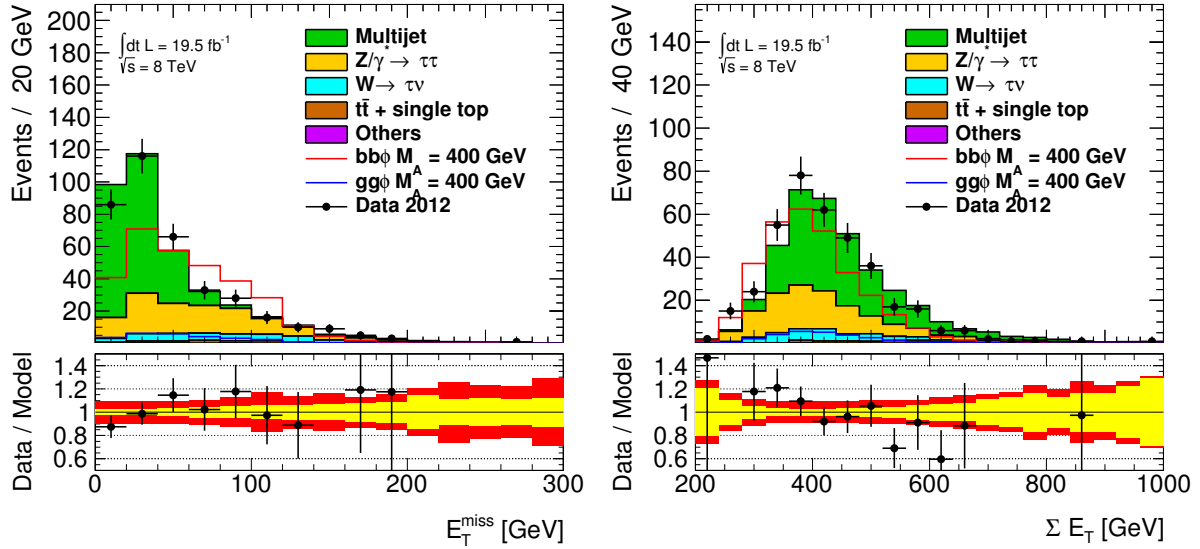


Figure 12.12: Key event distributions in the STT signal region. The multijet contribution is estimated using tau-ID fake-factors. All other contributions are estimated from MC simulation. Others include di-boson production and W/Z light lepton, i.e. e, μ , decays. The signal shown for illustration corresponds to $M_A = 400$ GeV and $\tan\beta = 40$ assuming the m_h^{\max} scenario. The statistical and systematic uncertainties on the model are indicated by the yellow and red bands in the ratio, respectively.

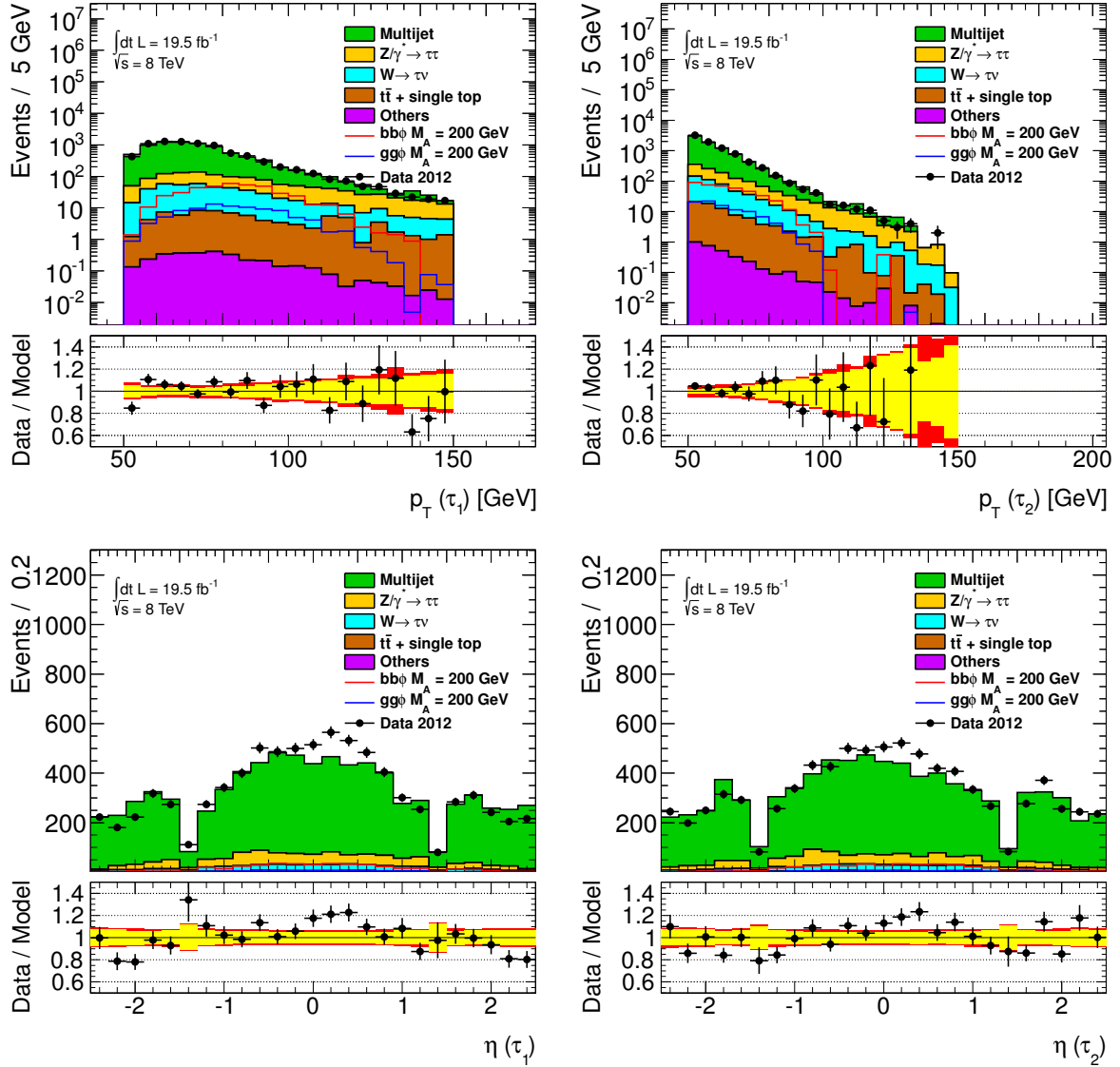


Figure 12.13: Kinematic distributions of the leading (left) and sub-leading (right) tau candidates in the DTT signal region. The multijet contribution is estimated using an ABCD method. All other contributions are estimated from MC simulation. Others include di-boson production and W/Z light lepton, i.e. e, μ , decays. The signal shown for illustration corresponds to $M_A = 200$ GeV and $\tan\beta = 15$ assuming the m_h^{\max} scenario. The statistical and systematic uncertainties on the model are indicated by the yellow and red bands in the ratio, respectively.

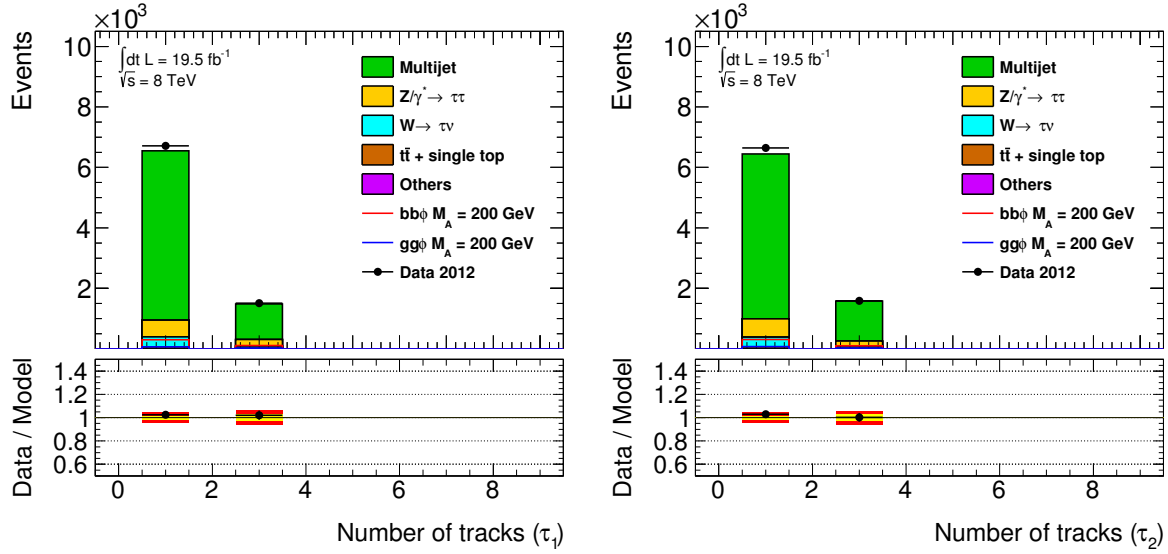


Figure 12.14: Track multiplicity distributions for the leading (left) and sub-leading (right) tau candidates in the DTT signal region. The multijet contribution is estimated using an ABCD method. All other contributions are estimated from MC simulation. Others include di-boson production and W/Z light lepton, i.e. e, μ , decays. The signal shown for illustration corresponds to $M_A = 200$ GeV and $\tan\beta = 15$ assuming the m_h^{\max} scenario. The statistical and systematic uncertainties on the model are indicated by the yellow and red bands in the ratio, respectively.

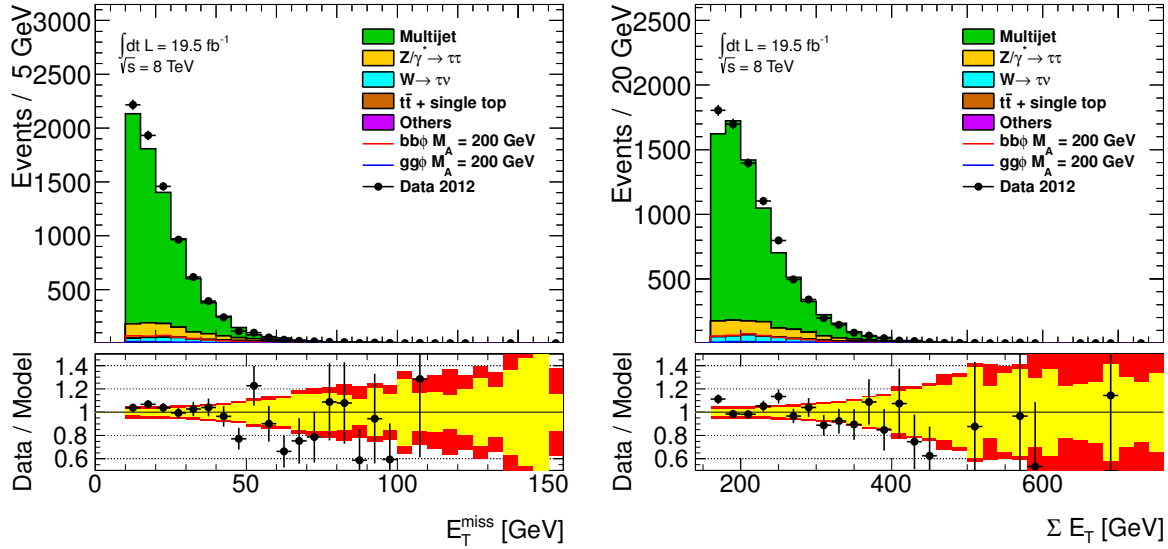


Figure 12.15: Key event distributions in the DTT signal region. The multijet contribution is estimated using an ABCD method. All other contributions are estimated from MC simulation. Others include di-boson production and W/Z light lepton, i.e. e, μ , decays. The signal shown for illustration corresponds to $M_A = 200$ GeV and $\tan\beta = 15$ assuming the m_h^{\max} scenario. The statistical and systematic uncertainties on the model are indicated by the yellow and red bands in the ratio, respectively.

12.5 Results

After the event selection, including the data-driven estimates of the various background processes, the final discriminating variable, the *total transverse mass*, m_T^{tot} (see Eq. 10.3), is calculated and fed into the machinery featured to perform the statistical analysis of the selected data. The resulting distributions of m_T^{tot} are shown in Figure 12.16 for the STT (left) and DTT (right) channels. Both are combined later (c.f. Section 12.6). As both channels are sensitive in a different mass range, the signal process shown for illustration purpose differs. In the STT channel, which is sensitive at high mass, the signal shown corresponds to $M_A = 400$ GeV and $\tan\beta = 40$. In the DTT category the sensitivity is higher at lower mass and lower $\tan\beta$, such that the expected mass distribution for $M_A = 200$ GeV and $\tan\beta = 15$ is shown. As discussed earlier, the H^0 and A^0 bosons become degenerated at high mass and large $\tan\beta$. This is the case for all considered parameter points of the benchmark scenarios studied. Hence, the shown signal is the sum of the contributions from the two Higgs bosons taking into account their respective branching ratio for the decay in two hadronically decaying tau leptons.

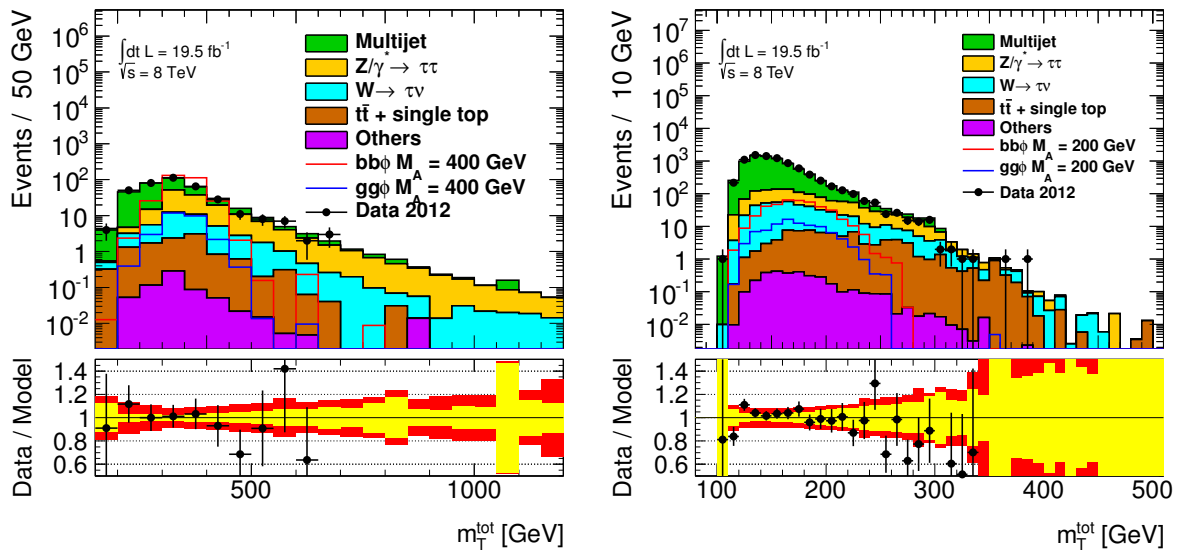


Figure 12.16: Total transverse mass distribution in the STT (left) and DTT (right) signal region. The multijet contribution is estimated using tau-ID fake-factors in the STT category, while a two-dimensional sideband extrapolation method is exploited in the DTT selection. All other contributions are estimated from MC simulation. Di-boson production and W/Z light lepton, i.e. e, μ , decays are summarised as Others. The signal template in the STT category corresponds to $M_A = 400$ GeV and $\tan\beta = 40$, while in the DTT channel $M_A = 200$ GeV and $\tan\beta = 15$ is shown. Both are derived assuming the m_h^{max} benchmark scenario. The statistical and systematic uncertainties on the model are indicated by the yellow and red bands in the ratio, respectively.

12.6 Statistical Analysis of the Results

The following sections will briefly introduce the statistical concepts exploited to interpret the observed data.

12.6.1 Hypothesis Testing

Hypothesis tests are the fundamental concept to discriminate between a null hypothesis, H_0 , and an alternative hypothesis, H_1 . It is used to select one hypothesis in favour of the other. Depending on the actual aim of the statistical analysis the null and alternative hypothesis can have different meaning. In

order to calculate a discovery significance, the null hypothesis is the expectation from known processes only, i.e. the *background-only* hypothesis, and the alternative hypothesis includes the signal, i.e. the *signal plus background* hypothesis. For the purpose of the exclusion of a potential signal, these hypothesis definitions are swapped. In high energy physics one introduces a *signal strength* parameter, μ , to distinguish between the two hypothesis, with $\mu = 0$ defining the background-only hypothesis and, $\mu = 1$ the nominal signal hypothesis. If one expects b background events from known processes and s signal events, the total number of observed events, N , can be written as $N = \mu s + b$. To test the compatibility of the observed data, \vec{x} , with a given hypothesis, H , one constructs a *test statistic*, $q_\mu(\vec{x})$, which is a function of the measured data. For each hypothesis the test statistic gets a probability density function (p.d.f.), $f(q_\mu|H)$, assigned. To test whether the measured data is in agreement with the hypothesis a critical value q_{crit} is defined, such that the probability observing a value of the test statistic with $q_{\mu,\text{obs}} = q_{\mu,\text{crit}}$ with H being true, is α , i.e:

$$\alpha = \int_{q_{\mu,\text{crit}}}^{\infty} f(q_\mu|H) dq_\mu . \quad (12.3)$$

α is called the *significance level*. If $q_{\mu,\text{obs}} < q_{\mu,\text{crit}}$ one does not reject the hypothesis, while for $q_{\mu,\text{obs}} > q_{\mu,\text{crit}}$ the hypothesis is rejected. The question though is how to construct the test statistic. According to the *Neyman Pearson lemma* [263] the optimal test statistic for an experiment with no systematic uncertainties is the likelihood ratio:

$$q_\mu(\vec{x}) = \frac{\mathcal{L}(H_0)}{\mathcal{L}(H_1)} . \quad (12.4)$$

The observed significance level is called *p-value*, which defines the probability of measuring data with equal or worse compatibility than the observed data given the hypothesis, H , under assumption. Since the p-value is a probability it follows $p \in [0, 1]$. The p-value can be related to a Gaussian significance, Z :

$$Z = \Phi^{-1}(1 - p) , \quad (12.5)$$

with Φ^{-1} being the inverse of the cumulative distribution, or quantile, of a normal distribution. In practice the p-value is a function of the signal strength parameter, μ . If one wants to test the background-only hypothesis the p_0 -value¹³, p_0 , is defined as:

$$p_0 = P(q_\mu \leq q_{\mu,\text{obs}}|H_0) = \int_{-\infty}^{q_{\mu,\text{obs}}} f(q_\mu|H_0) dq_\mu = 1 - \int_{q_{\mu,\text{obs}}}^{\infty} f(q_\mu|H_0) dq_\mu . \quad (12.6)$$

From this the confidence level for the background-only hypothesis, CL_b , is defined as:

$$\text{CL}_b = 1 - p_0 . \quad (12.7)$$

In particle physics one has agreed on a threshold of rejecting the background hypothesis if $Z_0 > 5$ which corresponds to $p_0 < 2.87 \cdot 10^{-7}$, i.e. the probability of observing the given data or less compatible data under the assumption of H_0 being true is less than $2.87 \cdot 10^{-7}$. If one tests the signal hypothesis the p-value, p_μ , reads as:

$$p_\mu = P(q_\mu \geq q_{\mu,\text{obs}}|H_1) = \int_{q_{\mu,\text{obs}}}^{\infty} f(q_\mu|H_1) dq_\mu . \quad (12.8)$$

The agreement within the particle physics community of rejecting the signal hypothesis is to exclude signal strengths with $Z_\mu > 1.64$ which corresponds to $p_\mu < 0.05$, i.e. the tested signal is excluded at 95% confidence level. The 95% C.L. upper limit on μ , i.e. on the cross section of the signal process, is obtained by finding the μ value such that:

$$p_\mu < \alpha , \quad (12.9)$$

with $\alpha = 0.05$, with the upper limit, μ_{up} , corresponding to $p_{\mu_{\text{up}}} = \alpha$. This is the so-called CL_{s+b} method.

¹³Note that p_0 is not a p-value, but rather one minus the p-value

12.6.2 The CL_s Method

An exclusion limit obtained by the CL_{s+b} method may be optimistic in case of low separation power. If the expected signal yield is small compared to the background yields, i.e. $\mu s \ll b$, the p.d.f.s of the test statistic of the two hypothesis will have a large overlap. This results in a 95% C.L. exclusion of μ even though one has only little or no sensitivity for the tested hypothesis. To avoid this issue the CL_s method [264] has been proposed. It is designed to be *conservative*, meaning that the excluded signal strength will always be greater than the CL_{s+b} limit, i.e. the confidence level will be larger than 95%. It is defined as:

$$\text{CL}_s = \frac{\text{CL}_{s+b}}{\text{CL}_b} = \frac{p_\mu}{1 - p_0}. \quad (12.10)$$

If the analysis has large sensitivity to the signal hypothesis, the p.d.f.s of the test statistic will be well separated, such that p_0 will be small, and thus $1 - p_0 \simeq 1$. In that case the obtained upper limit will be the same as if one would exploit the CL_{s+b} technique. If, however, the sensitivity is small, $1 - p_0$ will be small, and thus CL_s be large. To obtain the upper limit it is required that $\text{CL}_s < \alpha$ such that the upper limit will increase, i.e. it will get weaker. In that sense CL_s will always be a subset of CL_{s+b} providing more conservative limits, without suffering from low sensitivity analyses. Figure 12.17 illustrates the CL_s concept. This technique will be exploited in the presented analysis.

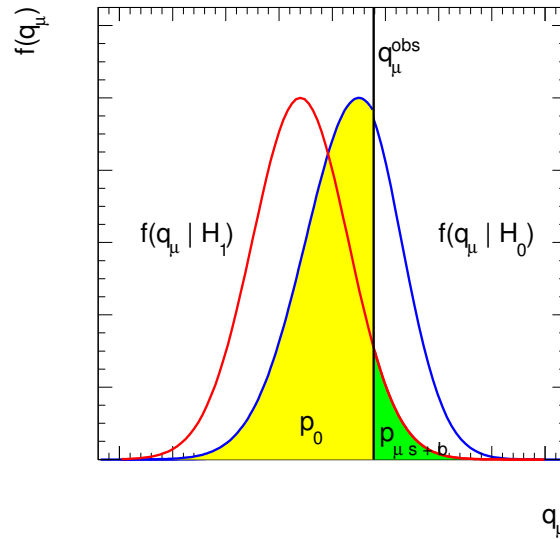


Figure 12.17: Illustration to support the CL_s method exploited to extract upper limits. The probability density function of the test statistic for the signal+background, $f(q_\mu|H_1)$, and background-only, $f(q_\mu|H_0)$, hypotheses are shown by the red and blue lines, respectively. The observed value of the test statistic is indicated by the black line. The p-values are obtained from the integrals which are marked by the yellow and green areas.

12.6.3 Construction of the Likelihood Function

As pointed out previously, the upper limit is obtained exploiting the CL_s approach in which the test statistic is defined as the likelihood ratio according to the Neyman-Person lemma. This section will outline the construction of the likelihood function, \mathcal{L} , used to model the two hypotheses. In the presented analysis the statistical analysis is based on the m_T^{tot} distribution, taking into account the entire shape information. The measured histogram can be expressed as a set of values, $\vec{m} = (m_1, m_2, \dots, m_N)$, in which m_i is the measured mass of the i -th event. The probability density function is given as:

$$f(m_i) = \frac{\mu s f_s(m_i) + b f_b(m_i)}{\mu s + b}, \quad (12.11)$$

with $f_s(m_i)$ and $f_b(m_i)$ being the normalised p.d.f.s of the signal and background hypothesis, respectively. The p.d.f. of measuring N events with masses \vec{m} is then given as:

$$\mathcal{L}(\mu) = P(\vec{m}|\mu) = \text{Pois}(N|\mu s + b) \prod_{i=1}^N f(m_i), \quad (12.12)$$

with $\text{Pois}(N|\mu s + b)$ being the *Poisson* distribution:

$$\text{Pois}(N|\mu s + b) = (\mu s + b)^N \frac{e^{-(\mu s + b)}}{N!}. \quad (12.13)$$

The best estimators for the signal and background p.d.f.s for a binned histogram evaluate to:

$$f_s(m_i) = \frac{s_j}{s\Delta_j} \quad f_b(m_i) = \frac{b_j}{b\Delta_j}, \quad (12.14)$$

with s_j, b_j being the number of signal and background events in bin j which has a width Δ_j . The binning of the histogram is related to the measured mass by a non-linear relation. For the entries in each bin the following relations hold:

$$N = \sum_{j=1}^{n_{\text{bins}}} N_j \quad s = \sum_{j=1}^{n_{\text{bins}}} s_j \quad b = \sum_{j=1}^{n_{\text{bins}}} b_j. \quad (12.15)$$

Using Eqs 12.11-12.15 this leads to the likelihood function:

$$\begin{aligned} \mathcal{L}(\mu) &= \text{Pois}(N|\mu s + b) \prod_{i=1}^N \frac{\mu s f_s(m_i) + b f_b(m_i)}{\mu s + b} \\ &= \frac{(\mu s + b)^N e^{-(\mu s + b)}}{N!} \prod_i \frac{1}{\mu s + b} \frac{\mu s_j + b_j}{\Delta_j} \\ &= \frac{1}{N!} \prod_j \frac{1}{\Delta_j} (\mu s_j + b_j) e^{-(\mu s_j + b_j)} \\ &= \frac{1}{N!} \prod_j \underbrace{\frac{N_j}{\Delta_j}}_{\text{constant}} \cdot \underbrace{\frac{(\mu s_j + b_j) e^{-(\mu s_j + b_j)}}{N_j}}_{\text{Pois}(N_j|\mu s_j + b_j)} \\ &= C \prod_j \text{Pois}(N_j|\mu s_j + b_j), \end{aligned} \quad (12.16)$$

with C being a normalisation constant. The analysis of the data is performed exploiting the *extended maximum likelihood approach* [265]. The underlying concept is the *maximum likelihood* (ML) method [265] which defines ML estimators to be the parameter estimators which maximise the likelihood function. Since this is a maximisation problem any monotonic transformation of the likelihood function will yield the same optimal value. Hence it is convenient to transform the maximisation problem into a minimisation problem by considering the *negative log-likelihood function* (NLL):

$$-\ln \mathcal{L}(\mu) = -\ln(P(\vec{m}|\mu)) = -\ln C - \sum_{j=1}^{n_{\text{bins}}} \left[\mu s_j + b_j + \ln(N_j!) - N_j \ln(\mu s_j + b_j) \right]. \quad (12.17)$$

The advantage is that the product turns into a sum and the exponential terms become simple factors. This simplifies the numerical treatment of the procedure. In practice the situation becomes more complicated by considering not only a single measurement, but many categories and auxiliary information from e.g. control regions constructed to constrain a given background. In the presented analysis both is true. Not just a single channel, but two categories (STT and DTT), are present and combined. Furthermore, the two

dimensional side band method featured to estimate the multijet background will yield further channels. However, the discussed procedure still holds, with some refinements. Rather than considering b being a vector of the bin contents of the m_T^{tot} histogram in a single channel, the bin contents of all channels are sequentially added to b , i.e.:

$$\vec{b} = (b_{1,1}, b_{2,1}, \dots, b_{1,n_{\text{bins}}^{ch_1}}, b_{2,1}, \dots, b_{2,n_{\text{bins}}^{ch_2}}, b_{n,1}, \dots, b_{ch_n, n_{\text{bins}}^{ch_n}}), \quad (12.18)$$

with $b_{ch_n, j}$ being the bin content of bin j in channel n and $n_{\text{bins}}^{ch_n}$ the total number of bins in channel n . \vec{s} and \vec{N} are defined accordingly.

12.6.4 Treatment of Systematic Uncertainties

In practice the expected signal and background yields in each bin in the m_T^{tot} distribution are not fixed constants, but rather expected mean values, which are subject to systematic uncertainties. Chapter 11 introduced the common experimental and theoretical sources of systematic uncertainties, while Section 12.3 outlined the systematic uncertainties dedicated to the search for heavy neutral Higgs bosons. Given that, the above mentioned procedure is only a simplified version of the real treatment. In the actual statistical analysis of the data a *nuisance parameter* (NP), α , is introduced for each source of systematic uncertainties. Nuisance parameters are not of direct interest (like the signal strength), but influence the parameter(s) of interest as both signal and background predictions depend on them. The signal and background yields are rewritten such that:

$$s_j = s_j(\vec{\alpha}) = s_j(\{\alpha_i\}_{i=1}^{n_{\text{syst}}}) \quad \text{and} \quad b_j = b_j(\vec{\alpha}) = b_j(\{\alpha_i\}_{i=1}^{n_{\text{syst}}}), \quad (12.19)$$

where $\vec{\alpha} = \{\alpha_i\}_{i=1}^{n_{\text{syst}}}$ is the set of nuisance parameters for the number of systematic uncertainties. In the construction of the likelihood function the following notation will be used: The nominal signal and background expectations are defined as $\alpha_i = 0$, while the altered yields are defined for $\alpha = \pm 1$ for the 1σ up and down variation, respectively. In general each systematic uncertainty can be composed of two components. One component will measure the effect on the normalisation, η_i^\pm , and one component affects the shape of the m_T^{tot} distribution, σ_i^{\pm} . It has to be noted that \pm does not necessarily refer to an upward or downward shift of the expected event yields, but rather it refers to the direction in which the corresponding systematic uncertainty is shifted. The exact treatment of the systematic uncertainties is subtle, though, as it might be difficult to consider correlations across different background components or signal samples correctly. An advantage of the histogram based approach is that one can track down the individual systematics explicitly. However, to form continuous nuisance parameters an interpolation algorithm and constraint terms have to be introduced, which leads to ambiguities. A detailed discussion is given in [266]. For nuisance parameters assigned to a shape systematic uncertainty a piecewise linear interpolation is applied, while for nuisance parameters affecting the normalisation a piecewise exponential interpolation is considered. The background yield modified by the nuisance parameters then reads as:

$$b_j(\vec{\alpha}) = \left[b_j^0 + \sum_{i=1}^{n_{\text{syst}}} L_{i,j}(\alpha_i) \right] \cdot \left[\prod_{i=1}^{n_{\text{syst}}} E_i(\alpha_i) \right], \quad (12.20)$$

with the linear interpolation term:

$$L_{i,j}(\alpha_i) = \begin{cases} \alpha_i (I_{i,j}^+ - b_j^0) & \alpha_i \geq 0 \\ \alpha_i (b_j^0 - I_{i,j}^-) & \alpha_i \leq 0. \end{cases} \quad (12.21)$$

In there b_j^0 is the nominal background yield and $I_{i,j}^\pm$ the $\pm 1\sigma$ variation of systematic uncertainty i in bin j :

$$\begin{aligned} I_{i,j}^+ &= \eta_i^+ \sigma_{i,j}^+, \\ I_{i,j}^- &= \eta_i^- \sigma_{i,j}^-, \end{aligned} \quad (12.22)$$

with normalisation factors:

$$\begin{aligned}\eta_i^+ &= \sum_{j=1}^{n_{\text{bins}}} b_j^0 / \sum_{j=1}^{n_{\text{bins}}} \sigma_{i,j}^+, \\ \eta_i^- &= \sum_{j=1}^{n_{\text{bins}}} b_j^0 / \sum_{j=1}^{n_{\text{bins}}} \sigma_{i,j}^-.\end{aligned}\tag{12.23}$$

The normalisation factors are introduced such that the histograms assigned to an uncertainty contains only the shape difference. Thus the exponential interpolation used for the shape uncertainty is given as:

$$E_i(\alpha_i) = \begin{cases} \left(\sum_{j=1}^{n_{\text{bins}}} \sigma_{i,j}^+ / \sum_{j=1}^{n_{\text{bins}}} b_j^0 \right)^{\alpha_i} & \alpha_i \geq 0 \\ \left(\sum_{j=1}^{n_{\text{bins}}} b_j^0 / \sum_{j=1}^{n_{\text{bins}}} \sigma_{i,j}^- \right)^{\alpha_i} & \alpha_i \leq 0 \end{cases}\tag{12.24}$$

Each nuisance parameter is constrained from auxiliary measurements, implemented by adding a Gaussian to the likelihood, i.e.:

$$\mathcal{L}_{\text{syst}}(\vec{\alpha}) = \prod_i^{n_{\text{syst}}} \text{Gaussian}(\alpha_i^0 | \alpha_i, 1),\tag{12.25}$$

where $\text{Gaussian}(\alpha_i^0 | \alpha_i, 1)$ denotes a standard normal Gaussian distribution with $\alpha_i^0 = 0$.

The decision whether a systematic uncertainty is treated as shape or normalisation uncertainty is based on a shape comparison via a *Kolmogorov-Smirnov-test* (KS-test) [229, 230]. KS-tests are suitable to distinguish whether two distributions arise from the same underlying p.d.f. or not. Hence, the shape of the nominal analysis of the normalised $m_{\text{T}}^{\text{tot}}$ distribution is compared to the one obtained after variation of a systematic uncertainty. As an example the shapes of the $m_{\text{T}}^{\text{tot}}$ distribution in the STT category is shown in Figure 12.18 for the variations assigned to the TES and tau trigger scale factor uncertainty. As expected the $m_{\text{T}}^{\text{tot}}$ shape is shifted if the TES is shifted up or down by one sigma. The variation of the tau trigger scale factors on the other hand only affects the normalisation. The outcome of the KS-test is the KS-value, which is the probability of the test. KS-values close to one indicate that the shapes are compatible, while KS-values much smaller than one indicate a considerable shape difference. For the considered experimental systematic uncertainties, for which the KS-values in the STT category are given in Table 12.11 for each sample and variation, only the TES uncertainty assigned to real taus shows KS-values different from one. Hence, all nuisance parameters assigned to systematic uncertainties are treated as normalisation uncertainty, except the ones assigned to the real tau component of the TES which is treated as shape systematic.

In total this analysis has 24 nuisance parameters assigned to the considered systematics. Table 12.12 shows a summary indicating also the name assigned to the nuisance parameter in the model for future reference. To simplify the fit model all nuisance parameters assigned to systematic uncertainties which either evaluate to exactly zero or less than 0.1% are dropped.

12.6.5 Treatment of Statistical Uncertainties

Statistical uncertainties can arise from different sources, such as a small amount of simulated events or low event yields in control regions used to estimate a background by a data-driven approach. A nuisance parameter γ_j is assigned to the total MC or CR estimate to each bin. This is a simplified treatment of the statistical uncertainties, as the proper treatment, i.e. assigning a nuisance parameter for each bin and each background component, would lead to several hundred nuisance parameters which is not feasible for the fit. The expected background yield then reads as

$$b_j(\vec{\alpha}, \gamma_j) = \gamma_j b_j(\vec{\alpha}),\tag{12.26}$$

with $b_j(\vec{\alpha})$ as defined in Eq. 12.20. For statistical uncertainties the auxiliary measurement is a Poisson processes, and hence the constraint term can not be modelled by a Gaussian function, but by a Poisson

	$b\bar{b}A \rightarrow \tau_{\text{had}}\tau_{\text{had}}$	$gg \rightarrow A \rightarrow \tau_{\text{had}}\tau_{\text{had}}$	$Z/\gamma^* \rightarrow \tau\tau + \text{jets}$	$W \rightarrow \tau\nu + \text{jets}$	Top	Others
τ -3p down	1.00	1.00	1.00	1.00	1.00	1.00
τ -3p up	1.00	1.00	1.00	1.00	1.00	1.00
τ -ID down	1.00	1.00	1.00	1.00	1.00	1.00
τ -ID up	1.00	1.00	1.00	1.00	1.00	1.00
τ -trigger down	1.00	1.00	1.00	1.00	1.00	1.00
τ -trigger up	1.00	1.00	1.00	1.00	1.00	1.00
JES down	1.00	1.00	1.00	1.00	1.00	1.00
JES up	1.00	1.00	1.00	1.00	1.00	1.00
MC fake-weight down	1.00	1.00	1.00	1.00	1.00	1.00
MC fake-weight up	1.00	1.00	1.00	1.00	1.00	1.00
MET (res.) down	1.00	1.00	1.00	1.00	1.00	1.00
MET (res.) up	1.00	1.00	1.00	1.00	1.00	1.00
MET(scale) down	1.00	1.00	1.00	1.00	1.00	1.00
MET(scale) up	1.00	1.00	1.00	1.00	1.00	1.00
TES fake down	1.00	1.00	1.00	1.00	1.00	1.00
TES fake up	1.00	1.00	1.00	1.00	1.00	1.00
TES real down	0.07	0.04	1.00	1.00	1.00	1.00
TES real up	0.02	0.04	0.97	1.00	1.00	1.00
k-factor $Z/\gamma^* \rightarrow \ell\ell$ down	1.00	1.00	1.00	1.00	1.00	1.00
k-factor $Z/\gamma^* \rightarrow \ell\ell$ up	1.00	1.00	1.00	1.00	1.00	1.00
k-factor $Z/\gamma^* \rightarrow \tau\tau$ down	1.00	1.00	1.00	1.00	1.00	1.00
k-factor $Z/\gamma^* \rightarrow \tau\tau$ up	1.00	1.00	1.00	1.00	1.00	1.00

Table 12.11: KS-values for all systematic uncertainties obtained from a compatibility test of the normalised $m_{\text{T}}^{\text{tot}}$ shape w.r.t. the nominal setup in the STT channel. The signal shown for illustration corresponds to $M_A = 400$ GeV.

nuisance parameter name	systematic uncertainty	type
ATLAS_TAU_TES_REAL	TES (real taus)	shape
ATLAS_TAU_TES_FAKE	TES (fake taus)	norm
ATLAS_MET_RESO	$E_{\text{T}}^{\text{miss}}$ resolution	norm
ATLAS_MET_SCALE	$E_{\text{T}}^{\text{miss}}$ scale	norm
ATLAS_TAU_JES	JES	norm
ATLAS_TAU_ID	tau-ID	norm
ATLAS_TAU_EWFAKES	jet-to-tau fake-rate	norm
ATLAS_TAU_QCDFAKES	fake-factors	norm
TAU_TRIG_HIGH	τ -trigger ($p_{\text{T}} > 100$ GeV)	norm
TAU_TRIG_LOW	τ -trigger ($p_{\text{T}} < 100$ GeV)	norm
TAU_RECO	3-prong reco.	norm
QCD_ROSS	R_{qcd}	norm
QCD_ABCDShape	R_{qcd}	shape
KFACTOR_DYtt	k-factors $Z/\gamma^* \rightarrow \tau\tau$	norm
Q2_X	acceptance of process X	norm
XS_X	cross section of process X	norm

Table 12.12: Summary of nuisance parameters assigned to systematic uncertainties.

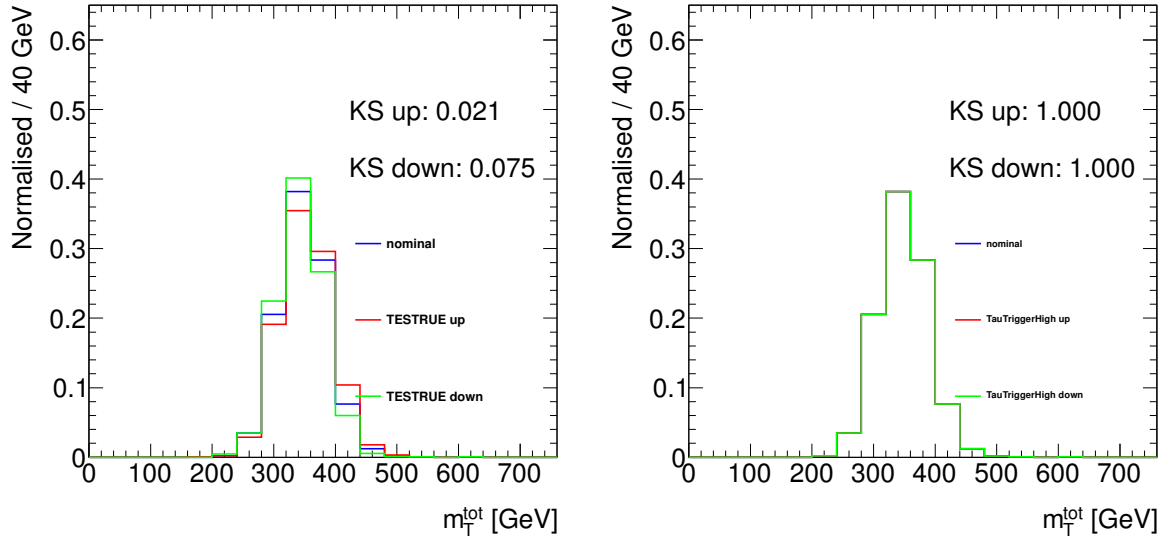


Figure 12.18: Comparison of the shapes of the m_T^{tot} distribution for a $M_A = 400$ GeV Higgs boson produced in association with b-quarks. The blue histogram indicates the nominal distribution while the red and green histograms represent the $\pm 1\sigma$ variation for TES (left) and tau trigger scale factor (right) uncertainty, respectively. The shown KS-values mark the calculated values of the Kolmogorov-Smirnov test comparing the shapes of the nominal setup and the given variation. KS-values close to one indicate that both samples arise from the same p.d.f., while values far from one indicate a shape difference.

distribution with mean $\gamma_j n_j^{\text{MC}}$. However, the number of events, n_j^{MC} , is not necessarily an integer number such that a Poisson constraint term may not be suitable either. Rather a Gamma constraint term is chosen to model the information of the auxiliary measurement:

$$\mathcal{L}_{\text{stat}}(\vec{\gamma}) = \prod_k^{n_{\text{stat}}} \text{Gamma}\left(\gamma_k^j | n_j^{\text{MC}} - 1, \frac{1}{n_j^{\text{MC}}}\right), \quad (12.27)$$

with

$$\text{Gamma}(x|\alpha, \beta) = \frac{\beta^\alpha}{\Gamma(\alpha)} x^{\alpha-1} e^{-\beta x}, \quad (12.28)$$

and the Gamma function defined as $\Gamma(\alpha) = \int_0^\infty x^{\alpha-1} e^{-x} dx$.

The final likelihood function is then given by the product of all terms and reads as

$$\mathcal{L}(\mu, \vec{\theta}) = \mathcal{L}(\mu) \cdot \mathcal{L}_{\text{syst}}(\vec{\alpha}) \cdot \mathcal{L}_{\text{stat}}(\vec{\gamma}). \quad (12.29)$$

12.6.6 Setting Upper Exclusion Limits

As discussed above setting upper limits exploiting the CL_s technique requires the definition of a test statistic. Once systematic uncertainties enter the statistical analysis of the measured data there is in general no single test statistic which yields optimal results. The fact that the signal strength is assumed to be positive, $\mu > 0$, is incorporated in the definition of the test statistic denoted by \tilde{q}_μ :

$$\tilde{q}_\mu = \begin{cases} -2 \ln \left(\frac{\mathcal{L}(\mu, \hat{\theta}(\mu))}{\mathcal{L}(\hat{\mu}, \hat{\theta})} \right) & , 0 \leq \hat{\mu} \leq \mu \\ -2 \ln \left(\frac{\mathcal{L}(\mu, \hat{\theta}(\mu))}{\mathcal{L}(0, \hat{\theta}(0))} \right) & , \hat{\mu} \leq 0 \\ 0 & , \hat{\mu} \geq \mu \end{cases}. \quad (12.30)$$

Here, $\hat{\mu}$ and $\hat{\theta}$ mark the unconditional *maximum likelihood estimators* of the signal strength and nuisance parameters, respectively, obtained from the unconditional fit, i.e. both μ and θ are allowed to float. In the numerator μ is fixed to the tested signal strength and $\hat{\theta}(\mu)$ is the ML estimator of the nuisance parameters for the given μ . If the best fit value of the signal strength becomes negative the denominator is evaluated at $\hat{\mu} = 0$ which recovers the physical interpretation of the test statistic, as the best level of agreement of the data with any model occurs for $\mu = 0$. In case the tested μ is smaller than the ML estimator, $\hat{\mu}$, the test statistic is set to zero. In doing so one avoids to take these values of \tilde{q}_μ into account for the calculation of the p-value, as this case corresponds to a signal+background hypothesis, which predicts less events than observed in data. This is an intrinsic feature of this particular analysis, though. For other statistical interpretations of measured data, like e.g. neutrino oscillations, which may yield lower observed events than predicted by the background model, the \tilde{q}_μ test statistic may not be applicable.

To obtain the upper limit one needs to generate the sampling distribution $f(\tilde{q}_\mu|H_1)$. The probability density functions for \tilde{q}_μ can be obtained either from pseudo data (toy MC) or exploiting *asymptotic approximations*. In order to get a sufficient amount of sampling points in the tails of the test statistic the number of toy MC data sets has to be large, and thus is computationally very expensive. In the presented analysis this will be done for the purpose of validation as outlined in Section 12.6.9. However, the upper limit can be obtained from asymptotic formulae defined in [41]. Their validity is based on *Wilks theorem* [267] and the *Wald approximation* [268]. The derivation of the upper limit is based on an artificial dataset, the *Asimov dataset* [41]. It is generated according to Eq. 12.16 with

$$N_{j,A} = E[N_j] = \mu' s_j(\vec{\theta}) + b_j(\vec{\theta}). \quad (12.31)$$

Here, μ' marks the assumed value of the signal strength, i.e. for the signal+background hypothesis it is assumed $\mu' = 1$, while for the background-only hypothesis μ' is set to zero. The nuisance parameters, $\vec{\theta}$, in Eq. 12.31 correspond to the MLE obtained from the unconditional fit with $\hat{\mu} = \mu'$. In the case of setting upper exclusion limits the Asimov dataset represents the background-only hypothesis. From the p.d.f. of \tilde{q}_μ one can then calculate the upper limit on the excluded signal strength without generating toy MC. Details on the calculation of the upper limit exploiting the asymptotic formulae can be found in [41].

12.6.7 Calculation of Local Discovery Significance

So far the test statistic used to obtain an upper limit has been introduced. If one observes an excess of events w.r.t. the background-only hypothesis in data one wants to obtain the local discovery significance. Local refers to the fact that the signal hypothesis is tested for a single value of the signal strength. For this purpose the definition of the test statistic changes to:

$$q_0 = \begin{cases} -2 \ln \left(\frac{\mathcal{L}(0, \hat{\theta}(0))}{\mathcal{L}(\hat{\mu}, \hat{\theta})} \right) & , \hat{\mu} \geq 0 \\ 0 & , \hat{\mu} < 0 \end{cases}. \quad (12.32)$$

This test statistic reflects that the considered signal can only yield an increase in the observed number of events. Apparently this is not a general assumption (c.f. e.g. neutrino oscillation) but is reliable in the search for new heavy bosons. The p-value is calculated according to Eq. 12.8:

$$p_0 = \int_{q_{0,\text{obs}}}^{\infty} f(q_0|0) dq_0. \quad (12.33)$$

To calculate the p_0 -value one needs to obtain the corresponding p.d.f., $f(q_0|0)$. Analogously to the case of setting upper exclusion limits one can either generate toy MC samples or exploit the asymptotic formulae.

12.6.8 Validation of the Minimisation Procedure

As the fit model is rather complicated it has to be guaranteed that the fit results will be stable and that the minimisation procedure will end up in the global minimum rather than in a local minimum. This has to be done before actually considering the measured data, based on the background model. For this purpose an Asimov dataset is created with all nuisance parameters fixed to their initial value, $\alpha_{i \neq j}$, but one which is under consideration, α_j . The latter is scanned between $\pm 5\sigma$ in steps of $\delta\alpha_j = 0.2\sigma$. For each scan point the unconditional fit is performed with all nuisance parameters being allowed to float, but α_j fixed to $\hat{\alpha}_j = \alpha_j + n\delta\alpha_j$, with $n \in [-25, 25]$ indicating the current step. The scan is performed for a single parameter point in the M_A - $\tan\beta$ -plane chosen as $M_A = 400$ GeV and $\tan\beta = 20$. The obtained negative log-likelihood (NLL) values, $-2 \ln \mathcal{L}$, are shown in Figure 12.19 for the nuisance parameter assigned to the real τ -component of the TES uncertainty (left) and the fake-factor uncertainty (right), respectively.

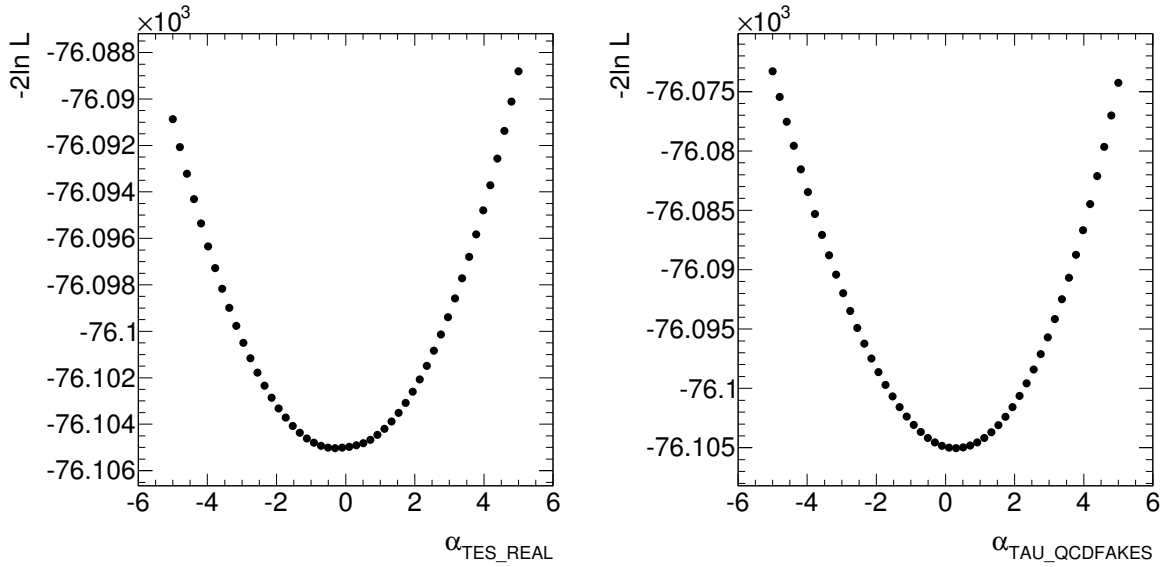


Figure 12.19: Negative log-likelihood values obtained from an unconditional fit with all, but one nuisance parameter free, which is scanned between $\pm 5\sigma$ around the mean value. Left: Nuisance parameter assigned to the real τ component of the TES uncertainty. Right: Nuisance parameter assigned to the fake-factors used to model the QCD multijet background.

It can be observed that only a single minimum is found for each nuisance parameter, which provides confidence in the chosen fit model. The scan of the nuisance parameter assigned to the fake-factor uncertainty further indicated that the best fit value is slightly shifted w.r.t. zero, which indicates that the QCD multijet background is slightly enhanced. However, neither of the scans shows any indication of serious problems of the chosen model, such as double minima or kinks. The NLL scan distributions for the remaining nuisance parameters can be found in Appendix D.3.

12.6.9 Validation using Pseudo Data

The lower limits on $\tan\beta$ in any of the benchmark scenarios are derived exploiting the asymptotic formulae. For the purpose of validation 10000 pseudo experiments (toy MC) have been produced. Each toy MC set is generated under the signal+background hypothesis with μ fixed to $\hat{\mu}$ obtained from a single unconditional fit to the measured data. For each toy MC an unconditional fit is performed from which the best fit values of each nuisance parameter is obtained. For each nuisance parameter, α_i , the *pull*, g_i , defined as:

$$g_i = \frac{\alpha_i^{fit} - \alpha_i^{gen}}{\sigma_i}, \quad (12.34)$$

is calculated, with α_i^{fit} being the best fit value for α_i , α_i^{gen} the mean value of the nuisance parameter used to generate the toy and σ_i the uncertainty on the fitted value of α_i . In case of infinite statistics, i.e. an infinite number of generated pseudo experiments, and α_i being the true value of the i -th nuisance parameter, the pull distribution will be a Gaussian distribution centred at zero with a variance of one. In practice this will not be achievable for all nuisance parameters, as on the one hand one cannot generate an infinite amount of toys, and on the other hand it will not be possible to get an estimate for each systematic uncertainty corresponding to the true value. The aim of this validation step is rather to figure out whether there are any nuisance parameters which are pathologically off. For instance, if an uncertainty is estimated in a too conservative way this may result in a strong over-constraint of the nuisance parameter in the fit, and thus may lead to a bias. Such over-constraints would be revealed in pull distributions with a variance much smaller than one. If one or more backgrounds are not estimated properly the minimisation procedure of the NLL function will address this by shifting the assigned nuisance parameters accordingly to recover the background component resulting in a shift of the mean value of the pull distribution. Figure 12.20 shows the pull distributions for the nuisance parameters assigned to the normalisation of the QCD multijet background obtained from a 2 dimensional sideband method and the jet-to-tau fake-rate. The pseudo experiments have been generated for $M_A = 400$ GeV and $\tan\beta = 20$. In addition a Gaussian fit to the pull distribution is shown for illustration by the black solid line.

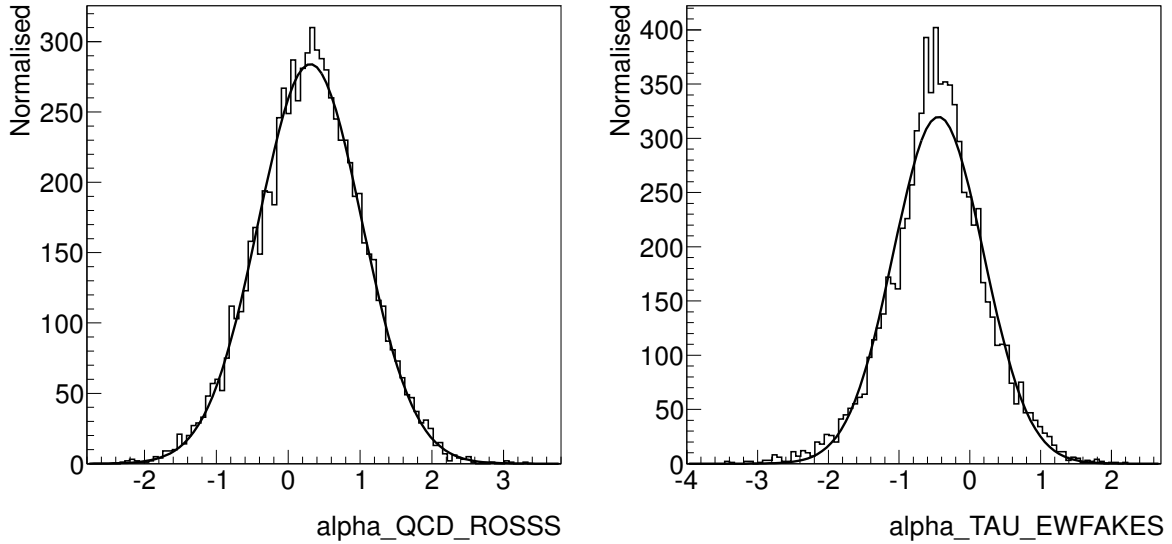


Figure 12.20: Pull distributions of nuisance parameters assigned to the normalisation of the QCD multijet background obtained from a 2D sideband method (left) and the jet-to-tau fake-rate (right) obtained from pseudo data under the H_1 hypothesis with $\mu = \hat{\mu}$ in which $\hat{\mu}$ is obtained from a single fit to data. The considered signal template corresponds to $M_A = 400$ GeV, $\tan\beta = 20$.

A summary of the mean and variance of the pull distributions for all nuisance parameters is provided in Figure 12.21. The green and yellow bands indicate the one and two sigma bands. The mean values of each nuisance parameters are within the one sigma band. Nuisance parameters assigned to the two-dimensional sideband extrapolation method exploited to estimate the QCD multijet background in the DTT category are shifted upwards by roughly 0.5σ , and are slightly over-constrained. This indicates that the QCD multijet contribution is about 2% larger and the uncertainty is estimated conservatively. Neither of them indicates an issue of the fit model. Furthermore, both the shape and the normalisation component ($\alpha_{QCD_ABCDShape}$ and α_{QCD_ROSS}) are shifted in the same direction. This is expected as they are fully correlated, since the offset term in the linear fit applied to R_{qcd} is constrained by the nominal measurement of R_{qcd} . The nuisance parameter assigned to the jet-to-tau fake-rate ($\alpha_{TAU_EWFakes}$) is also slightly constrained and shifted downwards. This indicates that the fit exploits additional information

and reduced the $W(\rightarrow \tau\nu)+\text{jets}$ background. The over-constraint is expected as the uncertainty is derived in a conservative approach.

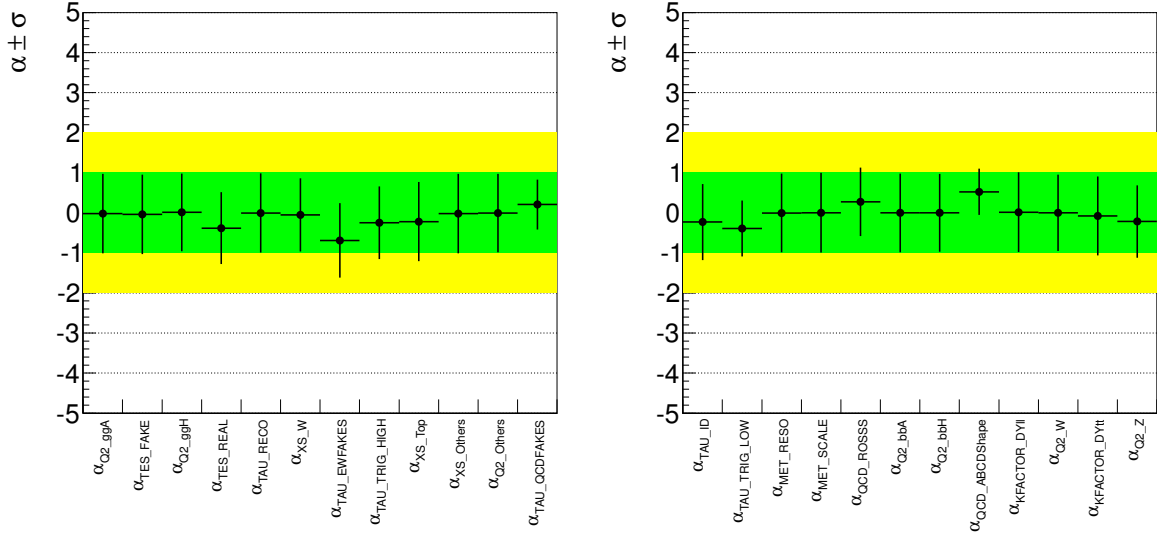


Figure 12.21: Summary of mean and variance of pull distributions of each nuisance parameter obtained from pseudo data generated under the H_1 hypothesis with $\mu = \hat{\mu}$ in which $\hat{\mu}$ is obtained from a single fit to data. The considered signal template corresponds to $M_A = 400 \text{ GeV}$ and $\tan\beta = 20$ assuming the m_h^{max} benchmark scenario.

12.6.10 Exclusion Limit on MSSM Parameter Space

Following the description above an exclusion limit at 95% C.L. is set on the MSSM parameter space assuming the m_h^{max} as well as the $m_h^{\text{mod+}}$ and $m_h^{\text{mod-}}$ benchmark scenario, respectively. Exploiting the asymptotic formulae the excluded signal strength at 95% C.L., μ_{excl} , is calculated for various grid points in the M_A - $\tan\beta$ -plane. The excluded lower value of $\tan\beta$ for a given Higgs mass, M_A , is obtained from a linear interpolation between the grid points, such that the excluded value corresponds to the value for which the excluded signal strength is equal to one. For each grid point the contributions of both the A^0 and H^0 boson are taken into account with their respective mass for the considered $\tan\beta$ value. Furthermore, each production mechanism is considered as a single component in the likelihood function. Figure 12.22 presents the 95% C.L. exclusion limit in the M_A - $\tan\beta$ -plane assuming the m_h^{max} benchmark scenario. The dashed black line indicates the expected limit, while the solid line represents the observed exclusion limit. One and two sigma uncertainties on the expected limit are marked by the green and yellow bands, respectively.

Table 12.13 presents the expected and observed lower bounds on $\tan\beta$ for the considered mass points in the m_h^{max} scenario. The excluded range extends from 13.3 to 55 at 200 GeV and 1 TeV, respectively.

As pointed out previously the m_h^{max} scenario serves as a "standard candle" to allow for comparisons with older results from LEP, Tevatron or the LHC experiments. Hence, to get a relevant interpretation in more realistic models, the limits have been obtained in the $m_h^{\text{mod+}}$ and $m_h^{\text{mod-}}$ benchmark scenarios as well. This is shown in Figure 12.23.

The strategy of determining the exclusion limits is the same as for the m_h^{max} scenario, but the Higgs production cross sections and their uncertainties have been replaced according to the prescription of these scenarios. The obtained limits on $\tan\beta$ for all considered Higgs masses are summarised in Table 12.14 and 12.15 for the $m_h^{\text{mod+}}$ and $m_h^{\text{mod-}}$ benchmark scenario, respectively.

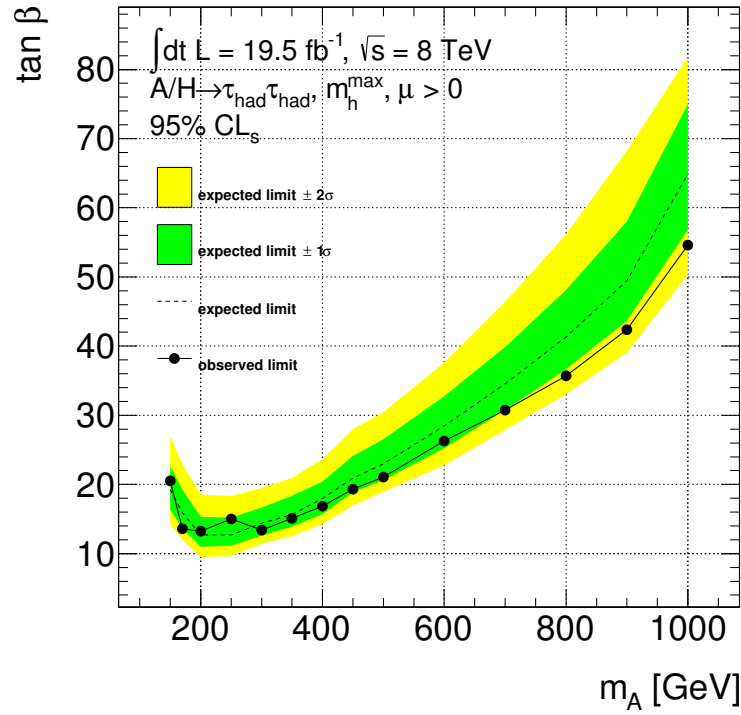


Figure 12.22: Expected (dashed line) and observed (solid line) 95% C.L. exclusion limit on $\tan\beta$ as a function of the Higgs mass, M_A , assuming the m_h^{\max} benchmark scenario. The STT and DTT channels are statistically combined. The green and yellow bands indicate the one and two sigma uncertainties on the expected limit.

M_A [GeV]	Observed	Expected	$+2\sigma$	$+1\sigma$	-1σ	-2σ
150	20.52	19.29	27.06	22.70	16.36	14.34
170	13.61	15.88	22.93	19.25	13.65	12.00
200	13.25	12.67	18.54	15.28	10.99	9.51
250	15.00	12.70	18.32	15.22	11.13	9.65
300	13.38	14.41	19.50	16.68	12.61	11.43
350	15.13	15.66	20.90	18.35	13.92	12.49
400	16.85	17.98	23.66	20.40	15.69	14.26
450	19.30	20.92	27.96	24.11	18.87	16.96
500	21.10	22.99	30.46	26.53	20.62	18.94
600	26.29	28.41	37.61	32.73	25.23	22.76
700	30.73	34.57	46.41	39.88	30.75	27.88
800	35.72	41.32	56.16	48.15	36.64	33.07
900	42.39	49.44	68.26	58.03	43.65	39.07
1000	54.63	64.86	81.78	74.96	56.80	50.36

Table 12.13: Expected and observed 95% C.L. excluded $\tan\beta$ in the m_h^{\max} benchmark scenario for $M_A \in [150, 1000]$ GeV. Uncertainties on the expected limit are quoted as $\pm 1\sigma$ and $\pm 2\sigma$.

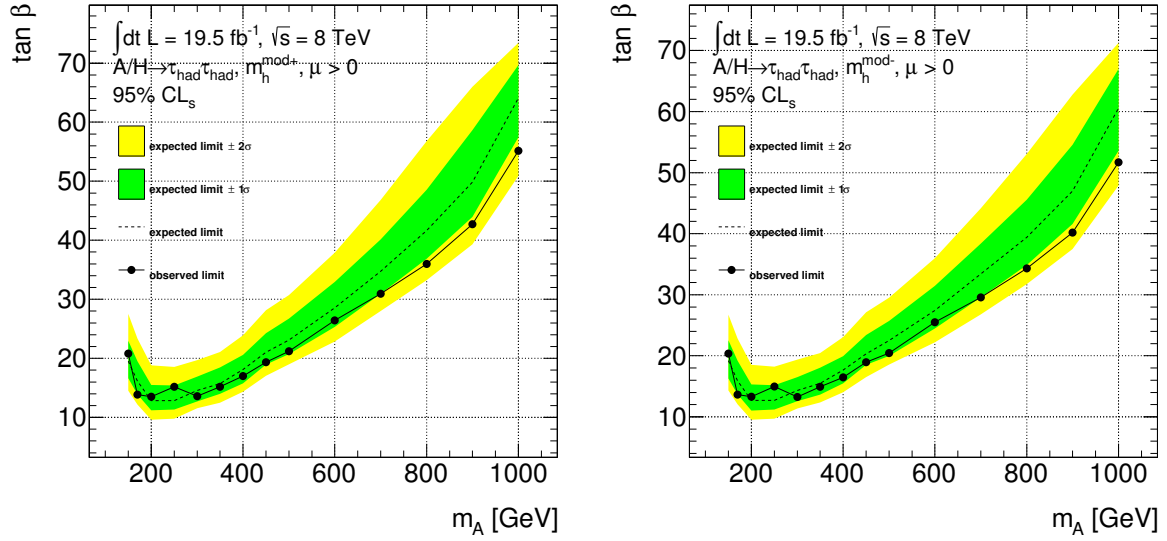


Figure 12.23: Expected (dashed line) and observed (solid line) 95% C.L. exclusion limit on $\tan\beta$ as a function of the Higgs mass, M_A , assuming the $m_h^{\text{mod}+}$ (left) and $m_h^{\text{mod}-}$ (right) benchmark scenario. The STT and DTT channels are statistically combined. The green and yellow bands indicate the one and two sigma uncertainties on the expected limit.

M_A [GeV]	Observed	Expected	+2 σ	+1 σ	-1 σ	-2 σ
150	20.82	19.50	27.51	22.97	16.64	14.53
170	13.86	16.14	23.36	19.50	13.91	12.17
200	13.51	12.82	18.82	15.48	11.18	9.63
250	15.18	12.84	18.56	15.41	11.35	9.81
300	13.58	14.58	19.68	16.93	12.71	11.57
350	15.18	15.71	21.08	18.46	13.97	12.50
400	16.99	18.10	23.89	20.58	15.76	14.34
450	19.36	21.04	28.17	24.27	18.94	17.05
500	21.19	23.12	30.72	26.72	20.72	19.00
600	26.44	28.55	37.88	32.92	25.32	22.83
700	30.92	34.73	46.83	40.16	30.95	28.00
800	35.98	41.65	56.78	48.54	36.89	33.24
900	42.71	49.82	66.00	58.63	43.96	39.30
1000	55.17	64.10	73.43	69.68	57.44	50.92

Table 12.14: Expected and observed 95% C.L. excluded $\tan\beta$ in the $m_h^{\text{mod}+}$ benchmark scenario for $M_A \in [150, 1000]$ GeV. Uncertainties on the expected limit are quoted as $\pm 1\sigma$ and $\pm 2\sigma$.

12.6.11 Upper Exclusion Limit on Generic 2HDM Models

Furthermore, upper limits on the cross section times branching ratio, $\sigma(pp \rightarrow \phi) \times BR(\phi \rightarrow \tau\tau)$, are calculated for a single Higgs boson, ϕ , produced in either association with b-quarks or via gluon-gluon fusion. This will allow an interpretation in almost any possible benchmark scenario in which the kinematics can be assumed to be the same. The 95% C.L. upper limit as a function of the Higgs mass is shown in Figure 12.24. In the past, the search in the fully hadronic final state was categorised in a b-tag

M_A [GeV]	Observed	Expected	$+2\sigma$	$+1\sigma$	-1σ	-2σ
150	20.35	19.22	26.73	22.55	16.31	14.31
170	13.64	15.90	22.83	19.22	13.70	12.04
200	13.29	12.70	18.52	15.29	11.05	9.55
250	14.97	12.71	18.24	15.20	11.19	9.72
300	13.27	14.31	19.36	16.51	12.57	11.39
350	14.91	15.46	20.47	18.05	13.65	12.34
400	16.47	17.64	23.07	19.95	15.50	14.01
450	18.95	20.33	27.12	23.41	18.51	16.49
500	20.47	22.50	29.51	25.71	19.98	18.55
600	25.49	27.43	35.96	31.44	24.47	22.21
700	29.56	33.42	44.15	38.39	29.57	26.80
800	34.31	39.40	53.06	45.57	34.87	31.74
900	40.16	46.99	62.77	54.54	41.57	37.46
1000	51.71	60.57	71.25	66.97	53.56	47.90

Table 12.15: Expected and observed 95% C.L. excluded $\tan\beta$ in the $m_h^{\text{mod-}}$ benchmark scenario for $M_A \in [150, 1000]$ GeV. Uncertainties on the expected limit are quoted as $\pm 1\sigma$ and $\pm 2\sigma$.

and a b-veto channel (c.f. Section 3.2) which lead to different selection efficiencies for the two considered production mechanisms. Since the presented analysis is performed inclusive in the number of additional jets the exclusion limits for both processes are very similar, as already expected due to the similar cut acceptance efficiency (c.f. Figure 12.9).

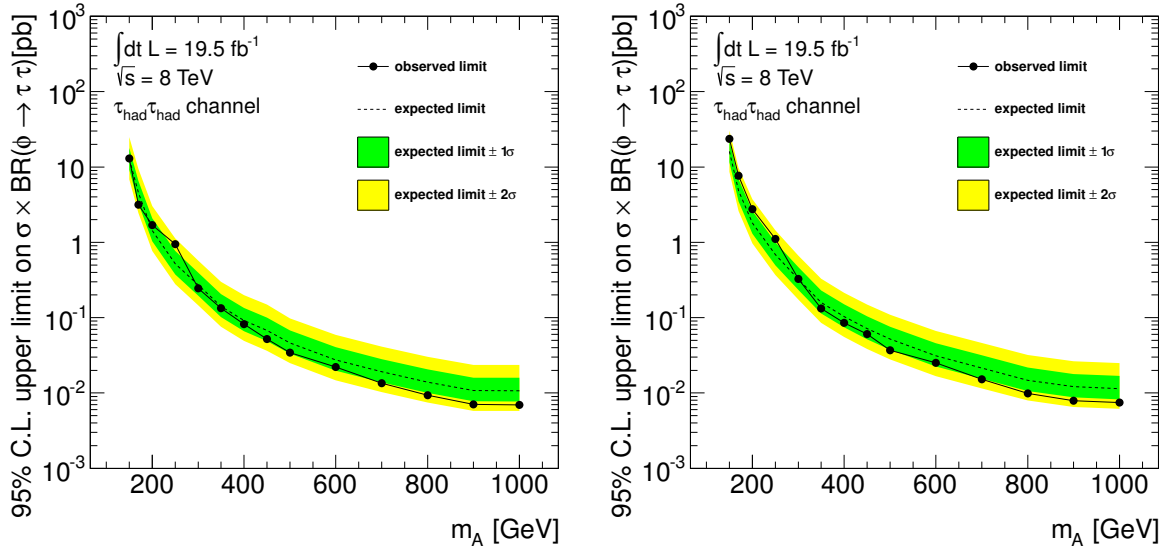


Figure 12.24: Upper limit on production cross section times branching ratio for neutral Higgs bosons produced in association with b-quarks (left) and via gluon-gluon fusion (right) as a function of the tested Higgs mass. The expected 95% C.L. exclusion limit is shown by the dashed line, while the solid line marks the observed limit. These upper bounds can be translated in various benchmark scenarios by rescaling.

Tables 12.16 and 12.17 summarise the numerical values of the excluded cross sections times branch-

ing ratios for each mass point for both production mechanisms.

M_A [GeV]	Observed	Expected	$+2\sigma$	$+1\sigma$	-1σ	-2σ
150	13013	12762	25018	17828	9196	6850
170	3151	4540	9408	6548	3271	2437
200	1691	1433	3022	2079	1032	768.9
250	946.7	520.3	1124	766.6	374.9	279.2
300	245.2	271.2	570.8	395.1	195.4	145.6
350	133.5	140.7	298.9	205.5	101.4	75.53
400	81.91	91.36	198.5	134.9	65.83	49.03
450	51.91	67.70	149.5	100.4	48.78	36.34
500	34.44	46.29	97.74	67.71	33.35	24.84
600	22.10	27.52	58.97	40.45	19.83	14.77
700	13.51	19.19	41.13	28.21	13.83	10.30
800	9.35	13.96	30.27	20.60	10.06	7.49
900	7.07	10.77	23.51	15.93	7.76	5.78
1000	6.97	10.73	23.52	15.89	7.73	5.76

Table 12.16: Numerical values of expected and observed 95% C.L. upper limits on the production cross section times branching ratio, $\sigma(pp \rightarrow \phi) \times BR(\phi \rightarrow \tau\tau)$ for Higgs production in association with b-quarks. One and two sigma bands on the expected limits are given in the last four columns. Numbers are given in fb^{-1} .

The excluded $\sigma(pp \rightarrow \phi) \times BR(\phi \rightarrow \tau\tau)$ range from 13.0 pb to 7.0 fb for b-associated production and from 23.6 pb to 7.5 fb for gluon-gluon fusion in the mass range between 150 GeV and 1 TeV.

12.6.12 Discovery Significance of the MSSM

The discovery significance has been calculated using the test statistic q_0 defined in Eq. 12.32. The local p-value, p_0 , is shown as a function of M_A for $\tan\beta = 20$ in Figure 12.25. The m_h^{max} benchmark scenario has been assumed. The expected p_0 -value is calculated under the signal+background hypothesis, while the observed p_0 -value is obtained from data. The lowest p_0 value is observed for $M_A = 1$ TeV. A p_0 value of 0.11 is observed, which corresponds to a discovery significance of 1.24σ according to Eq. 12.5.

M_A [GeV]	Observed	Expected	+2 σ	+1 σ	-1 σ	-2 σ
150	23623	16075	30497	22113	11583	8628
170	7648	4858.2	9713	6891	3501	2608
200	2751	1809.1	3730	2603	1304	971.0
250	1112	685.7	1445	1000	494.0	368.0
300	325.9	323.4	666.3	467.5	233.0	173.6
350	132.6	158.5	329.0	229.8	114.2	85.05
400	85.43	103.4	214.0	150.0	74.48	55.48
450	60.38	71.53	149.4	104.1	51.54	38.39
500	36.76	51.89	109.2	75.84	37.39	27.85
600	25.06	31.24	66.66	45.89	22.51	16.77
700	15.25	21.49	46.02	31.58	15.48	11.53
800	9.90	14.77	32.00	21.79	10.65	7.93
900	7.88	12.11	26.39	17.90	8.72	6.50
1000	7.49	11.44	25.00	16.91	8.24	6.14

Table 12.17: Numerical values of expected and observed 95% C.L. upper limits on the production cross section times branching ratio, $\sigma(pp \rightarrow \phi) \times BR(\phi \rightarrow \tau\tau)$, for Higgs production via gluon-gluon fusion. One and two sigma bands on the expected limits are given in the last four columns. Numbers are given in fb^{-1} .

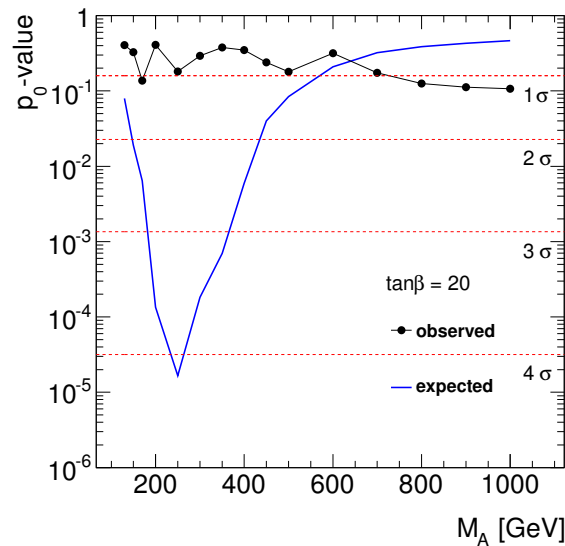


Figure 12.25: Local p_0 -value versus M_A in the m_h^{\max} scenario assuming $\tan\beta = 20$. The observed and expected local p_0 -values are represented by the black and blue lines. The lowest p_0 value is obtained for $M_A = 1 \text{ TeV}$ and evaluates to $p_0 = 0.11$. This corresponds to a local discovery significance of $Z_0 = 1.24 \sigma$. The dashed horizontal lines indicate the discovery significance thresholds.

12.7 Summary and Conclusion

In this chapter a search for heavy neutral Higgs bosons decaying into two tau leptons in the context of the MSSM was presented. It has been outlined in Section 2.5.2 that in the MSSM additional Higgs bosons beside the observed SM-like Higgs boson are likely to be heavy. The branching ratio of the CP-odd Higgs boson decaying into two tau leptons is about 10% over a wide mass range. Hence, given that the fully hadronic final state contributes to about 42%, the presented search is an essential probe for new physics in the context of the Higgs sector.

No deviation of the measured data w.r.t. the SM background model has been observed. Thus exclusion limits are set on the production cross section times branching ratio, $\sigma(pp \rightarrow \phi) \times \text{BR}(\phi \rightarrow \tau\tau)$ featuring the CL_s method. Contrary to previous analyses no dedicated selection of either the gluon-gluon fusion or b-associated production are applied, and hence the excluded production cross sections are similar. For the first time, the investigated mass range was extended up to $M_A = 1 \text{ TeV}$. The excluded production cross section times branching ratio ranges from 13.0 pb (23.6 pb) at 150 GeV to 7.0 fb (7.5 fb) at 1 TeV for the production in association with b-quarks (gluon-gluon production mechanism). The derived limits on the production cross section can then further be interpreted in dedicated benchmark scenarios, which configure the parameter space in the MSSM Higgs sector. The "standard candle" for these benchmark scenarios is the m_h^{max} scenario, which is defined by the CP-odd Higgs mass, M_A , and the ratio of the vacuum expectation values, $\tan\beta$. Lower limits on $\tan\beta$ are obtained for the considered mass hypotheses. The excluded $\tan\beta$ values range from 13.3 at 200 GeV to 55 at 1 TeV. After the discovery of a Higgs boson, new benchmark scenarios have been proposed to open the theoretically accessible parameter space. For the first time these benchmark scenarios have been investigated experimentally. Since the predicted production cross sections and branching ratios at high Higgs masses are similar to the prediction by the m_h^{max} scenario, the exclusion limits on $\tan\beta$ are similar. $\tan\beta$ above 13.5 (13.3) at 200 GeV and 55 (52) at 1 TeV can be excluded at 95% C.L. assuming the $m_h^{\text{mod}+}$ ($m_h^{\text{mod}-}$) scenario.

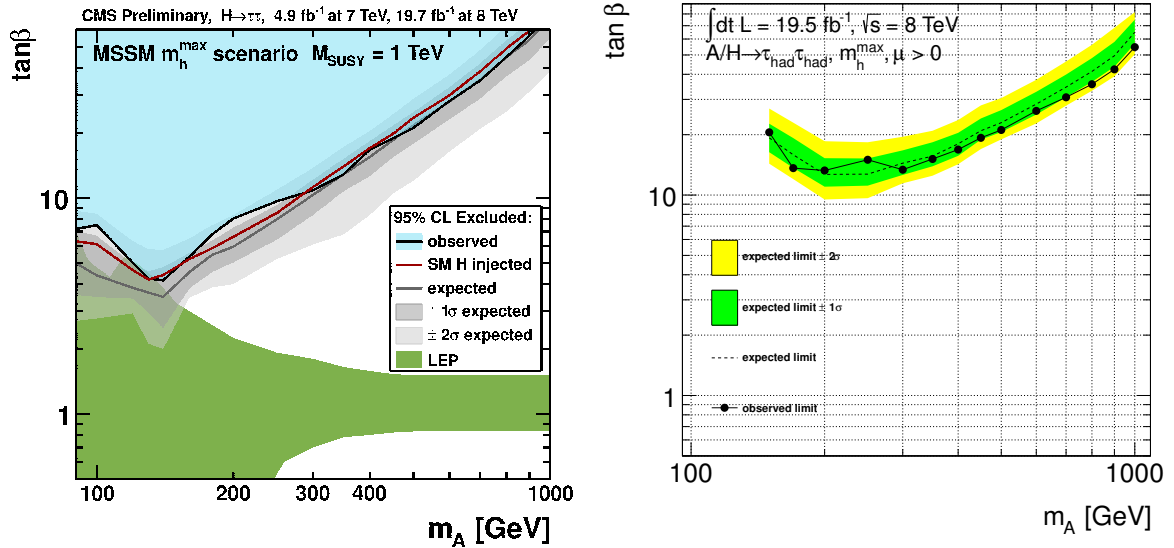


Figure 12.26: 95% C.L. exclusion limit on $\tan\beta$ as a function of the Higgs mass, M_A , assuming the m_h^{max} benchmark scenario obtained by the CMS collaboration [269] (left) and the presented analysis (right). The right plot is the same as shown in Figure 12.22, but with logarithmic axes.

The CMS collaboration has recently published an update on the search for neutral BSM Higgs bosons in the di-tau final state. For the first time they also investigated the fully hadronic final state and extend their considered Higgs boson mass range up to $M_A = 1 \text{ TeV}$. The analysis follows the one presented in Section 3.2. Details on the selection can be found in [269]. Figure 12.26 shows the obtained 95% C.L. exclusion limit in the M_A - $\tan\beta$ -plane by CMS (left) and the presented analysis (right) assuming the

m_h^{\max} scenario. It has to be noted that the CMS result is based on the combination of the leptonic and hadronic final states. Furthermore, it combines the results derived in the analysis of the 7 TeV and 8 TeV proton-proton collision data.

At low mass ($M_A \simeq 130$ GeV) the exclusion by CMS overlaps with the LEP exclusion, and thus this mass hypothesis can be excluded in the m_h^{\max} scenario. The excluded $\tan\beta$ values range from 4.16 at $M_A = 140$ GeV to 44.8 at $M_A = 800$ GeV. Above $M_A = 800$ GeV no exclusion limits are quoted as they are derived to be greater than 60, which is theoretically disfavoured. Apparently, in the low mass regime the result obtained by the CMS collaboration is much stronger than the one presented in this thesis. The main reason for this is the above mentioned combination with the leptonic final states, which dominate the sensitivity there. Furthermore, the presented analysis is optimised for heavy resonances, and thus not expected to be very sensitive in the low mass regime. However, for $M_A \geq 500$ GeV the expected sensitivity becomes similar or even better. In the presented analysis the observed (expected) 95% C.L. exclusion on $\tan\beta$ at $M_A = 500$ GeV is derived to be 21.1 (23.0), while CMS excludes 21.1 (28.8). For even higher mass hypotheses the exclusion on $\tan\beta$ by the presented analysis is between 7% and 25% lower than obtained by the CMS collaboration. The observed improvement of the sensitivity is due to the dedicated high mass selection driven by the STT category. In the future, the obtained results will be combined with the leptonic channels, which will improve the limits in the low mass regime and also slightly in the high mass regime, although the latter is expected to be small, as the sensitivity will be dominated by the fully hadronic final state.

13 Search for Heavy Z' Bosons

This chapter presents a search for heavy neutral gauge bosons decaying in the fully hadronic di-tau channel using proton-proton collision data taken at a centre-of-mass energy of $\sqrt{s} = 8 \text{ TeV}$ by the ATLAS experiment in 2012 corresponding to an integrated luminosity of $\mathcal{L} = 19.5 \text{ fb}^{-1}$. As discussed in detail in Section 2.6, new heavy Z' bosons are predicted by several models extending the SM, and thus addressing various problems of the SM describing nature. It has been pointed out that the coupling of a potential Z' boson to fermions of the third generation might be enhanced, such that the search in the di-tau final state provides an essential probe for these BSM models. The presented analysis has been published in [270], but since then further improvements, in particular concerning the background model, have been implemented and will be presented in the following sections. The dataset used for this analysis as well as the determination of the background model have been discussed extensively in previous chapters and will not be repeated here. First, Section 13.1 will introduce the signal model chosen for this search. In Section 13.2 specifics on the event selection are outlined. Results obtained by the presented analysis are given in Section 13.3 and 13.4. No signal has been found such that the search is interpreted as an upper limit on the production cross section of a Z' boson times the branching ratio of its decay into two tau leptons. This result can be translated into a lower limit on the Z' boson mass in specific models. Here, only the Sequential Standard Model is considered. The statistical analysis and its interpretation will be discussed in Section 13.5. Finally, Section 13.6 will associate the obtained results within the context of the current experimental knowledge of searches for new heavy resonances in the di-tau final state.

13.1 Signal Simulation

Monte Carlo samples for $Z' \rightarrow \tau\tau$ processes assuming the SSM have been produced for five mass points between $M_{Z'} = 250 \text{ GeV}$ and $M_{Z'} = 1250 \text{ GeV}$ in steps of $\Delta M_{Z'} = 250 \text{ GeV}$. These samples are not used to model the signal, but rather serve for the purpose of cross checks. The signal is modelled by reweighting the $Z/\gamma^*(\rightarrow \tau\tau)$ +jets samples according to a Z' signal using NNLO cross sections. This procedure has been developed by the $Z' \rightarrow \ell\ell$ analyses documented in [243, 271]. The advantage of this procedure is that one can model any mass hypothesis without producing full simulation samples for each of it. Furthermore, in principle it allows to consider various signal models besides the SSM by taking the model specific predictions into account in the reweighting. However, the latter is still under investigation and not considered here. Exploiting the reweighting procedure masses between $M_{Z'} = 500 \text{ GeV}$ and $M_{Z'} = 2125 \text{ GeV}$ in steps of $\Delta M_{Z'} = 125 \text{ GeV}$ are considered. Each event receives an event weight which depends on the generated invariant di-tau mass, following the cross section reweighting of the $Z/\gamma^*(\rightarrow \tau\tau)$ +jets background introduced in Section 8.1.1

$$w = \frac{|\mathcal{A}_{Z'}(M_{Z'})|^2}{\mathcal{A}_{Z/\gamma^*}}, \quad (13.1)$$

with the model and mass dependent helicity amplitude, $\mathcal{A}_{Z'}(M_{Z'})$, of the Z' boson and \mathcal{A}_{Z/γ^*} being the helicity amplitude of the SM Drell-Yan production. The latter is a function of the invariant di-tau mass and the quark-flavour of the initial state quarks. The weights as a function of the generated invariant di-tau mass are shown in Figure 13.1 for $M_{Z'} = 1.25 \text{ TeV}$ and $M_{Z'} = 1.75 \text{ TeV}$, respectively. The generated invariant di-tau mass for $Z/\gamma^* \rightarrow \tau\tau$ and the obtained Z' signal template after reweighting for $M_{Z'} = 1.25 \text{ TeV}$ is shown in Figure 13.1 (right).

Figure 13.2 shows the generated invariant di-tau mass obtained from full simulation using PYTHIA and reweighted $Z/\gamma^* \rightarrow \tau\tau$ MC. In here, a Z' mass of $M_{Z'} = 1250 \text{ GeV}$ is assumed. The interference of the signal helicity amplitude with the SM $Z/\gamma^* \rightarrow \tau\tau$ process is not included in the reweighting. It can be seen that in the PYTHIA simulation an arbitrary cut-off at $M_{\tau\tau}^{\text{gen}} = \frac{M_{Z'}^2}{2}$ is applied. This has been taken into account for the reweighted model, but just for the purpose of comparison to the PYTHIA simulated MC. Obviously, this cut-off is not applied in the actual analysis. A good agreement is obtained, although a slight shift of the peak position is observed due to missing spin effects in the reweighting. To validate the applicability of the reweighting procedure the distributions obtained via reweighting and the

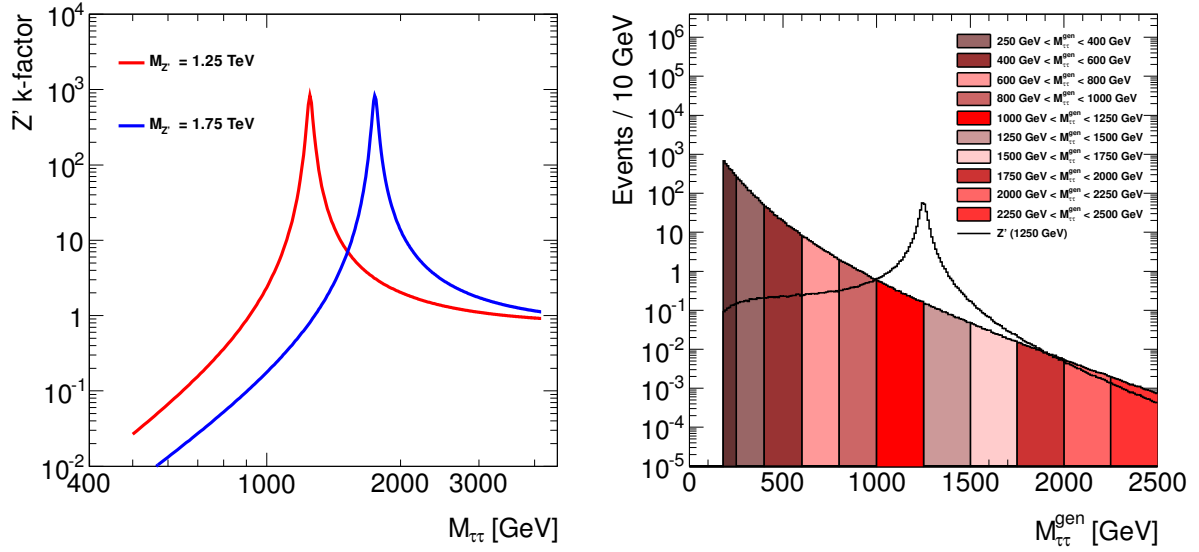


Figure 13.1: Left: Event weights applied to $Z/\gamma^* \rightarrow \tau\tau$ simulated MC to reweight to a Z' signal for $M_{Z'} = 1.25$ TeV (red) and $M_{Z'} = 1.75$ TeV (blue). Right: Generated invariant di-tau mass distribution of various $Z/\gamma^* \rightarrow \tau\tau$ samples and Z' signal template obtained via reweighting (black line) for $M_{Z'} = 1.25$ TeV.

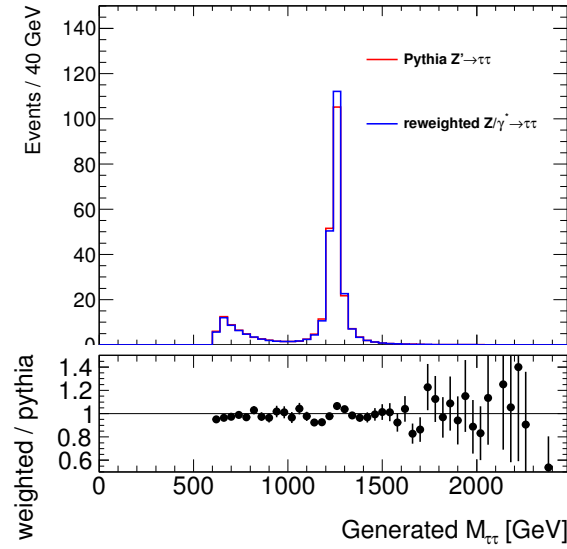


Figure 13.2: Generated invariant di-tau mass distribution in $Z' \rightarrow \tau\tau$ events generated by PYTHIA (red) and obtained from reweighting of $Z/\gamma^* \rightarrow \tau\tau$ events (blue). The bottom plot indicates the ratio between the reweighted model and the direct simulation by PYTHIA.

full simulation are compared. Figure 13.3 shows the generated transverse momentum of the leading and sub-leading tau lepton. The prediction by the Z' simulation and the reweighted $Z/\gamma^* \rightarrow \tau\tau$ agree well within uncertainties.

The visible component, i.e. without taking into account the escaping neutrinos, of the generated transverse momentum of the two tau leptons associated to the $Z'/Z/\gamma^*$ decay is shown in Figure 13.4. A clear discrepancy can be observed, which is due to missing corrections for polarisation affects. However, the considered p_T spectrum is softer in the reweighted signal model, such that the derived limit can be seen as a slightly conservative estimate.

Apparently, the softer generated visible p_T spectrum of the two tau leptons will lead to a shift in

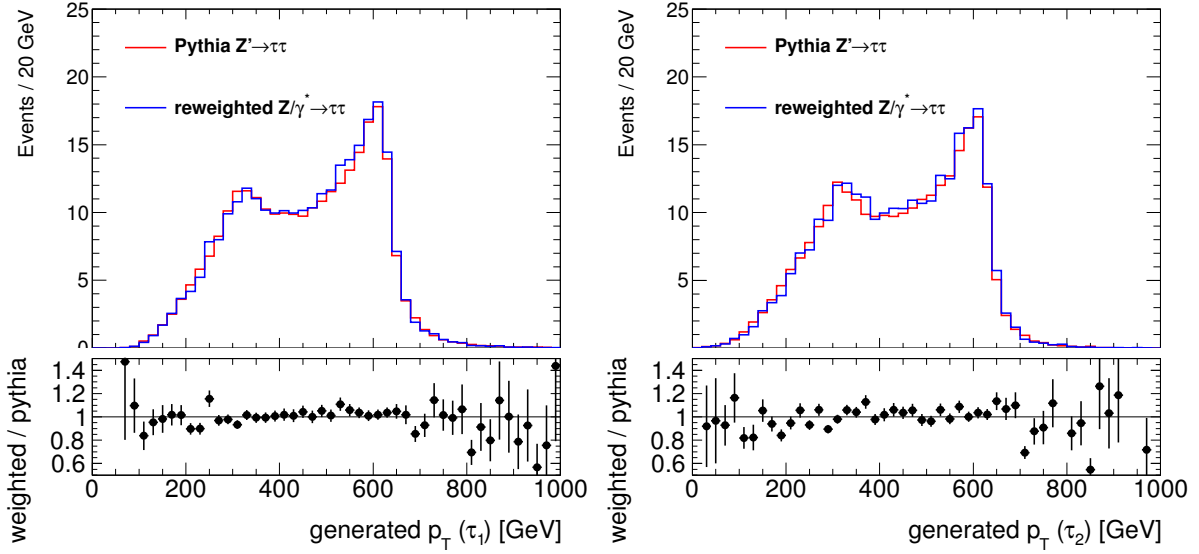


Figure 13.3: Generated p_T distribution of the leading (left) and sub-leading (right) tau lepton in $Z' \rightarrow \tau\tau$ events generated by PYTHIA (red) and obtained from reweighting of $Z/\gamma^* \rightarrow \tau\tau$ events (blue). The bottom plot indicates the ratio between the reweighted model and the direct simulation by PYTHIA.

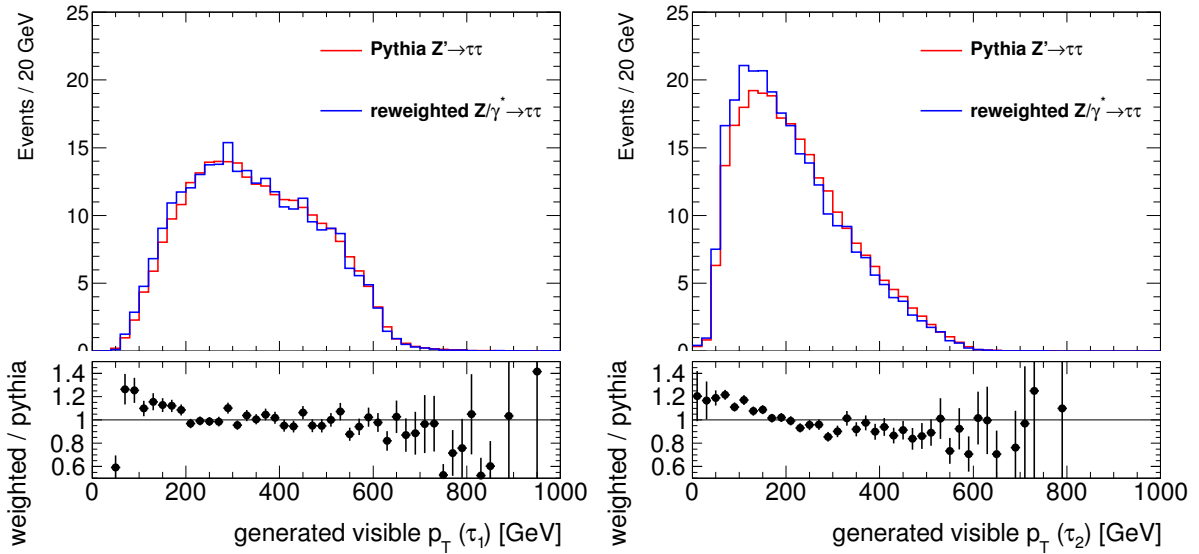


Figure 13.4: Generated visible p_T distribution of the leading (left) and sub-leading (right) tau lepton in $Z' \rightarrow \tau\tau$ events generated by PYTHIA (red) and obtained from reweighting of $Z/\gamma^* \rightarrow \tau\tau$ events (blue). The bottom plot indicates the ratio between the reweighted model and the direct simulation by PYTHIA.

the reconstructed tau- p_T distribution. This is shown in Figure 13.5, which presents the p_T of the reconstructed tau candidates geometrically matched to the generated tau leptons. In particular for the sub-leading tau candidate a shift towards lower p_T emerges in the reweighted signal template.

13.2 Event Selection

The event selection follows the search for MSSM Higgs bosons presented in Section 12.2. As pointed out there, the DTT category is only sensitive for low mass resonances. Since the exclusion limit of Z' bosons

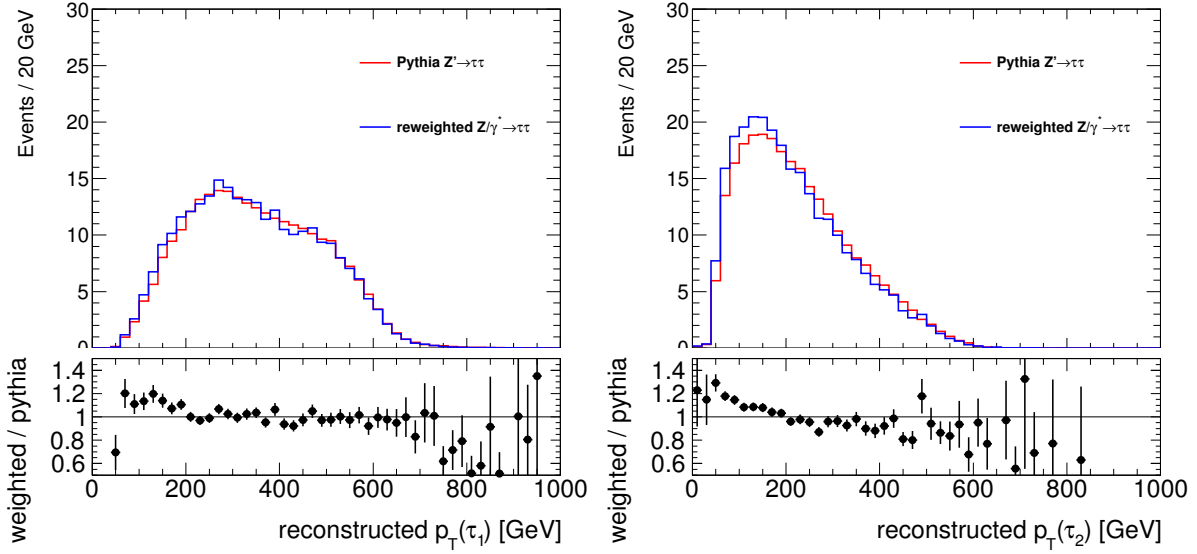


Figure 13.5: Reconstructed p_T distribution of the leading (left) and sub-leading (right) tau lepton in $Z' \rightarrow \tau\tau$ events generated by PYTHIA (red) and obtained from reweighting of $Z/\gamma^* \rightarrow \tau\tau$ events (blue). The bottom plot indicates the ratio between the reweighted model and the direct simulation by PYTHIA.

from ATLAS was found to be $M_{Z'} > 1.4 \text{ TeV}$ analysing 2011 proton-proton collision data [112] (c.f. Section 3.3), the DTT channel will not contribute to the sensitivity, and hence is dropped. Only the STT selection is considered. At very high mass the number of background events is expected to be very small, such that a shape based analysis is not suitable anymore. Hence, a cut-and-count experiment is performed in which only the event yields are considered. To provide an optimal sensitivity an additional threshold on m_T^{tot} is introduced on top of the selection outlined in Section 12.2.1. Obviously, this threshold depends on the tested mass hypothesis, and thus is tuned as a function of tested Z' mass. The figure of merit for this optimisation is the expected excluded cross section times branching ratio. Historically a Bayesian approach is considered in the search of heavy new resonances, which is exploited here as well. Details will be outlined in Section 13.5. It has been shown in previous analyses [234] that the obtained exclusion limits are compatible with CL_s limits obtained from pseudo experiments. The optimal threshold is chosen to be the one for which the lowest excluded cross section times branching ratio is obtained. The upper limits have been calculated for various Z' boson masses between $M_{Z'} = 500 \text{ GeV}$ and $M_{Z'} = 2125 \text{ GeV}$ in steps of $\Delta M_{Z'} = 125 \text{ GeV}$, scanning the threshold on the total transverse mass between $m_T^{\text{tot}} = 300 \text{ GeV}$ and $m_T^{\text{tot}} = 1100 \text{ GeV}$ in steps of $\Delta m_T^{\text{tot}} = 50 \text{ GeV}$. Figure 13.6 shows the obtained excluded signal strength in the $M_{Z'} - M_T^{\text{tot,threshold}}$ -plane. In addition to the scanned m_T^{tot} thresholds the expected sensitivity after the preselection is added for $m_T^{\text{tot}} = 160 \text{ GeV}$. To improve readability the excluded signal strength is scaled by 1000 and an arbitrary cut-off at $\mu = 200$ has been applied, but not considered for obtaining the optimal thresholds on m_T^{tot} .

As the tested mass becomes higher the optimal threshold increases up to $M_{Z'} = 850 \text{ GeV}$. For heavier Z' bosons the optimal threshold stays constant as the expected background yields become negligible and the expected signal rate increases. Table 13.1 summarises the m_T^{tot} thresholds for various mass ranges used in the statistical interpretation of the data.

Mass Point, $M_{Z'}$ [GeV]	500	625	750	875	1000	1125–1250	≥ 1375
m_T^{tot} [GeV]	>350	>400	>500	>550	>600	>700	>850

Table 13.1: Mass dependent lower thresholds on m_T^{tot} .

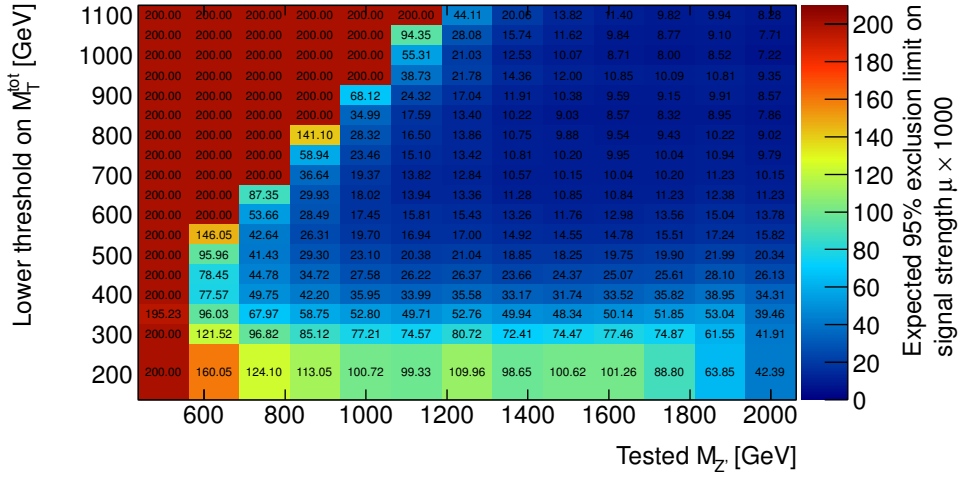


Figure 13.6: Obtained exclusion limit on the signal strength parameter for various thresholds on m_T^{tot} as a function of the tested Z' mass. For readability the signal strength is scaled by 1000 and an arbitrary cut-off at $\mu = 200$ is applied.

13.3 Results

The combined background model has already been validated in Section 12.4, and thus will not be repeated here. The number of selected events following the discussed event selection is summarised in Table 13.2.

As already discussed in Section 12.4.1 the dominant background after the event selection excluding the m_T^{tot} thresholds arises from QCD multijet production. One feature of the definition of m_T^{tot} is that the multijet distributions drops very steeply, and hence the multijet component is significantly reduced after the m_T^{tot} thresholds are applied. Already at very low thresholds ($m_T^{\text{tot}} \simeq 300$ GeV) it is comparable to the irreducible $Z/\gamma^*(\rightarrow \tau\tau)$ +jets expectation. Increasing the thresholds further leads to $Z/\gamma^*(\rightarrow \tau\tau)$ +jets being the dominant background component. With the considered thresholds being near the exclusion limit all backgrounds, except the $Z/\gamma^*(\rightarrow \tau\tau)$ +jets contribute only little. Above $m_T^{\text{tot}} = 700$ GeV no data events are observed, while from the SM processes 3.9 ± 0.2 events are expected. Assuming Poisson statistics the probability of such an expectation and observation is of the order of 2.1σ .

The distribution of the total transverse mass after the full event selection excluding the threshold on m_T^{tot} is shown in Figure 13.7. As expected a signal of a new heavy resonance would occur at very high m_T^{tot} as indicated by the shown signal hypotheses. No excess is observed in data, and hence exclusion limits on the cross section times branching ratio are derived.

13.4 Systematic Uncertainties

Systematic uncertainties introduced in Chapter 11 are applied in the search for Z' bosons accordingly. Contrary to the search for heavy neutral MSSM Higgs bosons discussed in the previous chapter, the treatment in this analysis is rather simple as the statistical interpretation of the data is based on event counts rather than on the mass shape. However, since the thresholds on m_T^{tot} depends on the signal mass hypothesis the systematic uncertainties have to be evaluated for each of them. Table 13.3 summarises the systematic uncertainties after the threshold of $m_T^{\text{tot}} > 850$ GeV is applied. The shown signal corresponds to a Z' boson with $M_{Z'} = 1750$ GeV. For completeness the expected event yields including their statistical uncertainty are shown in the first row. Corresponding tables for all other mass hypotheses considered for setting upper limits on the production cross section times branching ratio are given in Appendix E.2, outlining the expected signal yields as well.

cut	Z' (1750 GeV)	multijet	$Z/\gamma^* \rightarrow \tau\tau + \text{jets}$	$W \rightarrow \tau\nu + \text{jets}$	Top	Others	SM Total	Data
Preselection	10.0 ± 0.2	621.5 ± 5.6	266.6 ± 17.1	63.7 ± 1.4	22.1 ± 1.9	0.6 ± 0.3	974.5 ± 18.2	1017
Opposite signs	9.5 ± 0.2	322.0 ± 4.0	261.0 ± 17.1	52.9 ± 1.3	19.2 ± 1.9	0.6 ± 0.3	655.7 ± 17.7	690
$\Delta\phi(\tau_1, \tau_2) > 2.7$	9.3 ± 0.2	216.3 ± 3.3	113.7 ± 2.4	34.1 ± 1.0	10.2 ± 1.4	0.1 ± 0.0	374.4 ± 4.5	373
$m_T^{\text{tot}} > 160 \text{ GeV}$	9.3 ± 0.2	216.3 ± 3.3	113.7 ± 2.4	34.1 ± 1.0	10.2 ± 1.4	0.1 ± 0.0	374.4 ± 4.5	373
$m_T^{\text{tot}} > 300 \text{ GeV}$	9.3 ± 0.2	105.5 ± 2.4	102.7 ± 2.2	28.1 ± 0.9	7.1 ± 1.2	0.0 ± 0.0	243.4 ± 3.6	237
$m_T^{\text{tot}} > 350 \text{ GeV}$	9.1 ± 0.2	45.6 ± 1.6	63.4 ± 1.3	17.7 ± 0.7	5.0 ± 1.0	0.0 ± 0.0	131.8 ± 2.4	124
$m_T^{\text{tot}} > 400 \text{ GeV}$	8.8 ± 0.2	20.2 ± 1.1	36.7 ± 0.7	9.9 ± 0.5	2.0 ± 0.5	0.0 ± 0.0	68.9 ± 1.5	59
$m_T^{\text{tot}} > 450 \text{ GeV}$	8.5 ± 0.2	9.8 ± 0.8	22.1 ± 0.4	5.6 ± 0.3	1.2 ± 0.4	0.0 ± 0.0	38.8 ± 1.0	31
$m_T^{\text{tot}} > 500 \text{ GeV}$	8.2 ± 0.2	4.6 ± 0.5	14.1 ± 0.3	3.5 ± 0.2	0.6 ± 0.2	0.0 ± 0.0	22.8 ± 0.7	20
$m_T^{\text{tot}} > 550 \text{ GeV}$	7.8 ± 0.2	2.7 ± 0.4	9.0 ± 0.2	1.9 ± 0.1	0.4 ± 0.2	0.0 ± 0.0	13.9 ± 0.5	12
$m_T^{\text{tot}} > 600 \text{ GeV}$	7.5 ± 0.2	1.8 ± 0.3	6.0 ± 0.1	1.1 ± 0.1	0.1 ± 0.1	0.0 ± 0.0	9.0 ± 0.3	5
$m_T^{\text{tot}} > 650 \text{ GeV}$	7.1 ± 0.2	1.0 ± 0.2	4.1 ± 0.1	0.7 ± 0.1	0.1 ± 0.0	0.0 ± 0.0	5.9 ± 0.3	3
$m_T^{\text{tot}} > 700 \text{ GeV}$	6.7 ± 0.2	0.6 ± 0.2	2.8 ± 0.0	0.5 ± 0.1	0.0 ± 0.0	0.0 ± 0.0	3.9 ± 0.2	0
$m_T^{\text{tot}} > 750 \text{ GeV}$	6.3 ± 0.1	0.4 ± 0.2	1.9 ± 0.0	0.3 ± 0.0	0.0 ± 0.0	0.0 ± 0.0	2.8 ± 0.2	0
$m_T^{\text{tot}} > 800 \text{ GeV}$	5.9 ± 0.1	0.3 ± 0.1	1.4 ± 0.0	0.2 ± 0.0	0.0 ± 0.0	0.0 ± 0.0	1.9 ± 0.1	0
$m_T^{\text{tot}} > 850 \text{ GeV}$	5.5 ± 0.1	0.1 ± 0.1	1.0 ± 0.0	0.2 ± 0.0	0.0 ± 0.0	0.0 ± 0.0	1.3 ± 0.1	0
$m_T^{\text{tot}} > 900 \text{ GeV}$	5.1 ± 0.1	0.1 ± 0.1	0.7 ± 0.0	0.1 ± 0.0	0.0 ± 0.0	0.0 ± 0.0	1.0 ± 0.1	0
$m_T^{\text{tot}} > 950 \text{ GeV}$	4.7 ± 0.1	0.1 ± 0.1	0.5 ± 0.0	0.1 ± 0.0	0.0 ± 0.0	0.0 ± 0.0	0.7 ± 0.1	0
$m_T^{\text{tot}} > 1000 \text{ GeV}$	4.3 ± 0.1	0.1 ± 0.1	0.4 ± 0.0	0.1 ± 0.0	0.0 ± 0.0	0.0 ± 0.0	0.5 ± 0.1	0
$m_T^{\text{tot}} > 1050 \text{ GeV}$	3.9 ± 0.1	0.1 ± 0.1	0.3 ± 0.0	0.1 ± 0.0	0.0 ± 0.0	0.0 ± 0.0	0.4 ± 0.1	0
$m_T^{\text{tot}} > 1100 \text{ GeV}$	3.5 ± 0.1	0.0 ± 0.0	0.2 ± 0.0	0.1 ± 0.0	0.0 ± 0.0	0.0 ± 0.0	0.3 ± 0.0	0

Table 13.2: Expected and observed event yields from SM processes and a Z' signal with $M_{Z'} = 1.75 \text{ TeV}$ assuming the SSM after various selection criteria in the Z' event selection. The pre-selection includes the event cleaning, trigger decision and light lepton vetoes. Backgrounds from light lepton fakes or di-boson processes are summarised as *Others*.

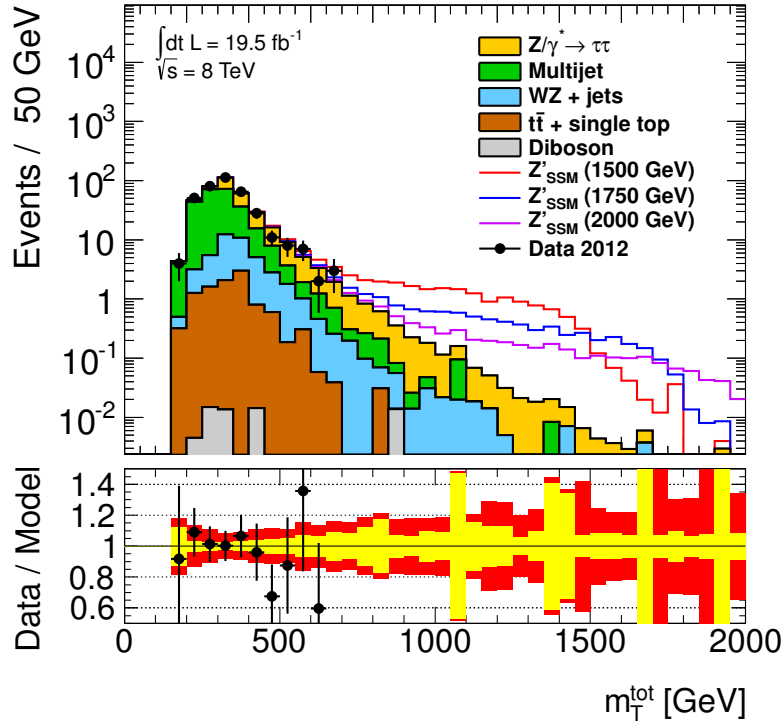


Figure 13.7: Total transverse mass distribution after the full event selection excluding the final m_T^{tot} threshold. Contributions from SM processes and various Z' signals ($M_{Z'} = 1.5 \text{ TeV}$ (red), $M_{Z'} = 1.75 \text{ TeV}$ (blue), $M_{Z'} = 2.0 \text{ TeV}$ (violet)) are stacked. The observed data is overlaid. Statistical and systematic uncertainties on the SM expectation are indicated by the yellow and red bands in the ratio, respectively.

	$Z/\gamma^* \rightarrow \tau\tau + \text{jets}$	multijet	W/Z + jets	Top	Di-boson	SM Total	$Z' (1750\text{GeV})$
Expected Events	0.99 ± 0.02	0.14 ± 0.08	0.18 ± 0.03	< 0.01	0.01 ± 0.01	1.32 ± 0.09	5.48 ± 0.14
Th. cross section	$\begin{smallmatrix} 8.6 \\ -6.2 \end{smallmatrix}$	—	± 27.5	± 12.1	± 5.0	$\begin{smallmatrix} 10.3 \\ -8.5 \end{smallmatrix}$	—
Multijet fake-factor	—	± 16.4	—	—	—	± 1.7	—
MC fake-weight	$\begin{smallmatrix} 2.7 \\ -0.5 \end{smallmatrix}$	—	$\begin{smallmatrix} 17.4 \\ -15.1 \end{smallmatrix}$	$\begin{smallmatrix} 60.3 \\ -35.7 \end{smallmatrix}$	± 60.0	$\begin{smallmatrix} 1.0 \\ -3.1 \end{smallmatrix}$	< 1
JES	—	—	—	—	—	—	—
MET (res.)	< 1	—	-1.9	—	—	< 1	—
MET(scale)	< 1	—	$\begin{smallmatrix} -1.9 \\ 0.0 \end{smallmatrix}$	—	—	< 1	—
τ -3p	± 4.3	—	± 1.5	± 16.3	—	± 3.4	± 4.0
τ -ID	± 7.5	—	± 3.2	± 3.6	± 2.4	± 6.1	± 7.4
τ -trigger	± 10.0	—	< 1	—	—	± 7.6	± 10.0
TES	$\begin{smallmatrix} 12.0 \\ -9.8 \end{smallmatrix}$	—	$\begin{smallmatrix} 4.0 \\ -5.0 \end{smallmatrix}$	$\begin{smallmatrix} -0.0 \\ -33.1 \end{smallmatrix}$	—	$\begin{smallmatrix} 9.5 \\ -8.0 \end{smallmatrix}$	± 2.3

Table 13.3: Summary of the total expected event yields and its statistical uncertainty and detector and theory related systematic uncertainties. Quoted numbers correspond to $M_{Z'} = 1750 \text{ GeV}$, i.e. $m_T^{\text{tot}} > 850 \text{ GeV}$. Uncertainties are given in %. Entries marked by — are either non applicable or evaluate to zero. W/Z+jets accounts for all contributions from W/Z decays into leptons accompanied by additional jets. The uncertainty on the total SM prediction can be lower than the relative uncertainty from individual contributions due to weights of the expected event yields.

13.5 Statistical Interpretation

Since no excess in data is observed upper limits on the production cross section times branching ratio for a heavy Z' boson decaying to two tau leptons in the fully hadronic final state are derived. This section will introduce the concept of Bayesian statistics to derive upper limits. First the Bayesian approach is discussed, followed by the introduction of the likelihood model. Finally, the obtained exclusion limits will be presented in Section 13.5.3.

13.5.1 Bayesian Approach

Historically, the Bayesian approach is considered in the statistical analysis of searches for heavy Z' bosons. It is based on the *posterior probability*, $P(H|\vec{x})$, i.e. the probability of the hypothesis H being true given the observed data, \vec{x} . The upper limit is derived from a *credibility* (or Bayesian) interval. Following the notation of Section 12.6.1, the signal is parametrised by the signal strength parameter, μ , such that the credibility interval can be written as:

$$\alpha = \int_0^\mu d\mu P(\mu|N), \quad (13.2)$$

where N is the number of observed data events. If one wants to set an upper limit at 95% C.L.¹⁴ one needs to find the value of μ such that $\alpha = 0.95$. The difficulty in this approach is that the posterior probability depends on the *prior probability*, $P(\vec{x}|H)$, which describes the knowledge or *degree of belief* about the input parameters of the model before accomplishing the measurement. The full prior probability can be written as

$$P(\vec{x}|H) = P(H)\pi(\vec{\theta}|H), \quad (13.3)$$

where $\vec{\theta}$ describes the internal parameters¹⁵ of the hypothesis H , $\pi(\vec{\theta}|H)$ the normalised p.d.f. of the parameters $\vec{\theta}$ and $P(H)$ the overall prior probability. The prior and posterior probability are related by *Bayes' theorem* [265]:

$$P(H|\vec{x}) = \frac{\int L(\vec{x}|\vec{\theta}, H)P(H)\pi(\vec{\theta}|H)d\theta}{P(\vec{x})}. \quad (13.4)$$

¹⁴C.L. in the Bayesian approach stands for credibility level, rather than for confidence level as in the Frequentist approach

¹⁵Here $\vec{\theta}$ includes both the signal strength parameter and the nuisance parameters.

In there, $P(\vec{x})$ is the *marginal likelihood* or *evidence* defined as

$$P(\vec{x}) = \int L(\vec{x}|\vec{\theta})\pi(\vec{\theta})d\vec{\theta}, \quad (13.5)$$

with $L(\vec{x}|\vec{\theta})$ being the likelihood function, i.e. the joint p.d.f. for the data under the assumption of the internal parameters, $\vec{\theta}$. The structure of the likelihood function will be outlined below. As discussed in Section 12.6.1 two hypotheses are considered, the background-only and the signal+background hypothesis. Which hypothesis is preferred by the data can be quantified using the *Bayes factor*, B , which describes the ratio of the posterior probabilities of the two hypotheses under investigation if the overall prior probabilities, $P(H_0)$ and $P(H_1)$, are equal

$$B = \frac{\int L(\vec{x}|\vec{\theta}_0, H_0)\pi(\vec{\theta}_0|H_0)d\vec{\theta}_0}{\int L(\vec{x}|\vec{\theta}_1, H_1)\pi(\vec{\theta}_1|H_1)d\vec{\theta}_1}. \quad (13.6)$$

Thus the Bayes factor is independent of the overall prior probabilities, but still requires the knowledge of the prior probabilities of the internal parameters.

13.5.2 Likelihood Model

The likelihood considered to parametrise the model depends on the signal strength and the nuisance parameters¹⁶, $\vec{\theta}$

$$\mathcal{L}(\mu, \vec{\theta}) = \text{Pois}(N|\mu s + b) \prod_i^{n_{\text{nuis}}} \text{Gaussian}(\theta_i, 0, 1). \quad (13.7)$$

For the nuisance parameters a Gaussian prior p.d.f. is assumed, while a uniform prior is taken on μ . The uniform prior states that each value of μ is equally likely between $\pm\infty$. It has been shown in previous analyses that the impact of the choice of the prior p.d.f. is small [112], and thus no other prior p.d.f.s are considered here.

13.5.3 Exclusion Limits

Making use of the aforementioned procedure 95% credibility upper limits on the production cross section times branching ratio, $\sigma(pp \rightarrow Z') \times \text{BR}(Z' \rightarrow \tau\tau)$, are set for various tested Z' boson mass hypotheses ranging from $M_{Z'} = 500 \text{ GeV}$ to $M_{Z'} = 2125 \text{ GeV}$. The *Bayesian Analysis Toolkit* (BAT) [110] is featured to sample the posterior p.d.f. utilising the *Markov Chain Monte Carlo* (MCMC) [173] technique to carry out the integration over the internal parameters (c.f. Eq. 13.4). Figure 13.8 shows the derived observed and expected limits and its corresponding one and two sigma bands. Theory predictions and their corresponding uncertainties on $\sigma(pp \rightarrow Z') \times \text{BR}(Z' \rightarrow \tau\tau)$ within the SSM are represented by the blue lines. From this, a lower limit on Z' boson mass can be extracted. From the search in the fully hadronic di-tau final state Z' bosons with masses less than 1.9 TeV can be excluded. As discussed above, the generated visible and thus the reconstructed tau p_T is softer in the reweighted signal templates due to mis-modelling effects of the polarisation. Hence, the derived limit has to be considered as slightly conservative. It has been shown in a previous search for Z' bosons decaying to two tau leptons using 2011 proton-proton collision data [234] that the obtained limit varies about 50 GeV considering pure $V - A$ and $V + A$ couplings.

13.6 Summary and Conclusion

In this chapter a search for heavy neutral Z' bosons decaying to two tau leptons has been presented. In this thesis only the fully hadronic final state is considered. As shown by previous searches for new heavy

¹⁶In the discussion above $\vec{\theta}$ was used for the internal set of parameters describing a model, while here it symbolises the nuisance parameters only.

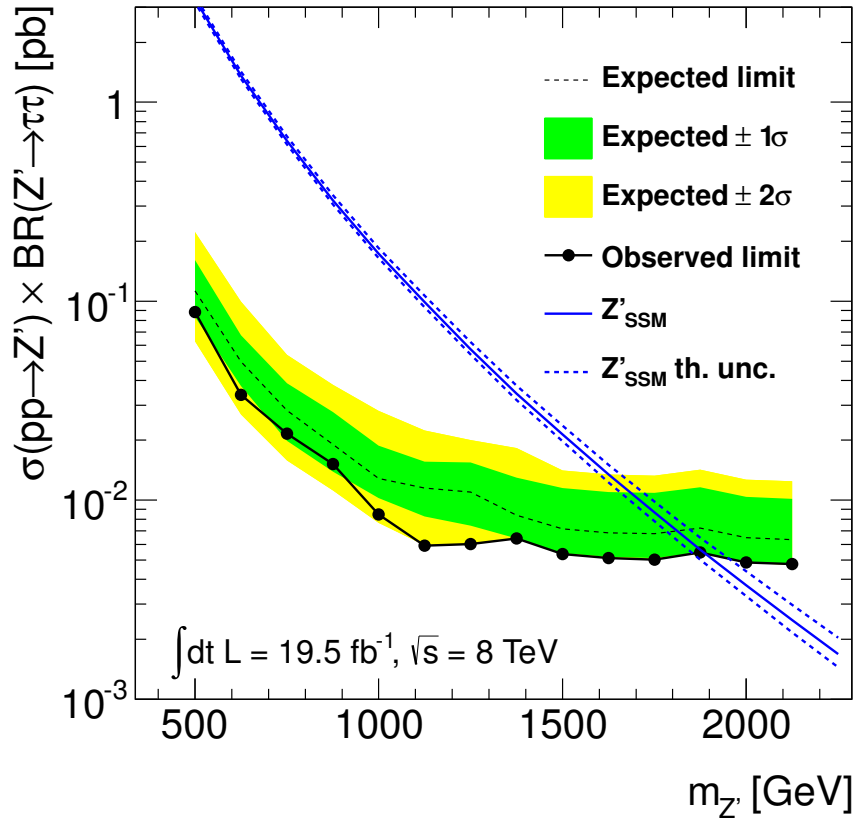


Figure 13.8: 95% credibility Bayesian upper limit on the production cross section times branching ratio, $\sigma(pp \rightarrow Z') \times \text{BR}(Z' \rightarrow \tau\tau)$, as a function of the tested Z' boson mass. The observed and expected limit is presented by the black solid and dashed line. The one and two sigma bands are shown in green and yellow, respectively. The theory prediction on $\sigma(pp \rightarrow Z') \times \text{BR}(Z' \rightarrow \tau\tau)$ in the Sequential Standard Model and its uncertainty are shown in blue. The observed and expected upper limits on the Z' mass in the SSM is derived to 1.9 TeV and 1.8 TeV, respectively.

neutral resonances, this final state dominates the sensitivity of such an analysis. The full proton-proton collision data taken by the ATLAS detector in 2012 has been analysed. Due to changes in the trigger configuration in the early period of data-taking, period A had to be discarded such that the analysed amount of data corresponds to an integrated luminosity of $\mathcal{L} = 19.5 \text{ fb}^{-1}$. Since no deviations from the SM prediction have been observed, an upper limit on the production cross section times branching ratio, $\sigma(pp \rightarrow Z') \times \text{BR}(Z' \rightarrow \tau\tau)$, has been derived following the Bayesian approach. The obtained excluded cross section reaches from 88.2 fb at $M_{Z'} = 500 \text{ GeV}$ to 4.8 fb at $M_{Z'} = 2125 \text{ GeV}$. This can be interpreted in the context of the Sequential Standard Model as an upper limit on the Z' mass. Z' bosons with a mass less than 1.9 TeV can be excluded at 95% credibility. Similar searches have been performed before by the ATLAS and CMS experiments at the LHC, as well as by the Tevatron experiments, as discussed in Section 3.4. Both the ATLAS and CMS collaborations could exclude Z' bosons with masses less than 1.4 TeV [112, 272] exploiting the 2011 dataset of proton-proton collisions.

This result therefore marks the strongest exclusion limit in the search for new heavy neutral resonances in the di-tau final state so far. This result will be improved even further once the remaining leptonic final states, i.e. $Z' \rightarrow \tau_e \tau_{\text{had}}$, $Z' \rightarrow \tau_\mu \tau_{\text{had}}$ and $Z' \rightarrow \tau_e \tau_\mu$, are combined with the presented search. Furthermore, the sensitivity of the fully hadronic channel could be increased considering e.g. additional triggers in the event selections, such as jet triggers which do not suffer from isolation inefficiencies at very high tau- p_T , or by recovering track reconstruction inefficiencies by considering 2-prong tau decays.

These issues are currently subject to further analyses performed by the ATLAS collaboration and might be included in the final ATLAS publication result expected in early 2014. Finally, in the future one would like to interpret the result in an extended theoretical context rather than just considering the SSM. In particular the interpretation within models with enhanced couplings to third generation fermions, like technicolour models (c.f. Section 2.6), is of great interest. This is currently under development and expected for the final publication by the ATLAS collaboration.

14 Summary and Outlook

The discovery of a new heavy resonance would be a direct indicator of new physics beyond the Standard Model. Thereby, the di-tau final state of such a particle is preferred by several models, and thus is an important ingredient in the physics program of the ATLAS experiment. The exclusion limits on the production cross section times branching ratio, $\sigma(pp \rightarrow X) \times \text{BR}(X \rightarrow \tau\tau)$, obtained in this thesis are hence a vital input for the phenomenology of BSM physics.

In this work searches for new heavy neutral Higgs bosons in the context of the MSSM and heavy Z' bosons decaying into two tau leptons, which both further decay hadronically, were presented. For this purpose the proton-proton collision data collected by the ATLAS detector in 2012 at a centre-of-mass energy of $\sqrt{s} = 8 \text{ TeV}$ was analysed. The amount of data corresponds to an integrated luminosity of $\mathcal{L} = 19.5 \text{ fb}^{-1}$. Both searches do not show a significant excess above the expectation of the SM. Hence exclusion limits on $\sigma(pp \rightarrow X) \times \text{BR}(X \rightarrow \tau\tau)$ were derived. These results can further be interpreted in the context of various phenomenological models. The search for heavy neutral Higgs bosons was analysed in the context of the m_h^{max} benchmark scenario, which serves as a standard candle for BSM Higgs searches and allows for comparison w.r.t. previous results obtained by the LEP, Tevatron and LHC experiments. After the discovery of a Higgs boson by the ATLAS and CMS collaborations in 2012, the benchmark scenarios for the MSSM Higgs sector have been refined and considered accordingly in this thesis. For the first time experimental results were obtained in the $m_h^{\text{mod}+}$ and $m_h^{\text{mod}-}$ scenarios. The derived exclusion limits in the high mass regime outperform previous combined results by one order of magnitude in the excluded cross section. This then relates to an improvement of about a factor of two in $\tan\beta$.

Furthermore, the data was analysed w.r.t. heavy Z' bosons. These will couple preferably to fermions of the third generation depending on the model. Hence the analysis of the di-tau final state is crucial to discover new particles proposed by these models. In this work, only the Sequential Standard Model was considered. From the obtained exclusion limit on $\sigma(pp \rightarrow Z') \times \text{BR}(Z' \rightarrow \tau\tau)$ a lower limit on the Z' mass could be derived.

A crucial ingredient for physics analyses involving tau leptons are outstanding tau trigger and identification algorithms. In this thesis a new triggering algorithm for tau leptons based on multivariate classifiers has been developed and became the default tau trigger for 2012 data-taking. These new algorithms significantly improve the performance of accepting tau leptons, while rejecting fakes originating from quark or gluon initiated jets, w.r.t. the previous cut-based approach. Further, they serve for the purpose of harmonisation between the trigger and offline selection.

Moreover, the log-likelihood based tau identification algorithm for offline selection of tau leptons has been optimised in 2011 and exploited by several physics analyses. Within this context, a new framework was developed, which was featured for subsequent optimisations, i.e. used for the tuning of data-taking in 2012 at $\sqrt{s} = 8 \text{ TeV}$.

An updated event selection w.r.t. the previous study analysing the 2011 proton-proton collision dataset was introduced for the search of heavy neutral Higgs bosons in the fully hadronic di-tau final state. A refined trigger selection allows for dedicated background estimation techniques, which provide a valid prescription up to high transverse momenta, and thus large invariant mass. In particular the background arising from jet fakes in QCD multijet events dominates in the lighter mass regime and is not negligible at high mass. Given the overwhelming production cross section of multijet events at a proton-proton collider, this background has to be extracted from data. Unlike the two-dimensional sideband extrapolation method used previously, the newly introduced tau-ID fake-factor method does not suffer from low amount of data events in the control region at high transverse momenta, and thus allows a proper description. In the low mass regime however, this approach is not applicable anymore due to the di-tau trigger requirement. An updated two-dimensional sideband extrapolation method has been introduced by considering low- E_T^{miss} and high- E_T^{miss} control regions, which unlike the construction of the control region based on the tau identification criteria, does not suffer from correlations between the phase space regions. Both techniques provide an outstanding model of the complicated QCD multijet background. In the high mass regime, the irreducible $Z/\gamma^*(\rightarrow \tau\tau)$ +jets background becomes dominant.

Since no signal-free control region can be constructed in order to extract this background component from data, new dedicated high-mass Z/γ^* MC simulated samples have been produced. These samples provide a sufficient amount of generated events to extract a reliable background template. The remaining background is dominated by $W(\rightarrow \tau\nu)+\text{jets}$ events, in which the leading tau is faked by the recoiling jet. Usually these backgrounds suffer from an improper model of the predicted fake-rate and from low statistics. Both issues were addressed by the novel fake-weight technique, in which the jet-to-tau fake-rate is measured in a $W(\rightarrow \mu\nu)+\text{jets}$ control region. This measurement provides a proper model of the jet-to-tau fake-rate, and thus corrects both the shapes and the normalisation of this background. Contrary to other analyses, like the SM $H \rightarrow \tau_{\text{had}}\tau_{\text{had}}$ search, the fake-rate is not applied as a correction factor, but rather the tau identification requirement in MC is dropped and an event weight according to the fake-rate is applied. This artificially increases the amount of available MC simulated proton-proton collision events, and thus improves the statistical significance of the derived template. These background estimation techniques permit to extend the analysis up to $M_A = 1 \text{ TeV}$, while previous analyses only considered $M_A \leq 500 \text{ GeV}$. The novel background estimation techniques and event categorisation have significantly improved the sensitivity of this search. Compared to the combined result of the 2011 data analysis, the excluded cross section is about one order of magnitude lower, which results in an excluded $\tan\beta$ of about a factor of two smaller than previously. The CMS collaboration has also updated their search combining all di-tau final states and the proton-proton collision data collected at centre-of-mass energies of $\sqrt{s} = 7 \text{ TeV}$ and $\sqrt{s} = 8 \text{ TeV}$. Apparently, in the low mass regime ($M_A \lesssim 400 \text{ GeV}$) the sensitivity is higher due to the combination with the leptonic final states. However, at high invariant masses, the presented analysis outperforms the combined CMS result, both in the observed and expected exclusion limit. The improvement is achieved by the single-tau triggered category, which is designed for high performance at high mass. Depending on the mass hypothesis, the excluded $\tan\beta$ value in the m_h^{max} scenario is between 7% to 25% lower than quoted by the CMS collaboration. This will even further improve once the combination with the leptonic final states is performed. The latter will also address the low mass sensitivity. In summary the presented result has a significant impact in the understanding and the constraint of BSM physics.

In addition to the search for BSM Higgs bosons, the data was analysed in the context of heavy Z' bosons. The strategy of the event selection and background estimation follows the previously discussed Higgs search. However, since the considered mass range is extended up to $M_{Z'} \leq 2125 \text{ GeV}$, the procedure of the derivation of the exclusion limits had to be revisited. The analysis does not rely on the mass shape, but rather an optimisation of the event selection was done by introducing thresholds on m_T^{tot} depending on the considered mass hypothesis. The optimisation was performed based on the expected sensitivity. From this measurement exclusion limits on $\sigma(pp \rightarrow Z') \times \text{BR}(Z' \rightarrow \tau\tau)$ were derived and interpreted as a lower bound on $M_{Z'}$ of 1.9 TeV in the SSM. Future analyses will consider further phenomenological models, where in particular models with enhanced couplings to fermions of the third generation, like TC2, are of great interest. For this purpose, the newly introduced concept of the signal modelling based on reweighting of $Z/\gamma^* \rightarrow \tau\tau$ simulation events will simplify these analyses. The remaining difficulty lies in the correct prediction of the polarisation of the tau leptons, which is currently under investigation. As pointed out in Section 11.1.2 the tau reconstruction at high transverse momenta suffers from track merging effects, which distort the reconstruction of three-prong tau candidates. In the future one might be able to improve the signal acceptance by also taking two track tau candidates into account. However, this will not only increase the signal acceptance, but also the background acceptance. Hence the expected sensitivity has to be derived and compared to the current approach.

Even though no evidence for new heavy neutral resonances predicted by several theories has been observed so far, the investigated models are nevertheless of strong interest for physics beyond the Standard Model. The available parameter space has been highly restricted by the presented analyses, but still many regions are not covered yet. Thus the search for new particles in the di-tau final state will continue in run-II, which promises higher luminosities and centre-of-mass energies. This opens the window for BSM Higgs bosons and/or Z' bosons to be discovered. There may be heavier resonances which the current analysis is not sensitive to due to the lower centre-of-mass energy and the restricted amount of

high transverse momentum data. However, it might also be that no evidence in the di-tau final state will be observed, and thus at some point the phenomenologically interesting allowed parameter space can be closed. At this point the physics program has to be extended and a larger variety of final states has to be considered. In the case of MSSM Higgs bosons it might be that the Higgs sector realised in nature has a decreased coupling strength to tau leptons, e.g. in τ -phobic or light stau benchmark scenarios. Consequently other decay modes, such as e.g. final states involving SUSY particles, or double-Higgs decays need to be considered. There are still many other analyses in parallel which can give a hint, such as e.g. charged Higgs or direct SUSY searches. In the case of Z' bosons the allowed parameter space could be restricted further w.r.t. previous analyses. However, the interpretation of the obtained results within theoretical models with enhanced couplings to tau leptons is still pending. The search will be continued in run-II, which will allow to extend the investigated mass regime to $M_{Z'} > 2 \text{ TeV}$. If no signal will show up in the di-tau final state, it might do in the di-electron or di-muon final states, which are sensitive to even higher masses. This would be the case if the couplings of the Z' boson to fermions is universal. To conclude there is still a wide allowed parameter space where new resonances may hide, and the continuation of searches in the di-tau final state are crucial to obtain a better understanding of particle physics and nature.

A Auxiliary Information for the Theoretical Framework

In this appendix some auxiliary information for the theoretical framework used to describe high energy physics are given. In A.1 the gamma matrices are introduced. The construction of a field theory is briefly outlined in Appendix A.2 using the example of QED.

A.1 Gamma Matrices

The *gamma* or *Dirac matrices* are an important ingredient in the mathematical description of field theories in the context of high energy physics. They are a set of 4×4 matrices generating a matrix representation of the Clifford algebra. They are given as (in the Dirac representation):

$$\gamma^0 = \begin{pmatrix} \mathbb{1} & \mathbf{0} \\ \mathbf{0} & -\mathbb{1} \end{pmatrix} \quad \gamma^i = \begin{pmatrix} \mathbf{0} & \sigma^i \\ \sigma^i & \mathbf{0} \end{pmatrix}, \quad (\text{A.1})$$

with $\mathbb{1}$ being the 2×2 identity matrix, $\mathbf{0}$ being a 2×2 matrix of zeros and σ^i the *Pauli matrices*:

$$\sigma^1 = \begin{pmatrix} 0 & 1 \\ 1 & 0 \end{pmatrix} \quad \sigma^2 = \begin{pmatrix} 0 & -i \\ i & 0 \end{pmatrix} \quad \sigma^3 = \begin{pmatrix} 1 & 0 \\ 0 & -1 \end{pmatrix}. \quad (\text{A.2})$$

Furthermore, the following anticommuting relation is guaranteed:

$$\{\gamma^\mu, \gamma^\nu\} = \gamma^\mu \gamma^\nu + \gamma^\nu \gamma^\mu = 2\eta^{\mu\nu} \mathbb{1}_{4 \times 4}, \quad (\text{A.3})$$

with $\eta^{\mu\nu}$ being the *Minkowski metric* with signature $(+ - - -)$.

A.2 Quantum Electrodynamics

Quantum Electrodynamics (QED) shall serve as an example how to create a quantum field theory by the principle of local gauge invariance. The simplest choice of a gauge group is a phase transformation as described by $U(1)$ symmetry. Let's assume the Lagrange density, \mathcal{L} , of a free Dirac field, ψ , with mass, m :

$$\mathcal{L} = \bar{\psi}(i\gamma_\mu \partial^\mu - m)\psi, \quad (\text{A.4})$$

in which γ_μ denotes the vector of Pauli matrices and $\partial^\mu = (\frac{\partial}{\partial t}, -\vec{\nabla})$ the derivative. This Lagrangian is invariant under a global phase transformation of the field, ψ :

$$\begin{aligned} \psi &\xrightarrow{U(1)} \psi' = e^{-ie\theta} \psi, \\ \mathcal{L} &\xrightarrow{U(1)} \mathcal{L}' = \bar{\psi} e^{ie\theta} (i\gamma_\mu \partial^\mu - m) e^{-ie\theta} \psi = \mathcal{L}. \end{aligned} \quad (\text{A.5})$$

Following the gauge principle the Lagrangian has to be invariant under local gauge transformation, i.e. the phase θ is a function of the space-time point, $x^\mu = (t, \vec{x})$ ($\theta \rightarrow \theta(x^\mu)$). It can be shown that the Lagrangian is not invariant under such a transformation. Thus one needs to introduce a new gauge field, $A^\mu = (V, \vec{A})$, with the known scalar potential, V , and the vector potential¹⁷ \vec{A} , by minimal coupling. This leads to the covariant derivative, D^μ :

$$\partial^\mu \rightarrow D^\mu = \partial^\mu + ieA^\mu. \quad (\text{A.6})$$

Simultaneously the gauge field, A^μ , has to transform as:

$$A^\mu \rightarrow A'^\mu = A^\mu - \frac{1}{e} \partial^\mu \theta(x^\mu). \quad (\text{A.7})$$

¹⁷The scalar and vector potential can be associated to the electric, \vec{E} , and magnetic, \vec{B} , field by $\vec{E}(x^\mu) = -\vec{\nabla}V(x^\mu) - \frac{\partial \vec{A}(x^\mu)}{\partial t}$, and $\vec{B}(x^\mu) = \vec{\nabla} \times \vec{A}(x^\mu)$.

It can be shown that by introducing those transformations the Lagrangian stays invariant, which leads to:

$$\mathcal{L}' = \mathcal{L} + ie\bar{\psi}\gamma_\mu A^\mu \psi. \quad (\text{A.8})$$

Hence, the application of the gauge principle introduces interaction terms, \mathcal{L}_{int} , which account for the coupling of the gauge field, A^μ , to the matter field, ψ , with a coupling strength of e . This is the theoretical formulation of electromagnetic interaction, i.e. the coupling of the photon to charged particles. Since the electromagnetic field tensor, $F^{\mu\nu} = \partial^\mu A^\nu - \partial^\nu A^\mu$, is invariant under local phase transformation, the Lagrange density:

$$\mathcal{L}_A = -\frac{1}{4}F_{\mu\nu}F^{\mu\nu} \quad (\text{A.9})$$

is invariant as well. The local gauge invariance together with the kinematic term for A_μ leads to QED with the Lagrange density, \mathcal{L}_{QED} :

$$\mathcal{L}_{QED} = \bar{\psi}(i\gamma_\mu D^\mu - m)\psi - \frac{1}{4}F_{\mu\nu}F^{\mu\nu}. \quad (\text{A.10})$$

Following the Hamiltonian principle the equations of motion can be extracted from the Lagrange density, known as the *Maxwell equations*:

$$\partial_\nu F^{\nu\mu} = j^\mu. \quad (\text{A.11})$$

The current, $j^\mu = (\rho, \vec{j})$, with ρ being the charge density and \vec{j} the current density, is given as $j^\mu = e\bar{\psi}\gamma^\mu\psi$.

Explicit mass terms for the gauge bosons, $\mathcal{L}_m = \frac{1}{2}m^2 A_\mu A^\mu$, break the gauge invariance. Hence, the mass of the gauge bosons have to be introduced in a different way, e.g. by spontaneous symmetry breaking as explained in detail in Section 2.3.

QED is one of the most successful theories tested by dozens of experiments, which all agree with its predictions up to high precision. Thus the principle of local gauge invariance has become an important procedure in construction of theories, and motivates its application for description of other interaction as discussed in Chapter 2.

B Auxiliary Information for the Tau Trigger Optimisation

This appendix provides additional information for the multivariate-based tau trigger at EF stage. Identification variables used by the BDT and LLH algorithm are summarised for 1- and 3-prong EF tau candidates in Figures B.1 and B.2, respectively.

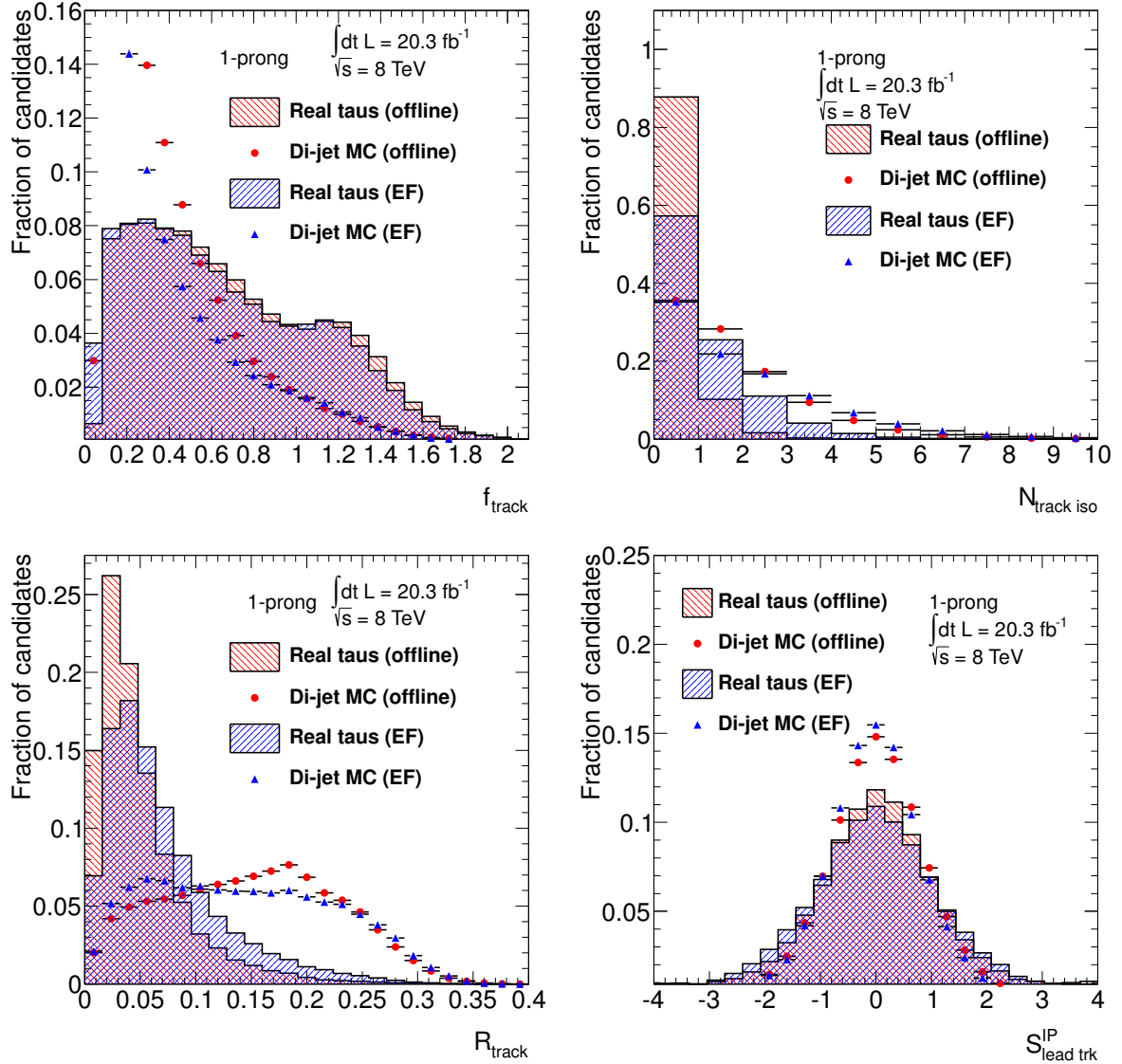


Figure B.1: Tau identification variables for one-prong tau candidates used by the multivariate EF trigger algorithms. The signal templates for EF tau candidates are shown by the blue histograms, while the background templates, extracted from di-jet MC simulation, are depicted by the blue triangles. For comparison the corresponding distributions of the offline reconstructed tau candidates are shown in red.

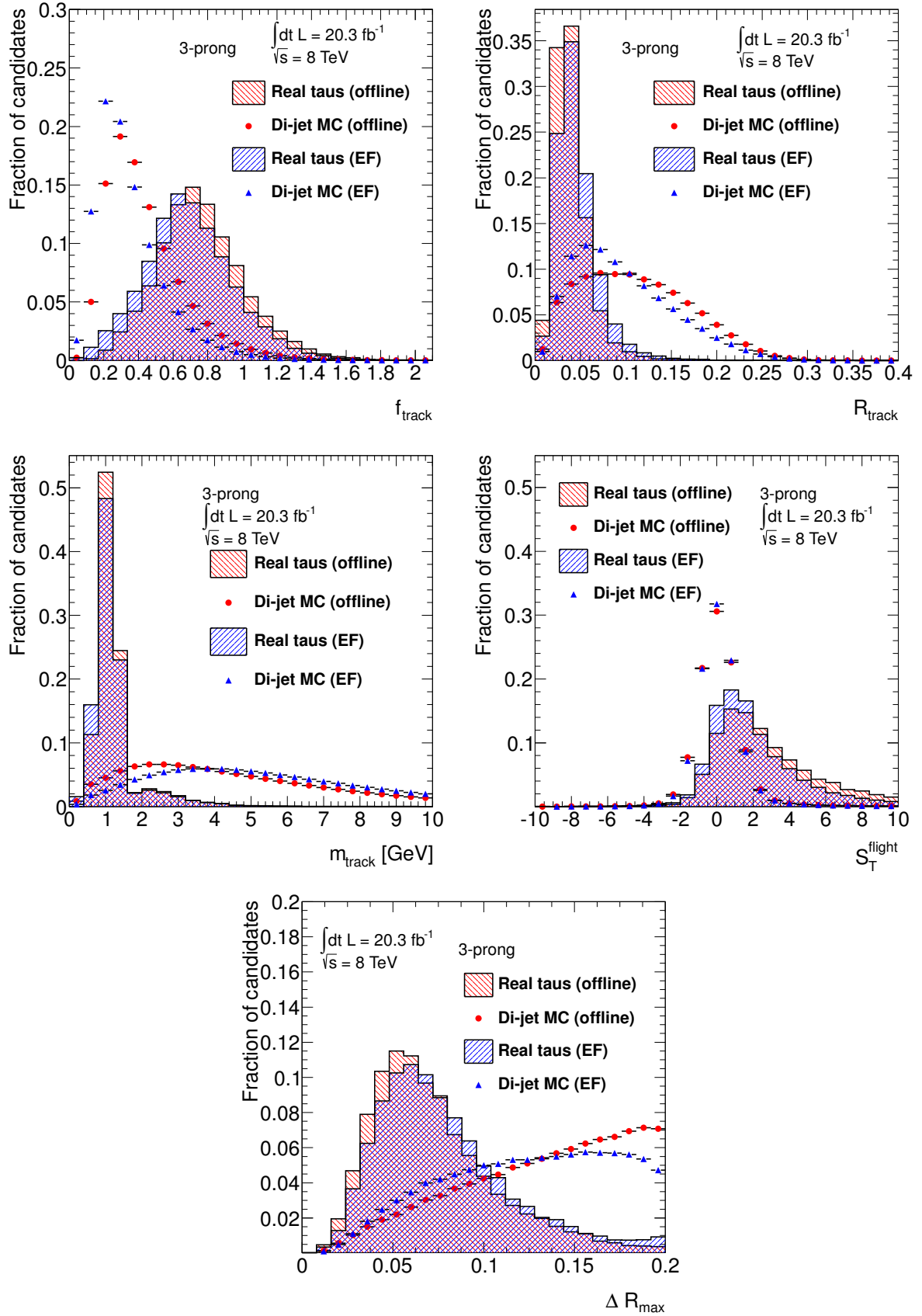


Figure B.2: Tau identification variables for multi-prong tau candidates used by the multivariate EF trigger algorithms. The signal templates for EF tau candidates are shown by the blue histograms, while the background templates, extracted from di-jet MC simulation, are depicted by the blue triangles. For comparison the corresponding distributions of the offline reconstructed tau candidates are shown in red.

C Auxiliary Information for the Monte Carlo Simulation Samples

This chapter provides auxiliary information for the MC simulation samples exploited in the presented analysis. In Section C.1 the samples for b-associated and gluon-gluon fusion BSM Higgs production are summarised, while Section C.2 tabular the background processes. Each of the tables provides an entire summary of the important information for each samples which includes a unique dataset ID, the cross section times branching ratio assigned to the process, the filter efficiency ϵ , the effective simulated luminosity, \mathcal{L}_{eff} , the amount of simulated events and the generator featured for production. The effective simulated efficiency is defined as

$$\mathcal{L}_{\text{eff}} = \frac{N_{\text{MC}}}{\sigma \cdot \epsilon_{\text{filter}}}, \quad (\text{C.1})$$

with N_{MC} being the number of simulated collision events.

C.1 BSM Higgs MC Samples

Tables C.1 and C.2 summarise the MC simulation datasets used to model the MSSM Higgs signal for b-associated and gluon-gluon fusion production mechanisms, respectively. Since the production cross section depends on the choice of $\tan\beta$, the number of generated events is given instead.

Process	Dataset number	k-factor	ϵ_{filter}	N_{MC}	Generator
$bb\phi, M_A = 100 \text{ GeV}$	109921	1	1	100000	Sherpa
$bb\phi, M_A = 110 \text{ GeV}$	125561	1	1	100000	Sherpa
$bb\phi, M_A = 120 \text{ GeV}$	109925	1	1	94900	Sherpa
$bb\phi, M_A = 130 \text{ GeV}$	125562	1	1	90000	Sherpa
$bb\phi, M_A = 140 \text{ GeV}$	125563	1	1	95000	Sherpa
$bb\phi, M_A = 150 \text{ GeV}$	125564	1	1	94900	Sherpa
$bb\phi, M_A = 170 \text{ GeV}$	125565	1	1	50000	Sherpa
$bb\phi, M_A = 200 \text{ GeV}$	109922	1	1	50000	Sherpa
$bb\phi, M_A = 250 \text{ GeV}$	125566	1	1	39999	Sherpa
$bb\phi, M_A = 300 \text{ GeV}$	109920	1	1	50000	Sherpa
$bb\phi, M_A = 350 \text{ GeV}$	125567	1	1	50000	Sherpa
$bb\phi, M_A = 400 \text{ GeV}$	109923	1	1	50000	Sherpa
$bb\phi, M_A = 500 \text{ GeV}$	109924	1	1	49999	Sherpa
$bb\phi, M_A = 600 \text{ GeV}$	109125	1	1	50000	Sherpa
$bb\phi, M_A = 700 \text{ GeV}$	125635	1	1	50000	Sherpa
$bb\phi, M_A = 800 \text{ GeV}$	125637	1	1	50000	Sherpa
$bb\phi, M_A = 900 \text{ GeV}$	181605	1	1	50000	Sherpa
$bb\phi, M_A = 1000 \text{ GeV}$	181788	1	1	50000	Sherpa

Table C.1: Signal MC samples for b-associated MSSM Higgs production.

C.2 Background MC Samples

The following tables will summarise the various MC simulated datasets used to estimate several backgrounds. In Table C.3 presents the samples for $Z/\gamma^*(\rightarrow \ell\ell)+\text{jets}$ production, Table C.4 for $W(\rightarrow \ell\nu)+\text{jets}$ production and Tables C.5 and C.6 for $t\bar{t}$, single top-quark and electroweak di-boson production, respectively.

Process	Dataset number	k-factor	ϵ_{filter}	N_{MC}	Generator
$gg\phi, M_A = 100 \text{ GeV}$	146651	1	1	100000	POWHEG
$gg\phi, M_A = 110 \text{ GeV}$	146652	1	1	74999	POWHEG
$gg\phi, M_A = 130 \text{ GeV}$	146655	1	1	100000	POWHEG
$gg\phi, M_A = 140 \text{ GeV}$	146656	1	1	100000	POWHEG
$gg\phi, M_A = 150 \text{ GeV}$	146657	1	1	99999	POWHEG
$gg\phi, M_A = 170 \text{ GeV}$	146658	1	1	50000	POWHEG
$gg\phi, M_A = 200 \text{ GeV}$	146659	1	1	49999	POWHEG
$gg\phi, M_A = 250 \text{ GeV}$	146660	1	1	50000	POWHEG
$gg\phi, M_A = 300 \text{ GeV}$	125605	1	1	50000	POWHEG
$gg\phi, M_A = 350 \text{ GeV}$	146662	1	1	49999	POWHEG
$gg\phi, M_A = 400 \text{ GeV}$	146663	1	1	49999	POWHEG
$gg\phi, M_A = 500 \text{ GeV}$	125609	1	1	50000	POWHEG
$gg\phi, M_A = 600 \text{ GeV}$	146666	1	1	50000	POWHEG
$gg\phi, M_A = 700 \text{ GeV}$	146667	1	1	50000	POWHEG
$gg\phi, M_A = 800 \text{ GeV}$	146668	1	1	49998	POWHEG
$gg\phi, M_A = 900 \text{ GeV}$	181469	1	1	50000	POWHEG
$gg\phi, M_A = 1000 \text{ GeV}$	181786	1	1	50000	POWHEG

Table C.2: Signal MC samples for gluon-gluon fusion MSSM Higgs production.

Process	Dataset number	$\sigma \times BR(pb)$	ϵ_{filter}	$\mathcal{L}_{eff}[\text{fb}^{-1}]$	Generator
$Z/\gamma^* \rightarrow \tau\tau$ (inclusive)	147818	878.04	1	17.08	Pythia
$Z/\gamma^* \rightarrow \tau\tau(180 \text{ GeV} < m_{ll} < 250 \text{ GeV})$	158731	1.25	1	120.14	Pythia
$Z/\gamma^* \rightarrow \tau\tau(250 \text{ GeV} < m_{ll} < 400 \text{ GeV})$	158732	0.44	1	343.97	Pythia
$Z/\gamma^* \rightarrow \tau\tau(400 \text{ GeV} < m_{ll} < 600 \text{ GeV})$	158733	0.07	1	$20.89 \cdot 10^2$	Pythia
$Z/\gamma^* \rightarrow \tau\tau(600 \text{ GeV} < m_{ll} < 800 \text{ GeV})$	158734	0.01	1	$12.26 \cdot 10^3$	Pythia
$Z/\gamma^* \rightarrow \tau\tau(800 \text{ GeV} < m_{ll} < 1000 \text{ GeV})$	158735	$3.07 \cdot 10^{-3}$	1	$47.19 \cdot 10^3$	Pythia
$Z/\gamma^* \rightarrow \tau\tau(1000 \text{ GeV} < m_{ll} < 1250 \text{ GeV})$	158736	$1.07 \cdot 10^{-3}$	1	$13.53 \cdot 10^4$	Pythia
$Z/\gamma^* \rightarrow \tau\tau(1250 \text{ GeV} < m_{ll} < 1500 \text{ GeV})$	158737	$3.00 \cdot 10^{-4}$	1	$50.04 \cdot 10^4$	Pythia
$Z/\gamma^* \rightarrow \tau\tau(1500 \text{ GeV} < m_{ll} < 1750 \text{ GeV})$	158738	$9.52 \cdot 10^{-5}$	1	$15.76 \cdot 10^5$	Pythia
$Z/\gamma^* \rightarrow \tau\tau(1750 \text{ GeV} < m_{ll} < 2000 \text{ GeV})$	158739	$3.26 \cdot 10^{-5}$	1	$46.00 \cdot 10^5$	Pythia
$Z/\gamma^* \rightarrow \tau\tau(2000 \text{ GeV} < m_{ll} < 2250 \text{ GeV})$	158740	$1.19 \cdot 10^{-5}$	1	$12.64 \cdot 10^6$	Pythia
$Z/\gamma^* \rightarrow \tau\tau(2250 \text{ GeV} < m_{ll} < 2500 \text{ GeV})$	158741	$4.46 \cdot 10^{-6}$	1	$33.66 \cdot 10^6$	Pythia
$Z/\gamma^* \rightarrow \mu\mu$ (inclusive)	147807	990.00	1	10.09	Powheg
$Z/\gamma^* \rightarrow \mu\mu(180 \text{ GeV} < m_{ll} < 250 \text{ GeV})$	129525	1.57	1	63.59	Powheg
$Z/\gamma^* \rightarrow \mu\mu(250 \text{ GeV} < m_{ll} < 400 \text{ GeV})$	129526	0.55	1	181.90	Powheg
$Z/\gamma^* \rightarrow \mu\mu(400 \text{ GeV} < m_{ll} < 600 \text{ GeV})$	129527	0.10	1	$10.34 \cdot 10^2$	Powheg
$Z/\gamma^* \rightarrow \mu\mu(600 \text{ GeV} < m_{ll} < 800 \text{ GeV})$	129528	0.02	1	$66.23 \cdot 10^2$	Powheg
$Z/\gamma^* \rightarrow \mu\mu(800 \text{ GeV} < m_{ll} < 1000 \text{ GeV})$	129529	$3.75 \cdot 10^{-3}$	1	$26.67 \cdot 10^3$	Powheg
$Z/\gamma^* \rightarrow \mu\mu(1000 \text{ GeV} < m_{ll} < 1250 \text{ GeV})$	129530	$1.29 \cdot 10^{-3}$	1	$77.26 \cdot 10^3$	Powheg
$Z/\gamma^* \rightarrow \mu\mu(1250 \text{ GeV} < m_{ll} < 1500 \text{ GeV})$	129531	$3.58 \cdot 10^{-4}$	1	$27.96 \cdot 10^4$	Powheg
$Z/\gamma^* \rightarrow \mu\mu(1500 \text{ GeV} < m_{ll} < 1750 \text{ GeV})$	129532	$1.12 \cdot 10^{-4}$	1	$88.96 \cdot 10^4$	Powheg
$Z/\gamma^* \rightarrow \mu\mu(1750 \text{ GeV} < m_{ll} < 2000 \text{ GeV})$	129533	$3.84 \cdot 10^{-5}$	1	$26.05 \cdot 10^5$	Powheg
$Z/\gamma^* \rightarrow \mu\mu(2000 \text{ GeV} < m_{ll} < 2250 \text{ GeV})$	129534	$1.39 \cdot 10^{-5}$	1	$71.99 \cdot 10^5$	Powheg
$Z/\gamma^* \rightarrow \mu\mu(2250 \text{ GeV} < m_{ll} < 2500 \text{ GeV})$	129535	$5.23 \cdot 10^{-6}$	1	$19.10 \cdot 10^6$	Powheg
$Z/\gamma^* \rightarrow ee$ (inclusive)	147806	1109.80	1	9.01	Powheg
$Z/\gamma^* \rightarrow ee(120 \text{ GeV} < m_{ll} < 180 \text{ GeV})$	129504	9.85	1	50.78	Powheg
$Z/\gamma^* \rightarrow ee(180 \text{ GeV} < m_{ll} < 250 \text{ GeV})$	129505	1.57	1	63.65	Powheg
$Z/\gamma^* \rightarrow ee(250 \text{ GeV} < m_{ll} < 400 \text{ GeV})$	129506	0.55	1	182.08	Powheg
$Z/\gamma^* \rightarrow ee(400 \text{ GeV} < m_{ll} < 600 \text{ GeV})$	129507	0.10	1	$10.35 \cdot 10^2$	Powheg
$Z/\gamma^* \rightarrow ee(600 \text{ GeV} < m_{ll} < 800 \text{ GeV})$	129508	0.02	1	$66.22 \cdot 10^2$	Powheg
$Z/\gamma^* \rightarrow ee(800 \text{ GeV} < m_{ll} < 1000 \text{ GeV})$	129509	$3.75 \cdot 10^{-3}$	1	$26.67 \cdot 10^3$	Powheg
$Z/\gamma^* \rightarrow ee(1000 \text{ GeV} < m_{ll} < 1250 \text{ GeV})$	129510	$1.29 \cdot 10^{-3}$	1	$77.34 \cdot 10^3$	Powheg
$Z/\gamma^* \rightarrow ee(1250 \text{ GeV} < m_{ll} < 1500 \text{ GeV})$	129511	$3.58 \cdot 10^{-4}$	1	$27.93 \cdot 10^4$	Powheg
$Z/\gamma^* \rightarrow ee(1500 \text{ GeV} < m_{ll} < 1750 \text{ GeV})$	129512	$1.12 \cdot 10^{-4}$	1	$84.15 \cdot 10^4$	Powheg
$Z/\gamma^* \rightarrow ee(1750 \text{ GeV} < m_{ll} < 2000 \text{ GeV})$	129513	$3.84 \cdot 10^{-5}$	1	$26.05 \cdot 10^5$	Powheg
$Z/\gamma^* \rightarrow ee(2000 \text{ GeV} < m_{ll} < 2250 \text{ GeV})$	129514	$1.39 \cdot 10^{-5}$	1	$71.99 \cdot 10^5$	Powheg
$Z/\gamma^* \rightarrow ee(2250 \text{ GeV} < m_{ll} < 2500 \text{ GeV})$	129515	$5.23 \cdot 10^{-6}$	1	$19.13 \cdot 10^6$	Powheg

Table C.3: Background MC samples: Z+jets samples. K-factors are mass dependent and given in Section 8.1.1 and 8.2.5, respectively.

Process	Dataset number	$\sigma \times BR(pb)$	k-factor	ϵ_{filter}	$\mathcal{L}_{eff}[\text{fb}^{-1}]$	Generator
$W \rightarrow e\nu + \geq 1 \text{ b-jet } (p_T^W > 0 \text{ GeV})$	167740	11000.00	1.10	0.012	103.23	Sherpa
$W \rightarrow e\nu + \geq 1 \text{ c-jet } (p_T^W > 0 \text{ GeV})$	167741	11000.00	1.10	0.048	17.20	Sherpa
$W \rightarrow e\nu + \text{light-jet } (p_T^W > 0 \text{ GeV})$	167742	11000.00	1.10	0.940	4.38	Sherpa
$W \rightarrow e\nu + \geq 1 \text{ b-jet } (70 \text{ GeV} < p_T^W < 140 \text{ GeV})$	167761	250.60	1.10	0.046	157.85	Sherpa
$W \rightarrow e\nu + \geq 1 \text{ c-jet } (70 \text{ GeV} < p_T^W < 140 \text{ GeV})$	167762	250.60	1.10	0.199	54.65	Sherpa
$W \rightarrow e\nu + \text{light-jet } (70 \text{ GeV} < p_T^W < 140 \text{ GeV})$	167763	250.60	1.10	0.755	24.02	Sherpa
$W \rightarrow e\nu + \geq 1 \text{ b-jet } (140 \text{ GeV} < p_T^W < 280 \text{ GeV})$	167770	31.16	1.10	0.063	461.32	Sherpa
$W \rightarrow e\nu + \geq 1 \text{ c-jet } (140 \text{ GeV} < p_T^W < 280 \text{ GeV})$	167771	31.16	1.10	0.220	264.49	Sherpa
$W \rightarrow e\nu + \text{light-jet } (280 \text{ GeV} < p_T^W < 280 \text{ GeV})$	167772	31.16	1.10	0.716	81.23	Sherpa
$W \rightarrow e\nu + \geq 1 \text{ b-jet } (280 \text{ GeV} < p_T^W < 500 \text{ GeV})$	167779	1.84	1.10	0.083	595.92	Sherpa
$W \rightarrow e\nu + \geq 1 \text{ c-jet } (280 \text{ GeV} < p_T^W < 500 \text{ GeV})$	167780	1.84	1.10	0.233	425.22	Sherpa
$W \rightarrow e\nu + \text{light-jet } (280 \text{ GeV} < p_T^W < 500 \text{ GeV})$	167781	1.84	1.10	0.684	361.47	Sherpa
$W \rightarrow e\nu + \geq 1 \text{ b-jet } (p_T^W > 500 \text{ GeV})$	167788	0.10	1.10	0.100	894.89	Sherpa
$W \rightarrow e\nu + \geq 1 \text{ c-jet } (p_T^W > 500 \text{ GeV})$	167789	0.10	1.10	0.242	368.22	Sherpa
$W \rightarrow e\nu + \text{light-jet } (p_T^W > 500 \text{ GeV})$	167790	0.10	1.10	0.660	671.57	Sherpa
$W \rightarrow \mu\nu + \geq 1 \text{ b-jet } (p_T^W > 0 \text{ GeV})$	167743	11000.00	1.10	0.012	103.23	Sherpa
$W \rightarrow \mu\nu + \geq 1 \text{ c-jet } (p_T^W > 0 \text{ GeV})$	167744	11000.00	1.10	0.048	17.20	Sherpa
$W \rightarrow \mu\nu + \text{light-jet } (p_T^W > 0 \text{ GeV})$	167745	11000.00	1.10	0.940	4.38	Sherpa
$W \rightarrow \mu\nu + \geq 1 \text{ b-jet } (70 \text{ GeV} < p_T^W < 140 \text{ GeV})$	167764	250.60	1.10	0.046	157.85	Sherpa
$W \rightarrow \mu\nu + \geq 1 \text{ c-jet } (70 \text{ GeV} < p_T^W < 140 \text{ GeV})$	167765	250.60	1.10	0.199	54.65	Sherpa
$W \rightarrow \mu\nu + \text{light-jet } (70 \text{ GeV} < p_T^W < 140 \text{ GeV})$	167766	250.60	1.10	0.755	24.02	Sherpa
$W \rightarrow \mu\nu + \geq 1 \text{ b-jet } (140 \text{ GeV} < p_T^W < 280 \text{ GeV})$	167773	31.16	1.10	0.063	461.32	Sherpa
$W \rightarrow \mu\nu + \geq 1 \text{ c-jet } (140 \text{ GeV} < p_T^W < 280 \text{ GeV})$	167774	31.16	1.10	0.220	264.49	Sherpa
$W \rightarrow \mu\nu + \text{light-jet } (280 \text{ GeV} < p_T^W < 280 \text{ GeV})$	167775	31.16	1.10	0.716	81.23	Sherpa
$W \rightarrow \mu\nu + \geq 1 \text{ b-jet } (280 \text{ GeV} < p_T^W < 500 \text{ GeV})$	167782	1.84	1.10	0.083	595.92	Sherpa
$W \rightarrow \mu\nu + \geq 1 \text{ c-jet } (280 \text{ GeV} < p_T^W < 500 \text{ GeV})$	167783	1.84	1.10	0.233	425.22	Sherpa
$W \rightarrow \mu\nu + \text{light-jet } (280 \text{ GeV} < p_T^W < 500 \text{ GeV})$	167784	1.84	1.10	0.684	361.47	Sherpa
$W \rightarrow \mu\nu + \geq 1 \text{ b-jet } (p_T^W > 500 \text{ GeV})$	167791	0.10	1.10	0.100	894.89	Sherpa
$W \rightarrow \mu\nu + \geq 1 \text{ c-jet } (p_T^W > 500 \text{ GeV})$	167792	0.10	1.10	0.242	368.22	Sherpa
$W \rightarrow \mu\nu + \text{light-jet } (p_T^W > 500 \text{ GeV})$	167793	0.10	1.10	0.660	671.57	Sherpa
$W \rightarrow \tau\nu + \geq 1 \text{ b-jet } (p_T^W > 0 \text{ GeV})$	167746	11000.00	1.10	0.012	102.80	Sherpa
$W \rightarrow \tau\nu + \geq 1 \text{ c-jet } (p_T^W > 0 \text{ GeV})$	167747	11000.00	1.10	0.048	17.21	Sherpa
$W \rightarrow \tau\nu + \text{light-jet } (p_T^W > 0 \text{ GeV})$	167748	11000.00	1.10	0.940	3.51	Sherpa
$W \rightarrow \tau\nu + \geq 1 \text{ b-jet } (70 \text{ GeV} < p_T^W < 140 \text{ GeV})$	167767	250.60	1.10	0.046	157.92	Sherpa
$W \rightarrow \tau\nu + \geq 1 \text{ c-jet } (70 \text{ GeV} < p_T^W < 140 \text{ GeV})$	167768	250.60	1.10	0.199	54.72	Sherpa
$W \rightarrow \tau\nu + \text{light-jet } (70 \text{ GeV} < p_T^W < 140 \text{ GeV})$	167769	250.60	1.10	0.755	24.03	Sherpa
$W \rightarrow \tau\nu + \geq 1 \text{ b-jet } (140 \text{ GeV} < p_T^W < 280 \text{ GeV})$	167776	31.16	1.10	0.063	462.38	Sherpa
$W \rightarrow \tau\nu + \geq 1 \text{ c-jet } (140 \text{ GeV} < p_T^W < 280 \text{ GeV})$	167777	31.16	1.10	0.220	264.84	Sherpa
$W \rightarrow \tau\nu + \text{light-jet } (280 \text{ GeV} < p_T^W < 280 \text{ GeV})$	167778	31.16	1.10	0.716	81.48	Sherpa
$W \rightarrow \tau\nu + \geq 1 \text{ b-jet } (280 \text{ GeV} < p_T^W < 500 \text{ GeV})$	167785	1.84	1.10	0.083	595.92	Sherpa
$W \rightarrow \tau\nu + \geq 1 \text{ c-jet } (280 \text{ GeV} < p_T^W < 500 \text{ GeV})$	167786	1.84	1.10	0.233	425.22	Sherpa
$W \rightarrow \tau\nu + \text{light-jet } (280 \text{ GeV} < p_T^W < 500 \text{ GeV})$	167787	1.84	1.10	0.684	361.69	Sherpa
$W \rightarrow \tau\nu + \geq 1 \text{ b-jet } (p_T^W > 500 \text{ GeV})$	167794	0.10	1.10	0.100	894.89	Sherpa
$W \rightarrow \tau\nu + \geq 1 \text{ c-jet } (p_T^W > 500 \text{ GeV})$	167795	0.10	1.10	0.242	368.22	Sherpa
$W \rightarrow \tau\nu + \text{light-jet } (p_T^W > 500 \text{ GeV})$	167796	0.10	1.10	0.660	675.60	Sherpa

Table C.4: Background MC samples: W+jets samples.

Process	Dataset number	$\sigma \times BR(pb)$	k-factor	ϵ_{filter}	$\mathcal{L}_{eff}[\text{fb}^{-1}]$	Generator
$t\bar{t}$ (no fully hadronic decays)	105200	238.06	1	0.543	115.99	MC@NLO
$t\bar{t}$ (fully hadronic decays)	105204	238.06	1	0.457	11.03	MC@NLO
single-top: s -channel $W \rightarrow e\nu$	108343	0.61	1	1	329.87	MC@NLO
single-top: s -channel $W \rightarrow \mu\nu$	108344	0.61	1	1	329.87	MC@NLO
single-top: s -channel $W \rightarrow \tau\nu$	108345	0.61	1	1	329.70	MC@NLO
single-top: t -channel $W \rightarrow e\nu$	117360	9.48	1	1	31.65	AcerMC
single-top: t -channel $W \rightarrow \mu\nu$	117361	9.48	1	1	31.65	AcerMC
single-top: t -channel $W \rightarrow \tau\nu$	117362	9.48	1	1	31.65	AcerMC
single-top: Wt -channel	108346	22.37	1	1	89.38	MC@NLO

Table C.5: Background MC samples: $t\bar{t}$ and single top-quark samples.

Process	Dataset number	$\sigma \times BR(pb)$	k-factor	ϵ_{filter}	$\mathcal{L}_{eff}[\text{fb}^{-1}]$	Generator
WW inclusive	105985	53.90	1	0.382	121.12	Herwig
ZZ inclusive	105986	7.32	1	0.212	161.36	Herwig
WZ inclusive	105987	22.30	1	0.305	146.78	Herwig

Table C.6: Background MC samples: Electroweak di-boson samples.

D Auxiliary Information for the Search for Heavy Neutral Higgs Bosons

In this appendix miscellaneous information on the search for heavy neutral Higgs bosons in the context of the MSSM are given. In Section D.1 auxiliary material concerning the applied production cross sections in several benchmark scenarios is given. Pull distributions of nuisance parameters obtained from pseudo data are summarised in Section D.2. Finally, in Section D.3 negative log likelihood values profiled for each nuisance parameter are presented.

D.1 Higgs Production Cross Section

This section will provide further detailed information on the cross sections used in this analysis to set upper limits on $\tan\beta$ in various scenarios. In Figures D.1 and D.2 the production cross section times branching ratio for both b-associated and gluon-gluon fusion production is shown for the heavy neutral Higgs bosons, A^0 and H^0 , in the $m_h^{\text{mod-}}$ and $m_h^{\text{mod+}}$ benchmark scenario, respectively. Numerical values for specific $\tan\beta$ values are presented in Tables D.1 - D.9.

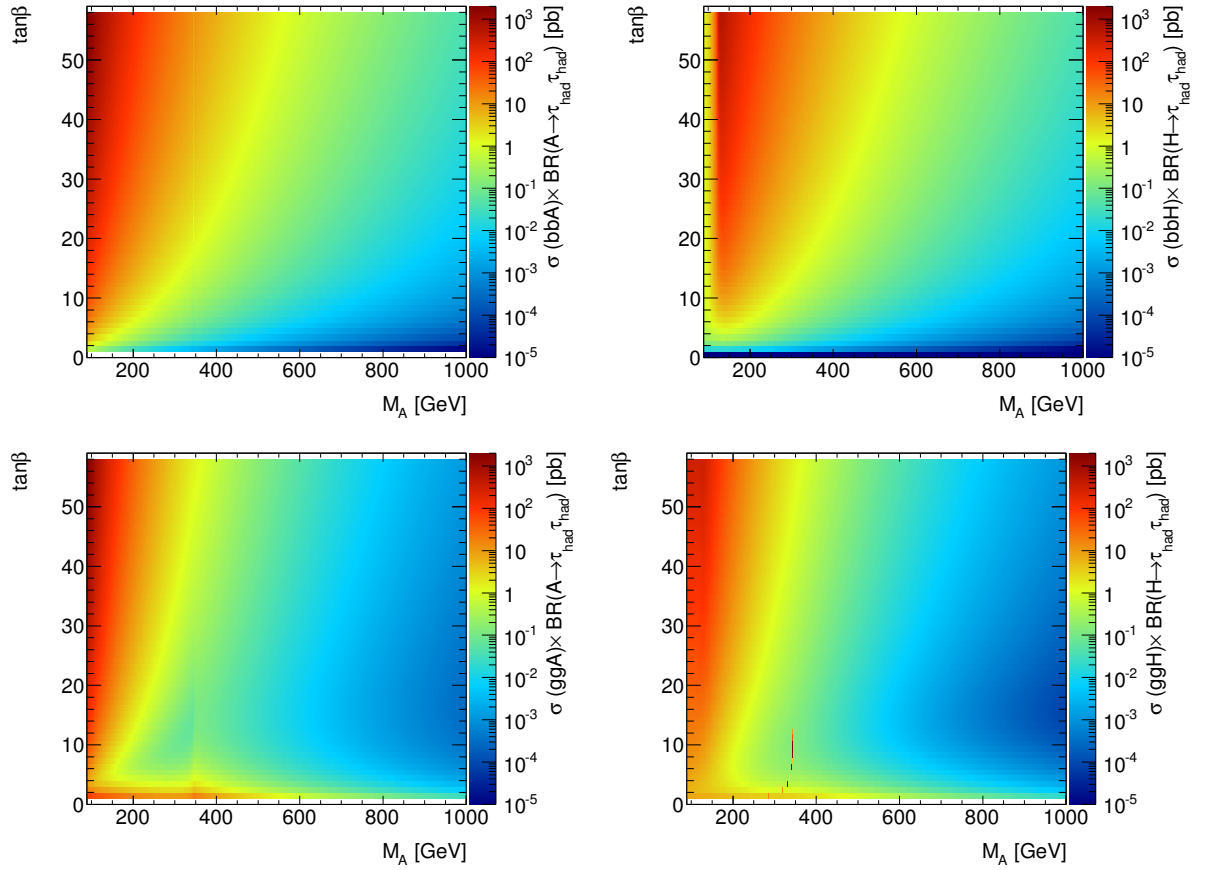


Figure D.1: Production cross section times branching ratio for Higgs production in association with b-quarks (top) and via gluon-gluon fusion (bottom) versus M_A in the $m_h^{\text{mod-}}$ scenario for the A^0 (left) and H^0 (right) boson.

m_A (GeV)	BR $\times \sigma$ bbA(fb)	BR $\times \sigma$ ggA(fb)	m_H (GeV)	BR $\times \sigma$ bbH(fb)	BR $\times \sigma$ ggH(fb)	m_h (GeV)	BR $\times \sigma$ bbh(fb)	BR $\times \sigma$ ggH(fb)
$\tan\beta = 5$								
170	64.24 ^{+8.02} _{-11.50}	30.75 ^{+4.22} _{-3.99}	178.382	31.50 ^{+3.88} _{-5.46}	66.87 ^{+7.43} _{-7.68}	120.164	55.34 ^{+8.09} _{-12.11}	367.92 ^{+54.42} _{-48.05}
200	26.44 ^{+3.17} _{-4.40}	14.82 ^{+2.01} _{-1.91}	205.915	20.36 ^{+2.43} _{-3.32}	35.22 ^{+4.00} _{-4.13}	122.402	30.34 ^{+4.39} _{-6.56}	351.67 ^{+51.74} _{-45.83}
250	6.17 ^{+0.72} _{-0.95}	5.66 ^{+0.73} _{-0.72}	254.142	7.46 ^{+0.87} _{-1.13}	12.28 ^{+1.43} _{-1.49}	123.928	17.00 ^{+2.44} _{-3.64}	327.83 ^{+47.89} _{-42.61}
300	1.11 ^{+0.13} _{-0.16}	2.01 ^{+0.27} _{-0.26}	303.291	2.16 ^{+0.25} _{-0.31}	4.13 ^{+0.48} _{-0.52}	124.589	12.35 ^{+1.77} _{-2.64}	310.92 ^{+45.25} _{-40.33}
350	0.2650 ^{+0.0314} _{-0.0371}	2.07 ^{+0.30} _{-0.29}	352.591	0.7345 ^{+0.0865} _{-0.1029}	2.15 ^{+0.27} _{-0.28}	124.928	10.18 ^{+1.46} _{-2.17}	297.89 ^{+43.36} _{-38.64}
400	0.1332 ^{+0.0162} _{-0.0184}	0.9456 ^{+0.1205} _{-0.1242}	401.857	0.2582 ^{+0.0311} _{-0.0359}	0.9393 ^{+0.1075} _{-0.1176}	125.129	8.96 ^{+1.28} _{-1.91}	289.12 ^{+42.08} _{-37.50}
500	0.0367 ^{+0.0047} _{-0.0052}	0.2274 ^{+0.0283} _{-0.0305}	501.188	0.0361 ^{+0.0046} _{-0.0051}	0.1328 ^{+0.0142} _{-0.0166}	125.359	7.64 ^{+1.09} _{-1.62}	278.48 ^{+40.53} _{-36.12}
600	0.0107 ^{+0.0015} _{-0.0015}	0.0588 ^{+0.0074} _{-0.0081}	601.245	0.0108 ^{+0.0015} _{-0.0015}	0.0362 ^{+0.0039} _{-0.0047}	125.483	6.98 ^{+1.00} _{-1.48}	272.57 ^{+39.67} _{-35.36}
700	0.0040 ^{+0.0006} _{-0.0006}	0.0197 ^{+0.0025} _{-0.0028}	700.992	0.0040 ^{+0.0006} _{-0.0006}	0.0125 ^{+0.0014} _{-0.0017}	125.558	6.66 ^{+0.95} _{-1.42}	271.74 ^{+39.40} _{-35.17}
800	0.0017 ^{+0.0003} _{-0.0003}	0.0077 ^{+0.0010} _{-0.0011}	800.803	0.0017 ^{+0.0003} _{-0.0003}	0.0049 ^{+0.0006} _{-0.0007}	125.610	6.50 ^{+0.93} _{-1.38}	269.36 ^{+39.06} _{-34.86}
900	0.0008 ^{+0.0001} _{-0.0001}	0.0033 ^{+0.0005} _{-0.0005}	900.652	0.0008 ^{+0.0001} _{-0.0001}	0.0021 ^{+0.0003} _{-0.0003}	125.647	6.40 ^{+0.91} _{-1.36}	267.71 ^{+38.82} _{-34.65}
1000	0.0004 ^{+0.0001} _{-0.0001}	0.0015 ^{+0.0002} _{-0.0002}	1000.527	0.0004 ^{+0.0001} _{-0.0001}	0.0000 ^{+0.0000} _{-0.0000}	125.675	6.33 ^{+0.90} _{-1.34}	266.51 ^{+38.64} _{-34.49}
$\tan\beta = 10$								
170	313.34 ^{+39.10} _{-56.10}	91.69 ^{+13.29} _{-12.50}	172.562	261.92 ^{+32.62} _{-46.12}	154.38 ^{+19.61} _{-19.48}	127.158	65.89 ^{+9.34} _{-13.88}	454.63 ^{+68.80} _{-59.66}
200	154.60 ^{+18.52} _{-25.74}	32.89 ^{+4.82} _{-4.50}	201.692	150.88 ^{+18.05} _{-24.82}	69.19 ^{+9.07} _{-9.06}	127.988	30.43 ^{+4.30} _{-6.38}	412.78 ^{+62.32} _{-54.19}
250	52.74 ^{+6.15} _{-8.09}	7.55 ^{+1.05} _{-1.00}	251.195	62.41 ^{+7.26} _{-9.51}	23.09 ^{+3.14} _{-3.14}	128.475	15.55 ^{+2.19} _{-3.25}	367.10 ^{+55.42} _{-48.19}
300	15.18 ^{+1.77} _{-2.20}	1.98 ^{+0.29} _{-0.26}	301.036	23.78 ^{+2.76} _{-3.44}	8.17 ^{+1.08} _{-1.14}	128.675	10.95 ^{+1.54} _{-2.29}	336.89 ^{+50.73} _{-44.24}
350	4.85 ^{+0.57} _{-0.68}	2.29 ^{+0.39} _{-0.35}	350.694	8.72 ^{+1.03} _{-1.22}	3.43 ^{+0.46} _{-0.48}	128.774	8.89 ^{+1.25} _{-1.86}	319.61 ^{+48.12} _{-41.97}
400	2.33 ^{+0.28} _{-0.32}	1.28 ^{+0.20} _{-0.19}	400.331	3.59 ^{+0.43} _{-0.50}	1.43 ^{+0.17} _{-0.19}	128.833	7.75 ^{+1.09} _{-1.62}	308.25 ^{+46.41} _{-40.48}
500	0.6279 ^{+0.0807} _{-0.0883}	0.3359 ^{+0.0521} _{-0.0506}	500.072	0.5937 ^{+0.0756} _{-0.0838}	0.1836 ^{+0.0171} _{-0.0219}	128.902	6.53 ^{+0.92} _{-1.36}	294.78 ^{+44.39} _{-38.71}
600	0.1812 ^{+0.0246} _{-0.0260}	0.0888 ^{+0.0139} _{-0.0137}	600.268	0.1794 ^{+0.0243} _{-0.0257}	0.0429 ^{+0.0035} _{-0.0050}	128.940	5.91 ^{+0.83} _{-1.23}	287.45 ^{+43.28} _{-37.75}
700	0.0673 ^{+0.0097} _{-0.0100}	0.0301 ^{+0.0047} _{-0.0048}	700.191	0.0672 ^{+0.0097} _{-0.0099}	0.0132 ^{+0.0010} _{-0.0016}	128.965	5.64 ^{+0.79} _{-1.18}	283.05 ^{+42.62} _{-37.17}
800	0.0285 ^{+0.0044} _{-0.0044}	0.0117 ^{+0.0019} _{-0.0019}	800.130	0.0284 ^{+0.0045} _{-0.0043}	0.0049 ^{+0.0004} _{-0.0006}	128.983	5.52 ^{+0.78} _{-1.15}	280.18 ^{+42.19} _{-36.79}
900	0.0132 ^{+0.0022} _{-0.0021}	0.0050 ^{+0.0008} _{-0.0008}	900.080	0.0131 ^{+0.0022} _{-0.0020}	0.0020 ^{+0.0002} _{-0.0003}	128.996	5.44 ^{+0.77} _{-1.14}	278.20 ^{+41.89} _{-36.53}
1000	0.0065 ^{+0.0012} _{-0.0011}	0.0023 ^{+0.0004} _{-0.0004}	1000.037	0.0064 ^{+0.0002} _{-0.0010}	0.0000 ^{+0.0000} _{-0.0000}	129.007	5.39 ^{+0.76} _{-1.12}	276.78 ^{+41.68} _{-36.35}

Table D.1: Production cross section, σ , times branching ratio, $BR(\phi \rightarrow \tau\tau)$, as a function of m_A and $\tan\beta$. Gluon-gluon fusion and b-associated production are shown separately. Only the fully hadronic final state is considered by multiplying the BR with $BR(\tau\tau \rightarrow \tau_{\text{had}}\tau_{\text{had}}) = 0.4198$. Given $\sigma \times BR$ are valid for the m_h^{max} scenario. For details on quoted uncertainties consult text. Values given correspond to $\tan\beta = 5$ and $\tan\beta = 10$.

m_A (GeV)	$BR \times \sigma$ bbA(fb)	$BR \times \sigma$ ggA(fb)	m_H (GeV)	$BR \times \sigma$ bbH(fb)	$BR \times \sigma$ ggH(fb)	m_h (GeV)	$BR \times \sigma$ bbh(fb)	$BR \times \sigma$ ggh(fb)
$\tan \beta = 20$								
170	1254.11 ^{+156.48} _{-224.55}	428.63 ^{+61.44} _{-58.64}	170.717	1203.32 ^{+150.39} _{-212.98}	466.36 ^{+66.00} _{-63.37}	129.419	73.51 ^{+10.32} _{-15.31}	981.20 ^{+151.76} _{-131.19}
200	671.03 ^{+80.37} _{-111.73}	172.01 ^{+25.20} _{-24.20}	200.482	668.63 ^{+80.11} _{-110.25}	205.26 ^{+29.78} _{-28.82}	129.654	31.53 ^{+4.42} _{-6.56}	810.27 ^{+124.91} _{-107.85}
250	266.03 ^{+31.01} _{-40.82}	45.23 ^{+6.78} _{-6.62}	250.388	277.68 ^{+32.29} _{-42.35}	62.10 ^{+9.31} _{-9.11}	129.786	15.63 ^{+2.19} _{-3.25}	706.59 ^{+108.92} _{-94.05}
300	108.94 ^{+12.70} _{-15.78}	12.77 ^{+1.98} _{-1.92}	300.430	124.52 ^{+14.45} _{-18.00}	22.34 ^{+3.38} _{-3.41}	129.840	10.91 ^{+1.53} _{-2.27}	646.10 ^{+99.60} _{-86.00}
350	44.19 ^{+5.23} _{-6.18}	4.72 ^{+0.84} _{-0.77}	350.194	56.02 ^{+6.59} _{-7.85}	8.92 ^{+1.38} _{-1.41}	129.865	8.82 ^{+1.24} _{-1.83}	609.41 ^{+93.94} _{-81.12}
400	22.18 ^{+2.69} _{-3.07}	2.85 ^{+0.54} _{-0.49}	399.937	27.10 ^{+3.26} _{-3.77}	3.59 ^{+0.53} _{-0.56}	129.881	7.67 ^{+1.07} _{-1.59}	585.60 ^{+90.27} _{-77.95}
500	6.47 ^{+0.83} _{-0.91}	0.7751 ^{+0.1478} _{-0.1390}	499.787	6.21 ^{+0.79} _{-0.88}	0.5328 ^{+0.0703} _{-0.0810}	129.900	6.44 ^{+0.90} _{-1.34}	557.70 ^{+85.97} _{-74.24}
600	2.05 ^{+0.28} _{-0.29}	0.2168 ^{+0.0422} _{-0.0402}	599.991	2.03 ^{+0.28} _{-0.29}	0.1186 ^{+0.0145} _{-0.0179}	129.912	5.75 ^{+0.81} _{-1.19}	542.68 ^{+83.66} _{-72.24}
700	0.7909 ^{+0.1140} _{-0.1174}	0.0741 ^{+0.0147} _{-0.0142}	699.954	0.7890 ^{+0.1144} _{-0.1162}	0.0335 ^{+0.0039} _{-0.0050}	129.920	5.50 ^{+0.77} _{-1.14}	533.70 ^{+82.27} _{-71.04}
800	0.3424 ^{+0.0524} _{-0.0531}	0.0287 ^{+0.0058} _{-0.0057}	799.922	0.3410 ^{+0.0534} _{-0.0520}	0.0111 ^{+0.0012} _{-0.0016}	129.926	5.43 ^{+0.76} _{-1.13}	527.88 ^{+81.37} _{-70.27}
900	0.1603 ^{+0.0262} _{-0.0257}	0.0122 ^{+0.0025} _{-0.0025}	899.894	0.1590 ^{+0.0272} _{-0.0247}	0.0041 ^{+0.0004} _{-0.0006}	129.932	5.38 ^{+0.75} _{-1.12}	523.89 ^{+80.76} _{-69.73}
1000	0.0796 ^{+0.0141} _{-0.0132}	0.0055 ^{+0.0012} _{-0.0012}	999.867	0.0785 ^{+0.0149} _{-0.0125}	0.0017 ^{+0.0002} _{-0.0002}	129.936	5.35 ^{+0.75} _{-1.11}	521.03 ^{+80.32} _{-69.55}
$\tan \beta = 30$								
170	2828.81 ^{+352.96} _{-506.49}	1005.30 ^{+143.32} _{-137.15}	170.347	2774.96 ^{+347.05} _{-491.68}	1019.45 ^{+147.47} _{-140.37}	129.952	77.86 ^{+10.91} _{-16.17}	1785.64 ^{+276.04} _{-241.77}
200	1532.44 ^{+183.54} _{-255.16}	414.51 ^{+60.32} _{-58.21}	200.246	1528.76 ^{+183.20} _{-252.19}	433.47 ^{+64.14} _{-61.58}	130.050	32.74 ^{+4.59} _{-6.80}	1581.10 ^{+244.42} _{-214.08}
250	624.75 ^{+72.82} _{-95.86}	115.66 ^{+17.30} _{-16.98}	250.229	636.01 ^{+73.97} _{-97.02}	129.46 ^{+19.76} _{-19.23}	130.103	16.10 ^{+2.25} _{-3.34}	1359.85 ^{+210.22} _{-184.12}
300	277.06 ^{+32.31} _{-40.14}	36.95 ^{+5.71} _{-5.65}	300.310	292.63 ^{+33.96} _{-42.31}	46.34 ^{+7.21} _{-7.18}	130.123	11.21 ^{+1.57} _{-2.33}	1234.58 ^{+190.85} _{-167.16}
350	124.23 ^{+14.71} _{-17.38}	13.06 ^{+2.22} _{-2.14}	350.092	140.49 ^{+16.52} _{-19.69}	18.59 ^{+2.98} _{-2.99}	130.131	9.05 ^{+1.27} _{-1.88}	1159.73 ^{+179.28} _{-157.03}
400	64.44 ^{+7.82} _{-8.92}	6.76 ^{+1.23} _{-1.17}	399.853	71.99 ^{+8.66} _{-10.00}	7.79 ^{+1.23} _{-1.27}	130.135	7.87 ^{+1.10} _{-1.63}	1111.59 ^{+171.84} _{-150.51}
500	19.96 ^{+2.56} _{-2.81}	1.75 ^{+0.33} _{-0.32}	499.710	19.47 ^{+2.48} _{-2.75}	1.41 ^{+0.22} _{-0.24}	130.139	6.59 ^{+0.92} _{-1.37}	1055.60 ^{+163.19} _{-142.93}
600	6.80 ^{+0.93} _{-0.98}	0.4975 ^{+0.0980} _{-0.0958}	599.897	6.77 ^{+0.92} _{-0.97}	0.3514 ^{+0.0565} _{-0.0620}	130.142	5.81 ^{+0.81} _{-1.21}	1025.67 ^{+158.56} _{-138.87}
700	2.72 ^{+0.39} _{-0.40}	0.1699 ^{+0.0347} _{-0.0342}	699.858	2.72 ^{+0.39} _{-0.40}	0.1072 ^{+0.0178} _{-0.0197}	130.144	5.58 ^{+0.78} _{-1.16}	1007.84 ^{+155.80} _{-136.46}
800	1.20 ^{+0.18} _{-0.19}	0.0655 ^{+0.0139} _{-0.0137}	799.823	1.20 ^{+0.19} _{-0.18}	0.0376 ^{+0.0064} _{-0.0072}	130.146	5.55 ^{+0.78} _{-1.15}	996.33 ^{+154.02} _{-134.90}
900	0.5707 ^{+0.0933} _{-0.0915}	0.0276 ^{+0.0061} _{-0.0060}	899.789	0.5664 ^{+0.0968} _{-0.0881}	0.0146 ^{+0.0026} _{-0.0029}	130.148	5.54 ^{+0.78} _{-1.15}	988.46 ^{+152.81} _{-135.84}
1000	0.2864 ^{+0.0508} _{-0.0476}	0.0124 ^{+0.0028} _{-0.0028}	999.756	0.2825 ^{+0.0536} _{-0.0450}	0.0061 ^{+0.0011} _{-0.0013}	130.150	5.52 ^{+0.77} _{-1.14}	982.83 ^{+151.94} _{-133.07}

Table D.2: Production cross section, σ , times branching ratio, $BR(\phi \rightarrow \tau\tau)$, as a function of m_A and $\tan\beta$. Gluon-gluon fusion and b-associated production are shown separately. Only the fully hadronic final state is considered by multiplying the BR with $BR(\tau\tau \rightarrow \tau_{\text{had}}\tau_{\text{had}}) = 0.4198$. Given $\sigma \times BR$ are valid for the m_h^{max} scenario. For details on quoted uncertainties consult text. Values given correspond to $\tan\beta = 20$ and $\tan\beta = 30$.

m_A (GeV)	BR $\times \sigma$ bbA(fb)	BR $\times \sigma$ ggA(fb)	m_H (GeV)	BR $\times \sigma$ bbH(fb)	BR $\times \sigma$ ggH(fb)	m_{H_u} (GeV)	BR $\times \sigma$ bbh(fb)	BR $\times \sigma$ ggH(fb)
$\tan \beta = 40$								
170	5050.94 ^{+630.22} _{-904.36}	1821.12 ^{+259.07} _{-248.15}	170.206	4993.31 ^{+624.66} _{-885.10}	1782.67 ^{+259.93} _{-246.63}	130.226	81.80 ^{+11.45} _{-16.96}	3161.84 ^{+484.74} _{-430.37}
200	2745.93 ^{+328.87} _{-457.21}	757.82 ^{+109.98} _{-106.30}	200.151	2740.72 ^{+328.46} _{-452.20}	756.57 ^{+112.71} _{-107.88}	130.264	34.01 ^{+4.76} _{-7.05}	2760.16 ^{+423.16} _{-375.70}
250	1129.63 ^{+131.66} _{-173.32}	216.07 ^{+32.26} _{-31.72}	250.158	1140.39 ^{+132.63} _{-173.97}	224.77 ^{+34.51} _{-33.52}	130.283	16.63 ^{+2.33} _{-3.45}	2342.76 ^{+359.17} _{-318.88}
300	514.68 ^{+60.02} _{-74.56}	72.33 ^{+11.15} _{-11.08}	300.249	528.88 ^{+61.38} _{-76.48}	80.24 ^{+12.60} _{-12.49}	130.287	11.56 ^{+1.62} _{-2.40}	2112.61 ^{+323.88} _{-287.56}
350	241.52 ^{+28.60} _{-33.80}	26.48 ^{+4.38} _{-4.31}	350.033	260.54 ^{+30.64} _{-36.52}	32.34 ^{+5.23} _{-5.23}	130.284	9.33 ^{+1.31} _{-1.93}	1976.95 ^{+303.08} _{-269.09}
400	127.44 ^{+15.46} _{-17.64}	12.84 ^{+2.26} _{-2.20}	399.796	136.82 ^{+16.45} _{-19.01}	13.87 ^{+2.26} _{-2.30}	130.280	8.10 ^{+1.13} _{-1.68}	1890.37 ^{+289.81} _{-257.31}
500	40.81 ^{+5.24} _{-5.74}	3.24 ^{+0.60} _{-0.59}	499.635	40.21 ^{+5.12} _{-5.68}	2.81 ^{+0.47} _{-0.49}	130.274	6.77 ^{+0.95} _{-1.40}	1790.39 ^{+274.48} _{-243.70}
600	14.54 ^{+1.98} _{-2.08}	0.9385 ^{+0.1814} _{-0.1809}	599.801	14.51 ^{+1.96} _{-2.08}	0.7497 ^{+0.1301} _{-0.1381}	130.270	5.90 ^{+0.83} _{-1.22}	1737.28 ^{+266.34} _{-236.47}
700	5.95 ^{+0.86} _{-0.88}	0.3218 ^{+0.0649} _{-0.0651}	699.747	5.95 ^{+0.86} _{-0.88}	0.2401 ^{+0.0436} _{-0.0464}	130.266	5.68 ^{+0.80} _{-1.18}	1705.76 ^{+261.51} _{-232.18}
800	2.67 ^{+0.41} _{-0.41}	0.1240 ^{+0.0262} _{-0.0262}	799.696	2.66 ^{+0.42} _{-0.41}	0.0874 ^{+0.0166} _{-0.0177}	130.264	5.70 ^{+0.80} _{-1.18}	1685.48 ^{+258.40} _{-229.42}
900	1.28 ^{+0.21} _{-0.21}	0.0522 ^{+0.0115} _{-0.0115}	899.646	1.27 ^{+0.22} _{-0.20}	0.0350 ^{+0.0070} _{-0.0074}	130.262	5.71 ^{+0.80} _{-1.18}	1671.65 ^{+256.28} _{-227.54}
1000	0.6467 ^{+0.1147} _{-0.1075}	0.0235 ^{+0.0054} _{-0.0054}	999.598	0.6387 ^{+0.1213} _{-0.1019}	0.0151 ^{+0.0031} _{-0.0033}	130.261	5.71 ^{+0.80} _{-1.18}	1661.80 ^{+254.77} _{-226.20}
$\tan \beta = 50$								
170	7940.45 ^{+990.75} _{-1421.72}	2882.72 ^{+409.68} _{-392.57}	170.125	7880.99 ^{+986.06} _{-1397.30}	2778.02 ^{+406.55} _{-385.16}	130.430	85.82 ^{+12.01} _{-17.78}	5162.50 ^{+784.02} _{-702.62}
200	4321.46 ^{+517.57} _{-719.54}	1204.15 ^{+174.52} _{-168.81}	200.088	4315.94 ^{+517.28} _{-712.20}	1176.76 ^{+175.85} _{-168.08}	130.435	35.33 ^{+4.94} _{-7.32}	4441.98 ^{+674.59} _{-604.56}
250	1784.16 ^{+207.95} _{-273.75}	346.68 ^{+51.69} _{-50.86}	250.100	1795.03 ^{+208.77} _{-273.86}	348.64 ^{+53.67} _{-52.08}	130.435	17.16 ^{+2.40} _{-3.56}	3720.46 ^{+565.02} _{-506.36}
300	822.44 ^{+95.90} _{-119.15}	118.57 ^{+18.23} _{-18.18}	300.187	835.14 ^{+96.92} _{-120.77}	124.23 ^{+19.60} _{-19.37}	130.426	11.90 ^{+1.66} _{-2.47}	3332.48 ^{+506.10} _{-453.56}
350	395.20 ^{+46.80} _{-55.30}	44.54 ^{+7.25} _{-7.21}	349.967	416.56 ^{+48.98} _{-58.39}	50.20 ^{+8.16} _{-8.14}	130.414	9.60 ^{+1.34} _{-1.99}	3106.74 ^{+471.81} _{-422.83}
400	210.49 ^{+25.53} _{-29.13}	20.96 ^{+3.60} _{-3.55}	399.724	221.48 ^{+26.63} _{-30.78}	21.84 ^{+3.60} _{-3.64}	130.404	8.32 ^{+1.16} _{-1.72}	2963.76 ^{+450.10} _{-403.37}
500	68.70 ^{+8.83} _{-9.66}	5.25 ^{+0.95} _{-0.95}	499.528	68.13 ^{+8.67} _{-9.62}	4.71 ^{+0.80} _{-0.83}	130.388	6.94 ^{+0.97} _{-1.44}	2799.75 ^{+425.19} _{-381.05}
600	25.13 ^{+3.42} _{-3.60}	1.53 ^{+0.29} _{-0.29}	599.663	25.14 ^{+3.40} _{-3.60}	1.31 ^{+0.23} _{-0.24}	130.376	5.97 ^{+0.84} _{-1.24}	2713.14 ^{+412.04} _{-369.26}
700	10.43 ^{+1.50} _{-1.55}	0.5284 ^{+0.1053} _{-0.1067}	699.582	10.45 ^{+1.51} _{-1.54}	0.4302 ^{+0.0808} _{-0.0848}	130.367	5.77 ^{+0.81} _{-1.20}	2661.96 ^{+404.26} _{-362.30}
800	4.72 ^{+0.72} _{-0.73}	0.2040 ^{+0.0426} _{-0.0432}	799.505	4.72 ^{+0.74} _{-0.72}	0.1599 ^{+0.0316} _{-0.0330}	130.360	5.83 ^{+0.82} _{-1.21}	2629.14 ^{+399.28} _{-357.83}
900	2.28 ^{+0.37} _{-0.37}	0.0859 ^{+0.0187} _{-0.0190}	899.429	2.27 ^{+0.39} _{-0.35}	0.0657 ^{+0.0136} _{-0.0142}	130.355	5.87 ^{+0.82} _{-1.22}	2606.84 ^{+395.89} _{-354.80}
1000	1.16 ^{+0.21} _{-0.19}	0.0387 ^{+0.0088} _{-0.0089}	999.354	1.15 ^{+0.22} _{-0.18}	0.0288 ^{+0.0062} _{-0.0065}	130.350	5.88 ^{+0.82} _{-1.22}	2591.00 ^{+393.49} _{-352.64}

Table D.3: Production cross section, σ , times branching ratio, $BR(\phi \rightarrow \tau\tau)$, as a function of m_A and $\tan\beta$. Gluon-gluon fusion and b-associated production are shown separately. Only the fully hadronic final state is considered by multiplying the BR with $BR(\tau\tau \rightarrow \text{ThadThad}) = 0.4198$. Given $\sigma \times BR$ are valid for the m_h^{max} scenario. For details on quoted uncertainties consult text. Values given correspond to $\tan\beta = 40$ and $\tan\beta = 50$.

m_A (GeV)	BR $\times \sigma$ bbA(fb)	BR $\times \sigma$ ggA(fb)	m_H (GeV)	BR $\times \sigma$ bbH(fb)	BR $\times \sigma$ ggH(fb)	m_h (GeV)	BR $\times \sigma$ bbh(fb)	BR $\times \sigma$ ggh(fb)
$\tan \beta = 5$								
170	63.16 ^{+8.99} _{-8.07}	29.28 ^{+4.43} _{-4.16}	177.977	34.98 ^{+4.93} _{-4.43}	64.93 ^{+7.94} _{-8.17}	116.259	54.02 ^{+8.85} _{-7.51}	402.27 ^{+66.62} _{-58.72}
200	26.46 ^{+3.64} _{-3.30}	14.24 ^{+2.06} _{-1.99}	205.756	21.44 ^{+2.94} _{-2.67}	33.73 ^{+4.17} _{-4.32}	118.245	30.92 ^{+5.03} _{-4.28}	387.32 ^{+63.68} _{-56.53}
250	6.30 ^{+0.84} _{-0.77}	5.52 ^{+0.76} _{-0.76}	254.102	6.52 ^{+0.87} _{-0.80}	10.04 ^{+1.27} _{-1.32}	119.642	18.07 ^{+2.92} _{-2.50}	366.39 ^{+59.89} _{-53.37}
300	1.15 ^{+0.15} _{-0.14}	2.00 ^{+0.27} _{-0.28}	303.286	2.09 ^{+0.49} _{-0.25}	3.78 ^{+0.51} _{-0.51}	120.259	13.44 ^{+2.17} _{-1.85}	349.08 ^{+57.06} _{-50.85}
350	0.3488 ^{+0.0466} _{-0.0424}	2.62 ^{+0.41} _{-0.39}	352.597	0.7298 ^{+0.0970} _{-0.0893}	2.04 ^{+0.27} _{-0.28}	120.591	11.23 ^{+1.81} _{-1.55}	339.90 ^{+55.38} _{-49.42}
400	0.1495 ^{+0.0202} _{-0.0184}	1.02 ^{+0.14} _{-0.14}	401.867	0.2599 ^{+0.0348} _{-0.0321}	0.9087 ^{+0.1100} _{-0.1213}	120.795	9.99 ^{+1.61} _{-1.38}	331.92 ^{+54.08} _{-48.26}
500	0.0402 ^{+0.0056} _{-0.0051}	0.2393 ^{+0.0314} _{-0.0340}	501.203	0.0375 ^{+0.0052} _{-0.0048}	0.1346 ^{+0.0151} _{-0.0178}	121.028	8.69 ^{+1.40} _{-1.20}	322.10 ^{+52.48} _{-46.83}
600	0.0116 ^{+0.0017} _{-0.0015}	0.0614 ^{+0.0081} _{-0.0090}	601.264	0.0113 ^{+0.0016} _{-0.0015}	0.0375 ^{+0.0042} _{-0.0051}	121.156	8.05 ^{+1.29} _{-1.11}	316.56 ^{+51.58} _{-46.03}
700	0.0043 ^{+0.0006} _{-0.0006}	0.0205 ^{+0.0028} _{-0.0031}	701.016	0.0043 ^{+0.0006} _{-0.0006}	0.0130 ^{+0.0015} _{-0.0018}	121.235	7.69 ^{+1.24} _{-1.06}	313.16 ^{+51.02} _{-45.53}
800	0.0018 ^{+0.0003} _{-0.0003}	0.0080 ^{+0.0011} _{-0.0012}	800.832	0.0018 ^{+0.0003} _{-0.0003}	0.0052 ^{+0.0006} _{-0.0008}	121.290	7.46 ^{+1.20} _{-1.03}	310.92 ^{+50.66} _{-45.21}
900	0.0008 ^{+0.0001} _{-0.0001}	0.0034 ^{+0.0005} _{-0.0006}	900.689	0.0008 ^{+0.0001} _{-0.0001}	0.0022 ^{+0.0003} _{-0.0003}	121.330	7.30 ^{+1.17} _{-1.01}	309.35 ^{+50.40} _{-44.98}
1000	0.0004 ^{+0.0001} _{-0.0001}	0.0016 ^{+0.0002} _{-0.0003}	1000.570	0.0004 ^{+0.0001} _{-0.0001}	0.0000 ^{+0.0000} _{-0.0000}	121.362	7.19 ^{+1.16} _{-0.99}	308.20 ^{+50.22} _{-44.81}
$\tan \beta = 10$								
170	307.79 ^{+43.79} _{-39.33}	90.60 ^{+13.85} _{-13.10}	172.475	264.54 ^{+37.61} _{-33.70}	149.23 ^{+20.00} _{-20.04}	123.112	62.56 ^{+9.99} _{-8.58}	505.56 ^{+84.32} _{-74.25}
200	153.34 ^{+21.07} _{-19.11}	32.90 ^{+5.11} _{-4.85}	201.693	150.64 ^{+20.69} _{-18.77}	65.71 ^{+9.02} _{-9.11}	123.847	30.85 ^{+4.91} _{-4.22}	466.80 ^{+77.73} _{-68.63}
250	53.16 ^{+7.11} _{-6.47}	7.63 ^{+1.17} _{-1.12}	251.221	60.77 ^{+8.11} _{-7.43}	21.70 ^{+3.05} _{-3.11}	124.301	16.57 ^{+2.64} _{-2.27}	427.59 ^{+71.20} _{-62.87}
300	15.74 ^{+2.09} _{-1.90}	1.99 ^{+0.29} _{-0.29}	301.065	23.74 ^{+3.15} _{-2.89}	7.89 ^{+1.12} _{-1.16}	124.492	11.92 ^{+1.89} _{-1.63}	402.34 ^{+67.00} _{-59.16}
350	5.43 ^{+0.73} _{-0.66}	2.39 ^{+0.43} _{-0.39}	350.720	8.91 ^{+1.18} _{-1.09}	3.38 ^{+0.48} _{-0.50}	124.594	9.80 ^{+1.56} _{-1.34}	381.09 ^{+63.35} _{-55.88}
400	2.51 ^{+0.34} _{-0.31}	1.29 ^{+0.21} _{-0.20}	400.354	3.71 ^{+0.50} _{-0.46}	1.43 ^{+0.17} _{-0.20}	124.657	8.63 ^{+1.37} _{-1.18}	370.30 ^{+61.56} _{-54.30}
500	0.6748 ^{+0.0935} _{-0.0859}	0.3386 ^{+0.0550} _{-0.0539}	500.091	0.6293 ^{+0.0864} _{-0.0801}	0.1890 ^{+0.0182} _{-0.0237}	124.731	7.43 ^{+1.18} _{-1.01}	357.26 ^{+59.39} _{-52.39}
600	0.1951 ^{+0.0279} _{-0.0260}	0.0898 ^{+0.0145} _{-0.0146}	600.288	0.1914 ^{+0.0273} _{-0.0252}	0.0451 ^{+0.0038} _{-0.0055}	124.773	6.84 ^{+1.09} _{-0.94}	350.04 ^{+58.19} _{-51.33}
700	0.0725 ^{+0.0108} _{-0.0101}	0.0305 ^{+0.0050} _{-0.0051}	700.211	0.0720 ^{+0.0108} _{-0.0098}	0.0140 ^{+0.0011} _{-0.0017}	124.801	6.51 ^{+1.03} _{-0.89}	345.65 ^{+57.46} _{-50.68}
800	0.0307 ^{+0.0048} _{-0.0045}	0.0119 ^{+0.0020} _{-0.0020}	800.152	0.0305 ^{+0.0049} _{-0.0043}	0.0051 ^{+0.0004} _{-0.0006}	124.821	6.31 ^{+1.00} _{-0.86}	342.77 ^{+56.98} _{-50.26}
900	0.0142 ^{+0.0023} _{-0.0022}	0.0051 ^{+0.0009} _{-0.0009}	900.105	0.0141 ^{+0.0024} _{-0.0021}	0.0021 ^{+0.0002} _{-0.0003}	124.836	6.17 ^{+0.98} _{-0.84}	340.78 ^{+56.65} _{-49.97}
1000	0.0070 ^{+0.0012} _{-0.0011}	0.0023 ^{+0.0004} _{-0.0004}	1000.060	0.0069 ^{+0.0013} _{-0.0010}	0.0009 ^{+0.0001} _{-0.0001}	124.848	6.07 ^{+0.96} _{-0.83}	339.34 ^{+56.41} _{-49.76}

Table D.4: Production cross section, σ , times branching ratio, $BR(\phi \rightarrow \tau\tau)$, as a function of m_A and $\tan\beta$. Gluon-gluon fusion and b-associated production are shown separately. Only the fully hadronic final state is considered by multiplying the BR with $BR(\tau\tau \rightarrow \tau_{\text{had}}\tau_{\text{had}}) = 0.4198$. Given $\sigma \times BR$ are valid for the $m_h^{\text{mod-}}$ scenario. For details on quoted uncertainties consult text. Values given correspond to $\tan\beta = 5$ and $\tan\beta = 10$.

m_A (GeV)	BR $\times \sigma$ bbA(fb)	BR $\times \sigma$ ggA(fb)	m_H (GeV)	BR $\times \sigma$ bbH(fb)	BR $\times \sigma$ ggH(fb)	m_h (GeV)	BR $\times \sigma$ bbh(fb)	BR $\times \sigma$ ggh(fb)
$\tan\beta = 20$								
170	1259.05 ^{+179.14} _{-160.87}	432.41 ^{+64.03} _{-61.91}	170.734	1216.77 ^{+173.44} _{-155.31}	459.44 ^{+67.18} _{-65.22}	125.322	69.21 ^{+10.97} _{-9.45}	1141.91 ^{+187.72} _{-166.81}
200	676.24 ^{+26.50} _{-84.29}	174.97 ^{+25.83} _{-25.83}	200.514	675.23 ^{+29.84} _{-84.17}	198.43 ^{+29.70} _{-29.10}	125.536	31.85 ^{+5.04} _{-4.35}	965.41 ^{+159.80} _{-141.44}
250	270.22 ^{+36.15} _{-32.91}	46.72 ^{+7.33} _{-7.21}	250.417	280.91 ^{+37.52} _{-34.34}	62.10 ^{+9.53} _{-9.48}	125.662	16.49 ^{+2.61} _{-2.25}	874.46 ^{+144.74} _{-128.12}
300	112.54 ^{+14.97} _{-13.61}	13.53 ^{+2.16} _{-2.16}	300.455	126.50 ^{+16.76} _{-15.59}	22.44 ^{+3.52} _{-3.55}	125.715	11.68 ^{+1.85} _{-1.59}	817.62 ^{+135.33} _{-119.79}
350	47.11 ^{+6.30} _{-5.72}	5.01 ^{+0.95} _{-0.87}	350.215	57.83 ^{+7.68} _{-7.08}	9.07 ^{+1.45} _{-1.47}	125.743	9.51 ^{+1.51} _{-1.30}	781.57 ^{+129.37} _{-114.51}
400	23.66 ^{+3.19} _{-2.91}	2.95 ^{+0.58} _{-0.53}	399.954	28.27 ^{+3.78} _{-3.49}	3.69 ^{+0.56} _{-0.59}	125.761	8.33 ^{+1.32} _{-1.14}	757.49 ^{+125.38} _{-110.98}
500	6.97 ^{+0.97} _{-0.89}	0.7990 ^{+0.1570} _{-0.1492}	499.798	6.72 ^{+0.92} _{-0.86}	0.5752 ^{+0.0787} _{-0.0908}	125.783	7.12 ^{+1.13} _{-0.97}	728.59 ^{+120.60} _{-106.75}
600	2.24 ^{+0.32} _{-0.30}	0.2249 ^{+0.0448} _{-0.0433}	600.000	2.22 ^{+0.32} _{-0.29}	0.1316 ^{+0.0168} _{-0.0207}	125.796	6.54 ^{+1.04} _{-0.89}	712.70 ^{+117.97} _{-104.42}
700	0.8677 ^{+0.1289} _{-0.1213}	0.0770 ^{+0.0156} _{-0.0153}	699.963	0.8682 ^{+0.1298} _{-0.1186}	0.0378 ^{+0.0046} _{-0.0059}	125.806	6.22 ^{+0.98} _{-0.85}	703.07 ^{+116.37} _{-103.01}
800	0.3767 ^{+0.0585} _{-0.0553}	0.0298 ^{+0.0062} _{-0.0061}	799.931	0.3765 ^{+0.0598} _{-0.0532}	0.0127 ^{+0.0015} _{-0.0020}	125.813	6.01 ^{+0.95} _{-0.82}	696.79 ^{+115.33} _{-102.09}
900	0.1766 ^{+0.0289} _{-0.0273}	0.0126 ^{+0.0027} _{-0.0027}	899.903	0.1759 ^{+0.0301} _{-0.0257}	0.0048 ^{+0.0006} _{-0.0008}	125.820	5.88 ^{+0.93} _{-0.80}	692.45 ^{+114.61} _{-101.45}
1000	0.0878 ^{+0.0152} _{-0.0142}	0.0057 ^{+0.0013} _{-0.0012}	999.877	0.0869 ^{+0.0162} _{-0.0131}	0.0020 ^{+0.0002} _{-0.0003}	125.825	5.78 ^{+0.91} _{-0.79}	689.33 ^{+114.10} _{-101.00}
$\tan\beta = 30$								
170	2897.53 ^{+412.26} _{-370.22}	1032.51 ^{+151.84} _{-147.37}	170.376	2848.64 ^{+406.28} _{-363.74}	1031.24 ^{+154.02} _{-148.16}	125.876	73.15 ^{+11.57} _{-9.97}	2048.36 ^{+332.56} _{-298.35}
200	1574.52 ^{+216.36} _{-196.25}	428.61 ^{+64.43} _{-62.96}	200.275	1571.44 ^{+216.10} _{-195.93}	441.60 ^{+67.21} _{-65.38}	125.966	32.88 ^{+5.20} _{-4.48}	1882.57 ^{+305.64} _{-274.20}
250	645.69 ^{+86.39} _{-78.64}	121.02 ^{+18.82} _{-18.61}	250.252	655.71 ^{+87.58} _{-80.16}	132.72 ^{+20.77} _{-20.51}	126.015	16.74 ^{+2.65} _{-2.28}	1691.38 ^{+274.60} _{-246.36}
300	289.35 ^{+38.50} _{-34.99}	39.38 ^{+6.32} _{-6.31}	300.327	302.72 ^{+40.11} _{-36.83}	47.70 ^{+7.67} _{-7.66}	126.033	11.76 ^{+1.86} _{-1.60}	1574.39 ^{+255.61} _{-225.32}
350	132.63 ^{+17.73} _{-16.11}	14.20 ^{+2.52} _{-2.44}	350.104	147.08 ^{+19.54} _{-18.00}	19.32 ^{+3.18} _{-3.21}	126.040	9.53 ^{+1.51} _{-1.30}	1500.85 ^{+243.67} _{-218.60}
400	69.15 ^{+9.33} _{-8.49}	7.21 ^{+1.35} _{-1.30}	399.860	75.99 ^{+10.17} _{-9.39}	8.18 ^{+1.33} _{-1.38}	126.044	8.32 ^{+1.31} _{-1.13}	1451.97 ^{+235.73} _{-211.48}
500	21.67 ^{+3.00} _{-2.76}	1.85 ^{+0.36} _{-0.35}	499.706	21.33 ^{+2.93} _{-2.72}	1.56 ^{+0.25} _{-0.27}	126.048	7.08 ^{+1.12} _{-0.97}	1393.54 ^{+226.24} _{-202.97}
600	7.50 ^{+1.07} _{-1.00}	0.5324 ^{+0.1063} _{-0.1056}	599.890	7.52 ^{+1.07} _{-0.99}	0.3985 ^{+0.0662} _{-0.0726}	126.051	6.49 ^{+1.03} _{-0.88}	1361.55 ^{+221.05} _{-198.31}
700	3.02 ^{+0.45} _{-0.42}	0.1821 ^{+0.0377} _{-0.0376}	699.847	3.04 ^{+0.45} _{-0.41}	0.1240 ^{+0.0213} _{-0.0235}	126.053	6.16 ^{+0.97} _{-0.84}	1342.23 ^{+217.91} _{-195.50}
800	1.34 ^{+0.21} _{-0.20}	0.0702 ^{+0.0150} _{-0.0151}	799.808	1.35 ^{+0.21} _{-0.19}	0.0443 ^{+0.0079} _{-0.0088}	126.054	5.95 ^{+0.94} _{-0.81}	1329.65 ^{+215.87} _{-193.67}
900	0.6369 ^{+0.1040} _{-0.0983}	0.0295 ^{+0.0066} _{-0.0066}	899.771	0.6379 ^{+0.1090} _{-0.0932}	0.0176 ^{+0.0033} _{-0.0036}	126.056	5.82 ^{+0.92} _{-0.79}	1320.99 ^{+214.47} _{-192.41}
1000	0.3197 ^{+0.0555} _{-0.0519}	0.0133 ^{+0.0031} _{-0.0031}	999.736	0.3185 ^{+0.0593} _{-0.0481}	0.0075 ^{+0.0015} _{-0.0016}	126.058	5.72 ^{+0.90} _{-0.78}	1314.79 ^{+213.46} _{-191.50}

Table D.5: Production cross section, σ , times branching ratio, $BR(\phi \rightarrow \tau\tau)$, as a function of m_A and $\tan\beta$. Gluon-gluon fusion and b-associated production are shown separately. Only the fully hadronic final state is considered by multiplying the BR with $BR(\tau\tau \rightarrow \tau_{\text{had}}\tau_{\text{had}}) = 0.4198$. Given $\sigma \times BR$ are valid for the m_h^{mod} -scenario. For details on quoted uncertainties consult text. Values given correspond to $\tan\beta = 20$ and $\tan\beta = 30$.

m_A (GeV)	$BR \times \sigma$ bbA(fb)	$BR \times \sigma$ ggA(fb)	m_H (GeV)	$BR \times \sigma$ bbH(fb)	$BR \times \sigma$ ggH(fb)	m_{h_i} (GeV)	$BR \times \sigma$ bbh(fb)	$BR \times \sigma$ ggh(fb)
$\tan \beta = 40$								
170	5268.43 ^{+749.58} _{-673.16}	1902.26 ^{+279.34} _{-270.94}	170.231	5198.62 ^{+741.61} _{-663.90}	1836.92 ^{+276.02} _{-265.34}	126.200	76.51 ^{+12.09} _{-10.42}	3366.32 ^{+538.88} _{-488.60}
200	2873.62 ^{+394.87} _{-358.16}	796.79 ^{+119.31} _{-116.80}	200.171	2862.34 ^{+293.67} _{-356.90}	785.30 ^{+120.34} _{-116.67}	126.235	33.84 ^{+5.35} _{-4.61}	3059.11 ^{+489.70} _{-444.01}
250	1188.67 ^{+159.04} _{-144.78}	229.56 ^{+35.53} _{-35.24}	250.168	1196.41 ^{+159.81} _{-146.26}	235.07 ^{+37.06} _{-36.47}	126.243	17.02 ^{+2.69} _{-2.32}	2723.07 ^{+435.91} _{-395.23}
300	545.73 ^{+72.60} _{-66.00}	77.95 ^{+12.45} _{-12.47}	300.250	556.96 ^{+73.80} _{-67.77}	84.31 ^{+13.66} _{-13.61}	126.239	11.86 ^{+1.87} _{-1.62}	2522.34 ^{+403.78} _{-366.10}
350	260.70 ^{+34.85} _{-31.67}	29.14 ^{+5.01} _{-4.95}	350.027	277.22 ^{+36.83} _{-33.92}	34.29 ^{+5.70} _{-5.73}	126.233	9.57 ^{+1.51} _{-1.30}	2397.45 ^{+383.78} _{-347.97}
400	138.32 ^{+18.66} _{-16.98}	13.95 ^{+2.51} _{-2.47}	399.782	146.61 ^{+19.63} _{-18.12}	14.86 ^{+2.48} _{-2.54}	126.226	8.33 ^{+1.32} _{-1.14}	2314.90 ^{+370.57} _{-335.99}
500	44.78 ^{+6.20} _{-5.70}	3.52 ^{+0.66} _{-0.66}	499.599	44.62 ^{+6.13} _{-5.68}	3.15 ^{+0.54} _{-0.57}	126.216	7.07 ^{+1.12} _{-0.96}	2216.71 ^{+354.85} _{-321.74}
600	16.18 ^{+2.32} _{-2.15}	1.03 ^{+0.20} _{-0.20}	599.754	16.32 ^{+2.33} _{-2.15}	0.8617 ^{+0.1539} _{-0.1633}	126.208	6.47 ^{+1.02} _{-0.88}	2163.22 ^{+346.29} _{-313.98}
700	6.67 ^{+0.99} _{-0.93}	0.3524 ^{+0.0720} _{-0.0729}	699.688	6.74 ^{+1.01} _{-0.92}	0.2812 ^{+0.0527} _{-0.0560}	126.202	6.13 ^{+0.97} _{-0.84}	2131.02 ^{+341.13} _{-309.30}
800	3.00 ^{+0.47} _{-0.44}	0.1358 ^{+0.0290} _{-0.0294}	799.626	3.03 ^{+0.48} _{-0.43}	0.1041 ^{+0.0205} _{-0.0217}	126.198	5.92 ^{+0.94} _{-0.81}	2110.12 ^{+337.79} _{-306.27}
900	1.44 ^{+0.24} _{-0.22}	0.0571 ^{+0.0127} _{-0.0128}	899.566	1.45 ^{+0.25} _{-0.21}	0.0425 ^{+0.0088} _{-0.0092}	126.195	5.76 ^{+0.91} _{-0.79}	2095.80 ^{+335.49} _{-304.19}
1000	0.7291 ^{+0.1265} _{-0.1184}	0.0257 ^{+0.0059} _{-0.0060}	999.508	0.7312 ^{+0.1361} _{-0.1104}	0.0187 ^{+0.0040} _{-0.0042}	126.192	5.68 ^{+0.90} _{-0.77}	2085.54 ^{+333.85} _{-302.70}
$\tan \beta = 50$								
170	8418.38 ^{+1197.75} _{-1075.63}	3058.12 ^{+448.68} _{-435.08}	170.134	8303.78 ^{+1184.76} _{-1060.56}	2902.72 ^{+437.10} _{-420.31}	126.481	79.62 ^{+12.57} _{-10.84}	4705.21 ^{+749.30} _{-681.80}
200	4599.29 ^{+632.00} _{-573.25}	1286.21 ^{+192.21} _{-188.37}	200.085	4569.22 ^{+628.47} _{-569.75}	1240.28 ^{+190.66} _{-184.57}	126.486	34.72 ^{+5.48} _{-4.73}	4221.32 ^{+672.24} _{-611.69}
250	1909.83 ^{+255.53} _{-232.62}	374.03 ^{+57.75} _{-57.34}	250.083	1912.77 ^{+255.51} _{-233.83}	370.85 ^{+58.68} _{-57.65}	126.463	17.26 ^{+2.72} _{-2.35}	3716.25 ^{+591.81} _{-538.50}
300	886.01 ^{+117.88} _{-107.15}	129.47 ^{+20.63} _{-20.69}	300.153	894.30 ^{+118.50} _{-108.81}	132.96 ^{+21.63} _{-21.50}	126.441	11.96 ^{+1.89} _{-1.63}	3422.63 ^{+545.05} _{-495.95}
350	432.46 ^{+57.81} _{-52.54}	49.61 ^{+8.38} _{-8.36}	349.920	450.59 ^{+59.85} _{-55.13}	54.25 ^{+9.06} _{-9.09}	126.420	9.61 ^{+1.52} _{-1.31}	3242.15 ^{+516.31} _{-469.80}
400	231.55 ^{+31.25} _{-28.42}	23.14 ^{+4.07} _{-4.06}	399.663	241.20 ^{+32.29} _{-29.80}	23.83 ^{+4.04} _{-4.11}	126.403	8.34 ^{+1.32} _{-1.14}	3123.69 ^{+497.44} _{-452.63}
500	76.34 ^{+10.58} _{-9.71}	5.79 ^{+1.07} _{-1.08}	499.422	76.72 ^{+10.53} _{-9.77}	5.44 ^{+0.95} _{-0.99}	126.376	7.06 ^{+1.11} _{-0.96}	2983.61 ^{+475.14} _{-432.34}
600	28.30 ^{+4.05} _{-3.77}	1.71 ^{+0.33} _{-0.34}	599.530	28.71 ^{+4.09} _{-3.78}	1.52 ^{+0.28} _{-0.29}	126.356	6.45 ^{+1.02} _{-0.88}	2907.73 ^{+463.05} _{-421.34}
700	11.82 ^{+1.76} _{-1.65}	0.5891 ^{+0.1190} _{-0.1217}	699.421	12.03 ^{+1.80} _{-1.64}	0.5158 ^{+0.0997} _{-0.1044}	126.341	6.11 ^{+0.96} _{-0.83}	2862.25 ^{+455.81} _{-414.75}
800	5.37 ^{+0.83} _{-0.79}	0.2275 ^{+0.0481} _{-0.0491}	799.316	5.47 ^{+0.87} _{-0.77}	0.1947 ^{+0.0395} _{-0.0413}	126.330	5.89 ^{+0.93} _{-0.80}	2832.84 ^{+451.13} _{-410.49}
900	2.60 ^{+0.42} _{-0.40}	0.0956 ^{+0.0211} _{-0.0215}	899.213	2.64 ^{+0.45} _{-0.39}	0.0805 ^{+0.0171} _{-0.0179}	126.320	5.75 ^{+0.91} _{-0.78}	2812.75 ^{+447.93} _{-407.58}
1000	1.32 ^{+0.23} _{-0.21}	0.0430 ^{+0.0099} _{-0.0101}	999.112	1.33 ^{+0.25} _{-0.20}	0.0358 ^{+0.0080} _{-0.0083}	126.313	5.65 ^{+0.89} _{-0.77}	2798.43 ^{+445.65} _{-405.50}

Table D.6: Production cross section, σ , times branching ratio, $BR(\phi \rightarrow \tau\tau)$, as a function of m_A and $\tan\beta$. Gluon-gluon fusion and b-associated production are shown separately. Only the fully hadronic final state is considered by multiplying the BR with $BR(\tau\tau \rightarrow \tau_{\text{had}}\tau_{\text{had}}) = 0.4198$. Given $\sigma \times BR$ are valid for the $m_h^{\text{mod-}}$ scenario. For details on quoted uncertainties consult text. Values given correspond to $\tan\beta = 40$ and $\tan\beta = 50$.

m_A (GeV)	BR $\times \sigma$ bbA(fb)	BR $\times \sigma$ ggA(fb)	m_H (GeV)	BR $\times \sigma$ bbH(fb)	BR $\times \sigma$ ggH(fb)	m_h (GeV)	BR $\times \sigma$ bbh(fb)	BR $\times \sigma$ ggH(fb)
$\tan\beta = 5$								
170	62.25 ^{+8.86} _{-7.95}	29.61 ^{+4.47} _{-4.20}	178.206	33.36 ^{+4.70} _{-4.23}	64.69 ^{+7.86} _{-8.11}	115.957	55.34 ^{+9.08} _{-7.70}	423.66 ^{+70.78} _{-62.25}
200	25.92 ^{+3.56} _{-3.23}	14.43 ^{+2.09} _{-2.02}	205.909	20.61 ^{+2.82} _{-2.56}	33.67 ^{+4.13} _{-4.29}	118.027	31.65 ^{+5.15} _{-4.39}	406.49 ^{+67.45} _{-59.68}
250	6.11 ^{+0.82} _{-0.74}	5.57 ^{+0.76} _{-0.77}	254.196	6.26 ^{+0.84} _{-0.77}	9.96 ^{+1.24} _{-1.30}	119.489	18.42 ^{+2.98} _{-2.54}	380.64 ^{+62.97} _{-55.80}
300	1.11 ^{+0.15} _{-0.13}	2.01 ^{+0.28} _{-0.28}	303.351	2.01 ^{+0.27} _{-0.24}	3.74 ^{+0.48} _{-0.50}	120.117	13.65 ^{+2.20} _{-1.88}	363.93 ^{+60.02} _{-53.77}
350	0.3357 ^{+0.0449} _{-0.0408}	2.62 ^{+0.41} _{-0.39}	352.648	0.7009 ^{+0.0931} _{-0.0858}	2.02 ^{+0.27} _{-0.28}	120.460	11.38 ^{+1.83} _{-1.57}	351.30 ^{+57.94} _{-51.42}
400	0.1438 ^{+0.0194} _{-0.0177}	1.02 ^{+0.14} _{-0.14}	401.910	0.2494 ^{+0.0334} _{-0.0308}	0.8978 ^{+0.1075} _{-0.1192}	120.669	10.11 ^{+1.63} _{-1.39}	345.07 ^{+56.73} _{-50.42}
500	0.0386 ^{+0.0054} _{-0.0049}	0.2385 ^{+0.0312} _{-0.0338}	501.235	0.0360 ^{+0.0049} _{-0.0046}	0.1329 ^{+0.0147} _{-0.0175}	120.907	8.78 ^{+1.41} _{-1.21}	334.39 ^{+54.98} _{-48.86}
600	0.0112 ^{+0.0016} _{-0.0015}	0.0611 ^{+0.0080} _{-0.0089}	601.289	0.0108 ^{+0.0015} _{-0.0014}	0.0370 ^{+0.0041} _{-0.0050}	121.036	8.12 ^{+1.31} _{-1.12}	328.40 ^{+53.99} _{-47.98}
700	0.0041 ^{+0.0006} _{-0.0006}	0.0204 ^{+0.0027} _{-0.0031}	701.035	0.0041 ^{+0.0006} _{-0.0006}	0.0129 ^{+0.0014} _{-0.0018}	121.116	7.75 ^{+1.25} _{-1.07}	324.72 ^{+53.38} _{-47.44}
800	0.0018 ^{+0.0003} _{-0.0003}	0.0079 ^{+0.0011} _{-0.0012}	800.846	0.0017 ^{+0.0003} _{-0.0002}	0.0051 ^{+0.0006} _{-0.0007}	121.170	7.52 ^{+1.21} _{-1.03}	322.30 ^{+52.99} _{-47.09}
900	0.0008 ^{+0.0001} _{-0.0001}	0.0034 ^{+0.0005} _{-0.0005}	900.698	0.0008 ^{+0.0001} _{-0.0001}	0.0022 ^{+0.0003} _{-0.0003}	121.209	7.36 ^{+1.18} _{-1.01}	320.61 ^{+52.71} _{-46.84}
1000	0.0004 ^{+0.0001} _{-0.0001}	0.0016 ^{+0.0002} _{-0.0003}	1000.580	0.0004 ^{+0.0001} _{-0.0001}	0.0000 ^{+0.0000} _{-0.0000}	121.239	7.25 ^{+1.17} _{-1.00}	319.38 ^{+52.51} _{-46.66}
$\tan\beta = 10$								
170	302.24 ^{+43.00} _{-38.62}	88.54 ^{+13.54} _{-12.80}	172.598	256.86 ^{+36.51} _{-32.72}	145.14 ^{+19.29} _{-19.39}	122.974	64.82 ^{+10.36} _{-8.89}	513.75 ^{+86.43} _{-75.97}
200	149.79 ^{+20.58} _{-18.67}	32.01 ^{+4.96} _{-4.71}	201.767	146.71 ^{+20.15} _{-18.28}	65.60 ^{+8.92} _{-9.04}	123.762	31.84 ^{+5.07} _{-4.36}	472.59 ^{+79.31} _{-69.75}
250	51.46 ^{+6.89} _{-6.27}	7.42 ^{+1.14} _{-1.09}	251.264	59.00 ^{+7.88} _{-7.21}	21.51 ^{+2.99} _{-3.07}	124.249	16.97 ^{+2.70} _{-2.32}	429.71 ^{+72.11} _{-63.42}
300	15.00 ^{+2.00} _{-1.81}	1.96 ^{+0.29} _{-0.28}	301.095	22.82 ^{+3.02} _{-2.78}	7.74 ^{+1.09} _{-1.13}	124.445	12.14 ^{+1.93} _{-1.66}	402.58 ^{+67.56} _{-59.42}
350	5.13 ^{+0.69} _{-0.62}	2.41 ^{+0.43} _{-0.39}	350.744	8.49 ^{+1.13} _{-1.04}	3.31 ^{+0.47} _{-0.49}	124.551	9.94 ^{+1.58} _{-1.36}	381.71 ^{+64.01} _{-56.24}
400	2.37 ^{+0.32} _{-0.29}	1.29 ^{+0.21} _{-0.20}	400.374	3.51 ^{+0.47} _{-0.43}	1.39 ^{+0.17} _{-0.19}	124.616	8.73 ^{+1.39} _{-1.19}	370.18 ^{+62.07} _{-54.34}
500	0.6342 ^{+0.0879} _{-0.0807}	0.3359 ^{+0.0541} _{-0.0532}	500.107	0.5905 ^{+0.0811} _{-0.0752}	0.1819 ^{+0.0169} _{-0.0224}	124.691	7.49 ^{+1.19} _{-1.02}	356.28 ^{+59.74} _{-52.49}
600	0.1828 ^{+0.0262} _{-0.0243}	0.0888 ^{+0.0143} _{-0.0144}	600.299	0.1793 ^{+0.0256} _{-0.0256}	0.0432 ^{+0.0034} _{-0.0052}	124.733	6.89 ^{+1.09} _{-0.94}	348.60 ^{+58.46} _{-51.36}
700	0.0678 ^{+0.0101} _{-0.0095}	0.0301 ^{+0.0049} _{-0.0050}	700.220	0.0674 ^{+0.0101} _{-0.0092}	0.0133 ^{+0.0010} _{-0.0016}	124.760	6.55 ^{+1.04} _{-0.90}	343.94 ^{+57.67} _{-50.67}
800	0.0288 ^{+0.0045} _{-0.0042}	0.0117 ^{+0.0019} _{-0.0020}	800.158	0.0286 ^{+0.0045} _{-0.0040}	0.0048 ^{+0.0003} _{-0.0006}	124.780	6.34 ^{+1.01} _{-0.87}	340.89 ^{+57.16} _{-50.22}
900	0.0133 ^{+0.0022} _{-0.0021}	0.0050 ^{+0.0008} _{-0.0009}	900.108	0.0132 ^{+0.0023} _{-0.0012}	0.0020 ^{+0.0001} _{-0.0003}	124.794	6.20 ^{+0.98} _{-0.85}	338.78 ^{+56.81} _{-49.91}
1000	0.0065 ^{+0.0011} _{-0.0011}	0.0023 ^{+0.0004} _{-0.0004}	1000.070	0.0064 ^{+0.0012} _{-0.0010}	0.0009 ^{+0.0001} _{-0.0001}	124.806	6.10 ^{+0.97} _{-0.83}	337.26 ^{+56.55} _{-49.69}

Table D.7: Production cross section, σ , times branching ratio, $BR(\phi \rightarrow \tau\tau)$, as a function of m_A and $\tan\beta$. Gluon-gluon fusion and b-associated production are shown separately. Only the fully hadronic final state is considered by multiplying the BR with $BR(\tau\tau \rightarrow \text{Thad}(\text{Thad})) = 0.4198$. Given $\sigma \times BR$ are valid for the $m_h^{\text{mod}+}$ scenario. For details on quoted uncertainties consult text. Values given correspond to $\tan\beta = 5$ and $\tan\beta = 10$.

m_A (GeV)	BR $\times \sigma$ bbA(fb)	BR $\times \sigma$ ggA(fb)	m_H (GeV)	BR $\times \sigma$ bbH(fb)	BR $\times \sigma$ ggH(fb)	m_h (GeV)	BR $\times \sigma$ bbh(fb)	BR $\times \sigma$ ggh(fb)
$\tan\beta = 20$								
170	1212.19 ^{+172.47} _{-154.88}	414.05 ^{+61.24} _{-59.23}	170.803	1166.72 ^{+166.29} _{-148.91}	446.43 ^{+64.78} _{-63.13}	125.234	73.57 ^{+11.66} _{-10.04}	1056.09 ^{+175.56} _{-155.08}
200	649.56 ^{+89.26} _{-80.96}	166.89 ^{+25.24} _{-24.62}	200.555	648.36 ^{+89.14} _{-80.82}	192.26 ^{+28.60} _{-28.10}	125.478	33.56 ^{+5.32} _{-4.58}	969.01 ^{+161.09} _{-142.29}
250	258.29 ^{+34.56} _{-31.46}	44.20 ^{+6.93} _{-6.81}	250.443	269.60 ^{+36.01} _{-32.96}	60.01 ^{+9.16} _{-9.13}	125.623	17.14 ^{+2.71} _{-2.34}	797.39 ^{+131.04} _{-114.11}
300	106.34 ^{+14.15} _{-12.86}	12.61 ^{+2.02} _{-2.00}	300.474	120.76 ^{+16.00} _{-14.69}	21.57 ^{+3.37} _{-3.40}	125.678	12.03 ^{+1.90} _{-1.64}	740.31 ^{+121.66} _{-105.94}
350	43.81 ^{+5.86} _{-5.32}	4.72 ^{+0.90} _{-0.82}	350.231	54.61 ^{+7.25} _{-6.68}	8.66 ^{+1.37} _{-1.40}	125.708	9.74 ^{+1.54} _{-1.33}	704.29 ^{+115.74} _{-100.78}
400	21.89 ^{+2.95} _{-2.69}	2.81 ^{+0.55} _{-0.51}	399.968	26.46 ^{+3.54} _{-3.27}	3.48 ^{+0.52} _{-0.55}	125.728	8.49 ^{+1.34} _{-1.16}	680.30 ^{+111.79} _{-97.35}
500	6.39 ^{+0.89} _{-0.81}	0.7615 ^{+0.1490} _{-0.1415}	499.810	6.14 ^{+0.84} _{-0.78}	0.5205 ^{+0.0683} _{-0.0803}	125.751	7.22 ^{+1.14} _{-0.98}	651.56 ^{+107.07} _{-93.24}
600	2.03 ^{+0.29} _{-0.27}	0.2132 ^{+0.0422} _{-0.0408}	600.009	2.02 ^{+0.29} _{-0.27}	0.1155 ^{+0.0138} _{-0.0175}	125.766	6.61 ^{+1.05} _{-0.90}	635.80 ^{+104.48} _{-90.98}
700	0.7843 ^{+0.1165} _{-0.1096}	0.0729 ^{+0.0147} _{-0.0144}	699.969	0.7846 ^{+0.1173} _{-0.1072}	0.0321 ^{+0.0035} _{-0.0048}	125.776	6.27 ^{+0.99} _{-0.85}	626.26 ^{+102.91} _{-89.62}
800	0.3396 ^{+0.0527} _{-0.0499}	0.0282 ^{+0.0058} _{-0.0057}	799.936	0.3395 ^{+0.0539} _{-0.0480}	0.0104 ^{+0.0011} _{-0.0015}	125.783	6.05 ^{+0.96} _{-0.83}	620.04 ^{+101.89} _{-88.73}
900	0.1590 ^{+0.0260} _{-0.0245}	0.0120 ^{+0.0025} _{-0.0023}	899.906	0.1584 ^{+0.0271} _{-0.0231}	0.0038 ^{+0.0004} _{-0.0005}	125.789	5.91 ^{+0.94} _{-0.81}	615.75 ^{+101.19} _{-88.11}
1000	0.0789 ^{+0.0137} _{-0.0128}	0.0054 ^{+0.0012} _{-0.0012}	999.879	0.0782 ^{+0.0146} _{-0.0118}	0.0015 ^{+0.0001} _{-0.0002}	125.795	5.81 ^{+0.92} _{-0.79}	612.67 ^{+100.68} _{-87.67}
$\tan\beta = 30$								
170	2733.07 ^{+388.86} _{-349.21}	969.20 ^{+142.11} _{-138.11}	170.428	2680.97 ^{+382.34} _{-342.31}	977.26 ^{+145.05} _{-139.85}	125.772	79.66 ^{+12.61} _{-10.86}	1770.32 ^{+290.64} _{-259.10}
200	1482.68 ^{+203.74} _{-184.80}	401.18 ^{+60.16} _{-58.85}	200.309	1480.09 ^{+203.53} _{-184.53}	417.66 ^{+63.23} _{-61.65}	125.887	35.37 ^{+5.59} _{-4.82}	1606.32 ^{+263.72} _{-235.10}
250	605.94 ^{+81.07} _{-73.80}	112.59 ^{+17.48} _{-17.29}	250.273	617.21 ^{+82.44} _{-75.45}	125.24 ^{+19.51} _{-19.30}	125.952	17.69 ^{+2.80} _{-2.41}	1423.57 ^{+233.71} _{-208.35}
300	269.53 ^{+35.86} _{-32.60}	36.22 ^{+5.80} _{-5.79}	300.344	284.02 ^{+37.63} _{-34.56}	44.85 ^{+7.17} _{-7.19}	125.973	12.26 ^{+1.94} _{-1.67}	1312.97 ^{+215.55} _{-192.16}
350	121.70 ^{+16.27} _{-14.78}	12.92 ^{+2.30} _{-2.22}	350.119	136.83 ^{+18.18} _{-16.74}	18.05 ^{+2.95} _{-2.99}	125.984	9.85 ^{+1.56} _{-1.34}	1243.62 ^{+204.17} _{-182.01}
400	63.09 ^{+8.51} _{-7.74}	6.64 ^{+1.24} _{-1.20}	399.874	70.13 ^{+9.39} _{-8.67}	7.55 ^{+1.21} _{-1.26}	125.991	8.54 ^{+1.35} _{-1.16}	1197.60 ^{+196.62} _{-175.28}
500	19.57 ^{+2.71} _{-2.49}	1.71 ^{+0.33} _{-0.32}	499.721	19.20 ^{+2.64} _{-2.44}	1.38 ^{+0.22} _{-0.24}	125.999	7.22 ^{+1.14} _{-0.98}	1142.66 ^{+187.59} _{-167.24}
600	6.68 ^{+0.96} _{-0.89}	0.4874 ^{+0.0973} _{-0.0964}	599.904	6.70 ^{+0.95} _{-0.88}	0.3414 ^{+0.0550} _{-0.0612}	126.004	6.58 ^{+1.04} _{-0.90}	1112.60 ^{+182.66} _{-162.84}
700	2.67 ^{+0.40} _{-0.37}	0.1663 ^{+0.0343} _{-0.0343}	699.860	2.69 ^{+0.40} _{-0.37}	0.1032 ^{+0.0171} _{-0.0192}	126.008	6.23 ^{+0.98} _{-0.85}	1094.45 ^{+179.68} _{-160.18}
800	1.18 ^{+0.18} _{-0.17}	0.0640 ^{+0.0137} _{-0.0137}	799.821	1.19 ^{+0.19} _{-0.17}	0.0358 ^{+0.0062} _{-0.0069}	126.011	6.01 ^{+0.95} _{-0.82}	1082.63 ^{+177.74} _{-158.45}
900	0.5607 ^{+0.0916} _{-0.0865}	0.0269 ^{+0.0060} _{-0.0060}	899.785	0.5612 ^{+0.0959} _{-0.0820}	0.0137 ^{+0.0025} _{-0.0028}	126.014	5.86 ^{+0.93} _{-0.80}	1074.50 ^{+176.40} _{-157.26}
1000	0.2810 ^{+0.0488} _{-0.0456}	0.0121 ^{+0.0028} _{-0.0028}	999.749	0.2798 ^{+0.0521} _{-0.0422}	0.0057 ^{+0.0011} _{-0.0012}	126.017	5.76 ^{+0.91} _{-0.78}	1068.67 ^{+175.45} _{-156.41}

Table D.8: Production cross section, σ , times branching ratio, $BR(\phi \rightarrow \tau\tau)$, as a function of m_A and $\tan\beta$. Gluon-gluon fusion and b-associated production are shown separately. Only the fully hadronic final state is considered by multiplying the BR with $BR(\tau\tau \rightarrow \tau_{\text{had}}\tau_{\text{had}}) = 0.4198$. Given $\sigma \times BR$ are valid for the $m_h^{\text{mod+}}$ scenario. For details on quoted uncertainties consult text. Values given correspond to $\tan\beta = 20$ and $\tan\beta = 30$.

m_A (GeV)	BR $\times \sigma$ bbA(fb)	BR $\times \sigma$ ggA(fb)	m_H (GeV)	BR $\times \sigma$ bbH(fb)	BR $\times \sigma$ ggH(fb)	m_h (GeV)	BR $\times \sigma$ bbh(fb)	BR $\times \sigma$ ggh(fb)
$\tan\beta = 40$								
170	4865.21 ^{+692.21} -621.64	1748.31 ^{+255.65} -248.45	170.277	4796.35 ^{+684.18} -612.50	1701.03 ^{+254.12} -244.70	126.050	85.26 ^{+13.48} -11.62	2741.86 ^{+444.58} -399.52
200	2649.83 ^{+364.12} -330.27	730.59 ^{+109.00} -106.86	200.203	2641.90 ^{+363.34} -329.40	725.94 ^{+110.59} -107.50	126.109	37.17 ^{+5.88} -5.06	2460.12 ^{+398.90} -358.47
250	1092.97 ^{+146.24} -133.12	209.47 ^{+32.31} -32.09	250.192	1103.29 ^{+147.37} -134.87	216.80 ^{+34.00} -33.53	126.135	18.28 ^{+2.89} -2.49	2158.00 ^{+349.91} -314.44
300	499.16 ^{+66.41} -60.37	70.52 ^{+11.23} -11.27	300.272	512.27 ^{+67.88} -62.33	77.51 ^{+12.49} -12.47	126.138	12.54 ^{+1.98} -1.71	1977.87 ^{+320.71} -288.20
350	235.31 ^{+31.45} -28.59	26.02 ^{+4.48} -4.42	350.048	253.21 ^{+33.64} -30.98	31.34 ^{+5.18} -5.22	126.138	10.01 ^{+1.58} -1.36	1865.62 ^{+302.50} -271.84
400	124.19 ^{+16.76} -15.25	12.56 ^{+2.27} -2.23	399.805	133.01 ^{+17.81} -16.44	13.43 ^{+2.22} -2.29	126.137	8.64 ^{+1.36} -1.18	1791.36 ^{+290.46} -261.02
500	39.81 ^{+5.51} -5.06	3.17 ^{+0.60} -0.60	499.629	39.55 ^{+5.43} -5.04	2.74 ^{+0.46} -0.49	126.134	7.25 ^{+1.15} -0.99	1702.93 ^{+276.12} -248.14
600	14.20 ^{+2.03} -1.89	0.9159 ^{+0.1796} -0.1811	599.787	14.31 ^{+2.04} -1.89	0.7288 ^{+0.1278} -0.1369	126.132	6.59 ^{+1.04} -0.90	1654.69 ^{+268.30} -241.11
700	5.81 ^{+0.86} -0.81	0.3136 ^{+0.0641} -0.0648	699.726	5.87 ^{+0.88} -0.80	0.2320 ^{+0.0426} -0.0457	126.130	6.22 ^{+0.98} -0.85	1625.60 ^{+263.59} -236.87
800	2.60 ^{+0.40} -0.38	0.1207 ^{+0.0257} -0.0260	799.668	2.63 ^{+0.42} -0.37	0.0839 ^{+0.0162} -0.0173	126.130	5.99 ^{+0.95} -0.82	1606.70 ^{+260.52} -234.11
900	1.25 ^{+0.20} -0.19	0.0507 ^{+0.0112} -0.0114	899.613	1.26 ^{+0.21} -0.18	0.0333 ^{+0.0067} -0.0072	126.129	5.84 ^{+0.92} -0.80	1593.71 ^{+258.41} -232.22
1000	0.6298 ^{+0.1093} -0.1022	0.0228 ^{+0.0053} -0.0053	999.559	0.6307 ^{+0.1174} -0.0952	0.0142 ^{+0.0030} -0.0032	126.129	5.74 ^{+0.91} -0.78	1584.41 ^{+256.91} -230.87
$\tan\beta = 50$								
170	7606.26 ^{+1082.20} -971.87	2749.41 ^{+401.23} -389.99	170.180	7505.22 ^{+1070.75} -988.53	2627.60 ^{+393.06} -378.80	126.265	90.69 ^{+14.33} -12.35	3718.70 ^{+597.76} -540.75
200	4149.70 ^{+570.23} -517.21	1153.93 ^{+171.59} -168.51	200.124	4130.54 ^{+568.11} -515.04	1120.88 ^{+171.19} -166.17	126.289	38.96 ^{+6.15} -5.31	3298.08 ^{+530.15} -479.56
250	1718.64 ^{+229.95} -209.33	334.16 ^{+51.36} -51.09	250.119	1726.92 ^{+230.68} -211.11	334.27 ^{+52.56} -51.78	126.289	18.88 ^{+2.98} -2.57	2863.60 ^{+460.31} -416.39
300	794.12 ^{+105.65} -96.04	114.90 ^{+18.23} -18.32	300.193	805.39 ^{+106.72} -97.99	119.46 ^{+19.32} -19.25	126.277	12.83 ^{+2.03} -1.75	2608.47 ^{+419.30} -379.29
350	383.06 ^{+51.20} -46.54	43.46 ^{+7.35} -7.32	349.963	403.32 ^{+53.58} -49.35	48.48 ^{+8.05} -8.10	126.267	10.17 ^{+1.61} -1.39	2450.42 ^{+393.89} -356.31
400	204.13 ^{+27.55} -25.06	20.40 ^{+3.60} -3.58	399.712	214.62 ^{+28.73} -26.52	21.08 ^{+3.54} -3.62	126.259	8.74 ^{+1.38} -1.19	2346.19 ^{+377.14} -341.15
500	66.68 ^{+9.24} -8.48	5.10 ^{+0.94} -0.95	499.493	66.83 ^{+9.18} -8.51	4.65 ^{+0.80} -0.84	126.245	7.30 ^{+1.15} -0.99	2222.40 ^{+357.24} -323.15
600	24.41 ^{+3.49} -3.25	1.49 ^{+0.29} -0.29	599.615	24.73 ^{+3.52} -3.26	1.27 ^{+0.23} -0.24	126.235	6.61 ^{+1.04} -0.90	2155.03 ^{+346.41} -313.36
700	10.13 ^{+1.51} -1.42	0.5126 ^{+0.1035} -0.1057	699.521	10.30 ^{+1.54} -1.41	0.4161 ^{+0.0794} -0.0837	126.228	6.23 ^{+0.98} -0.85	2114.49 ^{+339.89} -307.46
800	4.58 ^{+0.71} -0.67	0.1975 ^{+0.0417} -0.0426	799.432	4.65 ^{+0.74} -0.66	0.1554 ^{+0.0312} -0.0328	126.223	5.99 ^{+0.95} -0.82	2088.17 ^{+335.65} -303.63
900	2.21 ^{+0.36} -0.34	0.0830 ^{+0.0183} -0.0187	899.345	2.24 ^{+0.38} -0.33	0.0629 ^{+0.0132} -0.0139	126.219	5.83 ^{+0.92} -0.79	2070.12 ^{+332.76} -301.01
1000	1.12 ^{+0.19} -0.18	0.0373 ^{+0.0086} -0.0087	999.259	1.13 ^{+0.21} -0.17	0.0273 ^{+0.0060} -0.0063	126.216	5.72 ^{+0.90} -0.78	2057.21 ^{+330.68} -299.13

Table D.9: Production cross section, σ , times branching ratio, $BR(\phi \rightarrow \tau\tau)$, as a function of m_A and $\tan\beta$. Gluon-gluon fusion and b-associated production are shown separately. Only the fully hadronic final state is considered by multiplying the BR with $BR(\tau\tau \rightarrow \text{Thad}\tau_{\text{had}}) = 0.4198$. Given $\sigma \times BR$ are valid for the $m_h^{\text{mod}+}$ scenario. For details on quoted uncertainties consult text. Values given correspond to $\tan\beta = 40$ and $\tan\beta = 50$.

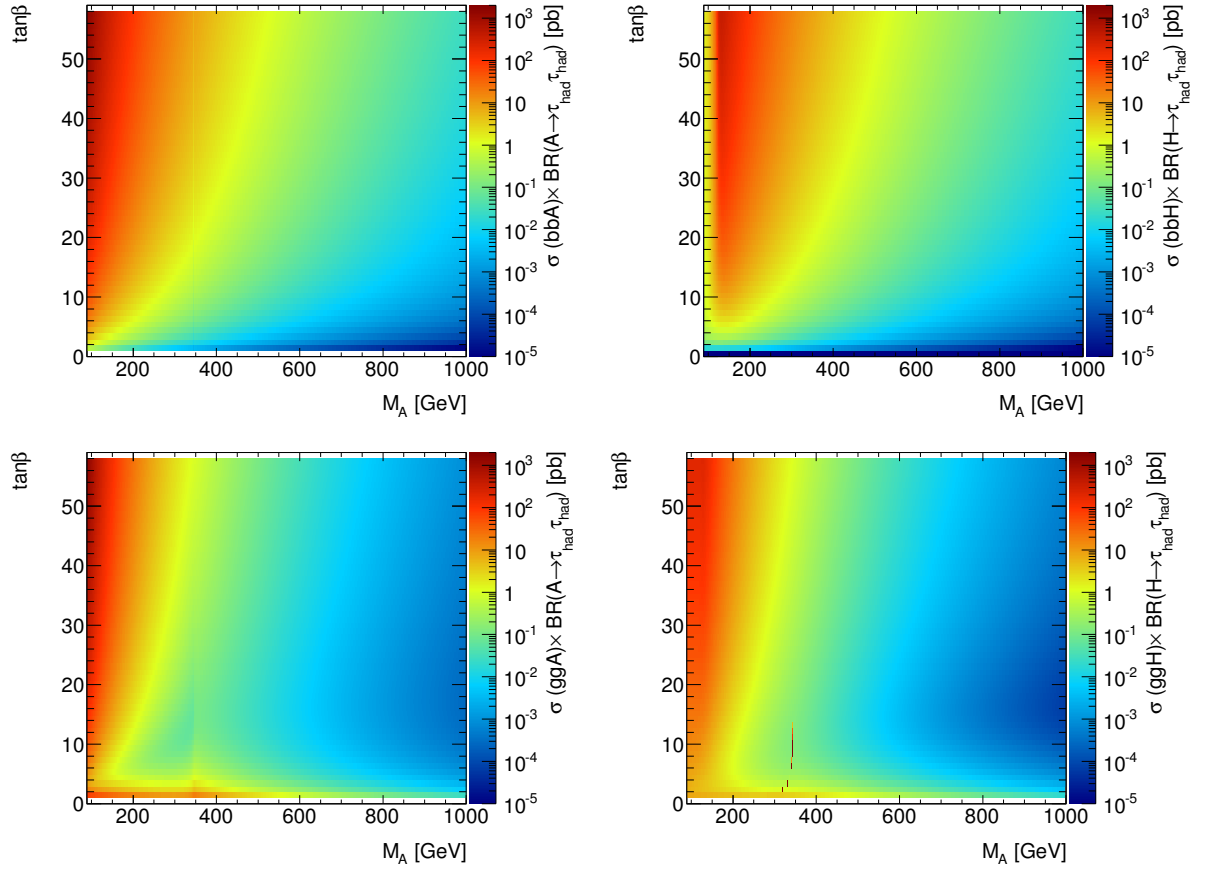


Figure D.2: Production cross section times branching ratio for Higgs production in association with b-quarks (top) and via gluon-gluon fusion (bottom) versus M_A in the $m_h^{\text{mod}+}$ scenario for the A^0 (left) and H^0 (right) boson.

D.2 Pull Distributions of Nuisance Parameters Obtained from Pseudo Data

Figures D.3 and D.4 summarise the pull distributions of the remaining nuisance parameters. For details consult Section 12.6.9.

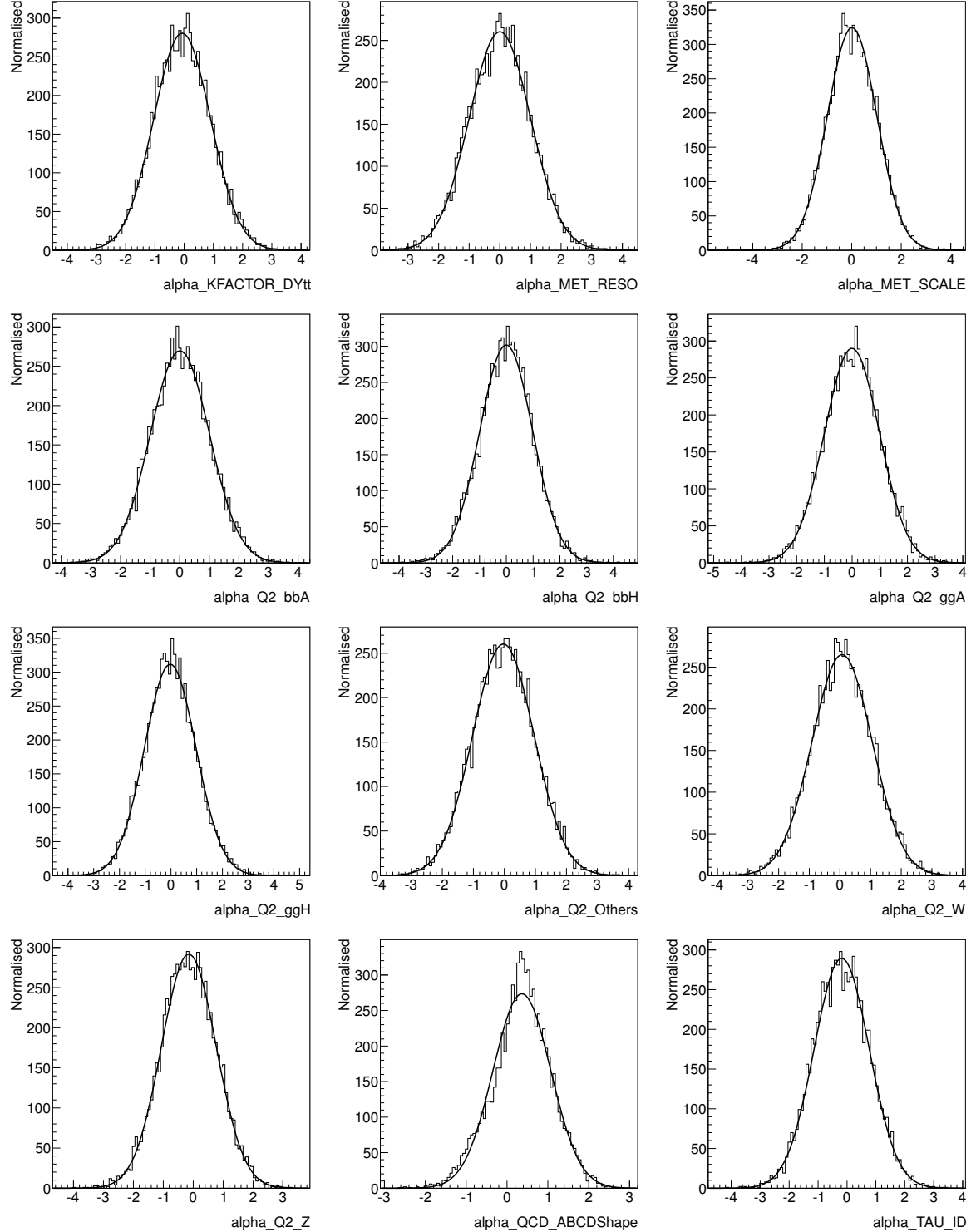


Figure D.3: Pull distributions of nuisance parameters obtained from pseudo data under the H_1 hypothesis with $\mu = \hat{\mu}$ in which $\hat{\mu}$ is obtained from a single fit to data. The considered signal template corresponds to $M_A = 400$ GeV and $\tan\beta = 20$.

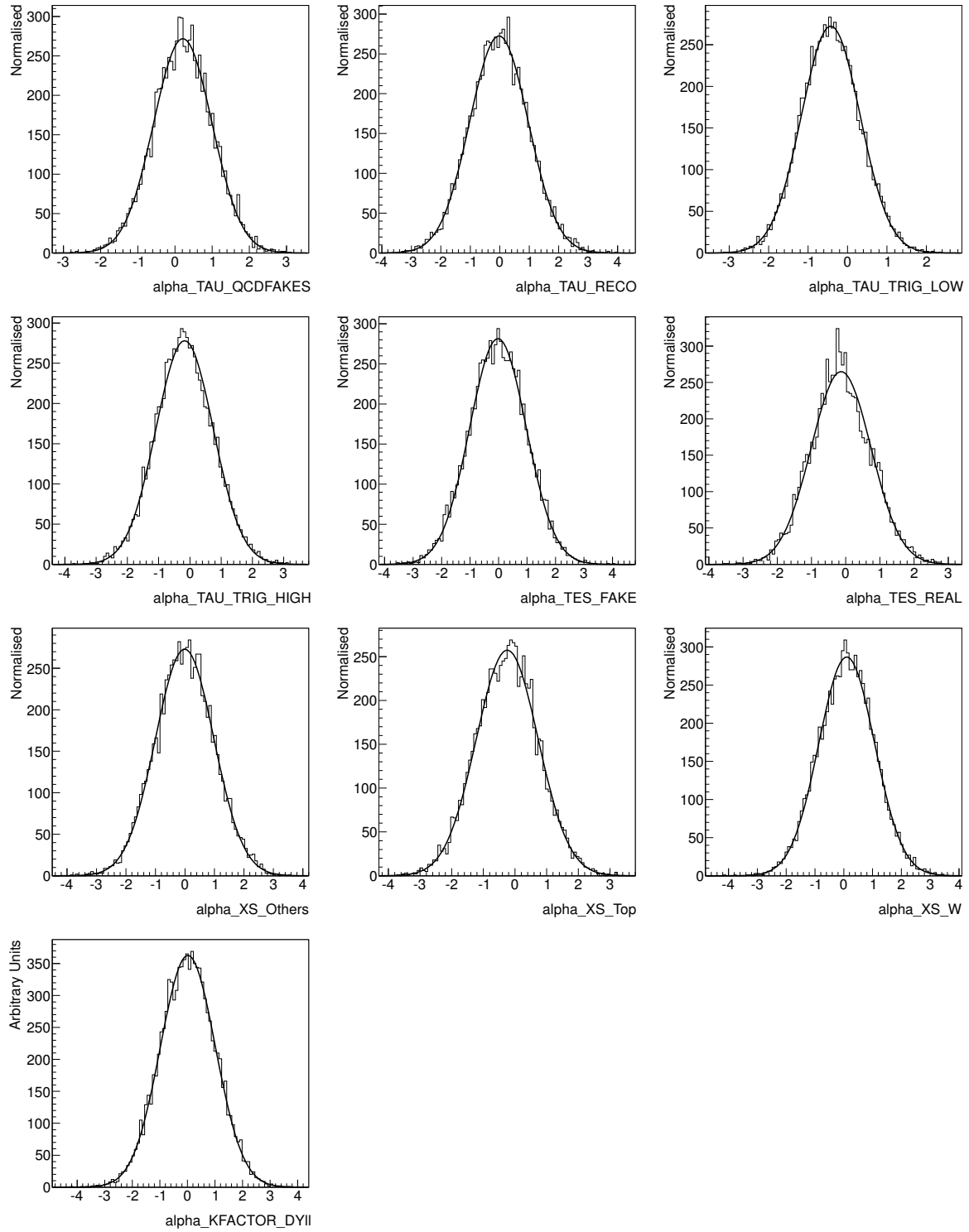


Figure D.4: Pull distributions of nuisance parameters obtained from pseudo data under the H_1 hypothesis with $\mu = \hat{\mu}$ in which $\hat{\mu}$ is obtained from a single fit to data. The considered signal template corresponds to $M_A = 400$ GeV and $\tan\beta = 20$.

D.3 Scans of Negative Log-Likelihood

Figure D.5 and D.6 shows the distributions of the negative log likelihood values profiled for each nuisance parameter.

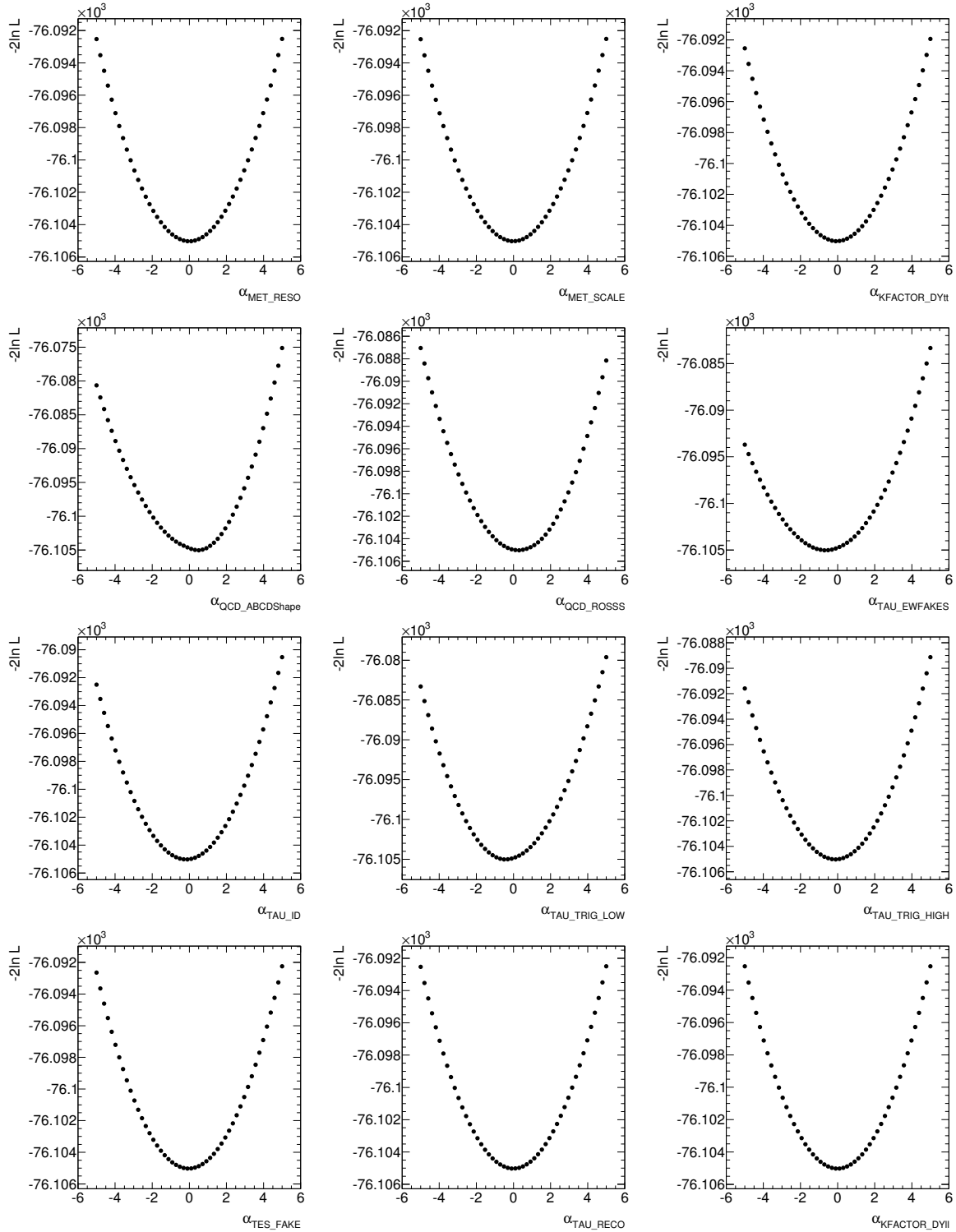


Figure D.5: Negative log-likelihood values obtained from a unconditional fit with all nuisance parameters free, but one, which is scanned between $\pm 5\sigma$ around the mean value.

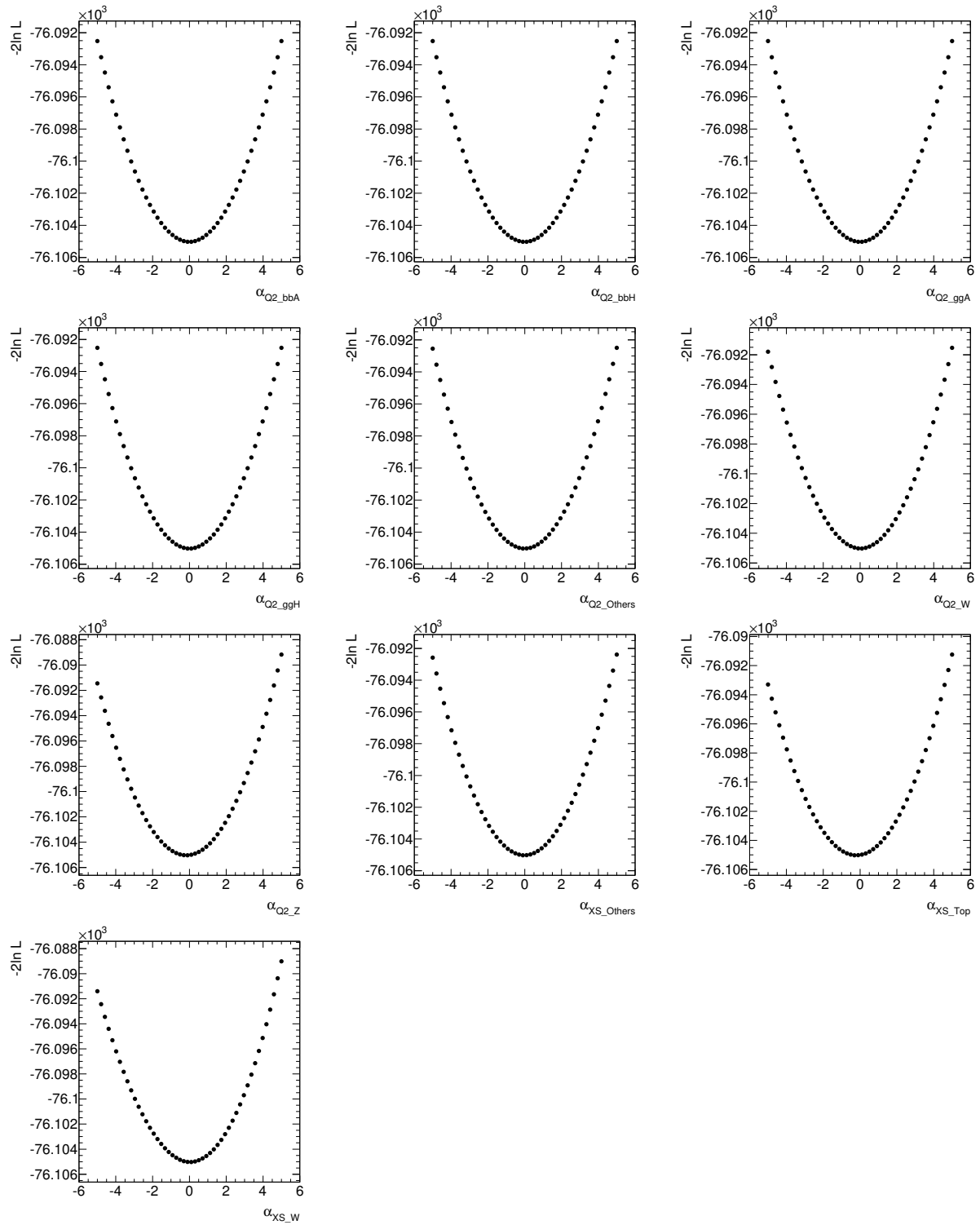


Figure D.6: Negative log-likelihood values obtained from a unconditional fit with all nuisance parameters free, but one, which is scanned between $\pm 5\sigma$ around the mean value.

E Auxiliary Information for the Search for Z' Bosons

This chapter provides auxiliary information for the search for heavy neutral Z' bosons. In Section E.1 MC simulated samples used to validate the signal reweighting procedure are summarised. Section E.2 summarises the systematic uncertainties and expected event yields for all considered mass hypotheses and various thresholds on m_T^{tot} .

E.1 Full Simulation Signal Monte Carlo Samples

$Z' \rightarrow \tau\tau$ Monte Carlo samples have been generated for several mass hypothesis featuring the PYTHIA generator. Tables E.1 lists the generated mass points and details on the samples.

Process	Dataset number	k-factor	ϵ_{filter}	N_{MC}	Generator
$Z' \rightarrow \tau\tau (M_{Z'} = 250 \text{ GeV})$	170201	1	1	384995	Pythia
$Z' \rightarrow \tau\tau (M_{Z'} = 500 \text{ GeV})$	170202	1	1	384995	Pythia
$Z' \rightarrow \tau\tau (M_{Z'} = 750 \text{ GeV})$	170203	1	1	399999	Pythia
$Z' \rightarrow \tau\tau (M_{Z'} = 1000 \text{ GeV})$	170204	1	1	399997	Pythia
$Z' \rightarrow \tau\tau (M_{Z'} = 1250 \text{ GeV})$	170205	1	1	399798	Pythia

Table E.1: MC samples for $Z' \rightarrow \tau\tau$ production.

E.2 Systematics

This section summarises the expected event yields and systematic uncertainties for all tested Z' boson mass hypotheses with m_T^{tot} thresholds applied according to Table 13.1. Tables E.2 - E.14 present the obtained results for $M_{Z'} = [500 - 2125] \text{ GeV}$.

	$Z/\gamma^* \rightarrow \tau\tau + \text{jets}$	multijet	W/Z + jets	Top	Di-boson	SM Total	$Z' (500\text{GeV})$
Expected Events	63.45 ± 1.31	45.60 ± 1.63	17.73 ± 0.70	4.99 ± 1.03	0.03 ± 0.02	131.80 ± 2.43	1477.83 ± 75.63
Th. cross section	$^{4.6}_{-3.6}$	—	± 27.5	± 10.3	± 5.0	$^{6.3}_{-5.8}$	—
Multijet fake-factor	—	± 9.5	—	—	—	± 3.3	—
MC fake-weight	$^{-1.8}_{-1.3}$	—	$^{16.8}_{-14.5}$	$^{27.4}_{-20.2}$	± 65.4	$^{2.4}_{-3.3}$	< 1
JES	—	—	—	—	—	—	—
MET (res.)	< 1	—	< 1	< 1	—	< 1	< 1
MET(scale)	—	—	< 1	< 1	—	< 1	< 1
τ -3p	± 1.2	—	< 1	< 1	< 1	< 1	± 1.0
τ -ID	± 6.6	—	± 3.3	± 5.7	± 2.2	± 3.9	± 6.7
τ -trigger	± 9.9	—	± 1.3	± 7.0	—	± 5.2	± 10.0
TES	$^{6.5}_{-7.5}$	—	$^{9.6}_{-7.3}$	$^{7.5}_{-12.5}$	$^{5.7}_{-0.0}$	± 4.7	$^{5.2}_{-6.6}$

Table E.2: Summary of the total expected event yields and its statistical uncertainty and detector and theory related systematic uncertainties. Quoted numbers correspond to $M_{Z'} = 500 \text{ GeV}$, i.e. $m_T^{\text{tot}} > 350 \text{ GeV}$. Uncertainties are given in %. Entries marked by — are either non applicable or evaluated to zero. W/Z+jets accounts for all contributions from W/Z decays into leptons accompanied by additional jets. The uncertainty on the total SM prediction can be lower than the relative uncertainty from individual contributions due to weights of the expected event yields.

	$Z/\gamma^* \rightarrow \tau\tau + \text{jets}$	multijet	W/Z + jets	Top	Di-boson	SM Total	Z' (625GeV)
Expected Events	36.68 ± 0.69	20.25 ± 1.10	9.92 ± 0.49	2.00 ± 0.49	0.03 ± 0.02	68.87 ± 1.47	814.30 ± 24.52
Th. cross section	$^{4.9}_{-3.8}$	—	± 27.5	± 10.4	± 5.0	$^{6.9}_{-6.3}$	—
Multijet fake-factor	—	± 10.2	—	—	—	± 3.0	—
MC fake-weight	< 1	—	$^{17.2}_{-14.8}$	$^{40.1}_{-29.0}$	± 60.5	$^{4.1}_{-3.5}$	$^{3.0}_{4.4}$
JES	—	—	—	—	—	—	—
MET (res.)	< 1	—	< 1	< 1	< 1	< 1	< 1
MET(scale)	< 1	—	—	—	< 1	< 1	< 1
τ -3p	± 1.6	—	< 1	< 1	< 1	< 1	± 1.6
τ -ID	± 6.8	—	± 3.3	± 4.4	± 2.2	± 4.2	± 6.7
τ -trigger	± 9.9	—	± 1.0	± 5.5	—	± 5.6	± 10.0
TES	$^{10.1}_{-6.7}$	—	$^{9.8}_{-5.5}$	$^{32.7}_{-16.8}$	< 1	$^{7.7}_{-4.8}$	± 4.3

Table E.3: Summary of the total expected event yields and its statistical uncertainty and detector and theory related systematic uncertainties. Quoted numbers correspond to $M_{Z'} = 625$ GeV, i.e. $m_T^{\text{tot}} > 500$ GeV. Uncertainties are given in %. Entries marked by — are either non applicable or evaluated to zero. W/Z+jets accounts for all contributions from W/Z decays into leptons accompanied by additional jets. The uncertainty on the total SM prediction can be lower than the relative uncertainty from individual contributions due to weights of the expected event yields.

	$Z/\gamma^* \rightarrow \tau\tau + \text{jets}$	multijet	W/Z + jets	Top	Di-boson	SM Total	Z' (750GeV)
Expected Events	14.07 ± 0.30	4.60 ± 0.50	3.45 ± 0.23	0.62 ± 0.22	0.01 ± 0.01	22.75 ± 0.67	357.80 ± 15.20
Th. cross section	$^{5.6}_{-4.3}$	—	± 27.5	± 10.4	± 5.0	$^{7.9}_{-7.1}$	—
Multijet fake-factor	—	± 11.7	—	—	—	± 2.4	—
MC fake-weight	$^{5.7}_{-0.8}$	—	$^{17.8}_{-15.3}$	$^{38.8}_{-32.9}$	± 60.6	$^{7.3}_{-3.8}$	$^{8.1}_{-0.1}$
JES	—	—	—	—	—	—	—
MET (res.)	< 1	—	< 1	< 1	—	< 1	$^{1.4}_{0.9}$
MET(scale)	< 1	—	< 1	—	—	< 1	< 1
τ -3p	± 2.5	—	< 1	± 2.1	< 1	± 1.7	± 2.4
τ -ID	± 7.2	—	± 3.4	± 5.3	± 2.4	± 5.1	± 7.1
τ -trigger	± 9.9	—	< 1	± 4.3	—	± 6.3	± 10.0
TES	$^{9.8}_{-11.1}$	—	$^{5.3}_{-6.8}$	$^{9.7}_{-3.4}$	—	$^{7.2}_{-8.0}$	$^{7.4}_{-5.3}$

Table E.4: Summary of the total expected event yields and its statistical uncertainty and detector and theory related systematic uncertainties. Quoted numbers correspond to $M_{Z'} = 750$ GeV, i.e. $m_T^{\text{tot}} > 500$ GeV. Uncertainties are given in %. Entries marked by — are either non applicable or evaluated to zero. W/Z+jets accounts for all contributions from W/Z decays into leptons accompanied by additional jets. The uncertainty on the total SM prediction can be lower than the relative uncertainty from individual contributions due to weights of the expected event yields.

	$Z/\gamma^* \rightarrow \tau\tau + \text{jets}$	multijet	W/Z + jets	Top	Di-boson	SM Total	Z' (875GeV)
Expected Events	8.96 ± 0.17	2.69 ± 0.39	1.85 ± 0.13	0.43 ± 0.21	0.01 ± 0.01	13.95 ± 0.49	193.81 ± 5.91
Th. cross section	$^{6.1}_{-4.5}$	—	± 27.5	± 10.0	± 5.0	$^{7.9}_{-6.9}$	—
Multijet fake-factor	—	± 11.1	—	—	—	± 2.1	—
MC fake-weight	$^{4.2}_{-0.3}$	—	$^{17.5}_{-15.1}$	± 33.2	± 60.6	$^{6.1}_{-3.3}$	$^{3.6}_{-0.1}$
JES	—	—	—	—	—	—	—
MET (res.)	< 1	—	< 1	—	—	< 1	$^{0.0}_{3.6}$
MET(scale)	< 1	—	—	—	—	< 1	< 1
τ -3p	± 2.8	—	< 1	± 2.9	< 1	± 2.0	± 2.9
τ -ID	± 7.3	—	± 3.1	± 6.3	± 2.4	± 5.3	± 7.3
τ -trigger	± 10.0	—	< 1	± 4.7	—	± 6.6	± 10.0
TES	± 10.0	—	$^{12.2}_{-10.1}$	$^{7.6}_{-58.3}$	< 1	$^{8.3}_{-9.1}$	± 4.6

Table E.5: Summary of the total expected event yields and its statistical uncertainty and detector and theory related systematic uncertainties. Quoted numbers correspond to $M_{Z'} = 875$ GeV, i.e. $m_{\text{T}}^{\text{tot}} > 550$ GeV. Uncertainties are given in %. Entries marked by — are either non applicable or evaluated to zero. W/Z+jets accounts for all contributions from W/Z decays into leptons accompanied by additional jets. The uncertainty on the total SM prediction can be lower than the relative uncertainty from individual contributions due to weights of the expected event yields.

	$Z/\gamma^* \rightarrow \tau\tau + \text{jets}$	multijet	W/Z + jets	Top	Di-boson	SM Total	Z' (1000GeV)
Expected Events	5.96 ± 0.10	1.78 ± 0.32	1.14 ± 0.08	0.13 ± 0.05	0.01 ± 0.01	9.02 ± 0.35	121.63 ± 3.92
Th. cross section	$^{6.5}_{-4.8}$	—	± 27.5	± 10.0	± 5.0	$^{7.9}_{-6.8}$	—
Multijet fake-factor	—	± 11.2	—	—	—	± 2.2	—
MC fake-weight	$^{2.4}_{-0.4}$	—	$^{17.7}_{-15.3}$	± 62.9	± 60.1	$^{4.8}_{-3.1}$	< 1
JES	—	—	—	—	—	—	—
MET (res.)	< 1	—	< 1	—	—	< 1	< 1
MET(scale)	< 1	—	—	—	—	< 1	< 1
τ -3p	± 3.1	—	< 1	< 1	< 1	± 2.2	± 3.6
τ -ID	± 7.4	—	± 3.1	± 3.9	± 2.4	± 5.3	± 7.5
τ -trigger	± 10.0	—	< 1	< 1	—	± 6.6	± 10.0
TES	$^{8.4}_{-9.7}$	—	$^{12.0}_{-6.6}$	$^{26.6}_{-1.1}$	—	± 7.5	$^{3.5}_{-4.8}$

Table E.6: Summary of the total expected event yields and its statistical uncertainty and detector and theory related systematic uncertainties. Quoted numbers correspond to $M_{Z'} = 1000$ GeV, i.e. $m_{\text{T}}^{\text{tot}} > 600$ GeV. Uncertainties are given in %. Entries marked by — are either non applicable or evaluated to zero. W/Z+jets accounts for all contributions from W/Z decays into leptons accompanied by additional jets. The uncertainty on the total SM prediction can be lower than the relative uncertainty from individual contributions due to weights of the expected event yields.

	$Z/\gamma^* \rightarrow \tau\tau + \text{jets}$	multijet	W/Z + jets	Top	Di-boson	SM Total	Z' (1125GeV)
Expected Events	2.81 ± 0.05	0.56 ± 0.18	0.51 ± 0.05	0.03 ± 0.02	0.01 ± 0.01	3.93 ± 0.20	62.46 ± 1.99
Th. cross section	$^{7.3}_{-5.3}$	—	± 27.5	± 10.1	± 5.0	$^{8.9}_{-7.5}$	—
Multijet fake-factor	—	± 13.2	—	—	—	± 1.9	—
MC fake-weight	$^{-2.0}_{-0.3}$	—	$^{17.5}_{-15.1}$	± 60.1	± 60.0	$^{1.6}_{-2.9}$	$^{-2.7}_{-0.1}$
JES	—	—	—	—	—	—	—
MET (res.)	< 1	—	—	—	—	< 1	< 1
MET(scale)	< 1	—	—	—	—	< 1	< 1
τ -3p	± 3.8	—	± 1.3	< 1	< 1	± 2.9	± 3.9
τ -ID	± 7.6	—	± 3.3	± 2.1	± 2.4	± 5.9	± 7.6
τ -trigger	± 10.0	—	< 1	—	—	± 7.2	± 10.0
TES	± 10.7	—	$^{2.3}_{-5.5}$	$^{101.6}_{-0.8}$	—	± 8.8	$^{3.8}_{-4.5}$

Table E.7: Summary of the total expected event yields and its statistical uncertainty and detector and theory related systematic uncertainties. Quoted numbers correspond to $M_{Z'} = 1125$ GeV, i.e. $m_T^{\text{tot}} > 700$ GeV. Uncertainties are given in %. Entries marked by — are either non applicable or evaluated to zero. W/Z+jets accounts for all contributions from W/Z decays into leptons accompanied by additional jets. The uncertainty on the total SM prediction can be lower than the relative uncertainty from individual contributions due to weights of the expected event yields.

	$Z/\gamma^* \rightarrow \tau\tau + \text{jets}$	multijet	W/Z + jets	Top	Di-boson	SM Total	Z' (1250GeV)
Expected Events	2.81 ± 0.05	0.56 ± 0.18	0.51 ± 0.05	0.03 ± 0.02	0.01 ± 0.01	3.93 ± 0.20	39.14 ± 1.22
Th. cross section	$^{7.3}_{-5.3}$	—	± 27.5	± 10.1	± 5.0	$^{8.9}_{-7.5}$	—
Multijet fake-factor	—	± 13.2	—	—	—	± 1.9	—
MC fake-weight	$^{-2.0}_{-0.3}$	—	$^{17.5}_{-15.1}$	± 60.1	± 60.0	$^{1.6}_{-2.9}$	$^{-5.1}_{-0.1}$
JES	—	—	—	—	—	—	—
MET (res.)	< 1	—	—	—	—	< 1	< 1
MET(scale)	< 1	—	—	—	—	< 1	—
τ -3p	± 3.8	—	± 1.3	< 1	< 1	± 2.9	± 3.9
τ -ID	± 7.6	—	± 3.3	± 2.1	± 2.4	± 5.9	± 7.5
τ -trigger	± 10.0	—	< 1	—	—	± 7.2	± 10.0
TES	± 10.7	—	$^{2.3}_{-5.5}$	$^{101.6}_{-0.8}$	—	± 8.8	± 3.5

Table E.8: Summary of the total expected event yields and its statistical uncertainty and detector and theory related systematic uncertainties. Quoted numbers correspond to $M_{Z'} = 1250$ GeV, i.e. $m_T^{\text{tot}} > 700$ GeV. Uncertainties are given in %. Entries marked by — are either non applicable or evaluated to zero. W/Z+jets accounts for all contributions from W/Z decays into leptons accompanied by additional jets. The uncertainty on the total SM prediction can be lower than the relative uncertainty from individual contributions due to weights of the expected event yields.

	$Z/\gamma^* \rightarrow \tau\tau + \text{jets}$	multijet	W/Z + jets	Top	Di-boson	SM Total	$Z' (1375\text{GeV})$
Expected Events	0.99 ± 0.02	0.14 ± 0.08	0.18 ± 0.03	< 0.01	0.01 ± 0.01	1.32 ± 0.09	18.84 ± 0.55
Th. cross section	$\begin{smallmatrix} 8.6 \\ -6.2 \end{smallmatrix}$	—	± 27.5	± 12.1	± 5.0	$\begin{smallmatrix} 10.3 \\ -8.5 \end{smallmatrix}$	—
Multijet fake-factor	—	± 16.4	—	—	—	± 1.7	—
MC fake-weight	$\begin{smallmatrix} -2.7 \\ -0.5 \end{smallmatrix}$	—	$\begin{smallmatrix} 17.4 \\ -15.1 \end{smallmatrix}$	$\begin{smallmatrix} 60.3 \\ -35.7 \end{smallmatrix}$	± 60.0	$\begin{smallmatrix} 1.0 \\ -3.1 \end{smallmatrix}$	< 1
JES	—	—	—	—	—	—	—
MET (res.)	< 1	—	-1.9	—	—	< 1	< 1
MET(scale)	< 1	—	$\begin{smallmatrix} -1.9 \\ 0.0 \end{smallmatrix}$	—	—	< 1	< 1
τ -3p	± 4.3	—	± 1.5	± 16.3	—	± 3.4	± 4.3
τ -ID	± 7.5	—	± 3.2	± 3.6	± 2.4	± 6.1	± 7.5
τ -trigger	± 10.0	—	< 1	—	—	± 7.6	± 10.0
TES	$\begin{smallmatrix} 12.0 \\ -9.8 \end{smallmatrix}$	—	$\begin{smallmatrix} 4.0 \\ -5.0 \end{smallmatrix}$	$\begin{smallmatrix} -0.0 \\ -33.1 \end{smallmatrix}$	—	$\begin{smallmatrix} 9.5 \\ -8.0 \end{smallmatrix}$	± 4.5

Table E.9: Summary of the total expected event yields and its statistical uncertainty and detector and theory related systematic uncertainties. Quoted numbers correspond to $M_{Z'} = 1375 \text{ GeV}$, i.e. $m_{\text{T}}^{\text{tot}} > 850 \text{ GeV}$. Uncertainties are given in %. Entries marked by — are either non applicable or evaluated to zero. W/Z+jets accounts for all contributions from W/Z decays into leptons accompanied by additional jets. The uncertainty on the total SM prediction can be lower than the relative uncertainty from individual contributions due to weights of the expected event yields.

	$Z/\gamma^* \rightarrow \tau\tau + \text{jets}$	multijet	W/Z + jets	Top	Di-boson	SM Total	$Z' (1500\text{GeV})$
Expected Events	0.99 ± 0.02	0.14 ± 0.08	0.18 ± 0.03	< 0.01	0.01 ± 0.01	1.32 ± 0.09	12.90 ± 0.36
Th. cross section	$\begin{smallmatrix} 8.6 \\ -6.2 \end{smallmatrix}$	—	± 27.5	± 12.1	± 5.0	$\begin{smallmatrix} 10.3 \\ -8.5 \end{smallmatrix}$	—
Multijet fake-factor	—	± 16.4	—	—	—	± 1.7	—
MC fake-weight	$\begin{smallmatrix} -2.7 \\ -0.5 \end{smallmatrix}$	—	$\begin{smallmatrix} 17.4 \\ -15.1 \end{smallmatrix}$	$\begin{smallmatrix} 60.3 \\ -35.7 \end{smallmatrix}$	± 60.0	$\begin{smallmatrix} 1.0 \\ -3.1 \end{smallmatrix}$	< 1
JES	—	—	—	—	—	—	—
MET (res.)	< 1	—	-1.9	—	—	< 1	< 1
MET(scale)	< 1	—	$\begin{smallmatrix} -1.9 \\ 0.0 \end{smallmatrix}$	—	—	< 1	< 1
τ -3p	± 4.3	—	± 1.5	± 16.3	—	± 3.4	± 4.5
τ -ID	± 7.5	—	± 3.2	± 3.6	± 2.4	± 6.1	± 7.5
τ -trigger	± 10.0	—	< 1	—	—	± 7.6	± 10.0
TES	$\begin{smallmatrix} 12.0 \\ -9.8 \end{smallmatrix}$	—	$\begin{smallmatrix} 4.0 \\ -5.0 \end{smallmatrix}$	$\begin{smallmatrix} -0.0 \\ -33.1 \end{smallmatrix}$	—	$\begin{smallmatrix} 9.5 \\ -8.0 \end{smallmatrix}$	$\begin{smallmatrix} 3.4 \\ -4.0 \end{smallmatrix}$

Table E.10: Summary of the total expected event yields and its statistical uncertainty and detector and theory related systematic uncertainties. Quoted numbers correspond to $M_{Z'} = 1500 \text{ GeV}$, i.e. $m_{\text{T}}^{\text{tot}} > 850 \text{ GeV}$. Uncertainties are given in %. Entries marked by — are either non applicable or evaluated to zero. W/Z+jets accounts for all contributions from W/Z decays into leptons accompanied by additional jets. The uncertainty on the total SM prediction can be lower than the relative uncertainty from individual contributions due to weights of the expected event yields.

	$Z/\gamma^* \rightarrow \tau\tau + \text{jets}$	multijet	W/Z + jets	Top	Di-boson	SM Total	$Z' (1625\text{GeV})$
Expected Events	0.99 ± 0.02	0.14 ± 0.08	0.18 ± 0.03	< 0.01	0.01 ± 0.01	1.32 ± 0.09	8.41 ± 0.20
Th. cross section	$\begin{smallmatrix} 8.6 \\ -6.2 \end{smallmatrix}$	—	± 27.5	± 12.1	± 5.0	$\begin{smallmatrix} 10.3 \\ -8.5 \end{smallmatrix}$	—
Multijet fake-factor	—	± 16.4	—	—	—	± 1.7	—
MC fake-weight	$\begin{smallmatrix} -2.7 \\ -0.5 \end{smallmatrix}$	—	$\begin{smallmatrix} 17.4 \\ -15.1 \end{smallmatrix}$	$\begin{smallmatrix} 60.3 \\ -35.7 \end{smallmatrix}$	± 60.0	$\begin{smallmatrix} 1.0 \\ -3.1 \end{smallmatrix}$	< 1
JES	—	—	—	—	—	—	—
MET (res.)	< 1	—	-1.9	—	—	< 1	< 1
MET(scale)	< 1	—	$\begin{smallmatrix} -1.9 \\ 0.0 \end{smallmatrix}$	—	—	< 1	—
τ -3p	± 4.3	—	± 1.5	± 16.3	—	± 3.4	± 3.8
τ -ID	± 7.5	—	± 3.2	± 3.6	± 2.4	± 6.1	± 7.3
τ -trigger	± 10.0	—	< 1	—	—	± 7.6	± 10.0
TES	$\begin{smallmatrix} 12.0 \\ -9.8 \end{smallmatrix}$	—	$\begin{smallmatrix} 4.0 \\ -5.0 \end{smallmatrix}$	$\begin{smallmatrix} -0.0 \\ -33.1 \end{smallmatrix}$	—	$\begin{smallmatrix} 9.5 \\ -8.0 \end{smallmatrix}$	± 3.0

Table E.11: Summary of the total expected event yields and its statistical uncertainty and detector and theory related systematic uncertainties. Quoted numbers correspond to $M_{Z'} = 1625$ GeV, i.e. $m_{\text{T}}^{\text{tot}} > 850$ GeV. Uncertainties are given in %. Entries marked by — are either non applicable or evaluated to zero. W/Z+jets accounts for all contributions from W/Z decays into leptons accompanied by additional jets. The uncertainty on the total SM prediction can be lower than the relative uncertainty from individual contributions due to weights of the expected event yields.

	$Z/\gamma^* \rightarrow \tau\tau + \text{jets}$	multijet	W/Z + jets	Top	Di-boson	SM Total	$Z' (1875\text{GeV})$
Expected Events	0.99 ± 0.02	0.14 ± 0.08	0.18 ± 0.03	< 0.01	0.01 ± 0.01	1.32 ± 0.09	3.32 ± 0.07
Th. cross section	$\begin{smallmatrix} 8.6 \\ -6.2 \end{smallmatrix}$	—	± 27.5	± 12.1	± 5.0	$\begin{smallmatrix} 10.3 \\ -8.5 \end{smallmatrix}$	—
Multijet fake-factor	—	± 16.4	—	—	—	± 1.7	—
MC fake-weight	$\begin{smallmatrix} -2.7 \\ -0.5 \end{smallmatrix}$	—	$\begin{smallmatrix} 17.4 \\ -15.1 \end{smallmatrix}$	$\begin{smallmatrix} 60.3 \\ -35.7 \end{smallmatrix}$	± 60.0	$\begin{smallmatrix} 1.0 \\ -3.1 \end{smallmatrix}$	< 1
JES	—	—	—	—	—	—	—
MET (res.)	< 1	—	-1.9	—	—	< 1	—
MET(scale)	< 1	—	$\begin{smallmatrix} -1.9 \\ 0.0 \end{smallmatrix}$	—	—	< 1	—
τ -3p	± 4.3	—	± 1.5	± 16.3	—	± 3.4	± 4.0
τ -ID	± 7.5	—	± 3.2	± 3.6	± 2.4	± 6.1	± 7.4
τ -trigger	± 10.0	—	< 1	—	—	± 7.6	± 10.0
TES	$\begin{smallmatrix} 12.0 \\ -9.8 \end{smallmatrix}$	—	$\begin{smallmatrix} 4.0 \\ -5.0 \end{smallmatrix}$	$\begin{smallmatrix} -0.0 \\ -33.1 \end{smallmatrix}$	—	$\begin{smallmatrix} 9.5 \\ -8.0 \end{smallmatrix}$	± 2.3

Table E.12: Summary of the total expected event yields and its statistical uncertainty and detector and theory related systematic uncertainties. Quoted numbers correspond to $M_{Z'} = 1875$ GeV, i.e. $m_{\text{T}}^{\text{tot}} > 850$ GeV. Uncertainties are given in %. Entries marked by — are either non applicable or evaluated to zero. W/Z+jets accounts for all contributions from W/Z decays into leptons accompanied by additional jets. The uncertainty on the total SM prediction can be lower than the relative uncertainty from individual contributions due to weights of the expected event yields.

	$Z/\gamma^* \rightarrow \tau\tau + \text{jets}$	multijet	W/Z + jets	Top	Di-boson	SM Total	Z' (2000GeV)
Expected Events	0.99 ± 0.02	0.14 ± 0.08	0.18 ± 0.03	< 0.01	0.01 ± 0.01	1.32 ± 0.09	2.39 ± 0.05
Th. cross section	$\begin{smallmatrix} 8.6 \\ -6.2 \end{smallmatrix}$	—	± 27.5	± 12.1	± 5.0	$\begin{smallmatrix} 10.3 \\ -8.5 \end{smallmatrix}$	—
Multijet fake-factor	—	± 16.4	—	—	—	± 1.7	—
MC fake-weight	$\begin{smallmatrix} -2.7 \\ -0.5 \end{smallmatrix}$	—	$\begin{smallmatrix} 17.4 \\ -15.1 \end{smallmatrix}$	$\begin{smallmatrix} 60.3 \\ -35.7 \end{smallmatrix}$	± 60.0	$\begin{smallmatrix} 1.0 \\ -3.1 \end{smallmatrix}$	$\begin{smallmatrix} 0.2 \\ 7.9 \end{smallmatrix}$
JES	—	—	—	—	—	—	—
MET (res.)	< 1	—	-1.9	—	—	< 1	< 1
MET(scale)	< 1	—	$\begin{smallmatrix} -1.9 \\ 0.0 \end{smallmatrix}$	—	—	< 1	—
τ -3p	± 4.3	—	± 1.5	± 16.3	—	± 3.4	± 3.9
τ -ID	± 7.5	—	± 3.2	± 3.6	± 2.4	± 6.1	± 7.4
τ -trigger	± 10.0	—	< 1	—	—	± 7.6	± 10.0
TES	$\begin{smallmatrix} 12.0 \\ -9.8 \end{smallmatrix}$	—	$\begin{smallmatrix} 4.0 \\ -5.0 \end{smallmatrix}$	$\begin{smallmatrix} -0.0 \\ -33.1 \end{smallmatrix}$	—	$\begin{smallmatrix} 9.5 \\ -8.0 \end{smallmatrix}$	$\begin{smallmatrix} 1.9 \\ -1.5 \end{smallmatrix}$

Table E.13: Summary of the total expected event yields and its statistical uncertainty and detector and theory related systematic uncertainties. Quoted numbers correspond to $M_{Z'} = 2000$ GeV, i.e. $m_T^{\text{tot}} > 850$ GeV. Uncertainties are given in %. Entries marked by — are either non applicable or evaluated to zero. Contributions from W/Z+jets decaying to light leptons, di-boson processes as well as $t\bar{t}$ and single-top are summarised as "Others". The uncertainty on the total SM prediction can be lower than the relative uncertainty from individual contributions due to weights of the expected event yields.

	$Z/\gamma^* \rightarrow \tau\tau + \text{jets}$	multijet	W/Z + jets	Top	Di-boson	SM Total	Z' (2125GeV)
Expected Events	0.99 ± 0.02	0.14 ± 0.08	0.18 ± 0.03	< 0.01	0.01 ± 0.01	1.32 ± 0.09	1.71 ± 0.03
Th. cross section	$\begin{smallmatrix} 8.6 \\ -6.2 \end{smallmatrix}$	—	± 27.5	± 12.1	± 5.0	$\begin{smallmatrix} 10.3 \\ -8.5 \end{smallmatrix}$	—
Multijet fake-factor	—	± 16.4	—	—	—	± 1.7	—
MC fake-weight	$\begin{smallmatrix} -2.7 \\ -0.5 \end{smallmatrix}$	—	$\begin{smallmatrix} 17.4 \\ -15.1 \end{smallmatrix}$	$\begin{smallmatrix} 60.3 \\ -35.7 \end{smallmatrix}$	± 60.0	$\begin{smallmatrix} 1.0 \\ -3.1 \end{smallmatrix}$	$\begin{smallmatrix} 0.2 \\ -4.0 \end{smallmatrix}$
JES	—	—	—	—	—	—	—
MET (res.)	< 1	—	-1.9	—	—	< 1	< 1
MET(scale)	< 1	—	$\begin{smallmatrix} -1.9 \\ 0.0 \end{smallmatrix}$	—	—	< 1	< 1
τ -3p	± 4.3	—	± 1.5	± 16.3	—	± 3.4	± 3.7
τ -ID	± 7.5	—	± 3.2	± 3.6	± 2.4	± 6.1	± 7.3
τ -trigger	± 10.0	—	< 1	—	—	± 7.6	± 10.0
TES	$\begin{smallmatrix} 12.0 \\ -9.8 \end{smallmatrix}$	—	$\begin{smallmatrix} 4.0 \\ -5.0 \end{smallmatrix}$	$\begin{smallmatrix} -0.0 \\ -33.1 \end{smallmatrix}$	—	$\begin{smallmatrix} 9.5 \\ -8.0 \end{smallmatrix}$	± 1.9

Table E.14: Summary of the total expected event yields and its statistical uncertainty and detector and theory related systematic uncertainties. Quoted numbers correspond to $M_{Z'} = 2125$ GeV, i.e. $m_T^{\text{tot}} > 850$ GeV. Uncertainties are given in %. Entries marked by — are either non applicable or evaluated to zero. W/Z+jets accounts for all contributions from W/Z decays into leptons accompanied by additional jets. The uncertainty on the total SM prediction can be lower than the relative uncertainty from individual contributions due to weights of the expected event yields.

Bibliography

ATLAS internal documents are listed for completeness, although not publically available

- [1] S. L. Glashow, *Partial Symmetries of Weak Interactions*, [Nucl. Phys. **22** \(1961\) 579 – 588](#).
- [2] S. Weinberg, *A Model of Leptons*, [Phys. Rev. Lett. **19** \(1967\) no. 21, 1264 – 1266](#).
- [3] A. Salam, *Weak and Electromagnetic Interactions*, [Conf. Proc. **C680519** \(1968\) 367–377](#).
- [4] F. Englert and R. Brout, *Broken Symmetry and the Mass of Gauge Vector Mesons*, [Phys. Rev. Lett. **13** \(1964\) 321 – 323](#).
- [5] P. W. Higgs, *Broken symmetries, massless particles and gauge fields*, [Phys. Lett. **12** \(1964\) 132 – 133](#).
- [6] P. W. Higgs, *Broken Symmetries and the Masses of Gauge Bosons*, [Phys. Rev. Lett. **13** \(1964\) 508 – 509](#).
- [7] P. W. Higgs, *Spontaneous Symmetry Breakdown without Massless Bosons*, [Phys. Rev. **145** \(1966\) 1156 – 1163](#).
- [8] G. S. Guralnik, C. R. Hagen, and T. W. B. Kibble, *Global Conservation Laws and Massless Particles*, [Phys. Rev. Lett. **13** \(1964\) 585 – 587](#).
- [9] L. R. Evans and P. Bryant, *LHC Machine*, [JINST **3** \(2008\) S08001](#). 164 p. This report is an abridged version of the LHC Design Report (CERN-2004-003).
- [10] ATLAS Collaboration, *The ATLAS Experiment at the CERN Large Hadron Collider*, [JINST **3** \(2008\) S08003](#).
- [11] CMS Collaboration, *The CMS Experiment at the CERN LHC*, [JINST **3** \(2008\) S08004](#).
- [12] ATLAS Collaboration, *Observation of a new particle in the search for the Standard Model Higgs boson with the ATLAS detector at the LHC*, [Phys. Lett. **B716** \(2012\) no. 1, 1–29](#).
- [13] CMS Collaboration, *Observation of a new boson at a mass of 125 GeV with the CMS experiment at the LHC*, [Phys. Lett. **B716** \(2012\) no. 1, 30–61](#), [arXiv:1207.7235 \[hep-ex\]](#).
- [14] WMAP Collaboration, *Nine-Year Wilkinson Microwave Anisotropy Probe (WMAP) Observations: Final Maps and Results*, [arXiv:1212.5225 \[astro-ph\]](#).
- [15] Planck Collaboration, *Planck 2013 results. I. Overview of products and scientific results*, [arXiv:1303.5062 \[astro-ph\]](#).
- [16] J. Beringer et al. (Particle Data Group), *Review of Particle Physics, 2012-2013*, [Phys. Rev. **D86** \(2012\) 010001](#).
- [17] S. P. Martin, *A Supersymmetry Primer*, [arXiv:9709356 \[hep-ph\]](#).
- [18] Y. A. Golfand and E. P. Likhtman, *Extension of the Algebra of Poincare Group Generators and Violation of p Invariance*, [JETP Lett. **13** \(1971\) 323–326](#).
- [19] J. Wess and B. Zumino, *Supergauge Transformations in Four-Dimensions*, [Nucl. Phys. **B70** \(1974\) 39–50](#).
- [20] P. Fayet, *Supersymmetry and Weak, Electromagnetic and Strong Interactions*, [Phys. Lett. **B64** \(1976\) 159](#).

- [21] P. Fayet, *Spontaneously Broken Supersymmetric Theories of Weak, Electromagnetic and Strong Interactions*, *Phys. Lett.* **B69** (1977) 489.
- [22] P. Fayet, *Relations Between the Masses of the Superpartners of Leptons and Quarks, the Goldstino Couplings and the Neutral Currents*, *Phys. Lett.* **B84** (1979) 416.
- [23] G. Farrar and P. Fayet, *Phenomenology of the Production, Decay, and Detection of New Hadronic States Associated with Supersymmetry*, *Phys. Lett.* **B76** (1978) 575–579.
- [24] D. Griffiths, *Introduction to Elementary Particles*. Wiley-VCH Verlag, 2008.
- [25] S. F. Novaes, *Standard Model: An Introduction*, [arXiv:0001283 \[hep-ph\]](#).
- [26] M. Gomez-Bock, M. Mondragón, M. Mühlleitner, M. Spira, and P. M. Zerwas, *Concepts of Electroweak Symmetry Breaking and Higgs Physics*, [arXiv:0712.2419 \[hep-ph\]](#).
- [27] A. Djouadi, *The anatomy of electroweak symmetry breaking Tome II: The Higgs bosons in the Minimal Supersymmetric Model*, *Phys. Rept.* **459** (2008) no. 1-6, 1–241.
- [28] P. Langacker, *The Physics of Heavy Z' Gauge Bosons*, *Rev. Mod. Phys.* **81** (2009) 1199–1228, [arXiv:0801.1345 \[hep-ph\]](#).
- [29] T. G. Rizzo, *Z' phenomenology and the LHC*, [arXiv:0610104 \[hep-ph\]](#). Published in Boulder, 2006, Colliders and Neutrinos (TASI 2006).
- [30] E. Noether, *Invarianten beliebiger Differentialausdrücke*, *Gött. Nachr.* (1918) 37–44.
- [31] E. Noether, *Invariante Variationsprobleme*, *Gött. Nachr.* (1918) 235–357.
- [32] W. Heisenberg, *Über den anschaulichen Inhalt der quantentheoretischen Kinematik und Mechanik*, *Zeitschrift für Physik* **43** (1927) 3–4.
- [33] H. Yukawa, *On the Interaction of Elementary Particles*, *Proc. Phys. Math. Soc. Jap.* **17** (1935) 48–57.
- [34] C. S. Wu, E. Ambler, R. W. Hayward, D. D. Hoppes, and R. P. Hudson, *Experimental Test of Parity Conservation in Beta Decay*, *Phys. Rev.* **105** (1957) no. 4, 1413–1415.
- [35] T. Nakano and K. Nishijima, *Charge Independence for V -particles*, *Prog. Theor. Phys.* **10** (1953) no. 5, 581–582.
- [36] M. Gell-Mann, *The interpretation of the new particles as displaced charge multiplets*, *Il Nuovo Cimento* **4** (1956) no. 2, 848–866.
- [37] M. Kobayashi and T. Maskawa, *CP -Violation in the Renormalizable Theory of Weak Interaction*, *Prog. Theor. Phys.* **49** (1973) 652–657.
- [38] Z. Maki, M. Nakagawa, and S. Sakata, *Remarks on the Unified Model of Elementary Particles*, *Progress of Theoretical Physics* **28** (1962) 870–880.
- [39] G. Bhattacharyya, *A Pedagogical Review of Electroweak Symmetry Breaking Scenarios*, *Rept. Prog. Phys.* **74** (2011) 026201, [arXiv:0910.5095 \[hep-ph\]](#).
- [40] ATLAS Collaboration, *Combined coupling measurements of the Higgs-like boson with the ATLAS detector using up to 25 fb^{-1} of proton-proton collision data*, *ATLAS-CONF-2013-034*.
- [41] G. Cowan, K. Cranmer, E. Gross, and O. Vitells, *Asymptotic formulae for likelihood-based tests of new physics*, *European Physical Journal C* **71** (2011) 1554, [arXiv:1007.1727](#).

- [42] ATLAS Collaboration, *Evidence for Higgs Boson Decays to the $\tau^+\tau^-$ Final State with the ATLAS Detector*, [ATLAS-CONF-2013-108](#).
- [43] CMS Collaboration, *Combination of standard model Higgs boson searches and measurements of the properties of the new boson with a mass near 125 GeV*, [CMS-PAS-HIG-13-005](#).
- [44] L. Landau, *On the angular momentum of a two-photon system*, Dokl. Akad. Nauk. Ser. Fiz. **60** (1948) 207–209.
- [45] C.-N. Yang, *On the angular momentum of a two-photon system*, [Phys. Rev. **77** \(1950\) 242–245](#).
- [46] ATLAS Collaboration, *Study of the spin of the new boson with up to 25 fb⁻¹ of ATLAS data*, [ATLAS-CONF-2013-040](#).
- [47] S. R. Coleman and J. Mandula, *All possible symmetries of the S matrix*, [Phys. Rev. **159** \(1967\) no. 5, 1251–1256](#).
- [48] R. Haag, J. T. Lopuszanski, and M. Sohnius, *All possible generators of supersymmetries of the S-matrix*, [Nucl. Phys. **B88** \(1975\) no. 2, 257–274](#).
- [49] D. Kazakov, *Beyond the Standard Model (In Search of Supersymmetry)*, [arXiv:0012288 \[hep-ph\]](#).
- [50] H. Baer and X. Tata, *Weak Scale Supersymmetry: From Superfields to Scattering Events*. Cambridge University Press, 2006.
- [51] S. Dimopoulos and D. Sutter, *The Supersymmetric Flavor Problem*, [arXiv:9504415 \[hep-ph\]](#).
- [52] J. Gunion and H. Haber, *Higgs Bosons in Supersymmetric Models. 1.*, [Nucl. Phys. **B272** \(1986\) 1](#).
- [53] H. P. Nilles, *Dynamically Broken Supergravity and the Hierarchy Problem*, [Phys. Lett. **B115** \(1982\) 193](#).
- [54] A. Chamseddine, R. Arnowitt, and N. P., *Locally Supersymmetric Grand Unification*, [Phys. Rev. Lett. **49** \(1982\) 970](#).
- [55] A. Chamseddine, R. Arnowitt, and N. P., *Gauge Hierarchy in Supergravity Guts*, [Nucl. Phys. **B227** \(1983\) 121](#).
- [56] R. Barbieri, S. Ferrara, and C. Savoy, *Gauge Models with Spontaneously Broken Local Supersymmetry*, [Phys. Lett. **B119** \(1982\) 343](#).
- [57] E. Cremmer, P. Fayet, and L. Girardello, *Gravity Induced Supersymmetry Breaking and Low-Energy Mass Spectrum*, [Phys. Lett. **B122** \(1983\) 41](#).
- [58] E. Ibanez, *Locally Supersymmetric SU(5) Grand Unification*, [Phys. Lett. **B118** \(1982\) 73](#).
- [59] H. P. Nilles, M. Srednicki, and D. Wyler, *Weak Interaction Breakdown Induced by Supergravity*, [Phys. Lett. **B120** \(1983\) 346](#).
- [60] LEP Working Group for Higgs boson searches, ALEPH Collaboration, DELPHI Collaboration, L3 Collaboration, OPAL Collaboration, *Search for Neutral MSSM Higgs Bosons at LEP*, [Eur. Phys. J. **C47** \(2006\) 547–587](#), [arXiv:0602042 \[hep-ex\]](#).
- [61] B. Allanach, M. Battaglia, G. Blair, M. S. Carena, A. De Roeck, et al., *The Snowmass Points and Slopes: Benchmarks for SUSY Searches*, [Eur. Phys. J. **C25** \(2002\) 113–123](#), [arXiv:0202233 \[hep-ph\]](#).

- [62] W. Siegel, *Supersymmetric Dimensional Regularization via Dimensional Reduction*, *Phys. Lett.* **B84** (1979) 193.
- [63] D. M. Capper, D. R. T. Jones, and P. van Nieuwenhuizen, *Regularization by Dimensional Reduction of Supersymmetric and Nonsupersymmetric Gauge Theories*, *Nucl. Phys.* **B167** (1980) 479.
- [64] M. Carena, S. Heinemeyer, O. Stål, C. Wagner, and G. Weiglein, *MSSM Higgs Boson Searches at the LHC: Benchmark Scenarios after the Discovery of a Higgs-like Particle*, *Eur. Phys. J.* **C73** (2013) 2552, [arXiv:1302.7033 \[hep-ph\]](#).
- [65] S. Heinemeyer, W. Hollik, and G. Weiglein, *The Masses of the Neutral CP-even Higgs Bosons in the MSSM: Accurate Analysis at the Two-Loop Level*, *Eur. Phys. J.* **C9** (1999) 343–366, [arXiv:9812472 \[hep-ph\]](#).
- [66] S. Heinemeyer, W. Hollik, and G. Weiglein, *FeynHiggs: a program for the calculation of the masses of the neutral CP-even Higgs bosons in the MSSM*, *Comput. Phys. Commun.* **124** (2000) 76–89, [arXiv:9812320 \[hep-ph\]](#).
- [67] G. G. Degrandi, S. Heinemeyer, W. Hollik, P. Slavich, and G. Weiglein, *Towards High-Precision Predictions for the MSSM Higgs Sector*, *Eur. Phys. J.* **C28** (2003) 133–143, [arXiv:0212020 \[hep-ph\]](#).
- [68] M. Frank, T. Hahn, S. Heinemeyer, W. Hollik, H. Rzehak, and G. Weiglein, *The Higgs Boson Masses and Mixings of the Complex MSSM in the Feynman-Diagrammatic Approach*, *JHEP* **02** (2007) 047, [arXiv:0611326 \[hep-ph\]](#).
- [69] R. Diener, S. Godfrey, and T. A. Martin, *Unravelling an Extra Neutral Gauge Boson at the LHC using Third Generation Fermions*, *Phys. Rev.* **D83** (2011) 115008, [arXiv:1006.2845 \[hep-ph\]](#).
- [70] A. Leike, *The Phenomenology of extra neutral gauge bosons*, *Phys. Rept.* **317** (1999) 143–250, [arXiv:9805494 \[hep-ph\]](#).
- [71] X.-G. He and G. Valencia, *$K^+ \rightarrow \pi^+ \nu \bar{\nu}$ and FCNC from non-universal Z' bosons*, *Phys. Rev.* **D70** (2004) 053003, [arXiv:0404229 \[hep-ph\]](#).
- [72] K. Cheung, C.-W. Chiang, N. Deshpande, and J. Jiang, *Constraints on flavor-changing Z' models by B_s mixing, Z' production, and $B_s \rightarrow \mu^+ \mu^-$* , *Phys. Lett.* **B652** (2006) 285 – 291, [arXiv:0604223 \[hep-ph\]](#).
- [73] S. King, S. Moretti, and R. Nevzorov, *Theory and Phenomenology of an Exceptional Supersymmetric Standard Model*, *Phys. Rev.* **D73** (2006) 035009, [arXiv:0510419 \[hep-ph\]](#).
- [74] Y. Hosotani, *Dynamical gauge symmetry breaking as the casimir effect*, *Phys. Lett.* **B129** (1983) 193–197.
- [75] V. Barger, P. Langacker, and H.-S. Lee, *Primordial Nucleosynthesis Constraints on Z' Properties*, *Phys. Rev.* **D67** (2003) 075009, [arXiv:0302066 \[hep-ph\]](#).
- [76] M. Cvetič and S. Godfrey, *Discovery and identification of extra gauge bosons*, [arXiv:9504216 \[hep-ph\]](#).
- [77] S. Weinberg, *Implications of Dynamical Symmetry Breaking*, *Phys. Rev.* **D13** (1976) 974–996.
- [78] L. Susskind, *Dynamics of Spontaneous Symmetry Breaking in the Weinberg-Salam Theory*, *Phys. Rev.* **D20** (1979) 2619.

- [79] C. T. Hill and E. H. Simmons, *Strong Dynamics and Electroweak Symmetry Breaking*, *Phys. Rept.* **381** (2004) 235–402, [arXiv:0203079 \[hep-ph\]](#).
- [80] R. S. Chivukula, M. Dugan, and M. Golden, *Electroweak Corrections in Technicolor Reconsidered*, *Phys. Lett.* **B292** (1992) 435–441, [arXiv:9207249 \[hep-ph\]](#).
- [81] G. Buchalla, G. Burdman, C. Hill, and D. Kominis, *GIM Violation and New Dynamics of the Third Generation*, *Phys. Rev.* **D53** (1996) 5185–5200, [arXiv:9510376 \[hep-ph\]](#).
- [82] T. Han, E. H. Logan, B. McElrath, and L.-T. Wang, *Phenomenology of the Little Higgs Model*, *Phys. Rev.* **D67** (2004) 095004, [arXiv:0301040 \[hep-ph\]](#).
- [83] N. Arkani-Hamed, A. Cohen, E. Katz, and A. Nelson, *The Littlest Higgs*, *JHEP* **07** (2002) 034, [arXiv:0206021 \[hep-ph\]](#).
- [84] U. Haisch and F. Mahmoudi, *MSSM: Cornered and Correlated*, *JHEP* **01** (2013) 061, [arXiv:1210.7806 \[hep-ph\]](#).
- [85] A. Arbey, M. Battaglia, A. Djouadi, and F. Mahmoudi, *An update of the constraints on the phenomenological MSSM from the new LHC Higgs results*, *Phys. Lett.* **B720** (2013) no. 1-3, 153–160, [arXiv:1211.4004 \[hep-ph\]](#).
- [86] Heavy Flavour Averaging Group (HFAG), *Averages of b -hadron, c -hadron, and tau-lepton properties as of early 2012*, [arXiv:1207.1158 \[hep-ex\]](#).
- [87] S. Playfer and S. Stone, *Rare b Decays*, *Int. J. Mod. Phys.* **A10** (1995) 4107–4138, [arXiv:9505392 \[hep-ph\]](#).
- [88] CMS Collaboration, *Combination of results on the rare decays $B_{(s)}^0 \rightarrow \mu^+ \mu^-$ from the CMS and LHCb experiments*, *CMS-PAS-BPH-13-007, LHCb-CONF-2013-012*, 2013.
- [89] XENON-100 Collaboration, *Analysis of the XENON100 Dark Matter Search Data*, [arXiv:1207.3458 \[astro-ph\]](#).
- [90] CDF and DØ Collaboration, *Combined CDF and DØ upper limits on MSSM Higgs boson production in tau-tau final states with up to 2.2 fb^{-1}* , [arXiv:1003.3363 \[hep-ex\]](#).
- [91] CDF and DØ Collaboration, *Search for Neutral Higgs Bosons in Events with Multiple Bottom Quarks at the Tevatron*, *Phys. Rev. D* **86** (2012) 091101, [arXiv:1207.2757 \[hep-ex\]](#).
- [92] E. Gross and O. Vitells, *Trial factors for the look elsewhere effect in high energy physics*, *Eur. Phys. J.* **C70** (2010) 552 – 530, [arXiv:1005.1891 \[physics.data-an\]](#).
- [93] ATLAS Collaboration, *Search for the neutral Higgs bosons of the Minimal Supersymmetric Standard Model in pp collisions at $\sqrt{s} = 7 \text{ TeV}$ with the ATLAS detector*, *JHEP* **02** (2013) 095, [arXiv:1211.6956 \[hep-ex\]](#).
- [94] CMS Collaboration, *Search for neutral Higgs bosons decaying to tau pairs in pp collisions at $\sqrt{s} = 7 \text{ TeV}$* , *Phys. Lett. B* **713** (2012) 68, [arXiv:1202.4083 \[hep-ex\]](#).
- [95] A. Elagin, P. Murat, A. Pranko, and A. Safonov, *A New Mass Reconstruction Technique for Resonances Decaying to di -tau*, *Nucl. Instrum. Meth.* **A654** 481–489, [arXiv:1012.4686 \[hep-ex\]](#).
- [96] CMS Collaboration, *Search for Neutral MSSM Higgs Bosons Decaying to Tau Pairs in pp Collisions at $\sqrt{s} = 7 \text{ TeV}$* , *Phys. Rev. Lett.* **106** 231801, [arXiv:1104.1619 \[hep-ex\]](#).

- [97] CMS Collaboration, *Search for a Higgs boson decaying into a b -quark pair and produced in association with b quarks in proton-proton collisions at 7 TeV*, *Phys. Lett. B* **722** (2013) 207 – 232, [arXiv:1302.2892 \[hep-ex\]](#).
- [98] ALEPH Collaboration, DELPHI Collaboration, L3 Collaboration, OPAL Collaboration, LEP Electroweak Working Group Collaboration, *A Combination of Preliminary Electroweak Measurements and Constraints on the Standard Model*, [arXiv:0612034 \[hep-ex\]](#).
- [99] ALEPH Collaboration, DELPHI Collaboration, L3 Collaboration, OPAL Collaboration, LEP Electroweak Working Group Collaboration, *Electroweak Measurements in Electron-Positron Collisions at W -Boson-Pair Energies at LEP*, *Phys. Rept.* **532** (2013) 119–244, [arXiv:1302.3415 \[hep-ex\]](#).
- [100] SLAC E158 Collaboration, *Precision Measurement of the Weak Mixing Angle in Møller Scattering*, *Phys. Rev. Lett.* **95** (2005) 081601, [arXiv:0504049 \[hep-ph\]](#).
- [101] C. Wood, S. Bennett, D. Cho, B. Masterson, J. Roberts, et al., *Violations of fundamental symmetries in atoms and tests of unification theories of elementary particles*, *Science* **275** (1997) 1759–1763.
- [102] J. Ginges and V. Flambaum, *Violations of fundamental symmetries in atoms and tests of unification theories of elementary particles*, *Phys. Rept.* **397** (2004) 63–154, [arXiv:0309054 \[physics\]](#).
- [103] CDF Collaboration, *Search for High-Mass e^+e^- Resonances in $p\bar{p}$ Collisions at $\sqrt{s}=1.96$ TeV*, *Phys. Rev. Lett.* **102** (2009) 031801, [arXiv:0810.2059 \[hep-ex\]](#).
- [104] DØ Collaboration, *Search for a heavy neutral gauge boson in the dielectron channel with 5.4 fb^{-1} of $p\bar{p}$ collisions at $\sqrt{s}=1.96\text{ TeV}$* , *Phys. Lett. B* **695** (2011) 88–94, [arXiv:1008.2023 \[hep-ex\]](#).
- [105] CDF Collaboration, *Search for High Mass Resonances Decaying to Muon Pairs in $\sqrt{s}=1.96$ TeV $p\bar{p}$ Collisions*, *Phys. Rev. Lett.* **106** (2011) 121801, [arXiv:1101.4578 \[hep-ex\]](#).
- [106] CDF Collaboration, *Search for new physics using high mass tau pairs from 1.96 TeV $p\bar{p}$ collisions*, *Phys. Rev. Lett.* **95** (2005) 131801, [arXiv:0506034 \[hep-ex\]](#).
- [107] ATLAS Collaboration, *Search for high-mass dilepton resonances with 6.1 fb^{-1} of pp collisions at $\sqrt{s}=8$ TeV with the ATLAS experiment*, *ATLAS-CONF-2012-129*.
- [108] CMS Collaboration, *Search for heavy narrow dilepton resonances in pp collisions at $\sqrt{s}=7$ TeV and $\sqrt{s}=8$ TeV*, *Phys. Lett. B* **720** (2013) 63, [arXiv:1212.6175 \[hep-ex\]](#).
- [109] ATLAS Collaboration, *Search for dilepton resonances in pp collisions at $\sqrt{s}=7$ TeV with the ATLAS detector*, *Phys. Rev. Lett.* **107** (2011) 272002, [arXiv:1108.1582 \[hep-ex\]](#).
- [110] A. Caldwell, D. Kollár, and K. Kröninger, *BAT - The Bayesian analysis toolkit*, *Comput. Phys. Commun.* **180** (2009) 2197–2209, [arXiv:0808.2552 \[physics.data-an\]](#).
- [111] CMS Collaboration, *Search for Resonances in the Dilepton Mass Distribution in pp Collisions at $\sqrt{s}=7$ TeV*, *JHEP* **1105** (2011) 093, [arXiv:1103.0981 \[hep-ex\]](#).
- [112] ATLAS Collaboration, *A search for high-mass resonances decaying to $\tau^+\tau^-$ in pp collisions at $\sqrt{s}=7$ TeV with the ATLAS detector*, *Physics Letters B* **719** (2013) no. 4–5, 242 – 260, [arXiv:1210.6604 \[hep-ex\]](#).
- [113] CMS Collaboration, *Search for high mass resonances decaying into tau-lepton pairs in pp collisions at $\sqrt{s}=7$ TeV*, *Phys. Lett. B* **716** (2012) 82, [arXiv:1206.1725 \[hep-ex\]](#).

- [114] LHCb Collaboration, *The LHCb Experiment at the CERN LHC*, *JINST* **3** (2008) S08005.
- [115] ALICE Collaboration, *The ALICE Experiment at the CERN LHC*, *JINST* **3** (2008) S08002.
- [116] ATLAS Collaboration, *A measurement of the inclusive W^\pm and Z/γ^* cross sections in the e and μ decay channels in pp collisions at $\sqrt{s} = 7$ TeV with the ATLAS detector*, *Phys. Rev.* **D85** (2011) 072004, [arXiv:1109.5141 \[hep-ex\]](#).
- [117] ATLAS Collaboration, *Statistical combination of top quark pair production cross-section measurements using dilepton, single-lepton, and all-hadronic final states at $\sqrt{s} = 7$ TeV with the ATLAS detector*, *ATLAS-CONF-2012-024*.
- [118] ATLAS Collaboration, *Charged-particle multiplicities in pp interactions measured with the ATLAS detector at the LHC*, *New J. Phys.* **13** (2011) 053033, [arXiv:1012.5104 \[hep-ex\]](#).
- [119] J. Campbell, J. Huston, and W. Stirling, *Hard Interactions of Quarks and Gluons: a Primer for LHC Physics*, [arXiv:0611148 \[hep-ph\]](#).
- [120] E. Lefèvre, *The CERN accelerator complex*, *CERN-DI-0812015*.
- [121] *LHC Performance and Statistics*, <http://lhc-statistics.web.cern.ch/LHC-Statistics/index.php>.
- [122] ATLAS Collaboration, *The ATLAS Inner Detector commissioning and calibration*, *Eur. Phys. J.* **C70** (2010) 787–821, [arXiv:1004.5293 \[hep-ex\]](#).
- [123] ATLAS Collaboration, *Readiness of the ATLAS Liquid Argon Calorimeter for LHC Collisions*, *Eur. Phys. J.* **C70** (2010) 723–753, [arXiv:0912.2642 \[hep-ex\]](#).
- [124] ATLAS Collaboration, *ATLAS Detector and Physics Performance: Technical Design Report*. CERN, 1999.
- [125] M. Aharrouche et al., *Measurement of the response of the ATLAS liquid argon barrel calorimeter to electrons at the 2004 combined test-beam*, *Nuclear Instruments and Methods in Physics Research Section A: Accelerators, Spectrometers, Detectors and Ass*.
- [126] ATLAS Collaboration, *Electron performance measurements with the ATLAS detector using the 2010 LHC proton-proton collision data*, *Eur. Phys. J.* **C72** (2012) 1909, [arXiv:1110.3174 \[hep-ex\]](#).
- [127] H. Stenzel, *Luminosity calibration from elastic scattering*, *ATL-LUM-PUB-2007-001*.
- [128] V. Cindro et al., *The ATLAS Beam Conditions Monitor*, *JINST* **3** (2008) P02004.
- [129] *ATLAS public luminosity results*, <https://twiki.cern.ch/twiki/bin/view/AtlasPublic/LuminosityPublicResults>.
- [130] *COMA Period Description Report*, https://atlas-tagservices.cern.ch/tagservices/RunBrowser/rBR_Period_Report.php.
- [131] M. Dobbs and J. Beck Hanser, *The HepMC C++ Monte Carlo event record for High Energy Physics*, *Comput. Phys. Commun.* **134** (2001) 41 – 46.
- [132] V. Gribov and L. Lipatov, *$e^+ e^-$ pair annihilation and deep inelastic $e p$ scattering in perturbation theory*, *Sov. J. Nucl. Phys.* **15** (1972) 675–684.
- [133] Y. L. Dokshitzer, *Calculation of the structure functions for deep inelastic scattering and $e^+ e^-$ annihilation by perturbation theory in quantum chromodynamics (in Russian)*, *Sov. Phys. JETP* **46** (1977) 641–653.

- [134] G. Altarelli and G. Parisi, *Asymptotic Freedom in Parton Language*, *Nucl. Phys.* **B126** (1977) 298.
- [135] ATLAS Collaboration, *The ATLAS Simulation Infrastructure*, *Eur. Phys. J.* **C 70** (2010) 823 – 874, [arXiv:1005.4568 \[physics.ins-det\]](#).
- [136] T. Sjöstrand, *Monte Carlo Generators*, [arXiv:0611247 \[hep-ph\]](#).
- [137] G. Soyez, *The SISCone and anti-kt jet algorithms*, [arXiv:0807.0021 \[hep-ph\]](#).
- [138] Y. L. Dokshitzer, G. D. Leder, S. Moretti, and B. R. Webber, *Better Jet Clustering Algorithms*, *JHEP* **9708** (1997) 001, [arXiv:9707323 \[hep-ph\]](#).
- [139] M. Wobisch and T. Wengler, *Hadronization Corrections to Jet Cross Sections in Deep-Inelastic Scattering*, [arXiv:9907280 \[hep-ph\]](#).
- [140] S. D. D. Ellis and D. E. Soper, *Longitudinally invariant K_t clustering algorithms for hadron hadron collisions*, *Nucl. Phys.* **B406** (1993) 187–224.
- [141] S. D. D. Ellis and D. E. Soper, *Successive Combination Jet Algorithm For Hadron Collisions*, *Phys. Rev.* **D48** (1993) 3160–3166, [arXiv:9305266 \[hep-ph\]](#).
- [142] V. Sudakov, *Vertex parts at very high energies in quantum electrodynamics*, *Sov. Phys. JETP* **3** (1956) 67–71.
- [143] S. Catani, F. Krauss, R. Kuhn, and B. R. Webber, *QCD Matrix Elements + Parton Showers*, *JHEP* **0111** (2001) 063, [arXiv:0109231 \[hep-ph\]](#).
- [144] F. Krauss, *Matrix Elements and Parton Showers in Hadronic Interactions*, *JHEP* **0208** (2002) 015, [arXiv:0205283 \[hep-ph\]](#).
- [145] S. Hoeche, F. Krauss, S. Schumann, and F. Siegert, *QCD matrix elements and truncated showers*, *JHEP* **0905** (2009) 053, [arXiv:0903.1219 \[hep-ph\]](#).
- [146] T. Gleisberg et al., *Event generation with SHERPA 1.1*, *JHEP* **02** (2009) 007, [arXiv:0811.4622 \[hep-ph\]](#).
- [147] T. Sjöstrand, S. Mrenna, and P. Skands, *PYTHIA 6.4 physics and manual*, *JHEP* **05** (2006) 026, [arXiv:0603175 \[hep-ph\]](#).
- [148] J. M. Butterworth, J. R. Forshaw, and M. H. Seymour, *Multiparton interactions in photoproduction at HERA*, *Z. Phys.* **C72** (1996) 637–646, [arXiv:9601371 \[hep-ph\]](#).
- [149] N. Davidson, G. Nanava, T. Przedzinski, E. Richter-Was, and Z. Was, *Universal Interface of TAUOLA Technical and Physics Documentation*, *Comput. Phys. Commun.* **183** (2012) 821–843, [arXiv:1002.0543 \[hep-ph\]](#).
- [150] P. Golonka and Z. Was, *PHOTOS Monte Carlo: A Precision tool for QED corrections in Z and W decays*, *Eur. Phys. J.* **C45** (2006) 97–107, [arXiv:0506026 \[hep-ph\]](#).
- [151] M. Schoenherr and F. Krauss, *Soft Photon Radiation in Particle Decays in SHERPA*, *JHEP* **0812** (2008) 018, [arXiv:0810.5071 \[hep-ph\]](#).
- [152] The ATLAS Computing Group, *ATLAS Computing*, [ATLAS-TDR-017](#), CERN-LHCC-2005-022, 2005.
- [153] S. Agostinelli [GEANT4 Collaboration], *GEANT4: A simulation toolkit*, *Nucl. Instr. and Meth. A* **506** (2003) 250.

- [154] E. Richter-Was, D. Froidevaux, and L. Poggioli, *ATLFAST 2.0 a fast simulation package for ATLAS*, [ATL-PHYS-98-131](#).
- [155] M. Duehrssen, *Study of Higgs bosons in the WW final state and development of a fast calorimeter simulation for the ATLAS experiment*. PhD thesis, University Freiburg, 2009.
- [156] ATLAS Collaboration, *Expected Performance of the ATLAS Experiment: Detector, Trigger and Physics*. CERN, Geneva, 2008. [arXiv:0901.0512](#). CERN-OPEN-2008-020.
- [157] V. Kartvelishvili, *Electron bremsstrahlung recovery in ATLAS*, [Nucl. Phys. Proc. Suppl. **172** \(2007\) 208–211](#).
- [158] R. Frühwirth, *A Gaussian-mixture approximation of the Bethe-Heitler model of electron energy loss by bremsstrahlung*, [Comp. Phys. Comm. **154** \(2003\) 131](#).
- [159] W. Lampl, S. Laplace, D. Lelas, P. Loch, H. Ma, S. Menke, S. Rajagopalan, D. Rousseau, S. Snyder, and G. Unal, *Calorimeter Clustering Algorithms: Description and Performance*, [ATL-LARG-PUB-2008-002](#).
- [160] T. Barillari et al., *Local Hadronic Calibration*, [ATL-LARG-PUB-2009-001](#).
- [161] *ATLAS egamma tracking in Release 17.2*, <https://twiki.cern.ch/twiki/bin/viewauth/AtlasProtected/EgammaTracking172>, 2012.
- [162] *ATLAS egamma performance IsEMIdentification*, <https://twiki.cern.ch/twiki/bin/viewauth/AtlasProtected/IsEMIdentification>, 2012.
- [163] *ATLAS egamma performance TechnicalitiesForMedium1*, <https://twiki.cern.ch/twiki/bin/viewauth/AtlasProtected/TechnicalitiesForMedium1>, 2012. Loose++ identification description.
- [164] *ATLAS Muon Combined Performance Guidelines for Analyses of 2012 Data*, <https://twiki.cern.ch/twiki/bin/viewauth/AtlasProtected/MCPAnalysisGuidelinesData2012>, 2012.
- [165] M. Cacciari and G. P. Salam, *Dispelling the N^3 myth for the K_t jet-finder*, [Phys. Lett. **B 641** \(2006\) 57 – 61](#), [arXiv:0512210 \[hep-ph\]](#).
- [166] M. Cacciari, G. P. Salam, and G. Soyez, *The anti- k_t jet clustering algorithm*, [JHEP **04** \(2008\) 063](#), [arXiv:0802.1189 \[hep-ph\]](#).
- [167] G. P. Salam, *Towards Jetography*, [Eur. Phys. J. **C 67** \(2010\) 637 – 686](#), [arXiv:0906.1833 \[hep-ph\]](#).
- [168] D. W. Miller, A. Schwartzman, and D. Su, *Jet-Vertex Association Algorithm*, [ATL-COM-PHYS-2008-008](#).
- [169] D. W. Miller, A. Schwartzman, and D. Su, *Measurement of Hadronic Event Shapes and Jet Substructure in Proton-Proton Collisions at 7.0 TeV Center-of-Mass Energy with the ATLAS Detector at the Large Hadron Collider*. PhD thesis, Stanford U., Menlo Park, CA, 2011.
- [170] ATLAS Collaboration, *Performance of Missing Transverse Momentum Reconstruction in ATLAS with 2011 Proton-Proton Collisions at $\sqrt{s} = 7$ TeV*, [ATLAS-CONF-2012-101](#).
- [171] ATLAS Collaboration, *Performance of Missing Transverse Momentum Reconstruction in Proton-Proton Collisions at 7 TeV with ATLAS*, [Eur. Phys. J. **C72** \(2012\) 1844](#), [arXiv:1108.5602 \[hep-ex\]](#).

- [172] ATLAS Collaboration, *Z $\rightarrow \tau\tau$ cross section measurement in pp collisions at 7 TeV with the ATLAS experiment*, [ATLAS-CONF-2012-006](#).
- [173] C. M. Bishop, *Pattern Recognition and Machine Learning*. Springer, 2007.
- [174] ATLAS Collaboration, *Performance of the Reconstruction and Identification of Hadronic Tau Decays in ATLAS with 2011 Data*, [ATLAS-CONF-2012-142](#).
- [175] ATLAS Collaboration, *Measurement of the jet fragmentation function and transverse profile in proton-proton collisions at a center-of-mass energy of 7 TeV with the ATLAS detector*, [Eur.Phys.J.C. 71 \(2011\) 1795](#), [arXiv:1109.5816 \[hep-ex\]](#).
- [176] ATLAS Collaboration, *Performance of the ATLAS Inner Detector Track and Vertex Reconstruction in the High Pile-Up LHC Environment*, [ATLAS-CONF-2012-042](#), 2012.
- [177] M. Trottier-McDonald, *A Cluster-based Approach to Reconstructing π^0 s in τ Decays*, Talk given at the Tau Substructure mini-workshop, 2012.
<https://indico.cern.ch/getFile.py/access?contribId=2&resId=0&materialId=slides&confId=>
- [178] ATLAS Collaboration, *Determination of the tau energy scale and the associated systematic uncertainty in proton-proton collisions at $\sqrt{s} = 8$ TeV with the ATLAS detector at the LHC in 2012*, [ATLAS-CONF-2013-044](#).
- [179] E. Khramov et al., *Study of the Response of the Hadronic Barrel Calorimeter in the ATLAS Combined Test-beam to Pions of Energies from 20 to 350 GeV for Beam Impact Points from 0.2 to 0.65*, [ATL-TILECAL-PUB-2009-007](#).
- [180] G. Folger and J. P. Wellisch, *String parton models in Geant4*, [arXiv:0306007 \[nucl-th\]](#).
- [181] H. W. Bertini, *Intranuclear-cascade calculation of the secondary nucleon spectra from nucleon-nucleus interactions in the energy range 340 to 2900 MeV and comparisons with experiment*, *Phys. Rev.* **188** (1969) 1711–1730.
- [182] M. Blann, B. L. Berman, and T. T. Komoto, *Precompound-model analysis of photonuclear reactions*, *Phys. Rev. C* **28** (1983) no. 6, 2286–2298.
- [183] B. Andersson, G. Gustafson, and B. Nilsson-Almqvist, *A model for low-pT hadronic reactions with generalizations to hadron-nucleus and nucleus-nucleus collisions*, *Nucl. Phys. B* **281** (1987) no. 1-2, 289 – 309.
- [184] ATLAS Collaboration, *Measurement of the Mis-identification Probability of τ Leptons from QCD Jets and from Electrons*, [ATLAS-CONF-2011-113](#).
- [185] A. Hoecker et al., *TMVA - Toolkit for Multivariate Data Analysis*, ArXiv Physics e-prints (2007) , [arXiv:0703039 \[physics\]](#).
- [186] Y. Freund and R. E. Schapire, *A Decision-Theoretic Generalization of On-Line Learning and an Application to Boosting*, *Journal of Computer and System Sciences* **55** (1997) 119 – 139.
- [187] ATLAS Collaboration, *Identification of Hadronic Decays of Tau Leptons in 2012 Data with the ATLAS Detector*, [ATLAS-CONF-2013-064](#).
- [188] *ATLAS tau systematics prescriptions for winter 2013*,
<https://twiki.cern.ch/twiki/bin/view/AtlasProtected/TauSystematicsWinterConf2013>, 2013.
- [189] ATLAS Collaboration, *Expected electron performance in the ATLAS experiment*, [ATL-PHYS-PUB-2011-006](#).

- [190] W. Davey, M. Morgenstern, P. Radloff, M. Shamim, A. Tanasijczuk, S. Tsuno, and P. Urquijo, *Tau Trigger Group Performance Plot*, [ATL-COM-DAQ-2012-035](#).
- [191] ATLAS, *Public Tau Trigger Plots for Collision Data*, <https://twiki.cern.ch/twiki/bin/view/AtlasPublic/TauTriggerPublicResults>.
- [192] ATLAS Collaboration, *Search for the Standard Model Higgs boson $H \rightarrow \tau\tau$ decays with the ATLAS detector*, [ATL-COM-PHYS-2013-722](#).
- [193] P. Rados, *Tau Trigger Efficiency Measurement from $Z \rightarrow \tau_{\text{had}}\tau_{\mu}$ Events*, Talk given in informal Tau Trigger Slice meeting, 2013.
<https://indico.cern.ch/getFile.py/access?contribId=6&resId=0&materialId=slides&confId=7>
- [194] P. Rados, *2013 Tau Trigger Scale Factors ($Z \rightarrow \tau\tau \rightarrow \mu\tau_{\text{had}}$ tag-and-probe method) Emulated Trigger Menu Reference Slides*, Talk given in informal Tau Trigger Slice meeting, 2013.
<https://indico.cern.ch/getFile.py/access?contribId=3&resId=2&materialId=slides&confId=7>
- [195] T. Sjöstrand, S. Mrenna, and P. Skands, *A Brief Introduction to Pythia 8.1*, [arXiv:0710.3820](#) [hep-ph].
- [196] R. Gavin, Y. Li, F. Petriello, and S. Quackenbush, *FEWZ 2.0: A code for hadronic Z production at next-to-next-to-leading order*, *Comput. Phys. Commun.* **182** (2011) 2388–2403, [arXiv:1011.3540](#) [hep-ph].
- [197] A. Martin, W. Stirling, R. Thorne, and G. Watt, *Parton distributions for the LHC*, *Eur. Phys. J.* **C63** (2009) 189–285, [arXiv:0901.0002](#) [hep-ph].
- [198] A. Martin, W. Stirling, R. Thorne, and G. Watt, *Uncertainties on α_S in global PDF analyses and implications for predicted hadronic cross sections*, *Eur. Phys. J.* **C64** (2009) 653–680, [arXiv:0905.3531](#) [hep-ph].
- [199] S. Frixione and B. R. Webber, *Matching NLO QCD computations and parton shower simulations*, *JHEP* **0206** (2002) 029, [arXiv:0204244](#) [hep-ph].
- [200] S. Frixione, E. Laenen, P. Motylinski, and B. R. Webber, *Single-top production in MC@NLO*, *JHEP* **03** (2006) 092, [arXiv:0512250](#) [hep-ph].
- [201] S. Frixione, E. Laenen, P. Motylinski, C. White, and B. R. Webber, *Single-top hadroproduction in association with a W boson*, *JHEP* **07** (2008) 029, [arXiv:0805.3067](#) [hep-ph].
- [202] G. Corcella et al., *HERWIG 6.5 release note*, [arXiv:0210213](#) [hep-ph].
- [203] H.-L. Lai et al., *New parton distributions for collider physics*, *Phys. Rev.* **D82** (2010) 074024, [arXiv:1007.2241](#) [hep-ph].
- [204] J. Gao, M. Guzzi, J. Huston, H.-L. Lai, Z. Li, P. Nadolsky, J. Pumplin, D. Stump, and C.-P. Yuan, *The CT10 NNLO Global Analysis of QCD*, [arXiv:1302.6246](#) [hep-ph].
- [205] ATLAS Collaboration, *New ATLAS event generator tunes to 2010 data*, Tech. Rep. [ATL-PHYS-PUB-2011-008](#).
- [206] M. Cacciari, M. Czakon, M. L. Mangano, A. Mitov, and P. Nason, *Top-pair production at hadron colliders with next-to-next-to-leading logarithmic soft-gluon resummation*, *Phys. Lett.* **B710** (2012) 612 – 622, [arXiv:1111.5869](#) [hep-ph].
- [207] P. Baernreuther, M. Czakon, and A. Mitov, *Percent level precision physics at the Tevatron: first genuine NNLO QCD corrections to $q\bar{q} \rightarrow t\bar{t} + X$* , *Phys. Rev. Lett.* **109** (2012) 132001, [arXiv:1204.5201](#) [hep-ph].

- [208] M. Czakon and A. Mitov, *NNLO corrections to top-pair production at hadron colliders: the all-fermionic scattering channels*, *JHEP* **1212** (2012) 054, [arXiv:1207.0236 \[hep-ph\]](#).
- [209] M. Czakon and A. Mitov, *NNLO corrections to top pair production at hadron colliders: the quark-gluon reaction*, *JHEP* **1301** (2013) 080, [arXiv:1210.6832 \[hep-ph\]](#).
- [210] M. Czakon, P. Fiedler, and A. Mitov, *The total top quark pair production cross-section at hadron colliders through $O(\alpha_s^4)$* , *Phys. Rev. Lett.* **110** (2013) 252004, [arXiv:1303.6254 \[hep-ph\]](#).
- [211] M. Czakon and A. Mitov, *Top++: a program for the calculation of the top-pair cross-section at hadron colliders*, [arXiv:1112.5675 \[hep-ph\]](#).
- [212] M. Botje et al., *The PDF4LHC Working Group Interim Recommendations*, [arXiv:1101.0538 \[hep-ph\]](#).
- [213] Ball, R. D. and others, *Parton distributions with LHC data*, *Nucl. Phys.* **B867** (2013) 244–289, [arXiv:1207.1303 \[hep-ph\]](#).
- [214] M. Aliev, H. Lacker, U. Langenfeld, S. Moch, P. Uwer, et al., *HATHOR: HAdronic Top and Heavy quarks crOss section calculatoR*, *Comput. Phys. Commun.* **182** (2011) 1034–1046, [arXiv:1007.1327 \[hep-ph\]](#).
- [215] ATLAS Collaboration, *Summary plots from the ATLAS Standard Model physics group*, <https://atlas.web.cern.ch/Atlas/GROUPS/PHYSICS/CombinedSummaryPlots/SM/>. Version of May, 8th, 2013.
- [216] N. Kidonakis, *Two-loop soft anomalous dimensions for single top quark associated production with a W- or H-*, *Phys. Rev.* **D82** (2010) 054018, [arXiv:1005.4451 \[hep-ph\]](#).
- [217] N. Kidonakis, *Next-to-next-to-leading-order collinear and soft gluon corrections for t-channel single top quark production*, *Phys. Rev.* **D83** (2011) 091503, [arXiv:1103.2792 \[hep-ph\]](#).
- [218] N. Kidonakis, *NNLL resummation for s-channel single top quark production*, *Phys. Rev.* **D81** (2010) 054028, [arXiv:1001.5034 \[hep-ph\]](#).
- [219] B. P. Kersevan and E. Richter-Was, *The Monte Carlo event generator AcerMC version 2.0 with interfaces to PYTHIA 6.2 and HERWIG 6.5*, [arXiv:0405247 \[hep-ph\]](#).
- [220] P. M. Nadolsky et al., *Implications of CTEQ global analysis for collider observables*, *Phys. Rev.* **D78** (2008) 013004, [arXiv:0802.0007 \[hep-ph\]](#).
- [221] ATLAS Collaboration, *Further ATLAS tunes of PYTHIA6 and Pythia 8*, [ATL-PHYS-PUB-2011-014](#).
- [222] J. Campbell and R. Ellis, *An update on vector boson pair production at hadron colliders*, *Phys. Rev.* **D60** (1999) 113006, [arXiv:9905386 \[hep-ph\]](#).
- [223] S. Alioli et al., *NLO Higgs boson production via gluon fusion matched with shower in POWHEG*, *JHEP* **0904** (2009) 002, [arXiv:0812.0578 \[hep-ph\]](#).
- [224] C. Oleari and L. Reina, *$W^\pm b\bar{b}$ production in POWHEG*, *JHEP* **1108** (2011) 061, [arXiv:1105.4488 \[hep-ph\]](#).
- [225] Data Preparation Group, *CheckListForPhysicsAnalysis*, <https://twiki.cern.ch/twiki/bin/viewauth/Atlas/DataPreparationCheckListForPhysicsAnalysis>.
- [226] ATLAS JetEtMiss Recommendations for how to clean jets in 2012 data, <https://twiki.cern.ch/twiki/bin/view/AtlasProtected/HowToCleanJets2012>, 2012.

- [227] ATLAS Detector, *TileTripReader*, <https://twiki.cern.ch/twiki/bin/viewauth/Atlas/TileTripReader>.
- [228] ATLAS Physics Analysis Tools, *PileupRewighting*, <https://twiki.cern.ch/twiki/bin/view/AtlasProtected/PileupRewighting>.
- [229] A. N. Kolmogorov, *Sulla Determinazione Empirica di una Legge di Distribuzione. (Italian) [On the empirical determination of a distribution law]*, Giornale dell'Istituto Italiano degli Attuari **4** (1933) 1–11.
- [230] N. V. Smirnov, *Ob uklonenijah empiričeskoj krivoj raspredelenija. (Russian). [On deviations from the empirical distribution curve]*, Recueil Mathématique (Matematičeskij Sbornik), N.S. **6** (1939) 3–26.
- [231] ATLAS Collaboration, *Search for Neutral MSSM Higgs Bosons $H \rightarrow \tau^+\tau^- \rightarrow \tau_h\tau_h + 2$ neutrinos with the ATLAS Detector in proton-proton collision at $\sqrt{s} = 7$ TeV with the ATLAS Experiment*, [ATL-COM-PHYS-2012-097](#).
- [232] O. Boeriu, W. Davey, S. Demers, J. Dingfelder, D. Duschinger, U. Klein, A. Leister, K. J. C. Leney, W. Mader, M. Morgenstern, R. Reece, F. Scutti, A. Straessner, A. Tuna, and H. H. Williams, *A search for high-mass ditau resonances decaying in the fully hadronic final state in pp collisions at $\sqrt{s} = 8$ TeV with the ATLAS detector*, [ATL-COM-PHYS-2013-125](#).
- [233] D. Duschinger, *Search for New Physics in Fully Hadronic Di-tau Final States with the ATLAS Detector*, [CERN-THESIS-2013-207](#).
- [234] W. Davey, J. Dingfelder, A. Florez, J. Glatzer, G. Palacino, R. Reece, A. Tuna, P. Wagner, and H. Williams, *A search for high-mass resonances decaying to tau+tau- in pp collisions at $\sqrt{s} = 7$ TeV with the ATLAS detector*, [ATL-COM-PHYS-2012-394](#).
- [235] R. Alon, L. Asquith, S. Baker, E. Bergeaas Kuutmann, B. Chapleau, S. Chekanov, A. R. Davison, E. Duchovni, T. Farooque, J. Ferrando, L. S. Gomez Fajardo, M. Karagoz, S. Livermore, A. Lewis, D. W. Miller, K. Moenig, E. Oliver, J. Proudfoot, C. Sandoval, A. Schwartzman, P. Sinervo, M. Villaplana, and M. Vos, *Backup Note for Jet Mass and Substructure in QCD Jets with the ATLAS Experiment*, [ATL-COM-PHYS-2011-1319](#).
- [236] M. Begel, A. Gaponenko, I. Hinchliffe, F. Paige, C. Ruwiedel, M. Shapiro, and S. Zenz, *A Study of Release 16 Tracking Performance in Jets Using 2010 Data*, [ATL-COM-INDET-2011-028](#).
- [237] T. Addy, *et al.*, *Search for high mass dilepton resonances in 5 fb^{-1} of pp collisions at $\sqrt{s} = 7$ TeV*, [ATL-COM-PHYS-2012-111](#).
- [238] ATLAS JetEtMiss Recommendations for 2012 data, <https://twiki.cern.ch/twiki/bin/viewauth/AtlasProtected/JetEtmissRecommendations2012>, 2012.
- [239] ATLAS Collaboration, *Jet energy scale and its systematic uncertainty in proton-proton collisions at $\sqrt{s} = 7$ TeV with ATLAS 2011 data*, [ATLAS-CONF-2013-004](#).
- [240] ATLAS JetEtMiss Recommendations for the analysis of 2012 data, <https://twiki.cern.ch/twiki/bin/view/AtlasProtected/JetEtmissDataAnalysisRecommendationSummer2010>, 2012.
- [241] ATLAS Collaboration, *Improved luminosity determination in pp collisions at $\sqrt{s} = 7$ TeV using the ATLAS detector at the LHC*, [arXiv:1302.4393 \[hep-ex\]](#).
- [242] ATLAS Standard Model Cross Section Recommendations for 7 TeV LHC Running, <https://svnweb.cern.ch/trac/atlasgrp/browser/Physics/StandardModel/xsectf/note/xsectf.pdf>, 2010.

- [243] ATLAS Collaboration, *Search for high-mass dilepton resonances in 21 fb⁻¹ of pp collisions at $\sqrt{s} = 8$ TeV*, [ATL-COM-PHYS-2013-087](#).
- [244] ATLAS Collaboration, *Search for the Standard Model Higgs boson in the $H \rightarrow \tau\tau$ decay mode with 4.7 fb⁻¹ of ATLAS data at 7 TeV*, [ATLAS-CONF-2012-014](#).
- [245] R. Hamberg, W. Van Neerven, and T. Matsuura, *A Complete calculation of the order α_s^2 correction to the Drell-Yan K factor*, [Nucl. Phys. B **359** \(1991\) 343 – 405](#).
- [246] ATLAS Collaboration, *Search for SM $H \rightarrow \tau^+\tau^- \rightarrow l\tau_{had}$ with the ATLAS Detector in 7 TeV Proton-Proton Collisions*, [ATLAS-COM-PHYS-2012-037](#).
- [247] S. Dittmaier, M. Krämer, and M. Spira, *Higgs Radiation off Bottom Quarks at the Tevatron and the LHC*, [Phys. Rev. **D70** \(2004\) 074010](#), [arXiv:0304035 \[hep-ph\]](#).
- [248] S. Dawson, C. B. Jackson, L. Reina, and D. Wackeroth, *Exclusive Higgs Boson Production with bottom quarks at Hadron Colliders*, [Phys. Rev. **D69** \(2004\) 074027](#), [arXiv:0311067 \[hep-ph\]](#).
- [249] D. Rainwater, M. Spira, and D. Zeppenfeld, *Higgs Boson Production at Hadron Colliders: Signal and Background Processes*, [arXiv:0203187 \[hep-ph\]](#).
- [250] T. Plehn, *Charged Higgs Boson Production in Bottom-Gluon Fusion*, [Phys. Rev. **D67** \(2003\) 014018](#), [arXiv:0206121 \[hep-ph\]](#).
- [251] F. Maltoni, Z. Sullivan, and S. Willenbrock, *Higgs-Boson Production via Bottom-Quark Fusion*, [Phys. Rev. **D67** \(2003\) 093005](#), [arXiv:0301033 \[hep-ph\]](#).
- [252] R. Harlander and W. Kilgore, *Higgs boson production in bottom quark fusion at next-to-next-to-leading order*, [Phys. Rev. **D68** \(2003\) 013001](#), [arXiv:0304035 \[hep-ph\]](#).
- [253] R. Harlander, M. Krämer, and M. Schumacher, *Bottom-quark associated Higgs-boson production: reconciling the four- and five-flavour scheme approach*, [arXiv:1112.3478 \[hep-ph\]](#).
- [254] LHC Higgs Cross Section Working Group, *Handbook of LHC Higgs Cross Sections: 2. Differential Distributions*, [arXiv:1201.3084 \[hep-ph\]](#).
- [255] LHC Higgs Cross Section Working Group, *Handbook of LHC Higgs Cross Sections: 1. Inclusive Observables*, [arXiv:1101.0593 \[hep-ph\]](#).
- [256] R. Harlander and W. Kilgore, *Next-to-Next-to-Leading Order Higgs Production at Hadron Colliders*, [Phys. Rev. Lett. **88** \(2002\) 201801](#), [arXiv:0201206 \[hep-ph\]](#).
- [257] M. Spira, *HIGLU: A Program for the Calculation of the Total Higgs Production Cross Section at Hadron Colliders via Gluon Fusion including QCD Corrections*, [arXiv:9510347 \[hep-ph\]](#).
- [258] LHC Higgs Cross Section Working Group, *Handbook of LHC Higgs Cross Sections: 3. Higgs Properties*, [arXiv:1307.1347 \[hep-ph\]](#).
- [259] R. Harlander, S. Liebler, and H. Mantler, *SusHi: A program for the calculation of Higgs production in gluon fusion and bottom-quark annihilation in the Standard Model and the MSSM*, [Comp. Phys. Comm. **184** \(2013\) 1605–1617](#), [arXiv:1212.3249 \[hep-ph\]](#).
- [260] R. D. Ball et al., *Impact of Heavy Quark Masses on Parton Distributions and LHC Phenomenology*, [Nucl. Phys. **B849** \(2011\) 296 – 363](#), [arXiv:1101.1300 \[hep-ph\]](#).

- [261] *Private communication during MC-physics meeting, Feb 28th, 2013.*
<https://indico.cern.ch/conferenceOtherViews.py?view=standard&confId=239089>.
- [262] A. Buckley et al., *Rivet user manual*, [arXiv:1003.0694 \[hep-ph\]](#).
- [263] J. Neyman and E. S. Pearson, *On the Problem of the Most Efficient Tests of Statistical Hypotheses*, *Philosophical Transactions of the Royal Society of London* **231** (1933) 289 – 337.
- [264] A.L. Read, *Presentation of search results: the CL_s technique*,
J. Phys. G: Nucl. Part. Phys. **28** (2002) 2693.
- [265] G. Cowan, *Statistical Data Analysis*. Oxford Science Publications, 1997.
- [266] K. Cranmer, G. Lewis, L. Moneta, A. Shibata, and W. Verkerke, *HistFactory: A tool for creating statistical models for use with RooFit and RooStats*, [CERN-OPEN-2012-016](#).
- [267] S. S. Wilks, *The Large-Sample Distribution of the Likelihood Ratio for Testing Composite Hypotheses*, *Annals Math. Statist.* **9** (1938) 60 – 62.
- [268] A. Wald, *Tests of Statistical Hypotheses Concerning Several Parameters When the Number of Observations is Large*, *Transactions of the American Mathematical Society* **54** (1943) 426 – 482.
- [269] CMS Collaboration, *Search for MSSM Neutral Higgs Bosons Decaying to Tau Pairs in pp Collisions*, [CMS-PAS-HIG-13-021](#), 2013.
- [270] ATLAS Collaboration, *A search for high-mass ditau resonances decaying in the fully hadronic final state in pp collisions at $\sqrt{s} = 8$ TeV with the ATLAS detector*, [ATLAS-CONF-2013-066](#).
- [271] ATLAS Collaboration, *Search for high-mass dilepton resonances in 20 fb^{-1} of pp collisions at $\sqrt{s} = 8$ TeV with the ATLAS experiment*, [ATLAS-CONF-2013-017](#), Mar, 2013.
- [272] CMS Collaboration, *Search for high mass resonances decaying into τ^- lepton pairs in pp collisions at $\sqrt{s} = 7$ TeV*, *Phys. Lett. B* **716** (2012) no. 1, 82 – 102,
[arXiv:1206.1725 \[hep-ex\]](#).

List of Figures

2.1	Higgs potential projected to $\phi_1 - \phi_2$ plane for negative μ^2	7
2.2	Observed local p_0 -value as a function of the SM Higgs mass	9
2.3	Observed best fit value of signal strength for individual Higgs decay channels from ATLAS and CMS	9
2.4	Evolution of the gauge coupling constants from the GUT to the weak scale	11
2.5	Examples for quantum loop corrections on the Higgs propagator entering the Higgs boson mass	12
2.6	Masses of the neutral MSSM Higgs bosons as a function of M_A for low and high $\tan\beta$ in the m_h^{\max} and $m_h^{\text{mod-}}$ scenario	17
2.7	Branching ratios of the neutral CP-odd Higgs boson	17
3.1	Parameter scans in the M_A - $\tan\beta$ -plane for the pMSSM	24
3.2	Exclusion limit of the MSSM Higgs production cross section from LEP	25
3.3	Exclusion limit of the CP-conserving m_h^{\max} scenario in the M_A - $\tan\beta$ -plane from LEP	25
3.4	95% C.L. exclusion limit on cross section times branching ratio for $\phi \rightarrow \tau\tau$ versus M_A and its interpretation within the m_h^{\max} scenario in the M_A - $\tan\beta$ -plane	26
3.5	95% C.L. exclusion limit on cross section times branching ratio for $\phi \rightarrow b\bar{b}$ versus M_A and its interpretation within the m_h^{\max} scenario in the M_A - $\tan\beta$ -plane	27
3.6	95% C.L. exclusion limit of $\phi \rightarrow \tau\tau$ interpreted in the m_h^{\max} benchmark scenario in the M_A - $\tan\beta$ -plane	28
3.7	95% C.L. exclusion limit on $\sigma_\phi \times \text{BR}(\phi \rightarrow \tau\tau/\mu\mu)$	28
3.8	95% C.L. exclusion limit on cross section times branching ratio for $\phi \rightarrow b\bar{b}$ versus M_ϕ and its interpretation within the m_h^{\max} scenario in the M_A - $\tan\beta$ -plane	29
3.9	Fit of the leptonic partial decay width of the Z boson and the leptonic mixing angle and comparison of predicted and measured SM observables obtained from global fits of electroweak data	30
3.10	95% C.L. upper bound on $\sigma(p\bar{p} \rightarrow Z') \times \text{BR}(Z' \rightarrow ee)$ depending on the Z' mass obtained by CDF and DØ	32
3.11	Upper bound on the production cross section of Z' bosons as a function of the Z' mass obtained in the di-muon analysis by the CDF collaboration and upper limits on production cross section times branching ratio for scalar and vector particle hypotheses in the di-tau channel	33
3.12	95% C.L. exclusion limit on Z' production cross section times branching ratio in the di-lepton analysis obtained by ATLAS and CMS	33
3.13	95% C.L. exclusion limit on Z' production cross section times branching ratio in the di-tau analysis obtained by ATLAS and CMS	34
4.1	Cross sections of Standard Model processes	38
4.2	Accelerator complex at CERN	39
4.3	Cut-away view of the ATLAS detector	40
4.4	ATLAS inner detector	41
4.5	Part view of the ATLAS inner detector	43
4.6	Sketch of the ATLAS calorimeter system	43
4.7	Schematic view of a barrel module of the electromagnetic calorimeter	44
4.8	Cumulative amount of material before and in the electromagnetic calorimeter	44
4.9	Cumulative amount of material in the hadronic calorimeter	46
4.10	Sketch of the ATLAS muon system	46
4.11	Placement of the forward detectors along the beam-line	47
4.12	Block diagram of the ATLAS trigger and data acquisition system	48
4.13	Total integrated luminosity delivered by the LHC and recorded by ATLAS over the 2012 data-taking period	48

4.14	Evolution of peak luminosity per fill and maximum number of interactions per bunch crossing during 2012 data-taking	49
5.1	Illustration of a hard scattering event taking place at a hadron collider	51
5.2	Work flow chart of the ATLAS reconstruction software chain	55
7.1	Pile-up dependence of track selection efficiency	63
7.2	Total tau energy scale uncertainty for 1-prong and multi-prong tau decays	65
7.3	Core energy fraction	67
7.4	Average distance of tracks to intermediate tau axis for reconstructed tau candidates . .	67
7.5	Momentum fraction of the highest- p_T track assigned to the tau candidate	68
7.6	Impact parameter significance of the highest- p_T track and number of tracks within the isolation annulus	69
7.7	Invariant mass of the track system and maximum distance of tracks associated to the tau candidate within $\Delta R < 0.2$ w.r.t. tau axis	70
7.8	Transverse flight path significance	70
7.9	Number of reconstructed neutral pions	71
7.10	Visible invariant mass of the track and neutral pion system	71
7.11	Ratio of the transverse momentum of the track and π^0 system w.r.t. the transverse momentum of the reconstructed tau candidate	72
7.12	Distribution of the LLH discriminator	73
7.13	Tau identification efficiency for one- and multi-prong tau candidates versus the visible p_T of the generated tau lepton for the LLH algorithm	74
7.14	Tau identification efficiency for one- and multi-prong tau candidates versus the average number of interactions per bunch crossing for the LLH algorithm	74
7.15	Tau mis-identification efficiency for one- and multi-prong tau candidates versus the p_T of the tau candidate for the LLH algorithm	75
7.16	Tau mis-identification efficiency for one- and multi-prong tau candidates versus the average number of interactions per bunch crossing for the LLH algorithm	76
7.17	Schematic view of a decision tree	76
7.18	Distribution of the BDT discriminator	77
7.19	Tau identification efficiency for one- and multi-prong tau candidates versus the visible p_T of the generated tau lepton for the BDT algorithm	77
7.20	Tau identification efficiency for one- and multi-prong tau candidates versus the average number of interactions per bunch crossing for the BDT algorithm	78
7.21	Tau mis-identification efficiency for one- and multi-prong tau candidates versus the p_T of the tau candidate for the BDT algorithm	78
7.22	Tau mis-identification efficiency for one- and multi-prong tau candidates versus the average number of interactions per bunch crossing for the BDT algorithm	79
7.23	Background rejection versus signal efficiency for the LLH and BDT tau identification algorithms for 1- and 3-prong tau candidates	80
7.24	Extended track distribution before applying the identification criterion and results of the template fit after applying jBDT medium identification for 1-prong probe taus . . .	81
7.25	Tau identification scale factors for 1-prong and 3-prong tau candidates derived from a $Z \rightarrow \tau_\mu \tau_{\text{had}}$ analysis	82
7.26	Background efficiency versus signal efficiency of the electron discrimination and electromagnetic energy fraction for taus and muons	83
7.27	Schematic view of tau trigger towers	85
7.28	Tau trigger efficiency for the 20 GeV tau trigger item at all stages of the trigger chain versus the number of reconstructed vertices	86
7.29	Core energy fraction for reconstructed 1-prong and 3-prong event filter tau candidates .	88
7.30	BDT and LLH scores for one- and multi-prong EF tau candidates	89

7.31	Fake rejection versus signal efficiency for the BDT- and LLH-based tau trigger identification algorithms	90
7.32	BDT-based tau trigger efficiency	90
7.33	Mis-identification efficiency of the BDT-based tau trigger identification	91
7.34	Tau trigger efficiency for EF_tau38T_medium1 derived from a $Z/\gamma^* \rightarrow \tau\tau$ tag-and-probe measurement	92
8.1	Examples of leading order Feynman diagrams of Z/γ^* +jets production	93
8.2	NNLO correction factors for $Z/\gamma^* \rightarrow \tau\tau$ MC simulation samples as a function of the generated invariant di-tau mass	94
8.3	Leading order Feynman diagrams of QCD di-jet production	95
8.4	Examples of leading and next-to-leading order Feynman diagrams of $W(\rightarrow \tau\nu)$ +jets production	95
8.5	Leading order Feynman diagrams of $t\bar{t}$ production	96
8.6	Summary of total production cross section measurements of various Standard Model processes compared to the corresponding theoretical expectations	97
8.7	Leading order Feynman diagrams of single top-quark production	97
8.8	NNLO correction factors for $Z/\gamma^* \rightarrow \ell\ell$ MC simulation samples as a function of the generated invariant di-lepton mass	98
9.1	Average number of interactions per bunch crossing	100
9.2	BDT discriminator at Event Filter	102
9.3	Angular distance between the two selected tau candidates after event cleaning and light lepton veto	103
10.1	Tau identification jBDT scores of the leading and sub-leading tau candidate	107
10.2	Fake-factors measured in a di-jet tag-and-probe style analysis versus the probe jet p_T for various triggers	108
10.3	Fake-factors measured in a di-jet tag-and-probe style analysis versus the probe jet p_T for various jet multiplicities	110
10.4	Fake-factors measured in a di-jet tag-and-probe style analysis versus the probe jet p_T for various jBDT thresholds	110
10.5	Fake-factors measured in a di-jet tag-and-probe style analysis for 1-prong and 3-prong probe jets versus the probe jet p_T	111
10.6	Kinematic distributions of the leading and sub-leading tau candidates in the same-sign control region	113
10.7	Track multiplicity distributions for the leading and sub-leading tau candidates in the same-sign control region	114
10.8	Key event distributions in the same-sign control region	114
10.9	Total transverse mass and visible mass distributions in the same-sign control region	115
10.10	Tau identification jBDT scores of the sub-leading tau candidate	116
10.11	Shape comparison of key kinematic variables of the two selected τ_{had} candidates measured in opposite- and same-sign data samples	117
10.12	Shape comparison of key event variables measured in opposite- and same-sign data samples	118
10.13	Total transverse mass distribution in the low- E_T^{miss} control region for opposite- and same-sign events	119
10.14	Kinematic distributions of the leading and sub-leading tau candidates in the fail-ID control region	121
10.15	Track multiplicity distributions for the leading and sub-leading tau candidates in the fail-ID control region	122
10.16	Key event distributions in the fail-ID control region	122
10.17	Total transverse mass and visible mass distributions in the fail-ID control region	123

10.18	Tau identification fake-rate for the loose jBDT tau identification working point measured in $W(\rightarrow \tau\nu)$ +jets MC and data events	124
10.19	$\sum_{\ell=\mu,\tau} \cos \Delta\phi(\ell, E_T^{\text{miss}})$ distribution in the $W(\rightarrow \mu\nu)$ +jets control region	126
10.20	Tau mis-identification efficiency measured in $W(\rightarrow \mu\nu)$ +jets data events	127
10.21	Combined tau trigger and identification fake-rate measured in $W(\rightarrow \mu\nu)$ +jets data events	128
10.22	Quark fraction of fake taus	129
10.23	Kinematic distributions of the leading and sub-leading tau candidates in the $Z/\gamma^* \rightarrow \tau\tau$ control region	132
10.24	Track multiplicity distributions for the leading and sub-leading tau candidates in the $Z/\gamma^* \rightarrow \tau\tau$ control region	133
10.25	Key event distributions in the $Z/\gamma^* \rightarrow \tau\tau$ control region	133
10.26	Total transverse mass and visible mass distributions in the $Z/\gamma^* \rightarrow \tau\tau$ control region	134
11.1	Tau identification efficiency for the loose jBDT working point for 1- and 3-prong tau candidates	136
11.2	Distribution of polar angle of the probe jet in the di-jet selection	137
11.3	Tau mis-identification efficiency for 1- and 3-prong tau candidates	138
11.4	Fraction of generated 3-prong tau decays reconstructed as 2-, 3- or 4-prong tau candidate	138
11.5	Fraction of charge flipped tau candidates	140
11.6	Tau-ID fake-factors derived in opposite- and same-sign events	141
11.7	QCD transfer factor as a function of the total transverse mass determined in the low- E_T^{miss} and fail-ID control sample	142
12.1	Examples of tree-level Feynman diagrams for neutral Higgs boson production in association with b-quarks	145
12.2	Total cross section of Higgs production in association with b-quarks in the m_h^{max} scenario	146
12.3	Higgs production cross section times branching ratio for Higgs production in association with b-quarks in the m_h^{max} scenario	147
12.4	Generated invariant di-tau mass and total decay width of heavy neutral Higgs bosons	148
12.5	Examples of Feynman diagrams of MSSM Higgs production via gluon-gluon fusion	148
12.6	Total cross section of Higgs production via gluon-gluon fusion in the m_h^{max} scenario	149
12.7	Higgs production cross section times branching ratio for Higgs production via gluon-gluon fusion in the m_h^{max} scenario	149
12.8	Trigger efficiency for the EF_tau125_medium1 tau trigger	150
12.9	Cut acceptance efficiency versus the tested Higgs mass hypothesis for the STT and DTT selection	153
12.10	Kinematic distributions of the leading and sub-leading tau candidates in the STT signal region	159
12.11	Track multiplicity distributions for the leading and sub-leading tau candidates in the STT signal region	160
12.12	Key event distributions in the STT signal region	160
12.13	Kinematic distributions of the leading and sub-leading tau candidates in the DTT signal region	161
12.14	Track multiplicity distributions for the leading and sub-leading tau candidates in the DTT signal region	162
12.15	Key event distributions in the DTT signal region	162
12.16	Total transverse mass distribution in the signal regions	163
12.17	Illustration to support the CL _s method	165
12.18	Comparison of the shapes of the m_T^{tot} distribution	170
12.19	Negative log-likelihood values obtained from an unconditional fit	172
12.20	Pull distributions of nuisance parameters obtained from pseudo data	173
12.21	Summary of mean and variance of pull distributions of each nuisance parameter obtained from pseudo data	174

12.22	Expected and observed 95% C.L. exclusion limit on $\tan\beta$ as a function of the Higgs mass assuming the m_h^{\max} benchmark scenario	175
12.23	Expected and observed 95% C.L. exclusion limit on $\tan\beta$ as a function of the Higgs mass assuming the $m_h^{\text{mod}+}$ and $m_h^{\text{mod}-}$ benchmark scenario	176
12.24	Upper limit on production cross section times branching ratio for neutral Higgs bosons	177
12.25	Local p_0 -value versus M_A in the m_h^{\max} scenario	179
12.26	95% C.L. exclusion limit on $\tan\beta$ as a function of the Higgs mass assuming the m_h^{\max} benchmark scenario obtained by the CMS collaboration and the presented analysis . . .	180
13.1	Event weights applied to reweight $Z/\gamma^* \rightarrow \tau\tau$ MC to a Z' signal and generated invariant di-tau mass distribution	184
13.2	Generated invariant di-tau mass in $Z' \rightarrow \tau\tau$ events generated by PYTHIA and obtained from reweighting of $Z/\gamma^* \rightarrow \tau\tau$ events	184
13.3	Generated p_T distribution of the leading and sub-leading tau lepton in $Z' \rightarrow \tau\tau$ events generated by PYTHIA and obtained from reweighting of $Z/\gamma^* \rightarrow \tau\tau$ events	185
13.4	Generated visible p_T distribution of the leading and sub-leading tau lepton in $Z' \rightarrow \tau\tau$ events generated by PYTHIA and obtained from reweighting of $Z/\gamma^* \rightarrow \tau\tau$ events . . .	185
13.5	Reconstructed p_T distribution of the leading and sub-leading tau lepton in $Z' \rightarrow \tau\tau$ events generated by PYTHIA and obtained from reweighting of $Z/\gamma^* \rightarrow \tau\tau$ events . . .	186
13.6	Obtained exclusion limit on the signal strength parameter for various thresholds on m_T^{tot} as a function of the tested Z' mass	187
13.7	Total transverse mass distribution after the full Z' event selection	188
13.8	95% credibility level on the cross section times branching ratio as a function of the Z' boson mass	191
B.1	Tau identification variables for one-prong tau candidates used by the multivariate EF trigger algorithms	199
B.2	Tau identification variables for multi-prong tau candidates used by the multivariate EF trigger algorithms	200
D.1	Higgs production cross section times branching ratio for Higgs production in the $m_h^{\text{mod}-}$ scenario	207
D.2	Higgs production cross section times branching ratio for Higgs production in the $m_h^{\text{mod}+}$ scenario	217
D.3	Pull distributions of nuisance parameters obtained from pseudo data	218
D.4	Pull distributions of nuisance parameters obtained from pseudo data	219
D.5	Negative log-likelihood values obtained from a unconditional fit	220
D.6	Negative log-likelihood values obtained from a unconditional fit	221

List of Tables

2.1	Matter particle content of the Standard Model	4
2.2	Fundamental interactions described by the Standard Model and mediating gauge bosons	4
2.3	MSSM Higgs boson couplings to gauge bosons and fermions with respect to SM Higgs couplings	15
2.4	Parameter setting of various MSSM Higgs benchmark scenarios	16
3.1	Lower limits on the Z' mass at 95% confidence level for E_6 , LRM and SSM models derived from forward-backward asymmetry measurements at LEP	31
3.2	95% C.L. observed limits on $M_{Z'}$ for various Z' models obtained by CDF and DØ from searches in the di-lepton channels	31
3.3	95% C.L. observed limits on $M_{Z'}$ for various Z' models obtained by ATLAS and CMS from searches in the di-lepton channels	34
4.1	Summary of pp collision data-taking periods in 2012 by the ATLAS detector	49
7.1	Decay modes and branching fractions of hadronic tau decays	61
7.2	Summary of tau identification variables	79
7.3	Set of identification variables used by the LLH and BDT algorithms at event filter stage	87
9.1	Summary of data periods, trigger configurations, and the integrated luminosity used in the analyses	101
10.1	Event yields in the multijet enriched control region in the single-tau triggered category	106
10.2	Summary of triggers used for the di-jet tag-and-probe fake-factor measurement	109
10.3	Event yields in the same-sign multijet enriched control region in the single-tau triggered category	112
10.4	Expected event yields in the signal and control regions used to estimate the multijet background exploiting an ABCD method	120
10.5	Expected event yields in the fail tau identification control regions	120
10.6	Number of events passing the $W(\rightarrow \mu\nu)$ +jets selection criteria	125
10.7	Expected and observed event yields in the $Z/\gamma^* \rightarrow \tau\tau$ control sample	131
11.1	Summary of simulated MC di-jet events	136
11.2	Expected and observed event yields in the opposite- and same-sign control samples used to derive the R_{qcd} transfer factor	142
11.3	Uncertainties on the cross section for all MC background samples	143
12.1	Expected event yields for SM backgrounds and Higgs signal for $m_A = 400$ GeV and $\tan\beta = 40$ for the STT selection	151
12.2	Expected signal event yields in the STT category for Higgs bosons produced in association with b-quarks	152
12.3	Expected signal event yields in the STT category for Higgs bosons produced via gluon-gluon fusion	152
12.4	Expected event yields for SM backgrounds and Higgs signal for $m_A = 200$ GeV and $\tan\beta = 15$ for the DTT selection	154
12.5	Expected signal event yields in the DTT category for Higgs bosons produced in association with b-quarks	155
12.6	Expected signal event yields in the DTT category for Higgs bosons produced via gluon-gluon fusion	155
12.7	Summary of PDF sets used to estimate the acceptance uncertainty	156
12.8	Systematic uncertainties arising from acceptance uncertainties estimated from altered generator configuration for various processes	157
12.9	Summary of detector and theory related systematic uncertainties in the STT category	158
12.10	Summary of detector and theory related systematic uncertainties in the DTT category	158
12.11	KS-values for all systematic uncertainties obtained from a compatibility test of the normalised $m_{\text{T}}^{\text{tot}}$ shape w.r.t. the nominal setup in the STT channel	169
12.12	Summary of nuisance parameters assigned to systematic uncertainties	169

12.13	Expected and observed 95% C.L. excluded $\tan\beta$ in the m_h^{\max} scenario	175
12.14	Expected and observed 95% C.L. excluded $\tan\beta$ in the $m_h^{\text{mod}+}$ scenario	176
12.15	Expected and observed 95% C.L. excluded $\tan\beta$ in the $m_h^{\text{mod}-}$ scenario	177
12.16	Numerical values of expected and observed 95% C.L. upper limits on $\sigma(pp \rightarrow \phi) \times$ $BR(\phi \rightarrow \tau\tau)$ for Higgs production in association with b-quarks	178
12.17	Numerical values of expected and observed 95% C.L. upper limits on $\sigma(pp \rightarrow \phi) \times$ $BR(\phi \rightarrow \tau\tau)$ for Higgs production via gluon-gluon fusion	179
13.1	Mass dependent lower thresholds on m_T^{tot}	186
13.2	Expected and observed event yields after various selection criteria in the Z' event selection	188
13.3	Summary of total expected event yields including statistical uncertainty and detector and theory related systematic uncertainties for $M_{Z'} = 1750$ GeV	189
C.1	Signal MC samples for b-associated MSSM Higgs production	201
C.2	Signal MC samples for gluon-gluon fusion MSSM Higgs production	202
C.3	Background MC samples: Z +jets samples	203
C.4	Background MC samples: W +jets samples	204
C.5	Background MC samples: $t\bar{t}$ and single top-quark samples	205
C.6	Background MC samples: Electroweak di-boson samples	205
D.1	Numerical values of Higgs production cross section for $\tan\beta = 5$ and $\tan\beta = 10$ in the m_h^{\max} scenario	208
D.2	Numerical values of Higgs production cross section for $\tan\beta = 20$ and $\tan\beta = 30$ in the m_h^{\max} scenario	209
D.3	Numerical values of Higgs production cross section for $\tan\beta = 40$ and $\tan\beta = 50$ in the m_h^{\max} scenario	210
D.4	Numerical values of Higgs production cross section for $\tan\beta = 5$ and $\tan\beta = 10$ in the $m_h^{\text{mod}-}$ scenario	211
D.5	Numerical values of Higgs production cross section for $\tan\beta = 20$ and $\tan\beta = 30$ in the $m_h^{\text{mod}-}$ scenario	212
D.6	Numerical values of Higgs production cross section for $\tan\beta = 40$ and $\tan\beta = 50$ in the $m_h^{\text{mod}-}$ scenario	213
D.7	Numerical values of Higgs production cross section for $\tan\beta = 5$ and $\tan\beta = 10$ in the $m_h^{\text{mod}+}$ scenario	214
D.8	Numerical values of Higgs production cross section for $\tan\beta = 20$ and $\tan\beta = 30$ in the $m_h^{\text{mod}+}$ scenario	215
D.9	Numerical values of Higgs production cross section for $\tan\beta = 40$ and $\tan\beta = 50$ in the $m_h^{\text{mod}+}$ scenario	216
E.1	MC samples for $Z' \rightarrow \tau\tau$ production.	223
E.2	Summary of total expected event yields including statistical uncertainty and detector and theory related systematic uncertainties for $M_{Z'} = 500$ GeV	223
E.3	Summary of total expected event yields including statistical uncertainty and detector and theory related systematic uncertainties for $M_{Z'} = 625$ GeV	224
E.4	Summary of total expected event yields including statistical uncertainty and detector and theory related systematic uncertainties for $M_{Z'} = 750$ GeV	224
E.5	Summary of total expected event yields including statistical uncertainty and detector and theory related systematic uncertainties for $M_{Z'} = 875$ GeV	225
E.6	Summary of total expected event yields including statistical uncertainty and detector and theory related systematic uncertainties for $M_{Z'} = 1000$ GeV	225
E.7	Summary of total expected event yields including statistical uncertainty and detector and theory related systematic uncertainties for $M_{Z'} = 1125$ GeV	226
E.8	Summary of total expected event yields including statistical uncertainty and detector and theory related systematic uncertainties for $M_{Z'} = 1250$ GeV	226

E.9	Summary of total expected event yields including statistical uncertainty and detector and theory related systematic uncertainties for $M_{Z'} = 1375$ GeV	227
E.10	Summary of total expected event yields including statistical uncertainty and detector and theory related systematic uncertainties for $M_{Z'} = 1500$ GeV	227
E.11	Summary of total expected event yields including statistical uncertainty and detector and theory related systematic uncertainties for $M_{Z'} = 1625$ GeV	228
E.12	Summary of total expected event yields including statistical uncertainty and detector and theory related systematic uncertainties for $M_{Z'} = 1875$ GeV	228
E.13	Summary of total expected event yields including statistical uncertainty and detector and theory related systematic uncertainties for $M_{Z'} = 2000$ GeV	229
E.14	Summary of total expected event yields including statistical uncertainty and detector and theory related systematic uncertainties for $M_{Z'} = 2125$ GeV	229

Acknowledgements

Amazing three years have passed in which I learnt so many new skills and had the opportunity to meet numerous fantastic people without whom this thesis would not have been achievable and I would like to spend the last words in honour of them.

First, I would like to thank my Doktorvater Arno Straessner who has allowed me to join his group and gave me the freedom to develop my interests. You always had an open door for discussions and guidance. It was a pleasure to work with you and I will always be grateful that you gave me this chance. I would like to further thank the head of our department, Michael Kobel, who always supported my ideas and interests. Thanks also to our IKTP team with whom I had many interesting and inspiring discussions. Many thanks in particular to Wolfgang Mader, Christian Gumpert, Peter Steinbach, Thomas Göpfert and Felix Friedrich. I would like to take the opportunity to express my gratitude to Christian Rudolph and Patrick Czodrowski with whom I had the chance not only to work together and share ideas, but also had a lot of fun during our coffee breaks, soccer competitions and all the other great events. Big thanks to Konrad "the famous" Jende with whom I had the honour to stay at CERN and having an awesome summer with many football matches and barbecues. It was a great time there. A special thank to all those who supported me while writing this thesis. Your useful comments and discussions helped a lot improving the quality of this thesis. Thanks to Arno Straesser, Christian Rudolph, Patrick Czodrowski, Anne Pfost, Alexander Voigt, Felix Friedrich and Frank Siegert. I further like to thank the Graduiertenkolleg, for their support in the past three years, which allowed me to attend many very interesting conferences. Special thanks to Martin zur Nedden for sharing your thoughts with me and all the useful discussion we had during many occasions.

Special thanks to all the incredible tau folks, with whom I had the pleasure to spend a lot of the past few years. It's impossible to name all of them, but I did like to take the opportunity to thank in particular Stan Lai, Stefania Xella, Martin Flechl, Soshi Tsuno, Will Davey, Elias Coniavitis, Ryan Reece, Alex Tuna, Dugon O'Neil, Noel Dawe and Felix Friedrich.

Many thanks also to all of those with whom I worked closely together in the trigger community, specially Mansoor Shamin, Cristobal Cuenca Almenar and Andres Tanasijczuk.

Thanks to the SM and BSM Higgs community with whom it was a pleasure to work with. Thanks to my former colleagues back in 2011, Julian Glatzer, Guilherme Hanninger, Sami Dhaliwal, Daniele Zanzi, Noel Dawe, Dugan O'Neil, KG Tan and Soshi Tsuno. Special thanks to my collaborators, John Keller, Matthew Beckingham, Wolfgang Mader, Lorenz Hauswald, Federico Scutti, Will Davey, Jürgen Kroseberg, Jochen Dingfelder, Felix Friedrich, Alessandro Manfredini, Stephen Sekula, Jianming Qian and especially Nikolaos Rompotis. Many thanks as well to our Editorial Board who helped to improve our analysis, Mogens Dam, Tony Liss, Keith Baker and Jaehoon Yu.

Thanks as well to the Z' and exotics team with whom I spent the last year and always had a lot of fun exchanging ideas. It was a great pleasure to work with you. Thanks to the analysis team, Dirk Duschinger, Kathrine Lenney, Ryan Reece, Alex Tuna, Matteo Volpi, Andrew Leister and Sarah Demers. A big thank to Will Davey. It was great to have someone like you to collaborate with.

Further, I would like to thank all my friends with whom I shared the past years in Dresden.

Finally, the biggest thank is awarded to my parents and my sister for their support during my whole life and particularly during the past few years. I'm very grateful for your belief in me and your encouragement.

Versicherung

Hiermit versichere ich, dass ich die vorliegende Arbeit ohne unzulässige Hilfe Dritter und ohne Benutzung anderer als der angegebenen Hilfsmittel angefertigt habe; die aus fremden Quellen direkt oder indirekt übernommenen Gedanken sind als solche kenntlich gemacht. Die Arbeit wurde bisher weder im Inland noch im Ausland in gleicher oder ähnlicher Form einer anderen Prüfungsbehörde vorgelegt.

Die vorliegende Dissertation wurde angefertigt unter der wissenschaftlichen Betreuung von Jun.-Prof. Dr. Arno Straessner (Institut für Kern- und Teilchenphysik, TU Dresden).

Es haben keine früheren erfolglosen Promotionsverfahren stattgefunden.

Hiermit erkenne ich die Promotionsordnung der Fakultät Mathematik und Naturwissenschaften der Technischen Universität Dresden vom 23.02.2011 an.

Marcus Matthias Morgenstern, Diplom-Physiker